Indonesian Journal of Chemistry
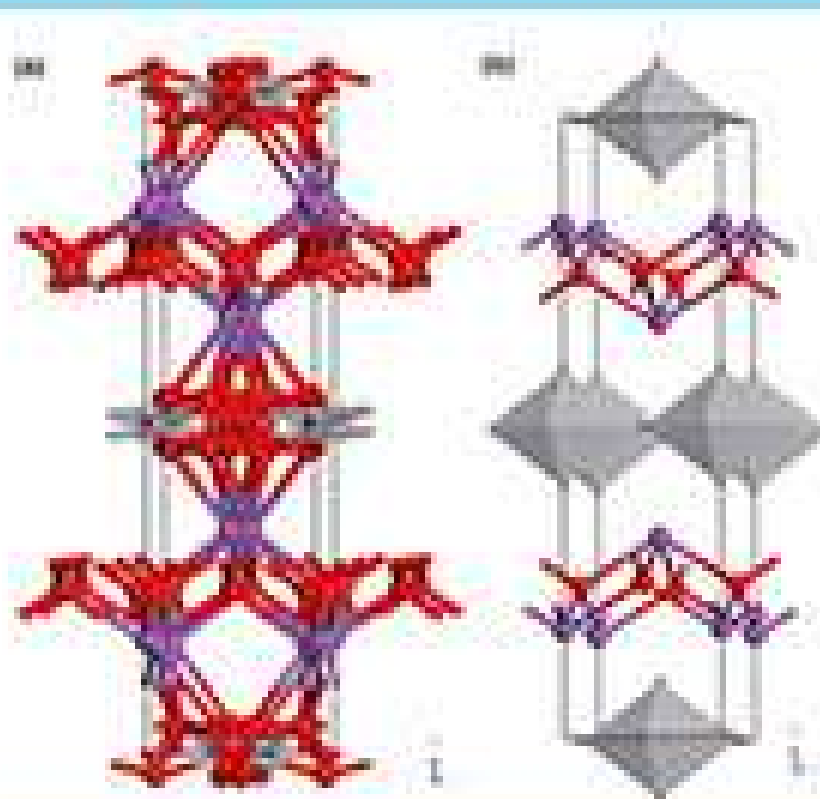
Levan Produced by the Halophilic Bacterium *Bacillus licheniformis* BK1 as a Nanoparticle for Protein Immobilization

Ira Oktavia, Aidah Nur Fithriah, Nur Umriani Permatasari, Enny Ratnaningsih, and Rukman Hertadi[*]

Biochemistry Research Division, Bandung Institute of Technology, Jl. Ganesa No. 10, Bandung 40132, Indonesia

* Corresponding author:

tel: +62-22-2502103
email: rukman@chem.itb.ac.id

Abstract: *This study examined the potential of levan from the halophilic bacterium* Bacillus licheniformis *BK1 as a nanoparticle system for protein immobilization. Levan produced by* B. licheniformis *BK1 was obtained by incubating the bacterium in the optimized Belghith medium, containing 15% (w/v) sucrose, 7.5% (w/v) NaCl and pH 8, in a rotary shaker at 150 rpm for 16 h, at 40 °C. The structure of the levan produced was verified by FTIR and NMR. It appeared that the levan had the same structure as that from* Erwinia herbicola. *The obtained levan was then used as a nanoparticle system to immobilize BSA and lysozyme proteins. The BSA-nanoparticle had a non-spherical shape with a surface charge of about -4.72 mV and a size distribution in the range of 83–298 nm. In contrast, the lysozyme-nanoparticle exhibited more spherical shapes with a surface charge of -2.57 mV and 206–285 nm size distribution. The efficiency of immobilization was about 74.26% and 81.77% for BSA and lysozyme, respectively. The study thus shows that levan produced by* B. licheniformis *BK1 can be used as a nanoparticle system for protein immobilization.*

Keywords: *levan; levansucrase; lysozyme-nanoparticle; bovine serum albumin-nanoparticle;* Bacillus licheniformis *BK1*

■ INTRODUCTION

Levan is a fructooligosaccharide (fructans) produced by certain types of microorganisms and plants. This biopolymer is a product of transfructosylation and polymerization reactions catalyzed by levansucrase with sucrose as a substrate. Levan is widely used in various industrial fields, such as medicine, food science, and cosmetics. In the medical field, levan has been used as an antitumor agent, an antioxidant, an anti-diabetic agent, an anti-inflammatory agent, and an immunity enhancer [1-5]. In the food science field, this biopolymer has been issued for prebiotics, cake stabilizers and low-calorie sweeteners [3]. In terms of cosmetics, it is used for skin whitening, skin moisturizers and hair care [6].

Levan application has now extended into the field of nanotechnology, where it is used as a material for constructing nanoparticles. Levan produced by *E. coli* carrying the recombinant levansucrase gene from *Bacillus licheniformis* has been utilized as a dietary supplement delivery nanoparticle, O-acetyl-α-tocopherol [7]. Levan produced by *Acetobacter xylinum* NCIM2526 has been used as a nanoparticle system for Au and Ag catalysts [8]. Furthermore, levan isolated from *Pseudomonas syringae* has been applied as Co, Fe and Se nanoparticles for dietary supplements. Meanwhile, levan produced by *B. polymyxa* PTCC1020 was employed as antibacterial nanocomposites and levan produced by *Acineto bacternectar* has been used to encapsulate 5-fluorouracil for cancer drug delivery systems [9-11].

The above-mentioned levan applications are mostly used for nano-carrier of small particles/molecules. In the previous study, *B. licheniformis* BK-AG21 was used as a levan producer. However, levan was mostly produced intracellularly instead of extracellular, since levansucrase that catalyzes the levan biosynthesis was not excreted. The advantage of using *B. licheniformis* BK1, is that the levan is produced extracellularly since the levansucrase produced by this bacterium is excreted. Therefore, levan purification becomes relatively easier. In this study, levan was applied to create a nanoparticle

for protein immobilization. BSA (Bovine Serum Albumin) and lysozyme were used as protein targets to be immobilized in the nanoparticles. In this study, the levan used was produced by a halophilic bacterium *Bacillus licheniformis* BK1 indigenous to a salty mud crater, Bledug Kuwu, Central Java, Indonesia. This study began with the optimization of levan production by *B. licheniformis* BK1 by modifying the production media and growth conditions. Furthermore, the structure of the resulting levan was verified by a spectroscopic method. After that, the levan was used for the production of nanoparticles for the immobilization of BSA and lysozyme. Thus, this study examines the potential of levan derived from the halophilic bacterium *Bacillus licheniformis* BK1 as a nanoparticle system for protein immobilization.

■ EXPERIMENTAL SECTION

Sources and Nature of Materials

A levan-producing bacterium, *B. licheniformis* BK1 indigenous from salty mud crater, Bledug Kuwu, Central Java, Indonesia was obtained from the collection at the biochemistry laboratory, Bandung Institute of Technology, Bandung. BSA and lysozyme, here the target proteins for immobilization, were purchased from Sigma Aldrich. Materials for bacterial growth, such as yeast extract, tryptone, bacto-agar were purchased from Sigma Aldrich, while other components such as NaCl and K_2HPO_{4b} were obtained from Merck. Other chemicals, such as DNS (Dinitrosalicyclic) (Sigma Aldrich) and Sucrose (Merck) were used for the activity measurement of levansucrase, Na_2SO_4 (Merck) was used for buffer preparation, and ethanol 95% (Merck) was used for levan extraction and purification.

Procedure

Potential assay for levan-producing bacteria

B. licheniformis BK1 was inoculated on a modified Belghith medium containing 20% of (w/v) sucrose as a carbon source, 10% (w/v) NaCl, 0.5% (w/v) as yeast extract, 1% (w/v) tryptone and 0.25% (w/v) K_2HPO_4 [12]. Then the inoculum was incubated at 37 ℃ for 24 h. A positive result in this assay was the appearance of a viscous mucus excreted by the bacterial colonies.

Bacterial tolerance assay against salinity level

B. licheniformis BK1 is a halophilic bacterium, therefore, in order to obtain the optimal growth, it was incubated in a liquid Luria Bertani medium with varying salinity levels. This was achieved by varying NaCl concentration within the range of 0–15% (w/v). The bacterium was incubated in a rotary shaking incubator at 37 ℃, 150 rpm, 24 h. Bacterial growth was monitored by measuring the optical density with a UV-Vis spectrophotometer at 600 nm [13].

Optimization of the production of levan

The other way to identify the potential of *B. licheniformis* BK1 to produce levan is by measuring levansucrase activity. Levansucrase activity was assayed by DNS colorimetric method, in which a unit activity is defined as the amount of enzyme needed to produce 1 μmol glucose resulted from the sucrose hydrolysis per minute [12]. Therefore, the optimization of the enzymatic reaction is a critical step to enhance the levan production rate. This step was carried out by optimizing the production medium compositions, pH, and temperature. *B. licheniformis* BK1 was grown in the modified Belghith medium with varied NaCl concentration within the range of 1–20% (w/v), 1–20% (w/v) sucrose concentration, pH 4–10, a temperature range of 25–50 ℃ and also varying the incubation time. The optimum medium and conditions were then used to produce levan.

Isolation and purification of levan

Isolation of levan was performed following the method developed by Tabernero et al. [11] with modifications. The modification was made because the original medium composition was made without the addition of NaCl. This study used halophilic bacteria so NaCl was added to the medium. The obtained culture was heated to boil, then subsequently cooled to room temperature and centrifuged at 7500 rpm for 20 min at 4 ℃. Afterwards, the resulting supernatant and pellet were separated. The collected supernatant was the mixed with 95% cold ethanol at a ratio of 3:1 (ethanol: supernatant) to precipitate the levan. The mixture was then centrifuged at $9,800 \times g$ at 4 ℃ for 15 min. The obtained levan was washed with 95% cold ethanol three times and

ddH₂O (double distilled water) twice. After that, it was dried in an oven at a temperature of 60 °C for 4 h.

Characterization of levan structure

Fourier Transform Infrared (FTIR) spectroscopy. The isolated levan from *B. licheniformis* BK1 was initially characterized using Fourier Transform Infrared (FTIR; Shimadzu IR Prestige-21) in order to identify functional groups that constituted its structure and then compared with a levan standard from *E. herbicola*. Levan was mixed with KBr in the ratio of 1:100 to make a KBr pellet of 1 mm thickness. A spectrum of the sample was taken from the wave number of 4500–500 cm⁻¹.

Nuclear Magnetic Resonance (NMR). The structure of the sample and the levan standard was further verified using ¹H-NMR and ¹³C-NMR spectroscopy (JEOL JNMECA 500). The sample of levan was dissolved in D₂O but the standard levan was dissolved in DMSO for both NMR measurements.

Preparation of protein-levan nanoparticles

Protein-carrying nanoparticles were prepared by following the method described by Sezer et al. [14]. A total of 0.5% (w/v) of the isolated levan was dissolved in 10 mL ddH₂O pH 3.5. Next, 0.1% (w/v) of the protein was dissolved in 10 mL of 20% (w/v) Na₂SO₄ solution and then mixed with the Levan solution. In this study, BSA and lysozyme were used as the target protein for immobilization. The mixture was stirred using a magnetic stirrer with the stirring rate of 500 rpm for 20 h at room temperature. After that, the mixture was centrifuged by 7500 rpm for 20 min at 4 °C to separate the pellet and the supernatant. The obtained pellet was washed with ddH₂O three times and then dried for 2 h.

Characterization of levan nanoparticles

Morphological analysis. The isolated levan and levan-protein nanoparticles were attached to a carbon adhesive and then gold coated with 10 mA sputter-coater (Hitachi MC 1000). The sample morphology was analyzed using Scanning Electron Microscopy (SEM; Hitachi SU-3500).

Size distribution analysis and determination of the surface charge. Prior to the measurements, the protein-levan nanoparticles were dissolved in phosphate buffer pH 7.3. Nanoparticle size and surface charge were measured with a particle size analyzer (Delsa™ Nano C Particle Analyzer, Beckman Coulter). The surface charge was expressed in Zeta Potential.

Determination of immobilization efficiency

Efficiency was determined by measuring protein uptake before and after immobilization using the Bradford method. The concentration of the protein uptake was interpolated on to the BSA standard curve to determine its concentration (Eq. (1)) [15]:

$$\text{Efficiency of Immobilization} = \frac{[P]_{prep} - [P]_{sptn}}{[P]_{prep}} \times 100\% \quad (1)$$

■ RESULTS AND DISCUSSION

Test of *B. licheniformis* BK1 as a Potential Levan Producer

The result showed that *B. licheniformis* could grow on Belghith medium containing 20% (w/v) sucrose and supplemented with the halophilic condition (10% NaCl). There was thick mucus observed around the medium after 24 h incubation at 37 °C. It was indicated that *B. licheniformis* BK1 had great potential as a levan producer (Fig. 1).

Optimization of Levan Production through Levansucrase Characterization

The first optimization for levansucrase activity was performed by varying the NaCl concentration of the production medium (liquid Belghith medium) in the range of 1–20% NaCl (w/v). Bacterial growth continued

Fig 1. The potential test result for *B. licheniformis* BK1 as levan producer on Belghith medium

up to 15% (w/v) NaCl, hence justifying the observation that *B. licheniformis* BK1 is moderately halophile. The highest activity of levansucrase was observed at 7.5% (w/v) NaCl (Fig. 2). In the next experiment, concentrations of sucrose in the production medium were varied in the range of 1–20% (w/v) with optimized NaCl. Both bacterial growth and levansucrase activity were observed after 24 h of incubation. The results showed that the sucrose tolerance for *B. licheniformis* BK1 was between 1–15% (Fig. 3). The specific activity of levansucrase excreted by the bacterium

reached the highest value at 15% (w/v) of sucrose. For the next test, the previously optimized NaCl and sucrose were used with varying temperatures, from 25 to 50 °C in increments of 5 °C. The bacterial growth apparently still continued up to 40 °C, but then decreased sharply above this temperature. Similarly, levansucrase specific activity also exhibited its highest activity at 40 °C (Fig. 4). Afterwards, *B. lichenicormis* BK1 was grown at the optimized concentration of NaCl, sucrose, and temperature in a serial medium containing different pH
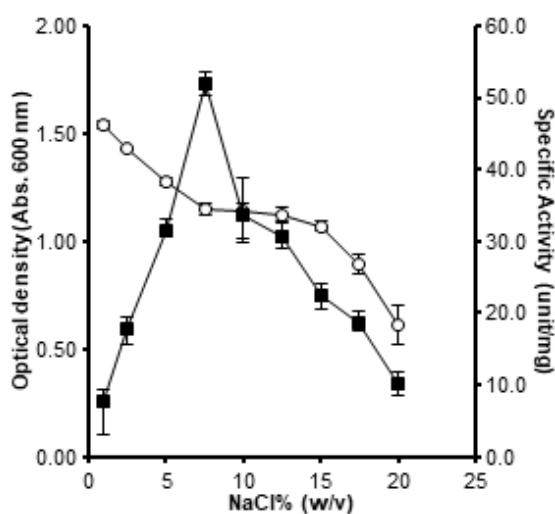

Fig 2. Effect of NaCl concentration variation on bacterial growth (white circle) and levansucrase activity (black square)
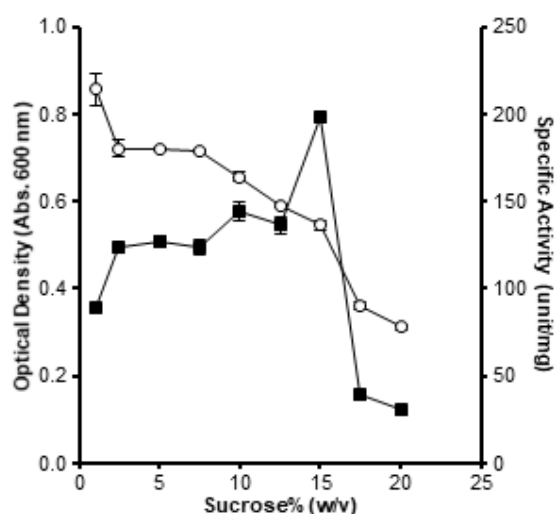

Fig 3. Effect of sucrose concentration variation on bacterial growth (white circle) and levansucrase activity (black square)
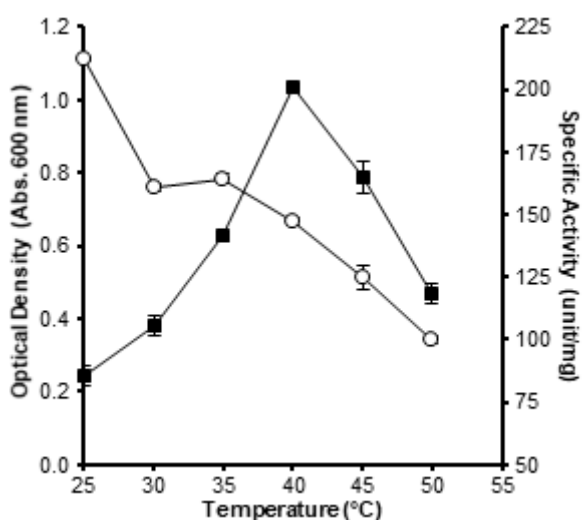

Fig 4. Effect of temperature variation on bacterial growth (white circle) and levansucrase activity (black square)
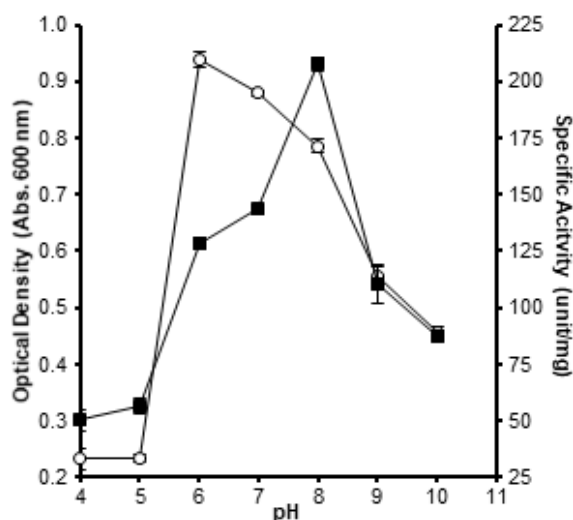

Fig 5. Effect of pH variation on bacterial growth (white circle) and levansucrase activity (black square)

from 4 to 10 with an increment of 1 pH unit. Optimum growth reached the highest point at pH 6 but levansucrase activity was observed at pH 8 (Fig. 5).

The result showed that bacterial growth increased in a log phase for 18 h and reached stationary above 18 h incubation with OD value of 1.10 A. The latest log phase showed the highest activity with a value of nearly 220 units/mg and declined dramatically to 40 units/mg above 18 h incubation (Fig. 6). The enzyme specific activity decreased most likely because, at the stationary phase, protease had been produced to provide additional carbon sources from proteins in the medium.

Characterization of Levan Structures

The structure of the levan sample isolated from *B. licheniformis* BK1 was elucidated with FTIR and NMR spectroscopic methods and then verified by comparing its spectra with those of a levan standard from *E. herbicola* (Fig. 7). The FTIR spectrum of the sample revealed the presence of –OH bond at a wavenumber of 3389 cm^{-1}, –CH bond at a wavenumber of 2885 cm^{-1}, C–OH bond at a wavenumber of 1018 cm^{-1}, furanose ring at a wavenumber of 1057–1271 cm^{-1}, and fingerprint area at wavenumber of 928–1271 cm^{-1} (Fig. 7(a)). These functional groups were similar to those of the levan from *E. herbicola* thereby

confirming that both were composed of similar functional groups (Fig. 7(b)).

Further structural verification of the sample was carried out by ^{1}H-NMR and ^{13}C-NMR. Similar to the above FTIR spectral pattern, the obtained ^{1}H-NMR spectrum had a similar pattern and chemical shifts with the levan standard from *E. herbicola* and the other halophilic *B. licheniformis* BK-AG21 [16] (Table 1). In
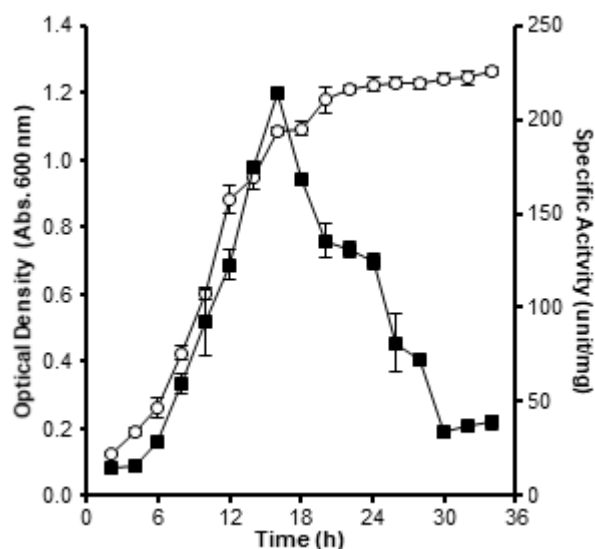
Fig 6. Effect of incubation time on the bacterial growth (white circle) and levansucrase activity (black square)
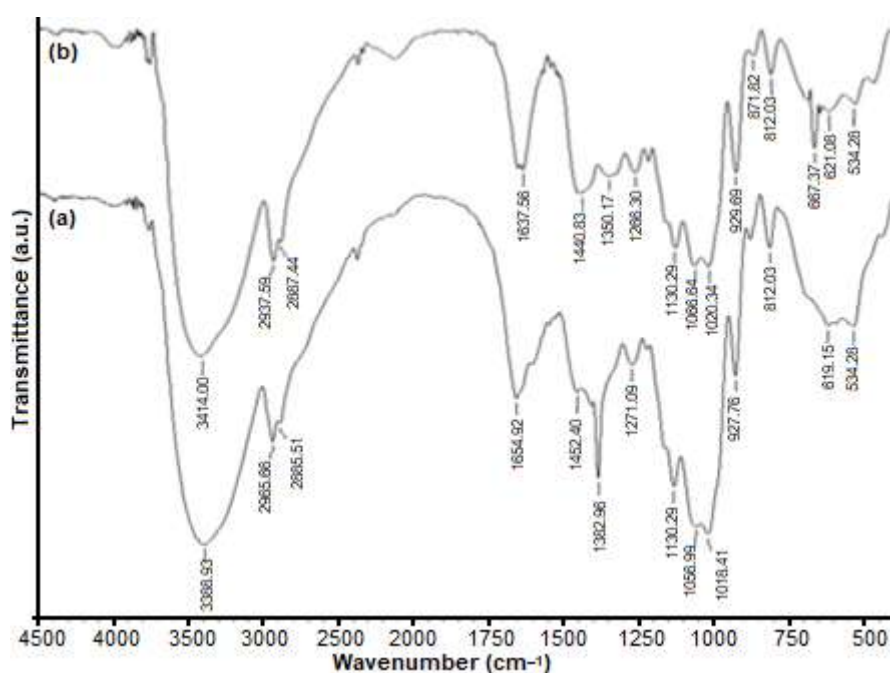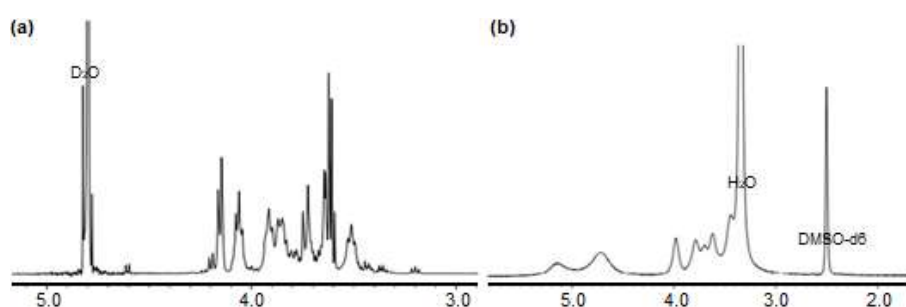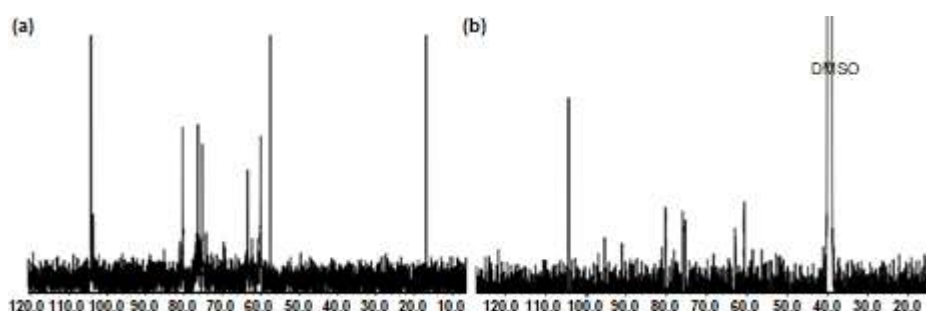
Fig 7. FTIR spectrum of levan from (a) sample of *B. licheniformis* and (b) standard of *E. herbicola*

Table 1. The comparison of ¹H-NMR chemical shifts for levan from *B. licheniformis*, *E. herbicola* and *B. licheniformis* BK AG21

Proton	Chemical shifts (ppm)		
	B. licheniformis BK1[a]	*E. herbicola*[b]	*B. licheniformis* BK AG21[c]
H-1a	3.64 (d)	3.61	3.61 (d)
H-1b	3.73 (d)	3.70	3.73 (d)
H-3	4.15 (d)	4.72	4.15 (d)
H-4	4.06 (t)	3.97	4.07 (t)
H-5	3.89 (m)	3.78	3.88 (m)
H-6	3.60 (t)	3.43	3.34(t)

*[a]Levan in this study; [b]Levan standard; [c]Levan from Mamay et al. [16]

Fig 8. The ¹H-NMR spectra of levan from (a) sample of *B. licheniformis* and (b) standard of *E. herbicola*

Fig 9. The ¹³C-NMR spectra of levan from (a) sample of *B. licheniformis* and (b) standard of *E. herbicola*
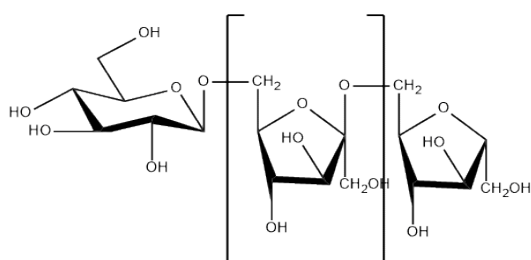
Fig 10. Levan structure

terms of the shape of the sample spectrum, the spectra of levan isolated from *B. licheniformis* BK1 (Fig. 8(a)) had sharper peaks compared to those of the standard levan (Fig. 8(b)).

Similar to ¹H-NMR result, similar spectral pattern and chemical shifts were observed between the ¹³C NMR spectrum of the levan sample with those of the *E. herbicola* standard (Fig. 9). The profile was also similar to the reference levan from *B. methylotrophicus* SK21.002 (Table 2). Based on all of these analyses, the isolated levan from *B. licheniformis* BK1 was confirmed to be levan with the structure depicted in Fig. 10.

Application of Bacterially Produced Levan as Nanoparticles for Protein Immobilization

The BSA-levan nanoparticles, as seen in the SEM image, exhibited a non-spherical morphological shape (Fig. 11(a)). The size distribution of these nanoparticles was in the range of 65–298 nm, but most of the

nanoparticles were around 65 nm (Fig. 12(a)). The amount of BSA that was successfully immobilized or incorporated into the levan nanoparticles was about 74.26%. In contrast, the SEM image and the size distribution of the lysozyme-levan nanoparticles showed more spherical shapes and more homogeneous particle sizes (Fig. 11(b)), which were in the range of 206–285 nm (Fig. 12(b)). Furthermore, the success rate for lysozyme immobilization on the levan-nanoparticle was also higher at, about 81.75%.

In order to verify the potential of *B. licheniformis* BK1 as a levan producer, it was grown on the modified Belghith medium containing 20% (w/v) sucrose as a major carbon source. Since *B. licheniformis* BK1 is a moderately halophilic bacterium, it was also added with 10% (w/v) NaCl. The potential of *B. licheniformis* BK1 as a levan producer can be seen in Fig. 1 and was exhibited by the appearance of a thick mucus secreted by the bacterial cells after 24 h of incubation at 37 °C. The high

Table 2. The comparison of ^{13}C-NMR spectral chemical shifts of levan from *B. licheniformis*, *Erwinia herbicola* and *B. methylotrophicus* SK21.002

Carbon	Chemical shifts (ppm)		
	B. licheniformis BK1[a]	*E. herbicola*[b]	*B. methylotrophicus* SK21.002[c]
C-1	60.09	62.20	61.20
C-2	104.27	105.80	102.66
C-3	76.26	78.60	77.51
C-4	75.26	77.20	76.10
C-5	80.35	81.90	80.77
C-6	63.44	65.00	63.94

*[a]Levan in this study; [b]Levan standard in this study; [c]Levan from Zhang et al. [17]
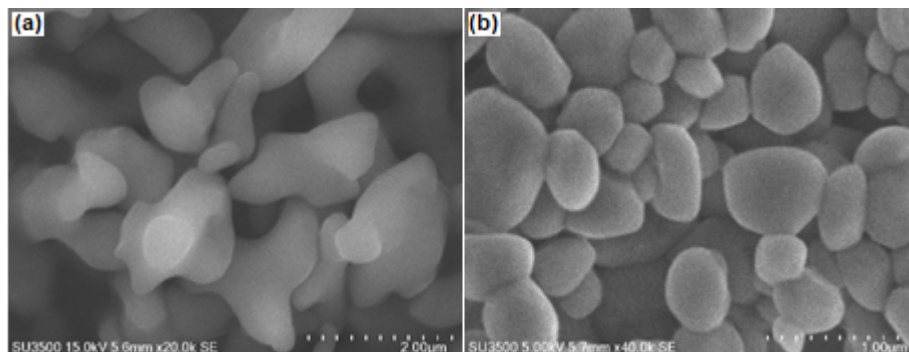

Fig 11. Scanning electron microscope image of the levan-nanoparticle system that interacted with (a) BVA and (b) lysozyme
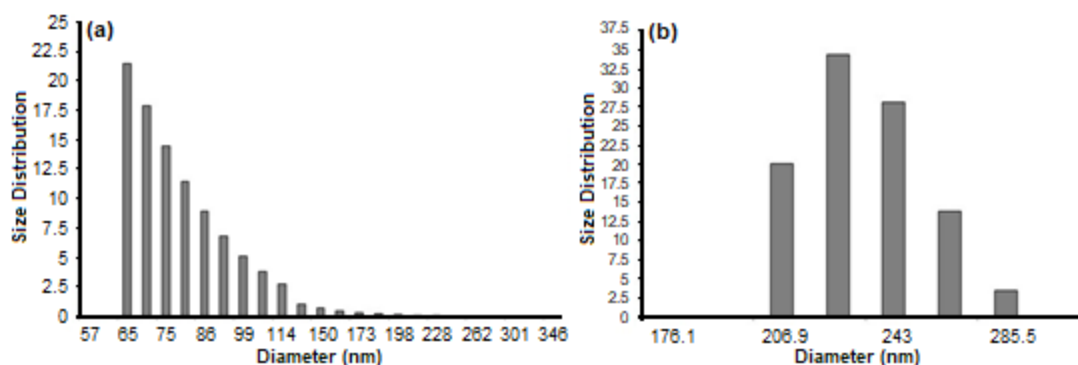

Fig 12. Particle size distribution of the levan-nanoparticle system that interacted with (a) BVA and (b) lysozyme

sucrose concentration stimulated the bacterial cells to release levansucrase to the medium which would then hydrolyze the sucrose into glucose and fructose and polymerize the fructose to become levan as well as performing uptake of some glucose for its growth [18].

Based on the result, *B. licheniformis* BK1 was categorized as moderately halophilic. These bacteria could grow up in Belghith medium supplemented with 15% (w/v) NaCl but the highest levansucrase activity was observed well at 7.5% (w/v) NaCl. The activity of levansucrase in catalyzing a reaction to produce levan is affected by sucrose concentration, pH, and temperature [3]. In addition, the use of halophilic bacterium in our study must also take into account the medium salinity [19].

This study revealed that levansucrase excretion was at the highest value when the medium was supplemented with 15% (w/v) sucrose. This study was in line with previous research that stated that when sucrose concentrations are greater than 10%, the transfructosylation reaction is preferred for the formation of levan. Concentrations of sucrose higher than 15% (w/v) apparently inhibited bacterial growth and thereby reduced the amount of enzyme excreted by the bacterium as indicated by a sharp decrease in its specific activity [12]. Therefore, 7.5% (w/v) NaCl and 15% (w/v) of sucrose were used in the next optimization.

All of the above-optimized parameters were then used to optimize the incubation time in the levan production. The bacteria were grown in the optimal production medium for 34 h and both the growth of the bacteria and the levansucrase specific activity was monitored every two hours. The results, as seen in Fig. 6, showed that the highest levansucrase specific activity was observed at 14 h of incubation, which was at the transition between the exponential and stationary phases. Levansucrase activity sharply decreased after entering the stationary phase. The enzyme specific activity decreased because, at the stationary phase, it is most likely that protease had been produced to provide additional carbon sources from proteins in the medium. All of the above-optimized parameters were used in further levan production by *B. licheniformis* BK1.

Temperature optimization showed the bacteria was able to grow in the temperature range of 25–50 °C. However, levansucrase activity exhibited the highest value at 40 °C and declined above that. These statements were supported with another study that stated that transfructosylation reaction of levan formation takes place within the temperature of 10–40 °C [19]. In addition, the study also showed that the bacterial growth reached the optimum level at pH 6 but levansucrase specific activity exhibited its highest activity at pH 8, which is within the range of the typical pH conditions for levan formation at pH 6–9 [12].

In this study, it was found that there were similar functional groups of between the observed levan produced by *B. licheniformis* and the levan standard which was produced by *E. herbicola*. FTIR spectrum revealed the presence of –OH, –CH, C–OH, furanose ring, and fingerprint area of the levan from *B. licheniformis* which was similar to that of *E. herbicola.* The NMR spectrum of ^{1}H and ^{13}C showed chemical shifts although similarities in the pattern could be detected. Spectra of the levan obtained from *B. licheniformis* had sharper peaks compared to those of the levan standard. This is likely due to the difference in chain length, in which the chain length of the sample was relatively shorter than that of the standard. The profile of the levan from *B. licheniformis* is more similar to the reference levan from *B. methylotrophicus* SK21.002, as seen in Table 2, rather than the levan standard from *E. Herbicola* [16]. Thus, the levan structure of *B. licheniformis* could be determined and confirmed as shown in Fig. 10.

It has been previously studied that levan has the potential to be developed as a nanomaterial for nanoparticles or nanocarrier of proteins and peptides for drugs or other applications [14]. The levan produced in this study, obtained from *B. licheniformis* BK1, was evaluated for its potential as a nanoparticle immobilizer for two proteins, BSA and lysozyme. The resulted nanoparticles were characterized by SEM and particle size analyzer to study their morphology, particle size distributions, and surface charge.

The result showed levan-BSA had a non-spherical shape with a size range of 65–298 nm (most of the nanoparticles were around 65 nm), but lysozyme-levan had a spherical shape with a size range of 206–285 nm and also had higher immobilization rate. The difference in morphology and the immobilization rate of proteins into the levan nanoparticle system was likely due to the difference of protein size. The result of the surface area measurement, calculated by using Getarea program to the crystal structure of both proteins revealed that the surface area of BSA was about 2.69×10^4 Å^2, which was significantly larger than that of the lysozyme structure that was only about 6.29×10^3 Å^2 [16]. In addition, as revealed from ^{1}H-NMR, levan produced by *B. licheniformis* BK1 on average had a shorter length than those from *E. herbicola*, such that they could not fully encapsulate the BSA molecular surface as well as the surface of the lysozyme. Therefore, the length of the biopolymer chain and the size of the protein or peptide molecules are critical factors to determine the success rate of producing a levan-nanoparticle system [15,17].

The analysis by using the particle size analyzer revealed that the surface charge value of the levan-nanoparticle that immobilized BSA and lysozyme were -4.72 and -2.57 mV, respectively. The negative value indicated that the outer surface of the proteins was not yet fully covered by levans. Since the levan-nanoparticle that immobilizes lysozyme had smaller negative value than that of BSA, it was likely that lysozyme surface was more covered than BSA. Sezer had successfully immobilized BSA to a levan nanoparticle, where the levan was produced by *Holomonas* sp. and obtained a positive surface charge [14]. Therefore, different bacteria may produce levans with different structural characteristics resulting in different morphologies and surface charges.

■ CONCLUSION

Levan produced by *B. licheniformis* BK1 was enhanced in this study through the optimization of levansucrase catalytic performance by varying medium composition and growth conditions. Levan isolated from *B. licheniformis* BK1 has a structural feature similar to levan from the other *Bacillus* sp. and the levan of *E. herbicola*. Levan produced from *B. licheniformis* BK1 can be used to immobilize proteins which have a molecular size that is similar to or lower than lysozyme. The success rate of levan to form a nanoparticle for protein immobilization depends on the size of the target protein and the average chain length of the levans.

■ REFERENCES

[1] Dahech, I., Belghith, K.S., Hamden, K., Feki, A., Belghith, H., and Mejdoub, H., 2011, Antidiabetic activity of levan polysaccharide in alloxan-induced diabetic rats, *Int. J. Biol. Macromol.*, 49 (4), 742–746.

[2] Abdel-Fattah, A.M., Gamal-Eldeen, A.M., Helmy, W.A., and Esawy, M.A., 2012, Antitumor and antioxidant activities of levan and its derivative from the isolate Bacillus subtilis NRC1aza, *Carbohydr. Polym.*, 89 (2), 314–322.

[3] Srikanth, R., Reddy, C.H.S.S.S., Siddartha, G., Ramaiah, M.J., and Uppuluri, K.B., 2015, Review on production, characterization, and applications of microbial levan, *Carbohydr. Polym.*, 120, 102–114.

[4] Srikanth, R., Siddartha, G., Sundhar Reddy, C.H.S.S.S., Harish, B.S., Ramaiah, M.J., and Uppuluri, K.B., 2015, Antioxidant and anti-inflammatory levan produced from *Acetobacter xylinum* NCIM2526 and its statistical optimization, *Carbohydr. Polym.*, 123, 8–16.

[5] Xu, X., Gao, C., Liu, Z., Wu, J., Han, J., Yan, M., and Wu, Z., 2016, Characterization of the levan produced by *Paenibacillus bovis* sp. nov BD3526 and its immunological activity, *Carbohydr. Polym.*, 144, 178–186.

[6] Öner, E.T., Hernández, L., and Combie, J., 2016, Review of Levan polysaccharide: From a century of past experiences to future prospects, *Biotechnol. Adv.*, 34 (5), 827–844.

[7] Nakapong, S., Pichyangkura, R., Ito, K., Iizuka, M., and Pongsawasdi, P., 2013, High expression level of levansucrase from *Bacillus licheniformis* RN-01 and synthesis of levan nanoparticles, *Int. J. Biol. Macromol.*, 54, 30–36.

[8] Ahmed, K.B.A., Kalla, D., Uppuluri, K.B., and Anbazhagan, V., 2014, Green synthesis of silver and gold nanoparticles employing levan, a biopolymer from *Acetobacter xylinum* NCIM 2526, as a reducing agent and capping agent, *Carbohydr. Polym.*, 112, 539–545.

[9] Bondarenko, O.M., Ivask, A., Kahru, A., Vija, H., Titma, T., Visnapuu, M., Joost, U., Pudova, K., Adamberg, S., Visnapuu, T., and Alamäe, T., 2015, Bacterial polysaccharide levan as stabilizing, non-toxic and functional coating material for microelement-nanoparticles, *Carbohydr. Polym.*, 136, 710–720.

[10] Taran, M., Etemadi, S., and Safaei, M., 2017, Microbial levan biopolymer production and its use for the synthesis of an antibacterial iron(II,III) oxide–levan nanocomposite, *J. Appl. Polym. Sci.*, 134 (12), 44613.

[11] Tabernero, A., González-Garcinuño, Á., Sánchez-Álvarez, J.M., Galán, M.A., and del Valle, E.M.M., 2017, Development of a nanoparticle system based on a fructose polymer: Stability and drug release studies, *Carbohydr. Polym.*, 160, 26–33.

[12] Belghith, K.S., Dahech, I., Belghith, H., and Mejdoub, H., 2012, Microbial production of levansucrase for the synthesis of fructooligosaccharides and levan, *Int. J. Biol. Macromol.*, 50 (2), 451–458.

[13] McBirney, S.E., Trinh, K., Wong-Beringer, A., and Armani, A.M., 2016, Wavelength-normalized spectroscopic analysis of *Staphylococcus aureus* and *Pseudomonas aeruginosa* growth rates, *Biomed. Opt. Express*, 7 (10), 4034–4042.

[14] Sezer, A.D., Kazak, H., Öner, E.T., and Akbua, J., 2011, Levan-based nanocarrier system for peptide and protein drug delivery: Optimization and influence of experimental parameters on the nanoparticle characteristics, *Carbohydr. Polym.*, 84 (1), 358–363.

[15] Sezer, A.D., Sarılmışer, H.K., Rayaman, E., Çevikbaş, A., Öner, E.T., and Akbuğa, J., 2017, Development and characterization of vancomycin-loaded levan-based microparticular system for drug delivery, *Pharm. Dev. Technol.*, 22 (5), 627–634.

[16] Mamay, Wahyuningrum, D., and Hertadi, R., 2015, Isolation and characterization of levan from moderate halophilic bacteria *Bacillus licheniformis* BK AG21, *Procedia Chem.*, 16, 292–298.

[17] Zhang, T., Li, R., Qian, H., Mu, W., Miao, M., and Jiang, B., 2014, Biosynthesis of levan by levansucrase from *Bacillus methylotrophicus* SK 21.002, *Carbohydr. Polym.*, 101, 975–981.

[18] Li, W., Yu, S., Zhang, T., Jiang, B., and Mu, W., 2015, Recent novel applications of levansucrases, *Appl. Microbiol. Biotechnol.*, 99 (17), 6959–6969.

[19] Ebel, C., Madern, D., and Zaccai, G., 2009, "Molecular Adaptation of Halophilic Proteins" in *Extremophiles*, vol. II, Eds., Gerday, C., and Glandsdorff, N., Eolss Publisher Co. Ltd., Oxford, England.

Synthesis of Dioxo-Dioxane and Dioxo-Dioxepane Ethyl Oleate Derivatives as Bio-Lubricant Base Stocks

Tutik Dwi Wahyuningsih[1,*] and Yehezkiel Steven Kurniawan[1,2]

[1]*Department of Chemistry, Faculty of Mathematics and Natural Sciences, Universitas Gadjah Mada, Sekip Utara, Yogyakarta 55281, Indonesia*

[2]*Ma Chung Research Center for Photosynthetic Pigments, Universitas Ma Chung, Malang 65151, Indonesia*

* Corresponding author:

tel: +62-818467863
email: tutikdw@ugm.ac.id

Abstract: *In this study, two novel compounds, i.e., ethyl 8-(3-octyl-5,6-dioxo-1,4-dioxan-2-yl)octanoate and ethyl 8-(3-octyl-5,7-dioxo-1,4-dioxepan-2-yl)octanoate were prepared from oleic acid as the starting material. Both compounds were obtained from the esterification of the ethyl 9,10-dihydroxyoctadecanoate with dicarboxylic acids in the presence of* p-*toluenesulfonic acid as a catalyst. The chemical structures of the synthesized products were confirmed by FTIR, ^{1}H-NMR, and MS spectrometers. The bio-lubricant properties of the products, such as density, total acid number, total base number, and iodine value, were determined and the effect of the dioxane and dioxepane heterocyclic rings to their bio-lubricant properties was discussed. The esterification of ethyl 9,10-dihydroxyoctadecanoate with oxalic acid gave ethyl 8-(3-octyl-5,6-dioxo-1,4-dioxan-2-yl)octanoate compound in 93.9% yield, while the esterification of ethyl 9,10-dihydroxyoctadecanoate with malonic acid gave ethyl 8-(3-octyl-5,7-dioxo-1,4-dioxepan-2-yl)octanoate compound in 89.6% yield. The density and total base number of the products were close to the standard commercial lubricant values. Meanwhile, the total acid number and the iodine value of the ethyl 8-(3-octyl-5,6-dioxo-1,4-dioxan-2-yl)octanoate were smaller than the standard commercial lubricant, showing that this compound is a promising bio-lubricant in a real application.*

Keywords: *synthesis; dioxane; dioxepane; bio-lubricant; oleic acid*

■ INTRODUCTION

Researches concerning bioenergy and biomaterial are increasing rapidly over the past several years [1-3]. Among them, bio-lubricant is gaining great interest because of the depleting oil-based lubricant reserves [4-5]. Bio-lubricant is an environmentally friendly product because it is biodegradable and does not contain either sulfur or harmful aromatic compounds [6-7]. Many researchers reported the availability to prepare bio-lubricant from vegetable oil, such as jatropha oil [8], canola oil [9], seed oil [10], and so on. However, the vegetable oil-derived bio-lubricant has several drawbacks, such as high acidic property caused by free fatty acids present and poor oxidation stability due to unsaturated fatty acids contained [11-13]. Therefore, many efforts are based on the chemical modification of vegetable oil to improve their physicochemical properties as bio-lubricants [14-15].

Madankar et al. modified fatty acids in canola oil through epoxidation, followed by ring-opening reaction with alcohols [9]. Furthermore, they also reported that the lubricant thermal stability increased by employing a longer carbon chain of the alkoxy ether substituent. Even though some chemical modifications of the vegetable oils were reported, ester-based lubricants were mostly developed due to the high yield obtained and the simple reaction process. Abdullah et al. prepared some polyesters of linoleic acid [16], while Salih et al. synthesized some triesters of oleic acid as bio-lubricant base stocks [17]. It was reported that polyester based lubricant performed a high viscosity index, a low pour point, a low volatility, and a high onset temperature.

However, the polyester-based lubricant is easily hydrolyzed at high temperatures; therefore, their total acid numbers (TAN) are quite high. Sammaiah et al. reported that the TAN of the hydroxy of jatropha fatty acid alkyl ester for methyl, *n*-butyl, isopropyl, isobutyl, and 2-ethylhexyl as alkyl groups were 220.13; 224.46; 220.46; 222.52; and 195.37 mg KOH/g, respectively [8], which is unfavorable.

In our previous works, we reported a wide application of oleic acid to prepare bio-lubricants and bio-greases [18-20]. The structure of the synthesized products in our previous work are shown in Fig. 1. The carboxylic acid functional group was modified to be an ester functional group to decrease the acidity property, and the unsaturated double bond was transformed into various heterocyclic rings to increase the oxidation stability [18]. Because of these chemical modifications, the TAN of the synthesized products were 14.53, 1.71, 11.00, and 5.46 mg KOH/g for ketal, acetal, D[4.4] and D[4.5] compounds, respectively, which are much lower than the Sammaiah et al. reports [8]. The other physicochemical properties are satisfying enough. However, the D[4.4] and D[4.5] compounds are less stable due to the presence of the bicyclic functional group.

In the present work, the other heterocyclic rings, i.e., dioxo-dioxane and dioxo-dioxepane, were evaluated for their bio-lubricant physicochemical properties. The ethyl 8-(3-octyl-5,6-dioxo-1,4-dioxan-2-yl)octanoate (abbreviated as Cyclic-6) and ethyl 8-(3-octyl-5,7-dioxo-1,4-dioxepan-2-yl)octanoate (abbreviated as Cyclic-7) were prepared through esterification between ethyl 9,10-dihydroxyoctadecanoate (EtDHO) and dicarboxylic acids. The physicochemical properties of the products as bio-lubricants were examined, and the effect of the heterocyclic rings was discussed.
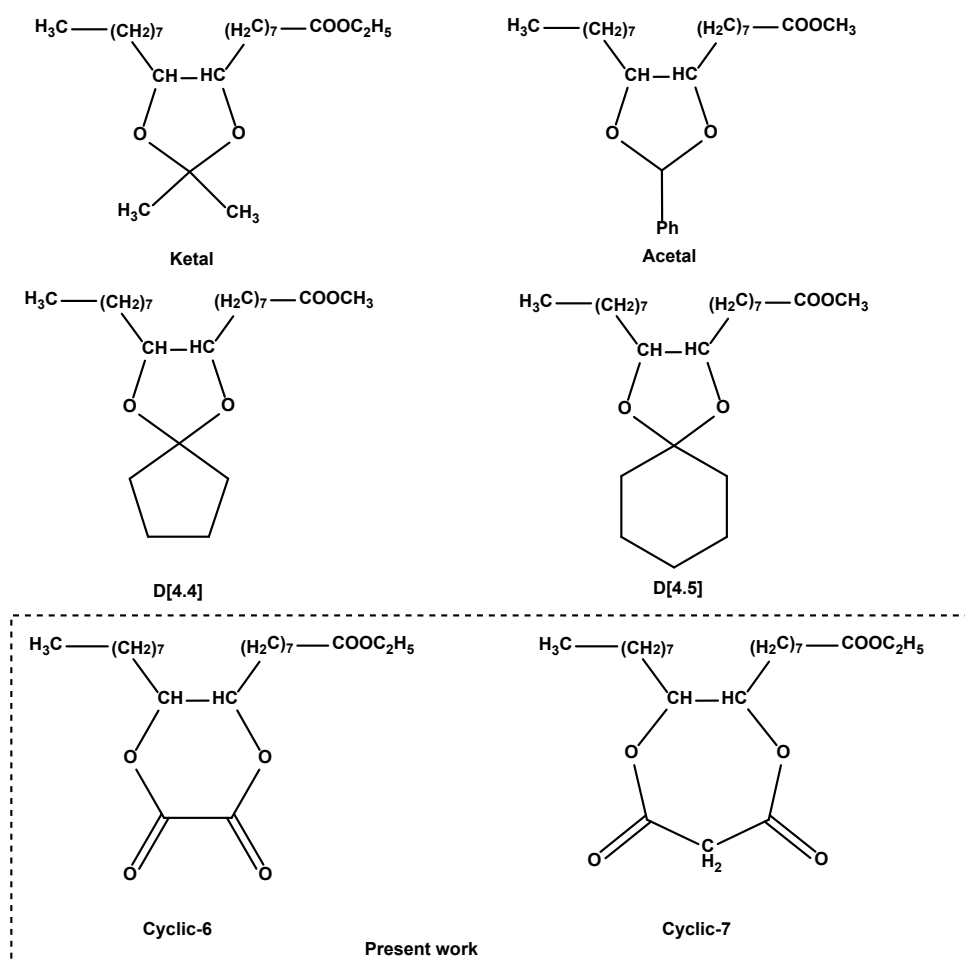

Fig 1. Prepared heterocyclic compounds derived from oleic acid in previous and present works

■ EXPERIMENTAL SECTION

Materials

Oleic acid was obtained from Sigma Aldrich, while other chemicals, such as oxalic acid dihydrate, malonic acid, *p*-toluenesulfonic acid monohydrate (*p*TSA), sodium bicarbonate, anhydrous sodium sulfate, acetonitrile, dichloromethane, and chloroform were in pro analysis grade and purchased from Merck. The 9,10-dihydroxyoctadecanoic acid (DHOA) and ethyl 9,10-dihydrooctadecanoate (EtDHO) were prepared as previously described [18]. Commercial lubricant, Pertamina Mesran Super 20W-50, was purchased and used as a standard for the lubricants' physicochemical properties test.

Instrumentation

The Fourier Transform Infrared (FTIR) spectra of the synthesized compounds were recorded on a Shimadzu Prestige-21 FTIR spectrophotometer, while the mass spectra (MS) of the synthesized products were recorded on a Shimadzu QP 2010S with Agilent GC Type 6890-MS Type 5973. The Proton Nuclear Magnetic resonance (^{1}H-NMR) spectra were recorded on a JEOL-MY500 NMR Spectrometer. Density, total acid number (TAN), total base number (TBN), and iodine value (IV) were determined by titration method according to American Society for Testing and Material (ASTM) in a similar manner as previously reported [18].

Procedure

Synthesis of ethyl 8-(3-octyl-5,6-dioxo-1,4-dioxan-2-yl)octanoate (Cyclic-6)

The EtDHO (0.68 g, 2.0 mmol) was dissolved into 25 mL of acetonitrile. The *p*TSA (0.10 g, 0.5 mmol) and oxalic acid dihydrate (1.01 g, 8.0 mmol) were added to the solution, and the mixture was refluxed for 5 h. The solvent was evaporated, and the residue was extracted with chloroform. The organic layer was washed twice with NaHCO$_3$ 10% (w/v) and then three times with distilled water. The organic layer was dried with anhydrous Na$_2$SO$_4$, and the solvent was evaporated to obtain the desired product as a light-yellow viscous liquid in a 93.9% yield. FTIR (KBr pellet, cm^{-1}): 2924 (C-H sp^3), 1721, and 1697 (C=O ester), 1458 (CH$_2$), and 1265 (C-O ester). ^{1}H-NMR (CDCl$_3$, ppm): 0.83 (t, 3H, -CH$_3$), 1.17–1.58 (m, 29H, -CH$_2$- and -CH$_2$COOCH$_2$C̲H̲$_3$), 2.23 (t, 2H, -C̲H̲$_2$COOCH$_2$CH$_3$), 3.56 (m, 2H, -CH-O), 4.10 (q, 2H, -CH$_2$COOC̲H̲$_2$CH$_3$). MS: 397 (M$^+$-H), 368 (M$^+$-H-C$_2$H$_5$), 355 (M$^+$-C$_3$H$_7$), 281, 263, 155, 69, 55, 43 (base peak).

Synthesis of ethyl 8-(3-octyl-5,6-dioxo-1,4-dioxepan-2-yl)octanoate (Cyclic-7)

The EtDHO (0.68 g, 2.0 mmol) was dissolved into 25 mL of acetonitrile. The *p*TSA (0.10 g, 0.5 mmol) and malonic acid (0.832 g, 8.0 mmol) were added to the solution, and the mixture was refluxed for 5 h. The solvent was evaporated, and the residue was extracted with dichloromethane. The organic layer was washed 3 times with NaHCO$_3$ 10% (w/v) and then 4 times with distilled water. The organic layer was dried with anhydrous Na$_2$SO$_4$, and the solvent was evaporated to obtain the desired product as a light-yellow viscous liquid in 89.6% yield. FTIR (KBr pellet, cm^{-1}): 2940 (C-H sp^3), 1713, and 1680 (C=O ester), 1427 (CH$_2$), and 1250 (C-O ester). ^{1}H-NMR (CDCl$_3$, ppm): 0.84 (t, 3H, -CH$_3$), 1.22–1.58 (m, 29H, -CH$_2$- and -CH$_2$COOCH$_2$C̲H̲$_3$), 2.25 (t, 2H, -C̲H̲$_2$COOCH$_2$CH$_3$), 3.55 (m, 2H, -CH-O), 3.98 (d, 2H, CO-CH$_2$-CO), 4.09 (q, 2H, -CH$_2$COOC̲H̲$_2$CH$_3$). MS: 410 (M$^+$-2H), 367 (M$^+$-2H-C$_3$H$_7$), 263, 155, 137, 69, 55 (base peak), 43.

■ RESULTS AND DISCUSSION

Synthesis of Cyclic-6 and Cyclic-7

The synthesis scheme of Cyclic-6 and Cyclic-7 compounds from oleic acid as the starting material is shown in Fig. 2. The first reaction is a hydroxylation by using potassium permanganate as the oxidation agent in an alkaline condition to give 9,10-dihydroxyoctadecanoic acid (DHOA) compound. Afterward, the carboxylic acid of DHOA was esterified with ethanol in the presence of montmorillonite KSF as an acid catalyst to form EtDHO compound. Finally, the desired compounds were obtained by cyclization through the esterification between the diol functional group of the EtDHO compound with a dicarboxylic acid. Cyclization of EtDHO with oxalic acid produced dioxane heterocyclic ring in the Cyclic-6 compound, while cyclization of EtDHO with malonic acid
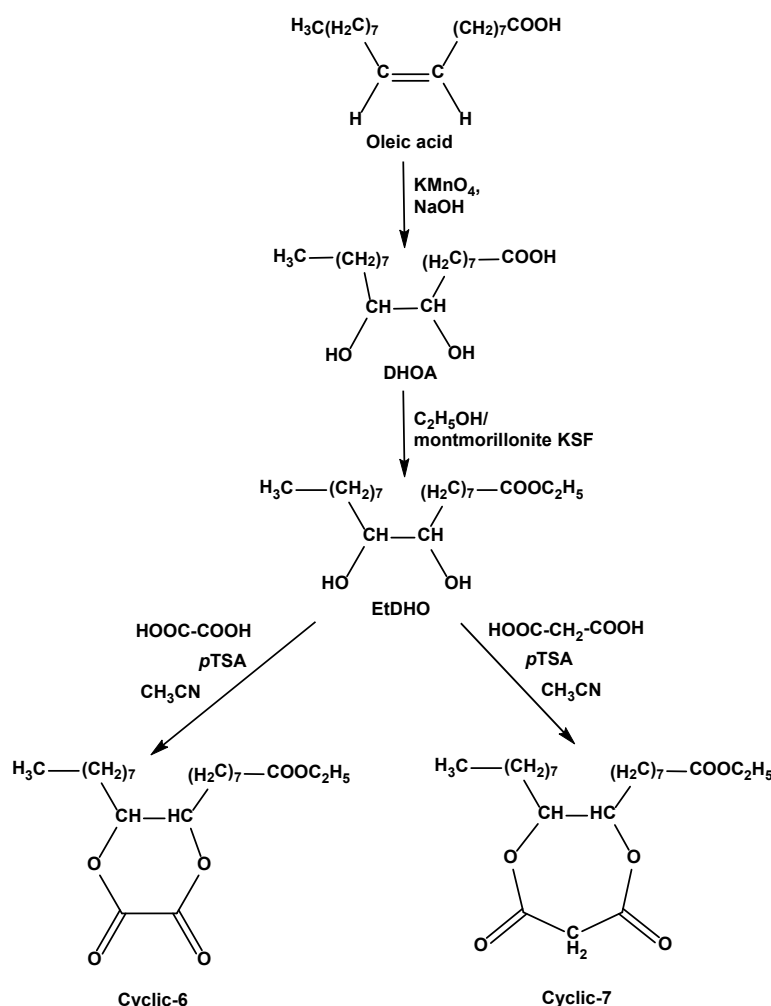
Fig 2. Synthesis scheme of Cyclic-6 and Cyclic-7 compounds from oleic acid

produced a dioxepane heterocyclic ring in the Cyclic-7 compound. The Cyclic-6 and Cyclic-7 were obtained in high yield, i.e., 93.9 and 89.6%, respectively, which is remarkable. Furthermore, both are novel compounds, which have never been reported before to the best of our knowledge.

The chemical structures of both products were confirmed by FTIR and ^{1}H-NMR analysis. The FTIR spectra of Cyclic-6 and Cyclic-7 compounds are shown in Fig. 3. The absence of a broad peak around 3000–3500 cm^{-1} showed that the hydroxyl (-OH) groups were completely esterified. The presence of two strong peaks at 1680-1725 cm^{-1} emphasized that each of the synthesized compounds has two C=O ester groups, which are chemically nonequivalent. The absorption peak of the methylene (-CH$_2$-) functional groups showed at 1458 and

1427 cm^{-1} for Cyclic-6 and Cyclic-7, respectively. Meanwhile, the absorption peak of the C-O ester functional groups was found at 1265 and 1250 cm^{-1} for Cyclic-6 and Cyclic-7, respectively.

The chemical structure of the Cyclic-6 was elucidated by ^{1}H-NMR spectra (data not shown). A triplet peak at 1.29 ppm and a quartet peak at 4.10 ppm confirmed that ethyl ester was formed. However, the dioxane heterocyclic ring could not be proven by using ^{1}H-NMR spectra because there is no additional proton after the esterification with oxalic acid. The ^{1}H-NMR spectrum of the Cyclic-7 product is shown in Fig. 4. The ethoxy functional group in Cyclic-7 was confirmed by the presence of triplet peak at 1.29 ppm (3H, overlapped with other peaks) and quartet peak at 4.09 ppm (2H). Furthermore, the methylene group from the malonic acid
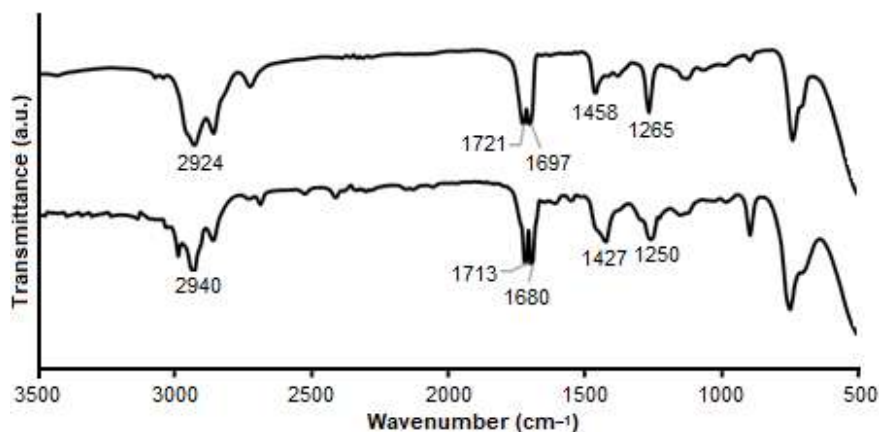
Fig 3. FTIR spectra of (a) Cyclic-6 and (b) Cyclic-7 compounds
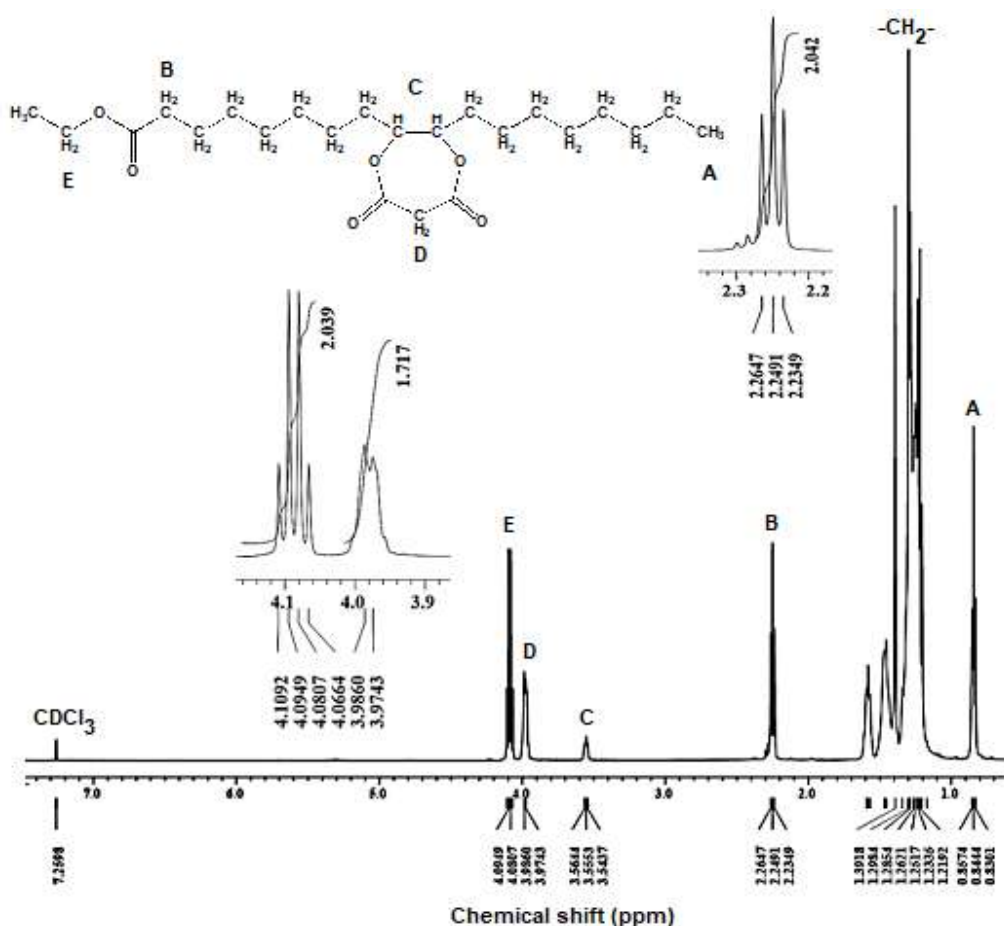
Fig 4. ^{1}H-NMR spectra of Cyclic-7 compound

appeared as a doublet at 3.98 ppm (2H) due to the geminal coupling. The other protons also appeared and were assigned, as shown in Fig. 3. Both FTIR and ^{1}H-NMR spectra confirmed that Cyclic-6 and Cyclic-7 compounds had been successfully prepared.

The Physicochemical Properties of Cyclic-6 and Cyclic-7 as Bio-lubricants

The physicochemical properties of Cyclic-6 and Cyclic-7 are shown in Table 1. The density of Cyclic-6 and Cyclic-7 are both higher than ketal, acetal, D[4.4],

Table 1. Bio-lubricant physicochemical properties of the products

No	Compounds	Physicochemical properties				Ref.
		Density (g/mL)	TAN (mg KOH/g)	TBN (mg KOH/g)	IV (mg I_2/g)	
1	Ketal	0.824	14.53	48.95	0.76	[19]
2	Acetal	-	1.71	14.12	0.25	[20]
3	D[4.4]	0.916	11.00	24.24	21.28	[18]
4	D[4.5]	0.913	5.46	14.04	17.73	[18]
5	Cyclic-6	1.045	1.37	3.53	0.72	This work
6	Cyclic-7	0.939	2.89	6.61	0.69	This work
7	Oleic acid	0.985	196.80	0.54	89.90	This work
8	Commercial lubricant	0.893	85.37	5.36	31.73	This work

and D[4.5] compounds. The higher density of Cyclic-6 and Cyclic-7 are probably caused by stronger intermolecular hydrophobic interaction. The density of Cyclic-6 was the highest due to the highest stability of the dioxane ring amongst all rings. It is well known that a six-membered ring is more stable and well-arranged than the seven-membered ring; therefore, it is in agreement with the measured density property [18].

The TAN value represents a possible corrosion level to the engine caused by using the lubricant. Compared to the hydroxy fatty acid alkyl ester of jatropha [8], the TAN values of the synthesized products decrease significantly by the formation of dioxane and dioxepane heterocyclic rings. It means that a cyclic ester functional group is preferable than polyester substituents. From Table 1, it is shown that the TAN values of Cyclic-6 and Cyclic-7 are lower than others, demonstrating that both compounds are preferable due to low corrosion level to the engine. The low TAN of Cyclic-6 and Cyclic-7 were caused by their stability against the acid hydrolysis process. The TAN value of Cyclic-6 is the lowest because of a stable six-member heterocyclic ring. Similar to the TAN results, the TBN value of the Cyclic-6 is the lowest, demonstrating that the Cyclic-6 compound is very stable to acid hydrolysis as well as the alkaline hydrolysis process.

The IV value represents the stability of the compound towards oxidation. Unsaturated fatty acid, such as oleic acid, has a high IV value due to the presence of the C=C double bond. Through chemical modifications of oleic acid, the IV significantly decreased, as shown in Table 1. The IV values of Cyclic-6 and Cyclic-7 compounds are less

than 1.00 mg I_2/g, showing that they are stable against the oxidation process. Compared to the commercial lubricant, Cyclic-6 and Cyclic 7 are better because their TAN and IV values are lower. Therefore, Cyclic-6 and Cyclic-7 are promising bio-lubricant candidates because of the shown excellent lubricant properties.

■ **CONCLUSION**

The Cyclic-6 and Cyclic-7 compounds were successfully synthesized from the esterification between EtDHO and oxalic acid and malonic acid, respectively. From the results, Cyclic-6 bio-lubricant gave lower TAN, demonstrating that Cyclic-6 is more stable than Cyclic-7 for acid hydrolysis. The density and TBN of the Cyclic-6 bio-lubricant are similar to the commercial lubricant. These findings are useful for the chemical design of fatty acids to improve the physicochemical properties of the bio-lubricant derived from vegetable oils.

■ **ACKNOWLEDGEMENTS**

■ **REFERENCES**

[1] Zhu, Y., Romain, C., and Williams, C.K., 2016, Sustainable polymers from renewable resources, *Nature*, 540, 354–362.

[2] Imawan, A.C., Kurniawan, Y.S., Lukman, M.F., Jumina, Triyono, and Siswanta, D., 2018, Synthesis and kinetic study of the urea controlled release composite material: Sodium lignosulfonate from

isolation of wood sawdust-sodium alginate-tapioca, *Indones. J. Chem.*, 18 (1), 108–115.

[3] Wahyuningsih, T.D., Kurniawan, Y.S., Amalia, S., Wardhani, T.A.K., and Muriningsih, C.E.S., 2019, Diethanolamide derivatives as potential enhanced oil recovery from Indonesian castor oil and used frying oil: Isolation, synthesis and evaluation as nonionic biosurfactants, *Rasayan J. Chem.*, 12 (2), 741–748.

[4] Zhou, Y., and Qu, J., 2017, Ionic liquids as lubricant additives: A review, *ACS Appl. Mater. Interfaces*, 9 (4), 3209–3222.

[5] Owuna, F.J., Dabai, M.U., Sokoto, M.A., Dangoggo, S.M., Bagudo, B.U., Birnin-Yauri, U.A., Hassan, L.G., Sada, I., Abubakar, A.L., and Jibrin, M.S., 2019, Chemical modification of vegetable oils for the production of biolubricants using trimethylolpropane: A review, *Egypt. J. Pet.*, In Press, Corrected Proof.

[6] Chan, C.H., Tang, S.W., Mohd, N.K., Lim, W.H., Yeong, S.K., and Idris, Z., 2018, Tribological behavior of biolubricant base stocks and additives, *Renewable Sustainable Energy Rev.*, 93, 145–157.

[7] Heikal, E.K., Elmelawy, M.S., Khalil, S.A., and Elbasuny, N.M., 2017, Manufacturing of environment friendly biolubricants from vegetable oils, *Egypt. J. Pet.*, 26 (1), 53–59.

[8] Sammaiah, A., Padmaja, K.V., and Prasad, R.B.N., 2014, Synthesis and evaluation of novel acyl derivates from Jatropha oil as potential lubricant base stocks, *J. Agric. Food Chem.*, 62 (20), 4652–4660.

[9] Madankar, C.S., Dalai, A.K., and Naik, S.N., 2013, Green synthesis of biolubricant base stock from Canola oil, *Ind. Crops Prod.*, 44, 139–144.

[10] Sonnenschein, M.F., Greaves, M.R., Bell, B.M., and Wendt, B.L., 2012, Design, polymerization, and properties of high-performance seed-oil-derived lubricants, *Ind. Eng. Chem. Res.*, 51 (25), 8386–8393.

[11] Soni, S., and Agarwal, M., 2014, Lubricants from renewable energy sources – A review, *Green Chem. Lett. Rev.*, 7 (4), 359–382.

[12] Panchal, T.M., Patel, A., Chauhan, D.D., Thomas, M., and Patel, J.V., 2017, A methodological review on bio-lubricants from vegetable oil based resources, *Renewable Sustainable Energy Rev.*, 70, 65–70.

[13] Reeves, C.J., Siddaiah, A., and Menezes, P.L., 2017, A review on the science and technology of natural and synthetic biolubricants, *J. Bio. Tribo. Corros.*, 3, 11.

[14] McNutt, J., and He, Q., 2016, Development of biolubricants from vegetable oils via chemical modification, *J. Ind. Eng. Chem.*, 36, 1–12.

[15] Hossain, M.A., Iqbal, M.A.M., Julkapli, N.M., Kong, P.S., Ching, J.J., and Lee, H.V., 2018, Development of catalyst complexes for upgrading biomass into ester-based biolubricants for automotive applications: A review, *RSC Adv.*, 8, 5559–5577.

[16] Abdullah, B.M., Zubairi, S.I., Huri, H.Z., Hairunisa, N., Yousif, E., and Basu, R.C., 2016, Polyester based on linoleic acid for biolubricant basestocks: Low-temperature, tribological and rheological properties, *PLoS ONE*, 11 (3), e0151603.

[17] Salih, N., Salimon, J., and Yousif, E., 2011, The physicochemical and tribological properties of Oleic acid based triester biolubricants, *Ind. Crops Prod.*, 34 (1), 1089–1096.

[18] Kurniawan, Y.S., Ramanda, Y., Thomas, K., Hendra, and Wahyuningsih, T.D., 2017, Synthesis of 1,4-dioxaspiro[4.4] and 1,4-dioxaspiro[4.5] novel compounds from oleic acid as potential biolubricant, *Indones. J. Chem.*, 17 (2), 301–308.

[19] Kurniawan, Y.S., Anwar, M., and Wahyuningsih, T.D., 2017, New lubricant from used cooking oil: Cyclic ketal of ethyl 9,10-dihidroxyoctadecanoate, *Mater. Sci. Forum*, 901, 135–141.

[20] Wahyuningsih, T.D., and Kurniawan, Y.S., 2017, Green synthesis of some novel dioxolane compounds from Indonesian essential oils as potential biogreases, *AIP Conf. Proc.*, 1823 (1), 020081.

Highest Ionic Conductivity of BIMEVOX (ME = 10% Cu, 10% Ga, 20% Ta): Computational Modeling and Simulation

Akram La Kilo[1,*], Alberto Costanzo[2], Daniele Mazza[2], Muhamad Abdulkadir Martoprawiro[3], Bambang Prijamboedi[3], and Ismunandar[3]

[1]*Department of Chemistry, Universitas Negeri Gorontalo, Jl. Jenderal Soedirman No. 6 Gorontalo 96128, Indonesia*

[2]*Dipartimento di Scienza dei Materiali e' Ingegneria Chimica, Politecnico di Torino, Corso Duca degli Abruzzi 24, 10129 Torino, Italy*

[3]*Inorganic and Physical Chemistry Research Group, Faculty of Mathematics and Natural Sciences, Institut Teknologi Bandung, Jl. Ganesha No. 10, Bandung 40132, Indonesia*

Abstract: *BIMEVOX had the potential to play an important role in solid oxide fuel cell, especially as the electrolyte due to their high ionic conductivity. In this work, oxide ion migrations of γ-Bi$_2$VO$_{5.5}$ and BIMEVOX were simulated using density functional theory (DFT), Mott-Littleton method, and molecular dynamics simulation. In γ-Bi$_2$VO$_{5.5}$, there were oxygen vacancies at the equatorial position in the vanadate layers. These vacancies could facilitate oxide ions migration. The Enthalpy of the oxide migration for γ-Bi$_2$VO$_{5.5}$ based on DFT calculation was 0.38 eV, which was in good agreement with experimental results. The γ-Bi$_2$VO$_{5.5}$ can be stabilized by partial substitution of V^{5+} with Cu^{2+}, Ga^{3+}, and Ta^{5+}. Defect simulation results using the Mott-Littleton method showed that the total maximum energies of region II were achieved at concentrations of 10, 10, and 20%, respectively, for Cu^{2+}, Ga^{3+}, and Ta^{5+}. The calculated concentration of Cu^{2+}, Ga^{3+}, and Ta^{5+} was in good agreement with those of experiment results, where the highest ionic conductivity was obtained. The results of the molecular dynamics simulation showed that the activation energies of oxide ion migration in γ-Bi$_2$VO$_{5.5}$ and BIMEVOX (ME = Cu and Ta) were 0.19, 0.21, and 0.10 eV, respectively, close to experimental values.*

Keywords: *simulation; vacancy defect; γ-Bi$_2$VO$_{5.5}$ and BIMEVOX; ionic migration*

■ INTRODUCTION

Solid electrolyte materials with high oxide ion conductivity intensively investigated in order to have a solid oxide fuel cell (SOFC). One of the oxide materials that had high oxide ion conductivity and the potential application was Bi$_2$V$_{1-x}$Me$_x$O$_{5.5-\sigma}$ (BIMEVOX), where ME was dopant [1-3]. Dopant at a certain concentration plays an important role in improving the ease of oxygen ions migration of Bi$_2$VO$_{5.5}$ [4-5]. Therefore, in addition to the migration path of oxygen ions, the search for a type of dopant with a certain concentration was needed to obtain BIMEVOX with high conductivity. The computational simulation method could be conducted first to predict the ease of ion migration.

BIMEVOX was a family of oxides derived from Bi$_2$VO$_{5.5}$ and obtained by doping into the vanadium site of Bi$_2$VO$_{5.5}$ by aliovalent or isovalent metal cations (ME). The structure of Bi$_2$VO$_{5.5}$ could be derived from Bi$_2$MoO$_6$ and δ-Bi$_2$MoO$_6$ by the formation of oxygen vacancies in the metal oxygen layers; thus, the compound can be formulated as (Bi$_2$O$_2$)(VO$_{3.5}\pi_{0.5}$), where π was corresponding to the intrinsic oxygen vacancies [6-7].

The Bi$_2$VO$_{5.5}$ goes to several structural transformations and known had several polymorphs, but essentially there were only three main polymorphs, namely α, β, and γ-Bi$_2$VO$_{5.5}$ with the transformations: $\alpha \rightarrow \beta$ at 720 K and $\beta \rightarrow \gamma$ at 840 K. The structures of α and

β-phases were more ordered, larger in unit cell and had lower conductivity. At the high temperature, γ-phase was formed and had a conductivity of 0.2 Scm⁻¹ at 943 K [6]. The γ-$Bi_2VO_{5.5}$ can be stabilized by partial substitution of V^{5+} with other metal cations (ME) [8-9]. The substitution does not only stabilize the structure but also increases ionic conductivity due to the creation of vacancies [10-11]. Therefore, the computational simulation carried out in this study was the gamma phase of $Bi_2VO_{5.5}$ and BIMEVOX (ME = Cu^{2+}, Ga^{3+}, and Ta^{5+}).

The experimental results of BIMEVOX compounds showed the contribution of electrons that affected BIMEVOX conductivity [12]. Moreover, the texture of compounds, surface conditions, pore existence, and the presence of impurities affect ionic conductivity. A single phase of BITAVOX could not be obtained by synthesis [13]. Dereeper et al. reported that BITAVOX conductivity increases with the increase in Ta dopant concentration. BIGAVOX had a smaller conductivity due to the contribution of electron conductivity [13]. Therefore, the single phase of the gamma-$Bi_2VO_{5.5}$ and BIMEVOX (Cu^{2+}, Ga^{3+}, and Ta^{5+}) through computational modeling and simulation was important to be conducted to predict the possibility of ease of migration of oxygen ions without the presence of electron conductivity.

Experimental studies on the oxide ionic conductivity of BIMEVOX have been reported elsewhere [14]. However, the experimental study could not reveal the detail of the mechanism of oxide ion conductivity and the role of dopant in the BIMEVOX on the structural properties. Computational studies could be used to study many material properties efficiently in order to save time and cost as well as to provide more detail mechanisms at the atomic level. Some computation study on the layered structure of Aurivillius phases similar to BIMEVOX has been carried out and reported [15-16]. It could reveal defect energies and maximum dopant concentrations in Aurivillius as ferroelectric material. From our best knowledge, the computational study on BIMEVOX was not reported yet.

Here, we report the computational study on BIMEVOX and its parent structure that cover the trajectory of ionic oxide in γ-$Bi_2VO_{5.5}$ and defect energy of BIMEVOX. The study was aimed to investigate the oxide ion pathways that were possible in the V^{5+} coordination environments of γ-$Bi_2VO_{5.5}$ as well as to predict dopant concentrations of Cu^{2+}, Ga^{3+}, and Ta^{5+} that give the higher ionic conductivity. Subsequently, transport properties and activation energy of migration of oxygen ions of the parent compound and BIMEVOX (ME = Cu^{2+} and Ta^{5+}), which were predicted to have the highest ionic conductivity, were simulated using the molecular dynamics method. Those dopants were selected because of their ionic radius close to the ionic radius of V^{5+}. This means that the dopant with an ionic radius close to the V^{5+} radius could enhance the conductivity [17].

■ COMPUTATIONAL METHODS

Enthalpy of Oxide Ion Migration

The enthalpies of oxide ion migration of γ-$Bi_2VO_{5.5}$ were calculated by using a computational simulation method that is based on density functional theory (DFT). This simulation used the CASTEP code of Material Studio Modeling from Accerys, series number 3.2.00, in Politecnico di Torino [18]. The methodology for electronic structure calculations in CASTEP is as follows: set of one-electron Schrodinger (Kohn-Sham) equations are solved using the plane-wave pseudopotential approach. The wave functions are expanded in a plane wave basis set defined by the use of periodic boundary condition and Bloch's Theorem. The electron-ion potential is described by means of *ab initio* pseudopotentials within both norm-conserving and ultrasoft formulations. Direct energy minimization schemes are used to obtain self-consistently, the electronic wave functions and its corresponding charge density. Lattice optimization is initially performed using exchange–correlation energy functions of Perdew–Burke–Ernzerhof (GGA-PBE). Structural optimizations were implemented to determine the best functional approximation to perform in examining the enthalpy of γ-$Bi_2VO_{5.5}$ at various oxygen positions of the tetragonal vanadate layer. A k-point grid of 1×1×1 generated using the Monkhorst–Pack method for Brillouin zone sampling with an energy cut-off of 600 eV.

Atomistic simulation and Molecular Dynamic

The main samples used in this simulation were of two types, namely (i) the tetragonal structure of γ-Bi$_2$VO$_{5.5}$ with an I4/mmm space group as reported by Mairesse et al. [17] and (ii) the tetragonal structure of γ-Bi$_2$VO$_{5.5}$ with P1 space group modified from the first structure. The two structures were then doped with a dopant (ME) of Cu, Ga, and Ta to obtain BIMEVOX compounds. In the first structure, the simulation method applied is atomistic simulation using GULP [19]. The simulation aims to calculate defect energy while predicting the ease of migration of oxygen ion in BIMEVOX based on the increase in dopant concentration. Meanwhile, the second structure applied molecular dynamics to determine the property of transport or activation energy of the migration of oxygen ions using the DLPOLY code [20]. Both simulation methods use Buckingham's short range potential defined:

$$\theta_{ij} = A_{ij}exp\left(-\frac{r_{ij}}{\rho_{ij}}\right) - \frac{C_{ij}}{r_{ij}^6} \qquad (1)$$

where A_{ij}, ρ_{ij} and C_{ij} were constant parameters, and r_{ij} was the distance between i and j ions. The first term in Eq. (1) describes short-range repulsion, while the second term shows induced dipole (van der Waals interaction).

Using DL_POLY, different defect concentrations were simulated by creating a supercell of 4×4×4 containing dopant concentrations (10% Cu and 20% Ta) and the respective amount of oxygen vacancies. The simulations were carried out for a step time of 0.0002 ps with an ensemble of constant temperature and volume (NVT) and algorithm of leapfrog that applied to the simulation box of 1088 ions.

Defect Energy of BIMEVOX

Calculation of energy defects in atomistic simulations is performed on the average structure of γ-Bi$_2$VO$_{5.5}$ and BIMEVOX with space group I4/mmm. The energy defect of BIMEVOX was calculated based on the Mott-Littleton method, which divides the crystal lattice into the two regions, namely regions I (inner sphere) and II (outer sphere). Region I is the spherical region surrounding defect, which is clearly in relaxation. Meanwhile, the region II is the outer spherical defect that

has relatively weak force, which is interpreted with the quasi-continuum approximation method. In this way, the lattice relaxation can be modelled effectively, and also the crystal is not as a simple rigid lattice where the diffusion of ions occurs. If the force on the region II is small, it can be assumed that the response of ions in this region is pure harmonic. There are two kinds of defects, namely impurity, and vacancy defects. Impurity defect with a defect center of V^{5+} is substituted partially with dopants of Cu^{2+}, Ga^{3+}, and Ta^{5+}, while the defect of oxygen vacancies are intrinsic defect as well as its being created in equatorial position of oxygen, O(3). The concentration of dopants, which substitutes V partially, was compensated by a reduction of concentrations of oxygen, O(3), to neutralize the charge in BIMEVOX structure. Defect energy calculations were performed at concentrations of 5, 10, 15, and 20% for each dopant, except for Ta^{5+} that was also carried out at the concentration of 25 and 30%.

■ **RESULTS AND DISCUSSION**

Geometry optimization of the parent structure, γ-Bi$_2$VO$_{5.5}$, was an initial procedure to check the structure stability. The structure of γ-Bi$_2$VO$_{5.5}$ reported by Mairesse et al. [17], tetragonal, space group I4/mmm, cell unit dimension, a = 3.99176(4), b = 3.99176(4), and c = 15.4309(3) Å was used as a starting model. The mean V–O octahedron was encaged between eight Bi sites. However, due to the O(2) and O(3) split-sites, it was observed that there were several short O–O contacts; these preclude simultaneous occupation of many of these O sites, as shown in Fig. 1.

In fact, the V–O environment, which appears as an octahedron squashed along the c stacking direction, must be viewed as the result of a superimposed polyhedral. Indeed, by selecting appropriate O sites among those drawn, the classical O environments of the V cation are easily recognized as octahedron, tetrahedron, trigonal bipyramid, and tetragonal pyramid with interatomic distances compatible with O atomic size [10]. Therefore, the structure, that has high symmetry and contains oxygen vacancy, can be represented using by space group P1 that had no symmetry, as shown in Fig. 2.
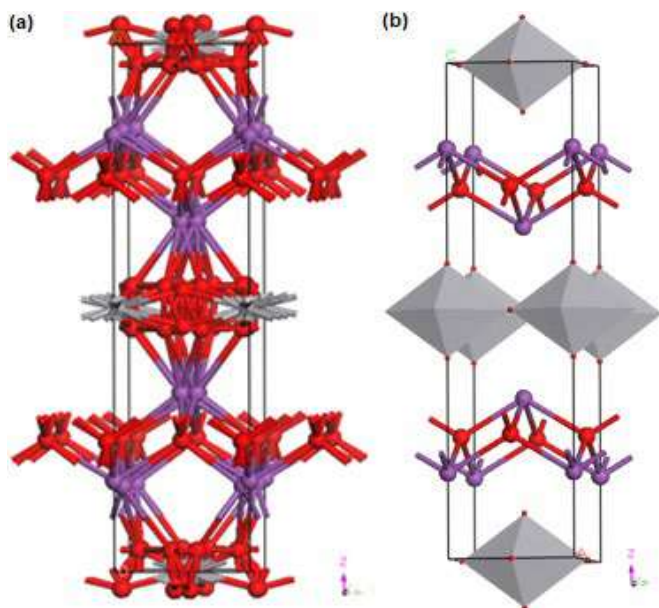
Fig 1. The crystal structures of $Bi_2VO_{5.5}$, (a) average crystallography structure, and (b) the refined structure oxygen vacancies were shown as oxygen atoms

Fig 2. The one possibility of a structure that has V - O tetrahedral environment with oxygen vacancy in the equatorial site

The structure in Fig. 2 was one of the models of structure γ-$Bi_2VO_{5.5}$, showing a special vanadium-oxygen anions coordination environment. The structure that is simulated based on DFT indicates that the coordination environment of V cations by O(3) and oxygen vacancy are in good agreement with the crystallography site of γ-$Bi_2VO_{5.5}$ structure, as depicted in Fig. 1(a) and 2. Therefore, the crystal structure (Fig. 2) can be used as a starting structure to determine activation energy that represents oxygen jump and the easiness of ionic conduction.

Pathway of Oxide Ion Migration of $Bi_2VO_{5.5}$

Oxygen ions, which surround the vanadium ions (Fig. 3), could be divided into two types, namely apical site, O(2), and equatorial site, O(3). Geometry optimization results of a γ-$Bi_2VO_{5.5}$ show that the angle that occupied O(3)-V-vacant O(3) against V was 70 degrees, with O(3)-V bond length of 1.72 Å. Throughout this 70 degrees angle, all the different positions of O(3) are optimized to describe oxygen pathways in the equatorial site as shown in Fig. 3.

Based on the result of the optimized geometry of γ-$Bi_2VO_{5.5}$, the enthalpies of O(3) migration were calculated. The O(3) was moved from one position to the other vacant
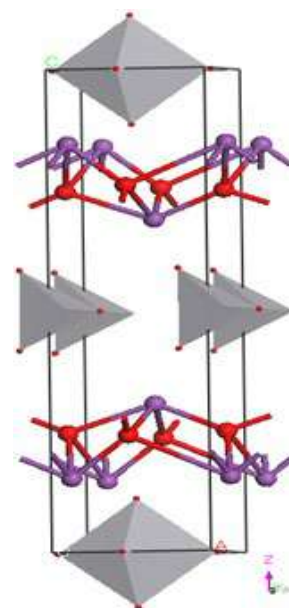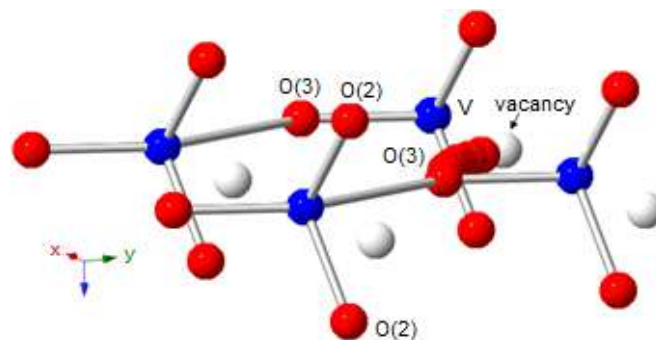

Fig 3. V coordination environments by oxide ions, O(3) equatorial oxygens and O(2) apical oxygens

position. The oxygen position with the highest energy, is in the middle between occupied position (initial position) and vacant position, as shown in Fig. 4.

The calculated activation energy of oxygen pathway was 0.38 eV and is in good agreement with experiment results, as given in Table 1.

Defect Energy of BIMEVOX

The calculation of defect energy was an important step to treat the lattice relaxation of point defect or migrating ion. In this study, the defect energy of BIMEVOX was calculated based on Mott-Littleton method. The number of ions involved in this defect energy

Table 1. Activation energies (eV) of oxygen ion motion in γ-Bi$_2$VO$_{5.5}$ based on this simulation work and these obtained from experiment work
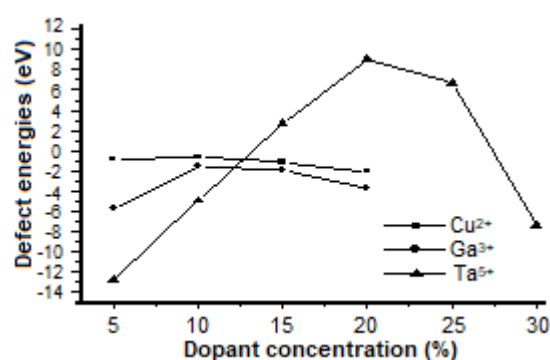
Calculation (this work	Experiment [ref.]	Description
0.384	0.3427 [14]	The temperature of 773 K, the sample obtained from a solid state reaction at sintering temperature of 1073 K for 10 and 12 h
	0.35 [15]	The temperature of 873 K, the sample obtained from a solid state reaction at a sintering temperature of 1113 K for 5 h
	0.4 [21]	High temperature, the sample obtained from solid state reaction at sintering temperature of 1103 k for 24 h
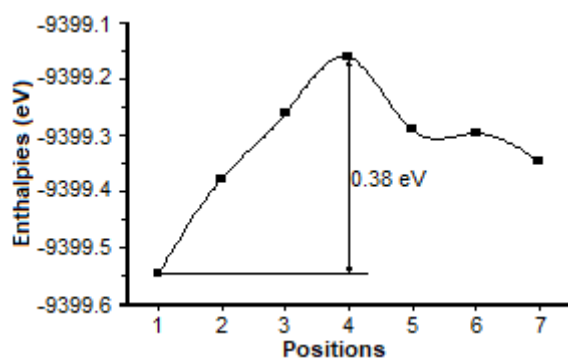
Fig 4. Enthalpies of oxygen migration as a function of the vacancy position in the γ-Bi$_2$VO$_{5.5}$ structure

Fig 5. Energy defect in region II as a function of dopant concentration. BIMEVOX structure was expected to more conductive at a dopant concentration of 10% Cu, 15% Ga, and 20% Ta

calculations was 5,604 ions for the region I and 103,016 ions for region II, with each radius was and 37 Å, respectively. The defect energy calculation results were summarized in Fig. 5.

The results of the defect energy calculations show that the defect energy values of region II vary according to the dopant type and concentration. Energy defect increases up to concentration of 10% for all dopants. However, for Ta^{5+}, defect energy increases with the concentration of up to 20%. This was as expected because of Ta is isovalence to V, with valence = +5. Maximum defect energy values were reached at concentrations of 10% for Cu and Ga, and 20% for Ta, with values of -0.63, -1.57 and 8.98 eV, respectively. BICUVOX and BIGAVOX defect energies are more negative at a concentration of more than 10%, and the BITAVOX defect energies have the highest negative values at concentrations of 5 and 30% Ta. The negative values of defect energy show that the response of ion is pure harmonic and unstable. However, the BIMEVOXes can be synthesized at the concentrations.

Oxygen vacancies can be varied in accordance with

the dopant valence and concentration. The dopant concentration increases the amount of oxygen vacancies in positions O(3). The preference of dopants affects symmetry and connectivity of polyhedral in the perovskite-like layer. Consequently, the performance of ionic conductivity is also expected to significantly depend on the defect structure and the effect of trapping on the diffusion pathway of oxygen [14]. Therefore, a stable structure is achieved when each dopant is at a certain concentration. Based on the defect energy values in this work, the concentration of dopants that stabilized γ-Bi$_2$VO$_{5.5}$ and were predicted to have the highest conductivity are 10% for Cu, 10% for Ga, and 20% for Ta. At these concentrations, the cation polarizability of dopants is predicted to have achieved maximum value so that it facilitates the oxide ion diffusion process in the like-perovskite layers. Again, we predict that sequences of decreasing conductivity of BICUVOX, BIGAVOX, and BITAVOX are 10>15>20% for Cu; 10>15>20% for

Ga; and 20>25>15>30% for Ta, respectively, as Fig. 5. These are in agreement with the experimental results reported by Kant et al., Lazure et al., and Murasheva et al. [22-24]. At concentrations of more than 10% Cu, the ionic conductivity of BICUVOX decreases with the increasing vacancy because in its like-perovskite volume increase.

Concentration value of 10% Cu in this study is in good agreement with experimental results reported by Kant et al. [22] which showed the stable structure of BICUVOX at 10%, which has a grain pattern and uniform in size with adequate porosity, compared to the concentrations of 15 and 20%. Concentration of 20% Ta also in good agreement with the experimental results reported by Lazure et al., which states that the best conductivity for BITAVOX achieved at a concentration of 20% Ta [23]. BIGAVOX has also the highest conductivity at a concentration of 10% Ga for the gamma phase. According to Kant et al., BIGAVOX has the highest conductivity at 10% for a beta phase, not the gamma phase [12]. While according to Murasheva et al. BIGAVOX phase was gamma at 10% Ga with more uniform grain [24].

Property of Transport and Activation Energy of BIMEVOX

Molecular dynamics simulations of $Bi_2VO_{5.5}$ starting with geometry optimization of the supercell (4×4×4) of $Bi_2VO_{5.5}$ using DLPOLY. In the perovskite layers of the supercell $Bi_2VO_{5.5}$, coordinations of V–O were 4 and 6 that arranged alternately between the bismuth layers (Fig. 6(a)). Coordination 4 of V–O (Fig. 6(c)) is square planar, and the coordination 6 is regular octahedral (Fig. 6). Since the superstructure is optimized, the ions were distorted in layers of bismuth and perovskite layer as shown in Fig. 6(d). The square planar of V–O turn
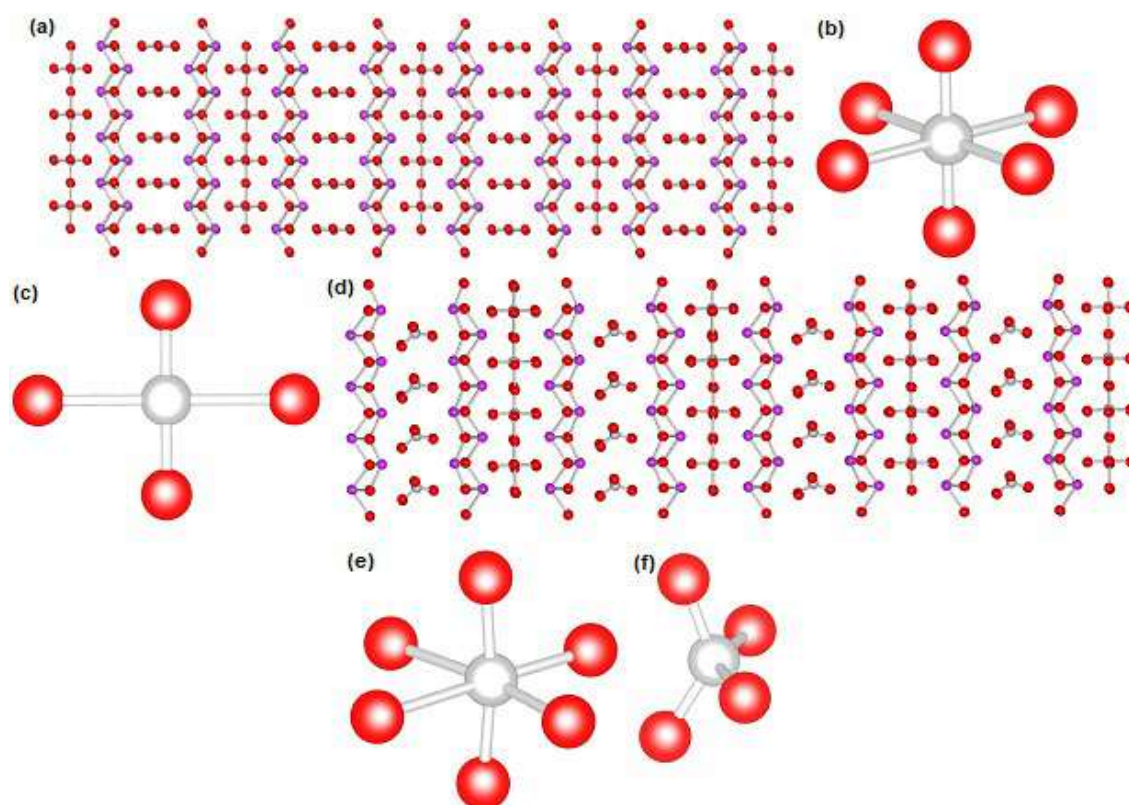
Fig 6. Super cell structure (4×4×4) $Bi_2VO_{5.5}$: (a) before optimization and (d) after optimization using DLPOLY code. In the perovskite-like layer, flat rectangular coordination (c) of the V–O has been changed into tetrahedral coordination (f), and the regular octahedral coordination (b) experienced distorted octahedral coordination (e). In an optimized structure, the ions in the bismuth layer are also distorted

into tetrahedral coordination (Fig. 6(f)), and the octahedral coordination is distorted (Fig. 6(e)). Therefore, the results of the supercell optimization of $Bi_2VO_{5.5}$ in accordance with the expected structure, which is also very similar to the results of the optimization of the unit cell $Bi_2VO_{5.5}$ using the DFT method.

The successful optimization of the $Bi_2VO_{5.5}$ supercell using DLPOLY has proven that this works well, and the short range potential of Buckingham between ions was also correct. Therefore, DLPOLY can be used to perform geometry optimization and molecular dynamics simulations of $Bi_2VO_{5.5}$. Furthermore, the transport properties (through molecular dynamics simulations) of $Bi_2VO_{5.5}$ studied by creating a supercell structure with VO coordinations were coordination mixtures of tetrahedral, coordination five, and octahedral. The coordination mixtures were representative to show the transport properties of the $Bi_2VO_{5.5}$ compound.

Molecular dynamics (MD) simulation were carried out on γ-$Bi_2VO_{5.5}$ and BIMEVOX that were predicted the easiest migration of oxygen ions as atomistic simulation results above, namely $Bi_2Cu_{0.1}V_{0.9}O_{5.35}$, $Bi_2Ga_{0.1}V_{0.9}O_{5.4}$, and $Bi_2Ta_{0.2}V_{0.8}O_{5.5}$. Before the MD simulation, the supercells of γ-$Bi_2VO_{5.5}$ and BIMEVOX were optimized first. The optimized structure was controlled at several temperatures to determine the properties of ion transport, such as mean square displacement (MSD) and activation energy. MSD was defined by the formula:

$$MSD_\beta(t) = \frac{1}{N}\sum_{i=1}^{N}\left[r_i(t) - r_i(0)\right]^2 \qquad (2)$$

where $r_i(t)$ was the position of ion i at time t. In a perfect lattice, the MSD of component ions usually ranges from the average value. Meanwhile, in the defect lattice, there were mobile ions, such as O^{2-} in γ-$Bi_2VO_{5.5}$, where MSD increases over time. Fig. 7 shows the MSD data of the γ-$Bi_2VO_{5.5}$ plotted as a function of time at temperatures of 500, 700 and 1100 K. This shown that there were migrating oxide ions, where the temperature rise was followed by an increase in the diffusion of oxide ion.

From the plot of slope MSD can be determined by the diffusion coefficient (D_β) using correlation:

$$MSD_\beta(t) = 6D_\beta(t) - MSD_\beta(0) \qquad (3)$$

where $MSD_\beta(0)$ was an atomic vibration factor arising from ion vibrations. The calculation of the diffusion coefficient at the three temperatures specified in Fig. 8. The calculation can be evaluated for the activation of ion migration using the Arrhenius relationship.

Based on the Arrhenius plot (ln D vs. 1/T) above, the activation energy obtained is 0.19 eV. This value was a value commonly found in experiments, as reported by Joubert et al. [25].

MSD of $Bi_2Cu_{0.1}V_{0.9}O_{5.35}$ increases with increasing temperature as shown in Fig. 9. This indicated that the diffusion of oxide ions increases with increasing temperature. At a temperature of 500, 773 and 823 K, the MSD plot rises to a straight line compared to the MSD plot

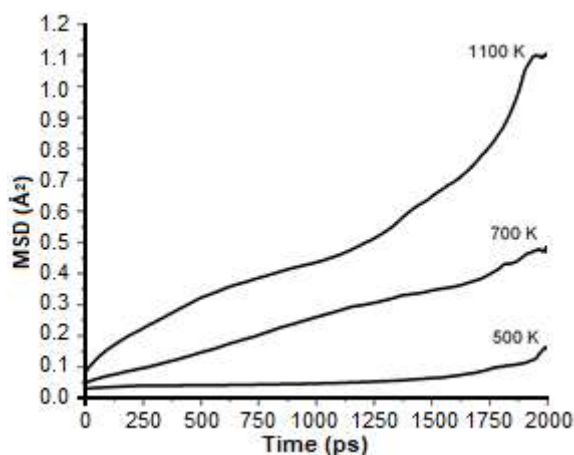**Fig 7.** MSD of the oxide ions of γ-$Bi_2VO_{5.5}$ at temperatures of 500, 700, and 1100 K. The MSD receives an increase in temperature, which indicates that the diffusion of oxide ions also increases
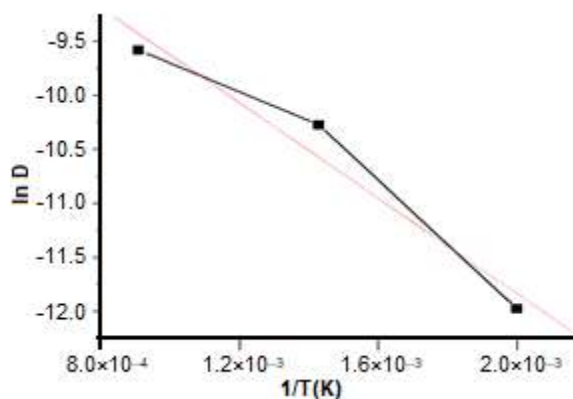

Fig 8. Plot ln D vs. 1/T for oxide ions of γ-$Bi_2VO_{5.5}$

at 873 K. At 873 K, the oxide ion migration rises rapidly to the timestep 160 ps, then the migration rises slowly to 480 ps, as shown in MSD with lines that are not straight (curved). At the timestep 160–480 ps, the migration of oxide ions was estimated to pass through the obstruction area. This kind of thing is observed in the migration of sodium ions of zeolites [26].

The diffusion coefficient of $Bi_2Cu_{0.1}V_{0.9}O_{5.35}$ at some temperatures was shown in Fig. 9. Based on this graph, the ion activation energy of $Bi_2Cu_{0.1}V_{0.9}O_{5.35}$ was 0.21 eV. This energy value was in accordance with the results of experiments reported by Guillodo et al. [27], but different from those reported by Krok et al. [28] and Simner et al. [29] as shown in Table 2. This difference can be caused by different synthesis methods.

The oxide ion MSD of $Bi_2Ta_{0.2}V_{0.8}O_{5.5}$ also increases with temperature rise (Fig. 10). Based on the plot of ln (oxide ion diffusion coefficient) on I/T (Fig. 10), the activation energy of the calculation result is 0.10 eV. Ion oxide MSD of $Bi_2Ta_{0.2}V_{0.8}O_{5.5}$ also increased with an increase in temperature. Based on the plot of ln (oxide ion

diffusion coefficient) versus I/T, the activation energy was 0.10 eV.

This activation energy was smaller than the activation energy calculated from γ-$Bi_2VO_{5.5}$ and $Bi_2Cu_{0.1}V_{0.9}O_{5.35}$. This indicated that the conductivity of the $Bi_2Ta_{0.2}V_{0.8}O_{5.5}$ was greater than the conductivity of the two types of compounds.

The addition of dopant partially to the parent compound (γ-$Bi_2VO_{5.5}$) gives rise to environmental irregularities in the vanadate layer, which can inhibit oxygen migration. The irregularity is caused by different size of vanadium (V^{5+} = 0.54 Å) with dopants (Cu^{2+} = 0.73 Å; Ga^{3+} = 0.62 Å; Ta^{5+} = 0.64 Å) and increase of oxygen vacancy due to substitution of V^{5+} partially by Cu^{2+}

Table 2. The activation energy of $Bi_2Cu_{0.1}V_{0.9}O_{5.35}$ based on the experimental results

Activation Energies (eV)	References
0.48	Krok et al. [28]
0.52	Simner et al. [29]
0.20	Guillodo et al. [27]
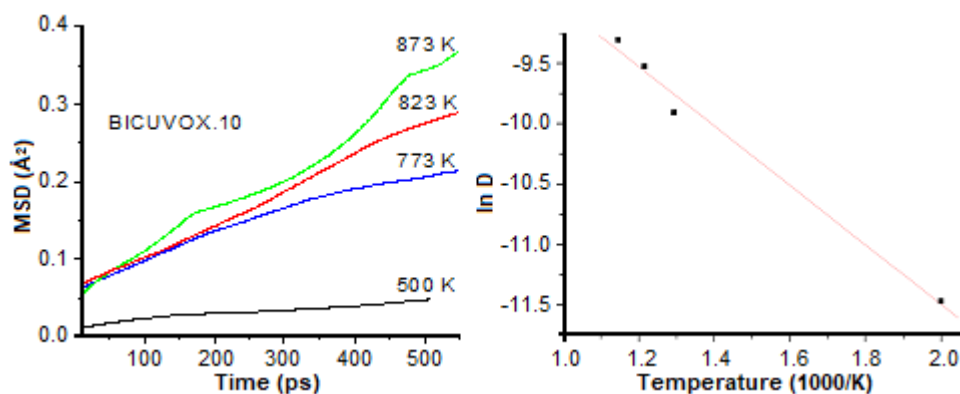
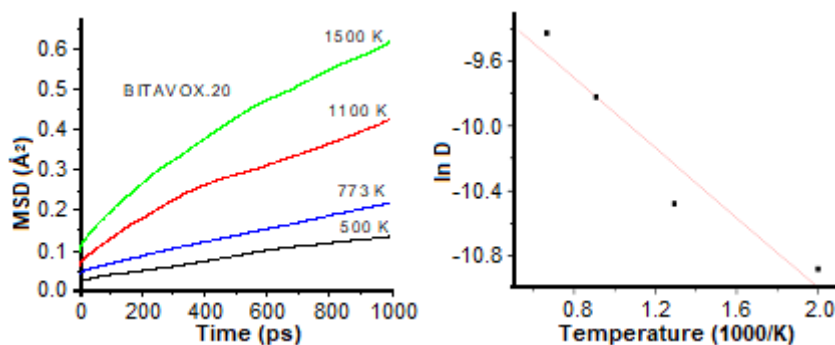**Fig 9.** MSD and Plot of ln D vs. 1/T of oxide ion of $Bi_2Cu_{0.1}V_{0.9}O_{5.35}$

Fig 10. Oxide ion MSD and ln D vs. I/T plot of $Bi_2Ta_{0.2}V_{0.8}O_{5.5}$

and Ga^{3+}. On the contrary, doping with Ta^{5+} does not add a vacancy because of Ta is isovalent with V.

The vacancy can cause a strong attraction between vacancies and V/dopants, thus increasing the activation energy of the migration of oxygen ion. The non-spherical d orbitals of Cu, with the configuration $3d^9$, also cause the vanadium environment to be distorted and can act as a trapping center in the process of oxygen ion migration.

Polarization of cations to oxygen ions can facilitate the hopping of oxygen ion to the vacancy site. This happens because the electron cloud of the oxide ion was pulled by the cation so that the oxide ion was easily moved from the site of the lattice. The polarization of the cations to the oxide ions that are getting stronger will further facilitate the oxide ions to migrate in the crystal lattice. Ta^{5+} cations, theoretically, will be stronger at polarizing oxide ions compared to Ga^{3+} and Cu^{2+} cations, because Ta^{5+} has a greater charge density. As a result, qualitatively it can be predicted that at the same concentration, the increase of ionic conductivity is BICUVOX<BIGAVOX< BITAVOX.

■ CONCLUSION

Computational simulation of ionic conductivity of BIMEVOX and γ-$Bi_2VO_{5.5}$ performed using DFT, Mott-Littleton method, and molecular dynamics simulation. The obtained enthalpy for γ-$Bi_2VO_{5.5}$ close to experimental results. Defect simulation using the Mott-Littleton method showed 10% Cu^{2+}, 10% Ga^{3+}, and 20% Ta^{5+}, where the highest ionic conductivity was in good agreement with the experiment results. The results of the molecular dynamics simulation showed that the activation energies of oxide ion migration in γ-$Bi_2VO_{5.5}$ and BIMEVOX (ME = Cu and Ta close to experimental values. The addition of oxygen vacancy at γ-$Bi_2VO_{5.5}$ due to doping with aliovalent dopants, such as Cu and Ga, causes disordering polyhedral in the vanadate layer where oxygen ion migration takes place. In contrast, ordering polyhedral due to the inclusion of isovalent dopants such as Ta causes easier ion migration. To synthesize BIMEVOX compounds that are expected to have high ion conductivity, the concentrations of aliovalent and aliovalent dopants are 10% and 20%, respectively.

■ REFERENCES

[1] Cho, H.S., Sakai, G., Shimanoe, K., and Yamazoe, N., 2005, Preparation of BiMeVOx (Me= Cu, Ti, Zr, Nb, Ta) compounds as solid electrolyte and behavior of their oxygen concentration cells, *Sens. Actuators, B*, 109 (2), 307–314.

[2] Chmielowiec, J., Paściak, G., and Bujło, P., 2008, Ionic conductivity and thermodynamic stability of La-doped BIMEVOX, *J. Alloys Compd.*, 451 (1-2), 676–678.

[3] Khaerudini, D.S., Guan, G., Zhang, P., Hao, X., and Abudula, A., 2014, Prospects of oxide ionic conductivity bismuth vanadate-based solid electrolytes, *Rev. Chem. Eng.*, 30 (6), 539–551.

[4] Tripathy, D., Saikia, A., and Pandey, A.C., 2019, Effect of simultaneous Ti and Nb doping on structure and ionic conductivity of $Bi_2V_{1-x}Ti_{x/2}Nb_{x/2}O_{5.5-\delta}$ (0.1≤ x≤ 0.25) ceramics, *Ionics*, 25 (5), 2221–2230.

[5] Tripathy, D., and Pandey, A., 2018, Structural and impedance studies of Ti^{IV} and Nb^V co-doped bismuth vanadate system, *J. Alloys Compd.*, 737, 136–143.

[6] Pernot, E., Anne, M., Bacmann, M., Strobel, P., Fouletier, J., Vannier, R.N., Mairesse, V.G., Abraham, F., and Nowogrocki, G., 1994, Structure and conductivity of Cu and Ni-substituted $Bi_4V_2O_{11}$ compounds, *Solid State Ionics*, 70-71, 259–263.

[7] Abrahams, I., Krok, F., Malys, M., and Bush, A.J., 2001, Defect structure and ionic conductivity as a function of thermal history in BIMGVOX solid electrolytes, *J. Mater. Sci.*, 36 (5), 1099–1104.

[8] Rusli, R., Abrahams, I., Patah, A., Prijamboedi, B., and Ismunandar, 2014, Ionic conductivity of $Bi_2Ni_xV_{1-x}O_{5.5-3x/2}$ (0.1 ≤ x ≤ 0.2) oxides prepared by a low temperature sol-gel route, *AIP Conf. Proc.*, 1589 (1), 178.

[9] Abraham, F., Boivin, J.C., Mairesse, G., and Nowogrocki, G., 1990, The BIMEVOX series: A new family of high performances oxide ion conductors, *Solid State Ionics*, 40-41, 934–937.

[10] Abrahams, I., and Krok, F., 2002, Defect chemistry of the BIMEVOXes, *J. Mater. Chem.*, 12 (12), 3351–3362.

[11] Khaerudini, D.S., Guan, G., Zhang, P., Hao, X., Kasai, Y., Kusakabe, K., and Abudula, A., 2014, Structural and conductivity characteristics of $Bi_4Mg_xV_{2-x}O_{11-\delta}$ ($0 \leqslant x \leqslant 0.3$) as solid electrolyte for intermediate temperature SOFC application, *J. Alloys Compd.*, 589, 29–36.

[12] Kant, R., Singh, K., and Pandey, O.P., 2010, Structural, thermal and transport properties of $Bi_4V_{2-x}Ga_xO_{11-\delta}$ ($0 \leq x \leq 0.4$), *Ionics*, 16 (3), 277–282.

[13] Dereeper, E., Briois, P., and Billard, A., 2017, BITAVOX coatings obtained by reactive magnetron sputtering: Influence of thickness and composition, *Solid State Ionics*, 304, 7–12.

[14] Kant, R., Singh, K., and Pandey, O.P., 2008, Synthesis and characterization of bismuth vanadate electrolyte material with aluminium doping for SOFC application, *Int. J. Hydrogen Energy*, 33 (1), 455–462.

[15] Krok, F., Abrahams, I., Zadrożna, A., Małys, M., Bogusz, W., Nelstrop, J.A.G., and Bush, A.J., 1999, Electrical conductivity and structure correlation in BIZNVOX, *Solid State Ionics*, 119 (1-4), 139–144.

[16] Mairesse, G., 1999, Advances in oxygen pumping concept with BIMEVOX, *C. R. Acad. Sci. IIC: Chim.*, 2 (11-13), 651–660.

[17] Mairesse, G., Roussel, P., Vannier, R.N., Anne, M., Pirovano, C., and Nowogrocki, G.L., 2003, Crystal structure determination of α, β and γ-$Bi_4V_2O_{11}$ polymorphs. Part I: γ and β-$Bi_4V_2O_{11}$, *Solid State Sci.*, 5 (6), 851–859.

[18] Payne M.C., and TCM group in Cambridge, 2005, *CASTEP of Material Studio Modeling from Accerys*, series number 3.2.00, with consumer is Politecnico di Torino.

[19] Gale, J.D., 1997, GULP: A computer program for the symmetry-adapted simulation of solids, *J. Chem. Soc., Faraday Trans.*, 93 (4), 629-637.

[20] Todorov, I.T., Smith, W., Trachenko, K., and Dove, M.T., 2006, DL_POLY_3: New dimensions in molecular dynamics simulations *via* massive parallelism, *J. Mater. Chem.*, 16 (20), 1911–1918.

[21] Voronkova, V.I., Yanovskii, V.K., Kharitonova, E.P., and Rudnitskaya, O.G., 2005, Superionic conductors in the Bi_2WO_6-$Bi_2VO_{5.5}$ system, *Inorg. Mater.*, 41 (7), 760–765.

[22] Kant, R., Singh, K., and Pandey, O.P., 2009, Microstructural and electrical behavior of $Bi_4V_{2-x}Cu_xO_{11-\delta}$ ($0 \leq x \leq 0.4$), *Ceram. Int.*, 35 (1), 221–227.

[23] Lazure, S., Vernochet, C., Vannier, R.N., Nowogrocki, G., and Mairesse, G., 1996, Composition dependence of oxide anion conduction in the BIMEVOX family, *Solid State Ionics*, 90 (1-4), 117–123.

[24] Murasheva, V.V., Fortalnova, E.A., Politova, E.A., Politova, E.D., Safronenko, M.G., Stefanovich, S.Y., and Venskovskii, N.U., 2008, Phase transitions in the BIMEVOX solid solutions with Me = Ga, Zr, *Mater. Sci. Forum*, 587-588, 114–117.

[25] Joubert, O., Jouanneaux, A., Ganne, M., Vannier, R.N., and Mairesse, G., 1994, Solid phase synthesis and characterization of new BIMEVOX series: $Bi_4V_{2-x}M_xO_{11}$ (M = Sb^v, Nb^v), *Solid State Ionics*, 73 (3-4), 309–318.

[26] Ramsahye, N.A., and Bell, R.G., 2005, Cation mobility and the sorption of chloroform in zeolite NaY: Molecular dynamics study, *J. Phys. Chem. B*, 109 (10), 4738–4747.

[27] Guillodo, M., Bassat, J.M., Fouletier, J., Dessemond, L., and Del Gallo, P., 2003, Oxygen diffusion coefficient and oxygen exchange coefficient of BIMEVOX.10 (ME = Cu, Co) ceramic membranes, *Solid State Ionics*, 164 (1-2), 87–96.

[28] Krok, F., Bogusz, W., Kurek, P., Wasiucionek, M., Jakubowski, W., and Dygas, J., 1993, Influence of preparation procedure on some physical properties of BICUVOX, *Mater. Sci. Eng., B*, 21 (1), 70–76.

[29] Simner, S.P., Suarez-Sandoval, D., Mackenzie, J.D., and Dunn, B., 1997, Synthesis, densification, and conductivity characteristics of BICUVOX oxygen-ion-conducting ceramics, *J. Am. Ceram. Soc.*, 80 (10), 2563–2568.

Determination of Total Phenolic Content and NIR-Chemometrics Classification Model of Queen and Local Varieties of Soursop (*Annonamuricata* L.) Leaf Powder

Lestyo Wulandari[*], Mellda Kusuma Candra Dewi, Nia Kristiningrum, and Raden Ajeng Yashinta Nirmala Siswanti

Faculty of Pharmacy, University of Jember, Jl. Kalimantan 37, Jember 68121, East Java, Indonesia

Abstract: *The leaves of soursop (Annonamuricata L.) are commonly used for health because of their antioxidant activity from its highest phytochemical content, namely phenolic compound, which is influenced by the varieties of this plant. In Indonesia, there are two soursop varieties, namely 'queen' and 'local' varieties which are difficult to determine morphologically. The aim of this study was to determine the total phenolic content of soursop leaves of both varieties and to establish a classification model of NIR spectroscopy combined with chemometrics for the identification of the varieties of soursop leaves. After the soursop leaves were dried and grinded, they were then scanned to obtain the spectra of NIR spectroscopy. NIR spectras were combined with chemometrics to classify the varieties of the soursop. The classification models used were Linear Discriminant Analysis (LDA), Support Vector Machines (SVM) and Soft Independent Modelling of Class Analogies (SIMCA). Total phenolic content of the soursop leaves was determined by UV-Vis spectroscopy using Folin-Ciocalteau reagent and gallic acid as reference. The result showed that the local variety had higher total phenolic content than the queen variety. NIR spectroscopy combined with chemometrics was able to classify the varieties of soursop leaves with 100% accuracy using LDA and SVM.*

Keywords: Annonamuricata *L.; phenolic total; NIR; chemometrics*

■ INTRODUCTION

Soursop plants are widely used for traditional medicine, especially the leaves [1]. A previous study reported that soursop leaves have antioxidant activity [2], which has a role in health related activities [3]. The highest phytochemical content in soursop leaves is phenolic compounds [4], which is considered as the major phytochemical responsible for the antioxidant activity [5], so it is necessary to determine the total phenolic content of the soursop leaves. Many factors influence phytochemical content, one of which is the plant varieties [6]. There are two varieties of soursop that grow in Indonesia, namely 'queen' and 'local' varieties. The queen variety has a sweet fruit flavor, while the local variety has a sour slightly sweet fruit flavor. Both of these varieties are easily identified from the taste of the fruit but are difficult to distinguish if compared morphologically.

The determination of the total phenolic content of two varieties of soursop leaves in this study was performed by UV-Vis spectroscopy with Folin-Ciocalteau reagents and gallic acid standard as reported by some researchers [7-9]. The purpose of determining the total phenolic content is to find out which variety has potentially more phenolic compound. After the variety of the soursop leaves which has potentially more phenolic source was known, then the classification model was determined. The classification model was needed to identify the soursop leaves varieties because it is difficult to identify morphologically. Determination of the classification model was performed by the NIR (Near Infra-Red) spectroscopy and chemometrics. NIR spectroscopy is an effective analysis technique because it is nondestructive, can analyze at high speed, does not cause pollution, uses simple sample preparations and do not require chemicals. However, the spectra data from

NIR spectroscopy is very complicated and overlapping, so chemometrics was used to analyze the spectral data. NIR coupled with chemometrics was used as a rapid analysis method in many studies [10-13]. NIR coupled with chemometrics was also used as high-speed sex identification and sorting of living silkworm pupae [14]. The classification models obtained were validated then the chosen model was applied for the determination of soursop varieties in the real sample. This study used samples in powder form because the preparations commonly used in traditional medicine are powder. The selected and validated classification model was then used to identify the varieties of soursop leaves from the supply of raw materials used for traditional medicines.

■ **EXPERIMENTAL SECTION**

Materials

The materials used in this study were leaves of the queen and local soursop (*Annonamuricata* L.) varieties taken from Jember Regency (6 local and 6 queen), Bondowoso (6 local and 6 queen), Malang (1 local), and Ngawi (1 local), East Java, Indonesia. Reagents were methanol, gallic acid standard (purity-100%, Sigma-Aldrich), Folin-Ciocalteau reagent (Merck), and Na_2CO_3, methanol 98%, and distilled water.

Instrumentation

The instruments used in this study were the Near Infra-Red Brimrose Luminar 3070 spectrophotometer (NIR Industry, France), Brimrose software (Brimrose Corp., USA), The Unscrambler X 10.2 software (CAMO, UK), UV-Vis Hitachi U-1800 spectrophotometer (Hitachi High-Technologies Corp., Japan), oven (Memmert, Germany), analytical balance (Sartorius, Germany), grinder, vials, desiccators, funnels, volumetric flasks, cuvettes, 100 mesh siever, and glassware.

Procedure

Sampling and sample preparation

The samples were divided into training sets and test sets. Training sets were used for making the model and test set samples were used as an independent sample for validating the model. The leaf of the samples used for training and test sets were obtained from Jember Regency (training set QJ1-QJ5 and LJ1-LJ5, test set Queen J sample, and test set Local B sample) and Bondowoso Regency (training set QB1-QB5 and LB1-LB5, test set Queen B sample, and test set Local B sample), while leaves from Malang Regency and Ngawi Regency were used as real samples for testing. The sampling was done based on the simple random sampling technique, it was picked randomly from the gardens belonging to residents in the area. Varieties were verified based on information from the taste of the fruit (sweet for queen varieties and sour for local varieties). The samples were sorted wetly, washed, drily sorted, and then dried. Dry leaves were mashed using a grinder until the powder was obtained, then the powder was sifted to obtain less than 100 mesh leaves powder. Determination of moisture content in the powdered sample was carried out using the gravimetric method. Moisture content determination was carried out by weighing empty vials without covering then as much as 1 g of soursop leaf powder was put in the vial and heated at 105 °C for 1 h then cooled in a desiccator in a closed vial state. After cooling down, the powder was then weighed. Heating with the oven was repeated for 30 min until a constant weight was obtained. Samples were restricted to < 10% of the moisture content. The water content was calculated as followed,

$$\text{Moisture content } (\%) = \frac{A - B}{A} \times 100\%$$

where A is the weight of the initial sample (g) and B is the sample weight after drying by the oven (g) [18].

Determination of total phenolic content using Folin-Ciocalteu reagents

This determination method of total phenolic content was validated by the authors in a previous study [19], the results of the validation are as seen in Table 2. Preparation of sample solutions and standards were carried out. Twenty five milligrams of each soursop leaves powder samples were weighed (replication three times) and dissolved with 98% methanol in a 10.0 mL volumetric flask, and were then filtered. The gallic acid was weighed 20.4 and 25.1 mg, each dissolved with 25.0 mL of 98% methanol in the volumetric flask so that the concentration of the gallic acid solution obtained was at 816 and 1004 μg/mL. Then the standard solution was

further diluted from 816 µg/mL to 8.16, 81.16, 5.02, 20.08, 30.12 and 50.02 µg/mL, 1004 µg/mL to 5.02, 20.08, 30.12, and 50.02 µg/mL by pipetting a certain amount of gallic acid standard solution in a measuring flask and then adding 98% methanol.

Optimization of maximum wavelength and incubation time was carried out using standard gallic acid solution concentration of 81.16 µg/mL added with 500 µL of Folin-Ciocalteu (1:10 v/v water) and 400 µL Na_2CO_3 (7.5 % w/v water). The mixture was then incubated at the incubation time, and the absorbance was measured at a wavelength of 400–800 nm. Determination of total phenolic content was carried out by pipetting 100 µL of each standard solution and the sample solution then added with 500 µL of Folin-Ciocalteu (1:10 v/v water). Then the mixture was incubated for 6 min, and then added with 400 µL Na_2CO_3 (7.5 % w/v water) [15-16]. The mixture was then allowed to stand at room temperature during the incubation time, and later the absorbance was measured at the optimum wavelength.

Spectra acquisition by NIR spectrophotometer

The sample was placed on the sample plate until it was fully filled and the surface was flat (parallel to the surface of the plate), then it was placed on the sample site and the spectra was measured using a NIR spectrophotometer. The sample was scanned 5 times at whole wavelengths (850–2000 nm) and specific wavelengths. Each of the acquisition of the scan was carried out 3 times.

Determination of the classification model and real sample application

The spectra data produced by the NIR spectrophotometer were then analyzed by chemometrics using the Unscrambler X version 10.2 software. The classification model used was a Linear Discriminant Analysis (LDA), Support Vector Machines (SVM) and Soft Independent Modelling of Class Analogies (SIMCA). The results obtained from the chemometric analysis evaluated the ability of the model to distinguish simulation samples into actual categories using % accuracy. The selected model was then validated using two cross-validation techniques, the first technique was Leave-One-Out-Cross-Validation (LOOCV) by taking 1

data set LB1, QB1, LJ1, RJ1 alternately and using the remaining 19 datasets as training sets. The second validation was 2-Fold-Cross-Validation (2FCV) which was performed by using 4 (four) independent samples as test set samples. The ideal model has accuracy value of 100%. After validated, the classification model was used to identify the varieties of real samples. The real samples used were local varieties of soursop leaves from Malang and Ngawi Regency.

■ RESULTS AND DISCUSSION

Preparation and Determining Moisture Content (MC) of Leaves Powder

The grounded powder was sieved in order to ensure uniformed particle size of the powder. This is because particle size can affect the length of light transmission that passes through the sample and affects the reflectance of the NIR spectra [17]. Well-controlled particle size and uniformity of samples are the basis for the formation of a good chemometric model [18]. In this study, 100 mesh was chosen to ensure particle size did not affect the spectra intensity produced. Powder samples sieved with 100 mesh (has particles sized ≤ 149 µm) resulted in spectra that were not affected by particle size [19]. The results of moisture content determination of queen and local varieties of soursop leaves powder were in the range of 3–5% as seen in Table 1.

Table 1 shows that the moisture content of soursop leaves powder was ≤ 10%. This result fulfilled the requirements of the moisture content for traditional medicine products in Indonesia. Moisture content greater than 10% will cause damage by microbes. Another purpose of determining moisture content was to ensure there is no effect on the calculation results of the determination of the total phenolic content and classification model. The spectral reflectance of samples with moisture content more than 10% and less than 10% can be seen in Fig. 1. A researcher has reported that the higher the moisture content, the higher the absorption and the reflectance gets smaller. This is because water consists of hydrogen bonds by hydrogen atoms which are the most powerful atoms absorbing NIR waves [20]. In conclusion, the moisture content was determined in
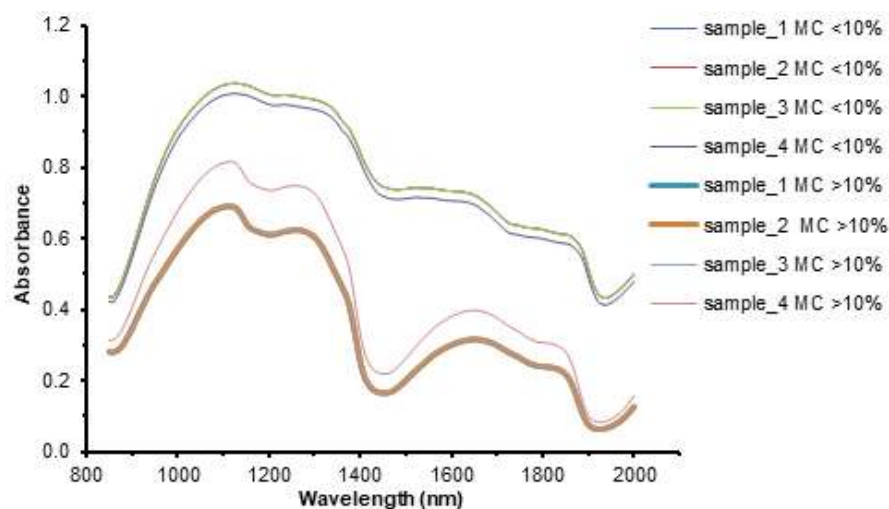
Fig 1. Spectra of samples wet powder with MC > 10% and dry powder with MC < 10%

Table 1. The results of sample moisture content

Code of sample	Water content ± % RSD (n = 3)
QB1	3.53% ± 1.72
QB2	4.07% ± 0.74
QB3	4.31% ± 1.68
QB4	3.85% ± 0.83
QB5	3.71% ± 2.30
QJ1	3.95% ± 2.59
QJ2	3.38% ± 2.14
QJ3	3.77% ± 2.62
QJ4	3.76% ± 2.93
QJ5	3.85% ± 2.34
LB1	4.75% ± 2.23
LB2	4.51% ± 1.26
LB3	4.35% ± 1.76
LB4	4.02% ± 1.74
LB5	4.59% ± 1.10
LJ1	4.86% ± 1.54
LJ2	3.89% ± 1.12
LJ3	4.84% ± 1.76
LJ4	4.60% ± 0.98
LJ5	4.66% ± 2.36
Test set Queen B	4.52% ± 1.84
Test set Queen J	3.64% ± 2.34
Test set Local B	4.48% ± 2.17
Test set Local J	4.76% ± 2.61

the sample to ensure the resulting spectra were not affected by moisture content.

Determination of Total Phenolic Content with Addition of Folin-Ciocalteu Reagents

In this study, gallic acid standards were chosen because it is one of the types of phenolic compound found

Table 2. The results of validation of the UV-Vis spectroscopy method for determination of total phenolic content

Parameter of Validation	Result
Linearity	
Linearity range (n=6)	4.08–12.24 ppm
Correlation coefficient	0.9943
Relative process standard deviation (Vxo)	4.91%
DL	1.13 ppm
QL	3.75 ppm
Precision (RSD, n=3)	0.73%
Accuracy (Recovery, mean ±%RSD)	
30% addition	99.807 ± 1.5
60% addition	98.142 ± 1.0

in soursop leaves [5]. Gallic acid was a recommended reference for the determination of total phenolic using Folin-Ciocalteau reagents [21]. Determination of total phenolic content by UV-Vis spectroscopy using Folin-Ciocalteau (FC) reagents was chosen because it is relatively fast, simple, reliable, and more accurate than other methods such as permanganate oxidation [22-23]. The principle reaction of this method is the reduction of Molybdate (VI) reaction on FC reagents by phenolic ions in the sample to form complex blue compounds that can be measured by UV-Vis spectrophotometer. The UV-Vis spectroscopy method for the determination of total phenolic content in this study was validated. The results of the assessment of validation parameters listed in Table 2 showed that the UV-Vis spectroscopy method

for the determination of total phenolic content was linear, precise, and accurate. 765 nm was chosen as the optimum wavelength because it had the maximum absorbance. In general, when the absorbance is to be measured at a single wavelength, the wavelength with the maximum absorbance is chosen [24]. Based on the research reported by Prior, it was shown that to provide reliable results on the supply of total phenolics with Folin-Ciocalteu reagents, it was recommended to use a wavelength of 765 nm.

The optimum incubation time is the time needed to obtain a steady state absorbance response. The result of the optimization of incubation time for the gallic acid solution, sample solutions of the queen variety) and sample solutions of the local variety were 40, 55 and 80 min, respectively. The longest incubation time (80 min) was applied for all sample solution. This study used six concentrations of standard solutions where the regression of the gallic acid standard curve was $y = 0.0877x + 0.0669$ and $r = 0.9983$. Determination of total phenolic content of soursop leaves powder of queen and local varieties was carried out by measuring the absorbance of each sample solution and then calculating the concentrations with the

standard gallic acid curve. Table 3 and Fig. 2 show the results of the total phenolic content in the samples obtained.

In Table 3 and Fig. 2, the phenolic content of soursop leaves powder clearly showed that the local variety had higher phenolic content than the queen variety at all planting areas. The results obtained showed that the soursop leaves powder of the local variety had more potential phenolic content, where the mean of the total phenolic content for the local variety and the queen variety was 38.478 mg GAE/g and 10.401 mg GAE/g, respectively. In this study, the results of the total phenolic content were varied among samples of the same variety. This is probably due to other factors that affect the total phenolic content of the sample, such as altitude, considering that samples of each varieties were taken in areas with different altitudes. For the local variety samples, LB2 that was taken from the highest location (792 masl) had the highest total phenolic content (54.583 mg/g). Meanwhile, for the queen variety, the highest phenolic content was QB3 which had phenolic content of 21.741 mg GAE/g that was obtained

Table 3. The results of determining the total phenolic content of the sample

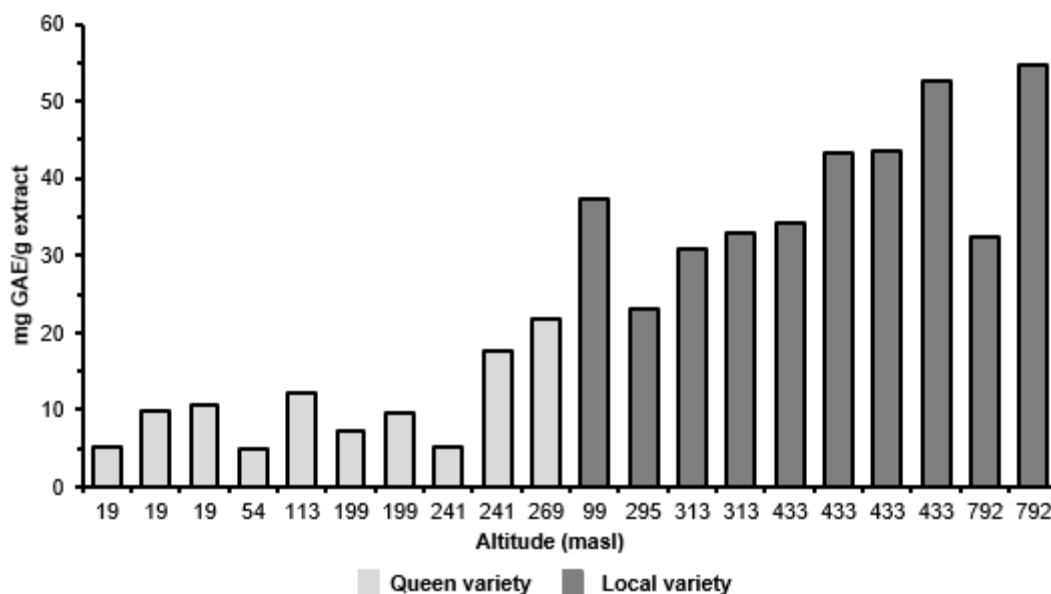| Code of Sample	mg GAE/g powder ± RSD (n = 3)	Altitude (masl)
QJ1	12.08 ± 1.87	113
QJ2	5.15 ± 2.44	19
QJ3	10.75 ± 2.45	19
QJ4	9.95 ± 0.95	19
QJ5	4.89 ± 2.12	54
QB1	5.20 ± 2.33	241
QB2	17.5 ± 1.34	241
QB3	21.7 ± 1.64	269
QB4	9.50 ± 1.67	199
QB5	7.28 ± 2.30	199
LJ1	37.4 ± 0.63	99
LJ2	43.3 ± 0.79	433
LJ3	52.6 ± 1.59	433
LJ4	34.1 ± 0.73	433
LJ5	43.5 ± 2.67	433
LB1	32.3 ± 0.12	792
LB2	54.6 ± 2.68	792
LB3	30.9 ± 2.15	313
LB4	33.0 ± 1.19	313
LB5	23.0 ± 1.57	295

Fig 2. Total phenolic content of queen and local varieties at all plantation area

from a sample taken from an altitude of 269 masl. The higher the place, the higher the stress of the environment, for example, the lower the temperature, the higher the humidity, the lower the intensity of sunlight, and the shorter the duration of irradiation. The stress of temperature, light, humidity, etc. can affect the production of plant secondary metabolites. When experiencing stress, the production of secondary metabolites increases. This is an attempt of plants to fight environmental stress. However, QB5 had total phenolic content lower than QJ1, even though QB5 was obtained from a place which had a higher altitude than QJ1. In addition, samples with the same variety and altitude also resulted in variations of the total phenolic content in LB1 and LB2 samples. This might have occurred because of other factors, namely the nutrients available because macro soil nutrients such as Nitrogen (N), Potassium (K), Organic Ingredients and Carbon (C) organically have a linear relationship with the formation of secondary metabolites [25].

Determination of the Classification Model

Determination of the classification model was performed by scanning the spectra data from each training set. The training set spectras were used to form the chemometric classification model namely LDA, SVM, and SIMCA. Basically, LDA, SVM, and SIMCA have the same working principle as supervised pattern recognition

which has better classification results than unsupervised pattern recognition. Supervised pattern recognition analysts have control over the classification of samples, which means the sample's category is determined previously by the analysts which are referred to as training sets in order to facilitate the process of determining the classification [26]. The three models were used to classify two types of categories, namely the queen and local categories. This category intended to classify samples based on their varieties. The results of the chart mapping of the LDA and SVM classification models are shown in Fig. 3. The accuracy of predictive ability of the LDA, SVM, and SIMCA classification models can be seen in Table 4.

The ability of the classification model can be seen from the percent accuracy of the mapping results of the LDA, SVM, and SIMCA models. Accuracy values showed the ability of the model to grouping simulation of the samples into two categories, namely queen and local. The accuracy of the LDA and SVM models were 100% while the SIMCA model was only 93.33%. The SIMCA model with percent accuracy of 93.33% showed that the SIMCA model that was created based on the PCA model from the training set was not able to group all samples in the correct category. This is because the SIMCA classification model was based on the PCA model.

Table 4. The predictive ability of LDA, SVM, and SIMCA

Model	Predictive ability (% Accuracy)		
	At whole NIR wavelength 850–2000 nm	At specific wavelength	
		850–1100 nm	1600–1650 nm
LDA	100%	91.67%	52.67%
SVM	100%	92.0%	54.33%
SIMCA	93.99%	-	-
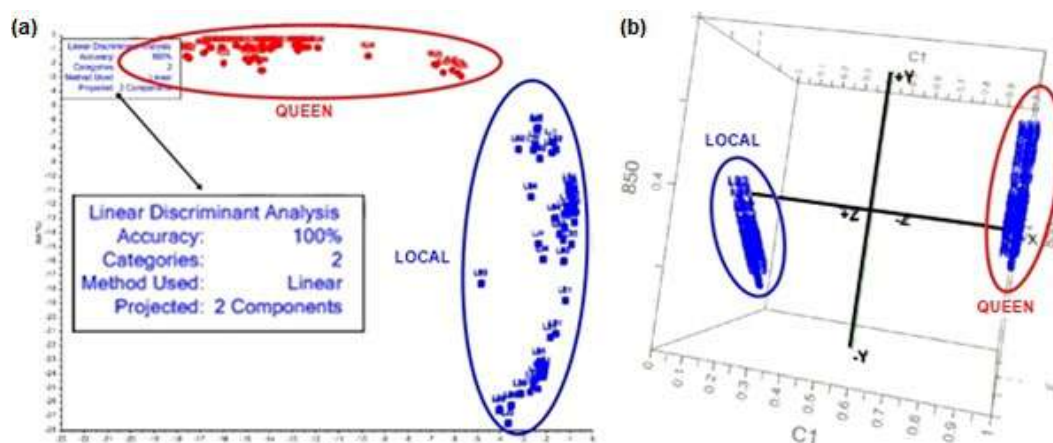
Fig 3. The mapping chart of classification models (a) LDA, (b) SVM
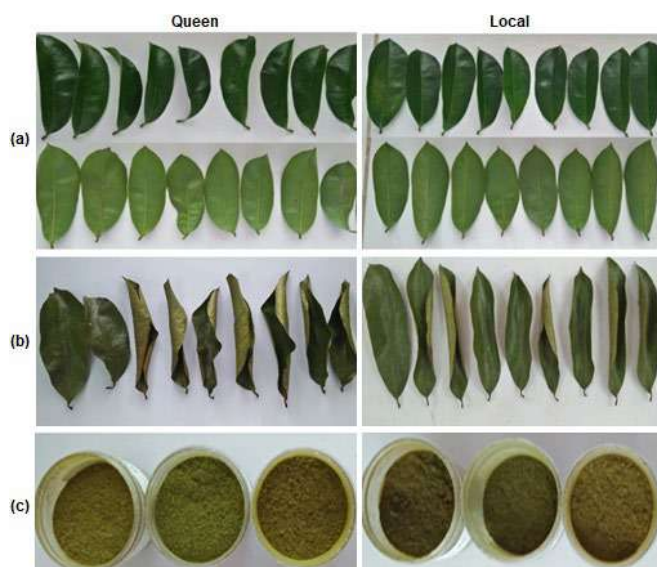
Fig 4. Queen and local soursop leaves (a) on wet, (b) dry, and (c) powder form

The PCA model has a disadvantage in being less optimal in the separation between classes so that the accuracy obtained was less than 100%. The 100% accuracy of the LDA and SVM models showed that the model was able to classify soursop leaves powder in correct varieties with the prediction accuracy of 100%. In this research, the classification models were also carried out at specific wavelengths which have functional groups characteristic of phenol compounds, namely Ar-OH and O-H. However, at these wavelengths, the classification model did not produce 100% accuracy. The accuracy of the LDA and SVM models at specific wavelengths can be seen in Table 4. Both varieties of soursop leaves were difficult to identify on wet and dry leaves, and also in powder form (Fig. 4), so the LDA and SVM classification model can help the identification of the two varieties of soursop leaves. The model's ability to recognize the identity of varieties of the plant can be used to control the quality of raw materials of traditional medicines that utilizes soursop leaves.

Validation of the Selected Classification Model

Cross-validation is a technique for assessing how far a statistical analysis result can be implemented into an independent data set. Cross-validation is used to estimate how accurate the prediction model is and how it is to be implemented. After 100% accuracy of prediction was

Table 5. The results of the model application in the real sample

Sample Codename	The Results of the Category Prediction by the Model (data)				Theoretical Category (data)	
	LDA		SVM			
	Queen	Local*	Queen	Local*	Queen	Local
Local Malang	0	15	0	15	0	15
Local Ngawi	0	15	0	15	0	15

*number of scanned spectra data

obtained, LDA and SVM models were then validated by cross validation. In this study, the validations were Leave-One-Out-Cross Validation and 2-Fold-Cross-Validation, because it has been proven effective for validating the classification chemometric model in previous studies [15,22]. The results of Leave-One-Out-Cross Validation obtained in this study were 100% accurate. This means there was no sample classified in the wrong variety. The 2-fold cross-validation in this study used 4 sample test sets in which their category were already known. The results of 2-fold cross-validation showed there was no sample grouped in the wrong category (100% accurate prediction).

Application on Real Samples

The real sample used was soursop leaves powder of the local variety originating from Malang and Ngawi Regencies. Samples were chosen from outside Jember and Bondowoso Regencies to ensure that the models could be used for determination of the plant varieties of soursop leaves from other planting areas, not only from Jember and Bondowoso Regencies. There were no samples collected from the market because the samples in the market were not attached with information on the raw material of the soursop leaves varieties. The classification model was able to predict correctly all varieties of the soursop leaves powder samples from Malang and Ngawi Regencies (100% correct prediction). The results of the model application in the real samples can be seen in Table 5, in which all spectra data of each real sample was categorized as the local variety.

CONCLUSION

The local variety of the soursop leaves has more potential as a source of total phenolic compound with an average content of 38.478 mg GAE/g, while the queen variety has an average content of 10.401 mg GAE/g. NIR and chemometric methods (LDA and SVM) can be used to classify queen and local varieties of soursop leaves powder.

REFERENCES

[1] Muizuddin, M., and Zubaidah, E., 2015, Studi aktivitas antibakteri kefir teh daun sirsak (*Annona muricata* Linn.) dari berbagai merk teh daun sirsak di pasaran, *Jurnal Pangan dan Agroindustri*, 3 (4), 1662–1672.

[2] Justino, A.B., Miranda, N.C., Franco, R.R., Martins, M.M., DaSilva, N.M., and Espindola, F.S., 2018, *Annona muricata* Linn. leaf as a source of antioxidant compounds with in vitro antidiabetic and inhibitory potential against α-amylase, α-glucosidase, lipase, non-enzymatic glycation and lipid peroxidation, *Biomed. Pharmacother.*, 100, 83–92.

[3] Roduan, M.R.M., Hamid, R.A., Sulaiman, H., and Mohtarrudin, N., 2017, *Annona muricata* leaves extracts prevent DMBA/TPA-induced skin tumorigenesis via modulating antioxidants enzymes system in ICR mice, *Biomed. Pharmacother.*, 94, 481–488.

[4] Minari, J.B., and Okeke, U., 2014, Chemopreventive effect of *Annona muricata* on DMBA-induced cell proliferation in the breast tissues of female albino mice, *Egypt. J. Med. Hum. Genet.*, 15 (4), 327–334.

[5] Coria-Téllez, A.V., Montalvo-Gónzalez, E., Yahia, E.M., and Obledo-Vázquez, E.N., 2018, *Annona*

muricata: A comprehensive review on its traditional medicinal uses, phytochemicals, pharmacological activities, mechanisms of action and toxicity, *Arabian J. Chem.*, 11 (5), 662–691.

[6] Chang, X., Ye, Y., Pan, J., Lin, Z., Qiu, J., Guo, X., and Lu, Y., 2018, Comparative assessment of phytochemical profiles and antioxidant activities in selected five varieties of wampee (*Clausena lansium*) fruits, *Int. J. Food Sci. Technol.*, 53 (12), 2680–2686.

[7] Toledo-Martín, E.M., Font, R., Obregón-Cano, S., De Haro-Bailón, A., Villatoro-Pulido, M., and Del Río-Celestino, M., 2017, Rapid and cost-effective quantification of glucosinolates and total phenolic content in rocket leaves by visible/near-infrared spectroscopy, *Molecules*, 22 (5), 851.

[8] Aleixandre-Tudo, J.L., and du Toit, W., 2019, "The role of UV-Visible spectroscopy for phenolic compounds quantification in winemaking" in *Frontiers and New Trends in the Science of Fermented Food and Beverages*, Eds. Solis-Oviedo, R.L., IntechOpen, London.

[9] Sasikala, S., and Radhaisri, S., 2017, Analysis of total phenol in developed nutraceutical by UV-VIS spectrophotometry, *Int. J. Sci. Res.*, 6 (11), 513–517.

[10] Jimenez, R., Molina, L., Zarei, I., Lapis, J.R., Chavez, R., Cuevas, R.P.O., and Sreenivasulu, N., 2019, Method development of near-infrared spectroscopy approaches for nondestructive and rapid estimation of total protein in brown rice flour, *Methods Mol. Biol.*, 1892, 109–135.

[11] Su, W.H., Bakalis, S., and Sun, D.W., 2019, Chemometrics in tandem with near infrared (NIR) hyperspectral imaging and Fourier transform mid infrared (FT-MIR) microspectroscopy for variety identification and cooking loss determination of sweet potato, *Biosyst. Eng.*, 180, 70–86.

[12] Ferreiro-González, M., Espada-Bellido, E., Guillén-Cueto, L., Palma, M., Barroso, C.G., and Barbero, G.F., 2018, Rapid quantification of honey adulteration by visible-near infrared spectroscopy combined with chemometrics, *Talanta*, 188, 288–292.

[13] Kutsanedzie, F.Y.H., Chen, Q., Hassan, M.M., Yang, M., Sun, H., and Rahman, M.H., 2018, Near infrared system coupled chemometric algorithms for enumeration of total fungi count in cocoa beans neat solution, *Food Chem.*, 240, 231–238.

[14] Zhu, Z., Yuan, H., Song, C., Li, X., Fang, D., Guo, Z., Zhu, X., Liu, W., and Yan, G., 2018, High-speed sex identification and sorting of living silkworm pupae using near-infrared spectroscopy combined with chemometrics, *Sens. Actuators, B*, 268, 299–309.

[15] Wulandari, L., Siswanti, R.A.Y.N., and Nugraha, A.S., 2019, Determination of total phenolic content and classification model of local variety soursop (*Annona muricata* L.) leaf powder in different altitudes using NIR and FTIR spectroscopy coupled with chemometrics, *Indones. J. Pharm.*, 30 (1), 7–14.

[16] Keskin-Šašić, I., Tahirović, I., Topčagić, A., Klepo, L., Salihović, M., Ibragić, S., Toromanović, J., Ajanović, A., and Velispahić, E., 2012, Total phenolic content and antioxidant capacity of fruit juices, *Glas. Hem. Tehnol. Bosne Herceg.*, 39, 25–28.

[17] Chang, C.W., Laird, D., Mausbach, M.J., and Hurburgh, C.R., 2001, Near-infrared reflectance spectroscopy principal component regression analyses of soil properties, *Soil Sci. Soc. Am. J.*, 65 (2), 480–490.

[18] Zhu, Z., Chen, S., Wu, X., Xing, C., and Yuan, J., 2018, Determination of soybean routine quality parameters using near-infrared spectroscopy, *Food Sci. Nutr.*, 6 (4), 1109–1118.

[19] Yang, J., Liu, Z., Liu, B., and Zhu, Q., 2012, Determination of *Coptis chinensis*' quality by FT-NIR spectroscopy, *Health*, 4 (4), 196–202.

[20] Agustina, S., Purwanto, Y.A., and Budiastra, I.W., 2015, Prediksi kandungan kimia mangga arumanis selama penyimpanan dengan spektroskopi NIR, *JTEP*, 3 (1), 57–63.

[21] Wulandari, L., Nuri, Retnaningtyas, Y., and Lukman, H., 2016, Analysis of flavonoid in medicinal plant extract using infrared spectroscopy

and chemometrics, *J. Anal. Methods Chem.*, 2016, 4696803.

[22] Prior, R.L., Wu, X., and Schaich, K., 2005, Standardized methods for the determination of antioxidant capacity and phenolics in foods and dietary supplements, *J. Agric. Food Chem.*, 53 (10), 4290–4302.

[23] Khoddami, A., Wilkes, M.A., and Robert, T.H., 2013, Techniques for analysis of plant phenolic compounds, *Molecules*, 18 (2), 2328–2375.

[24] Rouessac, F., and Rouessac, A., 2007, *Chemical Analysis: Modern Instrumentation Methods and Techniques*, 2nd Ed., John Wiley & Sons Ltd, England.

[25] Salim, M., Yahya, Y., Sitorus, H., Ni'mah, T., and Marini, M., 2016, Hubungan kandungan hara tanah dengan produksi senyawa metabolit sekunder pada tanaman duku (*Lansium domesticum* Corr var Duku) dan potensinya sebagai larvasida, *Jurnal Vektor Penyakit*, 10 (1), 11–18.

[26] Enderle, D.I.M., and Weih, R.C., 2005, Integrating supervised and unsupervised classification methods to develop a more accurate land cover classification, *J. Arkansas Acad. Sci.*, 59 (10), 65–73.

Electrochemical Removal of Copper Ions Using Coconut Shell Activated Carbon

Nur Azza Azyan Muin[1], Hawaiah Imam Maarof[2,*], Nur Alwani Ali Bashah[1], Nor Aida Zubir[1], Rasyidah Alrozi[1], and Norhaslinda Nasuha[1]

[1]*Faculty of Chemical Engineering, Universiti Teknologi MARA, Cawangan, 13500 Pulau Pinang, Malaysia*

[2]*Faculty of Chemical Engineering, Universiti Teknologi MARA, 40450 Shah Alam, Selangor, Malaysia*

Abstract: *In this work, coconut shell activated carbon (CSAC) electrode was evaluated to remove copper ions via electrochemical processes. CSAC electrode and graphite were applied as the cathode and the anode, respectively. The reusability of the electrode, the effects of initial pH, applied voltage and initial concentration were studied. The electrochemical process was carried out for 3 h of treatment time, and the electrodes (anode and cathode) were separated by 1 cm. The results revealed that CSAC is proven as a reusable electrode to remove copper ions, up to 99% of removal efficiency from an initial concentration of 50 ppm after it had been used three times. From the observation, the removal efficiency was optimum at an initial pH of 4.33 (without any initial pH adjustment). The applied voltage at 8 V showed a higher removal efficiency of copper ion compared to at 5 V.*

Keywords: *activated carbon; copper; electrosorption; coconut shell; wastewater*

■ INTRODUCTION

In recent years, the heavy metal content in waste and wastewater has become one of the major concerns in the environment. Its concentration must be limited to a minimum amount as regulated by the local authority. Metal processing, electroplating, battery production, fertilizer production, and mining industries are the main sources discharging effluents of industrial wastewater containing heavy metals [1]. Heavy metal exposure via drinking water is a serious problem faced by humans. Copper removal recently has been eagerly studied since it is widely used in industries, such as electroplating, circuit-board manufacturing and as catalysts. A large quantity of copper with high concentration is commonly found in industrial effluents, and most of them are incompletely removed from the wastewater [2]. United States Environmental Protection Agency (EPA) regulates that the maximum limit of copper concentration in drinking water is 0.05 ppm. Copper is a non-biodegradable element and might be persistent in the aquatic environment. It tends to contaminate agricultural fields, disturb natural balance and accumulate in the ecosystem. Thus, the

accumulation of copper in the food chain will affect aquatic life [3].

Several conventional treatments for heavy metal removal from wastewater and water such as adsorption, chemical precipitation, coagulation-flocculation and ion exchange process have been implemented. Adsorption is widely recommended and used in industries due to its low cost, high removal efficiency depending on the types of adsorbent and simple process of chemical reaction [4]. Chemical precipitation is removing the heavy metals by using a large amount of chemicals to precipitate the metal ions so that they are easily removed from the wastewater [5]. However, some researchers observed that conventional chemical-physical treatments have encountered several disadvantages such as complex process plant to build, the high cost for a large quantity of chemical used, and the use of high energy. Moreover, the environment will be affected due to the large amounts of sludge produced from the processes that would require high cost and a large area for disposal [6].

Electrochemical processes nowadays has become a popular method for treating industrial wastewater

containing heavy metals due to its cost-efficiency and the high ability for metal removal from water. Electrocoagulation, electro-flotation, electrodeposition, electro-sorption, and electrodialysis are examples of electrochemical processes. The electrochemical process offers several advantages such as being cost-effective by not consuming chemicals in the system, offers high efficiency on heavy metal removal and also the fact that the process occurs at ambient temperature and pressure [7]. In electrochemical processes, there are various types of electrodes either porous or non-porous materials.

A porous material basically refers to carbon-based materials (e.g., agricultural activated carbon, granular activated carbon) that allows the removal of heavy metal on the surface of the electrode. The non-porous material is referring to metal-based electrodes (e.g., platinum, silver, zinc). The carbon-based electrode can also be a non-porous material for example graphite [8]. Carbon-based electrodes are low-cost materials compared to metal-based electrodes which are expensive in the industry. The evaluation of coconut shell activated carbon (CSAC) characteristics and properties show the advantages and its capability of removing heavy metals from water [9]. Hence, this work aims to evaluate the performance of coconut shell activated carbon as a porous electrode for the removal of copper from aqueous solution.

■ EXPERIMENTAL SECTION

Preparation of Electrode

The CSAC was provided by a local supplier. The preparation of the electrode was adapted from Maarof et al. [1]. CSAC was ground to fine particles and sieved to obtain the desired particle size (< 100 μm). Carbon black (CB) (Super P, Alfa Aesar), and polytetrafluoroethylene (PTFE) suspension (Sigma Aldrich, 60 wt.%) were mixed with CSAC powder at a mass ratio of 1:1:4 for electrode preparation. CSAC with 20% of CB was labeled as CSAC20CB. The mixture was thoroughly hand-mixed with the addition of 1,3-propanediol as a solvent to produce an electrode paste. The paste was kneaded and pressed in a stainless-steel mold then dried at 80 °C for 2 h, 150 °C for 1 h and 250 °C for 1 h. The dried electrodes

were packed into a 25 mm diameter stainless steel mold and pressed at 20 N/m^2 by using mechanical load to produce approximately 0.5 mm thick CSAC electrodes.

Batch Electrochemical Removal of Copper

The electrochemical cell was filled with 100 mL of copper solution and 5 mL of NaCl as supporting electrolyte. Two electrodes were placed in the cell at 1 cm apart. CSAC and graphite were the cathode and the anode, respectively. A magnetic stirrer was placed inside the cell, and hot plate stirrer was used to allow the mixing of the solution at 250 rpm. The voltage of 8 V was introduced into the system to provide electricity for the process of the removal of copper. The initial current of 150 mA was recorded. There was no pH adjustment of the copper solution except for the study of the effect of initial pH. This electrochemical process was carried out for 3 h. The samples were collected at regular time intervals to analyze the residual metal content.

Effect of initial pH

The electrochemical cell was set up with a voltage of 8 V, and the same conditions were applied as described in the previous paragraph except for initial pH value. The copper solution was adjusted to acidic and alkaline pH to study the effect of initial pH on the electrochemical removal of copper. The pH was adjusted at the start of each run by using either 1 M NaOH or 1 M HCl. The initial concentration was fixed at 50 ppm. The subsequent experiments were conducted at the optimum initial pH.

Effect of applied voltage

For the effect of applied voltage on the electrochemical process, voltages at 5 and 8 V were supplied for each treatment. The initial concentration and treatment time were fixed at 50 ppm and 3 h, respectively.

Effect of initial concentration

The initial concentrations of the copper solution were 50 and 100 ppm. The voltage was fixed at 8 V and no pH adjustment was made to the copper solution. For the initial copper concentration of 50 ppm, the electrochemical process was conducted for 3 h, while, for

100 ppm, the treatment time was 5 h.

Reusability of CSAC electrode

The reusability of the electrode was determined by repeating the experiment three times using the same CSAC electrode. The electrochemical process conditions were fixed at the concentration of the copper solution of 50 ppm, voltage of 8 V, no pH adjustment and 3 h of treatment time. The electrodes were rinsed with distilled water after every treatment to prevent the carry-over effect of the copper solution.

Analysis using ICP-OES

The concentration of copper ion was analyzed by using Inductively Coupled Plasma-Optical Emission Spectrometry (ICP-OES) (Perkin Elmer, Optima 7000 DV). The dilution factor of 10 was applied for each sample whereby 1 mL sample of the copper solution was diluted with 9 mL of 1% nitric acid. All samples were collected at regular time intervals within 3 h. The concentration of copper was determined by using an external standard calibration method. The concentrations of copper used to prepare the calibration curve were 1, 2, 3, 4 and 5 ppm. The removal efficiency of CSAC electrode is calculated by using Eq. (1).

$$\text{Removal Efficiency (\%)} = \frac{C_{Initial} - C_{Final}}{C_{Initial}} \times 100 \%\qquad(1)$$

■ RESULTS AND DISCUSSION

Effect of Initial pH

The initial pH of the solution is an important operating parameter that influences the performance of electrochemical removal of copper ions. The aqueous solution (100 mL) had the initial concentration of 50 ppm copper ion and 5 mL 0.1 M NaCl as the supporting electrolyte. The pH of this solution was 4.33. The removal efficiency of copper ions was studied at acidic and alkaline conditions for which the pH was adjusted accordingly. The pH of the aqueous solution was adjusted by adding a few drops of 1 M NaOH to obtain alkaline pH in the range of 8–10. While adjusting the pH to alkaline condition, the solution became an emulsion for which the copper ion was observed to be insoluble in the aqueous solution. Hussin et al. [10] observed a similar outcome and

reported that at higher pH values (nearest to alkaline), solid copper was formed and precipitated out of the solution. The insoluble copper had affected the performance of the CSAC electrode to remove the copper ions; copper ions were not deposited on the surface of the electrode. While sampling the solution, copper in solid form was clearly observed in the syringe filter. Therefore, it is noted that the electrochemical removal of copper ion is not suitable under alkaline as well as neutral conditions. The copper solution was adjusted to an acidic condition by adding drops of 1 M HCl, and the obtained pH was 2.62. Fig. 1 illustrates the removal efficiency of copper ions by CSAC electrode at the acidic initial condition and without pH adjustment. The removal efficiency of copper ions at pH 4.33 (99.3%) was better than at pH 2.62 (96.4%). During the first 60 min, the removal efficiency at the initial pH 2.62 was below 70%, and only 90.1% removal was achieved after 2 h of treatment time.

In contrast, initial pH 4.33 shows higher removal efficiency of 81.4% after 1 h of treatment time. The result shows that some of the copper ions were not recovered because of the hydrogen ions were attached to the surface of the CSAC electrode [11]. Alebrahim et al. [12] described that at lower initial pH of electrolyte (lower than pH 2), the discharged hydrogen ions in the solution are competing with the discharged copper ions at the cathode surface. They also reported that increasing the initial pH of the solution resulted in precipitation. Chen et al. [13]
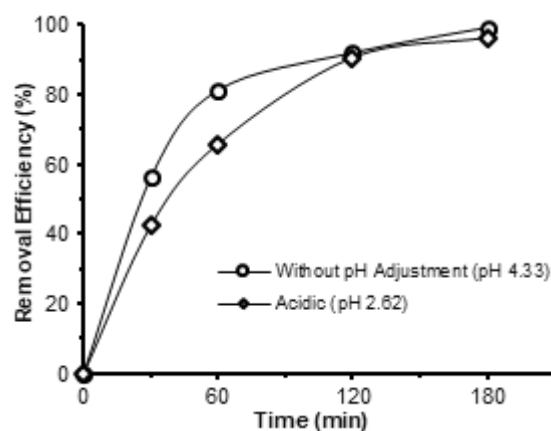

Fig 1. Removal efficiency of copper ions by CSAC electrode at acidic condition (pH 2.62) and without pH adjustment (pH 4.33)

reported that a lower pH resulted in a faster reaction rate due to the higher mass transfer rate. However, it tends to form concentration and electrochemical polarization which results in hydrogen evolution and reduce the current efficiency [13]. Thus, the competitive environment of hydrogen ions and copper ions occurred during the electrodeposition process. The optimum pH was reported at a value of 3.5. Therefore, the copper solution without initial pH adjustment (pH 4.33) is preferred compared to pH 2.62 for copper removal. Consequently, the initial pH of the copper solution at pH 4.33 (without any pH adjustment) was chosen as the optimum value and subsequently applied in the experiments for the other parameters studied.

Effect of Applied Voltage

The effect of the applied voltage was investigated at 5 and 8 V. The solution mixing rate was fixed at 250 rpm, the initial pH of the electrolyte was 4.33, and the initial copper ions concentration was 50 ppm. Fig. 2 shows the removal efficiency of copper ions by CSAC electrode at 5 V and 8 V applied voltage. As shown in Fig. 2, the removal of copper ions was at a higher rate for the first 60 min of treatment time using higher applied voltage (8 V). It achieved 81.4% of removal efficiency. At this point, the increase of percentage removal at 8 V, from 0 to 60 min was faster than at 5 V. At 60 min of treatment time, the difference in the percentage removal was 30.5%. As the treatment time was extended to 3 h, the removal efficiency at an applied voltage of 8 and 5 V was 99.3 and 94.9%,
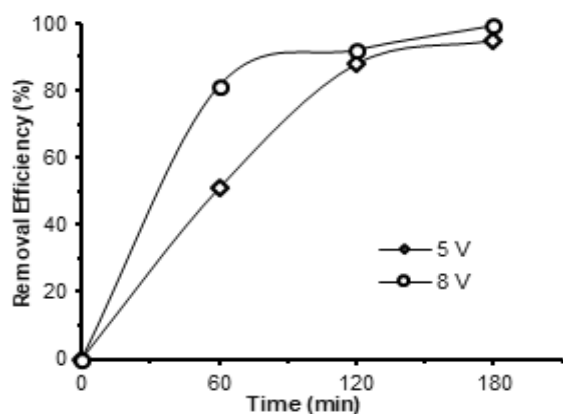
respectively. This indicates that the transfer of electrons and charged ions attached to the cathode is more effective at higher voltages. Marmaris et al. [14] studied the effect of the voltage supplied at 0.4, 0.8 and 1.2 V and reported that the highest removal efficiency of cadmium was at 1.2 V. It is also claimed that the electrochemical processes for cadmium using nano-carbon electrode required high supplied voltage to remove cadmium ion from solution. Elsherief [15] reported that low voltage supply resulted in the formation of hydrogen ions on the surface of the electrode (spiral wound steel electrode); thus, the removal efficiency was low. The electrostatic attraction of ions by the reticulated vitreous carbon electrode was effective at a higher voltage as it increased the flow velocity of electrons to be attached to the porous electrode [11]. Duan et al. [16] also described that electrodeposition rates of copper ion increased gradually when a higher cell voltage was supplied.

Effect of Initial Concentration

The effect of the initial concentration of copper by CSAC electrodes was carried out at the initial concentration of 50 and 100 ppm. Fig. 3 shows that the removal efficiency of the copper ion at 50 and 100 ppm were 99.3 and 94.2%, respectively. The results demonstrate that a lower initial concentration (50 ppm) gave higher removal efficiency than higher initial copper ion concentration (100 ppm). The higher removal efficiency was achieved at an initial concentration of 50 ppm copper solution after 3 h of treatment time. However,
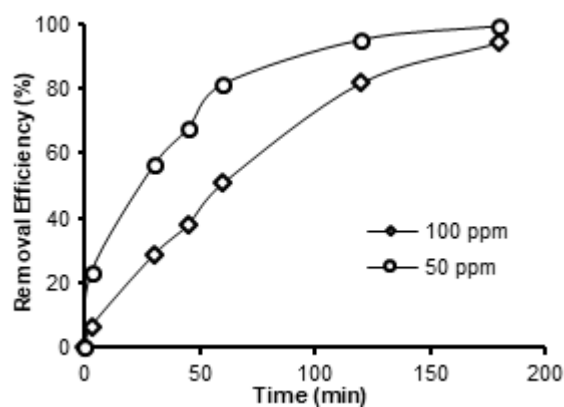

Fig 2. Removal efficiency of copper ions by CSAC electrode at applied voltage of 5 and 8 V

Fig 3. Effect of initial copper concentration on removal efficiency of CSAC electrode

at an initial concentration of 100 ppm, approximately similar efficiency (99.4%) was only achieved after the treatment time was prolonged to another 2 h. Khattab et al. revealed that the initial concentration has an influence on the removal efficiency of copper whereby high initial concentration tends to transport the ions through the pores easily. Therefore, it will be resulting in effective electrochemical removal of copper by carbon electrode [17].

Reusability of CSAC Electrode

The reusability of the CSAC electrode was studied by repeating the experiment three times using the same electrode for removal of copper ion from aqueous solution. Similar operating conditions of the electrochemical process were applied for the three experiments whereby, the initial concentration was fixed at 50 ppm, applied voltage at 8 V (approximately 150 mA), the solution was stirred at 250 rpm, initial pH of 4.33, and with the addition of 5 mL supporting electrolyte 0.1 M NaCl. The initial pH for copper solution was acidic for each experiment. Fig. 4 illustrates the removal efficiency of copper ions by CSAC electrode versus time, the removal efficiency of copper ion at the first run was 99.3%, higher than the subsequent second and third runs. The second and third run of the experiment gave the removal efficiency of 98.2 and 96.4%, respectively. This shows that at the first run, the removal of copper ion was the most effective. This is because of the charged particles of the surface electrode that was efficient in attracting the electrons of copper ions. The high porosity of electrode
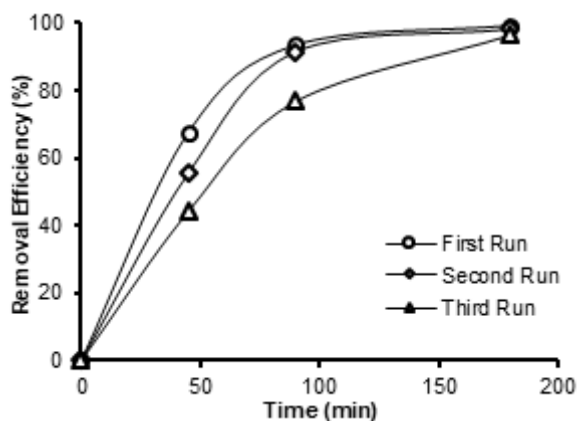

Fig 4. Successive copper ion removal efficiency of CSAC

gives the advantage in removing copper ion whereby it is allowing a greater mass transfer to occur during the electrochemical process [8].

In contrast, the performance of the CSAC electrode decreased slightly in its effectiveness for the second and third runs. The decrease in removal efficiency of copper ions after the first run is probably due to the less active surface area of the CSAC electrode. Reusability study of the electrode was carried out three times/runs, whereby CSAC electrode was rinsed with distilled water after each run was completed. Copper was observed to be deposited on the surface of the CSAC electrode. Thus, the availability of the active site of the surface of the electrode is lower due to the solid copper attached on the CSAC electrode.

■ CONCLUSION

Copper ions were recovered from synthetic wastewater by using the coconut shell activated carbon (CSAC) electrode via the electrochemical process. The reduction of copper ions was facilitated by the chemical reaction with the aid of applied voltage. CSAC, a carbon-based electrode was used as the cathode to attract the copper ions and deposit on the porous surface electrode. The CSAC electrode is an effective electrode with high removal efficiency and is a reusable electrode which can be used several times to remove copper ions, more than 99% removal efficiency was achieved after it had been used three times. The electrochemical removal of copper ions by the CSAC electrode was found more effective in acidic solution. In this work, the higher removal efficiency was achieved without any pH adjustment of the solution, which was at pH 4.33. The applied voltage of 8 V gave higher removal efficiency compared to 5 V. High initial concentration (100 ppm) required longer treatment time than 50 ppm whereby 5 h was needed to obtain 99.4% of copper removal. In contrast, 99% removal efficiency was achieved with only 3 h of treatment by 50 ppm copper ion. In conclusion, the CSAC electrode has high potential to remove copper ions through an electrochemical process. The CSAC electrode has the potential to replace metal-based electrode material as it has high removal efficiency due

to its porous properties and more importantly, it is cost effective. Coconut shell is an agricultural waste, available in large quantities in tropical countries globally that can be utilized to create value-added products.

■ REFERENCES

[1] Maarof, H.I., Ajeel, M.A., Daud, W.M.A.W., and Aroua, M.K., 2017, Electrochemical properties and electrode reversibility studies of palm shell activated carbon for heavy metal removal, *Electrochim. Acta*, 249, 96–103.

[2] Friedrich, J.M., Ponce-de-León, C., Reade, G.W., and Walsh, F.C., 2004, Reticulated vitreous carbon as an electrode material, *J. Electroanal. Chem.*, 561, 203–217.

[3] Huang, C.C., and Su, Y.J., 2010, Removal of copper ions from wastewater by adsorption/electrosorption on modified activated carbon cloths, *J. Hazard. Mater.*, 175 (1-3), 477–483.

[4] Peng, W., Li, H., Liu, Y., and Song, S., 2017, A review on heavy metal ions adsorption from water by graphene oxide and its composites, *J. Mol. Liq.*, 230, 496–504.

[5] Fu, F., and Wang, Q., 2011, Removal of heavy metal ions from wastewaters: A review, *J. Environ. Manage.*, 92 (3), 407–418.

[6] Barakat, M.A., 2011, New trends in removing heavy metals from industrial wastewater, *Arab. J. Chem.*, 4 (4), 361–377.

[7] Tran, T.K., Chiu, K.F., Lin, C.Y., and Leu, H.J., 2017, Electrochemical treatment of wastewater: Selectivity of the heavy metals removal process, *Int. J. Hydrogen Energy*, 42 (45), 27741–27748.

[8] Zhang, L.L., and Zhao, X.S., 2009, Carbon-based materials as supercapacitor electrodes, *Chem. Soc. Rev.*, 38 (9), 2520–2531.

[9] Iqbaldin, M.N.M., Khudzir, I., Azlan, M.I.M., Zaidi, A.G., Surani, B., and Zubri, Z., 2013, Properties of coconut shell activated carbon, *J. Trop. For. Sci.*, 25 (4), 497–503.

[10] Hussin, F., Abnisa, F., Issabayeva, G., and Aroua, M.K., 2017, Removal of lead by solar-photovoltaic electrocoagulation using novel perforated zinc electrode, *J. Cleaner Prod.*, 147, 206–216.

[11] Tramontina, J., Azambuja, D.S., and Piatnicki, C.M.S., 2002, Removal of Cd^{2+} ion from diluted aqueous solutions by electrodeposition on reticulated vitreous carbon electrodes, *J. Braz. Chem. Soc.*, 13 (4), 469–473.

[12] Alebrahim, M.F., Khattab, I.A., and Sharif, A.O., 2015, Electrodeposition of copper from a copper sulfate solution using a packed-bed continuous-recirculation flow reactor at high applied electric current, *Egypt. J. Pet.*, 24 (3), 325–331.

[13] Chen, X., Lin, H., Ren, H., and Xing, J., 2013, Experimental study on wastewater treatment containing copper with electrodeposition method, *Adv. Mater. Res.*, 779-780, 1670–1673.

[14] Marmanis, D.I., Dermentzis, K.I., Christoforidis, A.K., and Ouzounis, K.G., 2013, Cadmium removal from aqueous solution by capacitive deionization with nano-porous carbon electrodes, *J. Eng. Sci. Technol. Rev.*, 6 (5), 165–166.

[15] Elsherief, A.E., 2003, Removal of cadmium from simulated wastewaters by electrodeposition on spiral wound steel electrode, *Electrochim. Acta*, 48 (18), 2667–2673.

[16] Duan, W., Chen, G., Chen, C., Sanghvi, R., Iddya, A., Walker, S., Liu, H., Ronen, A., and Jassby, D., 2017, Electrochemical removal of hexavalent chromium using electrically conducting carbon nanotube/polymer composite ultrafiltration membranes, *J. Membr. Sci.*, 531, 160–171.

[17] Khattab, I.A., Shaffei, M.F., Shaaban, N.A., Hussein, H.S., and Abd El-Rehim, S.S., 2013, Electrochemical removal of copper ions from dilute solutions using packed bed electrode. Part I, *Egypt. J. Pet.*, 22 (1), 199–203.

Removal Efficiency of Acid Red 18 Dye from Aqueous Solution Using Different Aluminium-Based Electrode Materials by Electrocoagulation Process

Nurulhuda Amri[1,2], Ahmad Zuhairi Abdullah[1,*], and Suzylawati Ismail[1]

[1]School of Chemical Engineering, Universiti Sains Malaysia, Engineering Campus, 14300 Nibong Tebal, Penang, Malaysia

[2]Faculty of Chemical Engineering, Universiti Teknologi MARA (UiTM), Cawangan Pulau Pinang, 13500 Permatang Pauh, Penang, Malaysia

Abstract: *This work compares commercial aluminium electrode for use in the treatment of wastewater by electrocoagulation process against waste aluminium cans electrode. The applicability of the waste aluminium cans electrode was tested for decolorization of Acid Red 18 dye as a model pollutant. The batch electrocoagulation process using both types of electrode was conducted at a current density of 25 mA/cm^2, a pH of 3, an initial concentration of 100 mg/L and 25 min of reaction time. The elemental composition and surface morphology of both electrode materials and the sludge produced were analyzed using SEM-EDX to establish the correlation between the properties and characteristics of both electrode materials with their dye removal performance. The results demonstrated that waste aluminium cans performed better than commercial aluminium electrode with a removal efficiency of 100% in 25 min of reaction time. This was due to the higher Al dissolution of waste aluminium cans electrode that contributed to the larger amount of Al^{3+} released into the solution to consequently form more flocs to remove the dye molecules. In conclusion, the proposed waste aluminium electrode was considered as efficient and cost-effective and had the potential to replace the conventional ones in treating colored industrial wastewater using electrocoagulation process.*

Keywords: waste aluminium cans; commercial aluminium electrode; electrocoagulation process; Acid Red 18; removal efficiency

■ INTRODUCTION

Large amounts of disposed aluminium can contribute to solid wastes either in the form of industrial or domestic waste; they originate from products such as cans, food trays, pie plates, frozen foods containers, wrapping foil, etc. [1]. Annually, 1.5 million tons of waste is created worldwide by throwing away aluminium cans that not only fill up the landfills, but also cause wastage in energy and extensive environmental damage in creating new cans [2]. Recently, the attention of many researchers has shifted towards utilization of waste aluminium cans as a raw material in the preparation of catalysts [3] and nanomaterials [4]. The exploitation of this waste as a raw material in new research fields will present several environmental and economic benefits over a long-term period that will reduce the impact of aluminium wastes by converting them into valuable materials [5].

Aluminium (Al) is one of the electrode materials that has been extensively used, as this type of material presents high electro-dissolution rate and is effective in treating various pollutants using electrocoagulation (EC) process [6-8]. EC process is known as a potential technique for treating industrial effluent due to its simplicity in the design and operation, high efficiency, cost-effective treatment system, and environmental compatibility [9-10]. This process takes the benefits of the binding effect of charge neutralization/surface complexation/adsorption of pollutant onto the in-situ formation of metal hydroxide from the oxidation of sacrificial anode [11]. There have been numerous studies reported on the efficient performance of aluminium

electrodes used in the EC process for treatment of wastewater containing textile dyes [12-13].

Azo dyes are the largest group of dyes used in the textile industry that represent about 50% of all the commercial dyes available [10]. They generally have an azo group band (-N=N-) together with other chromospheres which are responsible for their intense color, high water solubility, and resistance to degradation under common biological treatment [9]. Acid Red 18 (AR18) dye is one of the dyes under the azo group that is commonly used during the dyeing process. The major environmental problem associated with the use of these dyes is their loss in the dyeing process. It is estimated that around 10–50% of these dyes are usually lost in the effluent [14]. Wastewaters containing dyes can cause aesthetic problems due to the color even at low concentration, and their intermediate products could be either toxic, carcinogenic, or mutagenic to aquatic life [14-15]. Therefore, the treatment of effluents containing azo dyes is crucial to minimize their harmful impacts on human beings and aquatic life.

Various treatment technologies, including physical, chemical, and biological methods, have been used for the treatment of textile effluents [16]. However, these treatment methods still have certain limitations such as high capital and operation cost, generation of a large amount of sludge and may not be effective for all types of dyes. In Malaysia, conventional wastewater treatment systems that are most commonly applied in textile industries are biological treatment alone or physicochemical treatments followed by a biological treatment [17]. Single conventional biological treatment does not always treat the textile effluent satisfactory as most of the dyes, especially azo dyes [18] are hardly biodegradable at high concentration [13]. Thus, certain pre-treatment, such as physical or chemical process is

necessary. In this respect, the EC process can be a good alternative pre-treatment method for biological treatment system due to its advantages.

In this study, waste aluminium cans (WAC) were utilized as a potential electrode for the removal of AR18 dye using an EC process. To the best of our knowledge, no study has been reported on the utilization of this waste material as an electrode in the EC process for the treatment of water or wastewater. Most of the studies available in literature utilized directly commercial electrode materials to evaluate their performance in the EC process [8-10].
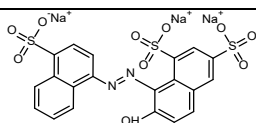
Thus, this study aimed to evaluate the applicability of WAC as an electrode and compare the removal performance between the WAC and commercial aluminium (COM) electrode in the decolorization of AR18 dye via the EC process. The Al ion (Al^{3+}) contents remaining in the solution after the EC process using both types of electrode material were also analyzed to ensure that the quality of treated water could achieve the permissible limit for industrial effluent discharged [19]. The characteristics of both electrodes in terms of elemental composition, the surface morphology of the electrodes before and after the EC process as well as the sludge produced were also examined to establish the correlation with the dye removal efficiency.

■ EXPERIMENTAL SECTION

Materials

All chemicals used in this study such as AR18 dye (> 99% purity), hydrochloric acid (HCl), sodium hydroxide (NaOH) and sodium chloride (NaCl) were of analytical grade and purchased from Merck. Table 1 shows the general properties of the AR18 dye. A stock solution of AR18 dye was prepared by dissolving 1 g of dye

Table 1. Properties of AR18 dye

Dye	Structure	Molecular formula	Molecular weight (g/mol)	λ_{max}* (nm)
Acid Red 18		$C_{20}H_{11}N_2Na_3O_{10}S_3$	604.48	507

*λ_{max} is the maximum absorbance of AR18 dye

in 1 L of deionized water. Then, the solution was diluted to give the initial concentration of 100 mg/L. The electrical conductivity of the solution was increased by the addition of 2 g/L of NaCl into the solution. Meanwhile, the pH of the solution was adjusted from the original pH of 6.8 to 3.0 using 0.1 M HCl solution.

The COM and WAC were used as materials for electrodes. The COM electrodes were purchased from Neilement Engineering Resources & Services. The dimensions of the COM electrode are illustrated in Fig. 1. Meanwhile, the WAC was collected from cafeterias in Universiti Sains Malaysia. The WAC was cut into dimensions similar to those of COM electrode but with a different thickness of 0.01 cm (original thickness of WAC). They were then subjected to a pre-treatment with sandpaper to remove the paint and epoxy coating on the outer and inner walls of the can, and rinsed with deionized water. Finally, the WAC was dried in an oven at 60 °C and ready to be used in the batch EC experiment.

Instrumentation

The solution pH was measured using a pH meter (Eutech pH2700, Thermo Scientific, Singapore). The concentration of AR18 dye solution was determined using a double beam UV-visible spectrophotometer (Shimadzu 1800, Japan) at a wavelength of 507 nm. The surface morphology and the elemental composition of both electrode materials and sludge produced after the EC process were examined using a scanning electron microscope (SEM) equipped with an energy-dispersive X-ray spectroscopy (EDX) facility (Quanta 450 FEG, FEI, Netherlands) operated at an accelerating voltage of 5 kV. The concentrations of Al^{3+} in the treated water were examined using an inductively coupled plasma-optical emission spectrometer (ICP-OES) (ICAP 7600, Thermo Scientific, USA).

Procedure

Batch monopolar EC experiments were carried out in a 1.1 L rectangular reactor, as shown in Fig. 2. Two pieces of flat WAC and COM plates were used as electrodes, and the distance between the electrodes was set at 0.5 cm. The area of each electrode dipped into the solution for both
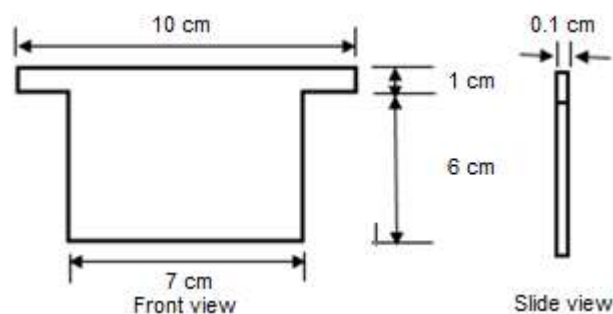
Fig 1. The specific dimensions of a COM electrode
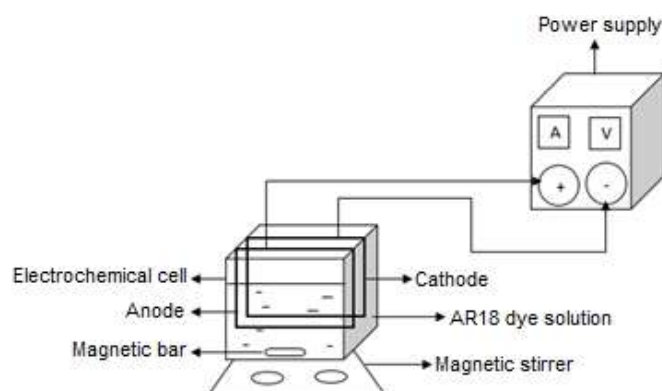
Fig 2. Schematic diagram of the experimental set-up for the EC system

WAC and COM was 6 cm × 7 cm. The electrodes were connected to a DC Power supply (Dazheng PS-305D, 0–5 A, 0–30 V) to supply and control the required current during the experiment. The water sample (800 mL) was initially fed into the EC cell, and the current density was set at 25 mA/cm² for 25 min. The solution was continuously stirred at 250 rpm during the experiment in order to get a homogeneous solution. All EC experiments for WAC and COM were operated at the best-operating conditions (current density of 25 mA/cm², pH of 3, initial concentration of 100 mg/L, electrode distance of 0.5 cm, NaCl concentration of 2 g/L and reaction time of 25 min) as obtained previously. In the preliminary work, a series of one-factor-at-a-time experiments for the effects of current density (10–30 mA/cm²), pH (3–9), contact time (0–60 min), NaCl concentration (2–5 g/L) and inter-electrode distance (0.5–2 cm) were conducted using the same batch EC system. However, the effect of operating parameters to obtain the best set of operating conditions is not reported in this paper.

Indones. J. Chem., 2020, 20 (3), 536 - 544

539

Samples of the treated wastewater were taken at different times and filtered through a Whatman filter paper no. 1 prior to its color measurement. Each analysis was conducted in triplicate. The AR18 dye removal efficiency is calculated using Eq. (1):

$$\text{Removal Efficiency (\%)} = \frac{C_0 - C_t}{C_0} \times 100\% \quad (1)$$

where, C_0 is the initial dye concentration (mg/L) and C_t is dye concentration at a time, t (mg/L).

■ **RESULTS AND DISCUSSION**

Elemental Composition

The elemental composition of WAC and COM were determined using EDX analysis, and the results are presented in Table 2. From the results, both WAC and COM electrodes were classified as aluminium alloys. Al was the main metal element in both electrode materials that represented about 85.67% and 79.05% by weight respectively for WAC and COM. The composition of Al was found to be higher in WAC than that of COM by about 6.62% with additional elements of Mg and Mn. Meanwhile, COM had Fe elemental composition of 0.41% by weight. The difference in the composition and alloying elements of these materials was believed to be one of the factors that contributed to the difference in the performance of AR18 dye removal in the EC process. Dura and Breslin [8] reported the performance of Al-Zn-In and Al-Mg alloy electrodes for the removal of phosphate, Zn^{2+}, and Orange II dye. It was observed that both types of Al alloy performed well in removing all the pollutants as compared to pure Al electrode due to their low overpotential values as obtained from the polarization and cyclic polarization experiment. These low overpotential

Table 2. Elemental compositions of WAC and COM electrodes

Element	WAC Weight (%)	COM Weight (%)
Al	85.67	79.05
C	9.60	16.54
O	2.55	3.99
Mg	1.16	-
Mn	1.02	-
Fe	-	0.41

values indicated a higher dissolution behavior of Al alloy than the pure Al electrode, which was more passive. However, the performance of Al-Zn-In was slightly better than Al-Mg, attributed to the instability of the passive film that was formed on the Al-Zn-In electrode to significantly enhance the dissolution of the electrode and the production of Al^{3+} ion.

Removal efficiency of AR18 dye using different electrode materials

In order to examine the potential of this waste electrode as a green alternative to the commercial Al electrode, the performance of WAC and COM in the decolorization of AR18 dye was investigated. The effect of different electrode materials on AR18 removal was conducted at the best-operating conditions as mentioned earlier. Fig. 3 illustrates the removal efficiency of AR18 dye and solution pH for WAC and COM electrodes with time. As can be observed, the removal trend was similar for both electrodes in which the decolorization efficiency increased drastically in the first 5 min of the reaction with up to 80% removals owing to higher precipitation rates under the acidic condition. After this point, the removal rates gradually increased, reaching a plateau in the next 20 min due to the transition of the dye removal mechanism from precipitation to the adsorption process [13]. However, it was found that the WAC performed better as compared to the COM with removal efficiencies of 100.00% and 87.56%, respectively after 25 min.

This finding was in agreement with the elemental analysis results (Table 2) as one of the Al alloying elements in WAC was Mg that could activate and enhance the Al dissolution through anode oxidation. Higher dissolution of WAC electrode produced a larger amount of Al^{3+} in the solution and subsequently proceeded through a hydrolysis reaction. This reaction generated various cationic monomeric and polymeric aluminium hydrolysis species. These cationic species were attracted to the negative charge of AR18 dye molecules, to result in the removal by either precipitation or adsorption mechanism. The result was consistent with Dura and Breslin [8]. They observed that the Al-Mg alloy electrode exhibited higher dissolution in
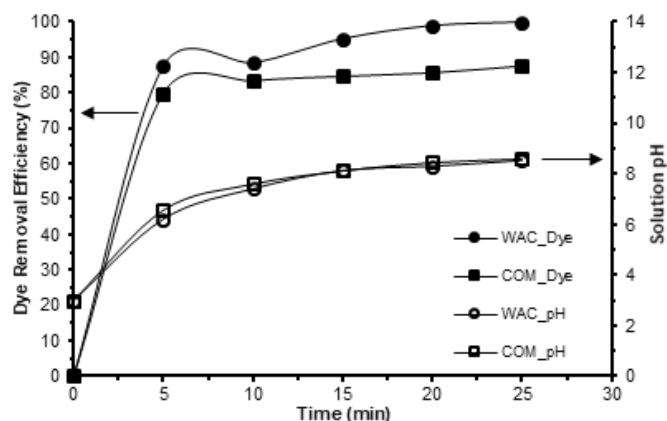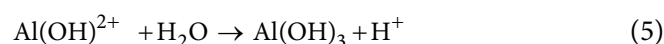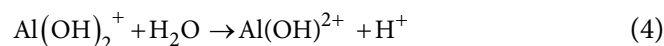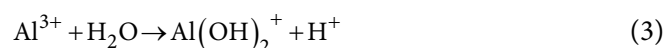
Fig 3. The removal efficiency of AR18 dye and the solution pH by WAC and COM electrodes

the presence of NaCl with more than 90% removal efficiencies of phosphate ions by the EC process.

Initial pH of the dye solution is also an important parameter affecting the predominance of coagulant species produced during the EC process. Generally, the pH of the treated water changes during the EC process. As can be seen in Fig. 3, the similar trends of increasing solution pH throughout the EC treatment were observed for both types of electrode material to indicate that the metal hydroxide species that formed in the solution were identical due to the constant initial solution pH of 3.0 set for WAC and COM electrodes. Overall, the solution pH increased rapidly to a maximum of 8.6 in 25 min. During the first 5 min, the initial solution pH increased drastically from 3.0 to 6.2 and 6.5 for WAC and COM electrodes, respectively. This was attributed to the hydroxyl ion release from water reduction occurring at the cathode during the EC treatment. Meanwhile, the dissolution of anode produced Al^{3+}, as expressed by Eq. (2). In acidic condition, Al^{3+} can directly undergo spontaneous hydrolysis reactions producing various monomeric species such as $Al(OH)_2^+$ and $Al(OH)^{2+}$ which then transform into $Al(OH)_3$ as shown in Eq. (3) to (5). However, the other ionic species ($Al(OH)_4^-$, $Al(OH)^{2+}$, $Al_2(OH)_2^{4+}$) and polymeric species ($Al_6(OH)_{15}^{3+}$, $AL_7(OH)_7^{4+}$, $Al_8(OH)_{20}^{4+}$, etc.) may also present in the system depending on the pH of the solution to be finally converted to $Al(OH)_3$ flocs. These $Al(OH)_3$ flocs are beneficial for the adsorption of soluble organic pollutants

due to their large surface area. The overall process of flocs formation can be described as [13]:

$$Al \rightarrow Al^{3+} + 3e^- \tag{2}$$

$$Al^{3+} + H_2O \rightarrow Al(OH)_2^+ + H^+ \tag{3}$$

$$Al(OH)_2^+ + H_2O \rightarrow Al(OH)^{2+} + H^+ \tag{4}$$

$$Al(OH)^{2+} + H_2O \rightarrow Al(OH)_3 + H^+ \tag{5}$$

The high decolorization efficiencies as demonstrated by both types of electrodes in the first 5 min were mainly due to the dye precipitation process by Al^{3+} as well as monomeric and polymeric species that formed in the solution at pH < 6.5. However, as the pH was increased exceeding 6.5, most of the aluminium hydroxide precipitated as Al coagulant, thus responsible for the adsorption of the remaining dye molecules. The finding in this work was in good agreement that of Khorram et al. [13]. They reported that dye precipitation process was the main mechanism that was responsible for the high removal efficiency followed by the adsorption of the dye polymeric colloidal species by $Al(OH)_3$ flocs which had a lesser effect. Thus, it can be summarized that the dye removal mechanisms for both WAC and COM electrodes were identical as the solution pH for both types of electrode material were almost the same throughout the EC process.

On the other hand, the finding was also consistent with that reported by Elabbas et al. [20]. They observed that changes in the solution pH were greatly influenced by the nature of the electrode materials. They found that the increase in the solution pH with time for aluminium alloy was slightly higher than that of pure aluminium leading to higher removal efficiency of chromium and COD. Since both types of electrode used in this study were categorized as the same nature of electrode material, which was aluminium alloys, they possessed rather similar behavior towards the pH change during the EC process.

Besides, the excellent removal performance of WAC could also be explained by the higher dissolution of WAC electrodes as compared to COM that was represented by the weight loss of electrodes, as shown in Fig. 4. Higher weight loss of WAC anode electrode
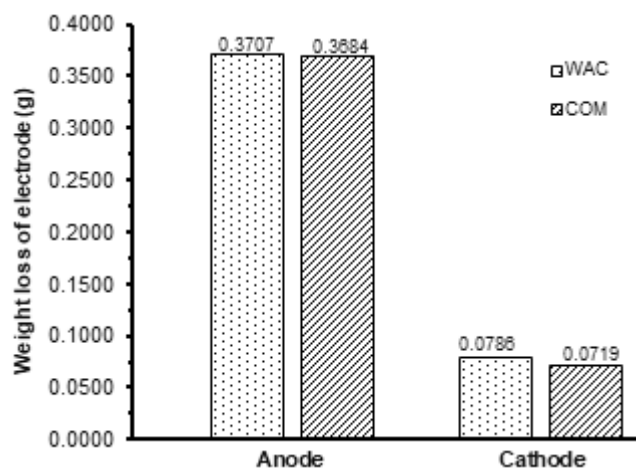
Fig 4. Weight loss of anodes and cathodes after the EC process

contributed to the higher amount of Al^{3+} released into the solution to destabilize the colloidal particles and form more flocs to remove the dye molecules. Results obtained in this work revealed that WAC was more superior to those reported in the literature. Khosravi et al. [10] reported that the highest AR18 removal of 92.3% was obtained by Al electrode at an optimum reaction time of 40 min, pH 4 and a current density of 26 mA/cm². In addition, Azarian et al. [15] observed that the highest AR18 removal of 95.0% was obtained by Al electrode under an optimum current density of 1.2 mA/cm², pH 7 and reaction time of 45 min.

The rate of AR18 dye decolorization can also be

confirmed by the absorption spectrum, as illustrated in Fig. 5. The absorbance by AR18 dye can be characterized by two peaks at 507 nm in the visible region and 320 nm in the ultraviolet region. As can be seen clearly, the main peak at 507 nm decreased significantly with time without the appearance of new absorbance peaks for both types of electrode during the EC process. However, the peak for WAC disappears faster than that of COM within 25 min of reaction time. This suggested that the decolorization involved the decomposition of AR18 dye through the breaking of -N=N- belonging to the chromophore group. A similar observation was reported by Azarian et al. [15], but the time taken for the 507 nm peak disappearance was relatively longer, i.e., between 30 to 120 min.

In order to ensure that the EC was a safe process and did not need any further treatment for treating excessive residual Al^{3+} ions after the process, the treated sample was then examined using ICP-OES. From the results in Table 3, it can be concluded that the residual Al^{3+}

Table 3. The concentrations of Al ion remaining in the treated water and the acceptable limit for Al ion from industrial effluent discharge [19]

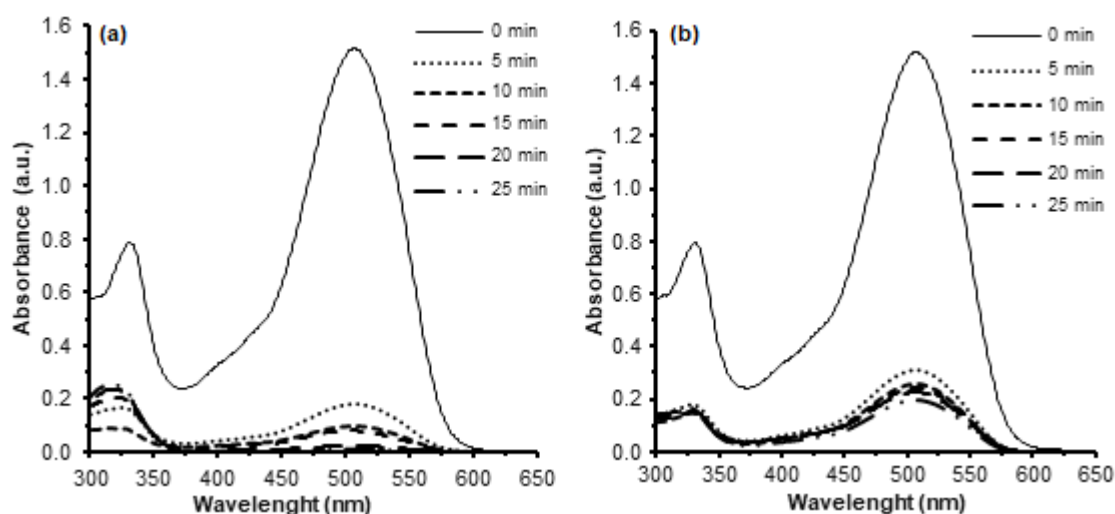| Electrode material	Treated water [Al^{3+}] (ppm)	Standard A [Al^{3+}] (ppm)	Standard B [Al^{3+}] (ppm)
WAC	0.6	10	15
COM	2.7		

Fig 5. Absorbance spectra of AR18 dye during the EC process at different reaction times using (a) WAC and (b) COM electrodes
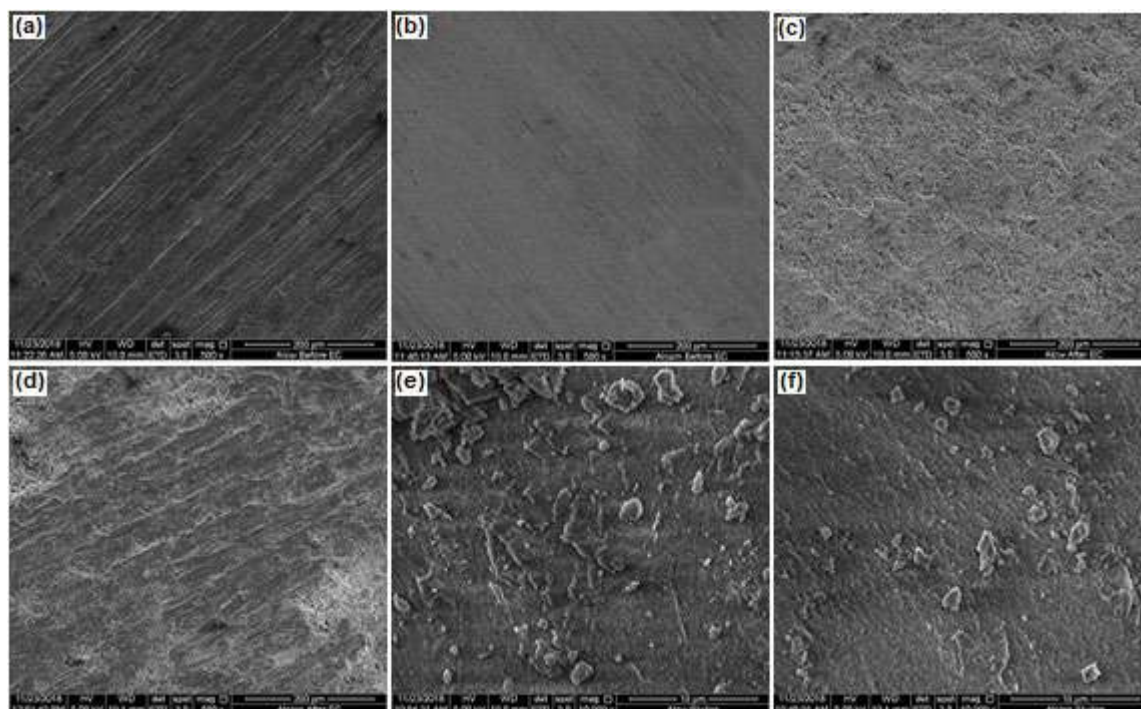
Fig 6. SEM images for (a) WAC before EC (500×), (b) COM before EC (500×), (c) WAC after EC (500×), (d) COM after EC (500×), (e) WAC sludge (10k×), (f) COM sludge (10k×)

concentrations in treated water using WAC and COM were 0.6 and 2.7 ppm, respectively. Thus, this was an additional benefit of the use of waste electrode as the concentration of Al^{3+} in the treated water was much lower compared to that of COM. This might be due to the fact that most of the Al^{3+} ions produced from the dissolution of WAC anode effectively combined with hydroxyl ions to form a higher amount of $Al(OH)_3$ flocs that ended up in the WAC sludge as confirmed by the surface morphology and EDX analysis as shown in Fig. 6(e) and 7(a), respectively. However, both electrodes still could be considered as harmless electrodes since they showed lower residual Al concentrations as compared to the permissible limit stated in the Malaysian's Fifth Schedule of Environmental Quality (Industrial Effluent) Regulation 2009 which are 10 ppm for Standard A and 15 ppm for Standard B[19].

Surface Characterization

Fig. 6(a–d) present the microscopic images of the surface morphology of both electrode materials while those of dried sludges produced after the EC process are shown in Fig. 6(e–f). The images of electrodes before treatment show that the WAC electrode had a relatively rougher surface structure as compared to COM, which features a relatively smooth surface. The rough structure surface of WAC was mainly caused by the pre-treatment of the electrode with sandpaper to remove the paint and epoxy coating on the outer and inner walls of the can. However, both material surfaces changed to rather coarser structures after the EC process. WAC surface presented a well uniform distribution of visible dents generated as a result of higher electrode dissolution.

Meanwhile, a non-uniform distribution of visible dents was observed on the surface of COM. Thus, it can be summarized that the more uniform dissolution of WAC electrodes led to the higher removal of AR18 dye as compared to the non-uniform dissolution of COM electrode. The produced sludge image exhibited similar features for both electrode materials indicating the presence of identical elemental constituents such as Al, O, Na, and Cl. However, it is observed that the number and size of particles existing in WAC were larger than those of COM sludge suggesting greater formation of
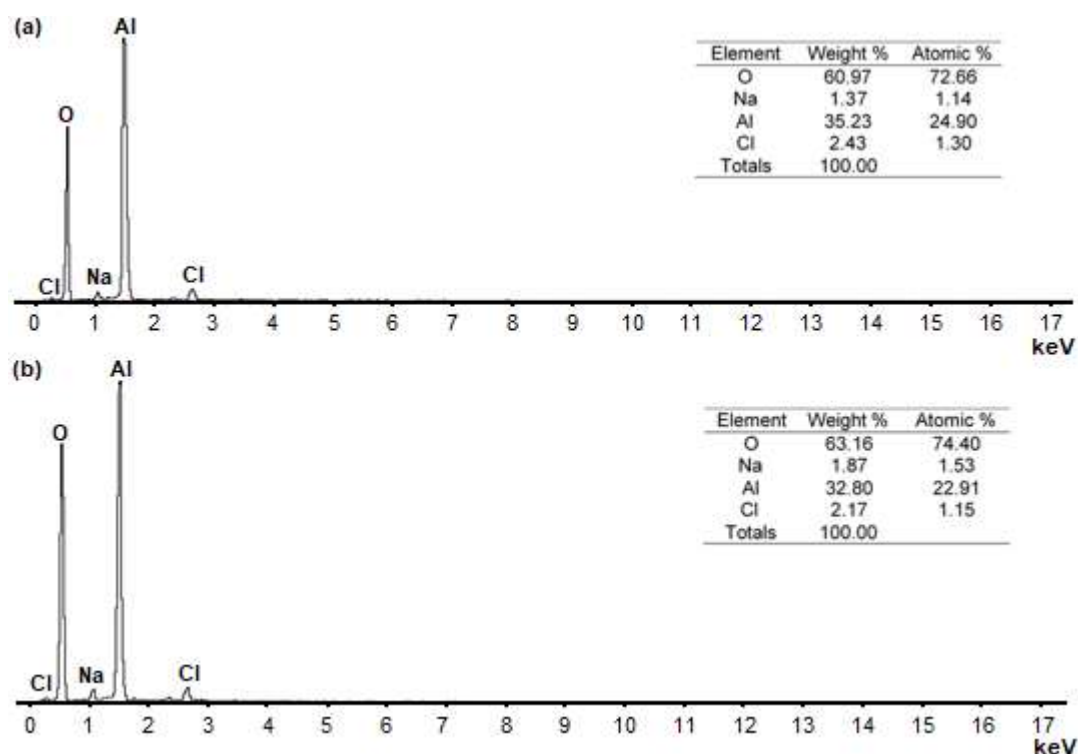
Fig 7. EDX Analysis results of sludge produced after the EC treatment using (a) WAC and (b) COM electrodes

$Al(OH)_3$ flocs in the WAC sludge. This can be confirmed by the EDX analysis results, as shown in Fig. 7(a) and 7(b) where the composition of Al element (by weight %) for WAC sludge was higher than COM with a difference of 2.43%. The presence of Na and Cl ion was also detected in both types of sludge due to the usage of NaCl as a supporting electrolyte in the EC process.

■ CONCLUSION

In the present work, the dye removal efficiency and changes in the solution pH with time as well as the quality of the treated water using WAC and COM electrodes via EC process were studied. The WAC electrode demonstrated better performance than COM electrode as it could decolorize the AR18 dye faster with 100% removal efficiency in 25 min and produced lower residual Al concentration of 0.6 ppm in the treated water after the EC treatment. During the EC process, it was also observed that pH of the solution increased considerably with both types of electrode materials reaching a maximum of 8.6, indicating that they performed similar dye removal mechanism due to the identical nature of the electrode

materials. In summary, the utilization of this material offered several advantages as it could reduce the cost for electrode material that needs to be replaced periodically and at the same time transforming this WAC into a valuable material.

■ REFERENCES

[1] Nogueira, F.G.E., Asencios, Y.J.O., Rodella, C.B., Porto, A.L.M., and Assaf, E.M., 2016, Alternative route for the synthesis of high surface-area η-Al_2O_3/Nb_2O_5 catalyst from aluminum waste, *Mater. Chem. Phys.*, 184, 23–30.

[2] Marck Industries, *Facts about Recycling Aluminum*, 2015, https://www.marck.net/facts-about-recycling-aluminum/, accessed on 10 December 2018.

[3] Abdelrahman, E.A., 2018, Synthesis of zeolite nanostructures from waste aluminum cans for efficient removal of malachite green dye from aqueous media, *J. Mol. Liq.*, 253, 72–82.

[4] Ahmedzeki, N.S., Hussein, S.J., and Abdulnabi, W.A., 2018, Synthesis of nano crystalline gamma alumina from waste cans, *Iraqi J. Chem. Pet. Eng.*, 19 (1), 45–49.

[5] Hu, Y., Bakker, M.C.M., and de Heij, P.G., 2011, Recovery and distribution of incinerated aluminum packaging waste, *Waste Manage.*, 31 (12), 2422–2430.

[6] Simanjuntak, W., Ginting, I., and Pandiangan, K.D., 2011, Removal of natural organic matter using electrocoagulation as a first step for desalination of brackish water, *Indones. J. Chem.*, 11 (1), 103–107.

[7] Ensano, B.M.B., Borea, L., Naddeo, V., Belgiorno, V., de Luna, M.D.G., Balakrishnan, M., and Ballesteros, F.C., 2019, Applicability of the electrocoagulation process in treating real municipal wastewater containing pharmaceutical active compounds, *J. Hazard. Mater.*, 361, 367–373.

[8] Dura, A., and Breslin, C.B., 2019, Electrocoagulation using aluminium anodes activated with Mg, In and Zn alloying elements, *J. Hazard. Mater.*, 366, 39–45.

[9] Ghalwa, N.M.A., Saqer, A.M., and Farhat, N.B., 2016, Removal of Reactive Red 24 dye by clean electrocoagulation process using iron and aluminum electrodes, *J. Chem. Eng. Process Technol.*, 7 (1), 1–7.

[10] Khosravi, R., Hazrati, S., and Fazlzadeh, M., 2016, Decolorization of AR18 dye solution by electrocoagulation: Sludge production and electrode loss in different current densities, *Desalin. Water Treat.*, 57 (31), 14656–14664.

[11] Zhang, X.D., Hao, J.D., Li, W.S., Jin, H.J., Yang, J., Huang, Q.M., Lu, D.S., and Xu, H.K., 2009, Synergistic effect in treatment of C.I. Acid Red 2 by electrocoagulation and electrooxidation, *J. Hazard. Mater.*, 170 (2-3), 883–887.

[12] El-Ashtoukhy, E.S.Z., and Amin, N.K., 2010, Removal of acid green dye 50 from wastewater by anodic oxidation and electrocoagulation-A comparative study, *J. Hazard. Mater.*, 179 (1-3), 113–119.

[13] Khorram, A.G., and Fallah, N., 2018, Treatment of textile dyeing factory wastewater by electrocoagulation with low sludge settling time: Optimization of operating parameters by RSM, *J. Environ. Chem. Eng.*, 6 (1), 635–642.

[14] Khandegar, V., and Saroha, A.K., 2013, Electro coagulation for the treatment of textile industry effluent–A review, *J. Environ. Manage.*, 128, 949–963.

[15] Azarian, G., Nematollahi, D., Rahmani, A.R., Godini, K., Bazdar, M., and Zolghadrnasab, H., 2014, Monopolar electro-coagulation process for azo dye C.I. Acid Red 18 removal from aqueous solutions, *Avicenna J Environ. Health Eng.*, 1 (1), e354.

[16] Fajriati, I., Mudasir, and Wahyuni, E.T., 2019, Adsorption and photodegradation of cationic and anionic dyes by TiO_2-chitosan nanocomposite, *Indones. J. Chem.*, 19 (2), 441–453.

[17] Pang, Y.L., and Abdullah, A.Z., 2013, Current status of textile industry wastewater management and research progress in Malaysia: A review, *Clean-Soil Air Water*, 41, 751–764.

[18] Baban, A., Yediler, A., Avaz, G., and Hostede, S.S., 2010, Biological and oxidative treatment of cotton textile dye-bath effluents by fixed and fluidized bed reactors, *Bioresour. Technol.*, 101 (4), 1147–1152.

[19] Ministry of Natural Resources and Environment Malaysia, 2010, *Environmental Requirements: A Guide for Investors*, 11th Ed., http://www.doe.gov.my/eia/wp-content/uploads/2012/03/A-Guide-For-Investors1.pdf, accessed on 10 December 2018.

[20] Elabbas, S., Ouazzani, N., Mandi, L., Berrekhis, F., Perdicakis, M., Pontvianne, S., Pons, M.N., Lapicque, F., and Leclerc, J.P., 2016, Treatment of highly concentrated tannery wastewater using electrocoagulation: Influence of the quality of aluminium used for the electrode, *J. Hazard. Mater.*, 319, 69–77.

Enhancing the Performances of Polymeric PVDF Membranes for Oil/Water Separation by Hydrophilic and Underwater Oleophobic Surfaces Modification

Faraziehan Senusi[1,2], Benjamin Ballinger[1], and Suzylawati Ismail[1,*]

[1]*School of Chemical Engineering, Universiti Sains Malaysia, Engineering Campus, 14300 Pulau Pinang, Malaysia*

[2]*Faculty of Chemical Engineering, Universiti Teknologi MARA (UiTM) Pulau Pinang, Permatang Pauh 13500 Pulau Pinang, Malaysia*

* Corresponding author:

tel: +604-5996458
email: chsuzy@usm.my

Abstract: *This paper investigates the permeability and separation performance of polyphenolic-amine coated PVDF membrane with hydrophilic (26.9 ± 5.6°) and underwater oleophobic (162.1 ± 5.1°) surface modification. Surface chemical structures, surface compositions and hydrophilicity of membranes were investigated by Attenuated Total Reflectance Fourier transform infrared (ATR-FTIR) spectroscopy, X-ray photoelectron spectroscopy (XPS) and contact angle analysis, respectively. The separation of emulsion oil solutions was evaluated using cross-flow filtration mode in terms of high permeation flux and excellent oil resistance. Then, the flux recovery ratio of filtration process was calculated at different transmembrane pressures (TMP) and initial concentrations of emulsion feed solutions. The results showed a decrease in the flux recovery ratio at higher pressures and initial oil concentrations. By applying Hermia's blocking model, formation of cake layer shows dominant fouling mechanism for the emulsion oil separation process.*

Keywords: *polyphenolic coating; hydrophilicity; underwater oleophobic; polymeric membrane; emulsion oil*

■ INTRODUCTION

The separation of oily wastewater, especially for surfactant-stabilized emulsions with droplet sizes smaller than 20 μm require a promising method in order to meet the requirements of high quality of the permeate flux with low operating costs [1-2]. Due to the micron sizes, emulsion droplets require a long time for effective gravity separation and ineffective breaking process, even after the addition of chemicals because of its high stability in water. Thus, the polymeric membrane filtration is one of the promising and advanced technology for the separation of various types of wastewater including emulsified oil/water mixtures.

However, the main problem for membrane separation is fouling phenomena due to the surfactant adsorption and pore blocking which can cause a severe decline of flux and rejection efficiency [3]. Generally, the fouling decreases with an increase in hydrophilicity of the membrane surface and it offers better membrane fouling resistance. In order to achieve better membrane performance, various strategies; bulk modification blending process [4-5] and the surface modification of membranes [6-8] have been applied which contributes to the enhancement in membrane performances. In addition, PVDF membranes are the most extensively used in the water treatment marketplace [9-10]. However, the performance need to be improved especially on the wettability and fouling behavior due to their hydrophobic properties [11].

To date, exciting findings have been constantly made through mussel and plant inspired chemistry using polydopamine [12] and plant (poly)phenols [13] as 'bio-glue' as well as a surface modifying agent that hydrophilize many substrates including; metals [14], glass [15] and a wide variety of polymers [16-17]. The surfaces of various substrates were improved by the existence of catechol and amine groups that have the capability to adhere on these substrates. In this study,

tannic acid as plant polyphenol derivatives have been used to transform the surface of hydrophobic polymer to become highly hydrophilic with underwater oleophobic properties and low oil adhesion for oily wastewater treatment. The polyvinylidene fluoride (PVDF) porous membrane were modified via facile deposition method using polyphenolic-amine coating by mussel-inspired coating approach [18]. It was found that the water permeability and removal efficiency of emulsion oils were improved significantly. In addition, this paper also emphasizes on the analysis of fouling mechanism of emulsion oil solutions based on a blocking model filtration on the modified membrane.

■ EXPERIMENTAL SECTION

Materials

Rolls of flat sheet polyvinylidene fluoride (PVDF) membranes (0.22μm, porosity 75%), tannic acid (TA) and tetraethylenepentamine (TEPA) were purchased from Merck Malaysia. Tris(hydroxymethyl) aminomethane and isopropanol (IPA) were supplied by Friendemann Schmidt Chemical and sodium hydroxide (NaOH) was obtained from R&M Chemicals. All chemicals were used as received. Diesel oil (Shell Malaysia) and Tween 80 (Friendemann Schmidt Chemical) were used in the preparation of emulsion oil as synthetic oil feed solution.

Procedure

Surface modification of flat sheet membrane

Prior to the coating process, the pristine PVDF membranes (M_0) with fixed size of 11.5 cm × 7 cm were immersed in 25% of IPA for 24 h to wet the pores, then soaked overnight with deionized water (DI). Next, 0.2 g of TA and 1.2 mL of TEPA were dissolved in 100 mL of 50 mM Tris-HCl buffer solution (pH 9) for 30 min. Then, the prewetted PVDF membranes were immersed into the solution with mild shaking in open containers for 6 h at 30 °C. Finally, the coated membranes, labelled as M_C, were immersed in 25% of IPA for 30 min and soaked with DI water for 12 h to remove redundant solution and later dried in air drying oven at 45 °C. Then, the membrane surface wettability was evaluated using a Dropmeter A-200

(Rame-Hart Instrument Co., U.S.A) contact angle system by detection of water contact angles using 1,2-Dichloroethane as a model oil to characterize the underwater oleophobicity. The surface chemical structure and chemical composition of the membranes were determined by attenuated total reflectance Fourier transform infrared spectra (ATR-FTIR, Thermo Scientific Nicolet iS10) and X-ray photoelectron spectroscopy (Axis Ultra DLD XPS, Kratos), respectively.

Pure water permeance experiments

The permeability of the membranes was evaluated using a laboratory scale crossflow filtration unit as shown in Fig. 1. The permeate exited at atmospheric pressure into a beaker sitting on an electronic balance (EK3000i, A&D Company). The balance was connected to a RSWeight WinCT software supplied by A&D Company, which automatically recorded the mass of permeate flux as function of time. The effective filtration area of membrane for this study was 33.6 cm². Prior to each filtration process, pure water was flowed through the membrane cell for 30 min under transmembrane pressures (TMP) of 0.20 MPa to compress the membrane. Then, the permeability tests were conducted in the range of 0.05–0.20 MPa. The pure water flux, J (LMH) was calculated as Eq. 1 where, Δm is the mass of permeated flux for a period of operation time (Δt), ρ_w is the density of water and A is the effective filtration area.

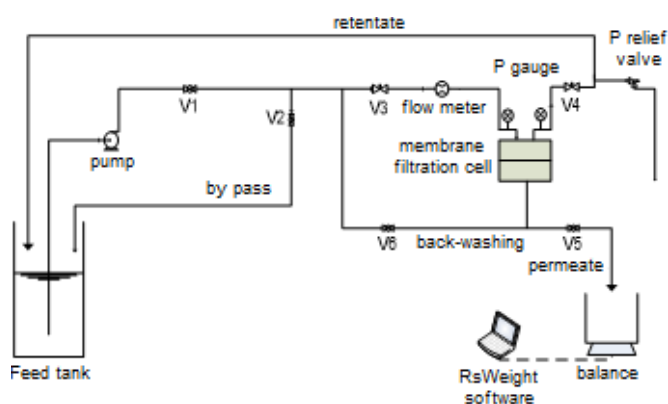$$J = \frac{\Delta m}{\rho_w A \Delta t} \qquad (1)$$

Fig 1. A laboratory scale crossflow filtration unit

Separation property and fouling studies

The foulant employed in this study was an emulsion of diesel oil in water, in which 4.82 mL of diesel oil and 0.42 mL of Tween 80 as surfactant were blended with 3 L of pure water at 6000 rpm for 30 min in a homogenizer (Ultra Turrax T-50, IKA). The droplet size of the emulsion was in the range of 0.20–10 μm with a mean diameter of 3.6 μm detected by the particle size analyzer (Cilas). The oil rejection was calculated by determining the oil concentration in the feed and permeate solution by UV spectrophotometer (DR 6000, Hach) at maximum wavelength of 198 nm which was observed using quartz cuvette. The relation between the absorbance and oil concentration was initially calibrated for different known oil concentrations as a linear calibration curve with $R^2 = 0.9948$. The removal efficiency, R (%) was calculated as follows:

$$R = \left(1 - \frac{C_P}{C_F}\right) \times 100\% \qquad (2)$$

where R (%) is the oil removal percentage, C_P and C_F are the emulsion oil concentrations in permeate and feed, respectively.

The filtration of emulsion oil solutions at different TMP and oil concentrations were applied using the recyclable steps after the compaction of the modified membrane at 0.20 MPa for 30 min. The stable water flux (J_W) was obtained by pure water filtration after 70 min. Then, the feed solution was changed to emulsion oil for 100 min until the stable flux of permeate (J_P) was obtained. The cleaning process was performed by flushing method using 0.005 M acid solution (HCl) without applying the hydraulic pressure for 5 min, followed by rinsing with pure water for the next 10 min. Finally, the feed solution was changed to pure water again to record the pure water flux (J_C) after the cleaning process. The water flux recovery ratio (FRR) indicates the degree of irreversible effects of emulsion oil on the membrane surface during filtration process and was calculated by the following equation:

$$FRR(\%) = \frac{J_C}{J_W} \times 100 \qquad (3)$$

The empirical models to describe permeate flux decline were presented by Hermia [19] based on constant pressure filtration laws that correspond to four basic types of fouling [20] as illustrated in Table 1: complete blocking (a), intermediate blocking (b), standard blocking (c) and cake layer formation (d). The characteristic form of Hermia model is given as:

$$\frac{d^2 t}{dV^2} = k \left(\frac{dt}{dV}\right)^n \qquad (4)$$
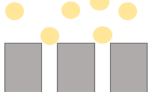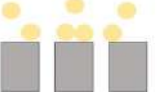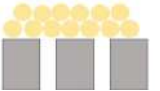
where, t and V are the filtration time and cumulative permeate volume, respectively, and k and n are two model parameters.

■ RESULTS AND DISCUSSION

Permeability and Separation Performance of Modified Membrane

The surface hydrophilicity of the pristine and modified membranes were evaluated by using pure water flux and contact angle analysis. The static water contact angle (WCA) and underwater oil contact angle (OCA) are displayed in Fig. 2(a). The pristine membrane (M_0) shows a hydrophobic nature surface with WCA of 90° and exhibited a low pure water flux of 86.7 LMH, 92.2 LMH and 187.2 LMH at 0.05, 0.10 and 0.20 MPa, respectively. The hydrophilicity of the modified membrane (M_C) had a great improvement, which was proven by the significant decrease of the WCA with the

Table 1. Blocking filtration models at constant filtration pressure

Blocking Models	Equations	Schematic view	Blocking Models	Equations	Schematic view
Complete pore blocking (n=2)	$\ln\left(\frac{1}{J}\right) = \ln\left(\frac{1}{J_0}\right) + k_b t$		Intermediate pore blocking (n=1)	$\frac{1}{J} = \frac{1}{J_0} + k_i t$	
Standard pore blocking (n=1.5)	$\frac{1}{\sqrt{J}} = \frac{1}{\sqrt{J_0}} + k_s t$		Cake layer formation (n=0)	$\frac{1}{J^2} = \frac{1}{J_0^2} + k_c t$	
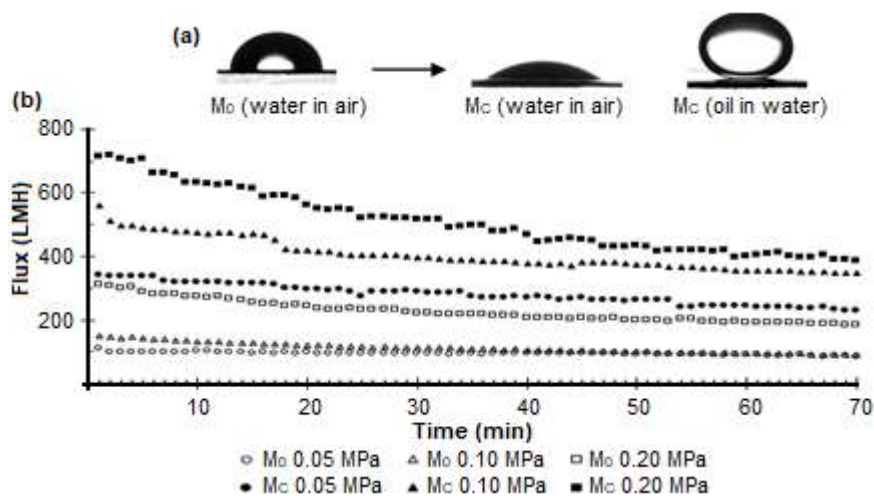
Fig 2. Contact angle in air and underwater (a) and pure water flux at different TMP (b) for membranes M_0 and M_C

modification to 26.9 ± 5.6°. Moreover, the pure water flux of M_C was significantly enhanced at each of the observed TMP as shown in Fig. 2(b) with the permeate flux for 0.05 MPa reaching 237.0 LMH. When the pressure was observed at 0.10 and 0.20 MPa, the pure water flux reached 351.8 and 398.7 LMH, respectively. The improvements on the flux are attributed to the large amount of hydrophilic hydroxyl groups on the modified M_C membrane surface which leads to higher water permeation [21].

The successful coating of the membrane surfaces that change the wetting properties could be confirmed by FTIR spectra analysis as shown in Fig. 3(b). The new broad peak between 3100 and 3600 cm^{-1} appears for M_C membranes which corresponded to the O-H stretching vibration [22]. It obviously indicated the successful adsorption of hydroxyl groups of polyphenolic tannic acid on the membrane surfaces. The new peak at 1668 and 1592 cm^{-1} was assigned to the aromatic ring (C=N) and N-H stretching of TEPA with polyphenolic, respectively,
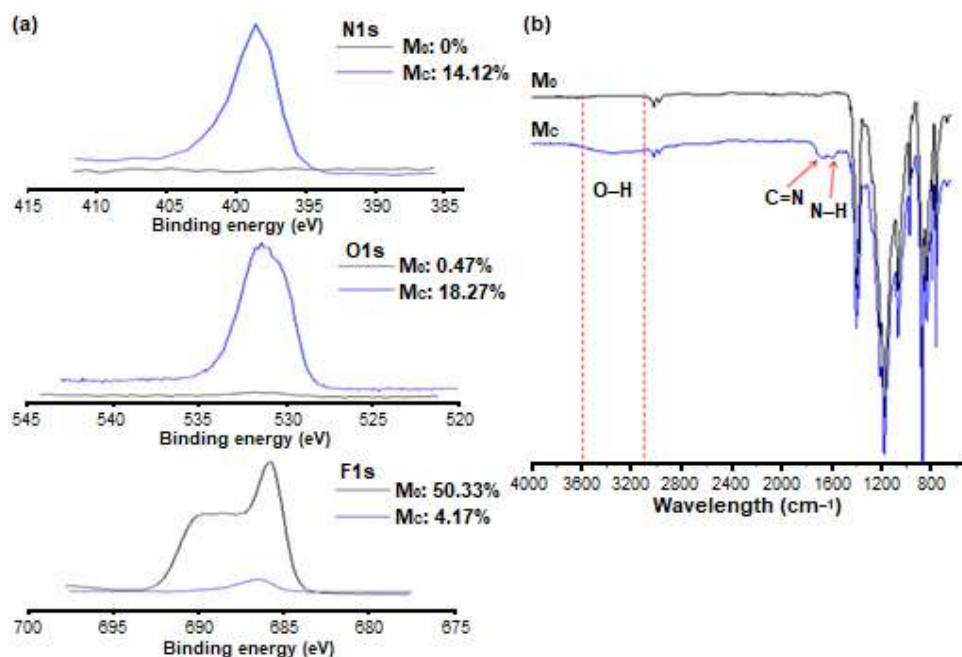
Fig 3. XPS high-resolution spectra of N1s, O1s and F1s narrow scans as a function of electron binding energy (a) and FTIR spectra (b) for membranes M_0 and M_C

during the Michael addition and Schiff bases reaction [23-24]. The similar results of FTIR spectra were also observed by other researchers for the hydrophilic coated membranes [25-26].

The ATR-FTIR results can also be confirmed by XPS analysis in Fig. 3(a), which showed the difference of surface composition for modified membranes, M_C. The new peaks of N1s and O1s elements appeared with 14.12 and 18.27% of atom percentages due to introduction of amine and –OH groups, respectively [27]. The peak intensities of F1s with atomic percentage decreased dramatically to 4.17% due to the defluorination of the pristine membrane, M_0 that occurred during this coating process. Sun et al. reported that the elimination of F⁻ occurred in the alkaline treatment for the surface modification of the PVDF membrane [28]. This concurred with the alkaline medium of polyphenolic-amine coating solution that can accelerate the interaction of hydroxyl-amine groups onto the M_C membrane surfaces through hydrogen bonding. Similar observation results were obtained for coated dual layer PVDF hollow fiber membranes reported by Shi et al. [29].

The hydrophilicity and underwater oleophobicity enable the modified membranes to achieve great potential in separating emulsified oil/water mixtures. The oil rejection and permeate flux were measured every 5 min by increasing the operation pressure from 0.025 to 0.20 MPa with an interval of 0.02 MPa as shown in Fig. 4. It was observed that oil removal efficiency and permeate flux were influenced by operating pressure. As concluded, when TMP rises, the rejection quickly decreased for the pristine M_0 membranes, while the permeate flux was lower compared to modified M_C membranes under the pressures from 0.025 to 0.06 MPa. The permeate flux start increasing from 0.08 MPa, however the separation of emulsion oil becomes worse at this state. This pressure was defined as emulsified oil critical pressure in which the suspended oil droplets on the surface would be pressed through the membranes, seriously deteriorating the separation efficiency [30].

For the modified M_C membranes, the oil rejections were maintained at approximately 90% with the higher flux from 0.025 MPa to 0.12 MPa and then slightly decreased to 83% at pressure of 0.20 MPa with the nearly constant flux. According to the above results, the surface wettability and low oil adhesion on the membrane surface of the modified M_C membranes improved further due to the enhancement of hydrophilicity. The better oil repelling ability is useful in reducing pore blockage by oil droplets especially under low precompacting pressures. It agrees with the results of underwater oleophobicity which demonstrate low oil adhesion of the membrane surfaces with oil contact angle of 162.1 ± 5.1°. The improvements on breakthrough pressure and separation efficiency was also observed by Xue et al. [31].
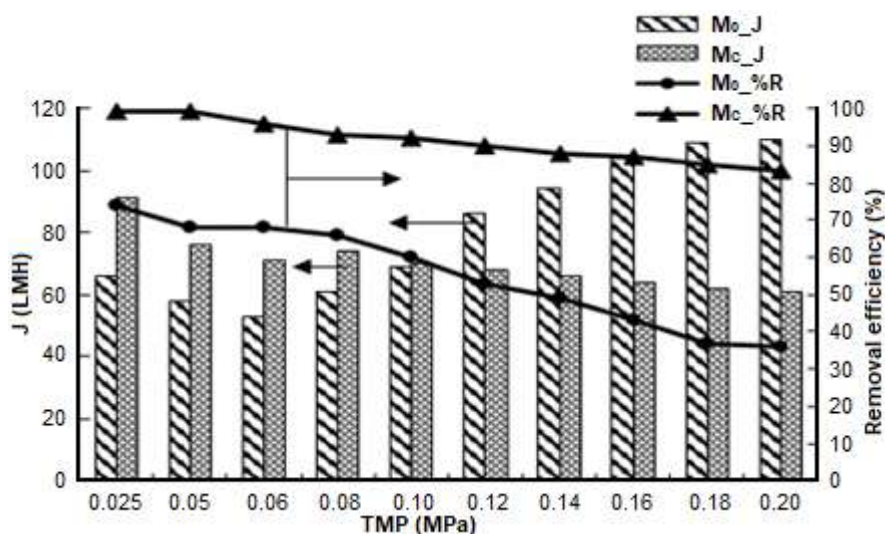

Fig 4. Permeate flux and separation efficiency of emulsion oil with increased pressure for membranes M_0 and M_C

Fouling Mechanism Studies

The separation of emulsion oil at different transmembrane pressures (TMP) is presented in Fig. 5(a). As can be observed, initial flux of pure water (J_w) increases with increasing TMP. Then, the steady state of permeation flux for emulsion oil (J_p) are 49.4 ± 1.6 LMH, 53.9 ± 0.7 LMH and 55.5 ± 0.9 LMH, for 0.05, 0.10 and 0.20 MPa, respectively. The results show that higher TMP results in droplets passing rapidly through the membrane pores due to the increase in driving force across the membrane. However, after the membranes were cleaned, the recovery flux decreased as the TMP increased.

The flux recovery ratio (FRR) for TMP values of 0.05, 0.10 and 0.20 MPa were 38.9, 35.9 and 32.8% respectively. These results indicate the increasing number of collisions between the emulsion droplets, which can break the film between the oil and water and cause many oil droplets to form a large droplet. As a result, a layer started to form above the membrane surface which may be compressed on the surface and throughout the pores at higher pressure [32]. The declines of the flux recovery ratio due to the emulsion oil had already blocked the pores and the fouling became more severe.

The effects of oil feed concentrations on the flux and recovery ratio are shown in Fig. 5(b). The results show that the steady state of permeation fluxes at 1500 ppm is slightly lower than the other two concentration values. It

may be due to the increase of resistance to permeate flow, which is attributed to the formation of thicker oil layer on the membrane surface with oil of higher concentration. Thus, the oil droplets accumulate and build up a boundary layer on the membrane surface which may reduce the permeate flux. Again, as the oil concentration increases, the flux recovery ratio after the cleaning process decreases due to the extension of interactions between emulsion droplets and the membrane surface [33].

Fig. 6 shows the representation of experimental data for permeation flux of emulsion oil as feed solution at 0.05 MPa with concentration of 500 ppm. The trends of permeate flux can be divided into three stages [34-35]. The rapid decline of flux in Stage I in the first 20 min was observed due to the build-up of oil layers on the membrane surface and within the pores. Then, the long gradual flux decline in Stage II for about 50 min was due to the accumulation of the retained oil droplets over the membrane surface. Stage III occurred after the cake layer build up on the membrane surface at maximum level and the steady state of flux was achieved until the end of the process.

In addition, the experimental filtration data of permeation flux of emulsion oil (J_P) were fitted and analyzed using the blocking model to explain the fouling phenomenon of membrane processes during constant TMP. The calculated model constants (K) and the values
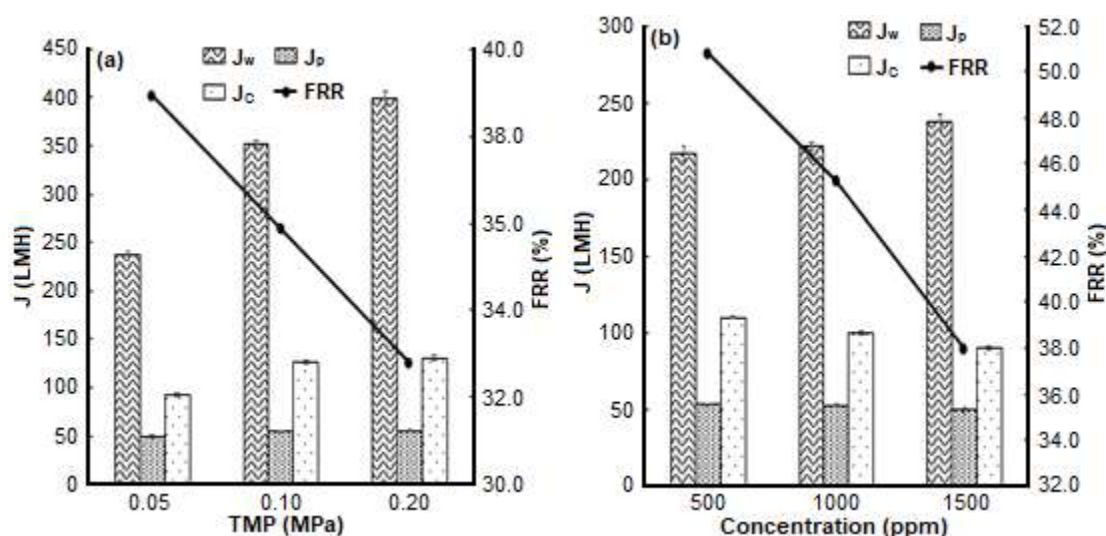

Fig 5. Permeation flux of emulsion oil and flux recovery at (a) different TMP and (b) different initial oil concentrations

Table 2. Parameter of Hermia Model for permeate of emulsion oil feed solution

Complete pore blocking			Standard pore blocking			Intermediate pore blocking			Cake layer formation		
R^2	k_b	J_0	R^2	k_s	J_0	R^2	$k_i \times 10^{-5}$	J_0	R^2	$k_c \times 10^{-6}$	J_0
0.8800	0.0061	89.7	0.9175	0.0004	90.4	0.9448	9.00	91.7	0.9739	3.00	100.0
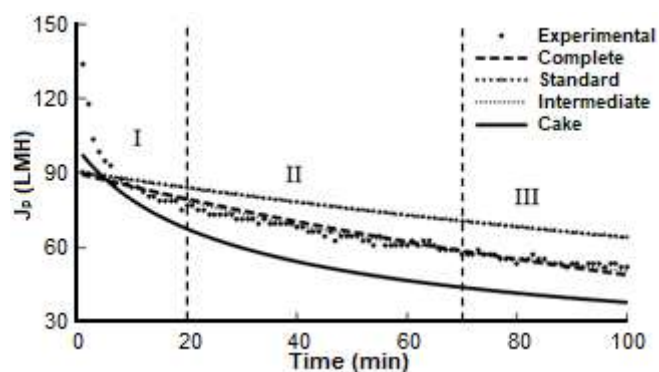
Fig 6. Permeation flux and model fitting of emulsion oil feed solution at 0.05 MPa

of coefficient of correlation (R^2) as shown in Table 2 were to determine whether the data agree with any of the considered models. The fitting of experimental permeate flux to the blocking models are illustrated in Fig. 6.

For all the models considered in this work, it can be concluded that the best of experimental data corresponds to the cake filtration model with R^2 of 0.9739 followed by the intermediate pore blocking with the R^2 value of 0.9448. The difference between experimentally measured initial permeate flux and the initial permeate flux predicted by cake filtration model was approximately 25%, while for the other three models it was above 32%. Therefore, the evidence suggests that the cake filtration phenomenon is due to the much smaller membrane pore size compared to the size of emulsion oil droplets, which indicates that there is a uniform solute cake layer that forms over the entire membrane surface which exert resistance for fluid flow [32].

■ CONCLUSION

In summary, facile modification of microfiltration PVDF membranes with high water permeation and separation performance using natural polyphenolic coating process was achieved. The inherent abundance of hydroxyl and amino groups induced by the coating process improved the membrane hydrophilicity. A significant enhancement of antifouling ability for emulsion oil separation was achieved due to the underwater oleophobic properties. Effect of transmembrane pressure and initial oil concentration had been investigated using cross-flow filtration. As expected, the results show that increasing the TMP increases permeation flux. However, it causes the reduction of flux recovery due to the compaction of cake layer formation thereby resulting in greater fouling. Also, the results on the higher oil concentration causes a decline in flux and flux recovery. The general blocking model has been evaluated at 0.05 MPa with 500 ppm of emulsified oil considering that the cake formation layer is the main fouling mechanism for the separations of emulsion oil.

■ ACKNOWLEDGMENTS

■ REFERENCES

[1] Zhu, Y., Wang, D., Jiang, L., and Jin, J., 2014, Recent progress in developing advanced membranes for emulsified oil/water separation, *NPG Asia Mater.*, 6, e101.

[2] Genc, A., and Bakirci, B., 2015, Treatment of emulsified oils by electrocoagulation: Pulsed voltage applications, *Water Sci. Technol.*, 71 (8), 1196–1202.

[3] Tripathi, B.P., Dubey, N.C., Subair, R., Choudhury, S., and Stamm, M., 2016, Enhanced hydrophilic and antifouling polyacrylonitrile membrane with

polydopamine modified silica nanoparticles, *RSC Adv.*, 6 (6), 4448–4457.

[4] Yin, J., Fan, H., and Zhou, J., 2016, Cellulose acetate/poly(vinyl alcohol) and cellulose acetate/crosslinked poly(vinyl alcohol) blend membranes: preparation, characterization, and antifouling properties, *Desalin. Water Treat.*, 57 (23), 10572–10584.

[5] Fang, L.F., Zhou, M.Y., Wang, N.C., Zhu, B.K., and Zhu, L.P., 2015, Improving the antifouling property of poly(vinyl chloride) membranes by poly(vinyl chloride)-g-poly(methacrylic acid) as the additive, *J. Appl. Polym. Sci.*, 132 (44), 42745.

[6] Zhu, H., and Zhu, S., 2015, A versatile and facile surface modification route based on polydopamine for the growth of MOF films on different substrates, *Can. J. Chem. Eng.*, 93 (1), 63–67.

[7] Bai, L., Liang, H., Crittenden, J., Qu, F., Ding, A., Ma, J., Du, X., Guo, S., and Li, G., 2015, Surface modification of UF membranes with functionalized MWCNTs to control membrane fouling by NOM fractions, *J. Membr. Sci.*, 492, 400–411.

[8] Kwon, Y.N., Hong, S., Choi, H., and Tak, T., 2012, Surface modification of a polyamide reverse osmosis membrane for chlorine resistance improvement, *J. Membr. Sci.*, 415-416, 192–198.

[9] Farahani, M.H.D.A., and Vatanpour, V., 2018, A comprehensive study on the performance and antifouling enhancement of the PVDF mixed matrix membranes by embedding different nanoparticulates: Clay, functionalized carbon nanotube, SiO_2 and TiO_2, *Sep. Purif. Technol.*, 197, 372–381.

[10] Otitoju, T.A., Ahmad, A.L., and Ooi, B.S., 2016, Polyvinylidene fluoride (PVDF) membrane for oil rejection from oily wastewater: A performance review, *J. Water Process Eng.*, 14, 41–59.

[11] Yu, S., Zhang, X., Li, F., and Zhao, X., 2018, Poly(vinyl pyrrolidone) modified poly(vinylidene fluoride) ultrafiltration membrane via a two-step surface grafting for radioactive wastewater treatment, *Sep. Purif. Technol.*, 194, 404–409.

[12] Ding, Y.H., Floren, M., and Tan, W., 2016, Mussel-inspired polydopamine for bio-surface functionalization, *Biosurf. Biotribol.*, 2 (4), 121–136.

[13] Sileika, T.S., Barrett, D.G., Zhang, R., Lau, K.H.A., and Messersmith, P.B., 2013, Colorless multifunctional coatings inspired by polyphenols found in tea, chocolate, and wine, *Angew. Chem. Int. Ed.*, 52 (41), 10766–10770.

[14] Kang, S.M., Hwang, N.S., Yeom, J., Park, S.Y., Messersmith, P.B., Choi, I.S., Langer, R., Anderson, D.G., and Lee, H., 2012, One-step multipurpose surface functionalization by adhesive catecholamine, *Adv. Funct. Mater.*, 22 (14), 2949–2955.

[15] Wei, Q., Zhang, F., Li, J., Li, B., and Zhao, C., 2010, Oxidant-induced dopamine polymerization for multi functional coatings, *Polym. Chem.*, 1 (9), 1430–1433.

[16] Wang, J., Hou, L., Yan, K., Zhang, L., and Yu, Q.J., 2018, Polydopamine nanocluster decorated electrospun nanofibrous membrane for separation of oil/water emulsions, *J. Membr. Sci.*, 547, 156–162.

[17] Kirschner, A.Y., Chang, C.C., Kasemset, S., Emrick, T., and Freeman, B.D., 2017, Fouling-resistant ultrafiltration membranes prepared via co-deposition of dopamine/zwitterion composite coatings, *J. Membr. Sci.*, 541, 300–311.

[18] Lee, H., Dellatore, S.M., Miller, W.M., and Messersmith, P.B., 2007, Mussel-inspired surface chemistry for multifunctional coatings, *Science*, 318 (5849), 426–430.

[19] Sousa, M.R.S., Lora-Garcia, J., and López-Pérez, M.F., 2018, Modelling approach to an ultrafiltration process for the removal of dissolved and colloidal substances from treated wastewater for reuse in recycled paper manufacturing, *J. Water Process Eng.*, 21, 96–106.

[20] Vela, M.C.V., Blanco, S.Á., García, J.L., and Rodríguez, E.B., 2009, Analysis of membrane pore blocking models adapted to crossflow ultrafiltration in the ultrafiltration of PEG, *Chem. Eng. J.*, 149 (1-3), 232–241.

[21] Chen, G.E., Sun, L., Xu, Z.L., Yang, H., Huang, H.H., and Liu, Y.J., 2015, Surface modification of poly(vinylidene fluoride) membrane with hydrophilic and anti-fouling performance via a two-step polymerizetion, *Korean J. Chem. Eng.*, 32 (12), 2492–2500.

[22] Zhao, X., and Liu, C., 2019, Efficient preparation of a novel PVDF antifouling membrane based on the solvent-responsive cleaning properties, *Sep. Purif. Technol.*, 210, 100–106.

[23] Bittner, S., 2006, When quinones meet amino acids: Chemical, physical and biological consequences, *Amino Acids*, 30 (3), 205–224.

[24] Ding, L., Gao, J., and Chung, T.S., 2019, Schiff base reaction assisted one-step self-assembly method for efficient gravity-driven oil-water emulsion separation, *Sep. Purif. Technol.*, 213, 437–446.

[25] Li, F., Ye, J., Yang, L., Deng, C., Tian, Q., and Yang, B., 2015, Surface modification of ultrafiltration membranes by grafting glycine-functionalized PVA based on polydopamine coatings, *Appl. Surf. Sci.*, 345, 301–309.

[26] Qin, A., Li, X., Zhao, X., Liu, D., and He, C., 2015, Engineering a highly hydrophilic PVDF membrane via binding TiO_2 nanoparticles and a PVA layer onto a membrane surface, *ACS Appl. Mater. Interfaces*, 7 (16), 8427–8436.

[27] Liu, C., Wu, L., Zhang, C., Chen, W., and Luo, S., 2018, Surface hydrophilic modification of PVDF membranes by trace amounts of tannin and polyethyleneimine, *Appl. Surf. Sci.*, 457, 695–704.

[28] Sun, C., and Feng, X., 2017, Enhancing the performance of PVDF membranes by hydrophilic surface modification via amine treatment, *Sep. Purif. Technol.*, 185, 94–102.

[29] Shi, H., Xue, L., Gao, A., Fu, Y., Zhou, Q., and Zhu, L., 2016, Fouling-resistant and adhesion-resistant surface modification of dual layer PVDF hollow fiber membrane by dopamine and quaternary polyethyleneimine, *J. Membr. Sci.*, 498, 39–47.

[30] Chen, P.C., and Xu, Z.K., 2013, Mineral-coated polymer membranes with superhydrophilicity and underwater superoleophobicity for effective oil/water separation, *Sci. Rep.*, 3, 2776.

[31] Xue, S., Li, C., Li, J., Zhu, H., and Guo, Y., 2017, A catechol-based biomimetic strategy combined with surface mineralization to enhance hydrophilicity and anti-fouling property of PTFE flat membrane, *J. Membr. Sci.*, 524, 409–418.

[32] Vela, M.C.V, Blanco, S.Á., García, J.L., Gozálvez-Zafrilla, J.M., and Rodríguez, E.B., 2007, Modelling of flux decline in crossflow ultrafiltration of macromolecules: Comparison between predicted and experimental results, *Desalination*, 204 (1-3), 328–334.

[33] Chakrabarty, B., Ghoshal, A. K., and Purkait, M. K., 2008, Ultrafiltration of stable oil-in-water emulsion by polysulfone membrane, *J. Membr. Sci.*, 325 (1), 427–437.

[34] Song, L., 1998, Flux decline in crossflow microfiltration and ultrafiltration: mechanisms and modeling of membrane fouling, *J. Membr. Sci.*, 139 (2), 183–200.

[35] Muhammad Sanusi, N.F.A., Mohd Yusoff, M.H., Seng, O.B., Marzuki, M.S., and Abdullah, A.Z., 2018, Ultrafiltration based on various polymeric membranes for recovery of spent tungsten slurry for reuse in chemical mechanical polishing process, *J. Membr. Sci.*, 548, 232–238.

Preparation of MWCNTS/Cr₂O₃-NiO Nanocomposite for Adsorption and Photocatalytic Removal of Bismarck Brown G Dye from Aqueous Solution

Emman Jassim Mohammad, Mohanad Mousa Kareem, and Abbas Jasim Atiyah Lafta*

Department of Chemistry, College of Science, University of Babylon, Hilla 51002, Iraq

Abstract: *This work describes the synthesis of nanocomposites of multiwall carbon nanotubes (MWCNTs) with co-oxide nanocomposite (MWCNTs)/MO. These nanocomposites were prepared using a simple evaporation and drying process. The obtained composites were characterized using X-Ray diffraction (XRD), Atomic force microscopy (AFM), Fourier Transform Infrared Spectroscopy (FTIR), and scanning electron microscopy (SEM). The activity of the prepared composites was investigated by following the removal of Bismarck brown G dye (BBG) from aqueous solution via adsorption processes and photocatalytic reactions. Different reaction parameters were performed, such as the effect of dosage of the used nanocomposite, pH value, and effect of temperature. In addition, adsorption isotherms and reaction kinetics were investigated. The efficiency of photocatalytic dye removal over the prepared composites was 99.9% after one hour of reaction at the optimal conditions, which were mass dosage (0.03 g), pH (5), and temperature (303 K). The adsorption isotherm data were fitted with Langmuir isotherm, and the kinetic data were fitted with the pseudo-second-order kinetic model.*

Keywords: *dyes removal; Bismarck brown G; carbon nanotubes; nanocomposite*

■ INTRODUCTION

In 1991, Summit discovered an inert carbonaceous compound that has very important and powerful properties that are called carbon nanotubes (CNTs) [1]. The first explored was of the type of multi walled carbon nanotubes (MWCNTs). This is a metallic compound and results from rolling single walled carbon nanotubes many times like (Russian doll) [2]. MWCNTs are bigger objects with diameters in the range of 1.4–100 nm and length from1 to several μm. It has a tensile strength about 100 times stronger as compared to steel and excellent thermal and electrical conductivities [3]. CNTs have a wide range of application due to its chemical, mechanical, electronic, and optical properties [4]. There are several types of carbon nanotubes likes single walled carbon nanotube (SWCNT), which has been discovered in 1993 by Iijima [5]. SWCNTs metallic or semiconductor depends on its diameter and chirality [6]. SWCNTs can be existing in three forms, Zigzag, Armchair, and chiral this depends on the way how to arrange the graphene into a cylinder. SWCNT have a diameter from 0.4 to 2.0 nm and length in

the range of 20–1000 nm [7]. Different methods are used to synthesize CNT/MOs nanocomposites, such as thermal decomposition of metal oxides precursor, chemical vapor deposition (CVD) synthesis route, hydrothermal crystallization, chemical precipitation, high-intensity ultrasonic radiation method and spontaneous formation of metal oxide nanoparticles on CNTs [8-11].

Activation (functionalization) of CNTs can be performed using various methods, including chemical, and physical methods. Chemical methods (covalent functionalization) consist of introducing functional groups on the surface of CNTs using oxidizing agents such as nitric acid, sulfuric acid, potassium permanganate or a mixture of sulfuric acid and nitric acid, hydrogen peroxide in the presence of nitric acid with oxygen-or microwave energy and water. Physical methods (Non-covalent functionalization) include using different adsorption forces, such as hydrogen bonds, Van der Waals force, electrostatic force, and π-stacking interactions. Non-covalent surface

functionalization frequently introduces little defects to the graphitic structure and does not destroy the conjugated system of the CNT sidewalls, which is important to maintain the pristine structure and properties of CNTs [12-13].

Before synthesizing the CNT/MO nanocomposite, CNTs should be functionalized [14-18]. Functionalization of CNTs plays an important step to make the CNTs soluble in water and have chemical functional groups on the surface of nanotubes, including alcoholic, carboxylic, aldehydic, ketonic, and esteric oxygenated functional groups [19]. Another activation method uses mechanical methods, which involving high shear mixing, grinding and impact mixing, or ultrasonication to open the agglomeration. These methods can separate nanotubes, but it is ineffective approaches due to breaking up of some nanotubes [20-21].

CNT, when combining with metal oxides (MOs), can produce new composites materials with new interesting properties. In addition, combining these materials in nanocomposite scales can reduce some of the disadvantages properties. As a result, the nanocomposites have large applications in comparison with the separated nanoparticles because CNTs act as a carrier to stabilize the nanoparticles. CNT/MOs nanocomposites have high specific surface areas with active surfaces for physical adsorption and chemical adsorption. In this context, different parameters need to be optimized, such as the initial concentration of the organic pollutant, contact time, adsorbent dosage, pH of reaction mixture and effect of the presence of other cations and anions in reaction mixture [22-23]. In the last few decades, high levels of pollution emerged as a result of the industrial revolution and a dramatic increase in population. Many factories over the world and especially from textile factories and dying factories discharge their waste directly into the environment without and pretreatment. This can lead to polluting each of rivers, soil, and even groundwaters. So, many types of research were directed to find proper approaches in order to reduce the level of pollutions, and among different types of pollution, pollution with textile dyes was an important type of pollution. In this context, many methods were applied to treat pollution of water with these dyes. Among these approaches, adsorption and photocatalytic dye treatment were undertaken as these routes can be performed and showed good removal efficiencies of polluted dyes from industrial water.

The present study describes the preparation of nanocomposites materials of functionalized multi-walled carbon nanotubes and Cr_2O_3-NiO co-oxide in different ratios. Then the activity of these prepared composites materials (MWCNTs/Cr_2O_3-NiO) would be investigated by following removal of Bismarck brown G dye (BBG) by adsorption and photocatalytic reaction over these prepared nanocomposites.

■ EXPERIMENTAL SECTION

Materials

MWCNTs were purchased from Nanoshel–the USA with a diameter of 13–18 nm, length in the range of 1–12 um, and purity 99%. Sulfuric acid and Nitric acid from (BDH), Bismarck brown G that has a molecular formula ($C_{21}H_{24}N_8 \cdot 2HCl$) was obtained from (Al-Hilla Textile Factory-Iraq).

Instrumentation

Atomic force microscope and Scanning Electron Microscope (FESEM) was used to investigate the surface morphology. Crystal structure of the prepared nanocomposite was investigated using powder X-Ray analysis, Phillips X-Ray diffraction with CuKα radiation (1.542 Å, 40 KV, 30 MA), in the 2θ range, 10–80 degrees. XRD6000, Shimadzu, Japan. Functional groups on the surface of the prepared composite were investigated using Fourier Transform spectroscopy (FTIR), 8400S Shimadzu Japan. FTIR spectra were recorded in the range of 400–4000 cm^{-1}, materials were mixed with powder of KBr in a ratio of 1.20. The topography of the surface of the prepared materials was investigated using an Atomic Force Microscope SPM-AA3000. Atomic Force Microscope/Contact Mode Angstrom Advanced Inc., 2005, USA. General morphological features and surface morphology of the prepared nanocomposites were investigated using SEM instrument JEOL JSM-6700F instrument (Germany). In addition, it was utilized in the calculation of the average particle size.

The EDX was used to measure the percentage of atomic ratio of MO, and factional group on the surface of the nanocomposites.

Procedure

Functionalization of MWCNTs

In order to convert MWCNTs from its inactive nature into the active form, 1 g. of raw MWCNTs was taken and added to a mixture of $HNO_3:H_2SO_4$ (1:3). The obtained mixture was then heated at 353 K and sonicated for 8 h. Then the obtained solution was filtered out by filter funnel borosilicate 3.3 (par. 3). The resulting suspension washed several times with distilled water until its pH reaching a value of 7. Then F-MWCNTs were dried at 373 K for 10 h [24]. Fig. 1 shows the preparation of MWCNTs/MO.

Synthesis of the nanocomposite

The nanocomposite of (MWCNTs/Cr_2O_3-NiO) was prepared using a simple evaporation and drying process [25]. This composite was prepared by adding MWCNTs to MO (MO = Cr_2O_3-NiO) in the mass ratio of 1:0.5 g., then MWCNTs were dispersed into 100 mL, and MO was added into 20 mL of distilled water. The MWCNTs mixture was stirred for 35 min, and MO mixture was stirred for 20 min. Then MWCNTs mixture was added into MO suspension along with stirring and heating to 353 K to evaporate water from the obtained mixture. After that, the obtained composite was dried overnight in an oven at 373 K. Fig. 2 shows the schematic diagram of the experimental procedure for the preparation of MWCNTs/MO nanocomposite by using simple evaporation and drying process.
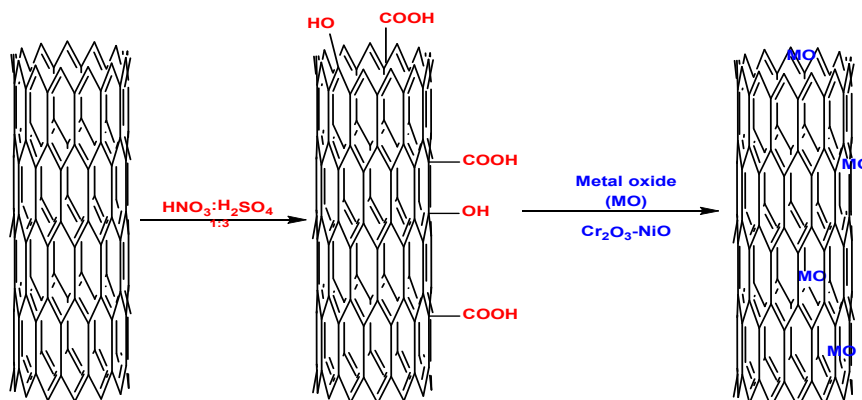

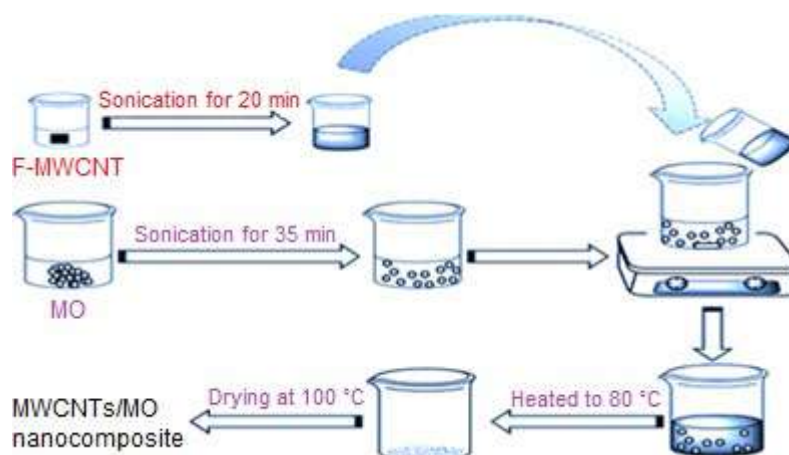**Fig 1.** Functionalization and synthesis of carbon nanotubes/metal oxide (CNT/MO) composites

Fig 2. Schematic diagram of the experimental procedure for the preparation of MWCNTs/Cr_2O_3-NiO nanocomposite by using simple evaporation and drying process

Photocatalytic removal of BBG

All experiments were performed by adding nanocomposite material into a reaction mixture, and each reaction patch consists of 30 mL, 50 ppm of the BBG dye aqueous solution. In all experiments, reactions were initiated by the stirring reaction mixture in the dark for ten minutes. Then the reaction was initiated by flushing UV radiation from a middle-pressure mercury lamp. The photocatalytic processes were performed using a mercury lamp (Philips Holland (250 W)) without cover glass as a source of UV radiation, magnetic stirrer, hot plate, and photoreaction cell which was made from Pyrex glass with quartz windows. Periodically, the reaction mixture was withdrawn at every 10 min for 1 h and centrifuged carefully. Then the absorbance's of the supernatant liquids was recorded at 460 nm using UV-Visible spectrophotometer (Shimadzu1100A). The efficiency of photocatalytic dye removal was calculated using the following equation:

$$\% \text{ Photodegradation efficiency} = \frac{A_0 - A_t}{A_0} \times 100 \qquad (1)$$

where the A_0, A_t is the initial, and the final absorbance of the used dye, respectively.

Study effect of pH, temperature and nanocomposite dosages on dye removal

In order to obtain optimum reaction conditions that can achieve high removal efficiency for dye over the prepared nanocomposites materials, a series of experiments were carried out to determine the optimum weight, pH, and temperature of the reaction mixture. To obtain an optimum used mass of the prepared composite (MWCNT/Cr_2O_3-NiO), a dye solution with a concentration of 50 ppm was suspended with graduated masses of materials nanocomposite (0.006, 0.01, 0.03, 0.05 g). The reaction was then initiated by irradiation with UV light at room temperature. From this study, the optimum mass of nanocomposite can be evaluated. Then the same arrangement would be followed to evaluate the optimum temperature by setting a series of experiments using an optimum mass that obtained from the previous study and by varying experiments at different temperatures (283, 288, 293, 298, 303, and 308 K). Then optimum pH would be investigated by performing a series of experiments with

different pH values (pH = 2, 4, 5, and 9). The pH values were adjusted at the desired level using 0.01 M NaOH or 1.0 M HCl solutions. These experiments were carried out using the same above arrangements under irradiation for 60 min. The absorbance for the above solutions was measured at λ_{max} = 460 nm, and the efficiency of photocatalytic removal of this dye was calculated using the relation that was mentioned in Eq. 1.

Adsorption ability of the prepared catalyst

The adsorption ability of the prepared nanocomposites materials was investigated using 50 ppm of BBG dye solution in 100 mL. These samples were stirred at room temperature without light using different masses of the nanocomposite (0.006, 0.01, 0.03, 0.05 g). In each case, the reaction mixture was stirred continuously at room temperature under normal atmospheric conditions. Then periodically, 1 mL of the reaction mixture was withdrawn and centrifuged, and the absorbance of the obtained supernatant liquid was recorded at 460 nm. Then removal efficiency was evaluated using the above relation in Eq. 1.

■ RESULTS AND DISCUSSION

Characteristics of Nanocomposites

XRD patterns of F-MWCNTs are shown in Fig. 3 and presented in Table 1. These patterns showed unfavorable amorphous carbon materials, a strong intense peak at $2\theta = 24.6°$, $26°$, and a low intense peak at $2\theta = 43.5°$. These peaks are corresponding to the (002) and (100) reflections, respectively. In comparison with that for MWCNTs, $2\theta = 25.2°$ and $2\theta = 44.0°$, these peaks showed a downhill shift which refers to a rise in the sp^2
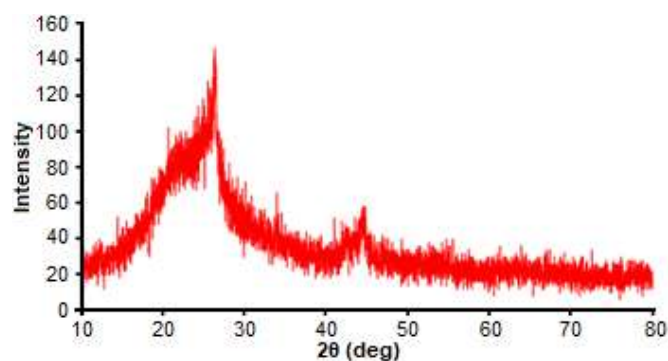
Fig 3. XRD pattern for F-MWCNT

Table 1. XRD patterns features of the MWCNTs and F-MWCNTs samples

Sample	2θ (deg)			
MWCNT		25.2		44.0
F-MWCNT	24.6	26.0	33.9	43.9
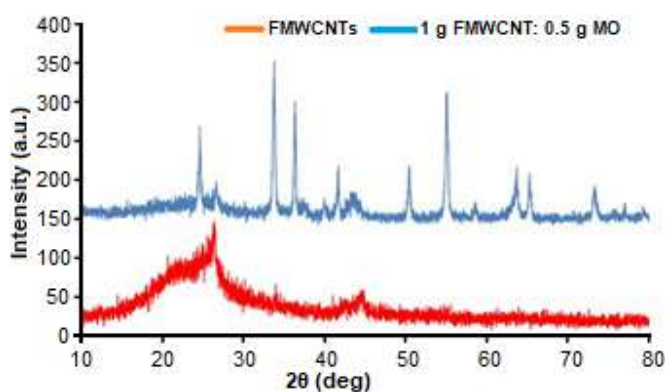
Fig 4. XRD patterns of nanocomposite MWCNTs/Cr_2O_3-NiO

Table 2. Values of angles diffraction 2θ, and particle size of nanocomposite/MWCNTs/Cr_2O_3-NiO

Sample	2θ (deg)	Crystalline size (nm) Average
Nanocomposite MOMWCNTs: 0.5 1 g	24.6557	
	26.6581	
	33.7712	
	36.3478	30.83
	37.1410	
	41.6543	
	43.3950	
	50.4008	
	55.0413	
	58.5748	
	63.6123	
	65.2709	
	73.2404	
	77.0343	
	79.2987	

C=C layer spacing and suggests that crystalline did not miss due to oxidative acid process. In this context, XRD patterns can be used to explain a relation between the degree of carbon nanotube and intensity of the oxidation MWCNTs (002) peak [26]. Table 1 shows a comparison of the XRD spectra features of the MWCNTs and F-MWCNTs samples.

X-Rays Diffraction of MWCNTs/Cr_2O_3-NiO Nanocomposite (XRD)

XRD patterns of MWCNTs/Cr_2O_3-NiO nanocomposites 1:0.5 g are shown in Fig. 4. XRD patterns of the nanocomposite are extremely similar to that of Cr_2O_3-NiO with the appearance of peaks at 24.6, 26.5, 43.3° for MWCNTs. The increase of FMWCNT ratio causes gradually decrease in the crystallite size of the MWCNTs/MO, and it becomes broader and more intense with an increase of the ratio of MWCNTs in the nanocomposite [27-28]. This observation can be related to the increase of the surface area of the composites with a reduction in the average particle size in comparison with the particle size of neat Cr_2O_3-NiO (36.18 nm). This probably arises from the high specific surface area of CNTs.

Fourier Transform Infrared Spectroscopy of MWCNTs and F-MWCNTs (FTIR)

Fourier Transform Infrared spectral data of MWCNTs and F-MWCNTs are presented in Fig. 5(a) and (b) for MWCNTs and F-MWCNTs respectively in the range of 400–4000 cm^{-1}. FTIR spectra of MWCNTs show a peak around 1680–1640 cm^{-1}, this peak is assigned to –C=C– of alkenes and that around 1500–1400 cm^{-1} is assigned to C–C stretching in the aromatic ring [29-31]. The peak around 2400 cm^{-1} is assigned to the compensation of carbon dioxide and water at the surface. The FTIR spectra of F-MWCNT show a peak around 1760–1690 cm^{-1} and this peak is assigned to C=O stretching vibration of the carboxyl group. The peak around 3500–3200 cm^{-1} is assigned to the OH vibration
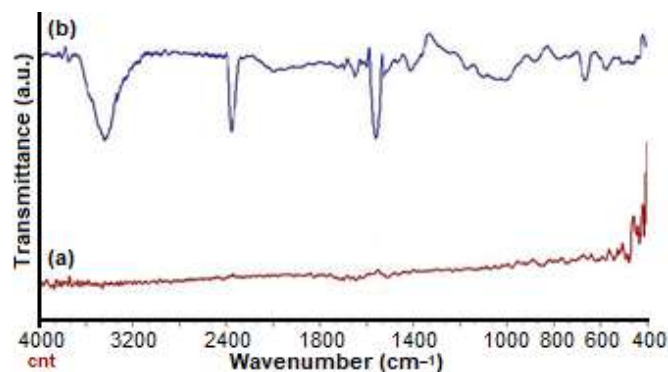
Fig 5. FTIR spectra of the MWCNTs (a), and FTIR spectra of the F-MWCNTs (b)

mode of O-MWCNTs. The peak around 1320–1000 cm⁻¹ is assigned to stretching vibration of C–O group in F-MWCNTs [32]. The peak around 2900–3100 cm⁻¹ can be attributed to the vibration of the C–H bond.

Fourier Transform Infrared Spectroscopy of MWCNTs/Cr_2O_3-NiO Nanocomposite

The FTIR spectra of the MWCNTs/MO nanocomposites are shown in Fig. 6. From these spectra, three obvious peaks correspond to the (MO) bonds around 432–619 cm⁻¹, which belong to metal-oxygen bond and the –OH bond around 1639–1681 cm⁻¹, and H bond at 3383 cm⁻¹. This is possibly arising from the intermolecular interaction at the surface of MO. However, the three absorption peaks of the MWCNTs/MO nanocomposite shifted towards higher wavelengths due to stronger interactions between the polar groups on the MO and functional groups at the surface of MWCNTs [33].

Atomic Force Microscopy (AFM) of the Prepared Nanocomposite

From the obtained results of AFM images, the average particle diameter of the prepared Cr_2O_3-NiO was around 74.65 nm at a calcination temperature of 773 K. This means that co-precipitation method effective to prepare catalysts in nanoscale and used in different industrial and environmental applications. Also, the
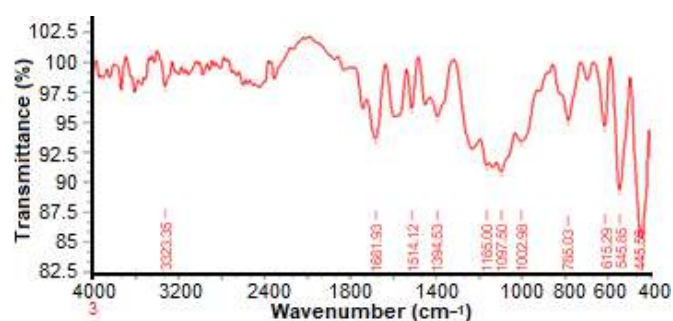
Fig 6. FTIR spectra of the MWCNTs/Cr_2O_3-NiO nanocomposite (1:0.5)
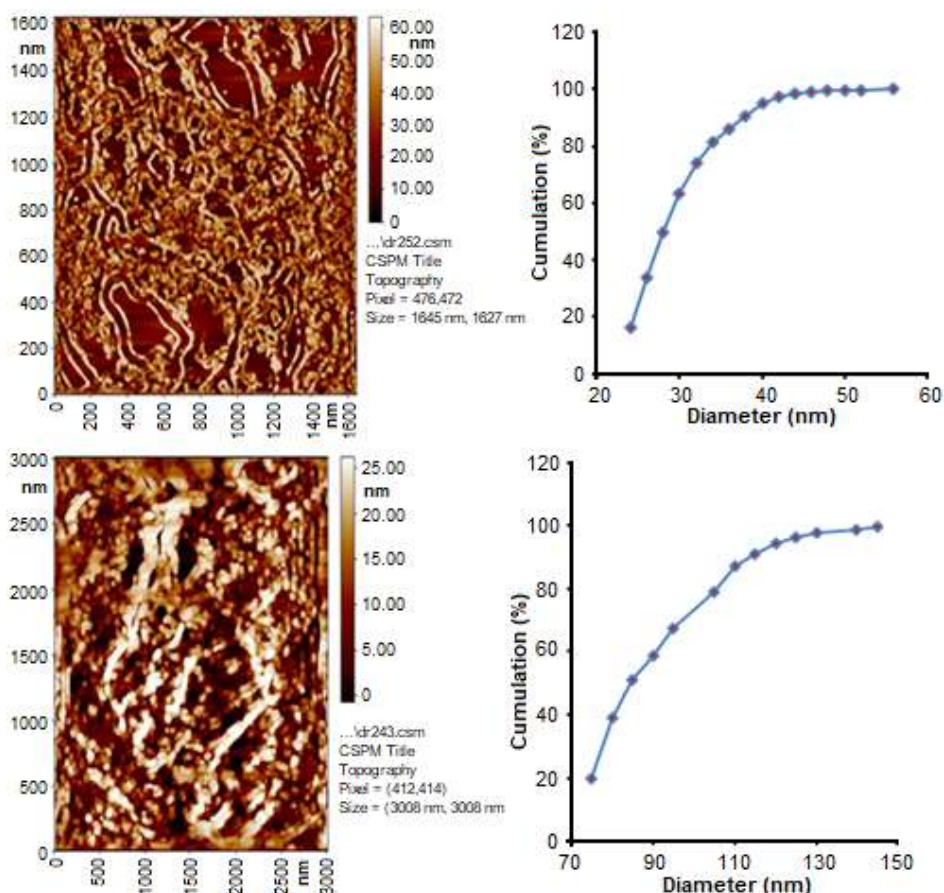
Fig 7. AFM images of nanocomposite F-MWCNTs/ Cr_2O_3-NiO (1:0. 5) g

average particle diameter of the F-MWCNTs was 29.24 nm due to having a high s surface area with small average particle size. The composite material showed an average particle diameter around 88.52 nm. This increment in particle size for a composite is probably due to the aggregation of particles that occurs at the surface of the prepared nanocomposite materials. AFM images of nanocomposite F-MWCNTs/Cr₂O₃-NiO (1:0.5) g are shown in Fig. 7.

Scanning Electron Microscope (SEM) of the Prepared Nanocomposites

The morphology of the prepared FMWCNT and MWCNTs/Cr₂O₃-NiO nanocomposite materials were investigated using SEM. This technique also was utilized to evaluate the average particle sizes. Fig. 8 and 9 show SEM images and ED's analysis for the MWCNTs, and MWCNTs/Cr₂O₃-NiO nanocomposite.

Fig. 8 shows SEM images of F-MWCNTs; from these images, it can be noted that the morphology shows the presence of smaller aggregates and tangled clusters after functionalization. The spectra of SEM-EDX of the F-MWCNTs show two important peaks corresponding to C and O result from the oxidation process with other impurities. Fig. 9 shows SEM images of the morphology F-MWCNTs/MO nanocomposites. The SEM images showed that the MWCNTs are homogeneously distributed throughout the MO matrix with an obvious agglomeration of the MO particles. SEM-EDX used for elemental analysis as shown in Fig. 9 shows that the nanocomposite elements F-MWCNTs/MO exhibited several peaks, which related to Ni, Cr, C, and O with few impurities in the prepared composite [34].
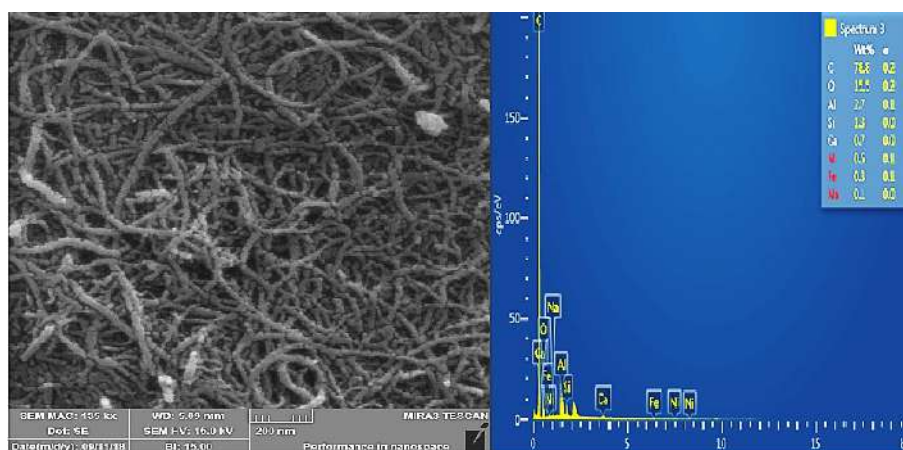
Fig 8. SEM images and EDS analysis of the prepared F-MWCNTs
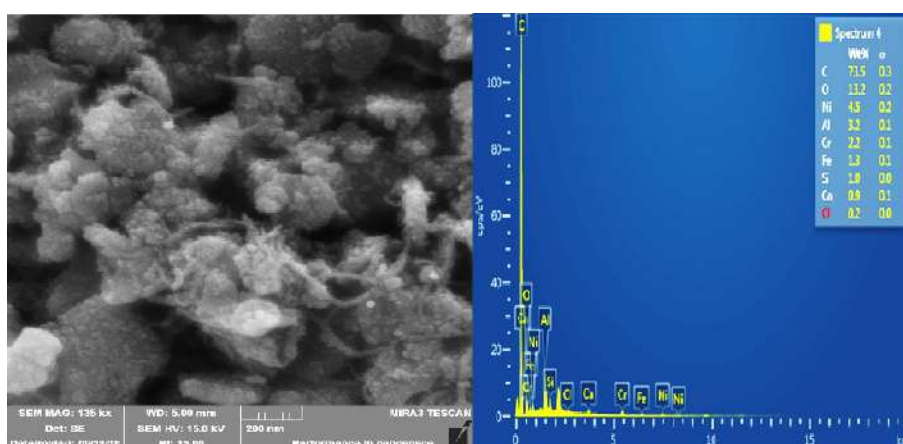
Fig 9. SEM images and EDS analysis of the prepared F-MWCNTs/ Cr₂O₃-NiO (1:0.5) g nanocomposites

Photocatalytic Activity of the Nanocomposite

Effect of the amount of nanocomposite on photocatalytic removal of BBG dye over nanocomposite

The obtained results of photocatalytic removal of BBG dye over nanocomposite under using different masses of the used composite are presented in Fig. 10. These used masses were as follows, 0.006, 0.01, 0.03, and 0.05 g. In each case, a required mass of the composite was suspended in 30 mL of dye aqueous solution (50 ppm) under irradiation with UV light at 298 K. All experiments were carried out for 60 min. From the obtained results, it was found that there was an increase in the efficiency of dye removal with an increase in the amount of the used composite. The higher efficiency of dye removal was achieved at mass equal to 0.03 g. After that, the increase in nanocomposite weight to 0.05 g leads to the reduction in efficiency of dye removal. At high concentrations of the nanocomposite upon using a same light source, the nanoparticles of $MWCNTs/Cr_2O_3$-NiO can form inner filter inside reaction mixture which leads to absorb the photons and prevent crossing passing them into the other side of the reaction mixture. This leads to reducing the number of excited particles, which results in a reduction in the formation of redox species including conduction band electrons and valence band holes. These redox species play a significant role in redox reaction at the surface of the used catalyst, which leads to a reduction in the efficiency of dye removal [35].

Effect of pH on photocatalytic BBG dye removal over $MWCNT/Cr_2O_3$-NiO

To investigate the effect of pH of the reaction mixture on the efficiency of BBG dye removal over prepared nanocomposite. A series of experiments were performed at different pHs values under constant other reaction parameters. For each case, 0.03 g of the nanocomposite was suspended in 30 mL of aqueous BBG dye solution 50 ppm under UV light at 298 K for 60 min. The obtained results of this part are presented in Fig. 11. From these results, the best result of removal efficiency was obtained at pH = 5 and in this case, the efficiency of dye removal was around 93.68%. Then after this value, any increase in the pH values up to 9 leads to a decrease in the removal efficiency. This can be resulted due to the repulsion between the negatively charged surface and the anionic groups in dye molecules [36-37].

Effect of temperature on photocatalytic removal of BBG over nanocomposite

The effect of reaction temperature on the efficiency of photocatalytic removal of BBG dye over nanocomposite was investigated by performing the reactions under different temperatures in the range from

Fig 10. Effect of the amount of nanocomposite on BBG dye removal over different masses of the composites
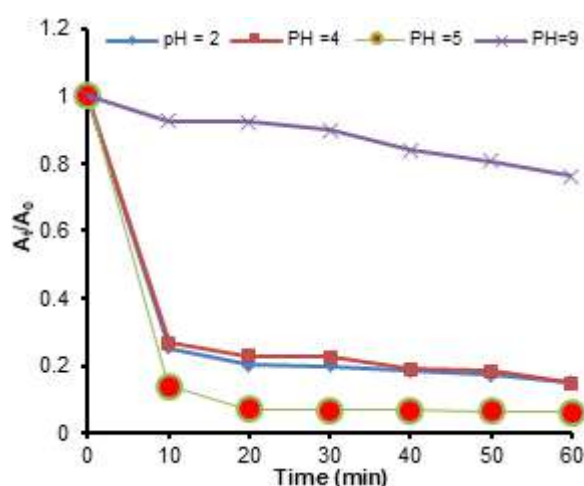
Fig 11. Effect of pHs of dye solution on the removal efficiency of BBG over nanocomposite

283–308 K with increasing by five degrees for each increment. Other reaction conditions were kept constant. These conditions involve using a dye in a concentration of 50 ppm in 30 mL, nanocomposite loading of 0.03 g, and the pH of the reaction mixture was kept at 5. The obtained results are shown in Fig. 12, and from these results, it was found that the efficiency of dye removal was enhanced with increasing temperature of the reaction mixture and the best removal efficiency was recorded at 303 K, and it was around 99.8%. This observation can be attributed to the formation of a high concentration of free radicals upon elevation in reaction temperature. These active species would contribute to the removal of dye molecules. Besides that, an increase in temperature leads to an increase of diffusion rate of dye molecules from the bulk solution to be adsorbed at the active sites on the surface. At higher temperatures, greater than 303 K, any increase in reaction temperature can affect the amount of adsorbed molecules at the surface and increase the rate of desorption of dye molecules away from the surface. This effect leads to reduce the efficiency of dye removal under these conditions [38].

Adsorption Isotherms

The results of the adsorption of BBG dye over nanocomposites are shown in Fig. 13 and 14, and Table 3. In this part, both Langmuir and Freundlich adsorption isotherm models were investigated for adsorption of BBG over nanocomposite.

From the presented results in Table 3, the value of the correction factor (R^2) to Langmuir is lower than the value of the correction coefficient (R^2) for Freundlich, but the number of adsorbed layers is 0.899. In this case, the formation of a single monolayer of adsorbate on the surface agrees on with the Langmuir adsorption model which make the adsorption seems to be more fitted with Langmuir adsorption isotherm. [39].

Kinetics of Adsorption of BBG over Nanocomposite

Kinetics study for adsorption of BBG dye over nanocomposite was investigated, and the obtained results are presented in Table 4 and Fig. 15 and 16. From
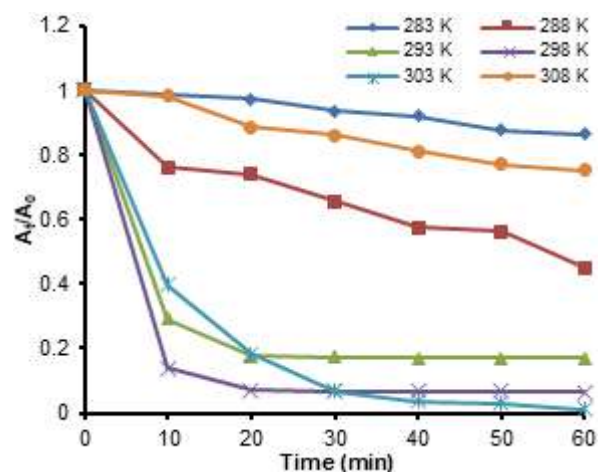
Fig 12. Effect of temperature on removal efficiency of BBG over nanocomposite

Fig 13. Langmuir adsorption isotherm for the adsorption of BBG over nanocomposite
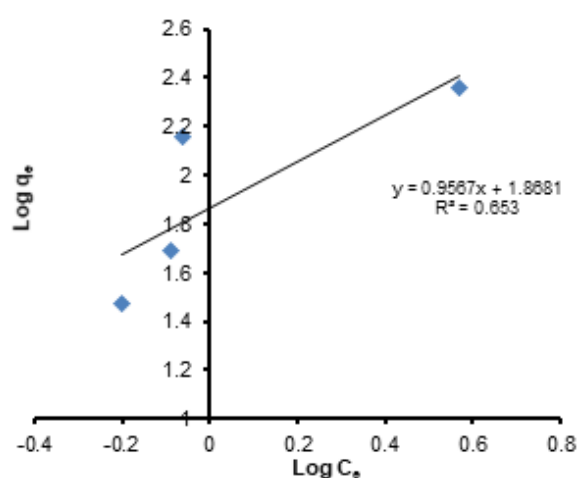
Fig 14. Freundlich adsorption isotherm for adsorption of BBG over the used nanocomposite

the obtained results, it was found that the value of the correction factor for the pseudo-first-order kinetic model was ranged from 0.8493 to 1.000. It was lower than the values of the pseudo-second-order kinetic model, which was ranged from 0.9987 to 1.000. From these results, it is clear that adsorption of BBG dye over nanocomposite was more fitted with a pseudo-second-order kinetic model.

The pseudo-first order kinetic model is given by Lagergren [39]

$$\ln(q_t - q_e) = \ln(q_e) - k_1 t \tag{2}$$

where q_e and q_t (mg/g) are the amounts of the BBG adsorbed at equilibrium and at time t (min), respectively, and k_1 (min^{-1}) is the adsorption rate constant. The pseudo-second-order kinetic model is given by the following equation:

$$\frac{t}{q_t} = \frac{1}{k_2 q_e^2} + \frac{t}{q_e} \tag{3}$$

where k_2 (g/mg min) is the rate constant of the second-order equation.

Table 3. Langmuir and Freundlich adsorption isotherms constants for adsorption of BBG over the used nanocomposite

Isotherms	Parameters	Values
Freundlich	K_F	5.682
	N	0.899
	R^2	0.9887
Langmuir	Q_m	909.09
	K_L	0.0576
	R^2	0.5888

Table 4. The adsorption parameters for BBG adsorption onto FMWCNTs/Cr₂O₃-NiO

Weight (g)	Pseudo-first-order model			
	q_e, exp (mg/g)	q_e, cal (mg/g)	K_1 (min^{-1})	R^2
0.006	231.3	64.32	0.1043	0.8553
0.01	147.39	10.41	0.0586	0.9611
0.03	49.18	2.57	0.0379	0.8493
0.05	29.62	34.12	0.0938	1
	Pseudo-second-order model			
	q_e, exp (mg/g)	q_e, cal (mg/g)	K_2 (g/mg min)	R^2
0.006	231.3	283.09	0.0026	0.9987
0.01	147.39	147.05	0.028	1
0.03	49.18	49.5	0.05	0.9998
0.05	29.62	29.67	0.151	0.9999
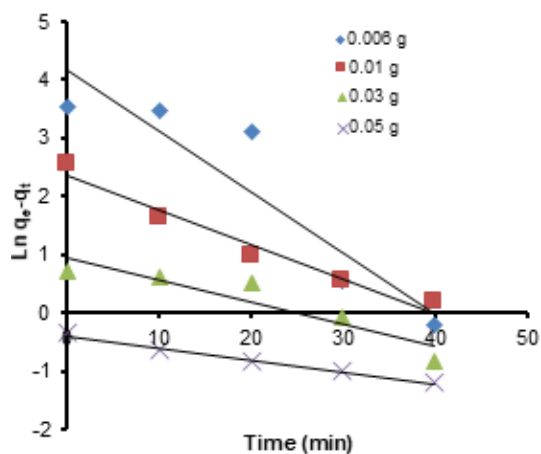
Fig 15. The pseudo-first-order onto FMWCNTs/Cr₂O₃-NiO for BBG adsorption
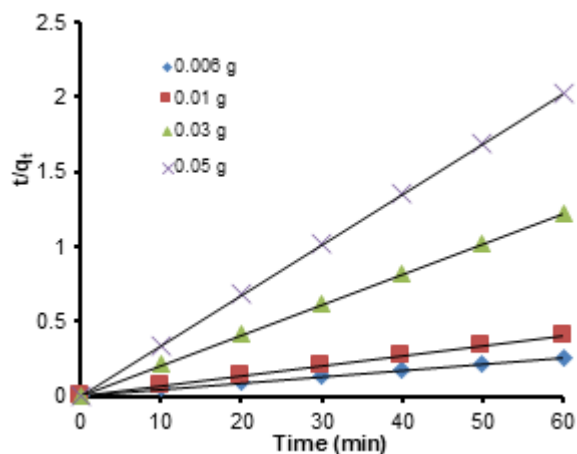
Fig 16. Pseudo-second order kinetic model over FMWCNT/ Cr₂O₃-NiO

■ **CONCLUSION**

The adsorption and photocatalytic removal of BBG dye over nanocomposite depend on the dosage of the nanocomposite, pH value, and reaction temperature. The complete photocatalytic removal of BBG dye was investigated by using F-MWCNT/MO under UV illumination. The optimal conditions of removal dye were found to be at pH of 5, nanocomposite dosage of 0.03 g/L, the temperature of 303 K with 50 ppm of the dye solution and illumination time of 60 min. From the obtained results of equilibrium, adsorption isotherm refers to the formation of monolayer adsorption, and hence it was more fitted with the Langmuir adsorption model. The adsorption process of BBG dye over the prepared nanocomposite was fitted with the pseudo-second-order kinetic model.

■ **REFERENCES**

[1] Xu, A.Z., Yang, M.S., Wu, Q., Hu, X.M., and Jiang, L., 2005, Flow field induced steady alignment of oxidized multi-walled carbon nanotubes, *Chin. Chem. Lett.*, 16 (6), 849–852.

[2] Iijima, S., and Ichihashi, T., 1993, Single-shell carbon nanotubes of 1-nm diameter, *Nature*, 363, 603–605.

[3] Ijima, S., 1991, Helical microtubules of graphitic carbon, *Nature*, 354 (7), 56–58.

[4] Wepasnick, K.A., Smith, B.A., Bitter, J.L., and Fairbrother, D.H., 2010, Chemical and structural characterization of carbon nanotube surfaces, *Anal. Bioanal. Chem.*, 396 (3), 1003–1014.

[5] Iijima, S., and Ichihashi, T., 1993, Single-shell carbon nanotubes of 1-nm diameter, *Nature*, 363, 603-605.

[6] Jishi, R.A., Venkataraman, L., Dresselhaus, M.S., and Dresselhaus, G., 1993, Phonon modes in carbon nanotubules, *Chem. Phys. Lett.*, 209 (1-2), 77–82.

[7] Wang, N., Tang, Z.K., Li, G.D., and Chen, J.S., 2000, Materials science: Single walled 4Å carbon nanotube arrays, *Nature*, 408 (6808), 50–51.

[8] Liu, X., Huber, T.A., Kopac, M.C., and Pickup, P.G., 2009, Ru oxide/carbon nanotube composites for supercapacitors prepared by spontaneous reduction of Ru(VI) and Ru(VII), *Electrochim. Acta*, 54 (27), 7141–7147.

[9] Leonov, A.A., Khasanov, A.O., Danchenko, V.A., and Khasanov, O.L., 2017, Spark plasma sintering of ceramic matrix composite based on alumina, reinforced by carbon nanotubes, *IOP Conf. Ser.: Mater. Sci. Eng.*, 286, 012034.

[10] Keshri, A.K., Huang, J., Singh, V., Choi, W., Seal, S., and Agarwal, A., 2010, Synthesis of aluminum oxide coating with carbon nanotube reinforcement produced by chemical vapor deposition for improved fracture and wear resistance, *Carbon*, 48 (2), 431–442.

[11] Bandow, S., Asaka, S., Saito, Y., Rao, A.M., Grigorian, L., Richter, E., and Eklund, P.C., 1998, Importance of transmission electron microscopy for carbon nanomaterials, *Phys. Rev. Lett.*, 80 (17), 3779–3782.

[12] Koval'chuk, A.A., Shevchenko, V.G., Shchegolikhin, A.N., Nedorezova, P.M., Klyamkina, A.N., and Aladyshev, A.M., 2008, Effect of carbon nanotube functionalization on the structural and mechanical properties of polypropylene/MWCNT composites, *Macromolecules*, 41 (20), 7536–7542.

[13] Amiri, A., Maghrebi, M., Baniadam, M., and Zeinali Heris, S.Z., 2011, One-pot, efficient functionalization of multi-walled carbon nanotubes with diamines by microwave method, *Appl. Surf. Sci.*, 257 (23), 10261–10266.

[14] Cuentas-Gallegos, A.K., Martínez-Rosales, R., Rincón, M.E., Hirata, G.A., and Orozco, G., 2006, Design of hybrid materials based on carbon nanotubes and polyoxometalates, *Opt. Mater.*, 29 (1), 126–133.

[15] Hojati-Talemi, P., and Simon, G., 2009, Microwave-based treatments for multi-walled carbon nanotubes, *Phys. Status Solidi C*, 6 (10), 2170–2173.

[16] Smith, B., Wepasnick, K., Schrote, K.E., Cho, H.H., Ball, W.P., and Fairbrother, D.H., 2009, Influence of surface oxides on the colloidal stability of multi-

walled carbon nanotubes: A structure-property relationship, *Langmuir*, 25 (17), 9767–9776.

[17] Lu, C., and Chiu, H., 2008, Chemical modification of multiwalled carbon nanotubes for sorption of Zn^{2+} from aqueous solution, *Chem. Eng. J.*, 139 (3), 462–468.

[18] Morales-Lara, F., Pérez-Mendoza, M.J., Altmajer-Vaz, D., García-Román, M., Melguizo, M., López-Garzón, F.J., and Domingo-García, M., 2013, Functionalization of multiwall carbon nanotubes by ozone at basic pH. Comparison with oxygen plasma and ozone in gas phase, *J. Phys. Chem. C*, 117 (22), 11647–11655.

[19] Eder, D., 2010, Carbon nanotube–inorganic hybrids, *Chem. Rev.*, 110 (3), 1348–1385.

[20] Fu, K., Huang, W., Lin, Y., Riddle, L.A., Carroll, D.L., and Sun, Y.P., 2001, Defunctionalization of functionalized carbon nanotubes, *Nano Lett.*, 1 (8), 439–441.

[21] Sun, Y., Wilson, S.R., and Schuster, D.I., 2001, High dissolution and strong light emission of carbon nanotubes in aromatic amine solvents, *J. Am. Chem. Soc.*, 123 (22), 5348–5349.

[22] Gupta, V.K., Agarwal, S., and Saleh, T.A., 2011, Synthesis and characterization of alumina-coated carbon nanotubes and their application for lead removal, *J. Hazard. Mater.*, 185 (1), 17–23.

[23] Wang, S., Shi, X., Shao, G., Duan, X., Yang, H., and Wang, T., 2008, Preparation, characterization and photocatalytic activity of multi-walled carbon nanotube-supported tungsten trioxide composites, *J. Phys. Chem. Solids*, 69 (10), 2396–2400.

[24] Mitróová, Z., Tomašovičová, N., Lancz, G., Kováč, J., Vávra, I., and Kopčanský, P., 2010, Preparation and characterization of carbon nanotubes functionalized by magnetite nanoparticles, *Proceeding of the 2nd NANOCON International Conference*, Olomouc, Czech Republic, 12–14 October 2010.

[25] Xu, Y.J., Zhuang, Y., and Fu, X., 2010, New insight for the enhanced photocatalytic activity of TiO_2 by doping carbon nanotubes: A case study on degradation of benzene and methyl orange, *J. Phys. Chem. C*, 114 (6), 2669–2676.

[26] Yu, Y., Yu, J.C., Yu, J.G., Kwok, Y.C., Che, Y.K., Zhao, J.C., Ding, L., Ge, W.K., and Wong, P.K., 2005, Enhancement of photocatalytic activity of mesoporous TiO_2 by using carbon nanotubes, *Appl. Catal.*, A, 289 (2), 186–196.

[27] Yudasaka, M., Kikuchi, R., Matsui, T., Ohki, Y., Yoshimura, S., and Ota, E., 1995, Specific conditions for Ni catalyzed carbon nanotube growth by chemical vapor deposition, *Appl. Phys. Lett.*, 67 (17), 2477–2479.

[28] Yukasaka, M., Kikuchi, R., Ohki, Y., Ota, E., and Yoshimura, S., 1997, Behavior of Ni in carbon nanotube nucleation, *Appl. Phys. Lett.*, 70 (14), 1817–1818.

[29] Skoog, D.A., Holler, F.J., and Crouch, S.R., 2007, Principles of Instrumental Analysis, Principles of Instrumental Analysis, 6th Ed., Thomson Brooks/Cole, Belmont, CA, USA.

[30] Wu, X., Hong, X., Luo, Z., Hui, K.S., Chen, H., Wu, J., Hui, K.N. Li, L., Nan, J., and Zang, Q., 2013, The effects of surface modification on the supercapacitive behaviors of novel mesoporous carbon derived from rod-like hydroxyapatite template, *Electrochim. Acta*, 89, 400–406.

[31] Pilehvar, S., Rather, J.A., Dardenne, F., Robbens, J., Blust, R., and De Wael, K., 2013, Carbon nanotubes based electrochemical detection of hydroxylated polychlorinated biphenyl in human blood aptasensing platform for the serum, *Biosens. Bioelectron.*, 54, 78–84.

[32] Fadaei, S., Moghadam, F.N., Hashemi, M., and Pourzamani, H., 2017, BTEX removal from aqueous solution by modified multi-walled carbon nanotubes with ozone, *Anuário IGEO*, 40 (1), 235–242.

[33] Yıldırım, A., and Seçkin, T., 2014, *In situ* preparation of polyether amine functionalized MWCNT nanofiller as reinforcing agents, *Adv. Mat. Sci. Eng.*, 2014, 356920.

[34] Kim, S.K., and Park, H.S., 2014, Multiwalled carbon nanotubes coated with a thin carbon layer for use as composite electrodes in supercapacitors, *RSC Adv.*, 4 (88), 47827–47832.

[35] Hayat, K., Gondal, M.A., Khaled, M.M., and Ahmed, S., 2010, Kinetic study of laser-induced photocatalytic degradation of dye (alizarin yellow)

from wastewater using nanostructured ZnO, *J. Environ. Sci. Health., Part A Toxic/Hazard. Subst. Environ. Eng.*, 45 (11), 1413–1420.

[36] Mohammad, E.J., Lafta, A.J., and Kahdim, S.H., 2016, Photocatalytic removal of reactive yellow 145 dye from simulated textile wastewaters over supported (Co, Ni)$_3$O$_4$/Al$_2$O$_3$ co-catalyst, *Pol. J. Chem. Technol.*, 18 (3), 1–9.

[37] Mohammad, E.J., Kareem, M.M., and Atiyah, A.J., 2018, Removal of dye Bismarck brown G by

photocatalytic reaction over prepared co-oxide Cr$_2$O$_3$-NiO: A kinetic study, *Asian J. Chem.*, 30 (11), 2527–2532.

[38] Soares, E.T., Lansarin, M.A., and Moro, C.C., 2007, A study of process variables for the photocatalytic degradation of rhodamine B, *Braz. J. Chem. Eng.*, 24 (1), 29–36.

[39] Lagergren, S., 1898, About the theory of so-called adsorption of soluble substances, *K. Sven. Vetensk.Akad. Handl.*, 24 (4), 1–39.

FTIR and HPLC-Based Metabolomics of Yacon Leaves Extracts (*Smallanthus sonchifolius* [Poepp & Endl.] H. Robinson) from Two Locations in Indonesia

Zuhelmi Aziz[1], Nancy Dewi Yuliana[2,*], Partomuan Simanjuntak[3], Mohamad Rafi[4], and Syamsudin[1]

[1]Doctoral Program of Pharmacy Faculty, University of Pancasila, Srengseng Sawah Jagakarsa, Jakarta Selatan 12640, Indonesia

[2]Department of Food Science and Technology, Faculty of Agricultural Technology, Bogor Agricultural University, Tanjung Street, IPB Dramaga Campus, Bogor 16680, Indonesia

[3]Research Center for Biotechnology, Indonesian Institute of Sciences (LIPI), Jl. Raya Bogor Km 46, Cibinong 16911, Indonesia

[4]Department of Chemistry, Faculty of Mathematics and Natural Sciences, Bogor Agricultural University, Tanjung Street, IPB Dramaga Campus, Bogor 16680, Indonesia

Abstract: Smallanthus sonchifolius *[Poepp. & Endl.] H. Robinson (Asteraceae) also known as Yacon or insulin plant, is traditionally used for treating diabetes. Varying geographical origins and postharvest handling, however, seem to affect quantitative and qualitative metabolites in the leaves of* Smallanthus sonchifolius *[Poepp. & Endl.] H. Robinson (Yacon). This study was conducted to compare and differentiate metabolites profile/fingerprint of Yacon leaves which were grown and obtained from different locations in Pulau Jawa i.e. Lembang (Jawa Barat) and Wonosobo (Jawa Tengah). Three different solvents (95% ethanol, 50% ethanol and water) were used to obtain Yacon leaves extracts, in order to determine the suitable solvent to produce discernable differentiation through FTIR and HPLC-based metabolomics. Principal Component Analysis (PCA) of FTIR data (4000–400 cm⁻¹ wavenumber) indicated that Yacon leaves extracted with 95% ethanol, had a distinctive FTIR fingerprint profile when compared to others. However, the FTIR-based PCA could not differentiate the extracts based on their geographical origins, although PCA analysis of HPLC-data successfully differentiated the extracts based on their geographical origins. Furthermore, the prominent peak for the leaves extract from Lembang and Wonosobo as regards to retention time, was observed at 21.59–25.10 min and 20.69–21.695 min respectively. Notably, R²Y and Q² values obtained by cross-validation and permutation tests showed all multivariate models were statistically reliable. Overall, there is a need to conduct further research using a more sophisticated tool such as LC-MS, to identify which metabolites were represented by the aforementioned FTIR and HPLC data.*

Keywords: *FTIR; HPLC; metabolomics;* Smallanthus sonchifolius*; Yacon*

■ INTRODUCTION

Smallanthus sonchifolius [Poepp. & Endl.] H. Robinson or Yacon is a perennial plant from the native Asteraceae family, located in the Andean regions of South America, spanning from Colombia to Argentina. This globally cultivated plant is also found in Europe, New Zealand and even Asia (Japan and Indonesia) [1]. Cultivated in Lembang, Jawa Barat Province, and in Wonosobo, Jawa Tengah Province; Yacon has been widely used as a traditional medicine to treat diabetes in Indonesia. Currently, its leaves are widely used as herbal medicine to also treat diabetes, often administered in the form of a single simplicia or mixed with other simplicia in the form of capsules or teabags.

The presence of phenolic constituents in Yacon has been linked to its antidiabetic (hypoglycaemic) and anti-hypertensive effects [2]. Studies by numerous researchers

have also reported its anti-inflammatory capacity, observed through metabolomics profiling of its compounds [3], and antidiabetic activity through α-glucosidase inhibition [4]. Despite several studies on the phytochemical content of Yacon, there have not been any reports on comparison and differentiation of Yacon metabolites profile, grown and obtained from different locations in Pulau Jawa. Such comparison and differentiation are necessary to ensure the quality of the potential effects that have been mentioned above, as the possibility of investigating and proving chemical variation as a result of geographical differences, may also have the potential within the field of pharmaco-botany, towards achieving optimal growth of Yacon to exhibit certain desired potency.

Previous phytochemical research of Yacon leaves has shown it contains sesquiterpene lactones such as sonchifolin, uvedalin, enhydrin, fluctuanin, polymatin B, fluctuadin, and polymatin C, and along with melampolide compounds [5]. Further analysis showed flavonoid compounds such as quercetin [6], polyphenolic compounds such as chlorogenic acid, ferulic acid, and caffeic acid derivatives such as 1.5-O-di-caffeoylquinic acid (1,5-CQA), 4,5-O-di-caffeoylquinic acid (4,5-CQA), and 3,5-O-di-caffeoylquinic acid (3,5-CQA) [7]. The reported caffeic acid derivative compounds were reported to have strong antioxidant properties, capable of blood glucose reduction through inhibition of the α-glucosidase enzyme. In addition, enhydrin has been observed in the increase of β-pancreatic cells in streptozotocin (STZ)-induced diabetogenic mouse pancreatic cells [5].

Currently, quality control of raw materials for herbal medicine is commonly performed through organoleptic evaluation, although scientific laboratories deem it comprehensively inadequate, as it relies simply on the subjective sensory evaluation of limited pool of experts. Furthermore, organoleptic tests have been shown to possess significant weaknesses and limitations, due to some sensory traits that cannot be described [8]. Hence edge-cutting instruments used within the field of analytical chemistry shows promise to devise a method for mentioned quality control using analytical instruments. Among these analytical instruments includes FTIR spectroscopy and HPLC, which is easy to use, cheap and

fast when investigating samples [9,11]. These instruments fulfilling efficient analysis criteria are also capable of investigating several components simultaneously, without damaging the samples [9,11].

The FTIR method produces a spectrum that provides complex data, which can be used to thoroughly describe the chemical characteristics of a sample [9]. Although IR spectrum pattern complexity is visually difficult to be interpreted, chemometrics method can be used to resolve this problem [10]. Juliani in his study used FTIR-based metabolomics, to identify an active compound with α-glucosidase inhibitory and antioxidant properties in aerial parts of *Orthosiphon stamineus* (OS) extract and its fractions [9]. Another option is using the HPLC method which produces chromatogram, illustrating the overall content and estimation of each content within a sample, based on the percent area of significant peaks. Ascertaining this capability, Feng et al. showed the potential of pairing HPLC with chemometric methods in order to analyze, obtain fingerprint and recognize the chemical pattern of ginger obtained from different markets in China [11].

In this study, we proposed to compare and differentiate metabolites profile/fingerprint of Yacon leaves grown and obtained from different locations in Pulau Jawa i.e. Lembang (Jawa Barat) and Wonosobo (Jawa Tengah). Three different solvents (95% ethanol, 50% ethanol and water) were used to make Yacon leaves extracts, in order to determine the suitable solvent to produce discernable differentiation through FTIR-based and HPLC-based metabolomics. It was assumed that the different condition between the two (2) locations and three (3) extraction solvents, would result in significant variations and levels of the chemical content in Yacon leaves, which would further affect the fluctuation of its bioactivity. This sought out differences, is targeted at improving the quality control of raw material for Yacon herbal products.

■ EXPERIMENTAL SECTION

Materials

Yacon leaves were collected from Perkebunan Najwa Herbal in Wonosobo, Jawa Tengah (J) and Perkebunan

Manoko in Lembang, Jawa Barat (B). Ethanol, acetonitrile (HPLC grade), and formic acid were purchased from Merck, Darmstadt, Germany. While potassium bromide for spectroscopy was purchased from Sigma Aldrich, St. Louis, USA.

Instrumentation

This study utilized an array of instruments which includes Sartorius TE214S analytical balance (Sartorius, Göttingen, Germany), ultrasonic LC 30 H Elma (Elma Schmidbauer Gmbh, Gottlieb-Daimler Straß 17 78224, Singen, Germany), FTIR spectrophotometer Tensor 37 (Bruker) equipped with OPUS software and HPLC LC-20 AD (Shimadzu, Kyoto, Japan).

Procedure

Sample preparation and extraction

The Yacon leaves were dried, grinded and sieved with a 40 mesh sieve. Approximately 20 g of Yacon leaves powder was extracted using 100 mL of 95% ethanol, after-which the extract was collected from the filtered mixture. The residue was extracted twice by ultrasonication for 30 min using ± 50 mL of 95% ethanol, which brought the total volume of solvents used to 200 mL. All of the extracts were pooled, while the residual solvent was evaporated using a vacuum rotary evaporator, after-which the extract was then dried using the freeze dryer. Similarly, the same procedure was repeated for 50% ethanol and water. Ten replications were made so 60 fractions were obtained. The resulted extracts were named according to the origin, extraction solvent and replicate numbers, for examples: B91 = Yacon from Lembang extracted with 95% ethanol replication 1, JW1 = Yacon from Wonosobo extracted with water replication 2.

Measurement of FTIR spectrum

The FTIR spectrum was obtained from each extract, with two (2) measurements approximately 2 mg of each Yacon leaves extract, mixed homogeneously with 0.2 g of potassium bromide, further pressed to form a tablet. Using OPUS 4.2 software (Bruker Optik GmbH, Karlsruhe, Germany), the FTIR spectrum was measured in the region of 4000–400 cm^{-1}.

HPLC analysis

HPLC analysis was conducted as follows: C18 stationary phase, UV detector 254 nm, 1 mL/min flowrate; 20 μL injection volume with gradient elution technique using mobile phase composition which was from 0–5 min (ACN 15%), 5–15 min (ACN 15–50%), 15–30 min (ACN 50–70%), 30–45 min (ACN 70–85%), and 45–60 min (ACN 85-95%) with a flowrate of 1 mL/min with an analysis time of 60 min. The waters column, columns × bride, dimensions were (4.6 mm × 150 mm × 5 μm), which was obtained from Waters Corporation, 34 Maple Street, Milford, Massachusetts, USA.

Data pre-processing treatments

The quantified chromatogram was categorized into variables based on its length and was pre-processed in four (4) steps to produce clear differentiation result. Firstly, the exclusion of variables which had a value of 0 was observed on at least 50% of the samples, either globally or locally within a group of samples, with further censoring of outliers through 90% winsorization. Secondly, the normality test was performed using four (4) different methods which include Shapiro-Wilk, Anderson-Darling, Lilliefors, and Jarque-Bera to evaluate the goodness of fit of the samples. Thirdly, comparison of variance using Levene's test and Bartlett's test to justify the relevance of PCA. Lastly, the Kaiser-Meyer-Olkin Test for Sampling Adequacy to determine whether the data obtained from quantified chromatogram was sufficient for factor analysis. Notably, these aforementioned tests were conducted using XLSTAT version 2014.5.03.

Principal component analysis (PCA)

PCA was done using SIMCA-P version 14 (Sartorius Stedim Biotech, Umea, Sweden), producing score plots, which was used to examine whether the sample groups were in accordance with their solvents and geographical origins. PCA investigation was conducted towards the absorption over certain ranges of wavelengths, while data as regards to the extracts with different solvents were obtained from quantification of FTIR spectra. Further PCA was performed on peak retention time and percentage of peak area (% A), as regards to the data obtained from quantification of

HPLC chromatograms. Notably, PCA also produces fingerprints of location origin and solvent, obtained from unique values of absorbance at certain wave numbers for certain extracts (FTIR), or from the unique percent area value (% A) at certain peak retention times for certain extracts (HPLC). PCA analysis for FTIR and HPLC data was done by using pareto scaling method. FTIR data had 60 observations and 1866 independent variables (FTIR wave numbers), while HPLC data had 60 observations and 31 independent variables (HPLC retention time).

■ RESULTS AND DISCUSSION

FTIR Spectra of Yacon Leaves Extracts

FTIR spectra were used to single out a functional group from the chemicals in the plant extract, which was made in the mid-infrared region (4000–400 cm⁻¹). A representative of the FTIR spectrum is obtained from different samples of Yacon leaves, in the mentioned infrared region observed in Fig. 1.

Results from the FTIR spectra indicated that samples from both regions, which were extracted using a similar solvent, showed a similar spectral pattern qualitatively albeit different values of absorption intensity. Therefore, it was concluded that direct

qualitative observation towards the spectra was not adequate to reveal the difference in geographical origins of the plant and any other inference towards the variation of the chemical composition of the samples.

Although direct qualitative observation failed to reveal the variation resulted from different geographical origins of the plant, variation resulting from different solvents was observed qualitatively on the spectra of samples from one region. Therefore it was assumed the variation as a result of the interactions between different solvents occurred because of the varying amount of the metabolite compounds, within the samples extracted with different solvents.

Visually, the spectrum of 95% ethanol extracts was sharper than the spectrum of 50% ethanol extract, and the spectrum of water extract inclusively (Fig. 1). Further comparison resulted in some typical absorbance peaks within the range of 3367–3391 cm⁻¹, indicating the absorption of the hydroxyl group (–OH), although the absorbance peaks within the range of 2925–2932 cm⁻¹ and around 2851cm⁻¹ demonstrated the absorption of the functional groups –CH stretching. Notably, the absorbance peaks around 1689, 1721 and 1740 cm⁻¹ denoted the absorption of the carbonyl functional group,
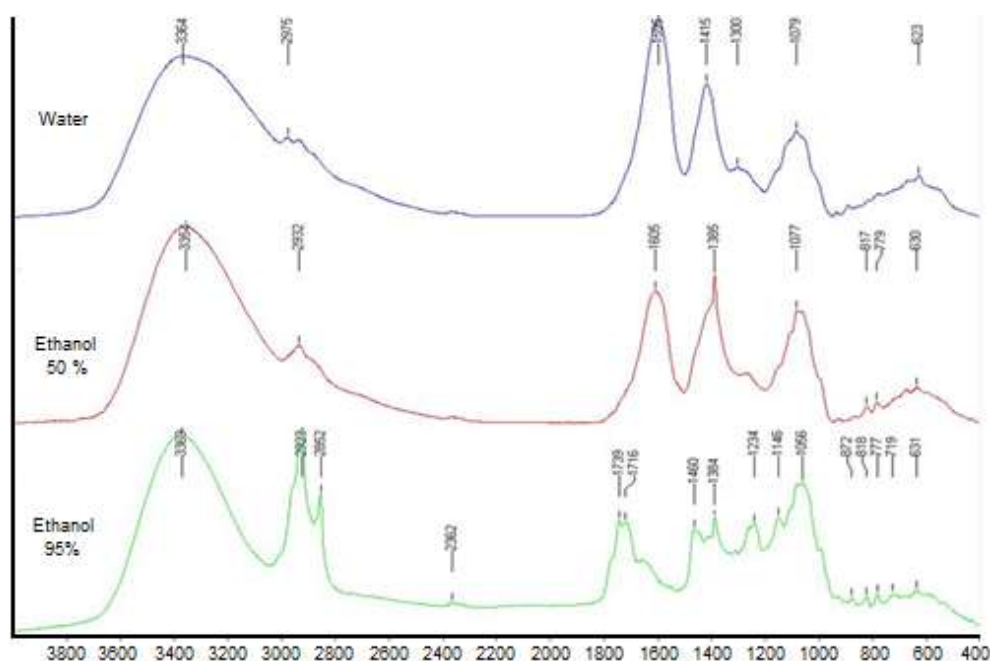
Fig 1. Example of FTIR-spectra of extracts of Yacon leaves, obtained from Jawa Tengah (J) in the range of 4000–400 cm⁻¹ wavenumbers

while peaks around 1384 cm⁻¹ indicated the presence of the methyl group (–CH₃). Furthermore, absorbance peaks within the range of 1250–1020 cm⁻¹ were marked by the absorption of aliphatic amine functional group (C–N stretching), while the peaks within the range of 1000–650 cm⁻¹ could be seen through the absorption of alkenes functional group C–H bend [12]. Lastly, in all spectral samples obtained, the absorbance peaks shown around 2300 cm⁻¹ was possibly due to CO_2 uptake from the air.

The complexity of the mentioned FTIR spectra was the result of various constituents of chemical compounds present within the samples. This noted complexity contributed towards the difficulty of making any direct visual interpretation, as the quantified FTIR spectra and the absorbance for each wave number was further analyzed using chemometric methods.

PCA of FTIR-Data

The quantified FTIR absorbance of Yacon leaves extract samples for each wave number, was used as input for PCA which was then transformed into a set of values of linearly uncorrelated variables called principal components (PCs) [13]. The observed transformation was conducted to investigate the geographical origins of each

sample and the solvents used for extractions. Subjecting the quantified FTIR spectra to data pre-processing, resulted in the elimination of variables in which at least 50% of them were 0, further winsorizing the outliers. The pre-processing also significantly showed that the quantified FTIR spectra were distributed normally with at least one sample group, where its variance significantly differed compared to other groups. The PCA model resulted in 4 components which explain 91.7% total variations where the value of Q^2 was recorded at 0.894, indicating that the transformation was reliable.

As shown by the PCA score plot (Fig. 2), the samples didn't display any remarkable differences, as there was no significant distinction between samples obtained from different regions. However, samples extracted using different solvents could be discerned into distinct groups (Fig. 3). The resulting distribution plot could be used to interpret the separation of samples respectively to their solvent, estimated by observing the centroids packing of each sample groups to each other. Explicitly, distribution plots which represented sample J extracted with three different solvents showed that they were significantly different from each other (Fig. 4).
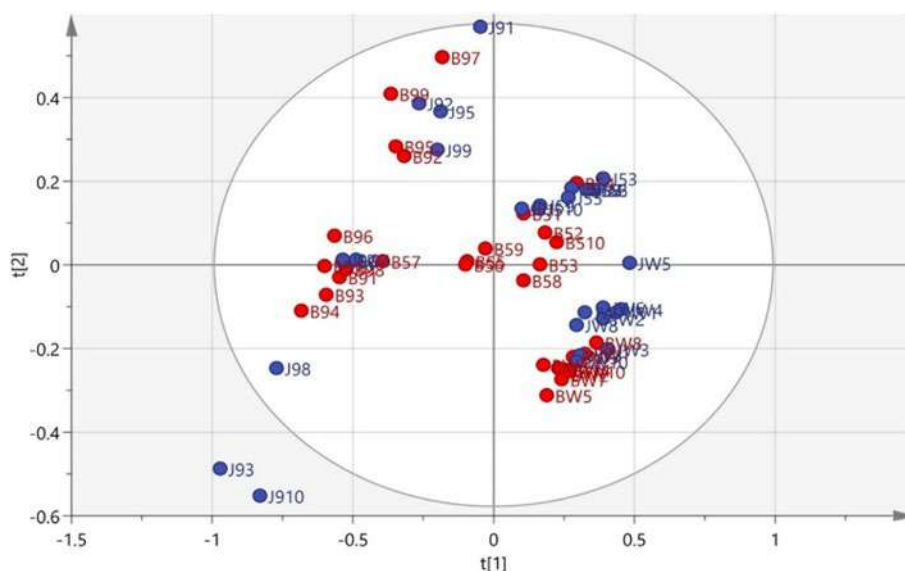
Fig 2. Geographical-origin-based PCA Score Plot of FTIR-data of Yacon leaves based on Pareto scaling (3800–400 cm⁻¹). Geographical origins denoted by color. Blue for Jawa Barat (B) and red for Jawa Tengah (J). For label explanation see Method section. R^2X cumulative = 0.956 and Q^2 = 0.932
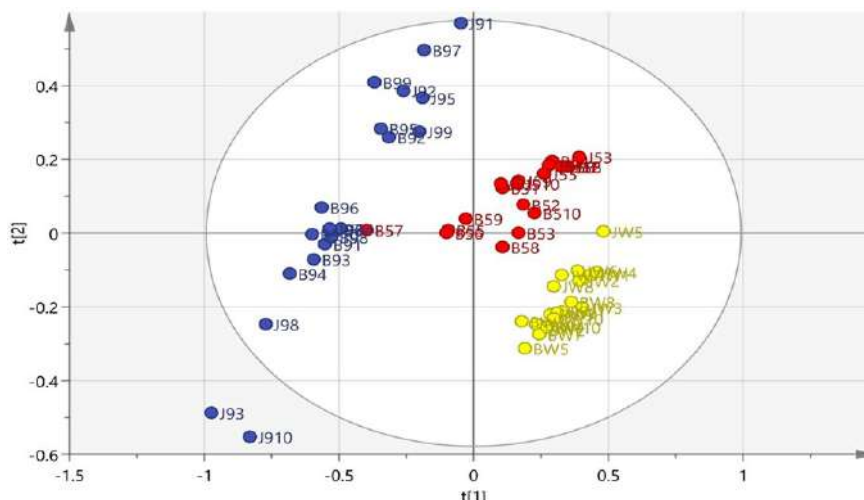
Fig 3. Solvent-based PCA Score Plot of FTIR-data of Yacon leaves based on Pareto scaling (3800–400 cm^{-1}). Solvents denoted by color. Yellow for water, blue for ethanol 50%, and red for 95% ethanol. R^{2}X cumulative = 0.917, Q^2 = 0.894
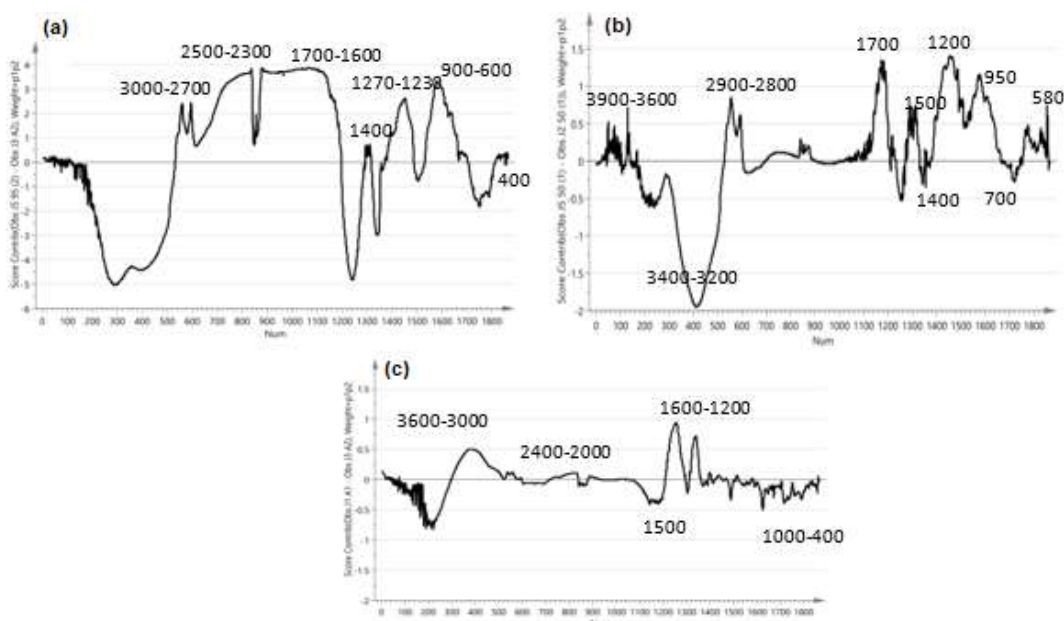
Fig 4. Representatives of PCA contribution plot of FTIR-data of Yacon leaves from Wonosobo (Jawa Tengah). (a) Yacon 95% ethanol extract, (b) Yacon 50 % ethanol extract, (c) Yacon water extract. In each contribution plots, the wave numbers positioned above the X-axis were present at a higher intensity at the respective extract as compared to those positioned below the X-axis

The 95% ethanol extract samples (Fig. 4(a)) showed a higher absorbance in an area within the range of 2700–1700 cm^{-1}, which was interpreted as having higher absorption of hydroxyl group from acid (OH within the range 2500–2700 cm^{-1}), alkanes (C–H, within the range of 2850–3000 cm^{-1}), C-H stretching (1450–1470) and carbonyl functional group (C=O) from aldehyde/ketone/carboxylic acids (1675–1740 cm^{-1}) and –C–O–C from ether (1230–1270). Meanwhile, 50% of ethanol extract samples showed lower absorbance within the range of 1700–400 cm^{-1}, indicating the presence of the methyl group (–CH$_3$ within the range of

1470–1340 cm⁻¹), alkenes (C–H within the range of 995–675 cm⁻¹), C–O functional group of alcohol, ether, carboxylic acids and esters [12], as compared to other groups. This finding resonates to numerous findings as regards to 50% ethanol extract samples (Fig. 4(b)) resembling 95% ethanol extract samples, except within the wavenumber range of 1700–1500 cm⁻¹ which can be attributed to the absorption of primary and secondary amines functional group N–H, amines bending (1575–1650 cm⁻¹) C=N: imines, oxime (1640–1690 cm⁻¹), C=O: amides (1640–1670 cm⁻¹) and within the range of 2853–2929 cm⁻¹. However, the 50% ethanol extract showed lower absorption of alkanes functional group C–H stretching, compared to 95% ethanol extract samples. Notably, water extract samples (Fig. 4(c)) also demonstrated the lowest absorption on the above-mentioned ranges.

The unique profiles of IR absorption could then be concluded from the fingerprints that differ the samples based on the solvents. Specifically, Fig. 4 shows functional groups present in the area as follows; –CH3, C–H, C=C–H, C–O and C–C, with the functional group predominantly present in the water extract.

PCA loading plot comprehensively illustrates absorbance intensities, which were used to cluster samples (Fig. 5). It was indicated that absorption at 3600–3000 cm⁻¹ of C–H stretching, free O–H stretching, O–H stretching, and N–H stretching; at 1700–1500 cm⁻¹ of C=C,

1500–1300 cm⁻¹ C–O–C asymmetric stretching, C–O stretching; and at 700–540 cm⁻¹ of C–H bending and C–O stretching were dominantly present in 95% ethanol extract. While at 3000–2800 and 2700–2400 cm⁻¹ of O-H stretching, 1300–700 cm⁻¹ of C–O stretching, C–H stretching and bending, with 540–400 cm⁻¹ of C–C skeletal vibration dominated the water and 50% ethanol extract.

PCA of HPLC-Data

HPLC chromatogram profiles of the Yacon leaves extracts from sample B and J (Fig. 6), shows similarities with the following details; 36 peaks were detected in each chromatogram extract, however in 50% ethanol extract and 95% Yacon B, peak numbers: 5 and 30 (P5 and P30) were detected with an area value of 0.000%. Notably, the similarities and number of peaks made the chromatogram profiles difficult to be distinguished visually. Hence, further investigation was conducted using PCA to differentiate the profiles of the samples.

The quantified chromatograms were subjected to data pre-processing and PCA, similar to FTIR-spectra. The resulting PCA had 3 components and captured 85% variations with Q^2 value at 0.68, which showed that the transformation was reliable. As illustrated by the PCA score plot (Fig. 7), samples could be distinguished based on the geographical origins and solvents used (Fig. 8). PCA biplot (Fig. 9) showed that the peaks were correlated with the geographical origin clusters, as samples
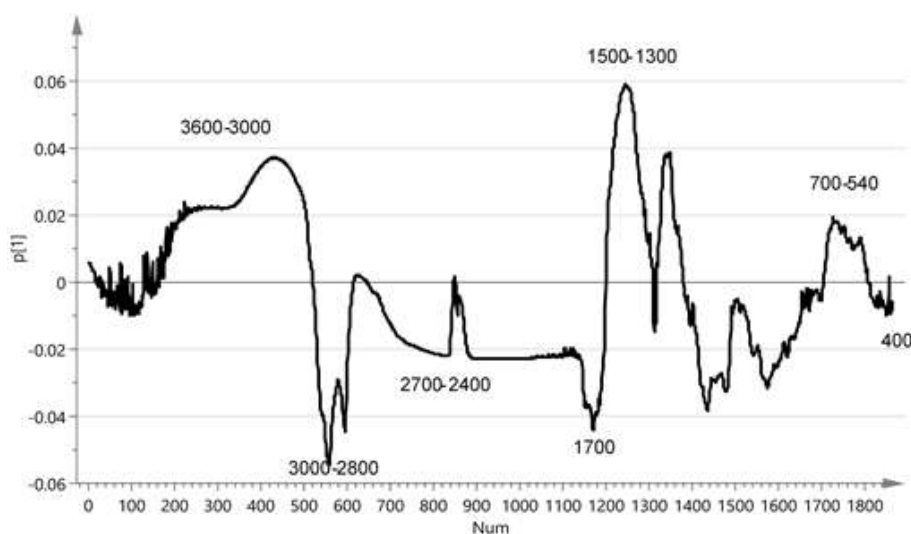
Fig 5. PCA loading line plot of FTIR data of Yacon extract obtained from different solvent extraction
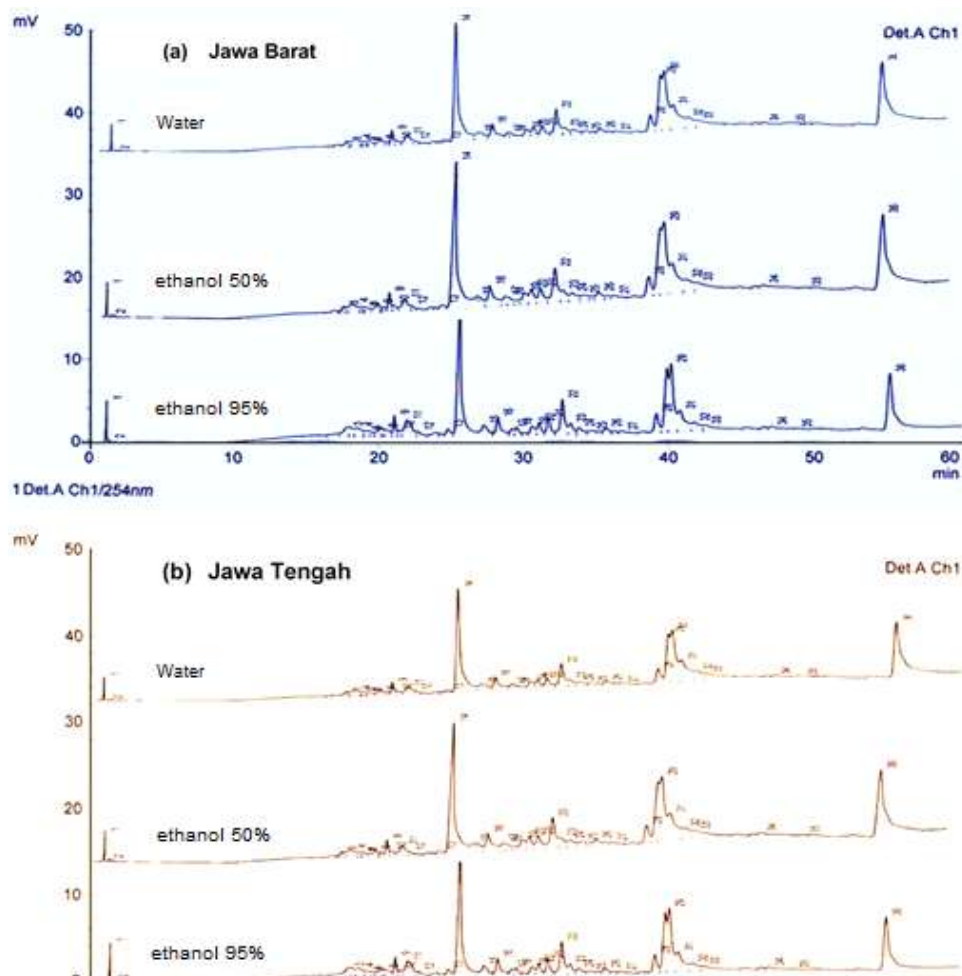
Fig 6. Example of HPLC- chromatograms of extracts of Yacon leaves from Lembang-Jawa Barat (a) and from Wonosobo-Jawa Tengah (b)
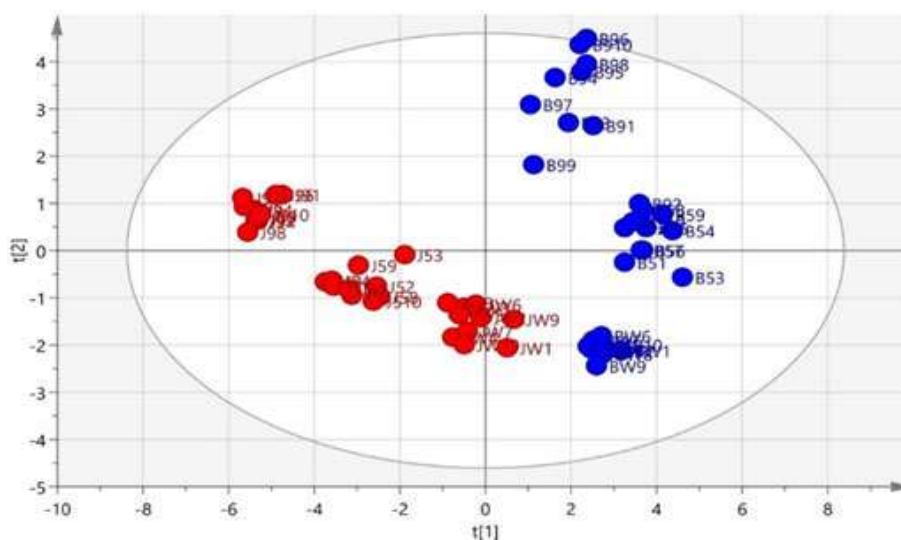
Fig 7. Geographical-origin-based PCA Score Plot of HPLC-data of Yacon leaves. Geographical origins denoted by color. Blue for Lembang-Jawa Barat (B) and red for Wonosobo-Jawa Tengah (J). R^2X cumulative = 0.85 and Q^2 = 0.68

Indones. J. Chem., 2020, 20 (3), 567 - 578

575
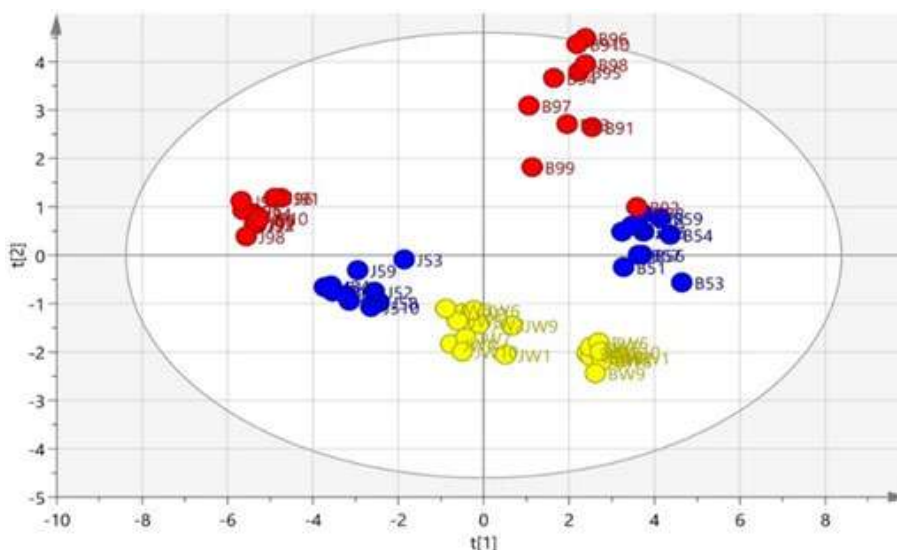
Fig 8. PCA score plot HPLC data of Yacon leaves extract colored in accordance with their extraction solvent, Blue = water extract; Red = ethanol 50% extract and Yellow = ethanol 95% extract
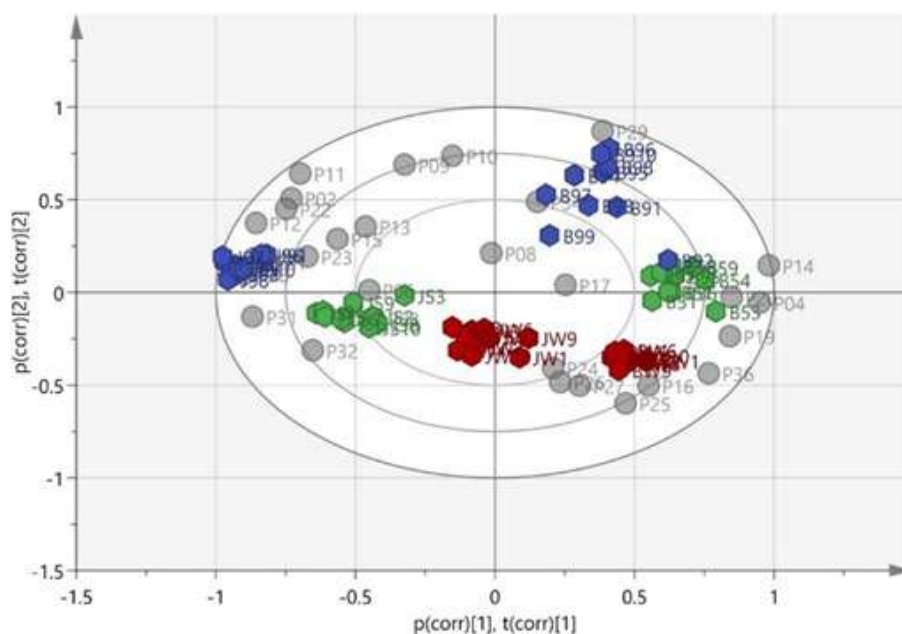
Fig 9. PCA loading biplot HPLC data of Yacon extract based on location origin. Blue = Yacon B (Lembang, Jawa Barat), purple = Yacon J (Wonosobo, Jawa Tengah), grey circle = peak number of the related retention time peak (P). The retention times abundantly found in particular extract were located nearby the associated extracts. For example, P32 (Peak no. 32) had high intensity in ethanol 50% extract

from Jawa Barat (B) were positively characterized by peak 04, peak 09 and peak 14.

Further analysis was conducted on water extracts from both regions (Fig. 10), by studying the contribution plot. Compared to overall samples, Yacon B water extract (BW) mainly exhibited higher intensities on peak 14, peak 16 and peak 36, with lower intensities at peak 11 and peak 29. Similarly, compared to overall samples, Yacon J water extract (JW) demonstrated lower intensities on peak 15 and peak 16, with higher intensity on peak 36.

In this preliminary study, we used FTIR and HPLC, thus the provided information is rather limited.
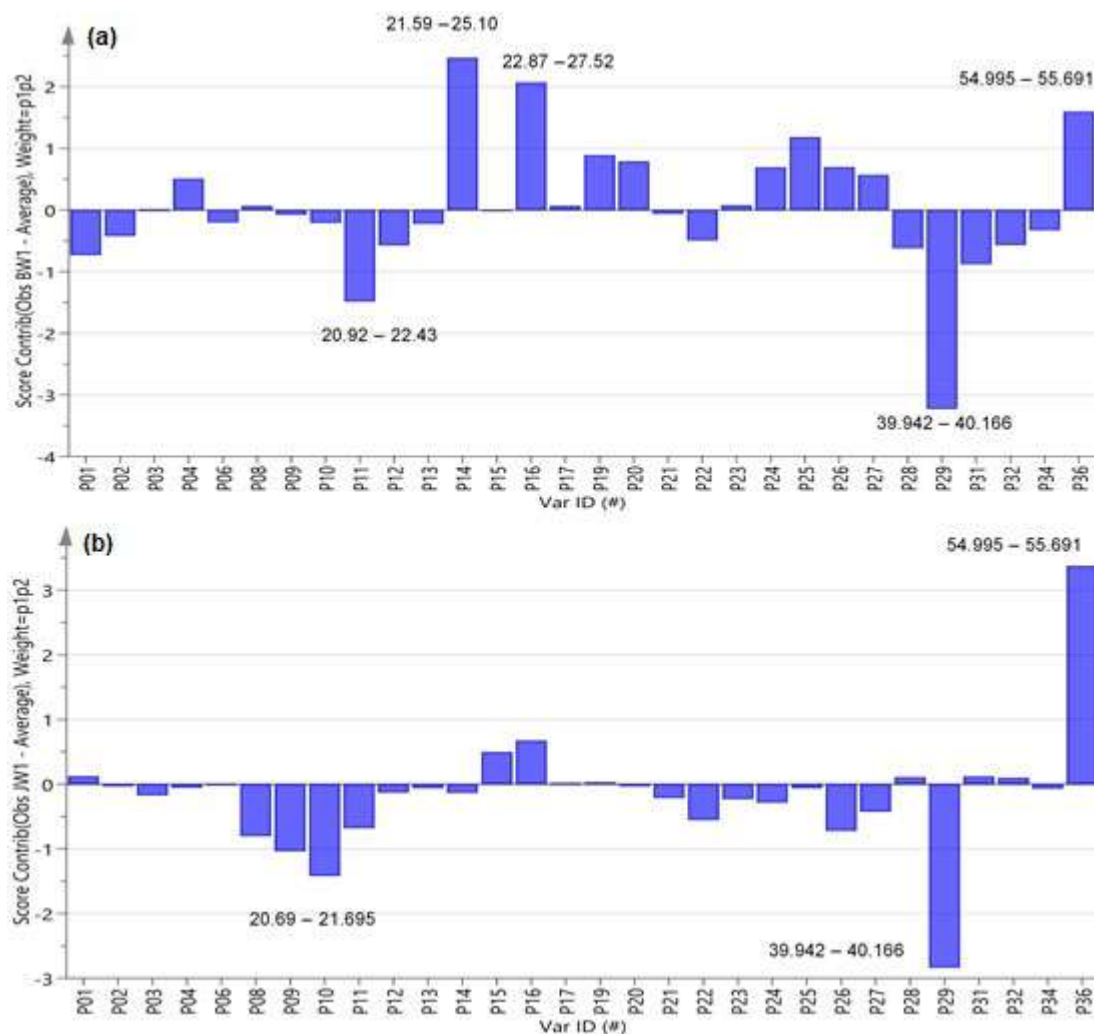
Fig 10. Two representative contribution plots of PCA Yacon HPLC data. (a) Contribution plot of Yacon water extract (Sample from Lembang Jawa Barat) and (b) Contribution plot of Yacon water extract from Wonosobo Jawa Tengah. Retention times mentioned in each figure representing metabolites were found to be more abundant in the associated extract if it is positioned above the X-axis. Oppositely, it is found to be less abundant if it is positioned below the X-axis. For example, Yacon water extract from Lembang contained peak at a retention time of 21.59–25.10 min with higher intensity, but it contained peak at a retention time of 20.92–22.43 min with lower intensity

No reports have been found regarding the identification of metabolites which discriminates Yacon leaves from different locations or extracted with different solvents. Thus, we could not compare the FTIR data obtained in this study with the data from the previous report. The commercially available compounds isolated from this plant is also not available. This is a hurdle of this research which hampers the identification of metabolites important for the separation. For a holistic view of this interaction, further research using a more robust tool such as NMR or LC-MS is recommended to disclose which compounds are represented by these discriminating peaks. We are currently conducting LC-MS based metabolomics of the Yacon's extract to further identify these metabolites markers.

■ **CONCLUSION**

The results of this study showed that FTIR and HPLC - Based Metabolomics supported by Principal Component Analysis (PCA), that was performed in

order to capture and discern the unique geographical origin of Yacon leaves and its accompanying solvent characteristics for extraction, would have been difficult to do just through direct visual observation and comparison. Notably, FTIR was able to distinctly cluster Yacon samples based on the solvents, but it was not capable to classify them based on their geographical origins. However, HPLC was able to distinctly cluster Yacon samples based on both the solvents and geographical origins. Demonstration of such capability can be used to construct hypothesis and evaluation for future researches, as regards to the metabolites compound variations on the activity of samples, e.g. anti-inflammatory activity or anti-diabetic activity, which can be evaluated through the combination of FTIR/HPLC and PCA for investigation.

■ ACKNOWLEDGMENTS

■ REFERENCES

[1] Grau, A., and Rea, J., 1997, "Yacon. *Smallanthus sonchifolius* (Poepp. & Endl.) H. Robinson" in Andean roots and tubers: Ahipa, arracacha, maca and yacon. Promoting the conservation and use of underulitized crops. 21, Eds. Hermann, M., and Heller, J., IPK & Gatersleben/International Plant Genetic Resources Institute, Rome, Italy, 203–204, 209, 221–223, 230.

[2] Genta, S.B., Carbrera, W.M., Mercado, M.I., Grau, A., Catalán, C.A., and Sánchez, S.S., 2010, Hypoglycemic activity of leaf organic extracts from *Smallanthus sonchifolius*: Constituents of the most active fractions, *Chem. Biol. Interact.*, 185, 143–152.

[3] Oliveira, R.B., Chagas-Paula, D.A., Secatto, A., Gasparoto, T.H., Faccioli, L.H., Campanelli, A.P., and Da Costa, F.B., 2013, Topical anti-inflammatory activity of yacon leaf extracts, *Rev. Bras. Farmacogn.*, 23 (3), 497–505.

[4] Djamil, R., Winarti, W., Simanjuntak, P., and Syamsudin, 2014, Standardization and α-glycosidase inhibition of extracts of *Vatica pauciflora* Blume stem barks and *Smallanthus sonchifolius* leaves, *J. Pharmacogn. Phytochem.*, 3 (4), 42–46.

[5] Honoré, S.M., Genta, S.B and Sánchez, S.S., 2015, *Smallanthus sonchifolius* (Yacon) leaves an emerging source of compounds for diabetes management, *J. Res. Biol.*, 5 (A), 021–042.

[6] Valentová, K., and Ulrichová, J., 2003, *Smallanthus sonchifolius* and *Lepidium meyenii* – Prospective Andean crops for the prevention of chronic diseases, *Biomed. Pap.*, 147 (2), 119–130.

[7] Russo, D., Valentão, P., Andrade, P.B., Fernandez, E.C., and Milella, L., 2015, Evaluation of antioxidant, antidiabetic and anticholinesterase activities of *Smallanthus sonchifolius landraces* and correlation with their phytochemical profiles, *Int. J. Mol. Sci.*, 16, 17696–17718.

[8] Soekarto, S.T., 2008, *Penilaian organoleptik untuk industri pangan dan hasil pertanian*, Bhratara Karya Aksara, Jakarta, 34.

[9] Juliani, Yuliana, N.D., Budijanto, S., Wijaya. C.H., and Khatib, A., 2016, Senyawa inhibitor α-glukosidase dan antioksidan dari kumis kucing dengan pendekatan metabolomik berbasis FTIR, *JTIP*, 27 (1), 17–30.

[10] Edi, D.P., Rafi, M., Utami, D.S., Nurcholis, W., and Agung, M., 2014, Identifikasi dan autentikasi jahe merah menggunakan kombinasi spektroskopi FTIR dan kemometrik, *Agritech*, 34 (1), 82–87.

[11] Feng, X., Kong, W., Wei, J., Ou-Yang, Z., and Yang, M., 2013, HPLC fingerprint analysis combined with chemometrics for pattern recognition of ginger, *J. Pharm. Biol.*, 52 (3), 362–367.

[12] Skoog. D.A., Holler. F.J., and Crounch. S.R., 2007, *Principles of Instrumental Analysis*, 6th Ed., Thomson Brooks/Cole, Belmont, CA.

[13] Sun, X., Wang, H., Han, X., Chen, S., Zhu, S., and Dai, J., 2014, Fingerprint analysis of polysaccharides from different *Ganoderma* by HPLC combined with chemometrics methods, *Carbohydr. Polym.*, 114, 432–439.

[14] Maser, W.H., Rusmarilin, H., and Yuliana, N.D., 2017, Aplikasi metabolomik berbasis HPLC untuk

mengidentifikasi waktu retenasi komponen antibakteri *Staphylococcus aureus* pada ekstrak bunga kecombrang (*Etlingera elatior*), *Alchemy*, 13 (2), 241–251.

[15] Tahir, H.E., Xiaobo, Z., Zhihua, L., Jiyong, S., Zhai, X., Wang, S., and Mariod, A.A., 2017, Rapid prediction of phenolic compounds and antioxidant activity of Sudanese honey using Raman and Fourier transform infrared (FT-IR) spectroscopy, *Food Chem.*, 226, 202–211.

[16] Isomaa, K., 2013, Chemometric Methods in Plant Metabolomic, *Thesis*, University of Helsinki.

[17] Silverstein, R.M., Bassler, G.C., and Morrill, T.C., 1981, *Spectrometric Identification of Organic Compounds*, 4th Ed., John Wiley & Sons, Inc., New York.

[18] Pomerantsev, A.L., 2014, *Chemometric in Excel*, John Wiley & Sons, Inc., Hoboken, New Jersey.

[19] Dejaegher, B., Alaerts, G., and Matthijs, N., 2010, Methodology to develop liquid chromatographic fingerprints for the quality control of herbal medicines, *Acta Chromatogr.*, 22 (2) 237–258.

[20] Khanmohammadi, M., 2015, *Current Applications of Chemometric*, Nova Science Publishers, Inc., Hauppauge, NY.

[21] Miller, J.N., and Miller, J.C., 2010, *Statistics and Chemometrics for Analytical Chemistry*, 6th Ed., Pearson Education Limited, Prentice Hall, UK.

[22] Rafi, M., Rohaeti, E., Miftahudin, A., and Darusman, L.K., 2011, Differentiation of *Curcuma longa, Curcuma xanthorrhiza* and *Zingiber cassumunar* by thin layer chromatography fingerprint analysis, *Indones. J. Chem.*, 11 (1), 71–74.

[23] Levandi, T., Püssa, T., Vaher, M., Ingver, A., Koppel, R., and Kaljurand, M., 2014, Principal component analysis of HPLC–MS/MS patterns of wheat *(Triticum aestivum)* varieties, *Proc. Est. Acad. Sci.*, 63 (1), 86–92.

[24] Valentová, K., Lebeda, A., Doležalová, I., Jirovský, D., Simonovska, B., Vovk, I., Kosina, P., Gasmanová, N., Dziechciarková, M., and Ulrichová, J., 2006, The biological and chemical variability of yacon, *J. Agric. Food Chem.*, 54 (4), 1347–1352.

[25] Liang, Y.Z., Xie, P., Chan, K., 2004, Quality control of herbal medicines, *J. Chromatogr. B*, 812 (1-2), 53–70.

[26] Yongyu, Z., Shujun, S., Jianye, D., Wenyu, W., Huijuan, C., Jianbing, W., and Xiaojun, G., 2011, "Quality control method for herbal medicine-Chemical fingerprint analysis" in *Quality Control of Herbal Medicines and Related Areas*, IntechOpen, Rijeka, Croatia.

[27] Barbara, M.M., and Nossar, R., 2015, Peluang usaha: *Budidaya tanaman obat diabetes mudah, tanam saja di tempat lembab*, http://www.tribunnews.com/bisnis/2015/09/03/peluang-usaha-budidaya-tanaman-obat-diabetes-mudah-tanam-saja-di-tempat-lembab, accessed on 21 March 2016.

Adsorption Analysis of Fluoride Removal Using Graphene Oxide/Eggshell Adsorbent

Norhusna Mohamad Nor[1,*], Nur Hidayahtul Nazrah Kamil[1], Amirul Izan Mansor[1], and Hawaiah Imam Maarof[2]

[1]Faculty of Chemical Engineering, Universiti Teknologi MARA, Cawangan Pulau Pinang, 13500 Permatang Pauh, Pulau Pinang, Malaysia

[2]Faculty of Chemical Engineering, Universiti Teknologi MARA, 40450 Shah Alam, Selangor, Malaysia

* Corresponding author:

tel: +604-3822539
email: norhusna8711@ppinang.uitm.edu.my

Abstract: *Graphene oxide with eggshells (GO/ES) adsorbent has been studied for fluoride ions (F⁻) removal. An adsorption study was conducted in batch experiments at different adsorption parameters, which are initial F⁻ concentration, contact time, and temperature. The effects of these adsorption parameters towards F⁻ removal by using GO/ES adsorbent were investigated. The adsorption parameters were then analyzed with adsorption isotherms (Langmuir and Freundlich), kinetics (pseudo-first-order and second-order) and thermodynamic studies. Under various parameters, GO/ES is proven as an effective adsorbent with an adsorption capacity of F⁻ are up to 48 mg/g. The experimental data were satisfactorily fitted with Langmuir isotherm, which illustrated the monolayer pattern of F⁻ adsorption into GO/ES adsorbent. The adsorption kinetic analysis indicated that the adsorption data could be well described by Pseudo-second-order kinetic model, which indicated the chemisorption process, while thermodynamic studies revealed that the adsorption of F⁻ was an exothermic process.*

Keywords: *graphene oxide; eggshell; fluoride; adsorption; isotherms; thermodynamics; kinetics*

■ INTRODUCTION

Contamination of fluoride (F⁻) in groundwater has been identified as a serious problem, which contributes to adverse effects on human health, aquatic life and indirectly to the environment as well. This occurrence is contributed by various sources, such as effluent from industrial activities, agricultural activities, and existing geological formation [1]. World Health Organization (WHO) has classified F⁻ as one of the main contaminants in water; hence, a maximum allowable limit for F⁻ in drinking water is suggested to be as low as 1.5 mg/L [3]. In addition, the Ministry of Health Malaysia has also set regulation for the National Standard for Drinking Water Quality, where it must be below than 0.4–0.6 ppm of F⁻ concentration [4]. According to the Environmental Quality (Industrial Effluent) regulations, the permissible F⁻ limit for industrial effluent in standard A and B are 2.0 mg/L and 5.0 mg/L, respectively [5]. Therefore, the wastewater effluent discharged from all industry must meet the allowable limit. Hence, concerning human health, developing efficient methods in F⁻ removal is significant to ensure F⁻ concentration is within acceptable limits.

The removal of F⁻ has become a great concern globally due to its toxic effect on the water towards humans and the environment. Various treatment methods are available for F⁻ removal, for instance, ion exchange, chemical precipitation, fluidized-bed precipitation, aluminum-solubility, membrane filtration, electrochemical method, and adsorption [1-2]. Among those methods, the adsorption process has been identified as the most efficient and economical method to be used in F⁻ removal [6]. The efficiency of adsorption depends on the type of adsorbents used, where high removal of F⁻ is anticipated based on the excellent development of the adsorptive materials. There are

many types of adsorbents that have been used for fluoride removal, such as activated carbon, biochar, raw biomass, fly ash, calcium-containing materials, and graphene oxide (GO) [1].

Calcium containing materials such as bone, eggshells, calcium carbonate ($CaCO_3$), and seashells have been used by researchers as adsorbents for F^- removal, due to their strong affinity towards the target pollutant [7]. GO is the combination of graphene and oxidizing agents, producing hydrophilic materials, and expands layer of separation [8]. The unique properties of GO are, it is a promising material for adsorption of F^-, due to its structure which can be altered, and it has excellent chemical, thermal and mechanical stability [8-9]. Furthermore, it also offers high surface areas with abundant binding sites, which is suitable for further modification. In this research work, the modification of GO with calcium-containing material, which is eggshells (ES) will be discussed in detail. ES has been selected, because of its low-cost material (waste) which is abundantly available, and its composition consists of a high percentage of $CaCO_3$. Thus, its combination with GO is a perfect match for F^- removal. The objective of this work is to investigate the effects of various adsorption parameters and adsorption analysis of F^- removal by using GO/ES adsorbent.

■ EXPERIMENTAL SECTION

Materials

Eggshells (ES) were obtained from a nearby cafeteria, UiTM Cawangan Pulau Pinang. Chemicals used for the synthesis of graphene oxide (GO) were graphite powder (99.99%), sodium nitrate ($NaNO_3$ 98%), sulphuric acid (H_2SO_4 98%), potassium permanganate, ($KMnO_4$), hydrogen peroxide (H_2O_2), and hydrochloric acid (HCl). As for the batch adsorption experiment, the chemical used was sodium fluoride (NaF).

Procedure

Synthesis of GO/ES adsorbent

Graphene oxide (GO) was prepared by using a modified Hummer's method [10]. 2.5 g of graphite powder and 1.25 g of $NaNO_3$ were added together with

60 mL of H_2SO_4 in a conical flask with continuous stirring for 2 h at constant temperature (10 °C). $KMnO_4$ (7.5 g) was added into the mixture, where the reaction temperature was controlled to be lower than 10 °C. The mixture was continued stirred at 30 °C for 2 h until the solution becomes pasty brownish. Next, 135 mL of deionized (DI) water was added slowly into the mixture. The reaction temperature was increased to 50 °C until the brownish color obtained. Finally, the mixture was terminated by the addition of 25 mL of H_2O_2, which turned the mixture into gold-yellow color. The mixture was filtered and washed with 400 mL of HCl and DI water repeatedly to remove any impurities. Then, it was dried in a drying oven at 60 °C for 24 h [11].

Pre-treatment of ES was done by washing it with DI water and drying in an oven at 45 °C for overnight. Then, ES was ground into a powder form, to obtain 250 μm size of particles size. One gram of GO in a slurry form was added into a beaker containing 300 mL of DI water and sonicated for 1 h at 45 °C. Then, 5 g of ES was added into the mixture. After 1 h, the suspension was collected and centrifuged for 15 min at 3000 rpm and dried at 60 °C overnight [12].

Batch experimental of fluoride removal

The effects of adsorption parameters (i.e., F^- initial concentration, contact time, and temperature) were conducted via a batch experiment. A stock solution of 1000 mg/L of fluoride was prepared by dissolving 1 g of NaF in 1 L of distilled water. The stock solution was diluted with distilled water to an achieved a concentration of 30 mg/L. A 200 mL of NaF stock solution was tested with 0.05 g of GO/ES adsorbent at 25 °C. The mixture was shaken by using an orbital shaker with 200 rpm for 60 min. The adsorbent was filtered through a 0.45 μm membrane filter. The steps were repeated at different concentrations (30, 40, 50, 60, 70 mg/L) contact times (30, 60, 90, 120 min) and temperatures (25, 45, 60, 75 °C). F^- final concentrations were measured by using DR 2800 Spectrophotometer before and after adsorption. SPADNS reagent was used as a standard to detect F^- concentration in samples. The adsorption capacity and percentage removal (%R) of F^- were calculated by using Eq. (1) and (2), respectively.

$$Q_e = \left[\frac{C_0 - C_t}{m}\right] \tag{1}$$

$$\% \, Removal = \left[\frac{C_0 - C_t}{C_0}\right] \times 100 \tag{2}$$

where Q_e is F⁻ adsorbed per unit mass of adsorbent (mg/g), C_t is the final concentration of F⁻ at equilibrium (mg/L), C_0 is an initial concentration of F⁻ (mg/L) and m is mass of adsorbent (g/L).

Adsorption isotherms

The analysis of adsorption isotherms were linearized as in Eq. (3) and (4) that represent Langmuir and Freundlich isotherms, respectively.

$$\frac{C_e}{q_e} = \frac{C_e}{q_{max}} + \frac{1}{q_{max} K_L} \tag{3}$$

$$\log q_e = \log K_F + \frac{1}{n} \log C_e \tag{4}$$

where C_e is equilibrium concentration of fluoride (mg/L), q_e is amount of fluoride adsorbed at equilibrium per gram of adsorbent (mg/g), q_{max} is adsorption for a complete monolayer (mg/g), k_L is a constant value of Langmuir (L/mg), K_F is Freundlich constant (L/mg), and 1/n is adsorption intensity.

Adsorption kinetics

The pseudo-first-order and pseudo-second-order adsorption kinetic models were used to investigate the adsorption kinetics of fluoride and to quantify the extent of uptake in the adsorption process, as shown in Eq. (5) and (6), respectively.

$$\log(q_e - q) = \log q_e - \frac{K_1 t}{2.303} \tag{5}$$

$$\frac{t}{q} = \frac{1}{K_2 q_e^2} + \left(\frac{1}{q_e}\right) t \tag{6}$$

where q_e is equilibrium adsorption capacity (mg/g), q is adsorption capacity at times (mg/g), K_1 is rate constant of pseudo-first-order adsorption, K_2 is rate constant of pseudo-first-order adsorption, and t is time.

Adsorption thermodynamics

Thermodynamic parameters such as standard free energy change (ΔG°), enthalpy change (ΔH°) and entropy change (ΔS°) were calculated to evaluate the spontaneous nature and the thermodynamic feasibility of the adsorption process [13]. The value of the equilibrium constant, K_0, is

calculated by using Eq. (7). The dependence of temperature on the adsorption of fluoride ions onto GO/ES adsorbent was evaluated using Eq. (8) and (9).

$$K_0 = \frac{C_0}{C_e} \tag{7}$$

$$\Delta G° = -RT \ln K_0 \tag{8}$$

$$Log K_0 = \frac{\Delta S°}{2.303R} - \frac{\Delta H°}{2.303RT} \tag{9}$$

where C_0 is the initial amount of adsorbate in solution (mg/L), C_e is equilibrium amount of adsorbate in solution (mg/L) R is universal gas constant (J/mol.K), and T is temperature (K).

■ RESULTS AND DISCUSSION

Batch adsorption studies were conducted on various adsorption parameters, which are F⁻ initial concentration, temperature, and contact time. The results of adsorption capacity and % removal of F⁻ at different adsorption parameters are shown in Fig. 1, respectively. Details discussion on the effect of each parameter will be discussed in the following subsections. According to Kashi et al. the eggshell is a promising material to be used as an adsorbent for F⁻ removal, which the fluoride removal was up to 100% [7]. The combination of eggshell and GO is expected to produce an excellent adsorbent since the use of GO modified with magnetic iron and aluminum oxide done by Liu et al. could remove F⁻ up to 64 mg/g [11]. The combination of GO with eggshells (GO/ES) in this research work can adsorb up until 56 mg/g.

Effect of Initial Fluoride Concentration

To study the effect of initial F⁻ concentration, the experiments were carried out with 0.05 g of adsorbent dosage, 60 min of contact time, and 25 °C of temperature. The % removal of F⁻ as shown in Fig. 1(a) decreases as F⁻ initial concentration increases. However, the adsorption capacities of F⁻ shown in Fig. 1 do not vary significantly, which are in the range of 44–46 mg/g. This is due to the vacant sites in GO/ES adsorbent which are capable of adsorbing up to a certain capacity, even though the higher initial concentration of F⁻ was introduced. The ratio of F⁻ to the number of available sites in GO/ES adsorbent is constant, where the vacant sites were saturated with F⁻

at certain concentration [7,13]. As the concentration gradient of F⁻ increased, the driving force will increase to overcome the mass transfer resistance of F⁻ from aqueous solution into a solid phase, which increases the adsorption equilibrium of GO/ES adsorbent until it achieved a saturated state. At the same time, this occurrence also resulted from the fixed adsorbent dosage used, where available vacant sites are limit with the increase of F⁻ initial concentration. These results are in agreement with the study done by Bhaumik et al. [13], where an increase of F⁻ concentration resulted in the decrement of the % removal.

Effect of Contact Time

The effect of contact time was varied at a given initial concentration (25 mg/L), adsorbent dosage (0.05 g) and temperature (25 °C). As illustrated in Fig. 1(b), the % removal of F⁻ increased as contact time increases from 30 to 90 min and remained constant afterward, where no significant changes are observed from 90 to 120 min. A similar trend is shown by the adsorption capacity of F⁻ in Fig. 1, where the values increase from 36 to 55 mg/g and start to reach equilibrium from 55–56 mg/g. The modification of ES into GO resulted in a large number of active binding sites, where the positive charge on Ca²⁺ extracted from CaCO₃ may be existed on GO's surface, thus enhancing the adsorption rate of F⁻ that is having negative charge [7]. Increasing the availability of active binding sites on the adsorbent surface might result in a high removal of F⁻. In this work, the adsorption of F⁻ to

reach equilibrium is started after 90 min, which is slower compared to other previous works [13-14]. It is presumed that the diffusion process of F⁻ from the bulk solution to the GO/ES adsorbent's surface is controlled by the affinity of F⁻ towards GO/ES's active binding sites, where longer time is needed for adsorption to reach equilibrium.

Effect of Temperature

The adsorption temperature of F⁻ was varied at 25, 45, 60 and 75 °C, with 25 mg/L of F⁻ initial concentration, 0.05 g of adsorbent dosage and 60 min of contact time. Fig. 1(c) showed that the % removal of F⁻ decreased with increase in temperature. This indicates that low temperature (25 °C) is favorable for F⁻ adsorption, which the highest % removal and adsorption capacity obtained were 48.12% and 48.12 mg/g, respectively. Inefficient removal of F⁻ was observed at elevated temperature, starting from 60 to 75 °C. Possibly, this is because high energy was received by F⁻, resulting in exciting movement of F⁻ molecules. Hence, the tendency of the molecules to escape from active binding sites is greater, which lead to less F⁻ being adsorbed into GO/ES adsorbent as the temperature is increased [15]. Therefore, lower temperature (less than 60 °C) is anticipated to be used to achieve high removal of F⁻, since sufficient energy will be delivered to the molecules. Indirectly, F⁻ will be steadily diffused into GO/ES's active binding sites without any resistances from the exciting movement of the molecules.
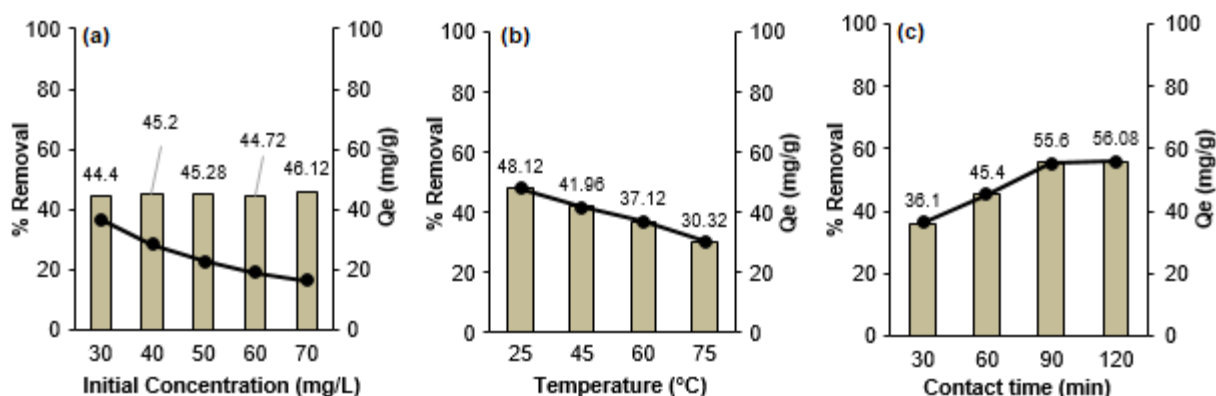
Fig 1. Effect of (a) initial concentration (b) contact time and (c) temperature on F⁻ percentage removal by using GO/ES adsorbent

Adsorption Isotherms

In this study, the adsorption mechanism of F$^-$ onto GO/ES adsorbent is further explained by using isotherm models, which are Langmuir and Freundlich. These isotherms are capable to describe the interaction between F$^-$ adsorbate and GO/ES adsorbent, which include homogeneity of the adsorbent and type of adsorption coverage [9]. The results of the isotherms are illustrated in Fig. 2, where higher R^2 value was obtained via the Langmuir isotherm model (0.9983) compared to the Freundlich isotherm model (0.5007). The experimental data were well fitted with the Langmuir model, where the adsorption of F$^-$ is defined as monolayer adsorption onto GO/ES adsorbent's surface that is containing a certain number of identical sites [8]. Thus, this indicates, the adsorption of F$^-$ is not effective for multilayer adsorption onto the heterogeneous surface (Freundlich model).

Constant parameters of adsorption isotherms that are shown in Table 1 were calculated according to the linearized isotherm models. The empirical constants for Langmuir isotherm, which are K$_L$ and q$_m$ were found to be 0.6221 L/mg and 46.73 mg/g, respectively. The K$_L$ constant measured in this study is relatively larger, which indicates a strong affinity between F$^-$ (adsorbate) and GO/ES adsorbent [14]. For Freundlich isotherm, the n constant should be obtained in the range of 1–10, to ensure favorable adsorption [13]. However, the n value in

this study is greater than 10, which agrees with the low R^2 value, where the adsorption mechanism of F$^-$ onto GO/ES adsorbent is not suitable to represent by Freundlich isotherm. Overall, Langmuir isotherm was very well fitted with this research data, which suggests that the binding energy on the whole surface of the GO/ES adsorbent was uniform and the adsorbed F$^-$ were adsorbed by forming monolayer adsorption, where sorbate-sorbate interaction can be neglected [13].

Adsorption Kinetics

The kinetics study of F$^-$ adsorption by using GO/ES adsorbent was analyzed by using linearized pseudo-first-order and pseudo-second-order models expressed as in Eq. (5) and (6), respectively with regard to adsorption on the solid surface system [16]. The experimental data obtained were fitted into the models, as illustrated in Fig. 3 and the K values were calculated and tabulated in Table 2.

From Fig. 3, the pseudo-second-order model represents the best F$^-$ adsorption kinetic on GO/ES adsorbent compared to Pseudo-first-order, with an R^2.

Table 1. Parameters of adsorption isotherms constant

	Langmuir		Freundlich
q$_m$ (mg/g)	46.73	n	32.79
K$_L$ (L/mg)	0.6221	K$_F$	0.4721
R^2	0.9983	R^2	0.5007
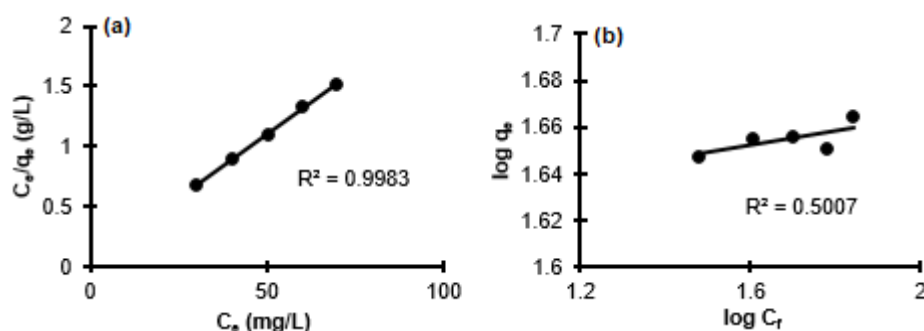
Fig 2. (a) Langmuir and (b) Freundlich isotherms for F$^-$ adsorption on GO/ES adsorbent

Table 2. Kinetics parameter for the adsorption of fluoride by GO/ES adsorbent

Pseudo-first-order		Pseudo-second-order	
Rate constant (K$_1$)	0.03020	Rate constant (K$_2$)	0.00047
R^2	0.95880	R^2	0.96970
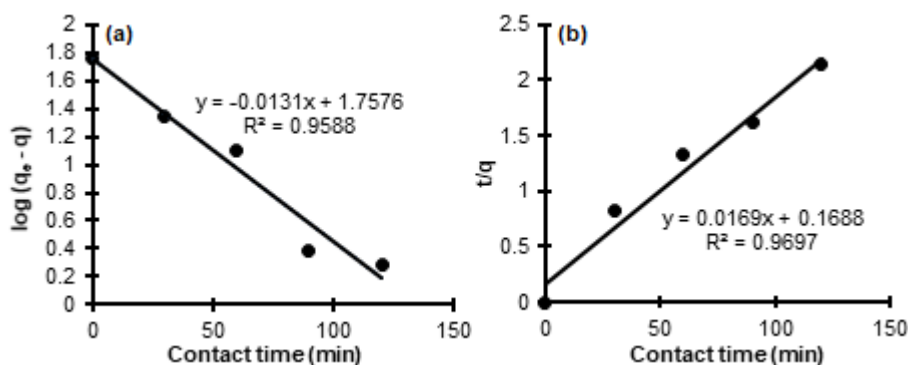
Fig 3. (a) Pseudo-first-order and (b) pseudo-second-order adsorption kinetics models for F⁻ removal by using GO/ES adsorbent

value of 0.9697 and K_2 value of 0.00047. According to pseudo-second-order theory, the adsorption of fluoride onto GO/ES adsorbent is a chemisorption process which involves sharing or exchange of electrons between the adsorbent and F⁻ [13]. There is a possibility that F⁻ may diffuse across a liquid phase prior to GO/ES's active sites through intraparticle diffusion and indirectly reacts with available active sites, such Ca^{2+} to produce CaF [17-20].

Adsorption Thermodynamics

Thermodynamic parameters, such as a change in Gibbs free energy ($\Delta G°$), enthalpy ($\Delta H°$) and entropy ($\Delta S°$), were evaluated in this study. K_0, which is the equilibrium adsorption constant calculated as the ratio between adsorption concentration and equilibrium concentration of the solution is shown in Eq. (7). The Gibbs free energy ($\Delta G°$) is calculated for adsorption of fluoride onto GO/ES adsorbent at all temperatures, where R is the gas constant (8.314 J/mol.K), and T is the temperature in Kelvin (K). The experimental data were fitted into the linearized Eq. (9), and illustrated in Fig. 4. All thermodynamic parameters were calculated and tabulated in Table 3.

From Fig. 4, the R^2 value obtained is 0.9726, which is not as high as the previous study done by other researchers [13]. Perhaps, this is due to less adsorption that happened at high temperature (348.15 K). From Table 3, the positive value of $\Delta G°$ indicates that the process is a physic-sorption process. The values of $\Delta G°$ in between 0 and to 20 kJ/mol indicate a physic-sorption process, while the values in between -80 to -400 kJ/mol correspond to the chemisorption process [15]. The increment in values of $\Delta G°$ with an increase in temperature suggests that higher temperature makes the
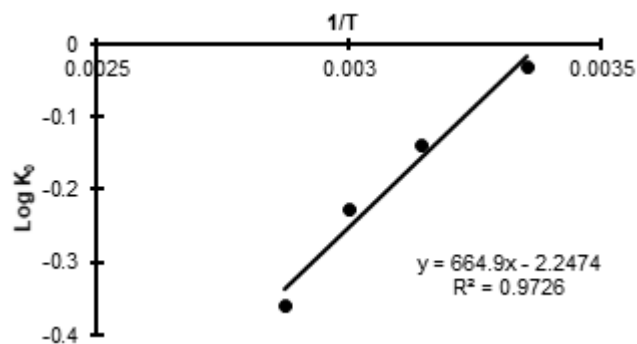
Fig 4. Thermodynamics study of F⁻ adsorption onto GO/ES adsorbent

Table 3. Thermodynamic parameters for the adsorption of F⁻ by GO/ES adsorbent

Temperature (K)	Thermodynamics parameters			
	K_0	$\Delta G°$ (kJ/mol)	$\Delta S°$ (J/mol.K)	$\Delta H°$ (kJ/mol)
298.15	0.9275	0.1865		
318.15	0.7230	0.8581	-43.04	-12.73
333.15	0.5903	1.4560		
348.15	0.4351	2.4085		

adsorption of F⁻ unfavorable, while the negative value of $\Delta S°$ indicates that the process is enthalpy driven and the negative value of $\Delta H°$ implies that the adsorption phenomenon is exothermic [12-13,19]. This explains that the adsorption of F⁻ by using GO/ES adsorbent is not suitable to be conducted at high temperature.

■ CONCLUSIONS

In this work, GO/ES adsorbent has been synthesized for F⁻ removal application. The maximum adsorption capacity of F⁻ (56 mg/g) was obtained at 25 °C, 25 mg/L of F⁻ initial concentration, 0.05 g of GO/ES adsorbent dosage and 120 min of contact time. Adsorption isotherms study show that the experimental data were best fitted with Langmuir isotherm, which indicates that F⁻ adsorption is following monolayer adsorption on a homogenous surface of GO/ES, with an R^2 value of 0.9983. The adsorption kinetics of F⁻ by using GO/ES is best presented by the pseudo-second-order model, involving a chemisorption process. From the thermodynamic analysis, F⁻ adsorption by using GO/ES adsorbent is a spontaneous and exothermic process; hence, a higher temperature is not favorable for this process.

■ ACKNOWLEDGMENTS

■ REFERENCES

[1] Mukherjee, S., and Halder, G., 2018, A review on the sorptive elimination of fluoride from contaminated wastewater, *J. Environ. Chem. Eng.*, 6 (1), 1257–1270.

[2] Jain, P.S., Prasad, S.B.B., and Raghu, A.V., 2017, A short review: Removal of fluoride ions from ground water by using various techniques, *IJRG*, 5 (4), 98–104.

[3] Nigri, E.M., Cechinel, M.A., Mayer, D.A., Mazur, L.P., Loureiro, J.M., Rocha, S.D., and Vilar, V.J., 2017, Cow bones char as a green sorbent for fluorides removal from aqueous solutions: Batch and fixed-bed studies, *Environ. Sci. Pollut. Res.*, 24 (3), 2364–2380.

[4] Engineering Services Division, 1983, *National standard for drinking water quality*, Ministry of Health Malaysia.

[5] Department of Environment Malaysia, 2010, *Environmental requirements: A guide for investors*, 11ᵗʰ Ed., Ministry of Natural Resources and Environment.

[6] Salifu, A., 2017, Fluoride removal from groundwater by adsorption technology - The occurrence, adsorbent synthesis, regeneration and disposal, *Dissertation*, Delft University of Technology, Delft, Netherlands.

[7] Kashi, G., Mehree, A., Zaeimdar, M., Khoshab, F., and Madaree, A.M., 2015, Removal of fluoride from urban drinking water by eggshell powder, *Bulg. Chem. Commun.*, 47, 187–192.

[8] Hasan, S.H., Mohan, S., Singh, D.K., and Kumar, V., 2015, Synthesis of graphene oxide and its application for efficient removal of fluoride from water, *J. Solid Waste Technol. Manage.*, 41 (4), 262–272.

[9] Kyzas, G.Z., Deliyanni, E.A., and Matis, K.A., 2014, Graphene oxide and its application as an adsorbent for wastewater treatment, *J. Chem. Technol. Biotechnol.*, 89 (2), 196–205,.

[10] Narasimharao, K., Venkata, R.G., Sreedhar, D., and Vasudevarao, V., 2016, Synthesis of graphene oxide by modified Hummers method and hydrothermal synthesis of graphene-NiO nano composite for supercapacitor application, *J. Mater. Sci. Eng.*, 5 (6), 1000284.

[11] Liu, L., Cui, Z., Ma, Q., Cui, W., and Zhang, X., 2016, One-step synthesis of magnetic iron–aluminum oxide/graphene oxide nanoparticles as a selective adsorbent for fluoride removal from aqueous solution, *RSC Adv.*, 6 (13), 10783–10791.

[12] Mohammad-Rezaei, R., Razmi, H., and Dehgan-Reyhan, S., 2014, Preparation of graphene oxide doped eggshell membrane bioplatform modified Prussian blue nanoparticles as a sensitive hydrogen peroxide sensor, *Colloids Surf., B*, 118, 188–193.

[13] Bhaumik, R., Mondal, M.K., Das, B., Roy, P., Pal, K.C., Das, C., Baneerjee, A., and Datta, J.K., 2012, Eggshell powder as an adsorbent for removal of fluoride from aqueous solution: Equilibrium,

586

Indones. J. Chem., 2020, 20 (3), 579 - 586

kinetic and thermodynamic studies, *E-J. Chem.*, 9 (3), 1457–1480.

[14] Raghav, S., and Kumar, D., 2019, Comparative kinetics and thermodynamic studies of fluoride adsorption by two novel synthesized biopolymer composites, *Carbohydr. Polym.*, 203, 430–440.

[15] Swain, S.K., Patnaik, T., Singh, V.K., Jha, U., Patel, R.K., and Dey, R.K., 2011, Kinetics, equilibrium and thermodynamic aspects of removal of fluoride from drinking water using meso-structured zirconium phosphate, *Chem. Eng. J.*, 171 (3), 1218–1226.

[16] Ahamad, K.U., Singh, R., Baruah, I., Choudhury, H., and Sharma, M.R., 2018, Equilibrium and kinetics modeling of fluoride adsorption onto activated alumina, alum and brick powder, *Groundwater Sustainable Dev.*, 7, 452–458.

[17] Sarma, G.K., and Rashid, M.H., 2018, Synthesis of Mg/Al layered double hydroxides for adsorptive removal of fluoride from water: A mechanistic and kinetic study, *J. Chem. Eng. Data*, 63 (8), 2957–2965.

[18] Di, H., Yu, Z., Ma, Y., Pan, Y., Shi, H., Lv, L., Li, F., Wang, C., Long, T., and He, Y., 2016, Anchoring calcium carbonate on graphene oxide reinforced with anticorrosive properties of composite epoxy coatings, *Polym. Adv. Technol.*, 27 (7), 915–921.

[19] Fathy, M., Moghny T.A., Mousa M.A., El-Bellihi A.H.A.A, and Awadallah A.E., 2016, Absorption of calcium ions on oxidized graphene sheets and study its dynamic behavior by kinetic and isothermal models, *Appl. Nanosci.*, 6 (8), 1105–1117.

[20] Kowanga, K.D., Gatebe, E., Mauti, G.O., and Mauti, E.M., 2016, Kinetic, sorption isotherms, pseudo-first-order model and pseudo-second-order model studies of Cu(II) and Pb (II) using defatted *Moringa oleifera* seed powder, *J. Phytopharmacol.*, 5 (2), 71–78.

Photocatalytic Degradation of Commercial Diazinon Pesticide Using C,N-codoped TiO₂ as Photocatalyst

Khoiriah Khoiriah[1], Diana Vanda Wellia[1], Jarnuzi Gunlazuardi[2], and Safni Safni[1,*]

[1]*Department of Chemistry, Faculty of Mathematics and Natural Sciences, Andalas University, Limau Manis, Padang 25163, Indonesia*

[2]*Department of Chemistry, Faculty of Mathematics and Natural Sciences, Universitas Indonesia, Kampus UI, Depok 16424, Indonesia*

* Corresponding author:

tel: +62-751-496818
email: safni@sci.unand.ac.id

Received: March 6, 2019
Accepted: May 24, 2019

DOI: 10.22146/ijc.43982

Abstract: *Diazinon (C₁₂H₂₁N₂O₃PS) is an effective pest controller that has been frequently used by farmers in agriculture. It is a nonspecific and highly toxic pesticide having low persistence in the environment and categorized as moderately hazardous class II. The degradation of commercial diazinon in aqueous solution was investigated by photocatalysis using low-energy activated C,N-codoped TiO₂ as catalyst under visible-light. The influence of some parameters, i.e., catalyst concentration, the initial concentration of diazinon, initial pH of diazinon, and irradiation time on the diazinon degradation was studied. The amount of diazinon degradation was strongly influenced by all the above parameters. The results show that titania-modified enhanced the degradation percentage of diazinon, from 44.08% without a catalyst to 86.93% by adding 12 mg of C,N-codoped TiO₂ catalyst after 30 min visible-light irradiation. UV-visible spectrophotometer, HPLC, and COD analysis verified that diazinon was successfully degraded under photocatalysis visible.*

Keywords: *degradation; photocatalysis; diazinon; C,N-codoped TiO₂*

■ INTRODUCTION

Diazinon(*O, O*-diethyl*O*-[6-methyl-2-(1-methyl ethyl)-4-pyrimidinyl]phosphorothioate (Fig. 1), an effective organophosphate chemical family and commercially introduced in 1952, is frequently used in Indonesia as an insecticide for various types of cultivation such as fruit trees, rice, palm, sugarcane, corn, tobacco, and horticultural plants. It is a nonspecific and highly toxic pesticide which has low persistence in the environment [1], immunotoxic [2] cytotoxic and genotoxic [3-5] and categorized as moderately hazardous class II by the World Health Organization (WHO) [6].

Diazinon at concentration 350 ng/L [7], 4.4 mg/L, 90–444 mg/kg may cause toxic for aquatic organisms, fish (48 h), and human, respectively. Inhibiting the enzyme acetylcholinesterase activity by overstimulation of nicotinic, muscarinic receptors [8] and increasing TNF-a production in rat serum and brain [9-10] are some toxic effects of

diazinon. The continuous application may lead to the common occurrence of diazinon residues in food crops, natural water systems, and soil [11]. Therefore, treating several water systems contaminated by diazinon is urgently demanded to protect human health. The use of advanced oxidation processes (AOPs) is essential because conventional treatment methods have high operational costs, longer reaction time, and producing secondary pollutant [12]. AOPs process produces and uses •OH and •O₂ radicals as reducing agents and strong oxidant to degrade organic pollutants to be environmentally friendly
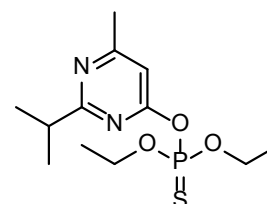
Fig 1. Structure of diazinon

compounds such as H_2O and CO_2 [13-14]. Photocatalysis, the use of light and semiconductor catalyst as reactive species source and having advantages such as non-selectivity, quickly completed oxidation and oxidation of pollutants in the ppb range, is one of the most promising AOPs for wastewater treatment [15].

The selected photocatalyst often used in the degradation process is titania (TiO_2) because of its abundance, effectiveness, stability against photo-corrosion, photoactive, and nontoxic to living things [16-17]. However, it has a fairly high band gap (3.2 eV), and a lot of research has reduced its band gap by modifying TiO_2 with metal, or non-metal elements [18].

Modified titania by the codoping method has higher photocatalytic activity than doping with only one element in the visible-light region [19]. The potential elements that can be used as dopants are carbon and nitrogen because their size is not much different from oxygen [20]. Several methods of synthesis of C,N-codoped TiO_2 have been reported such as sol-gel [21-23], and solvothermal [24-27], but these methods still use organic solvents which are less environmentally friendly and require high costs.

The modified titania with carbon and nitrogen (C,N-codoped TiO_2) has been successfully synthesized by the peroxo sol-gel method using environmentally friendly, water, as solvent [19,28] and reported that the presence of dopants carbon and nitrogen had been shown to provide a synergistic effect in absorbing visible-light to increase titania photocatalytic activity. The application has also been carried out on several organic pollutants [20,29-32] and inorganic pollutant [28]. In the present work, C,N-codoped TiO_2 synthesized by the peroxo sol-gel method was applied on photocatalysis of commercial diazinon pesticide under visible-light. Parameters affecting the degradation process, i.e., catalyst mass, doping on titania, pH of the initial solution, and irradiation time were studied.

■ **EXPERIMENTAL SECTION**

Materials

Materials used were commercial pesticide Diazinon 60 EC (600 g/L) manufactured by Petrokimia Kayaku, Co (Indonesia), double distilled water and ethanol 96% were from Dwipraga Chemical, Co (Indonesia), acetonitrile chromatography grade, Whatman filter (θ: 0.45 μm), undoped-TiO_2, and C,N-codoped TiO_2 catalyst were obtained from applied analytical chemistry laboratory of Andalas University with particle size about 44 nm.

Instrumentation

Centrifuge Nesco 80-2, analytical balance, UV-Vis spectrophotometer (Shimadzu Corp, serial A116352), HPLC (Hitachi-Trimaide, serial1202-005, Japan) and the Halogen lamp 500 Watt (Philips) were used in this investigation.

Procedure

Photodegradation experiments were conducted in 10 cm internal diameter Petridish as photoreactor that contained 20 mL of 18 mg/L diazinon pesticide in room temperature. The pesticide was treated by photocatalysis under visible-light irradiation using 12 mg TiO_2 and C,N-codoped TiO_2 for 5–30 min to investigate the doping effect on titania catalyst. C,N-codoped TiO_2 (0, 6, 12, 18, and 24 mg) was added into the photocatalysis system to study the effect of catalyst concentration. The effect of initial pH (3, 5, 7, 11) and initial concentration of diazinon over 9, 18, 36, 54, 72 and 90 mg/L were also studied. The pH of the solution was adjusted to 3, 5, 7, 11 by adding NaOH 0.01 N or HCl 0.01 N. The photolysis without catalyst and adsorption of catalyst (in dark place) were also investigated as a control. The degraded solution was collected and centrifuged for 20 min at 3000 rpm and then filtered through a Whatman 0.22 μm filter to separate the catalyst from the solution. The solution was kept in the dark bottles and measured with UV-Vis spectrophotometer. Degradation percentage of pesticide was calculated from spectrophotometric data using Eq. 1:

$$\frac{A_i - A_f}{A_i} \times 100\% \tag{1}$$

where A_i and A_f correspond to initial and final diazinon pesticide absorbance.

The untreated and treated diazinon by visible-light photocatalysis degradation was also analyzed by HPLC packed with a C18 column (150 mm × 4.6 mm) and detected by a UV detector at a wavelength of 247 nm to

identify the formed intermediates. The mobile phase was a mixture of acetonitrile and water, with a volumetric ratio of 75/25 with an injection flow rate of 0.6 mL/min. An injection volume of diazinon solution was 20 μL. The COD (chemical oxygen demand) of samples was determined by closed reflux, colorimetric methods (SNI 06-6989.2-2004).

■ RESULTS AND DISCUSSION

The Effect of Catalyst Concentration on Diazinon Degradation

The effect of C,N-codoped TiO_2 concentration (0–24 mg) was investigated for 18 mg/L diazinon degradation. As shown in Fig. 2, the increase of C,N-codoped TiO_2 addition from 0 to 12 mg improved the diazinon degradation percentage from 31.79% to 67.98% under visible-light photocatalysis for 15 min.

This preliminary improving diazinon degradation percentage with an increasing catalyst (0–12 mg) can be due to the increase in catalyst surface area, the easy light penetration, the enhanced amount of photon absorption on the catalyst surface, and consequently higher production of active species •OH radical by C,N-codoped TiO_2 [33]. However, using C,N-codoped TiO_2 catalyst up to 12 mg reduces degradation percentage. This phenomenon is caused by the higher suspension turbidity, which diminishes the amount of light to reach active surfaces [33-34]. Also, the agglomeration of C,N-codoped TiO_2 may deactivate the active sites [34-38]. Therefore, 12 mg of C,N-codoped TiO_2 is selected as the most efficient catalyst concentration for diazinon removal and used for other experiments.

The Effect of Titania Doping on Diazinon Degradation

The photocatalytic performance of the TiO_2 photocatalysts for the photodegradation of diazinon under visible-light was evaluated, as shown in Fig. 3. At first, catalyst adsorption and photolysis are performed as control with removal percentage 4.48%, 44.08%, respectively for 30 min reaction time. Under photolysis, a photon from the light source may break down the organic
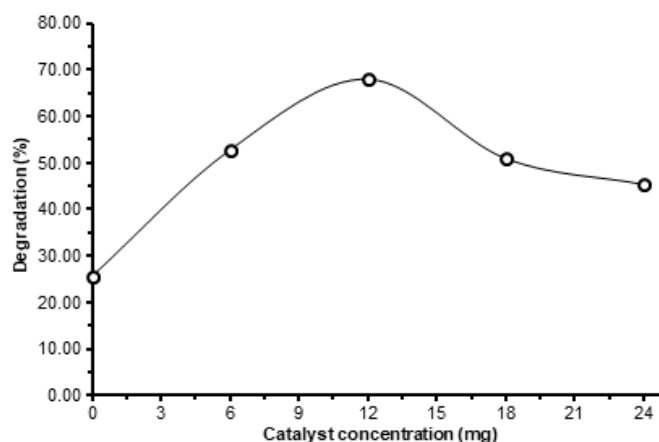
Fig 2. The effect of catalyst mass on photocatalysis of diazinon using C,N-codoped TiO_2 catalyst ([diazinon]$_o$ = 18 mg/L, catalyst = 0, 6, 12, 18, 24 mg, t = 15 min)
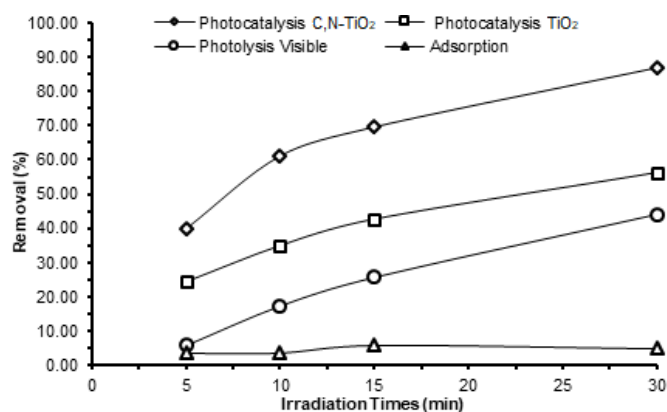
Fig 3. The effect of the catalyst on diazinon degradation by adsorption, photocatalysis using 12 mg C,N-codoped TiO_2 catalyst ([diazinon]$_o$ =18 mg/L, t = 5–30 min)

pollutant through chemical reaction [39]. Hence, the removal percentage increased significantly by adding the catalyst. The C,N-codoped TiO_2 photocatalysts were able to reduce 86.93% diazinon, which is higher than that is obtained in the presence of un-doped TiO_2 with 56.33% removal percentage of diazinon. Modification of titania using nonmetal elements such as carbon and nitrogen can lower its band gap, hasten the electron-hole process, and produce more •OH and $•O_2^-$ radicals, which resulted in more degraded diazinon pesticide. This result was attributed by the shifting edge of modification TiO_2, which can be attributed to the increased of TiO_2 optical absorption [28].

The Effect of Initial pH of Pesticide on Diazinon Degradation

pH is one of the most important parameters influencing the photocatalytic degradation behavior since it determines the photocatalyst surface charge and the size of the aggregate formed. The effect of initial pH in acidic, neutral, and alkaline (3, 5, 7, 11) on photocatalysis degradation of 18 mg/L diazinon using 12 mg C,N-codoped TiO$_2$ was investigated. As observed in Fig. 4, the percentage of diazinon degradation was 45.82, 69.46, 67.98, and 48.58% at pH 3, 5, 7, and 11, respectively. The maximum degradation of diazinon was achieved at pH 5. This term can be explained by electrostatic interaction between the catalyst surface and the target compound. In this study, the catalyst used was on the nanoscale, with a size of about 44 nm [28]. The zero point charge (zpc), pH$_{zpc}$, of nano-sized titania is reported around 6.3–6.9 [15, 40]. The TiO$_2$ surface is positively charged at a low pH (< pH$_{zpc}$), and negatively charged at a higher pH (> pH$_{pzc}$). On the other hand, the given pKa for diazinon is 2.6. It will be negatively charged above pH 2.6. Therefore, the optimal condition is found at pKa diazinon < pH < pH$_{zpc}$ C,N-codoped TiO$_2$ (between 2 < pH < 6.9) at which the positively charged catalyst and negatively charged diazinon should readily attract each other. The same result is also obtained by some researchers that degrade diazinon by photocatalysis using Pt-TiO$_2$ [34], and ZnO [35], TiO$_2$ [36] as catalysts.

The Effect of Initial Pesticide Concentration on Diazinon Degradation

The effect of initial pesticide concentration on diazinon degradation percentage is conducted with a dose of 9, 18, 36, 54, 72, and 90 mg/L at a constant condition; 15 min reaction time and 12 mg C,N-codoped TiO$_2$ catalyst dosage. The diazinon degradation decreases slightly with the higher initial concentrations of pesticides. The percentage of degradation diazinon at initial concentrations of 9, 18, 36, 54, 72 and 90 mg/L sequentially was achieved 72.43, 67.98, 66.07, 57.31, 49.38, and 22.91%, as illustrated in Fig. 5. The decrease in percentage degradation at high concentrations is caused by the competition between diazinon molecules each other
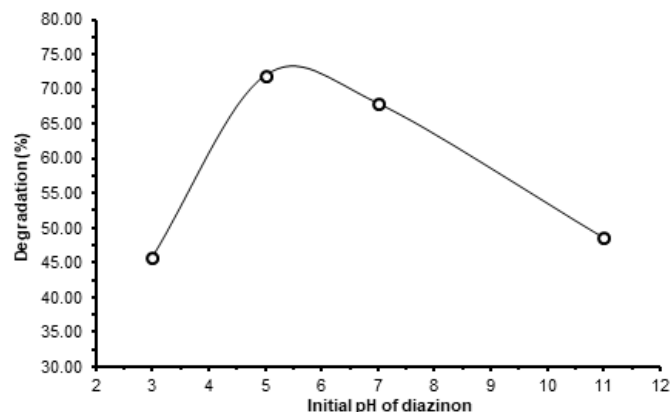
Fig 4. The effect of pesticide initial pH (3, 5, 7, 9) on photocatalysis of diazinon using 12 mg C,N-codoped TiO$_2$ catalyst ([diazinon]$_o$ = 18 mg/L, t = 15 min)
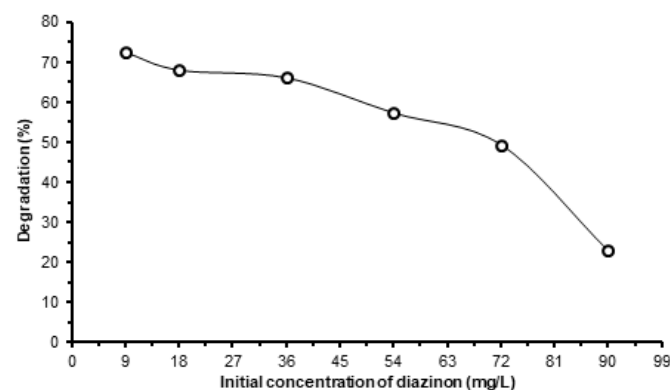
Fig 5. The effect of initial pesticide concentration on photocatalysis of diazinon using 12 mg C,N-codoped TiO$_2$ catalyst ([diazinon]$_o$ = 9 - 90 mg/L, t = 15 min)

to be absorbed on the C,N-codoped TiO$_2$ catalyst surface with the result reducing both of the availability of active sites and the pollutant oxidizing agents concentration (•OH and •O$_2^-$ radicals) [33]. More intermediates are generated and consumed the reactive species in the systems. In addition, the generated intermediates may adsorb on the catalyst surface, which causes deactivate of the active sites of photocatalyst and leads to a decrease in the degradation percentage. In contrast, at low concentrations, there is no lack of catalytic sites number, and the rate of degradation will be proportional to the substrate concentration [37].

Two kinds of terms regard to the effect of the initial concentration on degradation process, 1) the efficiency degradation decreases by increasing diazinon concentration [40-42] and 2) there is an optimum point
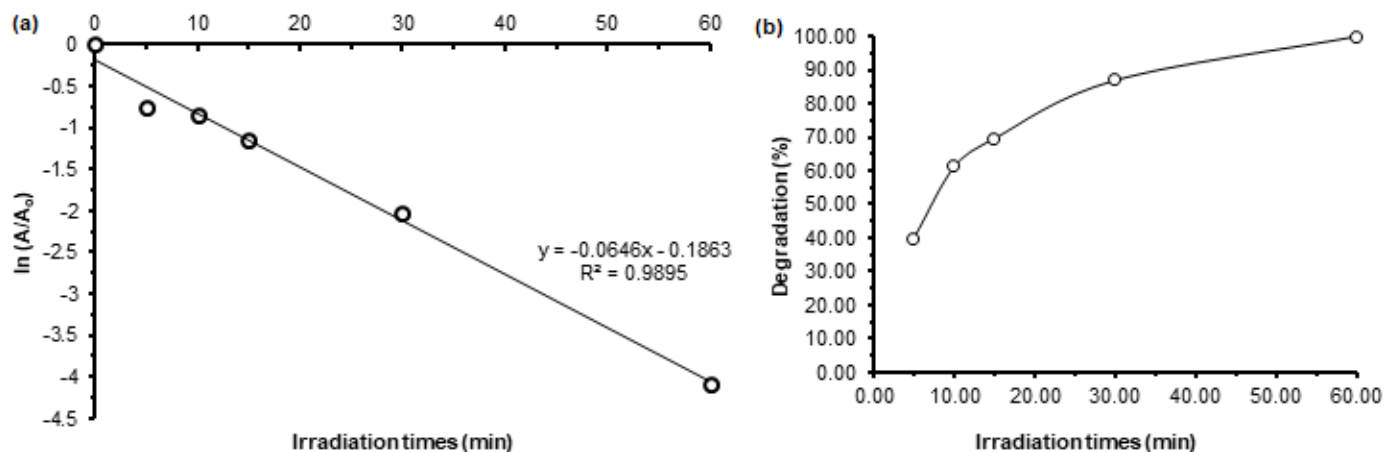
Fig 6. (a) The effect of irradiation times and (b) the first order model on photocatalysis of diazinon using 12 mg C,N-codoped TiO$_2$ catalyst ([diazinon]$_o$ = 18 mg/L, t = 5–60 min)

of efficiency degradation at a certain concentration [43-45]. This discrepancy may come from being the differences in the catalyst, organic pollutant properties, and experimental conditions.

The Effect of Irradiation Time on Diazinon Degradation

Time is one of the important parameters affecting the amount of organic pollutant degraded. The pesticide photocatalysis degradation was conducted over the range 5–60 min with constant catalyst weight. As can be seen in Fig. 6(a), the degradation of diazinon steadily improves by increasing time in the photocatalysis process. Diazinon was degraded from 39.86% to 100% when the radiation times were from 5 to 60 min. The contact between photon and C,N-codoped TiO$_2$ increases at a longer time, leading more number of radical actives species production, which improves diazinon degradation [30,46]. In addition, reactive species and pesticides react perfectly with increasing irradiation time [47].

In order to obtain kinetic information, experimental results were fitted with zero, first and second order equations. The linearity value of those order equations shows that the photocatalytic degradation of 18 mg/L diazinon is well fitted with the first-order model (R = 0.9893) as can be seen in Fig. 6(b). The rate constant calculated from the slope between ln ([diazinon]$_t$/[diazinon]$_0$) versus reaction time Eq. 2 is 0.0646 min^{-1}.

$$\ln \frac{A_t}{A_0} = -kt \qquad (2)$$

where A_t = diazinon concentration after irradiation, A_0 = initial concentration of diazinon, k = rate constant [48].

Fig. 7 represents the progressive degradation of diazinon after exposure under photocatalysis visible using C,N-codoped TiO$_2$. The UV–visible absorption spectrum of diazinon shows a peak at 247 nm. Its peak diminished gradually as exposure time increased, which confirm the progressive degradation of diazinon. The
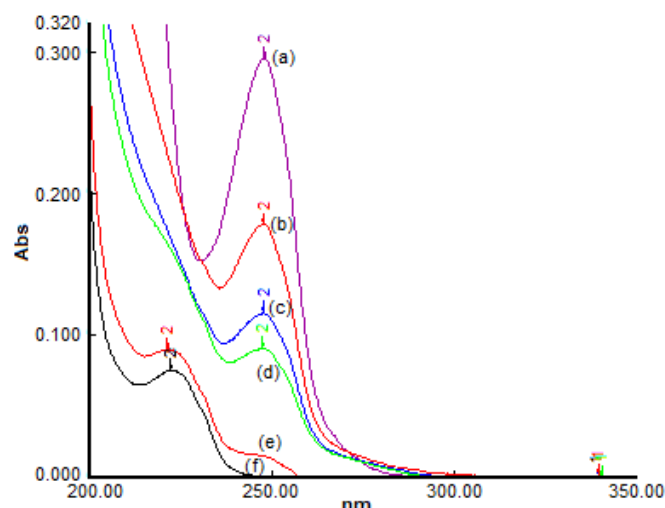
Fig 7. The change in UV-visible spectrum of Diazinon (a) before (0 min) and (b-f) after photocatalysis for 5–60 min, using 12 mg C,N-codoped TiO$_2$ catalyst ([diazinon]$_o$ = 18 mg/L, t = 5–60 min)

complete degradation was reached at 60 min irradiation by vanishing diazinon peak at 247 nm and appearing the new peak at 230 nm. The possible compound formed from this process is 2-isopropyl-6-methyl-4-pyrimidinol (IMP) as a less byproduct of diazinon degradation [49]. The IMP has UV-Vis absorbance spectra at 230 nm, as reported by Žabar [50]. Yielding IMP from diazinon occurs probably by two mechanisms; through oxidative desulfuration of hydroxyl radical attack on the thiono group to form diazoxon followed by hydrolysis, or through a directly oxidative mechanism on diazinon [49].

The HPLC Analysis of Degraded Diazinon

Generally, some intermediates and by-products will be produced during the degradation process. Sometimes they are more toxic than the initial target contaminants. Fig. 8 shows that diazinon concentration reduces after treatment indicating by the decrease in its peak at a retention time of 8.7 min. Diazinon almost completely disappears and transforms into other compounds after 60 min photocatalysis. This result is a good agreement with the UV-visible spectrophotometric data reaching 100% degradation percentage by disappearing diazinon spectrum and forming a new spectrum at 230 nm, as shown in Fig. 7. The existence of a new peak at retention time t_R = 1.67 min and t_R = 2.76 min in chromatogram signifies the possible formation of new compounds as the diazinon degradation products that need to be analyzed further.
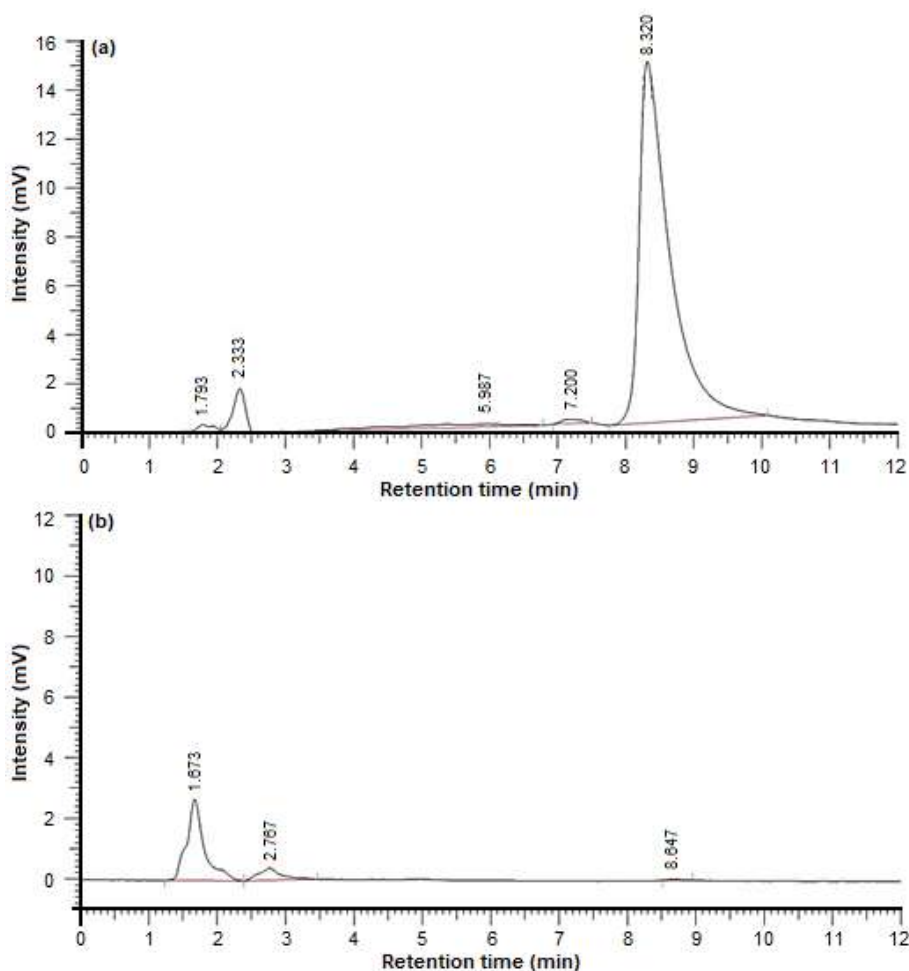
Fig 8. Chromatogram of (a) un-treated diazinon solution (b) treated diazinon by visible photocatalysis using 12 C,N-codoped TiO_2 catalyst ([diazinon]$_o$ =18 mg/L, t = 60 min)
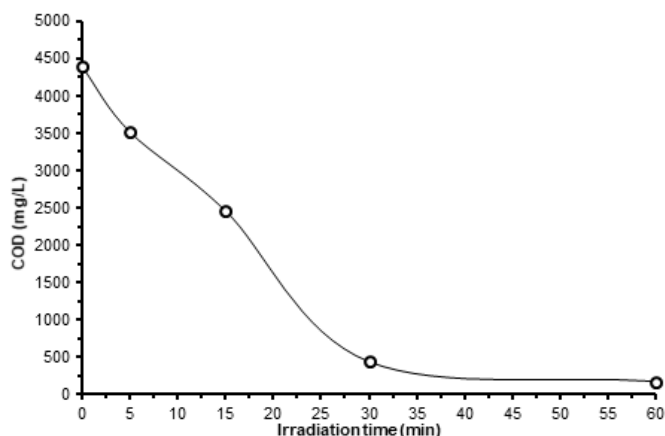
Fig 9. The chemical oxygen demand (COD) of diazinon after photocatalysis using 12 mg C,N-codoped TiO$_2$ catalyst ([diazinon]$_o$ = 18 mg/L, t = 5–60 min)

Chemical Oxygen Demand (COD) of Degraded Diazinon

The degree of diazinon mineralization was determined by using COD experiment. It is found that the COD of diazinon solution decreases from 4400 mg/L to 176 mg/L after 60 min of photocatalysis treatment. This indicates that 96% of diazinon was mineralized to carbon dioxide during photocatalysis [51]. When titania catalyst was irradiated by photon, its electron will excite from valence band to conduction gap, and this process generates electron-hole. The reaction between oxygen and water with generated electron-hole would form the strong oxidative hydroxyl radical (•OH). The radical would oxidize the organic pollutant into CO$_2$ and H$_2$O [52]. The COD, spectrophotometer UV-Visible, and chromatogram confirmed that photocatalysis using C,N-codoped TiO$_2$ under visible-light was successfully degraded the diazinon.

■ CONCLUSION

The diazinon degradation is accelerated by titania modified (C,N-codoped TiO$_2$) under the photocatalysis process. The diazinon can be completely degraded by C,N-codoped TiO$_2$ catalyzed visible photocatalysis for 60 min irradiation. The degradation was strongly affected by catalyst concentration, initial concentration of diazinon, initial pH of the solution, and irradiation time. UV-visible spectrophotometer, HPLC and COD analysis

verified that diazinon was successfully degraded by photocatalysis visible using 12 mg C,N-codoped TiO$_2$.

■ REFERENCES

[1] Čolović, M., Krstić, D., Petrović, S., Leskovac, A., Joksić, G., Savić, J., Franko, M., Trebše, P., and Vasić, V., 2010, Toxic effects of diazinon and its photodegradation products, *Toxicol. Lett.*, 193 (1), 9–18.

[2] Neishabouri, E.Z., Hassan, Z.M., Azizi, E., and Ostad, S.N., 2004, Evaluation of immunotoxicity induced by diazinon in C57bl/6 mice, *Toxicology*, 196 (3), 173–179.

[3] Muranli, F.D., Kanev, M., and Ozdemir, K., 2015, Genotoxic effects of diazinon on human peripheral blood lymphocytes, *Arh. Hig. Rada Toksikol.*, 66 (2), 153–158.

[4] Harchegani, A.B., Rahmani, A., Tahmasbpour, E., Kabootaraki, H.B., Rostami, H., and Shahriary, A., 2018, Mechanisms of diazinon effects on impaired spermatogenesis and male infertility, *Toxicol. Ind. Health*, 34 (9), 653–664.

[5] Ezzi, L., Haouas, Z., Salah, I.B., Sakly, A., Grissa, I., Chakroun, S., Kerkeni, E., Hassine, M., Mehdi, M., and Cheikh, H.B., 2016, Toxicopathic changes and genotoxic effects in liver of rat following exposure to diazinon, *Environ. Sci. Pollut. Res.*, 23 (11), 11163–11170.

[6] Jonidi-Jafari, A., Shirzad-Siboni, M., Yang, J.K., Naimi-Joubani, M., and Farrokhi, M., 2015, Photocatalytic degradation of diazinon with illuminated ZnO–TiO$_2$ composite, *J. Taiwan Inst. Chem. Eng.*, 50, 100–107.

[7] Li, P.C.H., Swanson, E.J., and Gobas, F.A.P.C., 2002, Diazinon and its degradation products in

agricultural water courses in British Columbia, Canada, *Bull. Environ. Contam. Toxicol.*, 69 (1), 59–65.

[8] Čolović, M.B., Krstić, D.Z., Ušćumlić, G.S., and Vasić, V.M., 2011, Single and simultaneous exposure of acetylcholinesterase to diazinon, chlorpyrifos and their photodegradation products, *Pestic. Biochem. Physiol.*, 100 (1), 16–22.

[9] Ahmed, M.A.E., Ahmed, H.I., and El-Morsy, E.M., 2013, Melatonin protects against diazinon-induced neurobehavioral changes in rats, *Neurochem. Res.*, 38 (10), 2227–2236.

[10] Hariri, A.T., Moallem, S.A., Mahmoudi, M., Memar, B., and Hosseinzadeh, H., 2010, Sub-acute effects of diazinon on biochemical indices and specific biomarkers in rats: Protective effects of crocin and safranal, *Food Chem. Toxicol.*, 48 (10), 2803–2808.

[11] Wu, J., Lan, C., and Chan, G.Y.S., 2009, Organophosphorus pesticide ozonation and formation of oxon intermediates, *Chemosphere*, 76 (9), 1308–1314.

[12] Yahiat, S., Fourcade, F., Brosillon, S., and Amrane, A., 2011, Photocatalysis as a pre-treatment prior to a biological degradation of cyproconazole, *Desalination*, 281, 61–67.

[13] Mirmasoomi, S.R., Ghazi, M.M., and Galedari, M., 2017, Photocatalytic degradation of diazinon under visible light using TiO_2/Fe_2O_3 nanocomposite synthesized by ultrasonic-assisted impregnation method, *Sep. Purif. Technol.*, 175, 418–427.

[14] Beduk, F., Aydin, M.E., and Ozcan, S., 2012, Degradation of malathion and parathion by ozonation, photolytic ozonation, and heterogeneous catalytic ozonation processes, *Clean-Soil Air Water*, 40 (2), 179–187.

[15] Chen, H., Shen, M., Chen, R., Dai, K., and Peng, T., 2011, Photocatalytic degradation of commercial methyl parathion in aqueous suspension containing La-doped TiO_2 nanoparticles, *Environ. Technol.*, 32 (13), 1515–1522.

[16] Sakkas, V.A., Dimou, A., Pitarakis, K., Mantis, G., and Albanis, T., 2005, TiO_2 photocatalyzed degradation of diazinon in an aqueous medium, *Environ. Chem. Lett.*, 3 (2), 57–61.

[17] Nadia, E.M., Moustapha, B., and Yahia, A.I., 2018, UV/TiO_2 photocatalytic oxidation of commercial pesticide in aqueous solution, *Am. J. Innov. Res. Appl. Sci.*, 7 (1), 36–43.

[18] Kumar, S.G., and Devi, L.G., 2011, Review on modified TiO_2 photocatalysis under UV/visible light: Selected results and related mechanisms on interfacial charge carrier transfer dynamics, *J. Phys. Chem. A*, 115 (46), 13211–13241.

[19] Xu, Q.C., Wellia, D.V., Yan, S., Liao, D.W., Lim, T.M., and Tan, T.T.Y., 2011, Enhanced photocatalytic activity of C-N-codoped TiO_2 films prepared via an organic-free approach, *J. Hazard. Mater.*, 188 (1-3), 172–180.

[20] Safni, Wellia, D.V., Komala, P.S., and Putri, R.A., 2015, Degradation of yellow-GCN by photolysis with UV-light and solar irradiation using C-N-codoped TiO_2 catalyst, *J. Chem. Pharm. Res.*, 7 (11), 306–311.

[21] Kakroudi, M.A., Kazemi, F., and Kaboudin, B., 2014, Highly efficient photodeoximation under green and blue LEDs catalyzed by mesoporous C-N-codoped nano TiO_2, *J. Mol. Catal. A: Chem.*, 392, 112–119.

[22] Chen, D., Jiang, Z., Geng, J., Wang, Q., and Yang, D., 2007, Carbon and nitrogen co-doped TiO_2 with enhanced visible-light photocatalytic activity, *Ind. Eng. Chem. Res.*, 46 (9), 2741–2746.

[23] Liu, G., Han, C., Pelaez, M., Zhu, D., Liao, S., Likodimos, V., Kontos, A.G., Falaras, P., and Dionysiou, D.D., 2013, Enhanced visible light photocatalytic activity of CN-codoped TiO_2 films for the degradation of microcystin-LR, *J. Mol. Catal. A: Chem.*, 372, 58–65.

[24] Dai, G., Liu, S., Liang, Y., Liu, H., and Zhong, Z., 2013, A simple preparation of carbon and nitrogen co-doped nanoscaled TiO_2 with exposed {001} facets for enhanced visible-light photocatalytic activity, *J. Mol. Catal. A: Chem.*, 368-369, 38–42.

[25] Wu, Y.C., and Ju, L.S., 2014, Annealing-free synthesis of C-N co-doped TiO_2 hierarchical spheres by using amine agents via microwave-assisted solvothermal method and their

Khoiriah et al.

photocatalytic activities, *J. Alloys Compd.*, 604, 164–170.

[26] El-Sheikh, S.M., Khedr, T.M., Hakki, A., Ismail, A.A., Badawy, W.A., and Bahnemann, D.W., 2017, Visible light activated carbon and nitrogen co-doped mesoporous TiO_2 as efficient photocatalyst for degradation of ibuprofen, *Sep. Purif. Technol.*, 173, 258–268.

[27] Wang, X., and Lim, T.T., 2010, Solvothermal synthesis of C–N codoped TiO_2 and photocatalytic evaluation for bisphenol A degradation using a visible-light irradiated LED photoreactor, *Appl. Catal., B*, 100 (1-2), 355–364.

[28] Wellia, D.V., Fitria, D., and Safni, 2018, C-N-codoped TiO_2 synthesis by using peroxo sol gel method for photocatalytic reduction of Cr(VI), *J. Pure Appl. Chem. Res.*, 7 (1), 25–31.

[29] Fitriyani, Y.O., Septiani, U., Wellia, D.V., Putri, R.A., Safni, 2017, Degradasi zat warna direct red-23 secara fotolisis dengan katalis C-N-codoped TiO_2, *Valensi*, 3 (2), 152–159.

[30] Safitri, V.Y., Santoni, A., Wellia, D.V., Khoiriah, and Safni, 2017, Degradation of paracetamol by photolysis using C-N-codoped TiO_2, *Molekul*, 12 (2), 189–195.

[31] Safni, Weillia, D.V., Komala, P.S., Putri, R.A., and Deliza, 2016, Photocatalytic degradation of yellow-GCN dye using C-N-codoped TiO_2 thin film in degradation reactor using visible-light irradiation, *Der Pharma Chem.*, 8 (19), 642–646.

[32] Safni, M., Putri, R.A., Wellia, D.V., and Septiani, U., 2017, Photodegradation of orange F3R dyes: Effect of light sources and the addition of CN-codoped TiO_2 catalyst, *Der Pharma Chem.*, 9 (10), 1–5.

[33] Kumar, A., and Pandey, G., 2017, A review on the factors affecting the photocatalytic degradation of hazardous materials, *Mater. Sci. Eng. Int. J.*, 1 (3), 1–10.

[34] Nakaoka, Y., Katsumata, H., Kaneco, S., Suzuki, T., and Ohta, K., 2012, Photocatalytic degradation of diazinon in aqueous solution by platinized TiO_2, *Desalin. Water Treat.*, 13 (1-3), 427–436.

[35] Daneshvar, N., Aber, S., Seyed Dorraji, M.S., Khataee, A.R., and Rasoulifard, M.H., 2007, Photocatalytic degradation of the insecticide diazinon in the presence of prepared nanocrystalline ZnO powders under irradiation of UV-C light, *Sep. Purif. Technol.*, 58 (1), 91–98.

[36] Jafari, S.J., Moussavi, G., and Hossaini, H., 2016, Degradation and mineralization of diazinon pesticide in UVC and UVC/TiO_2 process, *Desalin. Water. Treat.*, 57 (8), 3782–3790.

[37] Ahmed, S., Rasul, M.G., Brown, R., and Hashib, M.A., 2011, Influence of parameters on the heterogeneous photocatalytic degradation of pesticides and phenolic contaminants in wastewater: A short review, *J. Environ. Manage.*, 92 (3), 311–330.

[38] Jonidi-Jafari, A., Gholami, M., Farzadkia, M., Esrafili, A., and Shirzad-Siboni, M., 2017, Application of Ni-doped ZnO nanorods for degradation of diazinon: Kinetics and by-products, *Sep. Sci. Technol.*, 52 (15), 2395–2406.

[39] Speight, J.G., 2017, "Transformation of inorganic chemicals in the environment" in *Environmental Inorganic Chemistry for Engineers*, 1st Ed., Butterworth-Heinemann, 333–382.

[40] Kalantary, R.R., Shahamat, Y.D., Farzadkia, M., Esrafili, A., and Asgharnia, H., 2015, Photocatalytic degradation and mineralization of diazinon in aqueous solution using nano-TiO_2 (Degussa, P25): Kinetic and statistical analysis, *Desalin. Water. Treat.*, 55 (2), 555–563.

[41] Shirzad-Siboni, M., Jonidi-Jafari, A., Farzadkia, M., Esrafili, A., and Gholami, M., 2017, Enhancement of photocatalytic activity of Cu-doped ZnO nanorods for the degradation of an insecticide: Kinetics and reaction pathways, *J. Environ. Manage.*, 186 (Pt 1), 1–11.

[42] Mohagheghian, A., Karimi, S.A., Yang, J.K., and Shirzad-Siboni, M., 2016, Photocatalytic degradation of diazinon by illuminated WO_3 nanopowder, *Desalin. Water. Treat.*, 57 (18), 8262–8269.

[43] Baneshi, M.M., Rezaei, S., Sadat, A., Mousavizadeh, A., Barafrashtehpour, M., and Hekmatmanesh, H., 2017, Investigation of photocatalytic degradation of

diazinon using titanium dioxide (TiO₂) nanoparticles doped with iron in the presence of ultraviolet rays from the aqueous solution, *Biosci. Biotechnol. Res. Commun.*, 1, 60–67.

[44] Laoufi, N.A., Tassalit, D., and Bentahar, F., 2008, The degradation of phenol in water solution by TiO₂ photocatalysis in a helical reactor, *Global NEST J.*, 10 (3), 404–418.

[45] Tabasideh, S., Maleki, A., Shahmoradi, B., Ghahremani, E., and McKay, G., 2017, Sonophotocatalytic degradation of diazinon in aqueous solution using iron-doped TiO₂ nanoparticles, *Sep. Purif. Technol.*, 189, 186–192.

[46] Sari, M.I., Agustina, T.E., Melwita, E., and Aprianti, T., 2017, Color and COD degradation in photocatalytic process of procion red by using TiO₂ catalyst under solar irradiation, *AIP Conf. Proc.*, 1903, 040017.

[47] Wardhani, S., Purwonugroho, D., Fitri, C.W., and Prananto, Y.P., 2018, Effect of pH and irradiation time on TiO₂-chitosan activity for phenol photo-degradation, *AIP Conf. Proc.*, 2021, 050009.

[48] Hossaini, H., Moussavi, G., and Farrokhi, M., 2017, Oxidation of diazinon in cns-ZnO/LED photocatalytic process: Catalyst preparation, photocatalytic examination, and toxicity bioassay of oxidation by-products, *Sep. Purif. Technol.*, 174, 320–330.

[49] Shemer, H., and Linden, K.G., 2006, Degradation and by-product formation of diazinon in water during UV and UV/H₂O₂ treatment, *J. Hazard. Mater.*, 136 (3), 553–559.

[50] Žabar, R., 2012, Persistence, degradation and toxicity of transformation products of selected insecticides, *Dissertation*, University of Nova Gorica, Slovenia.

[51] Rajamanickam, D., and Shanthi, M., 2016, Photocatalytic degradation of an organic pollutant by zinc oxide – solar process, *Arabian J. Chem.*, 9 (Suppl. 2), S1858–S1868.

[52] Syafei, D., Sugiarti, S., Darmawan, N., and Khotib, M., 2017, Synthesis of TiO₂/carbon nanoparticle (C-dot) composites as active catalysts for photodegradation of persistent organic pollutant, *Indones. J. Chem.*, 17 (1), 37–42.

Enhancing Thermal and Mechanical Properties of UHMWPE/HA Composite as Tibial Tray

Yusuf Bramastya Apriliyanto[1], Sri Sugiarti[1,*], and Sulistioso Giat Sukaryo[2]

[1]*Department of Chemistry, Bogor Agricultural University, Chemistry Building, Wing 1, 3rd Floor, Tanjung St., IPB Darmaga Campus, Bogor 16680, Indonesia*

[2]*Center for Science and Advanced Material Technology, National Nuclear Energy Agency (PSTBM-BATAN), Puspiptek St., Tangsel-Banten 15314, Indonesia*

* Corresponding author:

tel: +62-251-8624567
email: sri.sw07@gmail.com

Abstract: *A bearing material in an artificial knee joint has to have good thermal and mechanical properties to prevent wear in order to be used as a tibial tray. Despite its well-known good properties, ultrahigh molecular weight polyethylene (UHMWPE) still needs to be modified to enhance its physical strength in its use in artificial joints. In this research, composites made from UHMWPE and hydroxyapatite (HA) were prepared by mechanical alloying and hot press method and their thermal and mechanical properties were modified using gamma rays. The composites were prepared using various HA loading ratios and irradiated using gamma rays at doses of 0, 25, 50, and 75 kGy. The effects of HA loading and gamma irradiation on thermal and mechanical properties were studied by various methods. The results showed that the addition of HA enhanced the hardness of UHMWPE by 8–15% and the maximum stress up to 38%. Gamma irradiation enhanced the crystallinity by 113–172%, the melting point by 0.6–0.7%, and decreased the break elongation of composites by 23–48%. Addition of polyvinyl alcohol (5% w/w) in composites reduced their rigidity by 16–47% and hardness by 3–9%.*

Keywords: *tibial tray; UHMWPE/HA composites; physical properties; irradiation, biomaterials*

■ INTRODUCTION

Joints are part of the body that are susceptible to damage caused by inflammation (osteoarthritis) and mechanical impact in case of accidents. One way that can be made to restore the normal function of a joint is by joint replacement surgery (arthroplasty). The most commonly replaced joints are knee and hip joints (> 90%). Statistically, the annual incidence rates of total knee replacement are higher compared to other artificial joints [1-2]. The artificial knee joint consists of the femoral component, the tibial tray, and the tibial component. Biomaterials used as a tibial tray must have good mechanical strength due to its function as a bearing material that connects the femur and tibia bones. In addition, implants used as artificial joints must also have a long lifetime [3]. Since it has to be placed within the corrosive environment of body fluids, it must be composed of non-biodegradable bioinert materials [4].

Ultrahigh molecular weight polyethylene (UHMWPE) is a polymer having good mechanical properties (e.g., resistant to wear, tear, abrasion, impact, chemicals) and good biocompatibility. UHMWPE has long been used as a bearing material in artificial knee joints because it has good physical properties [5]. However, in its use as a tibial tray, continuous pressure and friction can lead to wear of the material, shortening the lifetime of the artificial knee joints [6]. UHMWPE particles released due to wear may also cause inflammation in surrounding tissues leading to osteolysis [7]; therefore, further efforts are needed to enhance the physical properties of UHMWPE as a tibial tray. Ionizing radiation (e.g., gamma rays) is commonly used to initiate cross-linking between the polymer chains, and this approach successfully enhances the physical properties of many polymers [8]. However, oxidation related to

radical promoted reactions limits the use of this approach [9]. Oxidation especially occurs in large dose irradiations; thus, an antioxidant agent is needed to inhibit oxidation without limiting the cross-linking processes [10].

A polymer can also be modified to make a composite with improved physical properties by adding fillers into the matrix [11]. Some UHMWPE-based composites with improved properties have been reported in the literature, for instance UHMWPE-graphene oxide [12], UHMWPE-carbon fiber [13], UHMWPE-carbon nanotubes (CNT) [14], UHMWPE-HA [15-17], UHMWPE-Al_2O_3 [18], and even hybrid bio-composites of UHMWPE-HA-Al_2O_3-CNT [19]. Hydroxyapatite (HA) belongs to a class of bioactive ceramics that has high bio-affinity and biocompatibility. These properties arise from its chemical composition similarity with bone [20]. Therefore, hydroxyapatite is regularly used to improve the biocompatibility of an implant [21].

Moreover, the addition of hydroxyapatite into a polymer matrix can also increase its hardness and crystallinity [22]. Considering the importance of UHMWPE modification used for bearing material, UHMWPE/HA composites were prepared with and without the addition of polyvinyl alcohol (PVA) by mechanical alloying and hot press method and their thermal and mechanical properties were modified using gamma rays. PVA was used because of its biocompatibility, high lubricity, and cushioning properties [23].

■ EXPERIMENTAL SECTION

Materials

UHMWPE powder (molecular weight 3 to 6 × 10^6 g mol^{-1}) and PVA powder (molecular weight 8.9 to 9.8 × 10^4 g mol^{-1}) were purchased from Sigma Aldrich. Nanometer-sized HA (10 to 20 nm) was obtained from the Centre of Application Isotopes and Radiation (PAIR BATAN, Jakarta) that had been synthesized from *Lates calcarifer* fish.

Instrumentation

Instruments used in the mechanical alloying of UHMWPE/HA composites were a PW 700i high energy mill supported with a stainless steel vial and balls, and a Hydraulics Pj16h hot press apparatus. The products were characterized by using a Shimadzu XD 610X-ray diffractometer (XRD), a JEOL JED-2300 scanning electron microscope-energy dispersive X-ray spectrometer (SEM-EDX), and a Shimadzu IRPrestige-21 Fourier transform infrared spectrometer (FTIR). The composites were irradiated by using the gamma irradiator at the Centre of Application Isotopes and Radiation; prior to analyzing their hardness, tensile strength, and thermal properties by using a Zwick ISO/R 868 Shore A hardness tester, a Toyoseiki tensile tester, and a Perkin Elmer differential scanning calorimeter (DSC).

Procedure

Composites preparation

UHMWPE/HA composites were prepared by mixing UHMWPE and HA powder with HA loading ratios of 5, 10, and 15% w/w. PVA 5% w/w was also added into some of the powder mixtures while maintaining weight percentage of HA. Each of these powder mixtures had a total weight of 12 g. The prepared powder mixture was placed into a stainless steel vial, then stainless steel balls were added into the vial. The weight ratio between the powder and balls was fixed at 1:8. The mechanical alloying was performed for 90 min by using the PW 700i high energy mill at 1000 rpm. Each of these produced composites was molded to make films with a dimension of 15 cm × 15 cm × 0.05 cm using the hot press apparatus operated at 190 °C and 140 kg cm^{-2} for 5 min, then the hot films were cooled in a cold press apparatus for 5 min.

Composites characterization and irradiation

Composite films containing the lowest and highest HA content (UHMWPE + 5% HA, UHMWPE + 15% HA, UHMWPE + 5% HA + 5% PVA, and UHMWPE + 15% HA + 5% PVA) as well as the controls (pure UHMWPE, HA, and PVA) were characterized by using XRD at 2θ angle starting from 5° to 55°. Composite films containing the highest HA content (UHMWPE + 15% HA and UHMWPE + 15% HA + 5% PVA) were then analyzed for their surface morphology by using SEM-

EDX. After characterization, all composite films were irradiated to modify their properties. Irradiated films were prepared by exposing the films over gamma rays produced from Co^{60} isotope. Composite films were irradiated at doses of 0, 25, 50, and 75 kGy at 8 kGy h^{-1} dose rate. Irradiation was conducted in a chamber under atmospheric conditions.

Thermal and mechanical properties tests

Thermal properties of composites with the lowest HA content (UHMWPE + 5% HA: 0, 25, and 75 kGy) were investigated by using DSC under nitrogen gas atmosphere (20 cc min^{-1}). The operating temperature ranged from 25 °C to 200 °C with a heating rate of 20 °C min^{-1}. The peak of the endotherm plots indicated the melting points, while crystallinity was calculated by comparing the enthalpy of fusion of the composites with the enthalpy of fusion of 100% crystalline polyethylene (292.5 J g^{-1}) [5]. The hardness of all the composites was measured by using the Zwick ISO/R 868 Shore A tester; the results were then converted into Shore D units. Tensile tests were also applied to check the maximum stress and break elongation before and after irradiation. All of the mechanical tests were repeated three times for each composite. The effect of gamma radiation on polymer chains structure was observed by estimating the oxidation index (OI) and vinylene index (VI) of the composites with the lowest HA contents (UHMWPE +

5% HA: 0, 25, 50, and 75 kGy) by using FTIR. OI and VI values were calculated as follows [6,9].

$$OI = \left| \frac{I_{1720}}{I_{2022}} \right| \; ; \; VI = \left| \frac{I_{965}}{I_{2022}} \right|$$

I_{1720} is the absorption intensity around 1720 cm^{-1} for the carbonyl group, I_{965} is the absorption intensity around 965 cm^{-1} for vinylene group (mainly *trans*-vinylene), and I_{2022} is the absorption intensity around 2022 cm^{-1} for polyethylene vibration (amorphous and crystalline).

■ RESULTS AND DISCUSSION

Characterization of Composites

Composites are materials formed by combining two or more substances that are physically bound together, producing materials with different properties from their individual components. Physically bound means that each component remains separate and distinct inside a composite [16]. Each compound has a distinctive X-ray diffraction pattern; therefore, it can be utilized for qualitative analysis of a composite by comparing the diffraction pattern of the composite with its constituent compounds. If the diffraction pattern of the starting materials is lost or changed and there is a different diffraction pattern, this is an indication that there has been a chemical reaction producing a new material rather than a composite. Fig. 1 shows the diffractograms
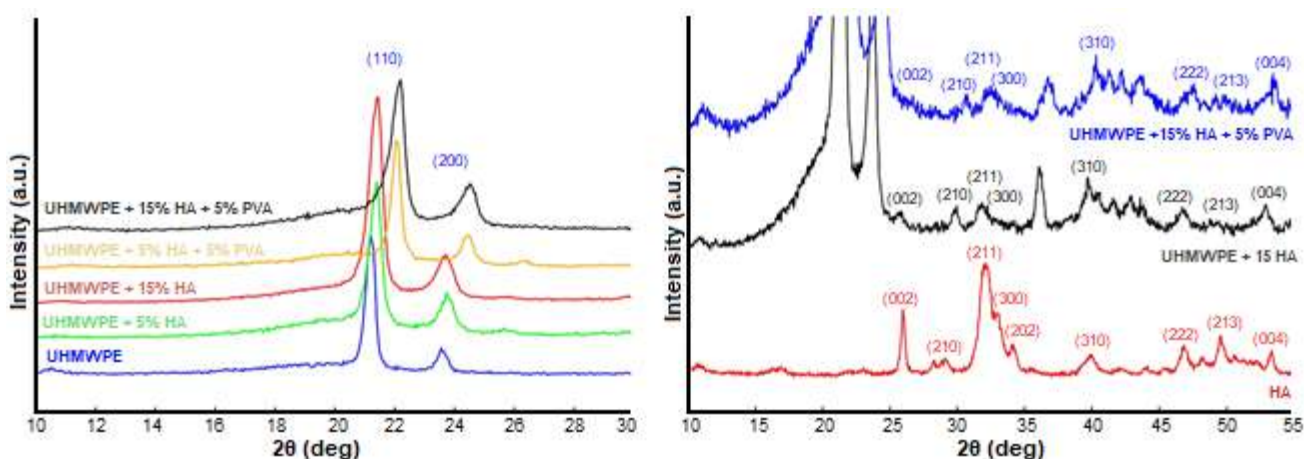
Fig 1. X-ray diffraction pattern of composites. UHMWPE identification in composites (left panel) and identification of HA in composites (right panel)

600

Indones. J. Chem., 2020, 20 (3), 597 - 607

of UHMWPE/HA composite with various HA loading ratios as well as its constituent compounds. Using these diffractograms, UHMWPE lattice parameters were calculated with the Joint Committee database on Powder Diffraction Standards (JCPDS) as a reference. The lattice parameters of UHMWPE are reported in Table 1.

The presence of UHMWPE in composites was identified by analyzing the diffraction patterns (Fig. 1) and comparing the lattice parameters in the UHMWPE sample with composite samples (Table 1). The emergence of peaks at almost the same 2θ angles and similar diffraction pattern on composites and UHMWPE can be clearly seen in the left panel of Fig. 1. Table 1 shows that UHMWPE lattice parameters on composites also have values close to UHMWPE lattice parameters. This indicates that there is a UHMWPE compound in the produced composites. However, the peaks of composites diffraction were slightly shifted to larger 2θ angle. This is caused by the milling process during composites preparation. The high energy ball milling process decreased the size of materials, as evidenced by the volume of UHMWPE unit cells (see Table 1).

HA in composites was also identified the same way, using samples with the highest HA content (Fig. 1, right panel). Those diffraction patterns show that the composites have diffraction peaks at 2θ angles similar to the diffraction peaks of HA. Since the HA content in composites is quite small (15% w/w), the intensity of the diffraction peaks is low. In addition, the HA lattice parameters and volume of HA unit cells in the composites

also have values close to the initial HA (reported in Table 2) indicating that there is HA compound in the composites. The case of the composites with PVA addition will be discussed further in the next section. Based on the above identification of the matrix (UHMWPE) and the filler (HA), it was concluded that UHMWPE-HA composites had been successfully formed from physically bound individual components.

The formation of composites can also be verified by looking at the SEM micrographs presented in Fig. 2. Fig. 2 shows that the individual components remain separate within the finished structures, and they can be distinguished by their physical appearances. Moreover, it can be seen from Fig. 2 that micro and sub-micrometer sized filler was randomly distributed over the polymer matrix. Although high energy ball milling technique was applied, dispersed nano-HA composites were difficult to obtain [18]. Since nano-HA has very high surface area and different functional groups (different polarity properties)

Table 1. Lattice parameters of orthorhombic unit cells of UHMWPE

Sample	a (Å)	b (Å)	c (Å)	V (Å³)
UHMWPE	7.4179	4.9336	2.5425	93.0477
UHMWPE + 5% HA	7.3866	4.9115	2.5416	92.2091
UHMWPE + 15% HA	7.4020	4.8976	2.5372	91.9795

Table 2. Lattice parameters of hexagonal unit cell of HA

Sample	a (Å)	c (Å)	V (Å³)
HA	9.3539	6.8797	521.2994
UHMWPE + 15% HA	9.3507	6.8805	520.9964
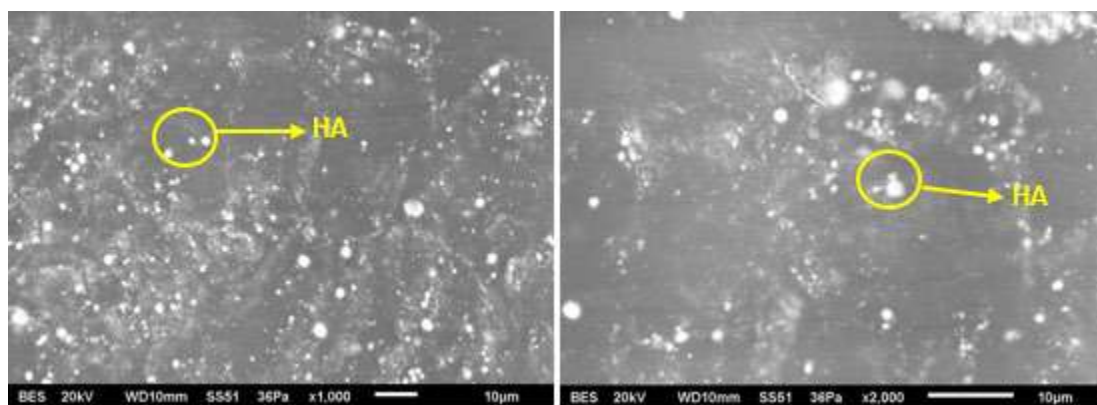
Fig 2. SEM micrographs of UHMWPE + 15% HA composite with 1000× (left panel) and 2000× (right panel) magnification

are present in HA and UHMWPE, agglomeration of HA particles is favored over dispersion. The agglomerated HA particles can be seen in Fig. 2 and from relatively high standard deviation value (SD) of the presence of elements (Ca, P, and O) at some different points over the surface obtained from EDX analysis (SD ranging from 0.4 to 6.5).

The Effect of Gamma Irradiation on Thermal Properties

Radiation dose affects melting point and fusion enthalpy of UHMWPE/HA composites. Melting point and fusion enthalpy of composites increased with increasing radiation dose (see Fig. 3). This increment corresponds to the increased crystallinity of composite presented in Fig. 4. Melting point depends on the size and perfection of a crystal, the larger and more perfect a crystal, the higher the melting point [5]. Therefore, the

energy required to melt the crystalline structure is higher than that of the amorphous particles [21]. In addition, the increment of melting point and fusion enthalpy could be regarded as an indication of cross-linking. A high cross-link level will decrease the degree of freedom between polymer chains; thus, the energy required to convert a solid phase into a liquid phase will even be higher. The higher the degree of crystallinity and cross-link level, the higher the energy required to convert the composite from solid to liquid [5].

The Effect of Gamma Irradiation on Hardness

The results of the composite hardness test (Fig. 5) show that their hardness was directly proportional to the radiation dose. Pure UHMWPE (0% HA) hardness values are in the range of 42 to 43 Shore D, while composites hardness values are in the range of 46 to 50 Shore D. The
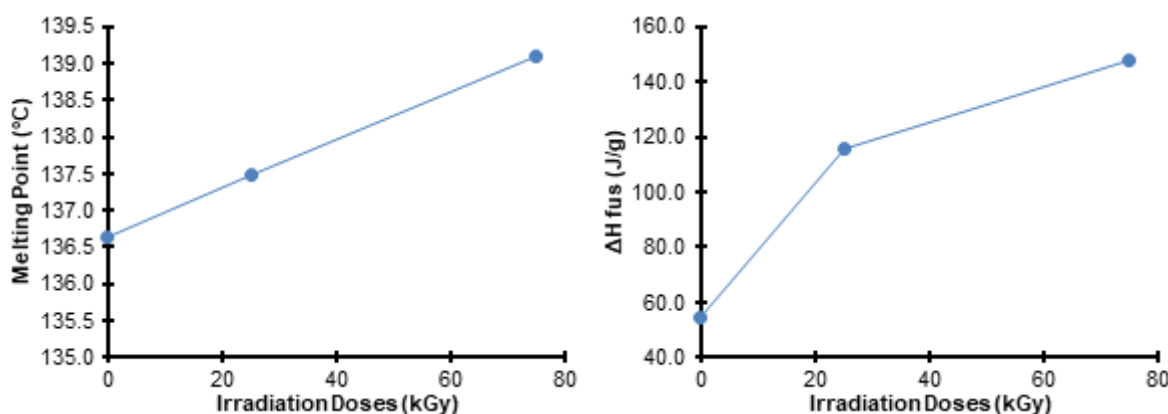
Fig 3. Melting point (left panel) and enthalpy of fusion of UHMWPE + 5% HA composites (right panel) plotted as a function of irradiation dose
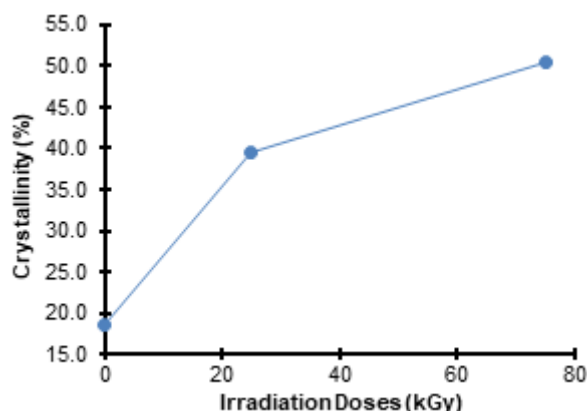
Fig 4. Crystallinity of UHMWPE + 5% HA composites plotted as a function of irradiation dose
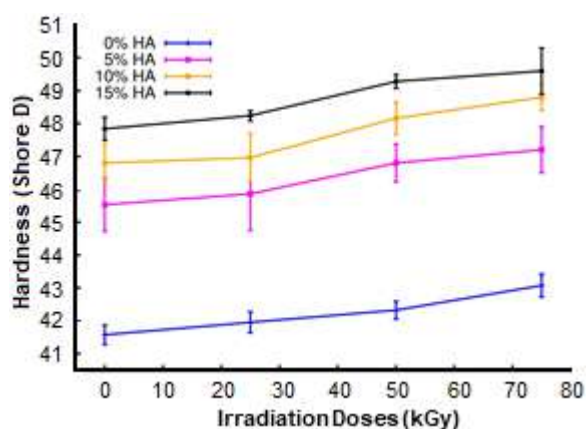
Fig 5. Hardness of composites plotted as a function of irradiation dose

hardness of composites is higher than pure UHMWPE. The hardness of composites is also higher than irradiated UHMWPE (0–150 kGy) reported by Sukaryo et al. [8] where the hardness ranged from 38 to 46 Shore D. The hardness values also increased with increasing HA content in the composites (Fig. 5). HA is a bioactive ceramic material whose structure and strength are similar to bone [16]. Therefore, the higher the HA content in the composite, the higher the value of composite hardness.

Composite hardness is also affected by the degree of crystallinity of the composite. As presented in Fig. 4, the crystallinity of composites increases with increasing radiation dose. The high degree of crystallinity will make a material resistant to the solvent, making the material harder and stiffer, thus improving its wear resistance [3,14]. Gamma irradiation initiates chain cutting and cross-linking. Cross-linking mainly occurs in amorphous areas, improving crystallinity in those areas. On the other hand, chain cutting mostly occurs in the folds of the polymer chain producing disconnected chains in the fold area, which may play a role in the additional

crystallization (thickening and refinement of lamella crystals) [6]. The level of cross-linking on the composites can be qualitatively determined by the vinylene groups absorbance in the FTIR spectrum and expressed by the vinylene index (VI). Cutting chains through homolytic cleavage can be terminated via radical recombination, forming oxide or non-oxide groups. The level of oxide group formation is expressed by the oxidation index (OI).

The VI/OI ratio was also calculated to gain more information related to the chemical processes that occurred during the irradiation. The effect of gamma radiation on VI, IO, and VI/OI ratio is shown in Fig. 6. Based on the VI, IO, and VI/OI ratio shown in Fig. 6, cross-linking is more dominant than oxidation at high doses, whereas at low doses oxidation rate is relatively dominant (see upper right panel of Fig. 6, at 25 kGy). This phenomenon can be explained by realizing that oxidation mainly occurs on the surface of composites, where radical oxygen is available from the bond breaking of atmospheric gas by gamma rays at low and high doses [9-10]. However, at low doses (25 kGy), the
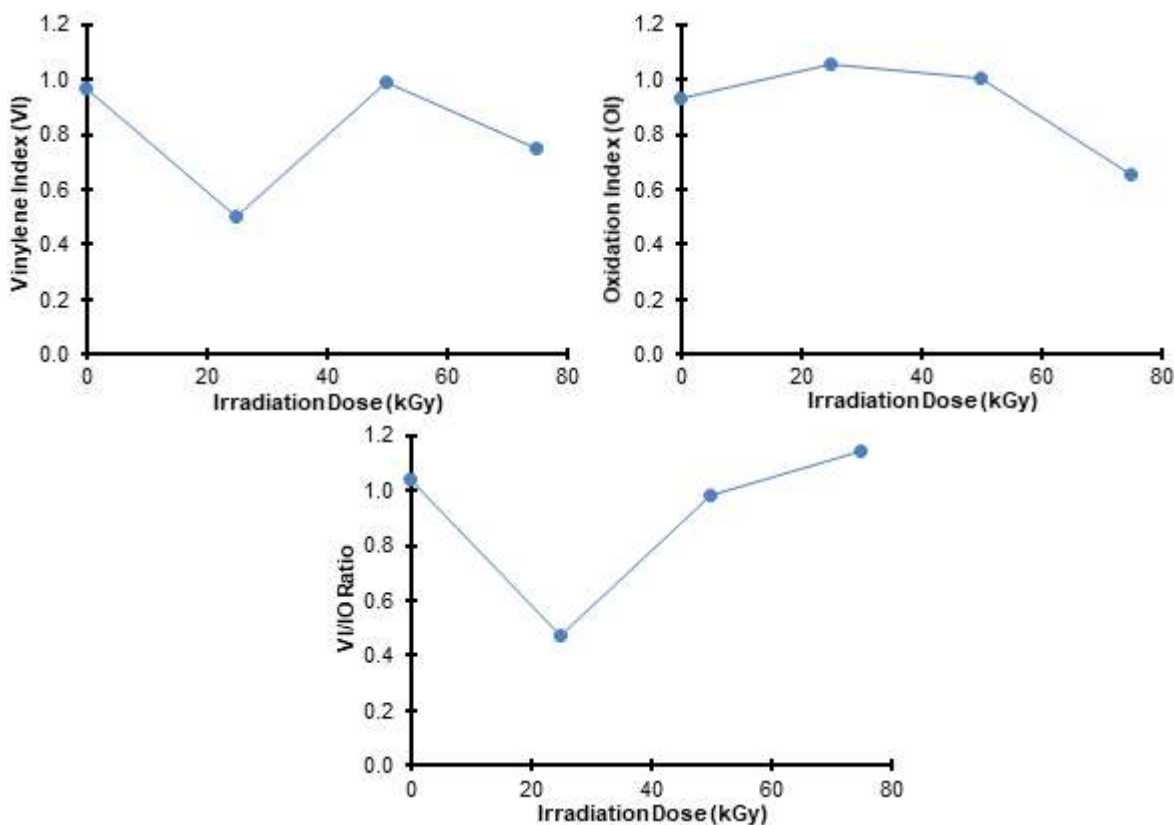
Fig 6. VI (upper left panel), OI (upper right panel), and VI/OI ratio (lower panel) of UHMWPE + 5% HA composite

inner side of composites receives low-intensity gamma rays, so cross-linking is not very effective compared to oxidation. This explains why UHMWPE-HA composites at 25 kGy have the lowest VI/OI ratio. The opposite result (high cross-linking) would happen if the radiation intensity received by the composites were high. Therefore, as can be seen in Fig. 6 (lower panel), composites at 50 and 75 kGy doses have higher VI/OI ratio. The composite without gamma irradiation (0 kGy) is acting as the control.

The Effect of Gamma Irradiation on Tensile Strength

The tensile test results are reported in Fig. 7. According to Fig. 7, the maximum stress and break elongation of composites ranged from 24 to 37 MPa and 106% to 264%, respectively. The maximum stress of composites tends to decrease with increasing radiation dose (Fig. 7, left panel). Increasing radiation dose intensifies the chain cutting level (oxidative and non-oxidative) of composites. Since chain cutting plays a role in the additional crystallization (Fig. 4), it lowers the maximum stress of composites by making composites have more crystalline properties (e.g., stiff yet brittle) [6]. In general, the maximum stress values decreased as the HA percentage increased. This was caused by a decreasing amount of UHMWPE that provides bending and ductile properties. However, most of the composites had higher maximum stress than pure UHMWPE (0% HA), although the composites contained HA (Fig. 7, left panel). This

shows that composite preparation and modification enhanced the maximum stress compared to pure UHMWPE.

On the other hand, break elongation of composites also decreased with increasing radiation dose (Fig. 7, right panel). This trend is related to the increasing number of cross-links relative to the oxidation rate (VI/OI ratio), as shown in Fig. 6. The high degree of crosslinks inhibits polymer chains movement when pulled, resulting in a low break elongation [21]. The VI/OI ratio at 25 kGy was lower than those at other doses (Fig. 6), this is why the break elongation of 5% HA at 25 kGy was the highest (264%). Break elongation of composites with 5% and 10% HA was higher than pure UHMWPE (0% HA), yet break elongation of pure UHMWPE was still higher than the composite with 15% HA. Large amounts of HA increases the influence of HA properties (e.g., rigid, fragile) in composites [21].

Physical Strength of Composite with Addition of Polyvinyl Alcohol (PVA)

In its use as an implant, a tibial tray should not be too hard to be comfortably used for daily activity. Moreover, it should alleviate the impact and friction generated by human movements. To increase the elasticity and lubricity of material, several researchers modified the surface of the artificial joint materials with PVA [23-24]. In this study, UHMWPE-HA composites with PVA addition (5% w/w) were successfully prepared using mechanical alloying and hot press method. X-ray
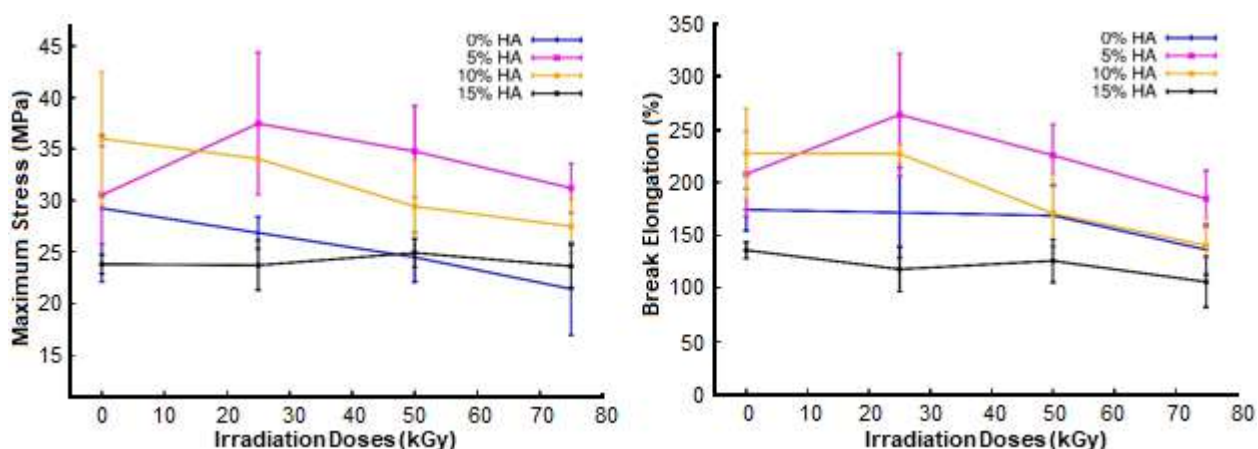
Fig 7. Maximum stress (left panel) and break elongation (right panel) of composites plotted as a function of irradiation dose

Table 3. Lattice parameters of orthorhombic UHMWPE in composites with PVA addition

Sample	a (Å)	b (Å)	c (Å)	V (Å³)
UHMWPE	7.4179	4.9336	2.5425	93.0477
UHMWPE + 5% HA + 5% PVA	7.1782	4.8891	2.5257	88.6382
UHMWPE + 15% HA + 5% PVA	7.1638	4.9455	2.5438	90.1223

Table 4. Lattice parameters of hexagonal HA in composite with PVA addition

Sample	a (Å)	c (Å)	V (Å³)
HA	9.3539	6.8797	521.2994
UHMWPE + 15% HA + 5% PVA	9.3489	6.8759	520.4495

diffractograms and lattice parameters reported in Fig. 8, Table 3 and Table 4, respectively, show that all three components (UHMWPE, HA, and PVA) are physically bound.

Non-PVA composites hardness is in the range of 46 to 50 Shore D (Fig. 5), while composites with PVA had hardness values lying in the range of 42 to 48 Shore D (Fig. 9, upper panel). The hardness of composites (without and with PVA addition) was higher than pure UHMWPE. However, in composites with additional PVA, the hardness value was lower than that of composites without additional PVA. This indicates that the addition of PVA decreased the hardness level of composites, yet the hardness was still
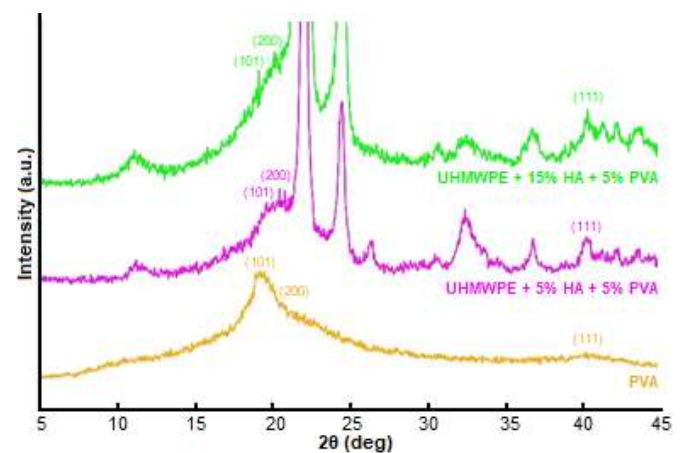
Fig 8. X-ray diffract pattern of PVA and composites with 5% (w/w) PVA addition
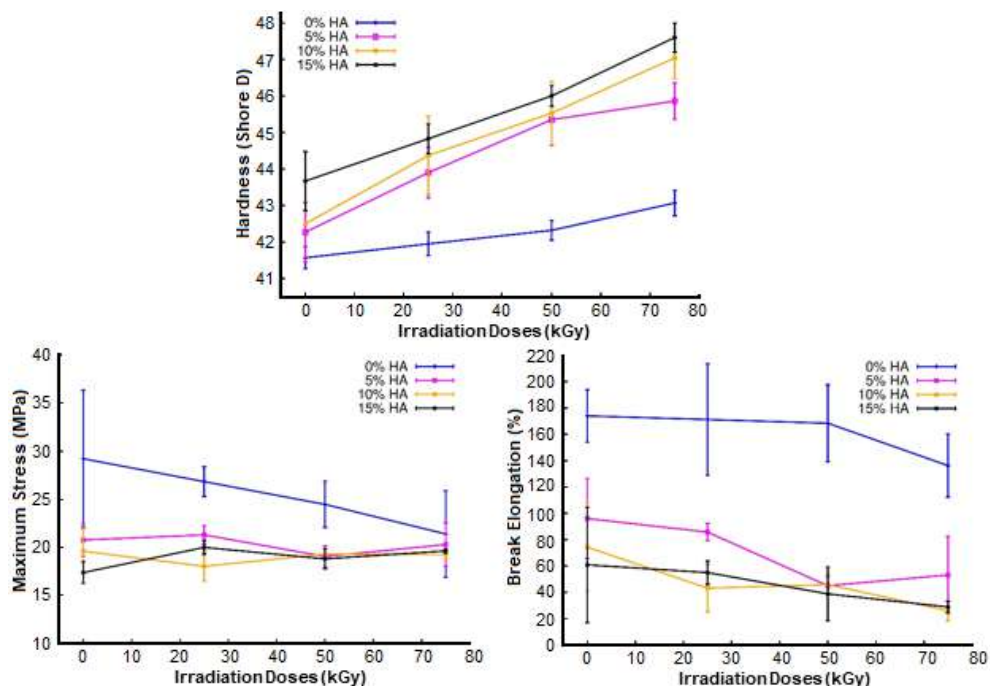
Fig 9. Hardness (upper panel), maximum stress (lower left panel) and break elongation (lower right panel) of composites with 5% (w/w) PVA addition plotted as a function of irradiation dose
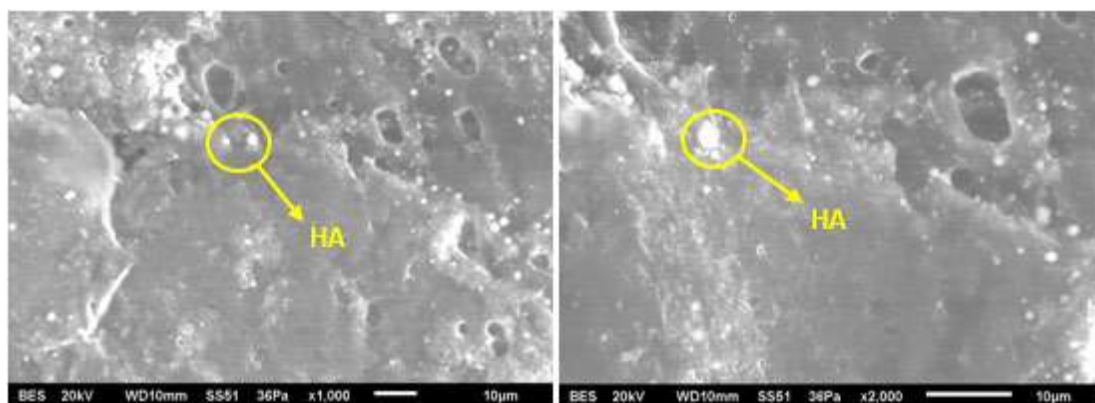
Fig 10. SEM micrographs of UHMWPE + 15% HA + 5% PVA composite with 1000× (left panel) and 2000× (right panel) magnification

higher than that of pure UHMWPE. The tensile test results of composites with PVA addition are presented in Fig. 9. Composites with PVA addition had lower maximum stress and lower break elongation compared to the pure UHMWPE. The maximum stress of composites tends to fluctuate and does not form a typical pattern (Fig. 9, left panel) while, in general, the break elongation of composites decreased with increasing radiation dose (Fig. 9, right panel).

The lower value of maximum stress and break elongation of composites with PVA addition compared to the pure UHMWPE (0% HA) can be explained by looking at the SEM micrographs in Fig. 10. Addition of PVA into composites induced micropores creation on the surfaces of the composites. This phenomenon is an indication of nonhomogeneity resulting from the different polarity between UHMWPE and PVA, so both materials tend to minimize their interface area. Moreover, the physical interaction between UHMWPE and PVA is relatively weak. If homogenous composites are desired, one must go beyond mechanical alloying by employing chemical grafting on the surface of composites, in order to bind PVA with UHMWPE through a strong chemical bond [23].

■ CONCLUSION

UHMWPE/HA composites were successfully synthesized using the high energy ball milling technique and hot press method. HA particles were physically bound with the UHMWPE matrix and could enhance the hardness of the polymer by 8–15% and the maximum stress up to 38%. Gamma irradiation promoted cross-linking and breaking of polymer chains, represented by VI and OI, respectively, which enhanced the crystallinity by 113–172%, melting point by 0.6–0.7%, and decreased break elongation of composites by 23–48%. Addition of PVA induced micropores creation on the surfaces of composites and thus reduced rigidity by 16–47% and hardness by 3–9%.

■ ACKNOWLEDGMENTS

■ REFERENCES

[1] Culliford, D., Maskell, J., Judge, A., Cooper, C., Prieto-Alhambra, D., and Arden, N.K., 2015, Future projections of total hip and knee arthroplasty in the UK: Results from the UK Clinical Practice Research Datalink, *Osteoarthritis Cartilage*, 23 (4), 594–600.

[2] Kremers, H.M., Larson, D.R., Crowson, C.S., Kremers, W.K., Washington, R.E., Steiner, C.A., Jiranek, W.A., and Barry, D.J., 2015, Prevalence of total hip and knee replacement in the United States, *J. Bone Joint Surg. Am.*, 97 (17), 1386–1397.

[3] Baena, J.C., Wu, J., and Peng, Z., 2015, Wear performance of UHMWPE and reinforced UHMWPE composites in arthroplasty applications: A review, *Lubricants*, 3 (2), 413–436.

[4] Maksimkin, A.V., Kaloshkin, S.D., Tcherdyntsev, V.V., Senatov, F.S., and Danilov, V.D., 2012, Structure and properties of ultra-high molecular weight polyethylene filled with disperse hydroxyapatite, *Inorg. Mater. Appl. Res.*, 3 (4), 288–295.

[5] Lednický, F., Šlouf, M., Kratochvil, J., Baldrian, J., and Novotná, D., 2007, Crystalline character and microhardness of gamma-irradiated and thermally treated UHMWPE, *J. Macromol. Sci. Part B Phys.*, 46 (3), 521–531.

[6] Slouf, M., Mikesova, J., Fencl, J., Stara, H., Baldrian, J., and Horak, Z., 2009, Impact of dose-rate on rheology, structure and wear of irradiated UHMWPE, *J. Macromol. Sci. Part B Phys.*, 48 (3), 587–603.

[7] Kandahari, A.M., Yang, X., Laroche, K.A., Dighe, A.S., Pan, D., and Cui, Q., 2016, A review of UHMWPE wear-induced osteolysis: The role for early detection of the immune response, *Bone Res.*, 4, 16014.

[8] Sukaryo, S.G., Arifin, N.L., Sudaryo, S., and Sudirman, S., 2012, Pengaruh radiasi gamma terhadap sifat mekanik UHMWPE untuk tibial tray, *Jurnal Kimia dan Kemasan*, 34 (2), 272–281.

[9] Slouf, M., Synkova, H., Baldrian, J., Marek, A., Kovarova, J., Schmidt, P., Doschner, H., Stephan, M., and Gohs, U., 2008, Structural changes of UHMWPE after e-beam irradiation and thermal treatment, *J. Biomed. Mater. Res. Part B*, 85 (1), 240–251.

[10] Peltzer, M., Wagner, J.R., and Jiménez, A., 2007, Thermal characterization of UHMWPE stabilized with natural antioxidants, *J. Therm. Anal. Calorim.*, 87 (2), 493–497.

[11] Selyutin, G.E., Gavrilov, Y.U., Voskresenskaya, E.N., Zakharov, V.A., Nikitin, V.E., and Poluboyarov, V.A., 2010, Composite materials based on ultra high molecular polyethylene: Properties, application prospects, *Chem. Sustainable Dev.*, 18, 301–314.

[12] Tai, Z., Chen, Y., An, Y., Yan, X., and Xue, Q., 2012, Tribological behavior of UHMWPE reinforced with graphene oxide nanosheets, *Tribol. Lett.*, 46 (1), 55–63.

[13] Dangsheng, X., 2005, Friction and wear properties of UHMWPE composites reinforced with carbon fiber, *Mater. Lett.*, 59 (2-3), 175–179.

[14] Martínez-Morlanes, M.J., Castell, P., Martínez-Nogués, V., Martinez, M.T., Alonso, P.J., and Puértolas, J.A., 2011, Effects of gamma-irradiation on UHMWPE/MWNT nanocomposites, *Compos. Sci. Technol.*, 71 (3), 282–288.

[15] Crowley, J., and Chalivendra, V.B., 2008, Mechanical characterization of ultra-high molecular weight polyethylene–hydroxyapatite nanocomposites, *Bio-Med. Mater. Eng.*, 18 (3), 149–160.

[16] Fang, L., Leng, Y., and Gao, P., 2006, Processing and mechanical properties of HA/UHMWPE nanocomposites, *Biomaterials*, 27 (20), 3701–3707.

[17] Li, F., Gao, L., Gao, H., and Cui, Y., 2017, The mechanical properties and modeling of creep behavior of UHMWPE/Nano-HA composites, *J. Mater. Eng. Perform.*, 26 (9), 4514–4521.

[18] Elmkharram, H.M.A., 2013, Mechanically processed alumina reinforced ultra-high molecular weight polyethylene (UHMWPE) matrix composites, *Thesis*, Virginia Tech, Blacksburg, Virginia, USA.

[19] Gupta, A., Tripathi, G., Basu, B., and Balani, K., 2012, Dependence of protein adsorption on wetting behavior of UHMWPE–HA–Al$_2$O$_3$–CNT hybrid biocomposites, *JOM*, 64 (4), 506–513.

[20] Gupta, A., Tripathi, G., Lahiri, D., and Balani, K., 2013, Compression molded ultra high molecular weight polyethylene–hydroxyapatite–aluminum oxide–carbon nanotube hybrid composites for hard tissue replacement, *J. Mater. Sci. Technol.*, 29 (6), 514–522.

[21] Alothman, O.Y., Almajhdi, F.N., and Fouad, H., 2013, Effect of gamma radiation and accelerated aging on the mechanical and thermal behavior of

HDPE/HA nano-composites for bone tissue regeneration, *Biomed. Eng. Online*, 12, 95.

[22] Kang, X., Zhang, W., and Yang, C., 2016, Mechanical properties study of micro-and nano-hydroxyapatite reinforced ultrahigh molecular weight polyethylene composites, *J. Appl. Polym. Sci.*, 133 (3), 42869.

[23] Chen, K., Zhang, D., Cui, X., and Wang, Q., 2015, Preparation of ultrahigh-molecular-weight poly ethylene grafted with polyvinyl alcohol hydrogel as an artificial joint, *RSC Adv.*, 5 (31), 24215–24223.

[24] Omata, S., Sawae, Y., and Murakami, T., 2015, Effect of poly(vinyl alcohol) (PVA) wear particles generated in water lubricant on immune response of macrophage, *Biosurf. Biotribol.*, 1 (1), 71–79.

Mixed Oxide Catalyst for the Oxidation of Glycerol to Lactic Acid: Influence of the Preparation Method and Calcination Temperature

Noraini Razali[1,*] and Ahmad Zuhairi Abdullah[2]

[1]Faculty of Chemical Engineering, Universiti Teknologi MARA, Cawangan Terengganu, Bukit Besi Campus, 23200, Dungun, Terengganu, Malaysia

[2]School of Chemical Engineering, Universiti Sains Malaysia, Engineering Campus, 14300 Nibong Tebal, Penang, Malaysia

Abstract: *The selective oxidation reaction of glycerol to produce lactic acid is a high-temperature reaction, and requiring a catalyst with high thermal stability. The mixed metal oxide is one of the potential catalysts to be explored. In this study, prepared CaCe supported on ZrO_2 catalyst with two preparation methods (co-precipitation and impregnation), and calcination temperatures (800 and 600 °C) were investigated. The oxidation reaction of glycerol to lactic acid was carried out at 250 °C for 2 h in a base-free condition using pure glycerol as a reactant. The catalysts were characterized using XRD, TGA, XPS, SEM and basicity test to evaluate and correlate the physical and chemical properties with their catalytic performance. It was found that the catalyst prepared by co-precipitation and calcined at 800 °C exhibited the highest catalytic performance. The high lactic acid yield of 38.8 and 95% glycerol conversion were achieved. The catalyst was successfully developed with sufficient porosity and high intensity of mixed metal structure that contributed to the desired high performance. Improvement in the basicity and formation of surface oxygen vacancies was attributed to cationic Ce^{4+}/Ce^{3+} elements leading to the promotion of lactic acid yield and high glycerol conversion.*

Keywords: *mixed metal oxide catalyst; oxidation; impregnation; co-precipitation; calcination*

■ INTRODUCTION

The production of lactic acid from glycerol has been receiving a lot of attention due to the efficient role of glycerol as a raw material in producing various useful chemicals [1]. Selective oxidation and hydrothermal reactions using solid catalyst have been found as potential techniques to promote high yield and selectivity of lactic acid. Different types of solid catalysts have been studied, such as monometallic, bimetallic, alkaline metal catalyst, alkaline earth metal catalyst, and supported catalyst [2-4].

One important application is the selective oxidation reaction which involves the roles of oxygen capacity in the reaction mechanism. Ceria catalysts feature in a variety of catalytic reactions. CeO_2 catalyst has attracted much attention due to its good oxygen storage capacity, thermal resistance and redox promotion property [5-7]. The chemical basicity property of the catalysts was contributed by CaO, as an important modification in the development of mixed oxide catalyst. It was evident that the strong basicity of the catalyst could enhance catalytic dehydration and benzylic acid rearrangement of the dihydroxyacetone intermediates to lactic acid. In addition, Ca leaching could be minimized by coupling with La_2O_3 or CeO_2 as appropriate support [8].

ZrO_2 could be suitable solid support due to its surface catalytic sites properties such as the high concentration of hydroxyl groups and coordinative unsaturated Lewis acidic-basic $Zr4^+O^{2-}$ pairs. These features are believed to potentially enhance the catalytic ability of the transition metal active sites [9]. Thus, this potential has created the interest to explore the suitability of a $CaOCeO_2/ZrO_2$ mixed oxide catalyst in the oxidative reaction of glycerol.

According to He et al. [10], the catalyst preparation

method is a critical factor in determining the interaction between the active metal components and the support. Therefore, it is important to compare the characterization and activity of the catalysts prepared by different synthesis methods and calcination temperatures. Hence, modification of the prepared catalyst would be expected to have an important influence in improving the activity. Thus, incorporation of CaO and CeO_2 into zirconia support seemed to result in a properly mixed oxide catalyst for further study, and its activity can be further improved with necessary modifications.

■ EXPERIMENTAL SECTION

Materials

Glycerols (98% purity), calcium nitrate hexahydrate, $Ca(NO_3)_2 \cdot 6H_2O$, cerium nitrate hexahydrate, $(Ce(NO_3)_2 \cdot 6H_2O)$, zirconyl chloride octahydrate $(ZrOCl_2 \cdot 8H_2O)$, ammonium hydroxide, NH_3OH (99% solution in water), sodium hydroxide, NaOH (90%) and sodium bicarbonate, Na_2CO_3 (90%) were purchased from Fluka. Deionized water (DI) was used throughout the study for the preparation of the support and catalysts. All chemicals were of reagent grade and were used as received without further purification.

Procedure

Preparation of mixed oxide catalysts

Zirconia (ZrO_2) support was prepared based on a work reported by Yang et al. [11] by using zirconium chloride octahydrate $(ZrOCl_2 \cdot 8H_2O)$, and adjusting the pH of the solution to 10–11 by dropwise addition of ammonium hydroxide solution (25%). The sample was then calcined at 500 °C for 3 h and used as the catalyst support. The support material was first dispersed in DI water and the required amounts of $Ca(NO_3)_2$ and $Ce(NO_3)_2$ solutions were added dropwise under stirring. Then, calculated amounts of 1 M NaOH and Na_2CO_3 were also added dropwise to maintain the pH at 10–11. The temperature of the mixture was set at 80 °C for 5 h on a hotplate stirrer. The suspension was then filtered, and the solid was thoroughly washed with deionized water to eliminate all traces of base (pH test). The catalysts were dried overnight at 80 °C followed by calcination at either 600 or 800 °C for 4 h.

Mixed oxide catalysts were also prepared using an impregnation method by mixing the calcined zirconia with an aqueous solution of metal precursors $(Ca(NO_3)_2$ and $Ce(NO_3)_2)$. The number of precursors used was calculated to obtain (30 wt.%) of active metal loading with a certain ratio of Ca and Ce. The solution was mixed for 24 h to ensure that metal dissolved and dispersed thoroughly on the surface of zirconia. The impregnated catalysts were then calcined in a muffle furnace at 600 and 800 °C for 4 h. The solids obtained were dried in an oven at 120 °C for 2 h before use in the oxidation reaction.

Characterization of the catalysts

The crystalline phases in the prepared catalyst samples and the average crystallite sizes were examined by X-ray diffraction (XRD) method using a Bruker diffractometer operated at 40 kV and 30 mA. The XRD patterns of the samples were obtained using with CuKα irradiation in the 2θ range of 5–90° with a step size of 0.03 °L. Thermal gravimetric analysis (TGA) was performed to observe any significant change in the weight loss of the catalysts. About 5 mg of the catalyst sample was heated from 31 to 800 °C at a heating rate of 10 °C/min in and an airflow of 25 mL/min by using simultaneous thermal analyzer (STA, 6000 from Perkin-Elmer USA).

X-ray photoelectron spectroscopy (XPS) study was carried using an AXIS Ultra DLD system equipped with AlKα X-ray source (1486.6 eV) by Kratos. Both of wide and narrow XPS scan spectra were obtained by scanning a 300 mm × 700 mm area at 7.5×10^{-9} torr ultravacuum environment inside the sample chamber. The analysis was performed using a hybrid lens mode with the slot aperture. The energy of the hemispherical analyzer was set at 160 eV for the survey scan and 20 eV for the narrow scan. The spectra were analyzed by a vision software with vision manager and processing abilities. For background subtraction and curve fitting, a linear method was used. The catalysts surface morphologies were studied utilizing a field emission scanning electron microscope (FESEM Carl Zeiss SMT, Oberkochen, Germany).

Hammett indicator method

Hammett indicator method was used to measure the basic strength of the catalyst samples (H_) [12]. In this procedure, 25 mg of the sample was first vigorously dispersed in 5.0 mL of Hammett indicator solutions and allowed to reach equilibrium for about 2 h until no significant change in the color intensity was observed. Results were reported as being higher than the weakest Hammett indicator which experienced color change, but lower than the strongest indicator that did not exhibit any color change. The Hammett indicators used in this study were 4-chloroaniline (H_ = 26.5), 4-nitroaniline (H_ = 18.4), 2,4-dinitroaniline (H_ = 15.0), phenolphthalein (H_ = 9.3), bromothymol blue (H_ = 7.2) and neutral red (H_ = 6.8).

Basicity test

The basicity of the catalysts was determined using Hammett indicator-benzoic acid titration method [13]. First, the 10 mg catalyst was shaken in a conical flask with 2.0 mL of Hammett indicator solution that had been diluted with methanol. 0.1 mol/L benzoic acid was then added dropwise into the conical flask, and the basic catalyst was neutralized using the benzoic acid. When the basic color disappeared, the volume of benzoic acid used was recorded. The basicity (mmol/g) of solid bases was evaluated by Hammett indicator-benzene carboxylic acid (0.02 mol/L anhydrous ethanol solution) titration until its color changed back to the original color.

Catalyst activity

Batch hydrothermal glycerol reaction was carried out in a 50 mL stainless steel autoclave at a stirring speed of 280 rpm. The standard reaction was carried out under the following reaction conditions: 99% aqueous glycerol, 20 wt.% of catalyst for 2 h of reaction. After being purged with O_2 for 15 min, the reactor was heated to the desired reaction temperature of 250 °C, and the O_2 pressure was maintained at about 7 bar. The liquid-phase products were analyzed through a gas chromatograph with a SHODEX capillary column (50 m × 0.32 mm × 0.25 μm) and a flame ionization detector. The catalytic performance demonstrated by the catalysts was evaluated based on glycerol conversion as well as the yield and selectivity of lactic acid.

■ RESULTS AND DISCUSSION

Characterization of the Prepared Catalyst

The XRD analysis confirmed the formation of crystalline CaO and CeO_2 on ZrO_2 in the synthesized samples. When prepared by co-precipitation, a solid with two independent phases of the two oxides was formed as indicated by XRD. The latter phase decorates the surface of ZnO as indicated by a clear role of calcium and cerium in the surface chemistry at (CeO_2ZrO_2, cubic, $2\theta = 28.3$ and 34.4°) and ($CaOZrO_2$, cubic: $2\theta = 60.3$ and 47.5°) of the mixed oxide catalyst. The CaCeZCP catalyst exhibited stronger diffraction peaks than the CaCeZIMP catalysts. Meanwhile, the CaCeZ800 catalyst exhibited higher crystallinity with a more intense peak due to the presence of CaO and CeO_2 phase compared to CaCeZ600 catalyst.

The sizes of the crystalline metal oxides of CaO and CeO_2 were calculated from the XRD diffraction peaks using the Scherrer equation. $CaCeZrO_2CP$ and $CaCeZrO_2800$ catalysts exhibited a larger size of crystalline oxides of CaO and CeO_2, with a crystal size of about to 200 nm, while $CaCeZrO_2IMP$ catalyst exhibited the smaller size of 140 nm. It is shown that the method of preparation and different calcination temperatures affected both the structure and crystalline size of the CeO_2 and CaO in the catalysts (Fig. 1). Increasing calcination temperature to 800 °C would increase the intensity of XRD reflexes due to the increase in the crystallinity, and it is in agreement with the findings by Al-Fatesh et al. [14].

In addition to the XRD analysis, thermogravimetric analysis (TGA) was also performed on the $CaCeZrO_2$ systems with the results, as shown in Fig. 2. TGA experiment provided information about water and nitrate ion losses as the catalyst was heated from 0–800 °C. The initial water loss was observed in the temperature range of 0–200 °C, followed by NO_3^{2-} ions decomposition between 600 °C and < 800 °C. Almost 10 wt.% mass decrease was observed in this temperature range due to the loss of nitrate ions from the ZrO_2 surface.

Nitrate ions contributed greatly to the catalyst's basicity and consequently the catalytic activity. It was,

Indones. J. Chem., 2020, 20 (3), 608 - 615

611
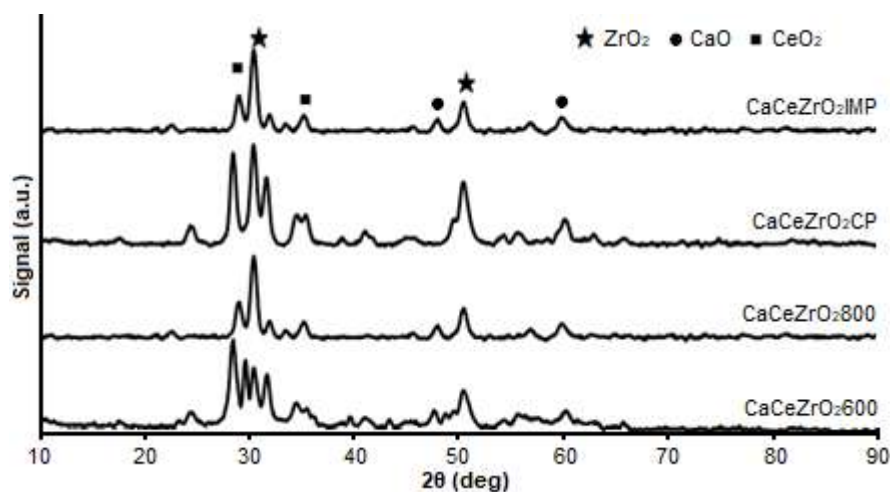
Fig 1. XRD patterns of the prepared catalysts
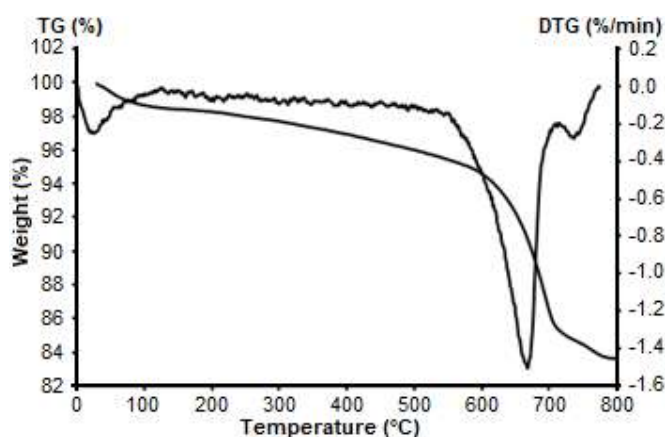
Fig 2. TGA profiles of CaCeZrO$_2$800 catalyst

therefore, important to understand the temperature range of nitrate loss to demonstrate the stability of the catalysts in terms of thermal stability of the synthesized materials. From the results, the catalyst was found to be thermally stable at a temperature of around 800 °C.

A significant change in the morphology was influenced by the preparation method and calcination temperature, as shown in Fig. 3. All of the catalytic materials had different morphologies. CaCeZrO$_2$IMP catalyst as shown in Fig. 3(a) appears to have a uniform and quasi-spherical particles with inner-aggregate pores particles. However, as for the CaCeZrO$_2$CP catalyst, the
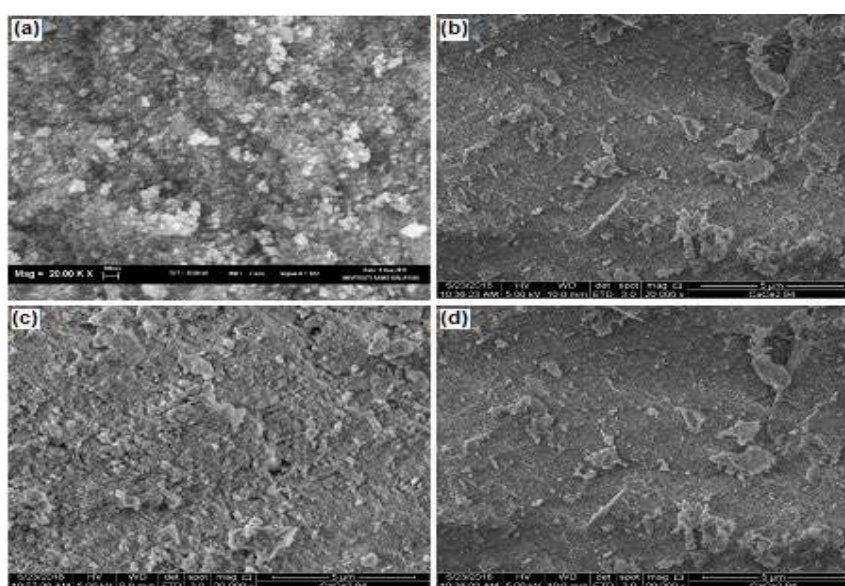
Fig 3. SEM of images at 20.0 k magnification of (a) CaCeZrO$_2$IMP (b) CaCeZrO$_2$CP (c) CaCeZrO$_2$600 (d) CaCeZrO$_2$800 catalysts

aggregates of metal oxide forming small porous structures are visible (Fig. 3(b)).

As the calcination temperature was increased, the morphology of CaCeZrO$_2$600 (Fig. 3(c)) and CaCeZrO$_2$800 (Fig. 3 (d)) also showed significant differences. The catalyst calcined at 800 °C exhibited more uniform and more porous surface suggesting high dispersion of Ca and Ce on the ZrO$_2$ support. In addition, calcination process could also contribute to the formation of a hollow, porous, and fluffy product as the reactions that occurred would release large amounts of gas and heat. Ozawa et al. [15] suggested that uniform dispersion of CeO$_2$ over the surface after calcination could result in better dispersion of the active phase. Uniform morphology and crystalline metal of CaCeZrO$_2$ mixed oxide catalyst indicated to the successful preparation method of coprecipitation at high calcination temperature.

Table 1 shows the X-ray photoelectron spectroscopy (XPS) results collected in order to study the chemical composition and state of the mixed oxide catalysts. It shows the XPS spectra in the O 1s, Ce 3d, Ca 2p, and Zr 3d BE ranges. For CaCeZrO$_2$600, the O 1s spectrum shows a peak at 528.7, while for CaCeZrO$_2$800, the O 1s spectrum shows a peak at 529.6, and this peak is attributed to chemisorbed oxygen. According to the Piumetti et al. [16], the signal at 528.6–528.9 eV corresponds to O (i.e. O^{2-}), whereas the peak at 529.9–531.4 eV can be ascribed to surface oxygens (i.e. O$_2^{2-}$, O$^-$, OH$^-$, CO$_3^{2-}$). For CaCeZrO$_2$800, the signal related to the O species appears at a slightly higher BE (529.6 eV); thus, revealing a lower nucleophilicity of the lattice oxygen ions. A richer population of O species was obtained for high-surface area materials rather than because of the richer population of surface hydroxyls, carbonates and adsorbed oxygen [16].

In the Ce 3d region, three peaks within 880–920 eV are recorded at 3d$_{5/2}$ and 3d$_{3/2}$. The Ce^{3+}/Ce^{4+} content of CaCeZrO$_2$800 (15.81%) is higher than that of CaCeZrO$_2$600 (10.70%) because of the higher thermal treatment used during the preparation method [16]. The mixed oxide catalyst showed the presence of CaO and CeO in both the cationic as well as in the metallic states. The occurrence of cationic Ca species confirms the interaction between CaO and CeO nanoparticles, which was expected to lead to Ce^{3+}/Ce^{4+} and oxygen deficient sites in the ceria [17].

The Zr 3d spectra in the 181.9–182.3 eV range denote the Zr 3d$_{5/2}$ state, whereas the signal at 184.4 eV corresponds to the Zr 3d$_{3/2}$ levels. Based on the binding energy of Zr 3d$_{5/2}$, Ce-Zr mixed oxide can be well distinguished from the ZrO$_2$ phase (182.9 eV) [18]. In the case of powder catalyst, a strong Ce-Ca interaction could lead to the formation of Ce–Ca–O mixed oxide system characterized by the enhancement of Ce^{3+}/Ce^{4+} ion concentration [18].

The basic properties (basic strength, surface basicity) seemed to influence the catalytic activity. The basicity values obtained by using Hammett indicator and benzoic acid titration were in good agreement with the catalytic activity results. The highest value of basicity (0.020 mmol/g) produced the highest yield (38.8%) and selectivity (40.6%) of lactic acid. The conversion of glycerol theoretically increases when the catalyst basicity increases [19]. The basic sites for CaZrO$_2$ and CeZrO$_2$ showed H_ in the range of 6.8–7.2. Upon the incorporation of Ca and Ce, higher basicity, H_ in the range of 9.8–15.0 was observed; thus, showing a higher yield of lactic acid due to the surface basic sites value.

Table 1. Summary of XPS results for CaCeZrO$_2$ catalysts calcined at 600 and 800 °C

Catalyst	Binding energy/eV (Atomic concentration (%))			
	Ce 3d	O 1s	Ca 2p	Zr 3d
CaCeZrO$_2$600	895.7	528.7	345.7	181.7
	(10.7)	(46.91)	(10.85)	(7.36)
CaCeZrO$_2$800	897.6	529.6	345.6	181.6
	(15.81)	(50.54)	(13.26)	(8.18)

Table 2. Performance of the CaCeZrO$_2$ catalysts at different preparation conditions

Catalyst	Hammett indicator	Basicity (mmol/g)	Glycerol conversion (%)	Yield (%)	Selectivity (%)
CaZrO$_2$	6.8–7.2	0.008	96.5	29.5	30.5
CeZrO$_2$	6.8–7.2	0.005	96.3	28.3	29.3
CaCeZrO$_2$CP	9.8–15.0	0.020	95.4	38.8	40.6
CaCeZrO$_2$IMP	9.8–15.0	0.015	90.2	32.5	36.1
CaCeZrO$_2$600	9.8–15.0	0.010	95.8	29.3	30.6
CaCeZrO$_2$800	9.8–15.0	0.020	95.4	38.8	40.6

Performance of the Prepared Catalyst

The activity of CaCeZrO$_2$ catalysts prepared with two preparation methods and calcination temperatures are shown in Table 2. Catalytic tests showed that CaCeZrO$_2$ catalysts prepared by coprecipitation gave higher glycerol conversion (95.4%) and lactic acid yield (38.8%) in comparison to those prepared by impregnation method (90.2%, 32.5%, respectively). According to Chen et al. [20], the production of lactic acid requires a strong base with a hydrophilic surface to facilitate the mass transfer between glycerol and the catalyst. It could be due to the fact that the pore structure of calcined catalyst was uniform and it was sufficiently porous to provide sufficient reaction to occur as shown in Fig. 3(a-b). Glycerol was expected to be able to diffuse easily inward into the pores of the catalyst. The interaction with CaO and CeO$_2$ on the internal and external of the basic sites catalyst surface generated with the cooperation of CaO and oxygen storage capability of CeO$_2$. The porous morphology and crystalline phase of mixed oxide were confirmed from SEM and XRD analysis results, respectively.

Effects of calcination temperature on the performance of the catalyst were investigated at 600 and 800 °C. Results showed that the conversion of glycerol remained at the same value (95%), but lactic acid yield increased from 29.30 to 38.80%, for CaCeZrO$_2$600 and CaCeZrO$_2$800, respectively. Based on the XPS results, the amounts of CeO$_2$, Ca and O of the catalyst produced with a calcination at 800 °C were relatively higher (15.80, 13.26, and 50.54%, respectively) as compared at those of the catalyst calcined at 600 °C (10.70, 10.85, and 46.91%, respectively). Thus, the conversion of glycerol to lactic acid was believed to be affected by the amount of active

CaO and CeO$_2$ with the presence of ZrO$_2$ at high calcination temperature as observed in the XPS results. Sietsma et al. [21] reported that low dispersion of active metal on support was due to the redistribution during drying at low temperature. Al-Fatesh and Fakeeha [22] suggested that high temperature should be employed to ensure sufficient decomposition of the salt used, solid state reactions of the support and reactions between deposited oxides. A nanocrystalline IrO$_2$ structure was studied by Xu et al. [23], and they showed that almost no IrO$_2$ nanoparticles were generated due to amorphous coating that was not fully decomposed at low calcination temperature. Consequently, it affected the total number of active sites available to catalyze their reaction.

Therefore, the highest activity achieved by CaCeZrO$_2$ catalyst was attributed to the significant formation of the desired surface structure of mixed metal oxide formed at a calcination temperature of 800 °C and prepared with the coprecipitation method.

■ **CONCLUSION**

Incorporations of calcium and cerium onto the zirconia support led to the formation of an efficient catalyst for lactic acid production from glycerol. High yield of lactic acid (38.80%) with 95.4% glycerol conversion was achieved. Investigation on the preparation method of catalyst and calcination temperature revealed the significant influences on the yield of lactic acid and glycerol conversion. Well-developed porous structure, high crystallinity of CaO, and CeO$_2$ supported on ZrO$_2$ and basicity properties made it possible to convert glycerol to lactic acid selectively. Thus, the CaCeZrO$_2$ catalyst was deemed and

suitable for application as a solid catalyst for lactic acid production from glycerol.

■ **REFERENCES**

[1] Quispe, C.A.G., Coronado, C.J.R., and Carvalho, J.A., 2013, Glycerol: Production, consumption, prices, characterization and new trends in combustion, *Renewable Sustainable Energy Rev.*, 27, 475–493.

[2] Zhao, Z., Arentz, J., Pretzer, L.A., Limpornpipat, P., Clomburg, J.M., Gonzalez, R., Schweitzer, N.M., Wu, T., Miller, J.T., and Wong, M.S., 2014, Volcano-shape glycerol oxidation activity of palladium-decorated gold nanoparticles, *Chem. Sci.*, 5 (10), 3715–3728.

[3] Dimitratos, N., Lopez-Sanchez, J.A., Anthonykutty, J.M., Brett, G., Carley, A.F., Tiruvalam, R.C., Herzing, A.A., Kiely, C.J., Knight, D.W., and Hutchings, G.J., 2009, Oxidation of glycerol using gold–palladium alloy-supported nanocrystals, *Phys. Chem. Chem. Phys.*, 11 (25), 4952–4961.

[4] Chieregato, A., Basile, F., Concepción, P., Guidetti, S., Liosi, G., Soriano, M.D., Trevisanut, C., Cavani, F., and López, J.M.L., 2012, Glycerol oxidehydration into acrolein and acrylic acid over W–V–Nb–O bronzes with hexagonal structure, *Catal. Today*, 197 (1), 58–65.

[5] Zeng, S., Zhang, X., Fu, X., Zhang, L., Su, H., and Pan, H., 2013, Co/$Ce_xZr_{1-x}O_2$ solid-solution catalysts with cubic fluorite structure for carbon dioxide reforming of methane, *Appl. Catal., B*, 136-137, 308–316.

[6] Kambolis, A., Matralis, H., Trovarelli, A., and Papadopoulou, C., 2010, Ni/CeO_2-ZrO_2 catalysts for the dry reforming of methane, *Appl. Catal., A*, 377 (1-2), 16–26.

[7] Maciel, C.G., Silva, T.F., Hirooka, M.I., Belgacem, M.N., and Assaf, J.M., 2012, Effect of nature of ceria support in CuO/CeO_2 catalyst for PROX-CO reaction, *Fuel*, 97, 245–252.

[8] Kim, M., DiMaggio, C., Yan, S., Salley, S.O., and Ng, K.Y.S., 2011, The effect of support material on the transesterification activity of CaO–La_2O_3 and CaO–CeO_2 supported catalysts, *Green Chem.*, 13 (2), 334–339.

[9] Kim, Y.H., Hwang, S.K., Kim, J.W., and Lee, Y.S., 2014, Zirconia-supported ruthenium catalyst for efficient aerobic oxidation of alcohols to aldehydes, *Ind. Eng. Chem. Res.*, 53 (31), 12548–12552.

[10] He, Y., Ford, M.E., Zhu, M., Liu, Q., Wu, Z., and Wachs, I.E., 2016, Selective catalytic reduction of NO by NH_3 with WO_3-TiO_2 catalysts: Influence of catalyst synthesis method, *Appl. Catal., B*, 188, 123–133.

[11] Yang, G.Y., Ke, Y.H., Ren, H.F., Liu, C.L., Yang, R.Z., and Dong, W.S., 2016, The conversion of glycerol to lactic acid catalyzed by ZrO_2-supported CuO catalysts, *Chem. Eng. J.*, 283, 759–767.

[12] Kouzu, M., Kasuno, T., Tajika, M., Sugimoto, Y., Yamanaka, S., and Hidaka, J., 2008, Calcium oxide as a solid base catalyst for transesterification of soybean oil and its application to biodiesel production, *Fuel*, 87 (12), 2798–2806.

[13] Huaping, Z., Zongbin, W., Yuanxiong, C., Ping, Z., Shijie, D., Xiaohua, L., and Zongqiang, M., 2006, Preparation of biodiesel catalyzed by solid super base of calcium oxide and its refining process, *Chin. J. Catal.*, 27 (5), 391–396.

[14] Al-Fatesh, A.S., Fakeeha, A.H., Ibrahim, A.A., Khan, W.U., Atia, H., Eckelt, R., Seshan, K., and Chowdhury, B., 2016, Decomposition of methane over alumina supported Fe and Ni–Fe bimetallic catalyst: Effect of preparation procedure and calcination temperature, *J. Saudi Chem. Soc.*, 22 (2), 239–247.

[15] Ozawa, M., Takahashi-Morita, M., Kobayashi, K., and Haneda, M., 2017, Core-shell type ceria zirconia support for platinum and rhodium three way catalysts, *Catal. Today*, 281, 482–489.

[16] Piumetti, M., Bensaid, S., Fino, D., and Russo, N., 2016, Nanostructured ceria-zirconia catalysts for

CO oxidation: Study on surface properties and reactivity, *Appl. Catal., B*, 197, 35–46.

[17] Purushothaman, R.K.P., van Haveren, J., van Es, D.S., Melián-Cabrera, I., Meeldijk, J.D., and Heeres, H.J., 2014, An efficient one pot conversion of glycerol to lactic acid using bimetallic gold-platinum catalysts on nanocrystalline CeO_2 support, *Appl. Catal., B*, 147, 92–100.

[18] Reddy, B.M., and Khan, A., 2003, Structural characterization of CeO_2-TiO_2 and V_2O_5/CeO_2-TiO_2 catalysts by Raman and XPS techniques, *J. Phys. Chem. B*, 107 (22), 5162–5167.

[19] Atia, H., Armbruster, U., and Martin, A., 2011, Influence of alkaline metal on the performance of supported silicotungstic acid catalysts in glycerol dehydration towards acrolein, *Appl. Catal., A*, 393 (1-2), 331–339.

[20] Chen, L., Ren, S., and Ye, X.P., 2014, Lactic acid production from glycerol using CaO as a solid base catalyst, *Fuel Process. Technol.*, 120, 40–47.

[21] Sietsma, J.R.A., Friedrich, H., Broersma, A., Versluijs-Helder, M., van Dillen, A.J., de Jongh, P.E., and de Jong, K.P., 2008, How nitric oxide affects the decomposition of supported nickel nitrate to arrive at highly dispersed catalysts, *J. Catal.*, 260 (2), 227–235.

[22] Al-Fatesh, A.S., and Fakeeha, A.H., 2012, Effects of calcination and activation temperature on dry reforming catalysts, *J. Saudi Chem. Soc.*, 16 (1), 55–61.

[23] Xu, W., Haarberg, G.M., Sunde, S., Seland, F., Ratvik, A.P, Zimmerman, E., Shimamune, T., Gustavsson, J., and Åkre, T., 2017, Calcination temperature dependent catalytic activity and stability of IrO_2–Ta_2O_5 anodes for oxygen evolution reaction in aqueous sulfate electrolytes, *J. Electrochem. Soc.*, 164 (9), 895–900.

Synthesis and Characterization of Controlled-Release Urea Fertilizer from Superabsorbent Hydrogels

Salih Muharam[1,*], Afria Fitri[1], Lela Mukmilah Yuningsih[1], Yulia Mariana Tessa Ayudia Putri[2], and Isnaini Rahmawati[2]

[1]Department of Chemistry, Faculty of Science and Technology, Muhammadiyah University of Sukabumi, Jl. R. Syamsudin S.H. No. 50, Cikole, Sukabumi 43113, West Java, Indonesia

[2]Department of Chemistry, Faculty of Mathematics and Natural Sciences, Universitas Indonesia, Pondok Cina, Depok 16424, West Java, Indonesia

Abstract: *It is very important to develop controlled-release fertilizers to ensure efficiency and environmental protection. This study aims to make a superabsorbent hydrogel-based controlled-release urea fertilizer. Superabsorbent hydrogels were prepared from the cellulose of corn cobs cross-linking with epichlorohydrin, and then an amount of urea as a fertilizer was stored inside the hydrogels (GEL-A). The GEL-A functionalization with carboxy-methyl was also carried out in this study to improve the hydrophilicity of hydrogels (GEL-B). GEL-A and GEL-B were immersed in water at a certain pH and temperature range and the urea concentration released from the hydrogels was monitored by a spectrophotometer. The results showed that the urea released by GEL-A and GEL-B was not much different. Respectively, the urea efficiency of GEL-A and GEL-B was around 5.29% and 5.56% for 180 min. The urea released from both hydrogels was not significantly affected by changes in the temperature of the solution. Urea release was influenced by pH, and the rate of urea release of GEL-B was faster than GEL-A, so pH control was needed in the application of this slow-release fertilizer.*

Keywords: *fertilizer; cellulose; superabsorbent hydrogel; slow-release fertilizer*

■ INTRODUCTION

Continuous use of fertilizers in agriculture, especially nitrogen fertilizers can cause environmental problems [1]. Urea is the most widely used fertilizer because it has high nitrogen content (46%). On the other hand, the efficiency of urea uptake by plants generally ranges under 50% due to surface runoff, washing, and evaporation, causing urea to be accumulated in the water and cause very serious environmental problems [2] when converted into a toxic compound of nitrite.

Agricultural technology has developed many fertilizers that can be released slowly or controlled in the soil [3-4]. The performance of such fertilizers provides a large amount of fertilizer, but protect it from rapid release due to evaporation and infiltration. The fertilizer release mechanism is the transfer of nutrients from the fertilizer-polymer interface to the polymer-soil interface [5] in the form of an adsorption-desorption process. The adsorption-desorption process is an equilibrium reaction, so it is influenced by changes in pH and temperature and also by the characteristics of the coating material, the type of fertilizer release material, and agronomic conditions.

The controlled release of fertilizers is carried out by materials such as hydrogels, polyolefins or resins and other polymer layers [1]. The formation of hydrogels with a cross-linking process will produce 3D macromolecules that have low solubility in water but absorb large amounts of water [6]. Hydrogels are generally obtained from natural sources (natural hydrogels) or are synthesized through chemical reactions. Naturally-sourced hydrogels are often called biopolymer-based hydrogels, which have some

advantageous attributes, unlike synthetic hydrogels, in terms of biocompatibility, biodegradability, non-toxicity, and bio-mimic traits. The appealing functions of cellulose-based hydrogels have inspired researchers throughout the globe to develop new materials for myriad applications in various fields, such as biomedical engineering (tissue engineering, wound dressing, drug delivery system), development of smart materials (sensors, actuators), advancement in healthcare and hygienic products (diapers, napkins) along with improvement in agriculture (pesticide carriers, water reservoir, water retention) [7].

Natural polymers have biocompatibility and lower toxic effects compared to the synthetic ones [8]. In this study, cellulose-based superabsorbent hydrogels was prepared using the epichlorohydrin crosslinking method to form a hollow or porous cellulose structure as a storage medium for fertilizers and release medium for the controlled release of urea.

■ EXPERIMENTAL SECTION

Materials

The materials used were corn cobs as a source of cellulose, epichlorohydrin, ethanol, $CaCO_3$, HNO_3, $NaNO_2$, Na_2SO_3, NaOCl, NaOH, $CO(NH_2)_2$, chloroacetic acid, 2-propanol, buffer solutions, $ZnSO_4$ and Nessler's reagent.

Instrumentation

The instruments used were SEM JEOL JED-2300, Bruker FTIR Spectrometer, and HACH DR-2000 Spectrophotometer.

Procedure

Isolation of α-cellulose

In 75 g of corn cobs, 3.5% HNO_3 (v/v) and 10 mg $NaNO_2$ were mixed, and then the mixture was heated at 90 °C for 2 h and the residue was refluxed with a mixture of 2% NaOH (w/v) and 2% Na_2SO_3 (w/v) at 50 °C for 1 h. Next, it was purified with 1.75% NaOCl (v/v) at 100 °C for 1 h and was then hydrolyzed with 17.5% NaOH (w/v) at 80 °C for 30 min. In the final stage, the residue was washed with distilled water and dried in an oven at 60 °C [9-10]. The produced dry powder was characterized using FTIR.

Synthesis of superabsorbent hydrogels

Preparation of GEL-A. In 3 g of cellulose, 98 g of a mixture of 6% NaOH (w/w), 4% urea (w/w), 90% water (w/w) and $CaCO_3$ were added, and then the mixture was stirred for 5 min and cooled for 24 h in the refrigerator to form a transparent cellulose gel. Epichlorohydrin 10% (v/v) was added to the mixture and stirred at 30 °C for 2 h and filtered to separate the gel. The gel was then washed with distilled water and dried at 40 °C to produce GEL-A [8]. GEL-A was characterized by FTIR.

Preparation of GEL-B. A certain amount of GEL-A was functionalized by adding 6.75 g NaOH, 40 mL of 2-propanol, and 10 mL of distilled water, and then the mixture was added by 7.5 g of chloroacetic acid in 10 mL of 2-propanol. The mixture was stirred for 4 h, filtered and washed with ethanol and dried at 40 °C for 3–12 h [11] to form GEL-B. Furthermore, it was characterized by FTIR.

Swelling capacity measurement. The swelling capacity of GEL-A and GEL-B in the water was measured by soaking both gels in nylon containers filled with water for 24 h at room temperature. The swelling ratio was calculated using this equation [12]:

$$\%Swelling = \frac{M_S - M_o - M_n}{M_o} \times 100 \qquad (1)$$

where M_S: swollen hydrogel weight, M_1: dried cellulose hydrogel and M_o: wet nylon bag weight.

Measurement of absorbed urea concentration. GEL-A and GEL-B were individually soaked in 100 ppm of urea solution for 24 h at room temperature and were then filtered, and the urea residue in the filtrate was measured by a spectrophotometer [13]. The amount of urea concentration absorbed into the gels is the deviation of the urea concentration in the solution from the urea concentration in the filtrate. Furthermore, the gels that had been soaked were characterized by SEM and FTIR [12].

Measurement of urea released from GEL-A and GEL-B. GEL-A and GEL-B were individually soaked in 250 mL of water for 15–180 min while being stirred constantly at room temperature. The urea which was released every 15 min was monitored by measuring the urea concentration in the solution with a

spectrophotometer [13]. In addition, the urea released from GEL-A and GEL-B was analyzed in media with pH 5–9 and temperatures 18–46 °C. The urea concentration in the solution was measured by the same technique.

■ RESULTS AND DISCUSSION

Isolation of α-Cellulose

Delignification process was carried out by a multistage pulping method using a mixture of 3.5% HNO$_3$ and NaNO$_2$. This process converts lignin to nitro lignin while eliminating hemicellulose [14]. The surface of the fibers at this stage appeared to be rougher, showing the removal of some outer non-cellulose layers such as hemicellulose, lignin, pectin and minerals [15]. Reheating was carried out in the second stage with a mixture of 2% NaOH and 2% Na$_2$SO$_3$ to complete lignin release. The next stage was the bleaching process by adding 1.75% NaOCl, accompanied by heating to form holocellulose [14]. Next, the hydrolysis process using 17.5% NaOH was conducted to produce pure α-cellulose [16].

Synthesis and Characterization of Superabsorbent Hydrogels

Hydrogels were prepared from cellulose in an aqueous solution of NaOH/urea with the addition of CaCO$_3$ as a pore forming material. Kabiri and Zohuriaan-Mehr [17] reported that the swelling ratio of superabsorbent hydrogels can be enhanced through porosity formed in the hydrogel structure. The physical gelation process was carried out through cooling for 24 h and the results showed that cellulose was well dispersed in the solution. Cellulose molecules in the aqueous solution below 0 °C have strong intermolecular interactions and

relatively more rigid chains, while those above 0 °C are converted to semi flexible chain conformation. Intermolecular interactions of cellulose are much stronger than between cellulose hydrates, NaOH hydrates, urea hydrates, and water molecules below 0 °C. Therefore, cellulose can be dissolved in NaOH/urea that is cooled to -10 °C, and the cellulose solution formed cannot remain in its liquid state below 0 °C for a certain time, indicating an irreversible sol-gel transition [18].

The cross-linking reaction of cellulose increases the specific degree of swelling and stable structure [19]. Epichlorohydrin (ECH) is a cross-linking agent whose reaction is catalyzed by bases (NaOH, LiOH, etc.) and is widely used for polysaccharide chains. The cross-linking process is controlled by the synergy between the chemical and physical cross-linking processes, namely the etherification reaction between the hydroxyl group of ECH and the cellulose chain (Fig. 1), as well as the cellulose chain winding through the reconstruction of hydrogen bonds in various alkaline media (NaOH, NaOH/urea, NaOH/thiourea, or LiOH/urea) [20].

Cellulose-ECH hydrogels are functionalized under alkaline conditions because the etherification reaction can be accelerated by the alkali/protonation process [11]. The hydroxyl group (–OH) of the cellulose molecules is activated and converted to a more reactive alkoxide (Cell-O⁻) form as shown in Fig. 2 [21]. Etherification takes place in the second stage. The role of the solvent in this reaction is to provide accessibility of the etherification reagent to the reaction center of the cellulose chain [22].

The swelling ratio has a linear correlation to the absorption capacity, where a high swelling ratio indicates
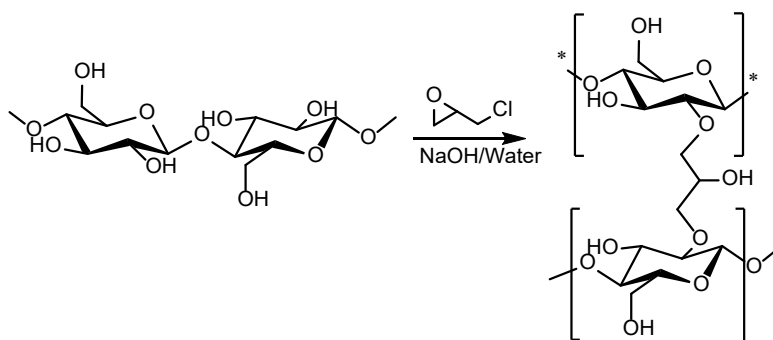
Fig 1. Mechanism of cellulose cross-linking with ECH [19]

Indones. J. Chem., 2020, 20 (3), 616 - 625

619
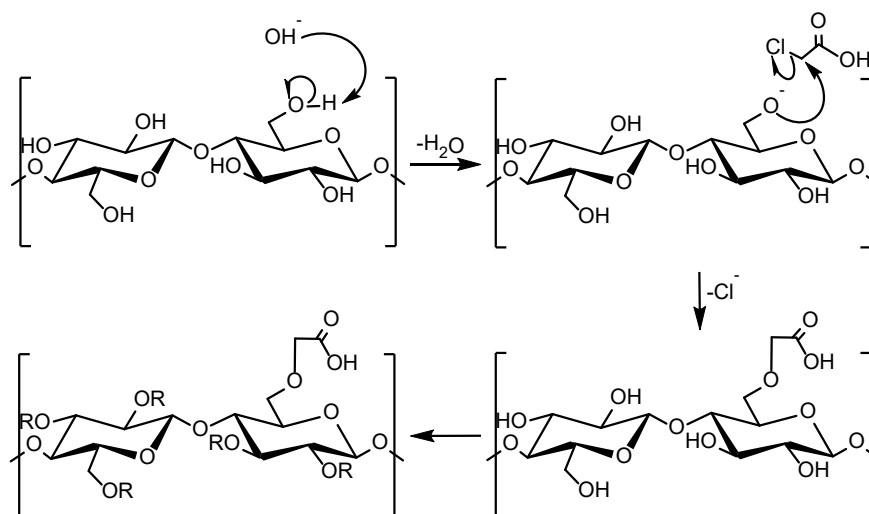
Fig 2. The mechanism for carboxymethylation of cellulose [23]

a high absorption capacity [12]. Table 1 shows the comparison of the swelling ratio of the hydrogels measured for 24 h. The swelling ratio of GEL-B was greater than that of GEL-A, due to the addition of the carboxymethyl group. The acidic characteristic of carboxymethyl causes hydrogels to be more polar, easily resonated and become more stable, resulting in greater water binding ability [11]. The swelling ratio of the hydrogels is affected by the degree of cross-linking, but it can also be affected by elasticity interaction, polymer-solvent interaction, electrostatic repulsion and osmotic pressure [12]. GEL-B after swelling appeared to be more transparent (Fig. 3(d)), showing greater water absorption, and this is the same as what was stated by Chang et al. [8], the increased space in a hydrogel material is caused by a highly hydrophilic carbonyl group

that can absorb many water molecules. When applied to agricultural land, a higher water retention capability can reduce the evaporation rate of water and consequently reduce the loss of fertilizer migrating to the soil surface [24]. It should be noted that on the ground, each hydrogel particle is surrounded by soil particles under the limiting pressure from the soil. Thus, the swelling rate of hydrogels would decrease in the soil [25].

The addition of fertilizer into hydrogel material was carried out by immersing GEL-A and GEL-B into the urea solution. Based on Table 2, greater urea absorption was achieved by GEL-B. In the urea solution, there is a group that has more hydrophilic sites such as $-NH_2^+$ and C=O and will interact with $-COOH$ group of hydrogels easily [26].

Table 1. Swelling ratio comparison of GEL-A and GEL-B

Sample Code	Ms (g)	Mo (g)	Mn (g)	% Swelling
GEL-A	2.4553	0.5005	0.9804	194.68
GEL B	5.4058	0.5017	0.9642	785.30
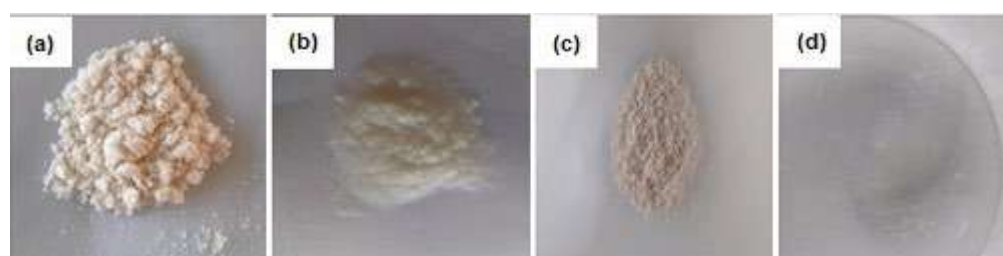
Fig 3. Hydrogels; (a) dried GEL-A, (b) swollen GEL-A, (c) dried GEL-B, (d) swollen GEL-B

Table 2. Urea absorption comparison of GEL-A and GEL-B

Sample Code	Total Urea Concentration (ppm)	Absorbed Urea Concentration (ppm)
GEL-A	100	97.75
GEL-B	100	98.33
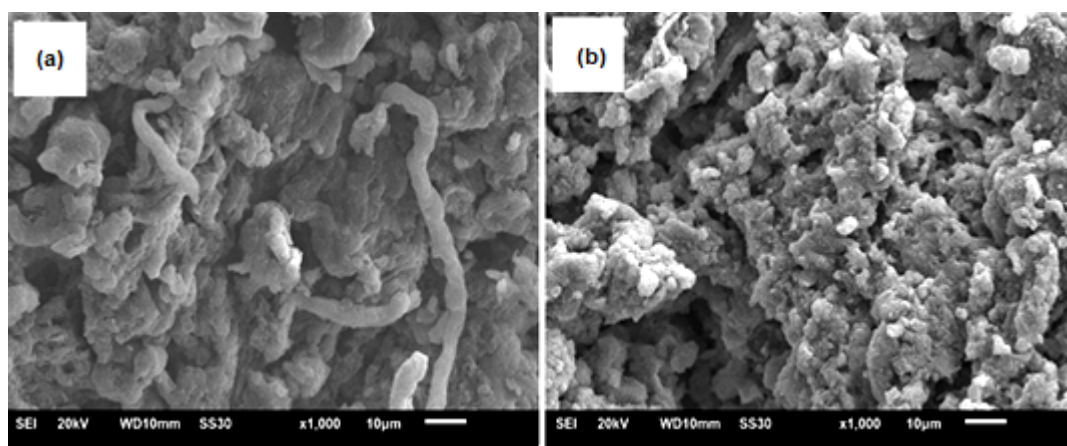
Fig 4. SEM micrograph; (a) GEL-A; (b) GEL-B

SEM characterization was used to study the morphological surface of the hydrogels. In Fig. 4, GEL-A displays a heterogeneous structure, while GEL-B has a relatively more uniform surface with the presence of several small pores. Interestingly, the structure of the fibrils can be observed on the surface (Fig. 4(a)). This fibrous structure is possible due to the cellulose chain's self-association at low temperature, which becomes more obvious and orderly with the increase of gelation concentration [8]. With the addition of the carboxymethyl group to GEL-B, it was observed that the particle size decreased. Moreover, the number of pores increased, leading to an open and loose structure (Fig. 4(b)). This shows that the electrostatic repulsion caused by the carboxylic anions ($-COO^-$) character had enlarged the space in the hydrogel network. Therefore, the swelling ratio increased because water molecules can easily diffuse in hydrogel material [27].

The differences in chemical structure between cellulose and hydrogels were characterized by FTIR, and the results are shown in Fig. 5. For the isolated cellulose spectrum (Fig. 5(a)), several typical absorption peaks can be seen, including the stretching of the –OH group at wave number 3447 cm^{-1} [28-29], the –CH group at wave number 2897 cm^{-1}, the C–C group at wave number 1643–1425 cm^{-1}, reinforced by the stretching vibrations of the C–O group at wave number 1273–1063 cm^{-1} [28], and the 1,4-β glycosidic bonds at wave number 895 cm^{-1} [30]. In the GEL-A spectrum (Fig. 5(b)), the broad absorption peak at wave number 3451 cm^{-1} is the stretching of the –OH group on the polymer backbone. The stretching of the aliphatic –CH group is shown at wave number 2922 cm^{-1} and the absorption peak shows the glycosidic bond (C–O–C) at 898 cm^{-1}. Meanwhile, in the GEL-B spectrum (Fig. 5(c)), changes in absorption bands and conical peaks for the –OH group at wave number 3439 cm^{-1} have been observed. On the other hand, the aliphatic –CH absorption band increases to 3173 cm^{-1}, and also the C–O–C group shifts to 866 cm^{-1} with a sharper peak [11]. Compared to GEL-A, the absorption band observed at wave number 1603 and 1460 cm^{-1} can be associated with asymmetric stretching of the carboxylic anion ($-COO^-$) and buckling –OH in the carboxylic spectrum [8,31]. The C–O group appears at wave numbers 1139 cm^{-1} and 1059 cm^{-1}. The results showed that there is a carboxyl group in GEL-B [32].

In Fig. 5(d) and Fig. 5(e), the FTIR spectrum of hydrogels after being soaked with urea solution is shown.
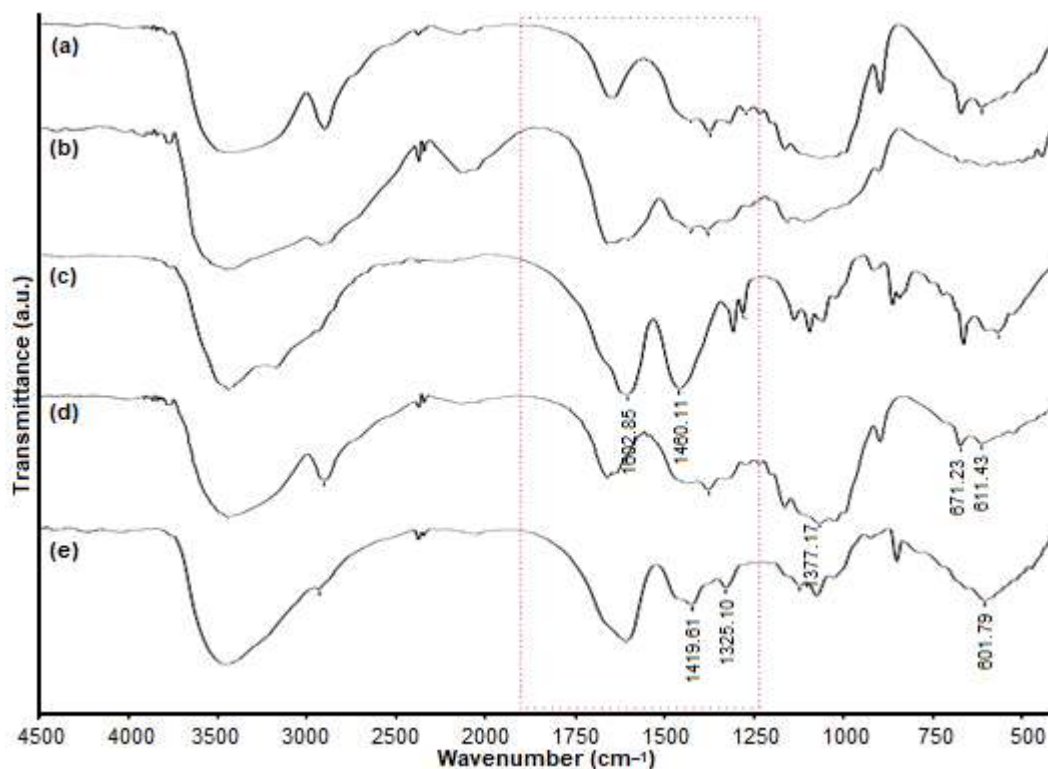
Fig 5. FTIR spectrum; (a) cellulose, (b) GEL-A before immersion, (c) GEL-B before immersion, (d) GEL-A after immersion, (e) GEL-B after immersion

The absorption peaks at wave numbers 3449 and 3445 cm^{-1} indicate the presence of the –OH group and the stretching of C–H was observed at wave numbers 2899 and 2928 cm^{-1} [33]. Other peaks observed are absorption bands at wave numbers 1659 and 1603, 1377 and 1325–1419, and areas around 1000–1250 cm^{-1}, indicating the presence of carboxylic anion (–COO^{-}) and N–H, as well as C–O or C–N [2,31,34]. Absorption peaks at wave numbers 611–671 and 602 cm^{-1} are associated with N–CO–N flexural vibrations, showing urea involvement in GEL-A and GEL-B [34].

Urea Released from GEL-A and GEL-B

The release of urea from the hydrogels is presented in Fig. 6. Due to its high urea solubility in water, it can be assumed that without a carrier matrix, almost 100% release of urea in water will occur within minutes [25].

In the hydrogels of controlled urea, the maximum release of urea concentration from GEL-A occurred in 90 min and it was shown by a decrease in urea concentration from 95.26 ppm to 94.46 ppm. Thus, the
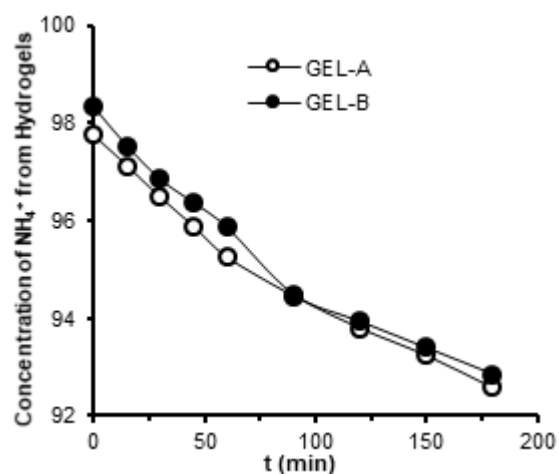
Fig 6. Slow-release of urea from hydrogels

total urea released in the 180 min period was 5.17 ppm or 5.29% of the amount of fertilizer absorbed. On the other hand, in GEL-B, the total urea released was 5.47 ppm or 5.56%. After the water entered the hydrogel layer, the fertilizer in the core was dissolved and then released in water [32]. In short, the hydrogels will gradually swell and act as a physical barrier that inhibits

the diffusion of nutrients from the polymer tissue, then the fertilizer will gradually dissolve and be released with increasing time through water exchange when the hydrogels are applied to the soil [24]. The mechanism of urea release from the hydrogel matrix is studied using the equation:

$$M_t / M_\infty = Kt^n \tag{2}$$

where M_t is the amount of urea released at time t, M_∞ is the total amount of urea present in the initial matrix, M_t/M_∞ is the fraction of urea released at time t. n = 1 is a continuous zero-order release, 0.5 < n < 1 is a non-Fickian diffusion release, and n < 0.5 is the release dominated by Fickian diffusion. The index n can be determined by plotting log M_t/M_∞ against the Kt^n log (Fig. 7 and Fig. 8) and determining the slope of the line obtained:

$$\log(M_t / M_\infty) = n\log(t) + \log(K) \tag{3}$$

Based on the above equation, the obtained n values of GEL-A (n = -0.0195) and GEL-B (n = -0.0207) showed the release of Fickian diffusion (n < 0.5). The recommended release mechanism to release the urea from the hydrogels is in a "partition" manner, where the solute moves through the interface and the area of the bound to the gel with polymer matrix [35].

The influence of pH on the release of urea from the hydrogel material is shown in Fig. 9. The release by GEL-B was faster than GEL-A. If the cation concentration increases, there is an increase in osmotic pressure in the gel system which eventually causes shrinkage within [26]. This is explained by the protonation of –COO⁻ to –COOH and the formation of hydrogen bonds between –COOH at acidic pH, which restrains the electrostatic repulsion of anions, increases the cross-linking of tissues, and consequently decreases water absorption [24]. However, in a certain pH range close to neutrality (pH 6–8), most of the base groups and acid groups are non-ionizing, so the H-bond between amine acid and carboxylic acid or carbox-amide group can produce a kind of cross-linking followed by a decreased swelling. With a further increase in pH, there is an electrostatic repulsion force between the –COO⁻ group and ionization of the carboxylic acid group. As a result, there is an expansion of the polymeric tissue which causes an increase in water absorption and swelling, subsequently, the release of urea increases and reaches a maximum at pH 9 [36]. The presence of additional ions can obviously
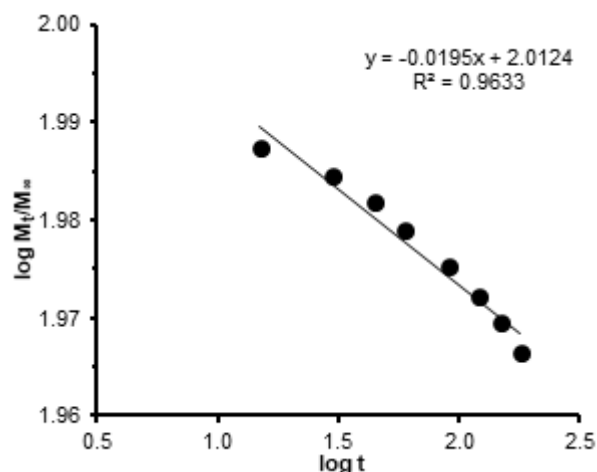
Fig 7. Index n of GEL-A
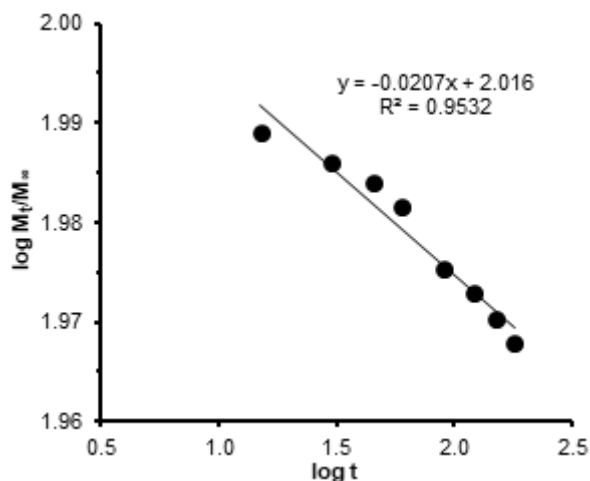
Fig 8. Index n of GEL-B
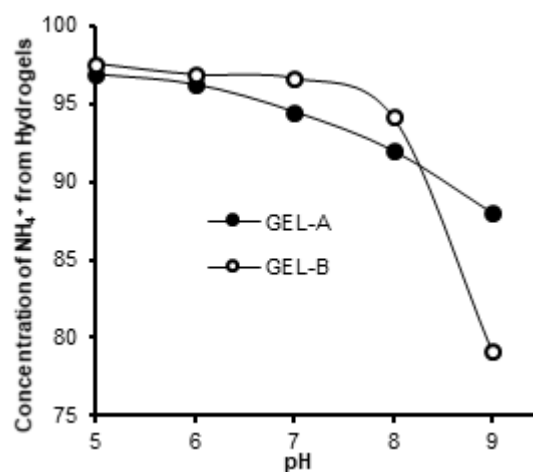
Fig 9. Effect of pH on urea release from hydrogels
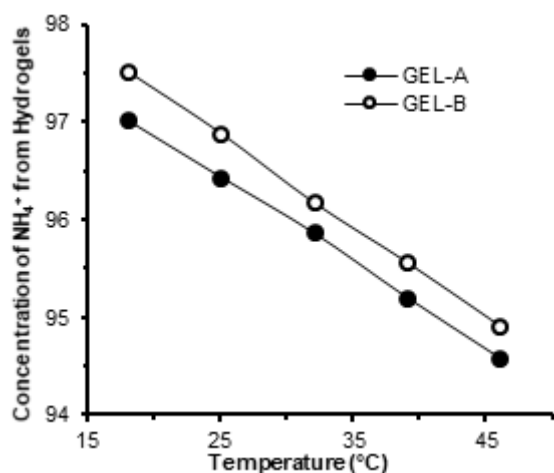
Fig 10. Effect of temperature on urea release from hydrogels

cause a slower rate of swelling and lower swelling capacity. Existing cations can produce greater fertilizer diffusion. Ions derived from the addition of a buffer solution can also play a role in increasing the concentration of urea in the release media. This means that the cations in water can accelerate the release of fertilizers by competing for adsorption sites, competitive complexing, etc. [37].

Slow-release fertilizer or controlled-release fertilizer can release nutrients due to two factors: humidity and temperature. Generally, the higher the temperature and the more available water vapors are, the faster the release of urea is [38]. This statement is in accordance with the graph in Fig. 10 which shows that as the temperature increases, the release of urea takes place quickly. Thus, the amount of urea in GEL-A has decreased from an initial concentration of 97.75 to 94.59 ppm. Whereas in GEL-B, the amount of urea released decreased from the initial concentration of 98.33 to 94.52 ppm. In the hydrophilic region, water molecules are connected by side chains through hydrogen bonds and work cooperatively to form a stable hydration shell around the hydrophobic groups. All of these interactions cause good solubility at room temperature. When the temperature rises, this system needs more energy to destroy this interaction and free trapped water molecules [39]. Lee and Yuan [40] also explained that the hydrophilic group in the polymer structure will form intermolecular hydrogen bonds between molecules with the surrounding water at low temperatures. Therefore, water that penetrates into the gel

is bound to a low temperature. The water molecule will gain enthalpy during the rise in temperature, and the hydrophilic groups in the gel will be converted into intramolecular hydrogen bonds under this condition. At the same time, hydrophobic strength will increase. These two results make the water molecules in the gel change from a bonded state to a free state and detached from the gel tissue with the release of urea. The level of immersion of the hydrogels that are sensitive to temperature also depends on the degree of water distribution. Faster response rate can be achieved if the water trapped in the hydrogels can quickly spread [36].

■ CONCLUSION

Superabsorbent hydrogels have been successfully synthesized and have shown their performance as the release material of controlled-release urea fertilizer. The formed GEL-A was better than GEL-B because the combination of urea and hydrogels produced a stable release of urea with a relatively lower amount of urea released (5.29%). Hydrogel application requires pH control.

■ REFERENCES

[1] Trenkel, M.E., 2010, *Slow and Controlled Release and Stabilized Fertilizers: An Option for Enhancing Nutrient Use Efficiency in Agriculture*, 2nd Ed., International Fertilizer Industry Association (IFA), Paris, France.

[2] Liu, M., Liang, R., Zhan, F., Liu, Z., and Niu, A., 2007, Preparation of superabsorbent slow release nitrogen fertilizer by inverse suspension polymerization, *Polym. Int.*, 56 (6), 729–737.

[3] Talaat, H.A., Sorour, M.H., Aboulnour, A.G., Shaalan, H.F., Ahmed, E.M., Awad, A.M., and Ahmed, M.A., 2008, Development of a multi-component fertilizing hydrogel with relevant techno-economic indicators, *Am. Eurasian J. Agric. Environ. Sci.*, 3 (5), 764–770.

[4] Puoci, F., Iemma, F., Spizzirri, U.G., Cirillo, G., Curcio, M., and Picci, N., 2008, Polymer in agriculture: A review, *Am. J. Agric. Biol. Sci.*, 3 (1), 299–314.

[5] Azeem, B., KuShaari, K., Man, Z.B., Basit, A., and Thanh, T.H., 2014, Review on materials and methods to produce controlled release coated urea fertilizer, *J. Controlled Release*, 181, 11–21.

[6] Zohuriaan-Mehr, M.J., and Kabiri, K., 2008, Superabsorbent polymer materials: A review, *Iran. Polym. J.*, 17 (6), 451–477.

[7] Kabir, S.M.F., Sikdar, P.P., Haque, B., Bhuiyan, M.A.R., Ali, A., and Islam, M.N., 2018, Cellulose-based hydrogels materials: Chemistry, properties, and their prospective applications, *Prog. Biomater.*, 7 (3), 153–174.

[8] Chang, C., Duan, B., Cai, J., and Zhang, L., 2010, Superabsorbent hydrogels based on cellulose for smart swelling and controllable delivery, *Eur. Polym. J.*, 46 (1), 92–100.

[9] Ibrahim, S.M., El Salmawi, K.M., and Zahran, A.H., 2007, Synthesis of crosslinked superabsorbent carboxymethyl cellulose/acrylamide hydrogels through electron-beam irradiation, *J. Appl. Polym. Sci.*, 104 (3), 2003–2008.

[10] Murthy, P.S.K., Mohan, Y.M., Varaprasad, K., Sreedhar, B., and Raju, K.M., 2008, First successful design of semi-IPN hydrogels-silver nanocomposites: A facile approach for antibacterial application, *J. Colloid Interface Sci.*, 318 (2), 217–224.

[11] Muharam, S., Yuningsih, L.M., and Sumitra, M.R., 2017, Characterization of superabsorbent hydrogels based on epichlorohydrin crosslink and carboxymethyl functionalization of cassava starch, *AIP Conf. Proc.*, 1862, 030083.

[12] Yusnaidar, Wirjosentono, B., Thamrin, and Eddiyanto, 2017, Synthesized superabsorbent based on cellulose from rice straw for controlled-release of urea, *Orient. J. Chem.*, 33 (4), 1905–1913.

[13] National Standardization Agency of Indonesia, 1991, *SNI 06-2479-1991, Metode pengujian kadar amonium dalam air dengan alat spektrofotometer secara nessler*, National Standardization Agency of Indonesia, Jakarta, Indonesia.

[14] Effendi, F., Elvia, R., and Amir, H., 2018, Preparasi dan karakterisasi mikrokristalin selulosa (MCC) berbahan baku tandan kosong kelapa sawit (TKKS), *Alotrop*, 2 (1), 52–57.

[15] Johar, N., Ahmad, I., and Dufresne, A., 2012, Extraction, preparation and characterization of cellulose fibres and nanocrystal from rice husk, *Ind. Crops Prod.*, 37 (1), 93–99.

[16] Zulharmitta, Viora, L., and Rivai, H., 2011, Pembuatan mikrokristalin selulosa dari batang rumput gajah (*Pennisetum purpureum* Schumach), *Jurnal Farmasi Higea*, 3 (2), 102–111.

[17] Kabiri, K., and Zohuriaan-Mehr, M.J., 2004, Porous superabsorbent hydrogels composites: Synthesis, morphology and swelling rate, *Macromol. Mater. Eng.*, 289 (7), 653–661.

[18] Cai, J., and Zhang, L., 2006, Unique gelation behavior of cellulose in NaOH/urea aqueous solution, *Biomacromolecules*, 7 (1), 183–189.

[19] Ciolacu, D.E., and Suflet, D.M., 2018, "Cellulose-based hydrogels for medical/pharmaceutical applications" in *Biomass as Renewable Raw Material to Obtain Bioproduct of High-Tech Value*, Eds. Popa, V., and Volf, I., Elsevier, Romania, 401–439.

[20] Udoetok, I.A., Dimmick, R.M., Wilson, L.D., and Headley, J.V., 2016, Adsorption properties of cross-linked cellulose-epichlorohydrin polymers in aqueous solution, *Carbohydr. Polym.*, 136, 329–340.

[21] Sangseethong, K., Ketsilp, S., and Sriroth, K., 2005, The role of reaction parameters on the preparation and properties of carboxymethyl cassava starch, *Starch/Stärke*, 57 (2), 84–93.

[22] Toğrul, H., and Arslan, N., 2003, Production of carboxymethyl cellulose from sugar beet pulp cellulose and rheological behaviour of carboxymethyl cellulose, *Carbohydr. Polym.*, 54 (1), 73–82.

[23] Adeyanju, O., Olademehin, O.P., Hussaini, Y., Nwanta, U.C., Adejoh, A.I., and Plavec, J., 2016, Synthesis, and characterization of carboxymethyl *Plectranthus esculentus* starch. A potential disintegrant, *J. Pharm. Appl. Chem.*, 2 (3), 189–195.

[24] Wen, P., Han, Y., Wu, Z., He, Y., Ye, B.C., and Wang, J., 2017, Rapid synthesis of a corncob-based

semi-interpenetrating polymer network slow-release nitrogen fertilizer by microwave irradiation to control water and nutrient losses, *Arabian J. Chem.*, 10 (7), 922–934.

[25] Mohammadi-Khoo, S., Moghadam, P.N., Fareghi, A.R., and Movagharnezhad, N., 2016, Synthesis of a cellulose-based hydrogels network: Characterization and study of urea fertilizer slow release, *J. Appl. Polym. Sci.*, 133 (5), 42935.

[26] Shah, R., Saha, N., and Saha, P., 2015, Influence of temperature, pH and simulated biological solutions on swelling and structural properties of biomineralized (CaCO$_3$) PVP-CMC hydrogels, *Prog. Biomater.*, 4, 123–136.

[27] Chang, C., Zhang, L., Zhou, J., Zhang, L., and Kennedy, J.F., 2010, Structure and properties of hydrogels prepared from cellulose in NaOH/urea aqueous solutions, *Carbohydr. Polym.*, 82 (1), 122–127.

[28] Mohadi, R., Saputra, A., Hidayati, N., and Lesbani, A., 2014, Studi interaksi ion logam Mn^{2+} dengan selulosa dari serbuk kayu, *Jurnal Kimia*, 8 (1), 1–8.

[29] Hutomo, G.S., Marseno, D.W., Anggrahini, S., and Supriyanto, 2012, Ekstraksi selulosa dari pod husk kakao menggunakan sodium hidroksida, *Agritech,* 32 (3), 223–229.

[30] Viera, R.G.P., Filho, G.R., de Assunção, R.M.N., Meireles, C.S., Vieira, J.G., and de Oliveira, G.S., 2007, Synthesis and characterization of methylcellulose from sugar cane bagasse cellulose, *Carbohydr. Polym.*, 67 (2), 182–189.

[31] Silverstein, R.M., Webster, F.X., and Kiemle, D.J., 2005, *Spectrometric Identification of Organic Compounds*, 7th Ed., John Wiley & Sons, Hoboken, New Jersey, USA.

[32] Wang, J., Liu, S., Qin, Y., Chen, X., Xing, R., Yu, H., Li, K., and Li, P., 2017, Preparation and characterization of controlled-release fertilizers coated with marine polysaccharides derivates, *Chin. J. Oceanol. Limnol.*, 35 (5), 1086–1093.

[33] Ni, B., Liu, M., and Lü, S., 2009, Multifunctional slow-release urea fertilizer from ethylcellulose and superabsorbent coated formulations, *Chem. Eng. J.*, 155 (3), 892–898.

[34] Wen, P., Wu, Z., He, Y., Han, Y., and Tong, Y., 2016, Characterization of p(AA-co-AM)/bent/urea and its swelling and slow release behavior in a simulative soil environment, *J. Appl. Polym. Sci.*, 133 (12), 43082.

[35] Lynch, I., and Dawson, K.A., 2004, Release of model compounds from "plum-pudding"-type gels composed of microgel particles randomly dispersed in a gel matrix, *J. Phys. Chem. B*, 108 (30), 10893–10898.

[36] Zhao, Y., Su, H., Fang, L., and Tan, T., 2005, Superabsorbent hydrogels from poly(aspartic acid) with salt-, temperature- and pH- responsiveness properties, *Polymer*, 46 (14), 5368–5376.

[37] Li, X., Li, Q., Xu, X., Su, Y., Yue, Q., and Gao, B., 2015, Characterization, swelling and slow-release properties of e new controlled release fertilizer based on wheat straw cellulose hydrogels, *J. Taiwan Inst. Chem. Eng.*, 60, 564–572.

[38] Rose, R., 2002, Slow release fertilizers 101, Dumroese, R.K., Riley, L.E., and Landis, T.D., Technical coordinators, *National Proceedings: Forest and Conservation Nursery Associations-1999, 2000, and 2001*, *Proceedings RMRS-P-24*, Ogden, UT., USDA Forest Service, Rocky Mountain Research Station, 304–308.

[39] Zhang, X., and Zhuo, R., 2000, Synthesis of temperature-sensitive poly(*N*-isopropylacrylamide) hydrogels with the improved surface property, *J. Colloid Interface Sci.*, 223 (2), 311–313.

[40] Lee, W.F., and Yuan, W.Y., 2000, Thermoreversible hydrogels X: synthesis and swelling behavior of the (*N*-isopropylacrylamide-co-sodium 2-acrylamido-2-methylpropyl sulfonate) copolymeric hydrogels, *J. Appl. Polym. Sci.*, 77 (8), 1760–1768.

Pollution Load Capacity Analysis of BOD, COD, and TSS in Karang Mumus River, Samarinda

Vita Pramaningsih[1,*], Slamet Suprayogi[2], and Ignasius Loyola Setyawan Purnama[2]

[1]*Department of Environmental Health, Universitas Muhammadiyah Kalimantan Timur,*
Jl. Ir. H. Juanda, No.15, Samarinda, East Kalimantan, Indonesia

[2]*Department of Environmental Geography, Faculty of Geography, Universitas Gadjah Mada,*
Bulaksumur, Sekip Utara 55281, Yogyakarta, Indonesia

Abstract: *The Rivers in Indonesia often accommodate pollution from all community activities. This happened due to a large number of people who use watersheds for living. One of those rivers is the Karang Mumus River in Samarinda City, East Kalimantan. This study aims to analyze the capacity of the Karang Mumus River pollution load in segments 2, 3 and 4. The analysis model used in this study was the QUAL2Kw and ArcGIS models. The former used to calculate the capacity of river pollution and the latter used to determine land use. The results of the QUAL2Kw Model analysis shown that the capacity of the BOD was exceeded in all segments, COD was exceeded in all segments except segment 3. The entire segment had an allocation of sectoral pollution load originated from domestic activities. This study concluded that the dominant land use of settlements was one of the main causes of this problem.*

Keywords: *capacity load; BOD; COD; TSS; QUAL2Kw model*

■ INTRODUCTION

Karang Mumus River is located in Samarinda City, East Kalimantan, and is also a subsidiary river of the Mahakam River. The length of the river from upstream to downstream reaches 17 km with a width of 10–15 m. This watershed had densely populated settlements. The majority of the population conducted bathing, washing, and toilet activities directly in this river, causing a lot of garbage thrown into the river and causing pollution. This condition was exacerbated by the existence of economic activities and traditional markets around the riverbanks. This worsened river water quality and affected public health. In addition, this also caused floods and pollution in rivers, household waste had also reduced the quality of water in this river.

Based on the ASPT and WQI, Karang Mumus River recently polluted with *Chironomus sp.* and *Melanoides tuberculata* as codominant taxa [1]. The contamination of PAHs in Karang Mumus River was relatively high because of polluted urban, suburban areas that a lot of commercial activity and residence [2]. Based on monitoring of water quality in Karang Mumus River in September 2015 held by Environment Agency (BLH) of Samarinda City, pH, BOD, COD, TSS, and Fecal Coliform at some points have exceeded the standard. These various studies were unsettling for the local government, and with various considerations PERDA East Kalimantan Province No. 2 of 2011 concluded that the Management of Water Quality and Water Pollution Control which states that the Karang Mumus River was classified as Class II meaning that the phosphate level in some river points was very high and dangerous.

Some earlier research mentioned several causes influencing the quality of river water, according to Effendy, the speed of river flow and various activities on the banks affected the quality of river water [3]. In line with this, according to Kalavaty, land use in upstream areas made the river water quality polluted [4]. Furthermore, in the rainy season, the flow of the river increased and caused pollution due to the increase in agricultural activities. These were the evidence of how

the use of river water in the upstream areas will affect the water quality in the downstream [5]. There were also social factors such as industrialization, urbanization, and agriculture activities that also affected the river's water physically and chemically for pH, TSS, BOD, COD, nitrate, and phosphorus parameters [6].

One attempt to make sure the level of pollution in the river is by using the Qual2Kw model. QUAL2Kw Model can be used to calculate the capacity of the pollution load according to the desired quality standard. The QUAL2Kw model was also used to determine the future river water quality, so the result of it can be used for the government's policy consideration [7]. The QUAL2Kw model was used to predict water quality in the next few years by calculating the projected population growth and sources of Point Source (PS) and Non Point Source (NPS) pollution [8]. The QUAL2Kw model is useful as a tool for simulating water quality in rivers and measuring the impact of NPS pollution from agriculture [9]. QUAl2Kw can also be used

to simulate DO, BOD, Total Coliform, and Total Nitrogen content in rivers for 10 years [10].

■ EXPERIMENTAL SECTION

Materials

Sampling for water quality checks carried out by purposive sampling. Determination of the sampling time was done by considering the backwater of the Mahakam River using the information that can be accessed at http://pasanglaut.com, accessed March 1, 2016, and the conditions of the collection at the river mouth. Based on these considerations, 17 sampling points were determined, namely 10 points in tributaries and drainage, and 7 points were taken in the main river. Sampling was carried out from upstream to downstream without being influenced by the Mahakam River backwater. Location of sampling and division of river segments was presented in Table 1, while the map of sampling points was presented in Fig. 1.
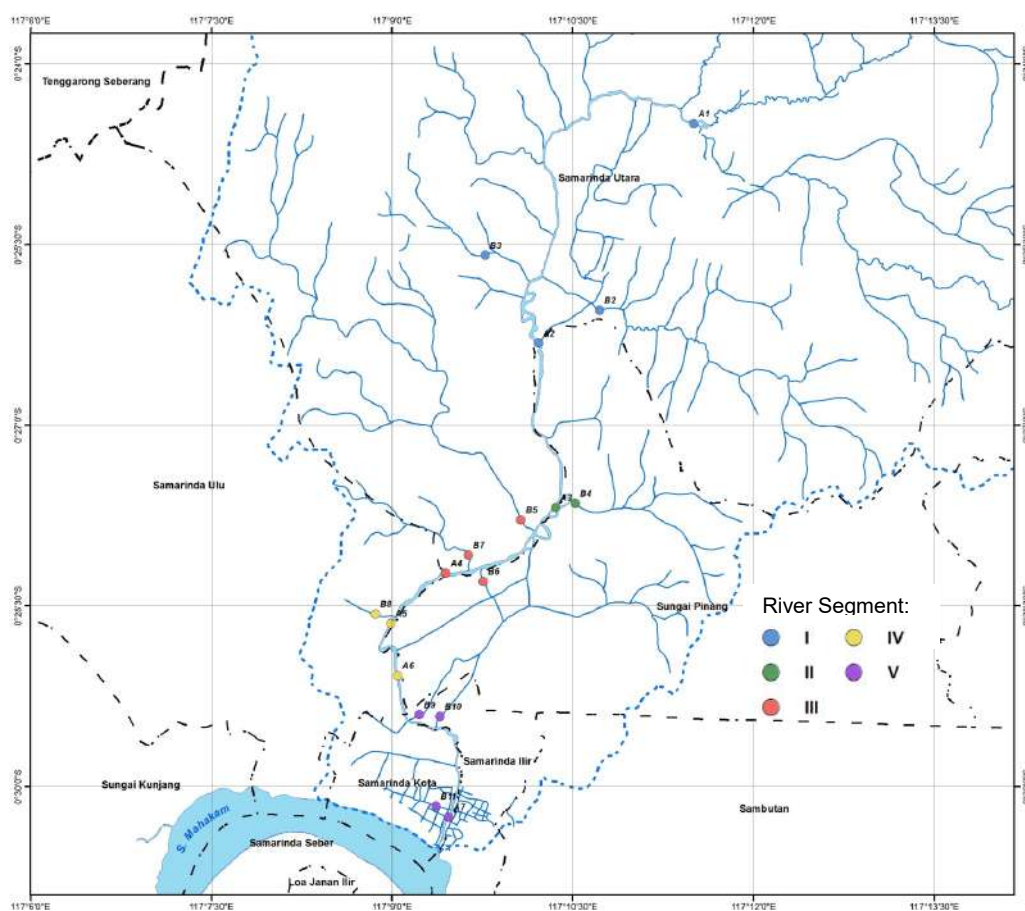
Fig 1. Map of sampling point and river segment

Table 1. Sampling location and river segment of Karang Mumus River

No.	Location	Coordinate		Code	Segment	Long (km)	Elevation (m)
		E (Longitude)	S (Latitude)				
1	Bridge after Benanga Reservoir	117° 11' 29.8357" BT	0° 24' 30.3840" LS	A1			11.647
2	Lempake Jaya River	117° 10' 43.4605" BT	0° 26' 2.7887" LS	B2	I	6.36	11.157
3	Bengkuring River	117° 09' 46.7605" BT	0° 25' 39.8136" LS	B3			11.210
4	Tepian Lempake Bridge	117° 10' 13.0293" BT	0° 26' 19.0643" LS	A2			10.870
5	Mugirejo-Gn. Lingai River	117° 10' 30.6227" BT	0° 27' 39.4128" LS	B4	II	2.71	7.419
6	Gunung Lingai (Jl. P.M. Noor)	117° 10' 23.9628" BT	0° 27' 36.8172" LS	A3			6.792
7	Sempaja River	117° 10' 4.8901" BT	0° 27' 47.1889" LS	B5			6.492
8	A. Yani (Gelatik-Pemuda) Drainage	117° 09' 32.6305" BT	0° 28' 18.4117" LS	B6	III	2.08	5.991
9	Pramuka-UNMUL River	117° 09' 39.2113" BT	0° 28' 4.9043" LS	B7			5.987
10	Gelatik Bridge	117° 09' 26.7660" BT	0° 28' 13.7029" LS	A4			5.624
11	Lembuswana-Vorvoo Drainage	117° 09' 1.3679" BT	0° 28' 34.8815" LS	B8			5.49
12	S. Parman Bridge	117° 09' 2.9383" BT	0° 28' 35.8637" LS	A5	IV	2.24	5.39
13	Perniagaan Bridge	117° 09' 3.4849" BT	0° 29' 4.5095" LS	A6			5.16
14	Jl. Gatot Subroto Drainage	117° 09' 10.1457" BT	0° 29' 27.6665" LS	B9			4.90
15	Jl. Lambung Mangkurat Drainage	117° 09' 21.6432" BT	0° 29' 31.4340" LS	B10	V	3.36	4.56
16	P. Hidayatullah Drainage	117° 09' 29.4943" BT	0° 30' 10.0386" LS	B11			4.19
17	Sei Dama Bridge	117° 09' 31.1835" BT	0° 30' 10.6989" LS	A7			3.96

A = Main River/Karang Mumus River

B = Tributary and Drainage

Instrumentation

Sample from the 17 point location is analyzed in the laboratory for BOD, COD, and TSS parameter. Analysis results were used as the input in the QUAL2Kw Model to determine the load capacity of the pollution of the river in each parameter. The modeling simulated two scenarios, namely, the scenario I in existing conditions and scenario II as a capacity load of pollution based on the standard of the Regulation Province East Kalimantan (No. 2 the Year 2011) about the management of water quality and water pollution control.

Procedure

There were Steps in the Model QUAL2Kw procedure, they were: first, doing data entry and then running the program. Second, the entry data QUAL2Kw program. The data includes the river segment, distance each segment from upstream to downstream, altitude/river elevation, coordinate segment, Point Source (PS), and Non Point Source (NPS). There were also the climatology and Hydrology data used; the climatology data includes the temperature, wind speed, cloud cover, and the hydrology data includes coefficient manning, wide river,

river discharge, discharge of PS, and NPS [11]. Output results could be viewed in two ways, using the graphs and tables. The output table could be seen on the worksheet WQ Output, while the output graph could be seen on the spatial chart worksheet [12].

The other steps were the calibration and validation of the simulations. The method used was the trial and error model. It included the use of the addition and subtraction of pollution load on the parameters, so the examination of the study will fit the scenario created. The operation of the model was done separately. The pollution load was calculated based on the approach to land use. Land use in the Karang Mumus watershed was dominated by 43.86% settlements and estates 25.42%. Pollution load was calculated by reduction value in scenario II (pollution load capacity) and scenario I (pollution load in the existing condition). The minus result (-) indicates that the pollution load has exceeded capacity and must be reduced. Conversely, if the result is positive (+), it indicates that the capacity still holds the burden of pollution. The output of the program was the magnitude maximum pollution load capable accepted the river [12].

■ RESULTS AND DISCUSSION

Pollution load capacity is the maximum amount of pollution loads allowed to be dumped into the water body without causing pollution. Then, the allocation of the burden of pollution is pollution load that can still be accommodated. Analysis of Point Source (PS) and Non Point Source (NPS) pollutants were used to calculate pollution loads. Tributaries and drainage that entered the main river (Sub DAS B2-B11) as PS and were added with NPS calculated from the land use approach. The map of land use and distribution of pollution sources of Karang Mumus watershed were presented in Fig. 2. The land use in Karang Mumus watershed was predominantly residential in the downstream as it is the location of the center of Samarinda City, East Kalimantan Province. Potential pollutant sources in each segment were presented in Table 2.

The settlements have the highest potential of being a polluting source in Karang Mumus River. It was in accordance with the percentage of land use in Karang Mumus watershed 43.86 of settlement and the city in the downstream area. The water quality of the Karang Mumus River decreased due to pollution. High Fe, Mn, COD, and TSS content in river water were affected by industrial waste, domestic waste, agriculture, and urban area runoff [13]. River water quality with urban land use indicated that water quality was physically polluted and was not suitable for consumption [4]. Fig. 3 presents an overview of the area around Karang Mumus River.

Pollution Load of BOD, COD, and TSS in Karang Mumus River

The pollution load analysis was done on each segment of the rivers, and it was originated from domestic activity, trash, livestock, agriculture, and building. The analysis of BOD, COD, and TSS are presented in Table 3, 4, and 5.
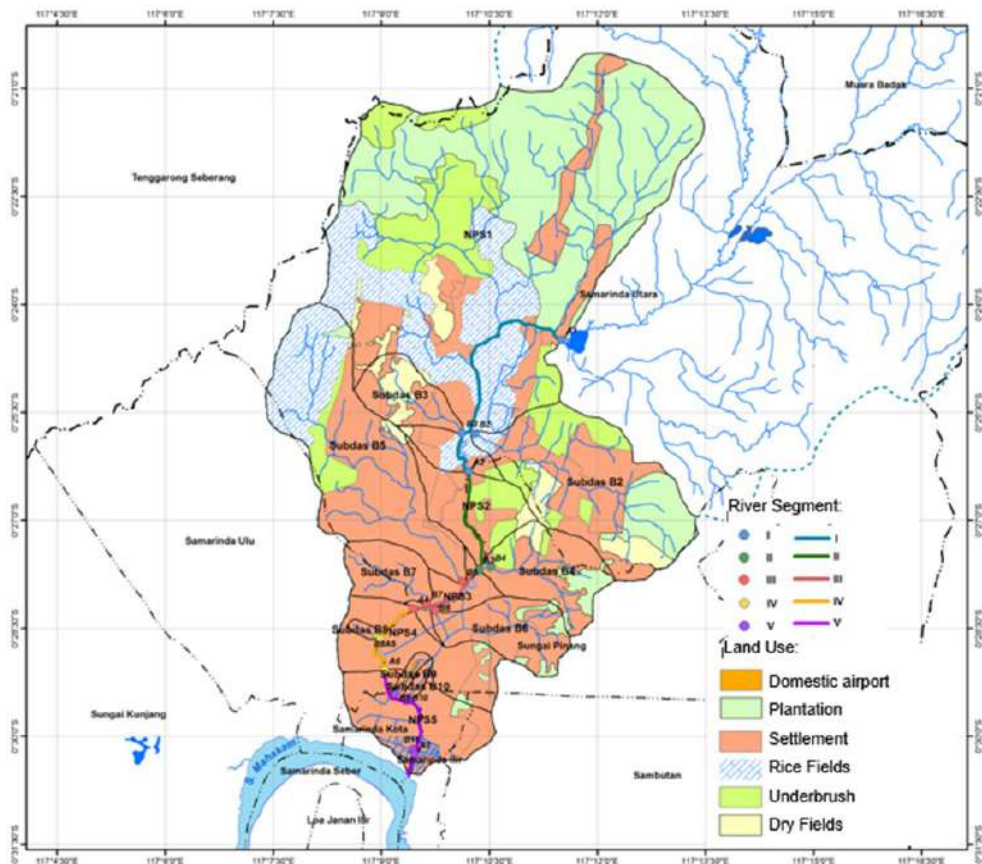
Fig 2. Land use and distribution of pollution source

Vita Pramaningsih et al.

Table 2. Potential pollutant sources each river segment

No.	Location	Code	Segment	Sub-District	Pollutant Source	Potential of Pollutant Source
1	Bridge after Benanga Reservoir	A1			NPS 1	Upstream activity
2	Lempake Jaya River	B2	I	Samarinda Utara	Sub DAS B2	Settlement
3	Bengkuring River	B3			Sub DAS B3	Bengkuring Residence, Traditional Bengkuring Market, Loundry
4	Tepian Lempake Bridge	A2				
5	Mugirejo-Gn. Lingai River	B4	II	Sungai Pinang	Sub DAS B4	Citra land Residence, Mugirejo Residence, Loundry
6	Gunung Lingai (P.M. Noor Street)	A3			NPS 2	
7	Sempaja River	B5	III	Sungai Pinang and Samarinda Utara	Sub DAS B5	Pondok Surya Indah Residence, Rapak Binuang Drainage, TVRI Drainage, Pinang Mas Drainage, Loundry
8	A. Yani (Gelatik-Pemuda) Drainage	B6			Sub DAS B6	The settlement around A. Yani Street, Pemuda Street, Sentosa Street, Hotel Grand Violand, Hotel Crystal
9	Pramuka-UNMUL River	B7			Sub DAS B7	The settlement around Pramuka Street, Loundry
10	Gelatik Bridge	A4			NPS 3	
11	Lembuswana-Vorvoo Drainage	B8	IV	Samarinda Ulu	Sub DAS B8	Mall Lebuswana, Mall Samarinda Square, Hotel Grand Victory, Settlements around Voorvo
12	S. Parman Bridge	A5			NPS 4	
13	Perniagaan Bridge	A6				Centre Market Segiri, settlements in river bank
14	Gatot Subroto Street Drainage	B9	V	Samarinda Kota and Samarinda Ilir	Sub DAS B9	Settlements around Gatot Subroto Street, Hotel Dragon,
15	Lambung Mangkurat Street Drainage	B10			Sub DAS B10	Settlements around Lambung Mangkurat Street, Hotel Diamond, Traditional Lambung Mangkurat Market,
16	P. Hidayatullah Drainage	B11			Sub DAS B11	Settlements around Hidayatullah Street, Mall SCP, Hotel ASTON, Hotel Borneo Swiss Bell
17	Sei Dama Bridge	A7			NPS 5	

A = Main River/Karang Mumus River;
B = Tributary and Drainage
Sub DAS B2-B11 are PS

Table 3. BOD pollution load

River Segment	BOD Pollution Load (kg/day)					
	Domestic	Trash	Livestock	Agriculture	Building	Total
Segment 1	371.71	3.14	25.79	415.89	-	816.53
Segment 2	536.29	4.54	18.05	30.85	-	589.73
Segment 3	982.28	8.31	34.24	81.69	-	1,106.53
Segment 4	891.02	7.54	11.93	0.39	-	910.87
Segment 5	2,905.46	24.58	1.13	0.21	1.12	2,932.49
Total	5,686.75	48.11	91.14	529.03	1.12	6,356.15
Percentage	89.47	0.76	1.43	8.32	0.02	100.00

Fig 3. Overview of the area around Karang Mumus River

Table 4. COD pollution load

River Segment	COD Pollution Load (kg/day)					
	Domestic	Trash	Livestock	Agriculture	Building	Total
Segment 1	511.10	4.32	61.92	623.83	-	1,201.17
Segment 2	737.40	6.24	43.19	46.27	-	833.09
Segment 3	1,350.64	11.43	82.02	122.53	-	1,566.61
Segment 4	1,225.15	10.36	28.49	0.59	-	1,264.59
Segment 5	3,995.00	33.80	4.02	0.32	1.67	4,034.81
Total	7,819.28	66.15	219.63	793.55	1.67	8,900.28
Percentage	87.85	0.74	2.47	8.92	0.02	100.00

Table 5. TSS pollution load

River Segment	TSS Pollution Load (kg/day)					
	Domestic	Trash	Livestock	Agriculture	Building	Total
Segment 1	353.12	2.99	22.38	3.36	-	381.84
Segment 2	509.47	4.31	15.49	0.14	-	529.41
Segment 3	933.17	7.89	29.49	0.22	-	970.78
Segment 4	846.46	7.16	10.19	0.02	-	863.84
Segment 5	2,760.18	23.35	1.44	0.01	0.56	2,785.54
Total	5,402.41	45.70	78.99	3.75	0.56	5,531.42
Percentage	97.67	0.83	1.43	0.07	0.01	100.00

The highest pollution load of BOD, COD, and TSS in all Karang Mumus River segments were originated from domestic activities. We can see from Fig. 2 that Segment 1 and 2 were dominated by the forestry. On the other hand, segment 3 to segment 5 were dominated by the land use of settlement, including density settlement

on the river banks. The highest pollution load of BOD, COD, and TSS was in segment 5. Urbanization and density of settlements on the river bank were contributed to the water pollution [4].

The high BOD was affected by the source of the contaminant from any famous tourist places [14]. BOD and COD were the indicators of organic pollutants sourced from agriculture and the settlement of domestic waste [15]. In the context of urbanization, many industries across the country also contributed a significant amount of PAHs (Polycyclic Aromatic Hydrocarbon). It was evidenced by the existence of organic pollutants in some rivers across Jakarta City [16].

Yet Geographically, Karang Mumus River has a little elevation in it and there is no any building floodgates that contributes the artificial aeration as the supply of oxygen of which can improve the quality of the water. In fact, the process of self-purification only occurs naturally without any aeration process because turbulence of the flow provides a supply of dissolved oxygen in the water [17].

Pollution Load Capacity

Calculation of pollution load capacity was done on segment 2, 3, and 4 only. It was because the data taken by the Model should not be influenced by backwater and also marshy areas of the river. After the measurement of discharge was done, it turned out that in segment 1 and 5 the discharge ware down on those segments. It happened because the location in segment 1 had a flat topography and the marsh area, while segment 5 was influenced by the backwater of Mahakam River. The pollution load capacity of BOD, COD, and TSS were presented in Table 6, 7, and 8.

Pollution load graphs on the existing conditions (scenario I) and pollution load capacity (scenario II) were presented in Fig. 4, 5, and 6. Zero points on the graph were upstream of Karang Mumus River. The graphs were presented for BOD, COD, and TSS parameters.

Based on Table 6, the pollution load of BOD in the entire segment exceeded the capacity. The highest allocation of the BOD pollution load in segment 4 was

Table 6. The pollution load capacity of BOD

Segment	Existing Pollution Load		Pollution Load Capacity		Allocation of Pollution Load	
	mg/L	kg/day	mg/L	kg/day	mg/L	kg/day
2	30.00	885.12	4.60	207.81	-25.40	-677.30
3	67.40	1,323.76	46.50	818.27	-20.90	-505.49
4	168.82	3,941.64	43.82	918.35	-125.00	-3,023.29
Total	266.22	6,150.52	94.92	1,944.43	-171.30	-4,206.09

Table 7. The pollution load capacity of COD

Segment	Existing Pollution Load		Pollution Load Capacity		Allocation of Pollution Load	
	mg/L	kg/day	mg/L	kg/day	mg/L	kg/day
2	184.63	4,836.21	170.63	4,497.60	-14.00	-338.61
3	133.10	2,623.44	531.10	12,249.59	398.00	9,626.15
4	279.86	6,396.73	199.86	4,461.83	-80.00	-1,934.90
Total	597.59	13,856.38	901.59	21,209.02	304.00	7,352.64

Table 8. The pollution load capacity of TSS

Segment	Existing Pollution Load		Pollution Load Capacity		Allocation of Pollution Load	
	mg/L	kg/day	mg/L	kg/day	mg/L	kg/day
2	21.05	1,073.55	418.05	10,442.73	397.00	9,369.18
3	35.48	714.68	216.08	5,018.99	180.60	4,304.31
4	287.93	373.68	283.73	6,102.93	-4.20	5,729.25
Total	344.46	2,161.91	917.86	21,564.65	573.40	19,402.74
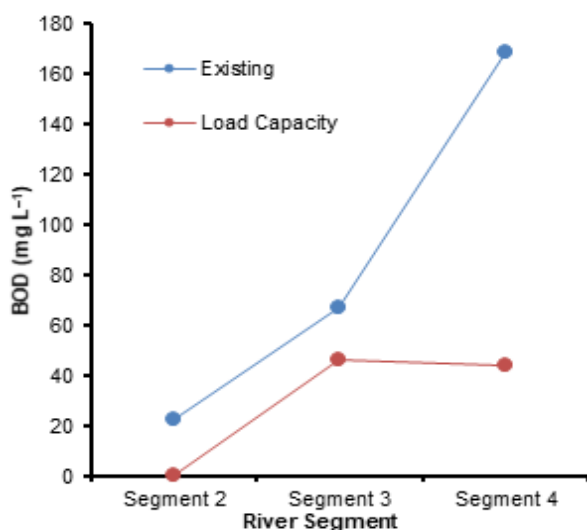
Fig 4. Pollution load capacity with the Existing condition of the BOD
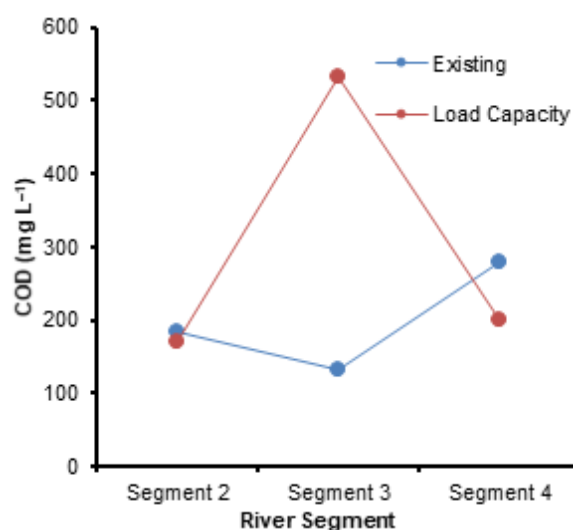
Fig 5. Pollution load capacity with the existing condition of the COD
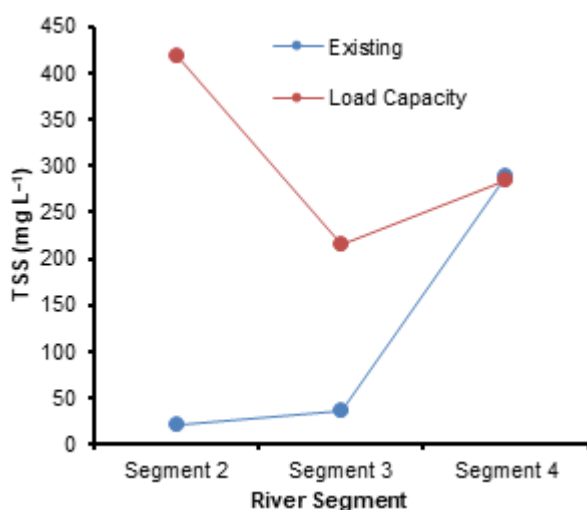
Fig 6. Pollution load capacity with the existing condition of the TSS

-3,023.29 kg/day, and it should be taken down. It was because the dominant land use in segment 4 was a settlement of 96.43%. This area is the center of Samarinda City with a density of settlement, Mall, Hospital and Traditional Market 'Segiri'. The result of the analysis BOD content in waters using QUAL2Kw concluded that the treatment to improve water quality in the location is needed. It was similar to the statements [8] that the simulation result of BOD by QUAL2Kw was used to determine location to improve water quality.

Based on Table 7, segment 3 still holds the COD pollution load of 398 mg/L with land use of settlement

71.11%. Segment 2 and 4 have COD pollution load exceeding capacity with the allocation of pollution load that must be reduced by 14 mg/L and 80 mg/L. The land use for settlement in segment 2 of 67.22%, and there were small 'tempeh' industries. Segment 4 has the highest COD pollution load is 279.86 mg/L. It was because of the influence of dominant land use settlement of 96.43%. This area is the center of Samarinda City density settlements, Mall, Hospital, and Big Market 'Segiri". A lot of residential settlements in riverbank with residents' daily activities such as bath, washing, and toilet to the river. It affected COD content because of the many organic compounds degraded in the water.

Based on Table 8, The TSS pollution load across the segment of the river still met the capacity. The pollution load of TSS in segment 4 was approaching capacity. It made sense because there are shopping malls/shopping centers, density residential, hotel, and hospital. TSS compound affected by runoff from the rainwater. The concentration of pollutants in the river is influenced by storm characteristic runoff and land uses [18]. Pollution load capacity for BOD, COD, and TSS was influenced by pollution load coming from the waste of community activities in settlements; it was necessary to be supervised [19].

The map of the capacity of pollution load BOD, COD and TSS presented in Fig. 7 showed the spatial
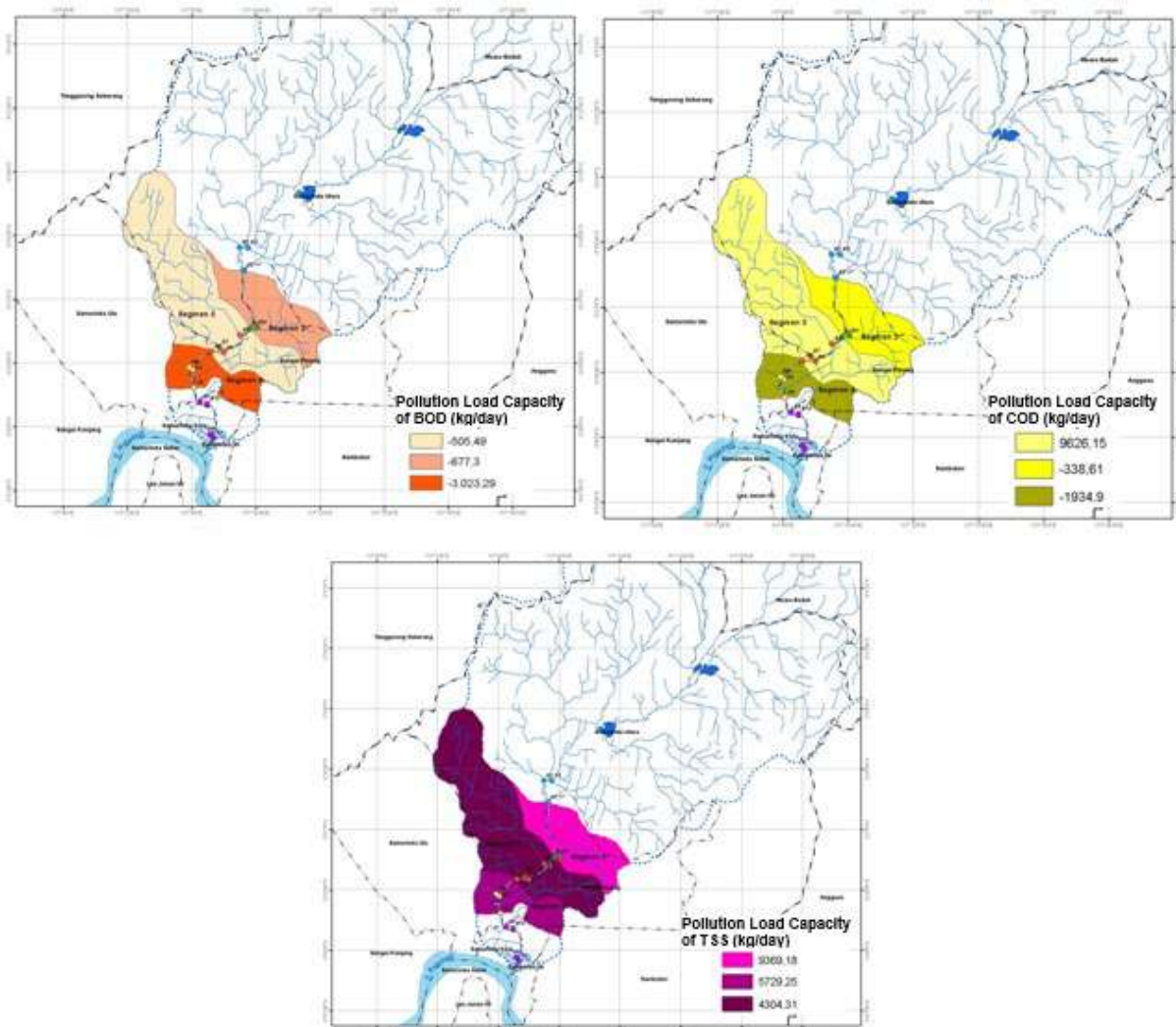
Fig 7. Spatial distribution of pollution load capacity for BOD, COD, and TSS

distribution of the pollution load capacity in the Karang Mumus watershed.

Allocation of Pollution Load

Allocation of sector pollution load for BOD, COD, and TSS were presented in Table 9, 10, and 11. It was calculated based on land use percentage in Karang Mumus watershed.

Based on Table 9, the highest allocation sector of pollution load for BOD were originated from the domestic activity from settlements. The highest domestic sector of the BOD pollution load that must be reduced is -2,957.37 kg/day in segment 4, with the dominant land use settlement of 96.43%.

Based on Table 10, the highest allocation sector of pollution load for COD was from the domestic sector. The highest domestic sector of COD pollution load that must be reduced is -1,874.55 kg/day in segment 4, with dominant land use settlement of 96.43%. Segment 3 was still capable of accommodating COD of 8,299.08 kg/day of the domestic sector. Settlements in segment 3 of 71.11% were smaller than segment 4. The allocation sector of pollution load for COD should be reduced in segment 2 is -299.71 kg/day with land use 67.22%. There were small 'tempeh' industries in segment 2, thus causing the pollution load of COD exceeding the capacity, although having the smallest settlement compared to segment 3 and 4.

Table 9. Allocation of sector pollution load for BOD

Segment	Allocation of Sector Pollution Load (kg/day)					Total
	Domestic	Trash	Livestock	Agriculture	Building	
2	-615.93	-5.21	-20.74	-35.43	0.00	-677.30
3	-448.74	-3.80	-15.64	-37.32	0.00	-505.49
4	-2,957.37	-25.02	-39.58	-1.31	0.00	-3,023.29
Total	-4,022.04	-34.03	-75.96	-74.06	0.00	-4,206.09

(-) indicates the pollution load must be reduced

Table 10. Allocation of sector pollution load for COD

Segment	Allocation of Sector Pollution Load (kg/day)					Total
	Domestic	Trash	Livestock	Agriculture	Building	
2	-299.71	-2.54	-17.55	-18.81	0.00	-338.61
3	8,299.08	70.21	503.96	752.90	0.00	9,626.15
4	-1,874.55	-15.86	-43.59	-0.91	0.00	-1,934.90
Total	6,124.82	51.82	442.82	733.18	0.00	7,352.64

(-) indicates the pollution load must be reduced

Table 11. Allocation of sector pollution load for TSS

Segment	Allocation of Sector Pollution Load (kg/day)					Total
	Domestic	Trash	Livestock	Agriculture	Building	
2	9,016.31	76.28	274.12	2.48	-	9,369.18
3	4,137.54	35.00	130.77	0.99	-	4,304.31
4	5,614.02	47.49	67.60	0.13	-	5,729.25
Total	18,767.87	343.18	1,853.82	210.81	-	42,972.41

Based on Table 11, the highest allocation sector of pollution load came from the domestic activity for segment 2, 3 and 4. The whole segment was still capable of holding TSS pollution load, the highest in segment 2 of 9,016.31 kg/day and lowest in segment 3 of 4,137.54 kg/day. It was due to the measurement was conducted at a time when the rain did not occur.

Similar to the statement of Baherem et al. [19], the pollution load capacity of BOD, COD, and TSS sources are originated from the waste of community activities in settlements. It means that public awareness and participation are not adequate to save the river from pollutants. Cooperation between stakeholder and communities are needed to manage bank erosion and agricultural practices aiming to minimize soil erosion in the catchment and sediment input to the river [20].

Based on the spatial distribution of pollution load capacity analysis, we can see more detailed information about the location that needs to be considered by the government as an effort to manage the environment. In addition, the calculation of sector pollution load allocation provided information about the dominant pollutant source. It can help the government efforts to control water pollution from the source. Hence, the collaboration involving all stakeholder are needed to develop a good river management especially for the communities who lives around the river to always maintain and improve river water quality [21].

■ CONCLUSION

The urban areas with the predominantly residential land have potential high pollution load to parameters of BOD, COD, and TSS. Karang Mumus River segment 2, 3 and 4 have a BOD capacity exceeded. Segment 3 was still capable of accommodating COD, and segment 2, 3 and 4 still holds the TSS.

■ ACKNOWLEDGMENTS

■ REFERENCES

[1] Patang, F., Soegianto, A., and Hariyanto, S., 2018, Benthic macroinvertebrates diversity as bioindicator of water quality of some rivers in east Kalimantan, Indonesia, *Int. J. Ecol.*, 2018, 5129421.

[2] Hadibarata, T., Syafiuddin, A., and Ghfar, A.A., 2019, Abudance and distribution of polycyclic aromatic hydrocarbon (PAHs) in sediments of the Mahakam River, *Mar. Pollut. Bull.*, 149, 110650.

[3] Effendy, H., 2016, River Water quality preliminary rapid assessment using pollution index, *Procedia Environ. Sci.*, 33, 562–567.

[4] Kalavaty, S., Sharma, T.R., and Sureshkumar, P., 2011, Water quality index of river Cauvery in Tiruchirappalli district, Tamilnadu, *Arch. Environ. Sci.*, 5, 55–61.

[5] Lai, Y.C., Yang, C.P., Hsieh, C.Y., Wu, C.Y., and Kao, C.M., 2011, Evaluation of non-point source pollution and river water quality using a multimedia two-model system, *J. Hydrol.*, 409 (3-4), 583–595.

[6] Yadav, S.S., and Rajesh, K., 2011, Monitoring water quality of Kosi river in Rampur district, Uttar Pradesh, India, *Adv. Appl. Sci. Res.*, 2 (2), 197–201.

[7] Kannel, P.R., Lee, S., Lee, Y.S., Kanel, S.R., and Pelletier, G.J., 2007, Application of automated QUAL2Kw for water quality modeling and management in the Bagmati river, Nepal, *Ecol. Modell.*, 202 (3-4), 503–517.

[8] Farhadian, M., Bozorg-Haddad, O., Pazoki, M., and Loaiciga, H.A., 2019, Minimal adverse impact of discharging polluted effluents to rivers with selective location, *Sustain. Cities Soc.*, 46, 101394.

[9] Gikas, G.D., 2014, Water quality of drainage canals and assessment of nutrient load using QUAL2Kw, *Environ. Processes*, 1 (4), 369–385.

[10] Sharma, D., Kansal, A., and Pelletier, G., 2015, Water quality modeling for urban reach of Yahuma river, India (1999–2009), using QUAL2Kw, *Appl. Water Sci.*, 7 (3), 1535–1559.

[11] Pelletier, G.J., and Chapra, S.C., 2008, *QUAL2Kw theory and documentation (version 5.1): A modeling framework for simulating river and stream water quality*, Environmental Assessment Program, Department of Ecology, Olympia, Washington.

[12] Pelletier, G.J., and Chapra, S.C., 2008, *QUAL2Kw user manual (version 5.1): A modeling framework for simulating river and stream water quality*, Environmental Assessment Program, Department of Ecology, Olympia, Washington.

[13] Yisa, J., and Jimoh, T., 2010, Analytical studies on water quality index of river Landzu, *Am. J. Appl. Sci.*, 7 (4), 453–458.

[14] Kumar, A., Bisht, B.S., Joshi, V.D., Singh, A.K., and Talwar, A., 2010, Physical, chemical and bacteriological study of water from rivers of Uttarakhand, *J. Hum. Ecol.*, 32 (3), 169–173.

[15] Venkatesharaju, K., Ravikumar, P., Somashekar, R.K., and Prakash, K.L., 2010, Physico-chemical and bacteriological investigation on the river Cauvery of Kollegal stretch in Karnataka, *Kathmandu Univ. J. Sci. Eng. Technol.*, 6 (1), 50–59.

[16] Rinawati, and Takada, H., 2017, Distribution and source of sedimentary Polycyclic Aromatic Hydrocarbon (PAHs) in river sediment of Jakarta, *Indones. J. Chem.*, 17 (3), 394–400.

[17] Arbie, R.R., Nugraha, W.D., and Sudarno, 2015, Studi kemampuan self purification pada sungai Progo ditinjau dari parameter organik DO dan BOD, *Jurnal Teknik Lingkungan*, 4 (3), 1–15.

[18] Chow, M.F., Yusop, Z., and Shirazi, S.M., 2013, Storm runoff and pollutant loading ffrom commercial, residential and industrial catchments in the tropic, *Environ. Monit. Assess.*, 185 (10), 8321–8331.

[19] Baherem, Suprihatin, and Indrasti, N.S., 2014, Strategi pengelolaan sungai Cibanten provinsi Banten berdasarkan analisis daya tampung beban pencemaran air dan kapasitas asimilasi, *JPSL*, 4 (1), 60–69.

[20] Hartwig, M., Schäffer, M., Theuring, P., Avlyush, S., M. Rode, M., and Borchardt, D., 2016, Cause-effect-

response chain linking source identification of eroded sediments, loss of aquatic ecosystem integrity and management options in a steppe river catchment (Khaara, Mongolia), *Environ. Earth Sci.*, 75 (10), 855.

[21] Endayani, S., Sadono, R., Kusumandari, A., and Hartono, 2019, Social and economic vulnerability in the sub-watershed of Karang Mumus, East Kalimantan Province, *JMHT*, 25 (2), 93-103.

Theoretical Study on Molecular Structure and Electronic Properties of New 1,3-Diaza-adamantan-6-ones Derivatives

Haithem Abdulhasan, Ahmed Al-Yasari*, and Rahman Alasadi

University of Kerbala, P.O. Box 1125, Kerbala, Iraq

Abstract: *In this study, the structural geometry and vibrational frequencies (IR) of 1,3-Diaza-adamantane-6-ones derivatives including Adamantane (A), 1,3-Diaza-adamantan (D), 1,3-Diaza-adamantan-6-one (DO), 5-Benzyl-1,3-diaza-adamantan-6-one (BD), 5-(4-Hydroxybenzyl)-1,3-diaza-adamantan-6-one (HBD), 5-(4-Methoxy benzyl)-1,3-diaza-adamantan-6-one (MBD), and 5-(4-Hydroxy-3-methoxybenzyl)-1,3-diaza-adamantan-6-one (HMBD) were theoretically studied. In addition, molecular orbital energies, including the highest occupied molecular orbitals (HOMOs), and lowest unoccupied molecular orbitals (LUMOs), and electronic properties of the titled molecules were theoretically studied using the computational method. Optimized molecular structures were obtained by DFT method with the hybrid B3LYP functional at a relatively small basis set of 6-31G. The calculated vibrational wavenumbers were obtained using the same level of the theory mentioned above. The contributions to the molecular orbitals of adamantane and substituted-phenyl groups in the title compounds were determined. Moving from A to HMBD, a decrease in the value of LUMO and total energy are noticed, while an increase in the value of HOMO is noted. These findings are supported by the decrease in the $E_{HOMO-LUMO}$ gap values. Furthermore, a decrease in the value of ionization potential (IP) is obtained, while an increase in the electron affinity (EA) is observed.*

Keywords: *Adamantane; 1,3-Diaza-adamantan; DFT/B3LYP*

■ INTRODUCTION

Adamantane and its derivatives have fascinating structures due to their various physiological, pharmaceutical, and medical activities [1-6]. It consists of a polycyclic cage molecule with high symmetry representing diamondoids–hydrogen-terminated hydrocarbons with a diamond-like structure [7-8]. Among these derivatives, 1,3-Diaza-adamantane derivatives have attracted great attention due to their interesting properties [9] such as antibacterial, and psychotropic activity [10-11]. Sharabi-Ronen et al. have reported the anti-neoplastic activity of 1,3-Diaza-2-functionalized-adamantan-6-one compounds against melanoma cells [12]. They showed that the ability of the reported compounds to introduce apoptosis in melanoma cells was significant.

1,3-Diazaadamantane-6-one derivatives have attracted considerable attention for diverse applications. Recently, we reported the synthesis of a new series of 1,3-Diaza-adamantane-6-ones derivatives [13]. However, their structural geometry and vibrational properties have not been studied yet. To the best of our knowledge, the quantum chemical calculations on these derivatives have not been done so far. In this study, the molecular structure and the full vibrational spectra have been reported. Moreover, the effect of substitution on electronic properties such as the ionization potential, the electron affinity, electronegativity, and the energy gap between HOMO–LUMO are generally studied.

■ COMPUTATIONAL METHODS

All computational procedures were carried out using GAMESS and Avogadro 1.1.1 [14-15]. The optimization structure of Adamantane (A), including 1,3-Diaza-adamantan (D), 1,3-Diaza-adamantan-6-one (DO), 5-Benzyl-1,3-diaza-adamantan-6-one (BD), 5-(4-Hydroxybenzyl)-1,3-diaza-adamantan-6-one (HBD), 5-

(4-Methoxybenzyl)-1,3-diaza-adamantan-6-one (**MBD**) and 5-(4-Hydroxy-3-methoxybenzyl)-1,3-diaza-adaman tan-6-one (**HMBD**) molecules have been performed using DFT method with the hybrid B3LYP functional at 6-31G level in the gas phase. The applied method is a combination of the Hartree–Fock method and the density functional theory using Becke's three parameter (B3) gradient corrected functionals [15] and Lee–Yang exchange-correlation functional (LYP) [16]. Molecular geometries of all systems were fully optimized at the B3LYP functional with a relatively small basis set of 6-31G level of theory. The stationary points determined with geometry optimization with minimal energy was

confirmed by calculating the normal vibration frequencies with the use of second derivatives at the same level of theory. The energy gap ($E_{HOMO\text{-}LUMO}$ gap), Ionization potential (IP), electron affinity (EA), and the electronegativity (X) have been calculated using equations 1, 2, 3, 4, respectively.

$$E_{HOMO-LUMO} \text{ gap} = E_{LUMO} - E_{HOMO} \qquad (1)$$
$$IP = -E_{HOMO} \qquad (2)$$
$$EA = -E_{LUMO} \qquad (3)$$
$$X = -0.5(E_{HOMO} + E_{LUMO}) \qquad (4)$$

Both the vibrational modes and frequencies were assigned, and the animations of normal modes were visualized by using Avogadro 1.1.1 [17].
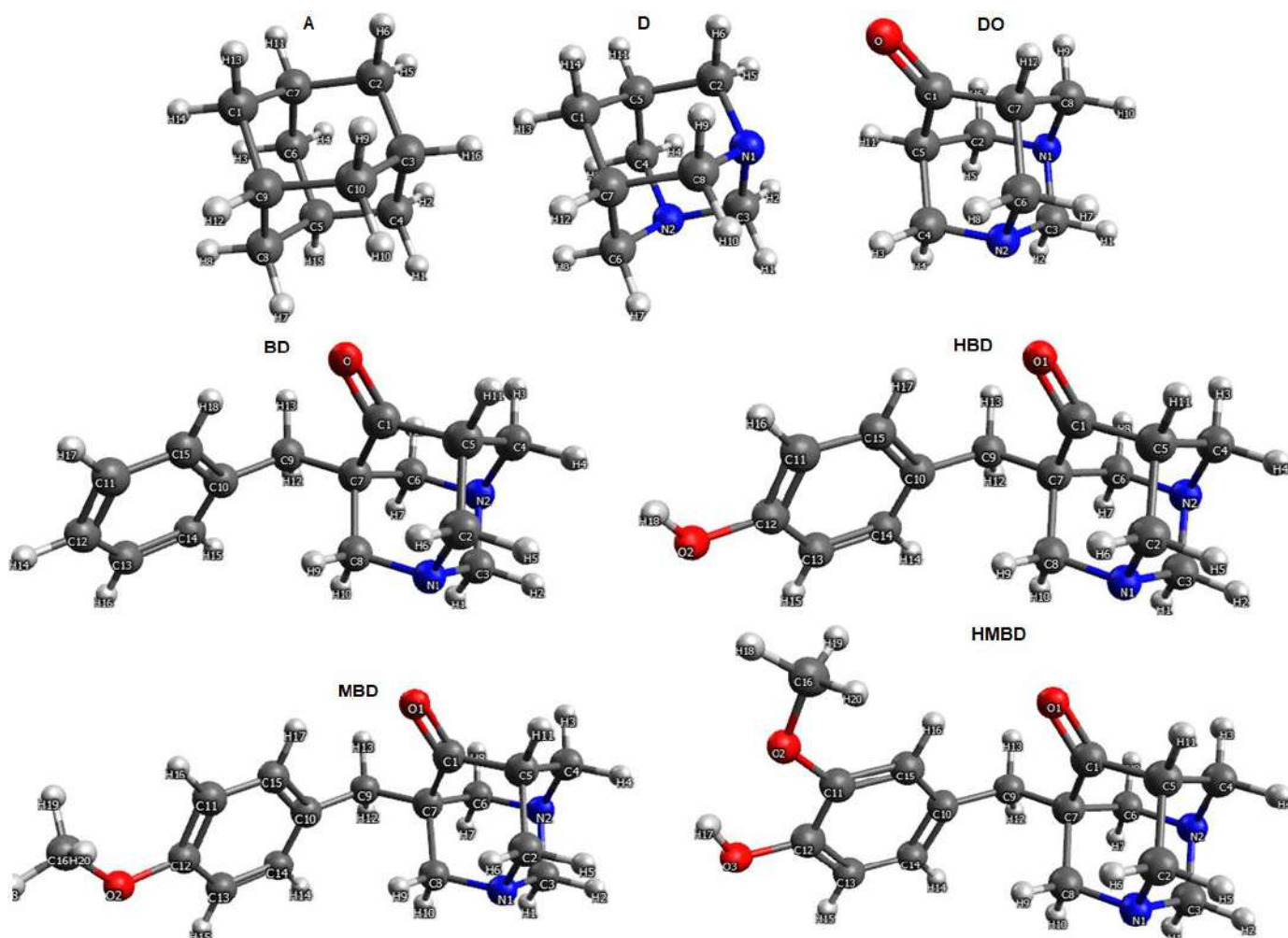
Fig 1. The optimized structure of molecules **A**, **D**, **DO**, **BD**, **HBD**, **MBD**, and **HMBD**

■ RESULTS AND DISCUSSION

Molecular Geometric Structure
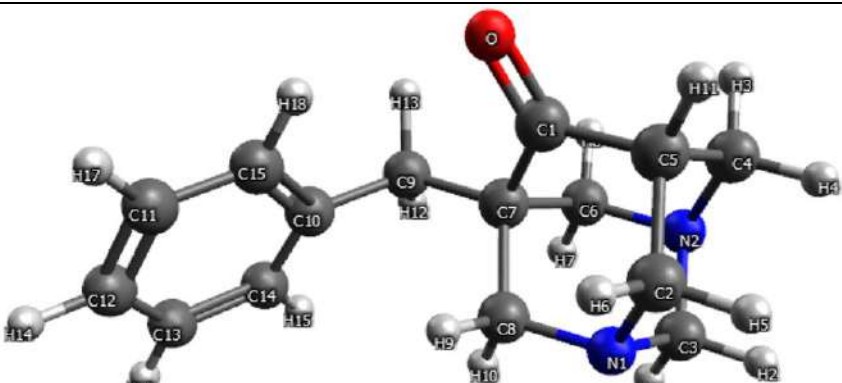
The chemical reactivity and hence, the chemical properties are affected by the change in molecular structure. Therefore, the effect of substitution of 1,3-diaza-adamantan derivatives with their parent Adamantane (**A**), including 1,3-Diaza-adamantan (**D**), 1,3-Diaza-adamantan-6-one (**DO**), 5-Benzyl-1,3-diaza-adamantan-6-one (**BD**), 5-(4-Hydroxybenzyl)-1,3-diaza-adamantan-6-one (**HBD**), 5-(4-Methoxybenzyl)-1,3-diaza-adamantan-6-one (**MBD**) and 5-(4-Hydroxy-3-methoxybenzyl)-1,3-diaza-adamantan-6-one (**HMBD**) have been studied.

Fig. 1 shows the geometric structures of the as-studied molecules as obtained by calculations. Selections of the most important structural parameters of all molecules

are listed in Table 1, and the full details of geometric parameters may be obtained from the author upon request. By considering the data for compound **A** and **D**, upon the substitution of two carbon by two nitrogen, the latter showed an increase in the angle value of N1-C3-N2 due to the effect of lone pair in the nitrogen of the heteroatom. Generally, in all compounds, N-C-N angles are slightly wider than C-N-C angles. In the case of compound **HMBD**, the bond length of C12-O2 is shorter than that in compound **MBD**, but the length of O3-C16 is longer. The C7-C9-C10 angle is slightly wider compared with compound **MBD**, and noticeably wider than the other studied compounds.

The same trend was noticed for the value of C5-C1-C7. The C4-N2-C6 showed a slight increase in its value when moving from compound **D** to **HMBD**. The

Table 1. Selected geometric parameters (bond distances, Å, bond and torsion angles, °) of **A**, **D**, **DO**, **BD**, **HBD**, **MBD**, and **HMBD**

Compound	A	D	DO	BD	HBD	MBD	HMBD
N1-C3-N2 (°)	109.7*	112.6	113	111.6	111.6	111.6	111.6
C2-N1-C8 (°)	-	109.8	109.9	110.2	110.1	110.1	110.2
C4-N2-C6 (°)	-	109.8	109.9	110.3	110.3	110.3	110.3
N1-C2 (Å)	-	1.494	1.464	1.482	1.482	1.483	1.481
N1-C3 (Å)	-	1.488	1.466	1.482	1.482	1.482	1.482
N2-C3 (Å)	-	1.488	1.466	1.486	1.486	1.486	1.486
C5-C1-C7 (°)	109.7"	108.6	110.7	113	112.9	112.9	113
C1-O1 (Å)	-	-	1.213	1.248	1.248	1.248	1.249
C7-C9-C10 (°)	-	-	-	116.5	116.4	117	117.2
C7-C9 (Å)	-	-	-	1.551	1.550	1.548	1.550
C9-C10 (Å)	-	-	-	1.521	1.522	1.522	1.522
C12-O2 (Å)	-	-	-	-	1.395	1.394	1.387
O3-C16 (Å)	-	-	-	-	-	1.451	1.453

In case of A, * = C3-C10-C9, " = C5-C6-C7

same trend was observed in the C2-N1-C8. The C1-O1 in compound **DO** is noticeably shorter than in all compounds due to the effect of the phenyl group in these compounds. The same was noticed for the N-C bond length, where it is remarkably shorter in **DO** compared to the others. The negative hyper-conjugative effect of lone pair in the nitrogen atom toward the carbonyl contributed to the decrease in the N-C bond lengths. These results are in line with those observed in earlier studies by Jiménez-Cruz et al. [18].

Vibrational Frequencies

The IR spectra of molecules were calculated in the range of 0–4000 cm^{-1}. Comparison of the calculated and experimental results show a relatively good agreement despite that the experimental values were recorded in the solid state while the calculated values were studied in the gas phase [13]. However, overestimation of some frequencies was noticed, such as the ν O-H stretching of **HBD**. Future works are needed to address these overestimations and to investigate further effects such as

solvation. Table 2 shows the IR data of the experimental and calculated values of studied molecules. In the case of compound **BD** that was chosen as a model of these series, experimentally [13] absorption bands were shown at 2952 cm^{-1} (ν C-H, benzene), 1464 cm^{-1} (ν C=C, benzene), 880 cm^{-1} (ν C-H, benzene), 1707 cm^{-1} (ν C=O, ketone), 1605 cm^{-1} (ν Ph), which almost coincide with those of maxima obtained theoretically, as shown in Fig. 2.

Generally, in the region of 1680-1730 cm^{-1}, the carbonyl C=O stretching vibrations are observed. In the case of compound **BD,** this band was obtained as a strong band at 1689 cm^{-1}. The band of stretching phenyl (ν Ph) group was noticed in the region of 1550–1650 cm^{-1}. Calculated spectra of the studied compounds can be provided upon request.

Molecular Orbital Energies (HOMO and LUMO Analyses)

The frontier molecule orbitals (FMOs) which refer to the HOMOs and LUMOs, have an important role in

Table 2. FT-IR data of the experimental [13] (and calculated) values of **BD**, **HBD**, **MBD**, and **HMBD**

Compound	ν C=O, ketone/cm^{-1}	ν Ph/cm^{-1}	ν O-H/cm^{-1}	ν OCH3/cm^{-1}
BD	1707	1605	-	-
	(1689)	(1637)		
HBD	1704	1600	3200	-
	(1686)	(1646)	(3600)	
MBD	1713	1609	-	1251, 1127
	(1682)	(1632)		(1250, 1172)
HMBD	1706	1569	3396	1270, 1145
	(1680)	(1561)	(3600)	(1270, 1168)
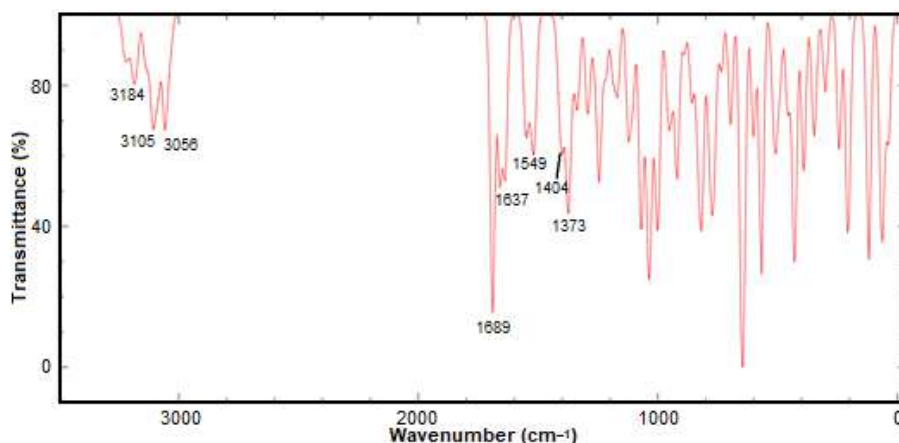
Fig 2. Calculated IR spectra of **BD** in the frequency range of 0–3300 cm^{-1}

chemical reactions, molecular electronic and physiochemical properties such as ionization potential, electron affinity, chemical reactivity, kinetic stability, electronegativity, and electrophilicity [19-20]. The calculated HOMOs and LUMOs of the titled molecules are shown in Fig. 3. Table 3 shows the electronic characteristics calculated for the given molecules: the frontier orbital energies (E_{homo}, E_{lumo}), the zero-point energy (ZPE), and the entropy (S) and final total energy (E_{final}). Generally, the results showed a decrease in final energy of optimized structures as follows: **A** > **D** > **DO** > **BD** > **HBD** > **MBD** > **HMBD**. The results also showed the same trend in the energy of E_{HOMO} and E_{LUMO}; an increase in the energy of E_{HOMO} and a decrease in the energy of E_{LUMO}. This is attributed to the effect of the replacement of carbon atoms with good donor atoms such as nitrogen and oxygen through comparison between molecules **A** and **D**.
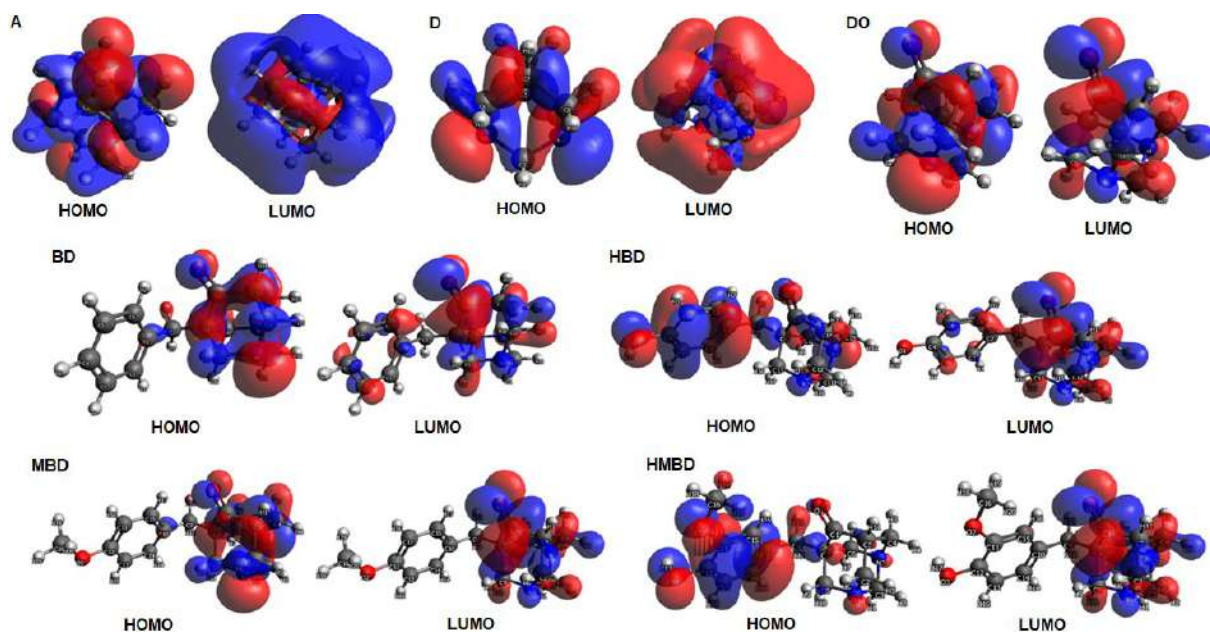
Fig 3. Frontier molecular orbitals of **A**, **D**, **DO**, **BD**, **HBD**, **MBD**, and **HMBD** molecules

Table 3. Calculated basic electronic energy characteristics of the studied compounds at room temperature (298.15 K)

Compound	E_{final}, a.u. (E_{final} kcal/mol)	E_{HOMO}, eV	E_{LUMO}, eV	S, cal/(mol K)	ZPE, kcal/mol
A	-390.348 (-244947.53)	-7.525	2.414	81.192	154.291
D	-422.359 (-265034.71)	-5.217	1.215	80.259	139.339
DO	-496.320 (-311446.10)	-5.797	-0.358	85.088	126.765
BD	-766.448 (-480954.36)	-5.784	-0.526	114.764	196.305
HBD	-841.608 (-528117.68)	-5.745	-0.478	119.739	198.515
MBD	-880.873 (-552756.73)	-5.721	-0.451	126.422	216.776
HMBD	-956.036 (-599922.67)	-5.382	-0.492	132.372	219.081

Table 4. Ionization potential **(IP)**, electron affinity **(EA)** and electronegativity **(X)** values of the studied compounds

Compound	$E_{HOMO-LUMO}$ gap/eV	IP/eV	EA/eV	X/eV
A	9.939	7.525	-2.414	2.5555
D	6.432	5.217	-1.215	2.001
DO	5.439	5.797	0.358	3.0775
BD	5.258	5.784	0.526	3.155
HBD	5.267	5.745	0.478	3.1115
MBD	5.27	5.721	0.451	3.086
HMBD	4.89	5.382	0.492	2.937

When comparing molecule **D** with **DO**, where C=O is introduced, it is clear that the energy E_{HOMO} is slightly decreased. While in the case of molecules **BD**, **HBD**, **MBD**, **HMBD** compared with molecule **A**, changes in the energy of E_{HOMO} and E_{LUMO} are the result from the introduction of the π-system (phenyl group) and donor groups. It is well known that the high value of the E_{HOMO} indicates a strong donor molecule, while the low value of the E_{LUMO} is likely referring to a good acceptor molecule to form stable bonds.

Electronic Properties: HOMO-LUMO Gap Energy ($E_{HOMO-LUMO}$ Gap), Electron Affinity (EA), Ionization Potential (IP), and Electronegativity (X)

The HOMO-LUMO gap energy ($E_{HOMO-LUMO}$ **gap**), Ionization potential (**IP**), electron affinity (**EA**) and electronegativity (**X**) were calculated by using the B3LYP with 6-31G level of theory for the titled molecules, as described in Computational Methods. Table 4 presents the calculated HOMO-LUMO gap energy ($E_{HOMO-LUMO}$ **gap**), Ionization potential (**IP**), electron affinity (**EA**), and electronegativity (**X**) values of the titled molecules calculated using equations 1-4. Generally, when comparing the titled molecules, the $E_{HOMO-LUMO}$ gap is changed as follows: **A > D > DO > BD < HBD < MBD > HMBD**. It is known that IPs and EAs are closely related to the energies of HOMO and LUMO, respectively. It can be seen from Table 4 that the highest IP value is for **A** indicating the more stable molecule with inertness in chemical reactivity. Meanwhile, the lowest IP value is for both **D** and **HMBD** due to the effect of the donor groups in these molecules, indicating more reactive molecules.

The calculated **EA** values of compound **A** and **D** are negative while for the rest of molecules are positive. A close look at these results, molecule **A** is more negative than that of molecule **D**. In the case of **BD**, **HBD**, **MBD**, and **HMBD,** the EA values are positive due to the presence of donor groups. From Table 4, it can also be noticed that the electronegativity (**X**) of the titled molecules are high (positive). These findings are important in many applications, such as corrosion inhibition. Further work is needed to investigate the properties of these materials as a corrosion inhibitor.

■ **CONCLUSION**

To sum up, the structure and physiochemical properties of Adamantane (**A**), 1,3-Diaza-adamantan (**D**), 1,3-Diaza-adamantan-6-one (**DO**), 5-Benzyl-1,3-diaza-adamantan-6-one (**BD**), 5-(4-Hydroxybenzyl)-1,3-diaza-adamantan-6-one (**HBD**), 5-(4-Methoxy benzyl)-1,3-diaza-adamantan-6-one (**MBD**), and 5-(4-Hydroxy-3-methoxybenzyl)-1,3-diaza-adamantan-6-one (**HMBD**) have been revealed at a relatively small basis set by using the DFT calculations with the hybrid B3LYP functional and 6-31G level of theory. The IR spectra of the titled molecules have been calculated in the gas phase. Moving from **A** to **HMBD**, a decrease in the values of LUMO and total energy are noticed, while the values of HOMO increase, indicating the more reactive molecule in the reactions with electrophiles with potential application as a corrosion inhibitor. These findings are supported by the decrease in the $E_{HOMO-LUMO}$ gap values, decrease in the values of **IP**, and increase in the values of **EA**.

■ **REFERENCES**

[1] Štimac, A., Šekutor, M., Mlinarić-Majerski, K., Frkanec, L., and Frkanec, R., 2017, Adamantane in drug delivery systems and surface recognition, *Molecules*, 22 (2), 297.

[2] Savel'eva, S.A., Leonova, M.V., Baimuratov, M.R., and Klimochkin, Y.N., 2018, Synthesis and transformations of aryl-substituted alkenes of the adamantane series, *Russ. J. Org. Chem.*, 54 (7), 996–1002.

[3] Ivleva, E.A., Tkachenko, I.M., and Klimochkin, Y.N.,

2017, Synthesis of adamantane functional derivatives basing on N-[(adamantan-1-yl)alkyl]acetamides, *Russ. J. Org. Chem.*, 52 (11), 1558–1564.

[4] Suslov, E., Zarubaev, V.V., Slita, A.V., Ponomarev, K., Korchagina, D., Ayine-Tora, D.M., Reynisson, J., Volcho, K., and Salakhutdinov, N., 2017, Anti-influenza activity of diazaadamantanes combined with monoterpene moieties, *Bioorg. Med. Chem. Lett.*, 27 (19), 4531–4535.

[5] Hickmott, P.W., Wood, S., and Murray-Rust, P., 1985, Introduction of pharmacophoric groups into polycyclic systems. Part 3. Amine derivatives of adamantane and diaza-adamantane, *J. Chem. Soc., Perkin Trans. 1*, 0, 2033–2038.

[6] Vrynchanu, N.A., Sergienko, O.V., and Maksimov Yu, N., 2009, Research of some sides of antifungal activity mechanism act of new adamantane derivative, *Морфологія*, 3 (2), 24–27.

[7] Schwertfeger, H., Fokin, A.A., and Schreiner, P.R., 2008, Diamonds are a chemist's best friend: Diamondoid chemistry beyond adamantane, *Angew. Chem. Int. Ed.*, 47 (6), 1022–1036.

[8] Gunawan, M.A., Hierso, J.C., Poinsot, D., Fokin, A.A., Fokina, N.A., Tkachenko, B.A., and Schreiner, P.R., 2014, Diamondoids: Functionalization and subsequent applications of perfectly defined molecular cage hydrocarbons, *New J. Chem.*, 38 (1), 28–41.

[9] Karthik, G., Sundaravadivelu, M., Rajkumar, P., and Manikandan, M., 2014, Diaza-adamantane derivatives as corrosion inhibitor for copper in nitric acid medium, *Res. Chem. Intermed.*, 41 (10), 7593–7615.

[10] Arutyunyan, G.L., Paronikyan, R.V., Saakyan, G.S., Arutyunyan, A.D., and Gevorkyan, K.A., 2008, Synthesis and reactions of polyhedral compounds. 29. Synthesis and antibacterial activity of 1,3-diazaadamantane derivatives, *Pharm. Chem. J.*, 42 (1), 18–22.

[11] Arutyunyan, G.L., Dzhagatspanyan, I.A., Nazaryan, I.M., Akopyan, A.G., and Arutyunyan, A.D., 2007, Synthesis and conversions of polyhedral compounds: 28. Synthesis and psychotropic activity of some 1,3-diazaadamantane derivatives, *Pharm. Chem. J.*, 41 (11), 591–593.

[12] Sharabi-Ronen, Y., Levinger, S., Lellouche, M.B., and Albeck, A., 2014, Anti-neoplastic activity of 1,3-diaza-2-functionalized-adamantan-6-one com pounds against melanoma cells, *Med. Chem.*, 10 (1), 27–37.

[13] Kuznetsov, A.I., Alasadi, R.T., Senan, I.M., and Serova, T.M., 2014, Synthesis of fragrant 1,3-diazaadamantan-6-ones, *Russ. Chem. Bull.*, 63 (9), 2195–2197.

[14] Gordon, M.S., and Schmidt, M.W., 2005, "Advances in electronic structure theory: GAMESS a decade later" in *Theory and Applications of Computational Chemistry: The first forty years*, Eds. Dykstra, C., Frenking, G., Kim, K., and Scuseria, G., 1st Ed., Elsevier Science, Amsterdam, 1167–1189.

[15] Becke, A.D., 1993, A new mixing of Hartree–Fock and local density-functional theories, *J. Chem. Phys.*, 98 (2), 1372.

[16] Fernández, M.J., Gálvez, E., Lorente, A., Camuñas, J.A., Sanz, J., and Fonseca, I., 1990, Synthesis, structural and conformational study of 6-hydroxy (or acyloxy) derivatives of the 1,3-dimethyl-1,3-diazoniatricyclo[3.3.1.1$^{3-7}$]decane system, *J. Heterocycl. Chem.*, 27 (5), 1355–1359.

[17] Hanwell, M.D., Curtis, D.E., Lonie, D.C., Vandermeersch, T., Zurek, E., and Hutchison, G.R., 2012, Avogadro: An advanced semantic chemical editor, visualization, and analysis platform, 2012, *J. Cheminform.*, 4 (1), 17.

[18] Jiménez-Cruz, F., Ríos-Olivares, H., and Gutiérrez, J.L.G., 2005, "Molecular structure in 1-azaadamantanes and 1,3-diazaadamantanes" in *Structural Analysis of Cyclic Systems*, Eds. Iriepa, I., Research Signpost, Trivandum, India, 101–125.

[19] Parr, R.G., Donnelly, R.A., Levy, M., and Palke, W.E., 1978, Electronegativity: The density functional viewpoint, *J. Chem. Phys.*, 68 (8), 3801.

[20] Figueredo, S., Páez, M., and Torresbc, F., 2019, The electrophilic descriptor, *Comput. Theor. Chem.*, 1157, 34–39.

Preliminary Study of Poly(Tetrahydrofurfuryl Acrylate) Thin Film as a Potential Material of Ion Selective Electrodes: The Case of Nitrate Ion-Selective Electrode

Sagir Alva[1,*], Robi Suherman[1], Vivi Friliandita[1], Deni Shidqi Khaerudini[1,2], Edy Herianto Majlan[3], and Aiman Sajidah Abd Aziz[4]

[1]*Mechanical Engineering Department, Faculty of Engineering, Universitas Mercu Buana, Jl. Meruya Selatan No. 01, Kembangan, Jakarta-11650, Indonesia*

[2]*Research Center for Physics, Indonesian Institute of Science (LIPI), Kawasan Puspiptek, Serpong, Tangerang Selatan 15314, Indonesia*

[3]*Fuel Cell Institute, Universiti Kebangsaan Malaysia, UKM, 43600 Bangi, Selangor, Malaysia*

[4]*Nanoelectronics Lab, MIMOS Semiconductor Sdn. Bhd., Technology Park Malaysia, 57000, Kuala Lumpur, Malaysia*

Abstract: *A preliminary study on the use of a photocurable poly-tetrahydrofurfuryl acrylate (pTHFA) has been successfully performed as an alternative membrane for application in the Ion-Selective Electrode (ISE) sensors such as Nitrate-ISE. The pTHFA membrane was synthesized using photopolymerization technique and further optimized by varying the concentration of the photo-initiator. The pTHFA photopolymer was characterized by C-NMR, H-NMR, FTIR, and DSC. The best sensing formulation comprising pTHFA photopolymer was obtained from composition II with T_g of -17.3 °C. In the Nitrate-ISE fabrication process, initially, the tetraoctylammonium nitrate (TOAN) ionophore was optimized. The optimum TOAN concentration of 4.2 mg was then immobilized onto composition II as a sensing matrix. Results showed that the pTHFA based ISE sensor exhibited a slope near the Nernstian number with a good linear response for detecting nitrate ion concentration between 10^{-1} to 10^{-4} M ($r^2 = 0.9994$) and limit of detection as low as 3.47×10^{-5} M. Furthermore, the selectivity behavior of pTHFA based nitrate-ISE sensor was determined in various types of interfering ions such as SO_4^{2-}, $H_2PO_4^-$, HPO_4^{2-}, Cl^- and I^-. The sensor has demonstrated selectivity coefficient of -2.27 ± 0.2, -2.49 ± 0.6, -2.18 ± 0.8, -1.31 ± 0.1 and 0.41 ± 0.2, respectively. The fabricated pTHFA ISE-Nitrate sensor was further tested in the fish ponds, soils, and also rivers. The sensors have shown excellent performance and is comparable to the standard method.*

Keywords: *pTHFA; Nitrate-ISE; photopolymer; T_g*

■ INTRODUCTION

In the last few decades, the measurement technology of the ion-selective electrodes (ISE) has been growing, including in terms of the electrode design, membrane type, material recognition, membrane preparation techniques, and the target ions [1]. Umezawa in 1990 had recorded over 190 types of anions, cations, or non-ionic elements that can be measured using the ISE, including the nitrate ions [2].

In addition, the measurements using ISE have been applied in various fields, such as health, the environment, food, agriculture, aquaculture, and many other fields [3]. The widespread use of ISE is inseparable from the benefits offered by ISE as it is capable of measuring in a wide range, unaffected by sample color or turbidity, does not require large samples, can be made portable, offers rapid process of the measurement, easy to operate and has lower cost of measurement compared to other methods [4].

Some research reports have used acrylic-based membrane materials to substitute conventional polyvinyl chloride (PVC) in the development of the ISE sensors [5-

646

Indones. J. Chem., 2020, 20 (3), 645 - 654

8]. Acrylate based membranes including photopolymerized tetrahydrofurfuryl acrylate (pTHFA) generally has several advantages over PVC based membranes, among others, this polymer can be prepared by rapid preparation time, requires minimal solvent, no plasticizer required and exhibits good adhesion properties to the electrode surface [9]. However, the most common acrylates used are based on poly(butyl acrylate) or methyl methacrylate-butyl acrylate copolymers, which show major physical deficiency such as being overly sticky or having a glue-like property. The acrylic-based membrane drawbacks will cause impurities to be easily attached to the membrane surface, which will later interfere with the sensing ions diffusion process into the membrane during the ISE measurement process. In addition, the acrylic-based membrane also demonstrated a low diffusion coefficient which will increase the resistance value. To overcome this, it is usually necessary to have a long hydration process time in order to obtain a stable sensor response [10].

Hence in this study, a simple and rapid fabrication of a photopolymerized tetrahydrofurfuryl acrylate (pTHFA) based membrane was introduced. This membrane has a hydrophilic characteristic, so the target ions are still able to diffuse into the membrane [11-12]. A preliminary study of using pTHFA photopolymer as an alternative ISE sensing matrix membranes to determine nitrate ions was also conducted.

The nitrate ion is a type of anion that is used as an indicator to determine water quality and soil fertility. The nitrate ion becomes dangerous if it accumulates in the human body in concentrations of more than 500 ppm, where the nitrate ions can be transformed into nitric acid through chemical reactions, which in turn can oxidize ferrous ions in the blood and could decrease the ability of blood to carry oxygen to the whole body [13]. In addition, nitrate ions can be transformed into toxic nitric ions through the reactions of the nitrogen cycle.

■ EXPERIMENTAL SECTION

Materials

The materials used in this study were tetrahydrofurfuryl acrylate monomer (THFA, ≤ 100%), tetraoctylammonium nitrate (TOAN, Selectophore, ≥

99.0%), 2-hydroxyethyl hethacrylate (HEMA, ≥ 99%), 1,6-hexanediol diacrylate (HDDA, technical grade, 80%) and 2-dimethoxy-2-phenylacetophenone (DMPP, 99%) from Sigma Aldrich, salts such as KCl (for molecular biology, ≥ 99.0%), KNO_3 (ReagentPlus®, ≥ 99.0%), $K_2HPO_4 \cdot 3H_2O$ (ReagentPlus®, ≥ 99.0%), KH_2PO_4 (ACS reagent, ≥ 98%), K_2SO_4 (ReagentPlus®, ≥ 99.0%), KI (ACS reagent, ≥ 99%), pyrrole monomer (Py, reagent grade, 98%), HCl (ACS reagent, 37%), CH_3Cl (≥ 99.5%) from Merck, and also deionized water.

Instrumentation

Cyclic voltammetry (CV) was performed using CS350 electrochemical workstation with a three-electrode system including a saturated calomel reference electrode (SCE) and a platinum (Pt) electrode counter electrode (Wuhan CorrTest Instruments Corp. Ltd). A screen-printed electrode (S3PE) working electrode was purchased from Scrint Print. Bhd, wherein the electrode consists of silver and carbon track on the same strip as shown in Fig. 1. An ultraviolet (UV) exposure box (Huanyu Instruments) was used for photopolymerization of the pTHFA membrane. The thermal analyzer device TGA/DSC (Linsesis DTA PT1600), FTIR (Thermoscientific Nicolet iS-10), and NMR 400 MHz (Bruker) were used to analyze polymeric material properties. UV-Vis Spectrophotometer UV1800/PC Laboratory (Shanghai Meipuda) were used for real samples and validation tests.

Procedure

Firstly, the pTHFA membrane was synthesized and characterized in order to obtain a photocurable sensing polymeric host matrix. The pTHFA photocurable polymer was prepared by varying the composition between THFA monomer, HDDA cross-linker agent, and DMPP photoinitiator as shown in Table 1.
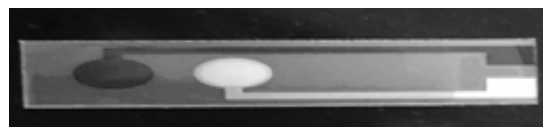

Fig 1. Single strip screen-printed electrode (S3PE) with double electrode (black = carbon electrode, grey = silver electrode)

Table 1. Composition of pTHFA membranes

Membrane	THFA (µL	HDDA (mg	DMPP (mg
I	100	1.6	0.8
II	100	1.6	1
III	100	1.6	2
IV	100	1.6	3
V	100	1.6	4
VI	100	1.6	5

The mixture was then deposited onto an aluminum plate placed in the UV exposure box. Photopolymerization process was carried out for 2.5 min under a nitrogen gas atmosphere until a thin film layer was formed on the aluminum plate. Subsequently, the photopolymerized thin films were analyzed using C-NMR, H-NMR, and FTIR instruments for structural determination while polymeric thermal properties analysis were characterized using the DSC instrument.

The selected pTHFA composition was used further for Nitrate-ISE sensor fabrication. S3PE carbon electrode was used as a sensor transducer. Polypyrrole (PPy) conducting polymer was deposited onto S3PE carbon surface using a cyclic voltammetry technique potential with sweep window of -1 V to 1 V and a scan rate of 100 mV/sec for 7 cycles. During the PPy coating process, the S3PE carbon electrode functioned as a working electrode, the Pt electrode acted as a counter electrode, and the SCE electrode was used as a reference electrode. The three electrodes were immersed in a mixture containing 0.5 M Py monomer and 0.1 M KCl, in which all three electrodes were also connected to a CS350 electrochemical workstation device. The dark purple layer formed on the S3PE carbon electrode surface indicated the formation of the Ppy conducting polymer.

As much as 1 µL of HEMA/DMPP mixture with a ratio of 200 µL:2 mg was further coated on the PPy electrode which had been prepared previously. The coated electrode was then placed into the UV exposure box and photopolymerized for 3.5 min under constant nitrogen gas flow. The pHEMA thin film layer formed was subsequently hydrated with 4.5 µL 0.01 M KNO_3 solution for 15 min. The pHEMA film functioned as an inner layer of the Nitrate-ISE system.

The selected pTHFA mixture from Table 1 was further added with TOAN nitrate sensitive ion exchange ranging from 3.6 to 4.5 mg. 5 µL of the mixture was fabricated onto the surface of the hydrated pHEMA layer and placed in the UV exposure box under constant nitrogen gas flow for 2.5 min to form a nitrate-ISE sensor. The nitrate ISE sensors were measured in the standard nitrate solution in the range of 10^{-1} to 10^{-8} M to determine the Nernstian number, linear range, and limit of detection (LOD). The selectivity coefficient of the fabricated sensor was further evaluated using a separate solution method (SSM), where the interference ions studied were Cl^-, $H_2PO_4^-$, HPO_4^{2-}, SO_4^{2-} and also I^-. The concentration of the test solution used for each ion was 0.1 M.

The best pTHFA based Nitrate-ISE was further used for testing real samples (fish ponds, soils, and rivers) and validated using the standard method of APHA Ed.22nd 4500-NO3-E2012. As much as 50 mL of filtered sample was added to 1 mL of 1 N HCl and mixed evenly. Furthermore, a calibration solution from 1 to 100 ppm of NO_3^- was added with 2 mL of CH_3Cl solution as a preservative. After that, absorbance measurements were carried out with a spectrophotometer equipment at 220 nm wavelength for NO_3^- and 275 nm readings for interference dissolved in organic matter. Then to calculate the NO_3^- concentration in the sample, a plot of the calibration curve was made between the concentration of the calibration solution and the absorbance value, where the absorbance value used was the difference between the observance at the measurement of 275 nm and 220 nm.

■ **RESULTS AND DISCUSSION**

Synthesis and Characterizations of pTHFA

The polymer membrane is one of the most important components in ISE sensor fabrication. Usually, the membrane used is a thin film placed on the surface of the transducer electrode [14]. The failure in the selection of a suitable membrane results in failure of the ISE sensor to function. One of the most important conditions of the membrane that can be used is the ability of the membrane to allow ions to enter the

membrane to the transducer surface so that it can be detectable, which depends on the value of T_g [15]. In addition, the membrane must have high mechanical strength; thus, it would not easily break when being used during sample measurements [7-8].

In this study, the membrane is based on acrylic, namely the pTHFA. The selection of the pTHFA membrane is based on the fact that so far, no membrane has been found to be ideal for ISE sensor fabrication. The typical ISE membrane used today is based on PVC, developed by Bloch and co-worker in the late 1960s [16]. However, the PVC membrane has several disadvantages.

In this study, the polymerization process of the THFA was carried out by the process of photopolymerization modified from a previous study [17]. In regards to its applications, pTHFA is still limited in medical applications such as artificial organs and for drug delivery [18]. In this preliminary study, it is necessary to optimize the synthesis of pTHFA and perform some basic characteristics tests such as structural analysis and Tg, wherein for structural analysis, the sample used is a sample with a THFA/DMPP ratio of 100:1 to represent the whole sample.
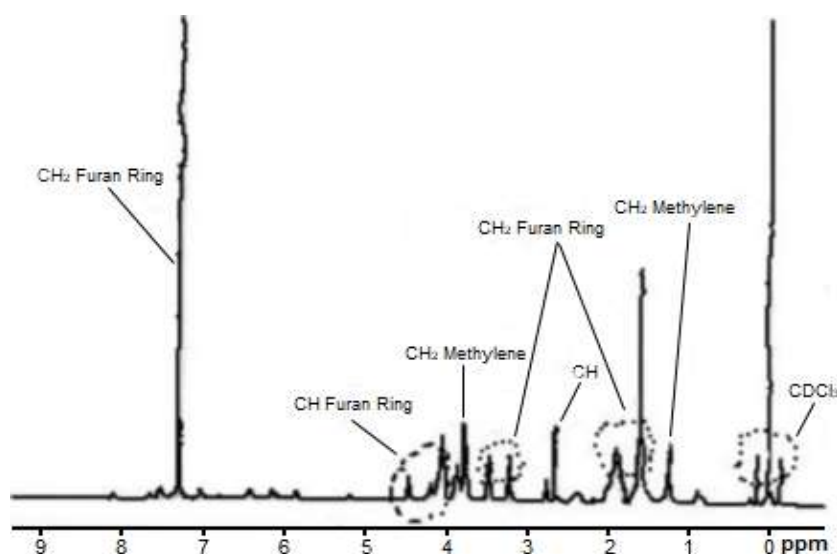

Fig 2. H-NMR graph of poly(tetrahydrofuryl acrylate) (pTHFA) photopolymer using NMR 400 MHz in CDCl₃
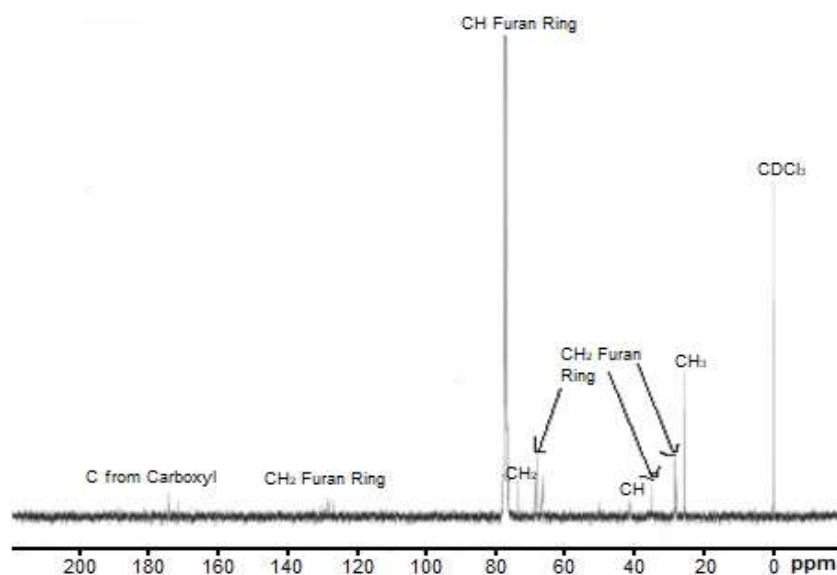
Fig 3. C-NMR graph of poly(tetrahydrofuryl acrylate) (pTHFA) photopolymer using NMR 400 MHz in CDCl₃
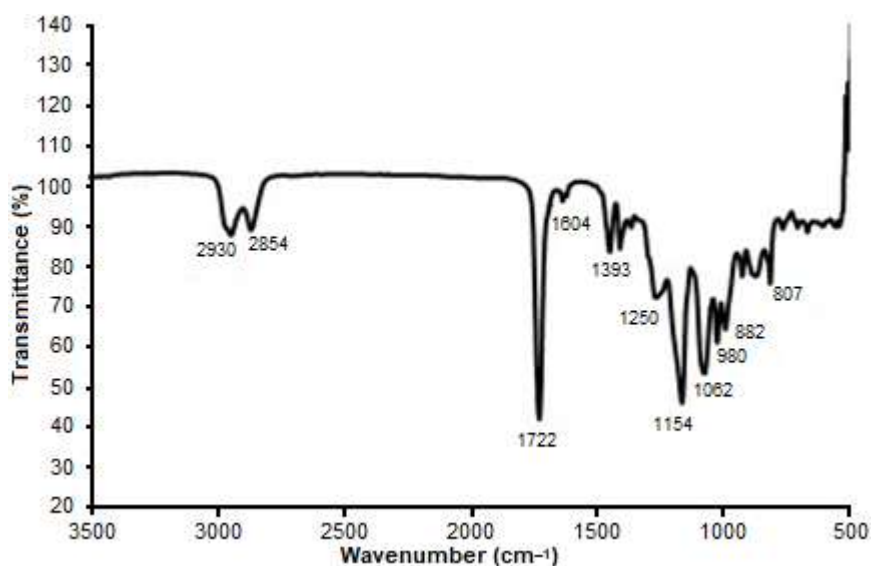
Fig 4. FTIR graph of poly(tetrahydrofuryl acrylate) (pTHFA) photopolymer

In this study, the structural analysis was performed by using C-NMR and H-NMR, in which the solvent used was $CDCl_3$, as shown in Fig. 2 and 3. The H-NMR analysis produced several peaks in chemical shift in regions 1.8, 2.6, 3.4, 3.8, 4, 4.4 and 7.2 ppm, whereas the peak of the C-NMR analysis was identified in 25.6, 28.2, 35, 41.37, 66.5, 73.7, 77.1, 125 and 174.2 ppm, whereas in regions 7.2 and 174.2, specific aromatic heteroatom groups were identified as furan rings [17].

Besides analysis using NMR, the analysis of the pTHFA structure was also done by using FTIR, in which the results can be seen in Fig. 4.

Fig. 4 shows several bands, two bands at 2930 cm^{-1} and 2854 cm^{-1} are stretching vibrations showing a set of C-H functional groups representing -CH$_3$ and -CH$_2$. Meanwhile, the band at 1722 cm^{-1} is a carbonyl functional group (C=O) derived from carboxylate acrylate. In this FTIR spectrum, there is also a weak bending vibration band at 1604 cm^{-1}. This band is attributed to the -OH functional group derived from the presence of a small amount of water from air trapped in the polymer. Two other bands are also seen at 1393 and 807 cm^{-1}, which are vibrations of the α-methyl functional group. Meanwhile, the stretching vibration is also seen in the band area of 1154 and 1210 cm^{-1} derived from -C-O-C-. Also seen from the FTIR spectra are the bands at 1062, 980, and 882 cm^{-1} regions, which are typical bands of the acrylic membranes [19].
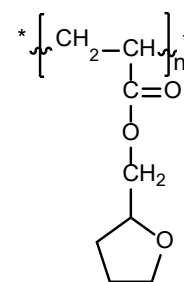
Fig 5. Structure of poly(tetrahydrofuryl acrylate) (pTHFA) photopolymer

Based on the combination of data obtained from NMR and FTIR, the structure of the pTHFA is shown in Fig. 5.

To obtain a suitable pTHFA membrane, the polymer synthesis optimization process was focused on adding a variety of the photo-initiator concentration into THFA monomer. In the process of the photopolymerization, the photo-initiator plays an important role to help the process of free radical formation of the monomer in which the photo-initiator will be active after exposure to UV lights [20-21]. The amount of the photo-initiators used should be appropriate since the amount of photo-initiators will affect the length of the polymer chain and the physical properties of the polymer which is certainly closely related to the resulting Tg of the polymer [22]. In this study, the T$_g$ of the polymer was measured using DSC and can be seen in Table 2.

Table 2. T_g of pTHFA photopolymer with the various weight of DMPP

Membrane	T_g (°C
I	not formed
II	-17.3
II	-15.2
III	-12.8
IV	-9.7
V	-7.2

From Table 2, we can see that the higher concentration of the added photoinitiator increased the T_g value. This indicates that the resulting pTHFA membrane was getting harder. This is inseparable from the fact that a large concentration of the photo-initiator will produce enough energy to form a polymer. Table 2 also shows that in membrane composition I (pTHFA I) with the use of 0.8 mg DMPP, the polymerization process did not occur. This is because, in the amount of DMPP < 1%, the polymerization process is very difficult to occur and requires a longer time between 10 min to 2 h [6]. The T_g value obtained in this study was not too different from the previous research that was between -7.5 °C–-17.3 °C [17], hence pTHFA II with the value of -17.3 °C was then selected to be applied to Nitrate-ISE fabrication. This value was chosen because of it was very close to the commonly used value for ISE sensor fabrication, i.e., between -40 °C to 15 °C [6,23-24].

Nitrate ISE

The nitrate ion is one of the most important nutrients for plants, but an excessive amount of nitrate in water can cause algae bloom which disrupts the environment [25]. In addition, a high level of nitrate concentrations may also affect human health as described in the introduction section of this article. Various analytical methods have been used to quantify nitrate level. One of the fast, on-site nitrate measurement is using ISE-nitrate [26].

In the ISE-nitrate sensor fabrication, the membrane plays a very important role in which it serves as a support matrix to contain the sensing active components which allow only the targeted ion to diffuse towards the sensor transducer [16]. In this study, the pTHFA II membrane was used as a support matrix for ISE-nitrate sensor fabrication. In order to form a sensing matrix, the pTHFA II membrane needs to be incorporated with active ingredients. TOAN is the most common active ingredient used in Nitrate-ISE sensor fabrication and has been used by previous researchers [27]. The insufficient amount of the active materials and TOAN ion exchanger in the membranes will affect the membrane characteristics, and this impacts the poor ISE response towards nitrate ions [28-29].

In this paper, the optimization process of the Nitrate-ISE sensor fabrication was conducted with four different compositions, in which the results of the performance tests can be seen in Table 3. The electromotive force (EMF) response curve of nitrate ISEs to varying TOAN amounts are shown in Fig. 6. In general, all the pTHFA membrane-based sensor compositions responded to the nitrate ions where the response slopes varied from -39.5 to -55.3 mV/dec. This indicates that the prepared pTHFA membrane has the potential to be applied as the ISE sensor host matrix membrane.

The photocurable pTHFA II membrane exhibited excellent soft and flexible physical characteristics. This is in agreement with its T_g value of -17.3 °C from the DSC study. Due to its excellent properties, pTHFA II host matrix allows diffusion of ions to enter the membrane to interact with TOAN and cause the potential changes on the surface of the C/PPy transducer [6].

Based on the data presented in Table 3, it showed that an optimized TOAN of 3.9 mg and 4.2 mg demonstrated values close to the Nernstian value of -59.16 mV/dec for the monovalent ion and lowest

Table 3. Performance of Nitrate-ISE within the variety of the TOAN

TOAN (mg	Slope (mV/dec	Linear Range (M	Detection Limit, (LOD (M	R^2
3.6	-39.5	$0.1–10^{-3}$	3.31×10^{-4}	0.9951
3.9	-55.3	$0.1–10^{-3}$	8.32×10^{-4}	0.9991
4.2	-52.7	$0.1–10^{-4}$	3.47×10^{-5}	0.9994
4.5	-46.2	$0.1–10^{-3}$	4.57×10^{-4}	0.9983
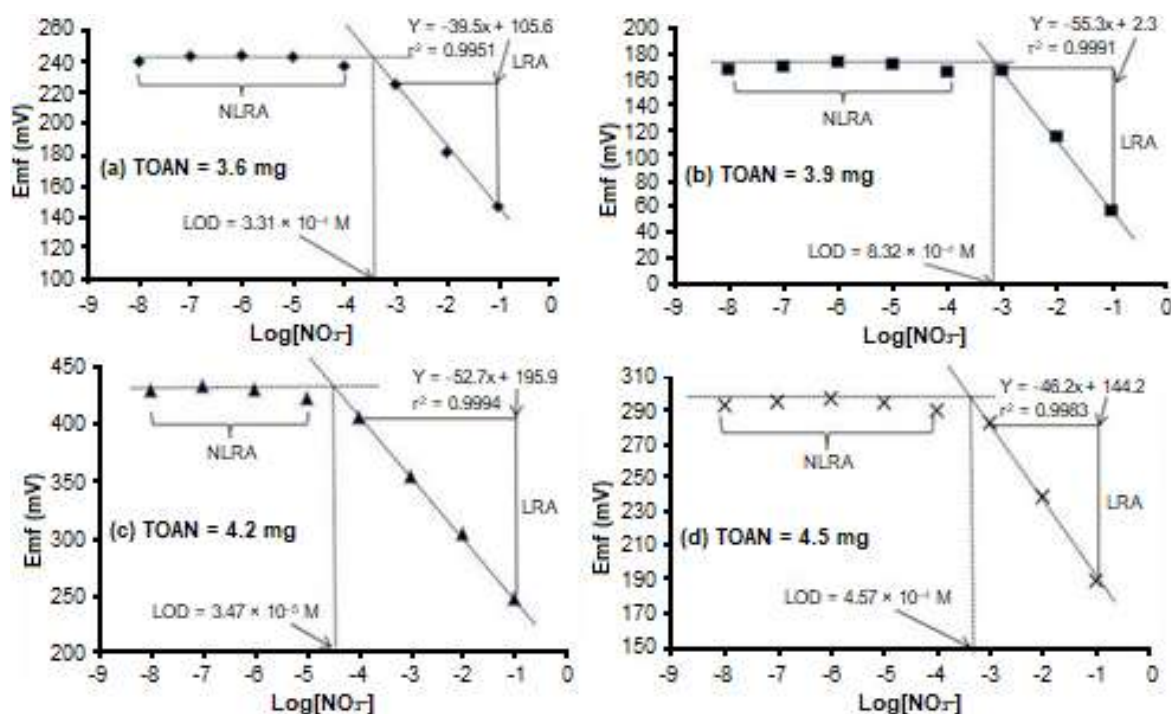
Fig 6. Response Nitrate-ISE sensors in various concentrations of the nitrate solutions

detection limit (LOD) of 8.32×10^{-4} M and 3.47×10^{-5} M. In contrast, a sensor with TOAN of less than 4.2 mg exhibited a shorter linear range detection area of 10^{-1} M to 10^{-3} M, including the use of 3.6 mg TOAN which only gave a slope value of -39.4 mV/dec which is far from the standard value of the Nernstian number. This is attributed to the lowest TOAN amount. The insufficient TOAN amount has caused disruption of the nitrate ions to diffuse into the pTHFA membrane. According to 1994 IUPAC, the slope value of the linear range area (LRA) is the Nernstian number, whereas the determination of the Nernstian number is done by measuring the different potential of each concentration of the calibration solution in the linear range area. Meanwhile, the determination of LOD is done by using the method of the intersection of imaginary lines between the lines of the linear range area with the line area of the non-linear range (NLRA) as shown in Fig. 6 [14].

The higher amount of sensitive ion exchange allowed more complexation to occur between nitrate ions and TOAN. Thus more influx of nitrate ions were attracted onto the membrane. When the TOAN amount increased over 4.2 mg, the slope of the ISE-nitrate sensor

reduced to -46.2 mV/dec. This was due to the change of membrane polarity where the membrane became more hydrophilic, which resulted in leaching of the active component from the sensing matrix. Sufficient amount of the TOAN ion exchanger is crucial to produce a good nitrate sensor performance [28-29].

Based on the sensor performance obtained from Table 3, the Nitrate-ISE sensor with 4.2 mg TOAN was selected for the selectivity coefficient test using the SSM method. This selectivity coefficient test is important in order to see the ability of the sensor response to the presence of the interfering ions [30]. The results of the coefficient test are presented in Table 4. Based on the

Table 4. Coefficient selectivity ($LogK_{a,b}^{pot}$ of the ISE - nitrate in various of interference ions with concentrations 0.1 M (N = 3 measurements

Interfering ions	$LogK_{a,b}^{pot}$
I^-	0.41 ± 0.2
Cl^-	-1.31 ± 0.1
$H_2PO_4^-$	-2.49 ± 0.6
HPO_4^{2-}	-2.18 ± 0.8
SO_4^{2-}	-2.27 ± 0.2

Table 5. Comparison of the measurement results of NO_3^-- ions in various real samples between sensors vs. APHA Ed.22nd 4500-NO3-E2012

Type of Samples	Sensors (ppm (n = 3	APHA Ed.22nd 4500-NO3-E2012 (ppm (n = 3
Fish ponds	23.8 ± 2.1	21.7 ± 1.5
Soils	32.1 ± 1.7	33.8 ± 0.7
Rivers	8.2 ± 0.5	7.9 ± 0.8

results, the highest logarithm, selectivity coefficient of the nitrate ion was towards iodide ion (I^-) which was 0.41 ± 0.2, and the lowest was towards dihydrogen phosphate ($H_2PO_4^-$) ion with a value of -2.49 ± 0.6. This result is inseparable from the Hofmeister series, which is a series of ionic ability to enter into the membrane, that shows iodide ion (I^-) can easily dissolve in an organic membrane. This will certainly accelerate the diffusion process of ion I^- into the membrane and impair the Nitrate-ISE sensor [31].

Real Sample Test

In developing a sensor, testing a real sample is a compulsory test that must be done. This is because real samples contain many other ion species, which makes it possible to cause interference with sensor readings. By testing with real samples, it can be seen whether the sensors that have been developed can work well even with the presence of other ions in the sample. Apart from that, testing with real samples must be followed by validation using the standard method, thus the measurement results from the sensors that have been developed can be believed to be true [32].

The real samples, i.e., soil samples, fish ponds, and river water, were used in this study. The selection of these samples was based on the fact that NO_3^- ions are one of the important parameters for the three samples. In soil, NO_3^- ions are needed by plants as a source nitrogen for the growth process. Meanwhile, in fish ponds and rivers, the number of excess NO_3^- ions can have a negative impact. This is because NO_3^- ions in the water can turn into NO_2^- ions or NH_3 molecules through the Nitrogen cycle, which are toxic to aquatic life. Besides that, the excess NO_3^- ions can cause Algae Bloom phenomena, which can greatly disrupt the aquatic ecosystem [25].

The test results of NO_3^- ions levels in the three real samples are shown in Table 5, where the results of measurements with the Nitrate-ISE sensors based on pTHFA films were also validated using the standard method, APHA Ed.22nd 4500-NO3-E2012.

Based on the data shown in Table 5, it can be seen through the measurement results that there is no significant difference between the sensors and the standard method. This indicates that the developed sensors could work well, and the interfering ions in the sample did not inhibit the response of the Nitrate-ISE sensor in the measurement process.

■ **CONCLUSION**

The pTHFA membranes prepared by photopolymerization technique have been successfully applied as an alternative membrane for the Nitrate-ISE sensor. The excellent sensor performance can be seen from the Nernstian number, LOD, linear range, and selectivity coefficient against some interfering ions. A low T_g polymeric membrane for sensing host matrix was achieved through this study. In addition, the pTHFA based Nitrate-ISE sensor tested in real samples had successfully demonstrated a comparable result to the standard method. It can be seen that there is a high potential of pTHFA application in ISE sensor technology.

■ **ACKNOWLEDGMENTS**

■ **REFERENCES**

[1] Makarychev-Mikhailov, S., Shvarev, A., and Bakker, E., 2008, "New trends in Ion-Selective Electrodes" in *Electrochemical Sensors, Biosensors and their Biomedical Applications Hand Book*, Eds. Zhang, X., Ju, H., and Wang, J., Academic Press, San Diego, 71–114.

[2] Umezawa, Y., 1990, CRC Handbook of Ion-Selective Electrodes: Selectivity Coefficients, 1st Ed., CRC Press, Boston.

[3] Criscuolo, F., Taurino, I., Stradolini, F., Carrara, S., and Micheli, G.D., 2018, Highly-stable Li+ ion-selective electrodes based on noble metal nanostructured layers as solid-contacts, *Anal. Chim. Acta*, 1027, 22–32.

[4] Alva, S., Aziz, A., Syono, M.I., and Sebayang, D., 2017, Development of solid-state reference electrode based on sodium polyanethol sulfonate immobilised on cellulose acetate, *J. Phys. Sci.*, 28 (2), 161–179.

[5] Dumschat, C., Frömer, R., Rautschek, H., Müller, H., and Timpe, H.J., 1991, Photolithographically patternable nitrate-sensitive acrylate-based membrane, *Anal. Chim. Acta*, 243, 179–182.

[6] Lee, Y.H., and Hall, E.A.H., 2001, Assessing a photocured self-plasticized acrylic membrane recipe for Na+ and K+ ion-selective electrodes, *Anal. Chim. Acta,* 443 (1), 25–40.

[7] Lee, Y.H., Alva, S., and Ahmad, M., 2004, Ammonium ion sensor based on photocured and self-plasticizing acrylic films for the analysis of sewage, *Sens. Actuator B-Chem.*, 98 (2-3), 160–165.

[8] Alva, S., Heng, L.Y., and Ahmad, M., 2006, Screen-printed potassium ion sensor fabricated from photocurable and self-plasticized acrylic film, *J. Phys. Sci.*, 17 (2), 141–150.

[9] Lee, Y.H., and Hall, E.A.H., 2000, Producing "self-plasticizing" ion-selective membranes, *Anal. Chem.*, 72 (1), 42–51.

[10] Michalska, A., Wojciechowski, M., Bulska, E., Mieczkowski, J., and Maksymiuk, K., 2009, Poly(n-butyl acrylate) based lead(II) selective electrodes, *Talanta*, 79 (5), 1247–1251.

[11] Takebe, Y., and Shirota, Y., 1994, Poly (tetrahydrofurfryl acrylate) as a new host polymer for polymer-salt hybrid ionic conductors, *Solid State Ionics*, 68 (1-2), 1–4.

[12] Mochizuki, A., Hatakeyama, T., Tomono, Y., and Tanaka, M., 2009, Water structure and blood compatibility of poly(tetrahydrofurfuryl acrylate), *J. Biomater. Sci., Polym. Ed.*, 20 (5-6), 591–603.

[13] Khanfar, M.F., Al-Faqheri, W., and Al-Halhouli, A., 2017, Low-cost lab on a chip for the colorimetric detection of nitrate in mineral water products, *Sensors*, 17 (10), 2345.

[14] Buck, R.P., and Lindner, E., 1994, Recommendations for the nomenclature of ion-selective electrodes, *Pure Appl. Chem.*, 66, 2527–2536.

[15] Yun, S.Y., Hong, Y.K., Oh, B.K., Cha, G.S., Nam, H., Lee, S.B., and Jin, J.I., 1997, Potentiometric properties of ion-selective electrode membranes based on segmented polyether urethane matrices, *Anal. Chem.*, 69 (5), 868–873.

[16] Pretsch, E., 2007, The new wave of ion-selective electrodes, *TrAC, Trends Anal. Chem.*, 26 (1), 46–51.

[17] Kaya, N.U., Onen, A., and Guvenilir, Y., 2017, Photopolymerization of acrylates by enzymatically synthesized PCL based macro-photoinitiator, *eXPRESS Polym. Lett.*, 11 (6), 493–503.

[18] Sato, C., Aoki, M., and Tanaka, M., 2016, Blood-compatible poly(2-methoxyethyl acrylate) for the adhesion and proliferation of endothelial and smooth muscle cells, *Colloids Surf., B*, 145, 586–596.

[19] Duan, G., Zhang, C., Li, A., Yang, X., Lu, L., and Wang, X., 2008, Preparation and characterization of mesoporous zirconia made by using a poly(methyl methacrylate) template, *Nanoscale Res. Lett.*, 3 (3), 118–122.

[20] Karaca, N., Ocal, N., Arsu, N., and Jockusch, S., 2016, Thioxanthone-benzothiophenes as photoinitiator for free radical polymerization, *J. Photochem. Photobiol., A*, 331, 22–28.

[21] Sangermano, M., Roppolo, I., and Chiappone, A., 2018, New horizons in cationic photopolymerization, *Polymers*, 10 (2), 136.

[22] Kim, W.S., Houbertz, R., Lee, T.H., and Bae, B.S., 2004, Effect of photoinitiator on photopolymerization of inorganic-organic hybrid polymers (ORMOCER®),

654

Indones. J. Chem., 2020, 20 (3), 645 - 654

J. Polym. Sci., Part B: Polym. Phys., 42 (10), 1979–1986.

[23] Wotring, V.J., Prince, P.K., and Bachas, L.G., 1991, Evaluation of poly(vinylidene chloride) as a matrix for polymer membrane ion-selective electrodes, *Analyst*, 116 (6), 581–584.

[24] Totu, E., Ruse, E., and Josceanu, A.M., 2006, Influence of plasticizers on ion-selective polyimide membranes, *Anal. Chim.*, 96 (3-4), 237–246.

[25] West, M., Fenner, N., Gough, R., and Freeman, C., 2017, Evaluation of algal bloom mitigation and nutrient removal in floating constructed wetlands with different macrophyte species, *Ecol. Eng.*, 108, 581–588.

[26] Alizadeh, N., and Nabavi, S., 2014, Synthesis and characterization of novel tetra cyclo[4]pyrrole ether as an anion recognition element for nanocomposite nitrate ion selective carbon paste electrode, *Sens. Actuators, B*, 205, 127–135.

[27] Nuñez, L., Cetó, X., Pividori, M.I., Zanoni, M.V.B., and del Valle, M., 2013, Development and application of an electronic tongue for detection and monitoring of nitrate, nitrite and ammonium levels in waters, *Microchem. J.*, 110, 273–279.

[28] Telting-Diaz, M., and Bakker E., 2001, Effect of lipophilic ion-exchanger leaching on the detection limit of carrier-based ion-selective electrodes, *Anal. Chem.*, 73 (22), 5582–5589.

[29] Żubrowska, M., Wróblewski, W., and Wojciechowski, K., 2011, The effect of lipophilic salts on surface charge in polymeric ion-selective electrodes, *Electrochim. Acta*, 56 (17), 6114–6122.

[30] Fan, Y., Xu, C., Wang, R., Hu, G., Miao, J., Hai, K., and Lin, C., 2017, Determination of copper(II) ion in food using an ionic liquids-carbon nanotubes-based ion-selective electrode, *J. Food Compos. Anal.*, 62, 63–68.

[31] Garajová, K., Balogová, A., Dušeková, E., Sedláková, D., Sedlák, E., and Varhač, R., 2017, Correlation of lysozyme activity and stability in the presence of Hofmeister series anions, *Biochim. Biophys. Acta, Proteins Proteomics*, 1865 (3), 281–288.

[32] Yi, T.H., Huang, H.B., and Li, H.N., 2017, Development of sensor validation methodologies for structural health monitoring: A comprehensive review, *Measurement*, 109, 200–214.

Ionic Conductivity of Chitosan-Lithium Electrolyte in Biodegradable Battery Cell

Benouar Ali[1,2,*] and Ahmed Bacha Reda Mohammed[2]

[1]Laboratoire de Physico-Chimie des Matériaux, Environnement et Catalyse, Université des Sciences et de la Technologie d'Oran Mohammed Boudiaf, M'Nouar BP, 1505, Oran, Algérie

[2]Ecole Supérieure en Génie Électrique et Énergétique, Oran, Algérie

Abstract: *The electrical conductivities of salts (LiCl, LiOH) in chitosan as an electrolyte in biodegradable batteries have been measured at the concentration range 10–100 mol m^{-3} in the temperature range 278–308 K. The data were interpreted in terms of ion–ion and ion–solvent interactions using the Fuoss paired ion. The fitting of Fuoss' equation of 1978 to these data led us to an estimate of the ionic association by computing the conductimetric pairing constants. In order to optimize the use of the electrolyte in the clean lithium battery, the temperature dependency of conductivity will be studied using Arrhenius empirical equation. This equation was applied successfully in the temperature range used in this study.*

Keywords: *electrical conductivity; biodegradable batteries; chitosan; clean energy*

■ INTRODUCTION

In recent years, the development of polymer electrolytes has been a central challenge to be faced by academic and industrial interests [1-2]. These materials have vast potential applications in various electrochemical devices [3-5]. They offer many advantages under liquid electrolytes, such as no internal shorting, leakage of electrolytes and non-combustible reaction products at the electrode surface existing in the liquid electrolytes [6]. Chitosan has been under extensive research on account of its specific properties, such as being non–toxic and biodegradable and also because of its promising potential in biomedical, pharmaceutical, and industrial applications [7-8]. Chitosan also constitutes a polymer host for electrolyte as it is able to dissolve ionic salts [9].

Electrical conductivity, the most vital electrolyte properties of chitosan, can be increased by several methods. Rosli et al. [10] studied the effect of TiO$_2$ filler on the structure and electrical properties of hexanoyl chitosan/polystyrene based electrolytes. The conductivity for filler-free polymer electrolyte is 7.21×10^{-5} S cm^{-1}. The addition of 4 wt.% TiO$_2$ increased the conductivity by one order of magnitude to 2.27×10^{-4} S cm^{-1}. Yulianti et al. [11] have successfully studied Ion Implantation Technique to prepare a solid-state electrolyte based on chitosan. Various ion salts (Li, Cu, Ag) was involved in the chitosan matrix. The results show that after implanted with Li, Cu or Ag ion, the conductivity of chitosan film increased significantly. Traditional lithium salts used in polymer electrolytes are LiPF$_4$, LiClO$_4$, LiBF$_4$, etc.

Up to now the lithium – ion batteries used specific electrolytes LiPF$_4$, LiPF$_6$, etc., dissolved in organic solvents such as Propylene Carbonate (PC) Acetonitrile (AN), etc. Our goal in this research is to substitute the toxic solvents (PC, AN) by the biodegradable and non-toxic solvent "Chitosan", with a view to elaborate a lithium-ion battery based on this clean and biodegradable solvent. We find it interesting to make measurements of conductivity with a lithium salt. This is performed in order to optimize the electrolyte composition to be used in a clean lithium battery without the use of toxic solvents like Propylene Carbonate (PC) and Acetonitrile (AN). The experimental conductance data will be analyzed by the known equations of the literature namely the Fuoss equation of 1978, Casteel–Amis empirical equation and Arrhenius empirical equation for the temperature dependence of the conductivity.

■ **EXPERIMENTAL SECTION**

Electrolytes with lithium salts, lithium chloride (LiCl) and Lithium hydroxide (LiOH) were prepared with distilled water and Chitosan. The LiCl and LiOH salts had a purity grade of 99.5% and 99%, respectively. The initial solution concentration for each electrolyte was prepared by weight using the electronic balance Ohaus As200. For the electrolyte solution, the concentrated solution was obtained by simply adding the necessary mass of lithium salts to the previous solution. Depending on its mass, lithium salts will require a period between 1–4 h to be completely dissolved using a magnetic stirrer. To prepare the polymer electrolyte, 0.5 g of chitosan was dissolved in 50 mL of acetic acid at 3% vol/vol. For the desired concentration, the lithium salt was added, and the mixture was placed in a magnetic stirrer at 313 K for 18 h. All prepared solutions were covered by paraffin.

The conductivity measurements were carried out using the EC215 conductivity meter (Hanna Instruments) having a resolution of 0.01 μS cm⁻¹, a precision of 1% and an automatic correction of temperature shift during the measurement. Before use, the instrument was calibrated using the standard KCl solution HI 7031. The solution was placed into a special dual wall cell suitable for temperature control and connected to the cryostat (Lauda RE1050- CP) filled with ethylene glycol where the desired temperature was kept constant (Fig. 1).

Theoretical Equations

Fuoss's model

According to Fuoss's paired ion model, an equilibrium may be established through the following reaction [12]:

$$A^+ + B^- \leftrightarrow \left(A^+\cdots B^-\right) \leftrightarrow \left(A^+B^-\right) \leftrightarrow \left(AB\right)$$
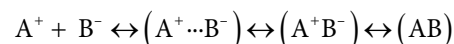
A⁺ and B⁻ are free ions; (A⁺⋯B⁻) are solvent separated pairs; (A⁺B⁻) are contact pairs and (AB) are neutral molecules.

In this theory, the effects of ion–ion and ion–solvent interactions enter through two adjustable parameters, the parameter α and Gurney radius (R_g). The parameter Rg is the radius of the spherical portion of the solvent that encloses the ion. The parameter (α) is a fraction defined by
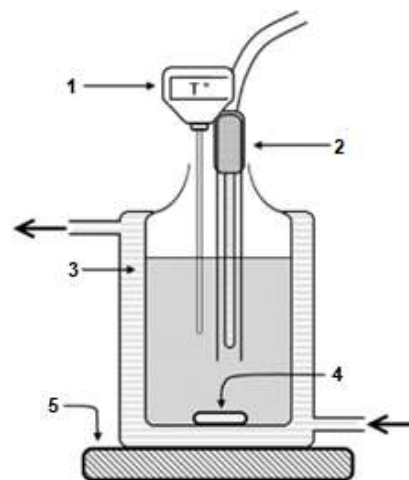
Fig 1. Experimental diagram. 1: Thermometer; 2: Electrical conductivity probe; 3: Heat-transfer fluid (Ethylene glycol); 4: Magnetic stir bars; 5: Magnetic stirrer

classifying each ion according to the magnitude of r, the distance from the center of the ion to that of the nearest neighbor of opposite sign. If r > R, then the ion is unpaired, otherwise the ion is said to be paired. If r << R, the paired ion and its neighbor constitute a contact pair which does not contribute to the conduction process. The experimental data were analyzed using Fuoss' conductance equation, expressed as:

$$\Lambda = P\left[\Lambda_0(1+RX)+EL\right] \tag{1}$$

$$P = 1-\alpha(1-\gamma) \tag{2}$$

$$\gamma = 1-K_A C\gamma^2 f^2 \tag{3}$$

$$-\ln f = \frac{\beta\kappa}{2(1+\kappa R)} \tag{4}$$

$$\beta = \frac{e^2}{\varepsilon k_b T} \tag{5}$$

$$K_A = K_R(1+K_S) \tag{6}$$

In these equations, R represents the Gurney radius; γ the fraction of unpaired ions (free ions); p the fraction of solvent-separated pairs; α the fraction of contact pairs; K_A the overall pairing constant evaluated from the association constant of contact-pairs (K_S) and the association constant of solvent-separated pairs (K_R). The variables f, β, and κ have their usual meanings; RX (relaxation effect) and EL (electrophoresis effect) are parameters depending on the physical properties of the solvent and the temperature, given, in SI units, by:

$$RX = \frac{-\beta\kappa}{6(1+1/\sqrt{2})(1+t)(1+t/\sqrt{2})} + \frac{\beta^2\kappa^2}{12}\ln t + \beta^2\kappa^2 FH2$$
$$+\beta^3\kappa^3 FH3 + [\frac{\beta_0 C^{1/2}\gamma^{1/2}}{\Lambda_0}](\frac{\beta\kappa}{8})\,[0.5 H2 - \ln t] \tag{7}$$

$$EL = -\beta_0 C^{1/2}\gamma^{1/2}[\frac{1}{1+t} + \beta\kappa(0.125\ln t) + 0.5 H1] \tag{8}$$

$$\beta_0 = \frac{Fe\kappa}{3\pi\eta C^{1/2}} \tag{9}$$

$$t = \kappa R \tag{10}$$

FH2, FH3, H1, and H2 are the interpolation polynomials introduced by Fuoss in order to facilitate solving the equation of conductance [12].

The method was used as follows: In our computer program, we used the interpolation polynomials established by Fuoss based on its model of ion pairs (1978) Eq. (1-10). In our case, we have adopted the method of calculation mentioned below. Indeed, we worked with the molar conductivity value at infinite dilution Λ_0 graphically obtained by extrapolation using the Debye-Huckel limiting law-Onsager. Indeed, for each electrolyte and for each concentration, we used a simple method to reproduce the experimental data of conductivity. Afterwards, we set an arbitrary value of α and varied the value of R_g until a standard deviation of σ is minimum, Eq. (11). Then, we fixed the value of R_g and varied the value of α until a minimum standard deviation σ was obtained to vary the radius of Gurney (R_g), by setting an arbitrary value of (α). Finally, we deduced the remaining Fuoss's parameters already described: molar conductivity at infinite dilution (Λ_0), the fraction (α) and the association constant (K_A). The calculated value was compared to the measured value of (R_g) and (α), seeking the minimum standard deviation:

$$\sigma^2 = \frac{\sum\left(\Lambda_{J(cal)} - \Lambda_{J(obs)}\right)^2}{n-2} \tag{11}$$

n is the number of concentrations used during the experiment.

Casteel-Amis empirical model

To describe the relationship between the electrical conductivity with concentration, the empirical Castel-Amis equation was used [13]. The empirical equation was written as follows:

$$\kappa = \kappa_{max}\left(\frac{C}{C_{max}}\right)^a \exp\left[b(C - C_{max})^2 - \frac{a}{C_{max}}(C - C_{max})\right] \tag{12}$$

In this equation, C_{max} is the concentration at which the specific conductivity maximum κ_{max} is attained. The constants (a) and (b) are arbitrarily chosen and adjusted by the least-squares method.

Arrhenius equation

On the basis of transport theory of solutions, we use the Arrhenius type temperature conductivity, which can be written as [14]:

$$\kappa = A\exp(\frac{E_a}{k_B T}) \tag{13}$$

where $A = \kappa_\infty$ represents the maximum electrical conductivity at infinite temperature, E_a is the activation energy for ionic conduction and k_B is the Boltzmann constant.

■ RESULTS AND DISCUSSION

The variation of the molar conductivity data for LiCl and LiOH in chitosan were analyzed by Fuoss, while the specific conductivity data were analyzed using the Casteel–Amis equation. These data are given in Table 1.

Table 1. Molar conductivities Λ of LiOH and LiCl in chitosan at 298 K

C (mol m^{-3})	Λ LiOH (S m^2 mol^{-1})	Λ LiCl (S m^2 mol^{-1})
10	0.220	0.135
20	0.205	0.120
30	0.200	0.116
40	0.192	0.112
50	0.190	0.112
60	0.186	0.110
70	0.185	0.107
80	0.184	0.106
90	0.183	0.105
100	0.182	0.104

Table 2. Fuoss' parameters Λ_0, α, R and K_A for LiOH and LiCl in chitosan at 298 K

	Λ_0 (S m^2 mol^{-1})	α	R (nm)	K_A (m^2 mol^{-1})
LiOH	0.139	0.3	0.85	2.8×10^{-3}
LiCl	0.235	0.45	0.65	6.2×10^{-3}
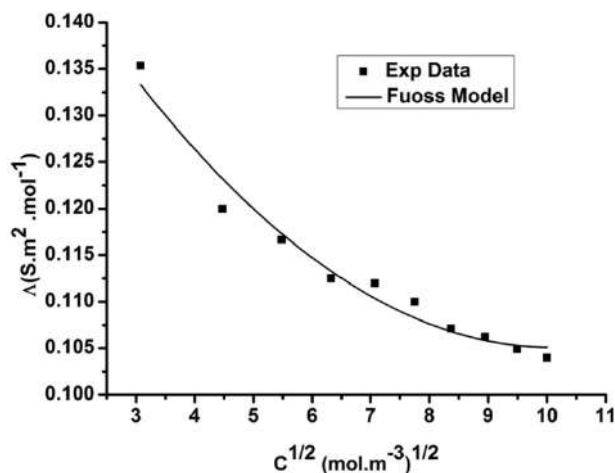
Fig 2. Molar conductivity of LiCl in chitosan versus $C^{1/2}$ at 25 °C. The solid line represents the Fuoss conductance equation

Fig 3. Molar conductivity of LiOH in chitosan versus $C^{1/2}$ at 25 °C. The solid line represents the Fuoss conductance equation

The molar conductivities are plotted against the square root of the salt concentration according to the model of Fuoss in Fig. 2 and 3. As can be seen in these figures, the molar conductivity decrease when the square root of the concentration increase. The solid line was calculated using equation 1 in the model of Fuoss. Values of Λ_0, α, R and K_A obtained by this method are listed in Table 2.

The conductivity data (κ) for two electrolytes were analyzed using the semi-empirical Casteel-Amis equation. They are plotted in Fig. 4. The values of the parameters C_{max}, κ_{max}, a and b are given in Table 3.

The value of (b) tends to be small and negative in all systems and seem to be influenced by dielectric constant. This result was previously found for LiCl in glycerol [15]. However, the coefficient (a) was all positive

Table 3. Casteel–Amis parameters κ_{max}, C_{max}, a and b for LiOH and LiCl in chitosan

	κ_{max} (S m⁻¹)	C_{max} (mol dm⁻³)	a	b
LiOH	126.9	1420	1.12	-0.55
LiCl	32.9	590	1.01	-0.45

Fig 4. The specific conductance κ as a function of concentration C of LiOH and LiCl in chitosan at 298 K

Fig 5. The specific conductance κ as a function of temperature T of LiOH and LiCl in chitosan

Table 4. The conductivities κ of LiCl and LIOH in chitosan in the temperature range 278–308 K

K (S m^{-1})	T = 308 K	T = 298 K	T = 288 K	T = 278 K
LiOH	20.2	18.2	17.8	17.1
LiCl	12.2	10.4	10.0	9.7
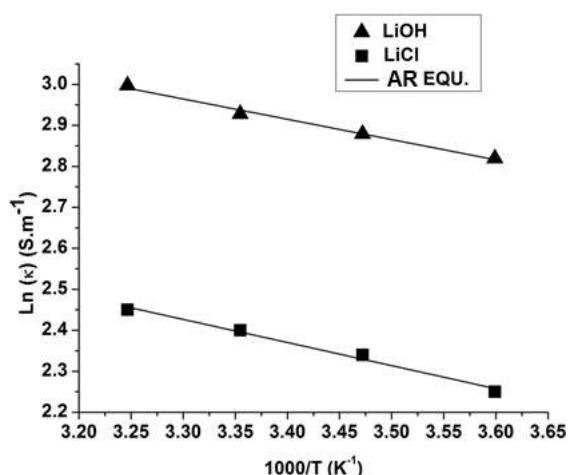
Fig 6. Arrhenius plot of the specific conductance κ of LiOH and LiCl in chitosan

and appears to be influenced by the solution viscosity, as they have been already noticed by Christie et al. when studying conductivities of lithium salt complexes in propylene carbonate [16].

Ionic conductivity data (κ) for LiCl and LiOH in chitosan, using the concentration 0.1 mol dm^{-3} and in the temperature range 278–308 K are presented in Table 4 and represented in Fig. 5. We can see that the conductivity increases when the temperature increases because the viscosity of the electrolyte is reduced. In Fig. 6, we plot the natural logarithm of κ versus 1/T K.
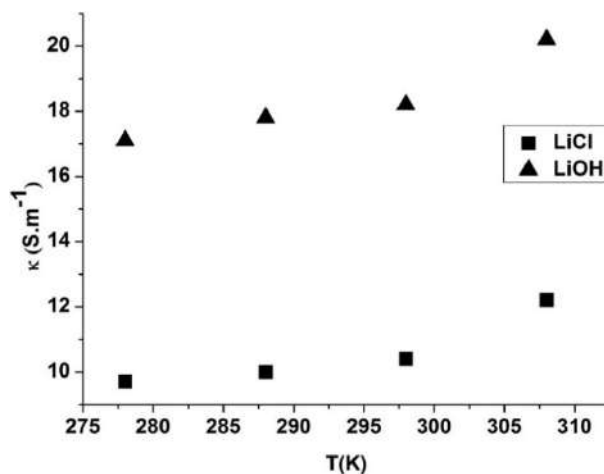
The maximum electrical conductivity (κ$_\infty$) was determined by assuming a linear fit of ln (κ) versus 1/T. In our case, κ$_\infty$ of LiOH and LiCl in chitosan were equal to 98.5 S m^{-1} and 72.24 S m^{-1}, respectively. Then, the activation energy (E$_a$ = 4.22 meV for LiOH and E$_a$ = 4.83 meV for LiCl) was evaluated from the slope (B = E$_a$/kB). It is noticeable that these results were also previously found by other researchers [17].

■ CONCLUSION

The purpose of the present study was to test simple models for the conductivity of biodegradable electrolyte used in a clean battery. The variations of the molar conductivity with salt concentration followed Fuoss's ion paired model. The electrical conductivities of above-mentioned systems have been determined to fit the empirical Gasteel–Amis equation. It was found that the values of (b) were all negative. The study presented in this paper proved that Arrhenius equation can also be used to describe the temperature dependence of the electrical conductivities. The activation energy of the electrolyte was obtained by the linear fit of ln (κ) versus 1/T. In view of these results, the electrolyte based on chitosan has been optimized and can be used in clean batteries.

■ REFERENCES

[1] Zong, Z., Kimura, Y., Takahashi, M., and Yamane, H., 2000, Characterization of the chemical and solid state structure of acylated chitosan, *Polymer*, 41 (3), 899–906.

[2] Ji, K.S., Moon, H.S., Kim, J.W., and Park, J.W., 2003, Role of functional nano-sized inorganic fillers in poly(ethylene) oxide-based polymer electrolytes, *J. Power Sources*, 117 (1-2), 124–130.

[3] Mohamed, N.S., Subban, R.H.Y., and Arof, A.K., 1995, Polymer batteries fabricated from lithium complexed acetylated chitosan, *J. Power Sources*, 56 (2), 153–156.

[4] Yahya, M.Z.A., and Arof, A.K., 2003, Effect of oleic acid plasticizer on chitosan–lithium acetate solid polymer electrolytes, *Eur. Polym. J.*, 39, 897–902.

[5] Yahya, M.Z.A., and Arof, A.K., 2004, Conductivity and X-ray photoelectron studies on lithium acetate doped chitosan films, *Carbohydr. Polym.*, 55 (1), 95–100.

[6] Gray, F.M., 1991, Solid Polymer Electrolytes: Fundamentals and Technological Applications, Wiley-VCH, Weinheim, New York.

[7] Khiar, A.S.A., Puteh, R., and Arof, A.K., 2006, Conductivity studies of a chitosan-based polymer electrolyte, *Physica B*, 373 (1), 23–27.

[8] Fuentes, S., Retuert, P.J., and González, G., 2007, Lithium ion conductivity of molecularly

compatibilized chitosan–poly(aminopropyltriethoxy silane)–poly(ethylene oxide) nanocomposites, *Electrochim. Acta*, 53 (4), 1417–1421.

[9] Singh, A.V., Nath, L.K., and Singh, A., 2010, Pharmaceutical, food and non-food applications of modified starches: A critical review, *Electron. J. Environ. Agric. Food. Chem.*, 9 (7), 1214–1221.

[10] Rosli, N.H.A., Chan, C.H., Subban, R.H.Y., and Winie, T., 2012, Studies on the structural and electrical properties of hexanoyl chitosan/polystyrene-based polymer electrolytes, *Physics Procedia*, 25, 215–220.

[11] Yulianti, E., Karo, A., Susita, L., and Sudaryanto, 2012, Synthesis of electrolyte polymer based on natural polymer chitosan by ion implantation technique, *Procedia Chem.*, 4, 202–207.

[12] Fuoss, R.M., 1978, Paired ions: Dipolar pairs as subset of diffusion pairs, *Proc. Natl. Acad. Sci. U.S.A.*, 75 (1), 16–20.

[13] Casteel, J.F., and Amis, E.S., 1972, Specific conductance of concentrated solutions of magnesium salts in water-ethanol system, *J. Chem. Eng. Data*, 17 (1), 55–59.

[14] Vogel, H., 1921, Das temperatur-abhängigkeitsgesetz der viskosität von flüssigkeiten, *Phys. Z.*, 22, 645–646.

[15] Benouar, A., Kameche, M., and Bouhlala, M.A., 2015, Molar conductivities of concentrated lithium chloride–glycerol solutions at low and high temperatures: Application of a quasi-lattice model, *Phys. Chem. Liq.*, 54 (1), 62–73.

[16] Christie, A.M., and Vincent, C.A., 1996, Conductivities of selected lithium salt complexes in propylene carbonate, *J. Phys. Chem.*, 100 (11), 4618–4621.

[17] Bouhlala, M.A., Kameche, M., Tadji, A., and Benouar, A., 2017, Chitosan hydrogel-based electrolyte for clean and biodegradable batteries: Energetic and conductometric studies, *Phys. Chem. Liq.*, 56 (2), 266–278.

Synthesis, Characterization and Morphological Study of Nicotinamide and *p*-Coumaric Acid Cocrystal

Mohamad Nor Amirul Azhar Kamis[1,2], Hamizah Mohd Zaki[1,2,*], Nornizar Anuar[3], and Mohammad Noor Jalil[1]

[1]*Faculty of Applied Sciences, Universiti Teknologi MARA, 40450 Shah Alam, Selangor, Malaysia*

[2]*Atta-ur-Rahman Institute for Natural Product Discovery, Universiti Teknologi MARA (UiTM), Puncak Alam Campus, 42300 Bandar Puncak Alam, Selangor, Malaysia*

[3]*Faculty of Chemical Engineering, Universiti Teknologi MARA, 40450 Shah Alam, Selangor, Malaysia*

Abstract: *Cocrystallization is one of the potent methods used to modify the physicochemical properties of drugs. Cocrystal of nicotinamide (NIC):p-coumaric acid (COU) was synthesized by a slow evaporation method using acetonitrile. The cocrystals with different feed molar ratios (NIC:COU : 1:1, 1:2, and 2:1) were characterized using DSC, PXRD, and FTIR, which revealed the formation of different polymorphs for each feed molar ratio. A single crystal of the NIC:COU (1:1) cocrystal was analyzed using single crystal X-ray diffraction (SCD), and ¹H-NMR revealed a greater cocrystal structure stability compared to the previously published cocrystal. The intermolecular hydrogen bonds, N-H···O, and O-H···O interactions played a major role in stabilizing the cocrystal structure. A molecular modeling technique was used for prediction, and surface chemistry assessment of the morphology showed an elongated (along the y-axis) octagonal crystal shape, which was in a reasonable agreement with the experimental crystal morphology. The reduction in values of the cocrystal solubility in ethanol was supported by the DSC data and simulation of crystal facets, where most of the crystal facets exposed to polar functional groups. At the concentration of 31.3 µM, NIC:COU (1:1) cocrystal showed more effective DPPH scavenging with 77.06% increased activity compared to NIC at the same concentration.*

Keywords: *physicochemical properties; cocrystal; molecular interaction; single crystal XRD; computational simulation*

■ INTRODUCTION

Pharmaceutical cocrystal is defined as multiple component crystals that contains an active pharmaceutical ingredient (API) and one or more pharmaceutically acceptable coformers with a well-defined stoichiometry through non-covalent interactions. The molecules in the cocrystal lattice are usually linked by hydrogen bonds, which tend to collapse once dissolved in a solvent if the interactions are weak. The formation of cocrystals is able to fine-tune or even customize the physicochemical properties of APIs in terms of their solubility, dissolution rate, moisture sorption, and stability without affecting the intrinsic bioactivity [1-2]. The cocrystals can be prepared by using several methods such as solution cooling, ambient co-milling, cryogenic co-grinding, slurry, solvent evaporation, or melt [3-4].

Nicotinamide (NIC) is an API, commercially known as vitamin B₃, is a water-soluble vitamin which able to form hydrogen bonds with other compounds containing hydrogen bond donor and acceptor groups [5]. There are four known polymorphs of NIC, the most stable at 126–128 °C, followed by the metastables at 112–117 °C, 107–111 °C, and 101–103 °C respectively [6]. NIC is widely used for acne vulgaris, anti-inflammatory, and exhibits many potential promising applications

such as improving the cognition in Alzheimer's disease transgenic mice, and able to reduce hyperpigmentation for patients with melisma [7].

The nitrogen atom on the pyridine ring of NIC often forms strong hydrogen bonds with the carboxylic acid group in the cocrystal designs [8-14], which makes the COU (*p*-coumaric acid) as the best compound to be used as the cocrystal former. The successful carboxylic acids used in the cocrystallization with NIC were ibuprofen (both *R/S* and *S* forms), salicylic acid, fenbufen, and flurbiprofen [15], fenamic acid [11], prulifloxacin [4], and (R)-mandelic acid [16]. Other compounds used in the cocrystallization with NIC were artesunate [17], baicalein [2], carbamazepine [5,18], celecoxib [19], ethylparaben [20], and simvastatin [21]. The single crystal of NIC:theophylline cocrystal showed the participation of the amide group forming the N-H···O, and O···H-N hydrogen bonds [22-23].

Nicotinamide (NIC), Fig. 1(a) is used in many cocrystallization experiments due to the presence of two hydrogen bonding groups ready to form the intermolecular hydrogen bond. The amide group has two proton donors and two lone pairs on the carbonyl group, which act as hydrogen bond acceptors. Another hydrogen bond acceptor group is the nitrogen atom on the pyridine ring with a lone pair, which is reported as the best hydrogen bonding acceptor [24]. Etter's empirical rule specified that the best proton donor and acceptor remained after intramolecular hydrogen bond formation will form the intermolecular hydrogen bonds [25]. The carboxylic acid proton was reported as the best hydrogen bond donor, which will interact with the nitrogen atom of pyridine ring (best hydrogen bond acceptor) as observed occurring in 10 out of 11 of the reported NIC-acid cocrystals [24].

The donor/acceptor pair of amide *syn*-proton and the carbonyl oxygen of the amide can form a homomeric $R_2^2(8)$ hydrogen bond ring [26-27]. The hydrogen bonding between the carboxylic acid group with the amide of NIC forms the heteromeric $R_2^2(8)$ hydrogen bonding dimer [28].

p-Coumaric acid (COU), Fig. 1(b) is one of the hydrocinnamic acids which widely spread in the plant
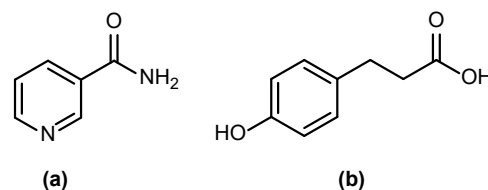
Fig 1. (a) Nicotinamide (NIC), (b) *p*-Coumaric acid (COU)

kingdom with useful biological activities, such as antioxidant, anti-inflammatory, antimicrobial, anticancer, antiplatelet, anti-melanogenic, antidiabetic, cardioprotective, suppression of tumor growth, and anti-anxiety activities [29-30]. *p*-Coumaric acid can be found abundantly as compared with the other two isomers, *ortho*-, *meta*-coumaric acid [31-32]. COU has been widely used in food, medicine, and cosmetic industries, which able to treat cosmetic imperfection [7,33-34].

COU has a hydroxyl group at *para* position of the aromatic ring and a carboxylic acid functional group, which are the possible sites for the hydrogen bonding to occur. A study between COU and quinine resulted in the formation of hybrid salt-cocrystal solvate composed of a quinine ion (Q$^+$), a coumarate ion (COU$^-$), water molecule, and methanol molecule, where water and methanol molecules acted as a bridge connecting Q$^+$ and COU$^-$ ions [35]. A study on a cocrystal between COU and theophylline and caffeine showed the utilization of both proton donor groups of COU, which built the cocrystal structures [31]. The cocrystal of COU with isoniazid showed that −OH phenol of COU prefers to form a hydrogen bond with the best hydrogen bond donor of the nitrogen atom of the pyridine ring of isoniazid [25,32], which does not follow the hydrogen bonding hierarchy. The same case has been observed in cocrystal between caffeic acid and isoniazid [36]. These occurrences show that the behavior of hydrogen bonding interactions between molecules is still specifically cannot be predicted.

Bevill et al. [7] had successfully synthesized and characterized the NIC:COU cocrystal using methanol with three polymorphic forms of 1:1 cocrystal, and one 1:2 cocrystal resulted from the induction in water. However, the study focused on the cocrystal

characterization, relative solid-state stability, and conversion to alternate stoichiometries of the polymorphic forms [7].

The molecular modeling simulation method is a widely used technique in crystal research [37], commonly used to predict crystal morphology and examine the growth mechanism at the atomistic/molecular level [38]. Validation of the predicted crystal morphology (commonly carried out in a vacuum environment) is a complex and challenging process in which in an actual situation, the crystals are grown in an environment with the presence of solvents and additives [39-40]. Molecular structure of a crystal is packed in a unit cell as a building unit and heavily depending on intermolecular interaction such as hydrogen bond and van der Waals between the molecules and are the important parameters, which affect the crystal shape, and hence the degree of solubility [41]. The crystal morphology also has a significant impact on processing and product performances [42]. In most cases, the use of different solvents results in different crystal morphology, the polar solvent will form the elongated crystal morphology, while high packing density will form the needle-like and plate-like crystal [43-45].

The traditional method used to predict the crystal morphology is via a periodic bond chain (PBC) by Donnay Harker analysis, and the attachment energy calculation, E_{att} (AE model) [44]. Hartman and Bennema reported that the E_{att} is related to the growth rate of the crystal [45]. Attachment energy is defined as the energy released upon the attachment of a slice with a d_{hkl} width of a growing crystal facet [42].

$$E_{lat} = E_{att} + E_{sli} \qquad (1)$$

where E_{lat} is the lattice energy that is proportional to the crystal growth rate, hence the larger attachment energy will result in faster crystal facet growth, thus less morphologically important [42,45-47]. E_{sli} is the slice energy, which is the energy of a growth slice with the thickness d_{hkl} surface of a growing crystal [45]. This calculation has been successfully used in a diverse range of contemporary applications such as the morphology prediction of pharmaceuticals [48], explosives [49], organic pigments [50], phases constituting kidney stones [51], and interpretation of inverse gas chromatography

data [52]. This method also has proven to be useful in the prediction of the crystal morphology, which involves the anisotropic energies in the crystal unit cell [39,53-54].

The exposed groups on the crystal facets play an important role when the crystal is in contact with external material such as the solvent. Exposure of a polar group will make the particular facet to be a polar facet, and vice versa [39]. The use of a polar solvent (or mixtures of them) on the polar crystal tends to shorten the crystal habit [44], as the solvent stops the growth of the fast-growing crystal.

In this study, NIC:COU cocrystal was synthesized with different feed molar ratios of 1:1, 1:2, and 2:1 using acetonitrile, and characterized. Acetonitrile is a common solvent used in the cocrystallization such as nicotinamide: 3-hydroxybenzoic acid (1:1) and pyrazinamide:2,5-dihydroxybenzoic acid (1:1) cocrystals [55]. The use of acetonitrile mixture solvent also resulted in the formation of enthenzamide:gentisic acid cocrystal polymorphs [56]. This study also suggested the effect of combined molecular structures in the cocrystal on the solubility in ethanol and the bioactivity by an antioxidant study using DPPH assay. The solubility data is vital as it is an important physicochemical property that affects the bioavailability of the drug, while the changes in antioxidant activity were studied at different concentrations to determine the potential of the cocrystal towards health promotion as rendered by many dietary supplements. A molecular modeling technique was also carried out in this study for the morphology prediction of the NIC:COU (1:1) cocrystal and the examination of its surface chemistry.

■ **EXPERIMENTAL SECTION**

Materials

Nicotinamide ($C_6H_6N_2O$, MW = 122.13 g/mol, > 99.0% purity) was purchased from Across Organic, Belgium. *p*-Coumaric acid ($C_9H_8O_3$, MW = 164.05 g/mol, 98.0% purity) was purchased from Sigma Aldrich, UK. 2,2-diphenyl-1-picryl-hydrazyl-hydrate (DPPH) free radical ($C_{18}H_{12}N_5O_6$, MW = 394.32 g/mol) used in the antioxidant test was purchased from Merck, Germany.

The solvent, acetonitrile (99.9% purity), and ethanol (HPLC purity > 99.9%) were purchased from RCI Labscan, Thailand, and the DMSO-d_6 ($\geq$ 99.8% deuteration degree) used for the NMR analysis was purchased from Merck, Germany. All chemicals and solvents were used as received without further purification.

Procedure

Preparation of cocrystal for characterization experiment

Cocrystals used in the characterization experiments were prepared using a rotary evaporation method (RTV) (Rotavapor R-210, BUCHI, Switzerland), at 50 °C, 100 atm, and 100 rpm speed. Three different feed molar ratios of NIC:COU were used, 1:1, 1:2, and 2:1 in acetonitrile to produce the NIC:COU cocrystal.

Synthesis of NIC:COU (1:1) single crystal

The single crystal of NIC:COU (1:1) was synthesized using slow evaporation method, in which an equimolar mixture of NIC (122 mg, 1 mmol) and COU (164 mg, 1 mmol) was dissolved in acetonitrile (10 mL) at 50 °C in a 20 mL vial. The solution was allowed to slowly evaporate in the vial with a perforated cap for four days until the crystal formed, harvested, and sent for crystal packing analysis using a single crystal X-ray diffractometer.

Solid state characterization

The cocrystals were characterized using differential scanning calorimeter (DSC), powder X-ray diffractometer (PXRD), Fourier transform infrared (FTIR) with attenuated total reflection (ATR) technique, and single crystal X-ray diffractometer (SCD).

The thermal analyses of the cocrystals were carried out using a Mettler Toledo differential scanning calorimeter (DSC). The temperature and cell constants were calibrated using indium. Samples (1–3 mg) were crimped in a nonhermetic aluminium DSC pan, heated from 30 °C to 300 °C, with a heating rate of 10 °C/min on continuous nitrogen purge (40 mL/min).

Powder X-ray diffraction (PXRD) analyses were performed at ambient temperature using a Rigaku powder diffractometer with Cu-K$_\alpha$ radiation (λ = 1.5406 Å) source. The tube voltage and amperage were set at 40 kV and 40 mA, respectively. The samples were analyzed in

the range of 2θ from 5° to 55° with a scanning speed of 2°/min, and a step size of 0.02°. The diffraction patterns of the cocrystals were compared to the patterns of the pure compounds (controls).

A Perkin Elmer FTIR spectrophotometer using the ATR technique with Omnic software version 5.2 was used to determine the functional groups of NIC:COU cocrystals with a spectral resolution of 1 cm^{-1}. The background spectrum composed of moisture and CO_2 molecules was collected prior to the analyses, which will be automatically subtracted from the sample spectrum. The data were collected in the range of 4000–400 cm^{-1}.

Single crystal X-ray diffraction data were collected using a Bruker D8 Quest diffractometer model using the graphite monochromatized Mo-K$_\alpha$ radiation (λ = 0.7107 Å) with APEX3 system. The crystal structure was refined using DOS-SHELXTL software, where all non-hydrogen atoms were refined anisotropically. The determination of intra and intermolecular hydrogen bonding was done using the PLATON software [57], and the preparation of figures was done using the MERCURY 3.8 software.

Liquid state characterization

The ^{1}H-NMR analysis was used to verify the chemical structure of the NIC:COU (1:1) cocrystal, which will support the SCD data. The spectrum was collected using a Bruker NMR-600 MHz model. The analysis was carried out using DMSO-d_6 solvent containing TMS.

The solubility of NIC, and NIC:COU (1:1) cocrystal was measured using the gravimetric method in ethanol from 10 °C to 60 °C. An excess amount of sample was added to ethanol (10 mL) in a 50 mL jacketed glass vessel. The flask was placed in a water bath with a controlled temperature ($\pm$ 0.1 °C) and continuously stirred for 24 h. The solution was allowed to settle for 12 h before sampling. The supernatant was withdrawn using a syringe (5 mL), filtered, and placed in an evaporating dish (pre-weighed). The weight of the solution was recorded before drying in an oven at 50 °C for 4 days. The dried sample was then reweighed and recorded.

The antioxidant capacities of the samples were determined using a DPPH free radical scavenging assay. A fresh solution of DPPH (0.1 mM) was prepared in ethanol. The samples were prepared in serial dilution

from 1000 μM to 2 μM in ethanol. The DPPH solution (10 μL) was added to the sample (1 μL) and the respective blank (1 μL). The samples were incubated in the dark for 30 min. The absorbance of the samples after the incubation period was measured using a BMG LABTECH microplate reader at 517 nm [58]. The DPPH radical scavenging capacity was calculated using Eq. (2) [59-60].

$$\text{DPPH radical scavenging capacity } (\%) = \frac{A_0 - A_1}{A_0} \times 100\% \quad (2)$$

A_0 and A_1 correspond to the absorbance of antioxidant at 517 nm of the DPPH radical for the blank and the sample, respectively.

Computational techniques

The modeling of NIC:COU (1:1) cocrystal morphology was carried out using the Material Studio (MS) package, from Accelrys Inc., using the embedded modules and protocols in determining the atomic charges, lattice energy, and the prediction of the crystal growth morphology under vacuum environment. The force fields applied were Compass, Dreiding, and Universal. Compass is a force field with most of the parameters was derived based on the derivation of *ab initio* calculation, while other parameters were fitted empirically. Dreiding force field with the application of the general force constants and geometry parameters [61] is widely applicable for simulation of biological, organic, and main-group inorganic molecules to determine the structures and dynamics. The dreiding force field is believed to be the most relevant force field available in MS for treating the organic molecules [47]. The Universal force field is acknowledged as a moderately accurate prediction for the geometries and conformational energies of organic molecules, some inorganics, and metal complexes [53].

Atomic charges determination

The atomic charges of the molecules of NIC:COU (1:1) cocrystal were calculated using the density functional theory (DFT) of the quantum mechanical code in the MS. DFT quantum code is an *ab initio* method with high accuracy in the estimation of the electronic properties of the atoms. Three types of atomic charges were used to determine the most suitable charges for the

cocrystal, Mulliken, Hirshfeld, and electrostatic potential fitting (ESP). This was done by applying the DFT quantum mechanical code with a PW91 gradient-corrected functional correlation, an 'all electrons' core treatment, and the DNP basis set [53]. The calculated charges were then assigned to the molecules.

Lattice energy determination and morphology prediction

MS software was used to calculate the lattice energy and simulate the cocrystal morphology using the attachment energy (AE) summation method.

The protocols adopted for the morphology prediction of NIC:COU (1:1) cocrystal were as follows: The NIC:COU (1:1) cocrystal structure with CCDC deposition number of 1587901, the chemical name of 3-(4-hydroxyphenyl)-prop-2-enoic acid pyridine-3-carboxamide was obtained from the refined structure using DOS-SHELXTL software. The atomic charges were calculated using the methods described earlier, which then assigned to the molecules. The molecules were subjected to two stages of the minimization process, (1) the molecules in the unit cell were minimized while the conformations of the molecules were kept fixed, but the molecules were allowed to move within the crystal packing, and (2) the conformation of the molecules were relaxed in the unit cell, and the molecules were allowed to move during the minimization process. The predicted morphology of the cocrystal was calculated using the growth morphology module in the MS software with assigned atomic charges/force fields pairs. Each set of atomic charges/force field produced different crystal morphology, which was then compared with the experimental cocrystal morphology for validation purposes.

■ **RESULTS AND DISCUSSION**

Differential Scanning Calorimetry (DSC)

Fig. 2 shows the DSC thermogram of the NIC, COU, and the NIC:COU mixtures with the feed molar ratios of 1:1, 1:2, and 2:1. NIC showed a sharp endotherm at 129.94 °C without any phase transformation, while COU melted at a higher temperature of 221.62 °C with a
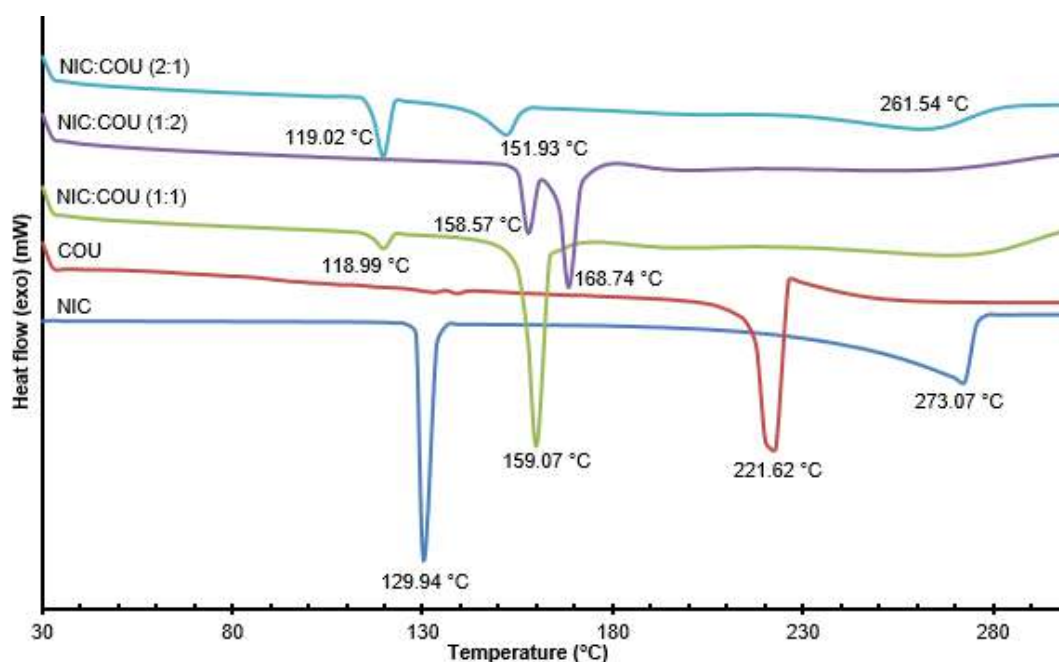
Fig 2. DSC thermogram of NIC, COU, and NIC:COU cocrystals

single endotherm upon heating. The NIC:COU (1:1) mixture melts at 159.07 °C, which is in between NIC and COU melting temperatures. Another minor melting event observed for 1:1 cocrystal is at 118.99 °C with very low intensity. A cocrystal is commonly identified from a DSC thermogram in which the melting temperature of the cocrystal is usually located in between or below of the parent compounds [5,22,62], which was observed in this work. The melting temperature of the NIC:COU (1:1) cocrystal produced in this work is in between the melting temperatures of the polymorphic forms of the NIC:COU (1:1) cocrystals, which were 158 °C (Form 2) and 160 °C (Form 3) [7]. There was no melting event recorded in the same research [7] for 118.99 °C, which perhaps indicating the development of a new crystal phase of the NIC:COU (1:1) cocrystal, discovered in this study. The other two polymorphs of NIC:COU cocrystal were recorded by the previous researcher [7] named Form 1, and Form 4 with melting temperatures of 154 °C and 174 °C, respectively.

The NIC:COU (1:2) mixture shows a phase transformation with two melting temperatures at 158.57 °C, and 168.74 °C respectively. The first melting temperature is in agreement with the Form 2 polymorph of the NIC:COU cocrystal with a melting point of 158 °C [7]. The melting temperature at 168.74 °C is also suspected as

a new crystal phase of NIC:COU (1:2) cocrystal, since there was no data recorded. There is no melting event of Form 4 NIC:COU cocrystal at 174 °C [7], which has a similar feed molar ratio, signifying that the use of a different solvent is able to form different characteristics of the crystal [43].

The NIC:COU (2:1) mixture shows a much similar pattern as NIC:COU (1:1) cocrystal, with the obvious difference, observed in the intensity of the minor melting peak in NIC:COU (1:1) mixture at the comparable melting temperature of 119.02 °C. This confirmed the development of a new crystal phase of the NIC:COU. The second melting temperature located at 151.93 °C, which likely to form Form 1 NIC:COU cocrystal, with a melting temperature of 154 °C [7]. The differences in melting temperatures of the synthesized cocrystals as compared to the parent compounds reflect the changes in the crystal lattice, intermolecular interaction, molecular symmetry, or conformational degree of freedom, which are responsible for the change in physicochemical properties of the cocrystals [2].

Powder X-ray Diffraction (PXRD)

The PXRD patterns of NIC, COU, and the NIC:COU cocrystals are presented in Fig. 3. The

comparison between diffractograms of NIC:COU cocrystals with NIC and COU revealed the feasible interaction between NIC and COU, which anticipated the formation of new crystalline phases due to the additional peaks. The new major peaks observed in all feed molar ratios of NIC:COU (1:1, 1:2, and 2:1) are at 2θ of 15.62°, 16.66°. The development of a new diffraction peak in NIC:COU (1:1) cocrystal at 2θ of 24.66° confirmed the formation of the pure cocrystal. On the other hand, NIC:COU mixtures with 1:2 and 2:1 molar ratios revealed the formation of the cocrystal with the mixture of the pure

compounds since most of the diffraction peaks of the pure compounds are observed.

Fourier Transform Infrared (FTIR)

The molecular interaction between NIC and COU was analyzed using FTIR spectroscopy with the ATR method. Fig. 4 shows the FTIR spectra of the NIC:COU cocrystals stacked with the pure compounds, NIC, and COU. The regions with potential functional groups which are able to form the hydrogen bond are observed, which are the pyridine ring and amide groups of NIC, and carboxylic acid and phenol groups of COU.
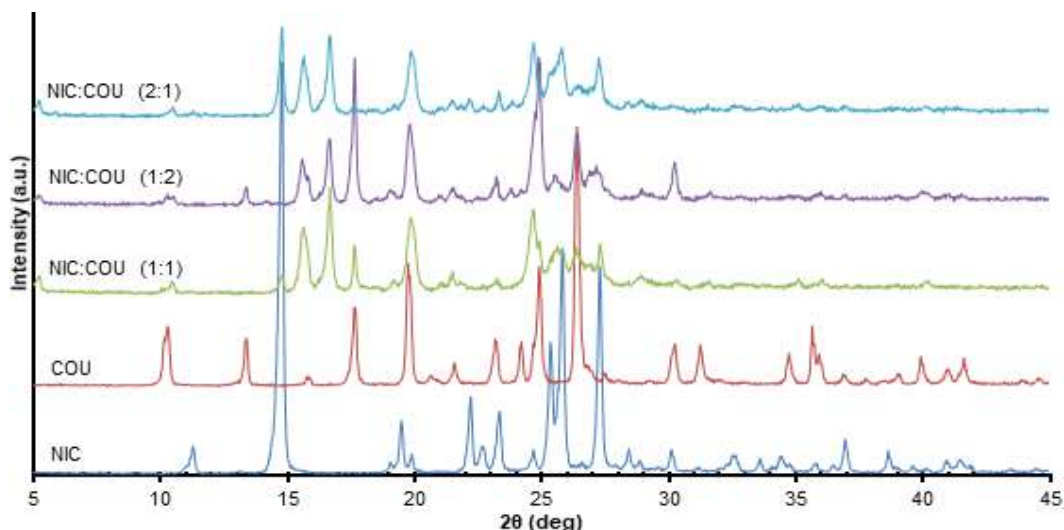

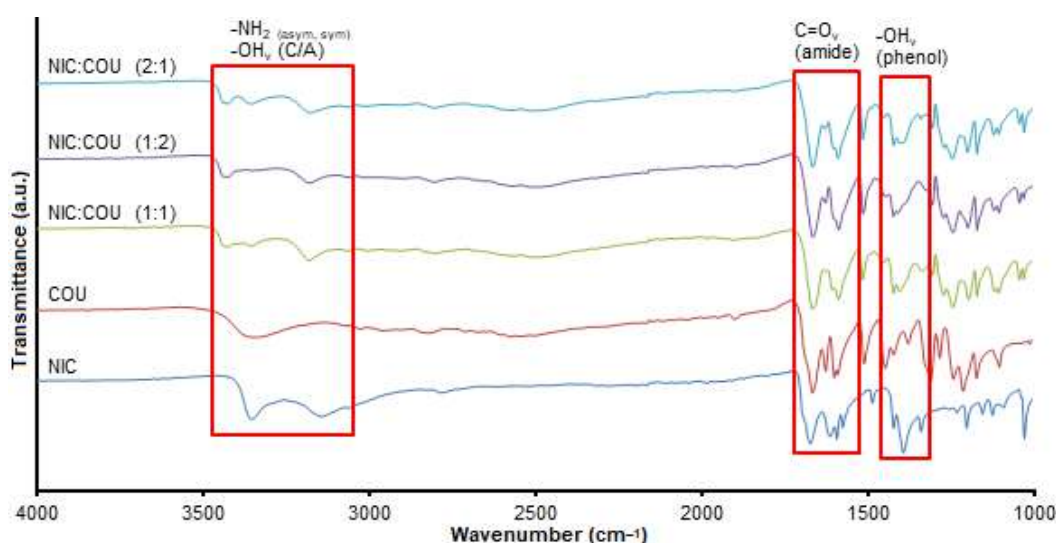**Fig 3.** PXRD patterns of NIC, COU, and NIC:COU cocrystals

Fig 4. FTIR spectra of NIC, COU, and NIC:COU cocrystals

NIC:COU (1:1) cocrystal shows that the C=O stretching of NIC is shifted from 1674 cm⁻¹ to 1667 cm⁻¹, which demonstrates the formation of hydrogen bonding on the oxygen which acts as hydrogen bond acceptor. The stretching of asymmetrical and symmetrical –NH₂ amide of NIC is shifted to higher wavenumber from 3354 cm⁻¹ and 3145 cm⁻¹ to 3355 cm⁻¹ and 3181 cm⁻¹ respectively. The shifts of these bands show the formation of a new phase due to the intermolecular hydrogen bonding from the two proton donors of the –NH₂ group. This is supported by the bending vibration of –NH band [4], which also shifted from 1614 cm⁻¹ to 1607 cm⁻¹. The stretching vibration of the nitrogen atom of the pyridine ring of NIC at 1393 cm⁻¹ is shifted to 1404 cm⁻¹ confirmed the utilization of the nitrogen as the best hydrogen acceptor group [24]. The additional peak at 3425 cm⁻¹ shows the involvement of the acidic proton of COU in the formation of hydrogen bonding with NIC. The band observed at 1900 cm⁻¹ attributes to the additional O-H···N hydrogen bonds [7] present in the cocrystal. The –OH stretching vibration of phenol is shifted from 1378 cm⁻¹ to 1336 cm⁻¹ explains the participation of the –OH group in the formation of hydrogen bonding.

Due to the fact of different crystal phases produced as discussed in the previous sections, the shifting of vibration peaks for NIC:COU cocrystals with 1:2 and 2:1 feed molar ratios were also analyzed successfully. In NIC:COU (1:2) cocrystal, the stretching vibrations of C=O amide and pyridine of NIC are shifted to the same wavenumber as NIC:COU (1:1) cocrystal at 1667 cm⁻¹, and 1404 cm⁻¹ respectively. This confirmed that the same hydrogen bonding interaction pattern occurs in the NIC:COU (1:2) cocrystal. For –NH₂ stretching vibration, only the symmetrical band is observed at 3178 cm⁻¹, and the bending vibration of –NH is shifted to 1627 cm⁻¹. An additional peak at 3426 cm⁻¹ is due to the formation of hydrogen bonding from the acidic proton of COU, and the peak at 1895 cm⁻¹ corresponds to the formation of the O-H···N hydrogen bond. The stretching vibration peak of –OH phenol is also diminished which is another characteristic of the hydrogen bonding behavior of the

NIC:COU (1:2) cocrystal.

The 2:1 feed molar ratio of NIC:COU cocrystal also shows the C=O amide stretching vibration at the same wavenumber as NIC:COU cocrystal with 1:1 and 1:2 feed molar ratios at 1667 cm⁻¹. The asymmetric and symmetric stretching of –NH₂ bands are shifted to 3356 cm⁻¹ and 3177 cm⁻¹ respectively, while no –NH bending vibration observed in the spectrum. The pyridine stretching vibration is shifted to 1394 cm⁻¹, and no peak observed for the O-H···N hydrogen bond formation. The acidic proton stretching vibration is shifted to 3426 cm⁻¹, and –OH phenol stretching vibration is shifted to 1340 cm⁻¹. These differences in the FTIR spectrum again confirmed the formation of different crystal phases with different hydrogen-bonding interactions. The summary of the differences in the vibration bands observed in the NIC:COU cocrystals can be found in Supplementary Material, section S1.

Nuclear Magnetic Resonance (NMR)

¹H-NMR was carried out to confirm the chemical structure of the synthesized cocrystal supporting the data from single crystal X-ray diffraction (SCD) analysis. The chemical structures of NIC and COU were confirmed by comparing the ¹H-NMR signals with previous researchers [63-64]. The ¹H-NMR signals of the NIC:COU (1:1) cocrystal are consistent with the signals of NIC and COU with a slight difference or no difference in terms of the chemical shift. The integration of NMR signals of the cocrystals reveals the same number of protons with the results from SCD analysis, which will be discussed in the next section. Table 1 shows the chemical shifts with the multiplicity of the NIC:COU (1:1) cocrystal in comparison with NIC and COU. The signal from NIC at 7.48 ppm (m, 1H) overlaps with a signal from COU at 7.49 ppm (m, 3H) results in a multiplet signal with four protons. The use of DMSO-d₆ as the NMR solvent was able to reveal the proton signal of the –OH (carboxylic acid and phenol) of COU, which is observed downfield, at 9.96 pm, and 12.12 ppm due to the high polarity of the –OH groups.

Table 1. The comparison of chemical shifts between NIC:COU (1:1) cocrystal with NIC and COU

Nicotinamide (NIC)		*p*-Coumaric acid (COU)		NIC:COU (1:1)	
Chemical shift, ppm (δ)	Multiplicity	Chemical shift, ppm (δ)	Multiplicity	Chemical shift, ppm (δ)	Multiplicity
		6.26	d	6.26	d
		6.77	d	6.77	d
7.48	m			7.47	m
		7.49	m	7.47	m
7.59	s			7.59	s
8.15	s			8.15	s
8.18	d			8.18	d
8.68	d			8.68	d
9.01	s			9.01	s
		9.96	s	9.96	s
		12.12	s	12.14	s

s: singlet, d: doublet, m: multiplet
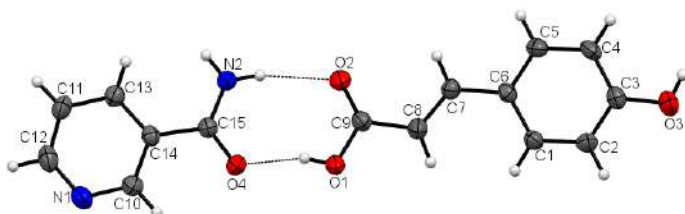
Fig 5. ORTEP drawing of NIC:COU (1:1) cocrystal with the atom labeling in the asymmetric unit

Crystallography Analysis of NIC:COU (1:1) Cocrystal

Fig. 5 and Table 2 show the ORTEP drawing of the asymmetric unit of NIC:COU (1:1) cocrystal and the crystallographic data of the cocrystal, respectively.

The NIC:COU (1:1) cocrystal was synthesized using the slow evaporation method with acetonitrile. The interaction is expected to occur between the nitrogen atom on the pyridine ring of NIC and acid group of COU, amide-amide, and amide-acid [11], and phenol-pyridine [32,36] hydrogen bonding linkages. The assessment of the asymmetric unit of the cocrystal shows that the 1:1 molecule crystallizes in a monoclinic crystal lattice with P 2_1/c space group, similar to the published Form 1 NIC:COU (1:1) cocrystal structure [7]. The synthesized cocrystal revealed greater stability with a higher melting temperature compared to the published cocrystal. All bond lengths and angles for both independent molecules are within the expected values, tabulated in the Supplementary Material, section S1, S2, and S3, respectively. The crystal structure

data comparison between the synthesized cocrystal with the published cocrystal are presented in Table 4.

Table 2. Crystal data and structure refinement parameters of NIC:COU (1:1) cocrystal

Empirical formula	$C_{15}H_{14}N_2O_4$
Moiety formula	$C_6H_{62}O$, $C_9H_8O_3$
Formula weight (g/mol)	286.28
Crystal system	monoclinic
Space group	P 2_1/c
R1-value	0.0751
Crystal size (mm³)	0.40 × 0.50 × 0.50
a (Å)	15.675(2)
b (Å)	6.3538(8)
c (Å)	14.433(2)
α (°)	90
β (°)	106.945(4)
ϒ (°)	90
V (Å³)	1375.1(3)
Z	4
D_c (g cm⁻³)	1.3828(3)
μ (mm⁻¹)	0.102
λ (Å)	0.7107
T (K)	273(2)
F(000)	600
2θ range (°)	2.951-28.352
Reflection collected/unique	28920/3404 [R(int) = 0.0806]
Data/parameters/restraints	3404/195/1
Goodness of fit	1.086
Data collection	Bruker APEX2
Data reduction	Bruker SAINT
Structure solution	SHELXS-97 (Sheldrick 2008)
Structure refinement	SHELXL-2013 (Sheldrick 2013)

The crystal structure shows no intramolecular interaction, no π-π stacking interaction, and no proton transfer from –COOH group of COU. The crystal structure is stabilized by intermolecular hydrogen-bonding interactions O1-H1A···O4 (2.554 Å), N2-H2A···O2 (2.922 Å), N2-H2B···O1 (2.976 Å), and O3-H3···N1 (2.713 Å). These intermolecular interactions are in good agreement with the FTIR result, which anticipated in the formation of the cocrystal. The hydrogen bond geometries were summarized in Table 3. Based on the hydrogen bonding interaction observed, the homomeric $R_2^2(8)$ ring is formed between a pair of –NH amide hydrogen-bonded to the oxygen of carbonyl group linking the tetrameric hydrogen-bonded rings into an infinite ribbon.

The hydrogen bonding interaction pattern in NIC:COU (1:1) cocrystal was consistent with Form 1 NIC:COU (1:1) cocrystal synthesized by the previous researcher [7]. Although the hydrogen bonding interaction patterns are similar, the hydrogen bonding geometry of the synthesized cocrystal in this study are off-plane for N2-H2B···O1, and O3-H3···N1 compared to the reported data. Bevill et al. [7] revealed a more planar geometry of N2-H2B···O1, and O3-H3···N1 hydrogen bonding interactions with 161.5°, and 164°, compared to the synthesized NIC:COU (1:1) cocrystal in this study with 153°, and 139° respectively. This supports the difference in the melting point of the synthesized cocrystal in this study with the cocrystals synthesized by Bevill et al. [7], which reflects the different solvent used for the cocrystal synthesis is able to change the properties of the cocrystal. The change of the properties of the cocrystal is crucial where it indicates the bioavailability and the stability of the compound.

Table 3. Hydrogen bond geometry (Å and °) in NIC:COU (1:1) cocrystal

D-H···A	D(D-H)	d(H···A)	D(D···A)	∠D-H···A
O1-H1A···O4	0.82(3)	1.76(3)	2.554(3)	162(3)
N2-H2A···O2	0.86	2.08	2.922(3)	167
N2-H2B···O1	0.86	2.18	2.976(3)	153
O3-H3···N1	0.82	2.04	2.713(3)	139

Table 4. Comparison between the synthesized NIC:COU (1:1) cocrystal with reported data

	Experiment, NIC:COU (1:1)	Literature [7]	
		Form 1	Form 3
Melting temp (°C)	159.07	154	160
Empirical formula	$C_{15}H_{14}N_2O_4$	$C_{15}H_{14}N_2O_4$	$C_{15}H_{14}N_2O_4$
Crystal habit	gold, plate	colorless, plate	colorless, rod
Crystal system	monoclinic	monoclinic	monoclinic
Space group, Z	P2$_1$/c, 4	P2$_1$/c, 4	C2/c, 16
a (Å)	15.675(2)	15.5106(10)	40.076(2)
b (Å)	6.3538(8)	6.2871(4)	7.1979(12)
c (Å)	14.433(2)	14.1238(10)	22.2876(12)
β (°)	106.945(4)	106.086(3)	122.479(2)
Volume (Å³)	1375.1(3)	1323.38(15)	5423.5(5)
D$_c$ (g/cm³)	1.3828(3)	1.437	1.402
T (K)	273(2)	120(2)	120(2)
μ (mm^{-1})	0.102	0.106	0.103
F (000)	600	600	2400
θ range (°)	2.951–28.352	2.73–32.58	1.83–31.00
R-int	0.0806	0.028	0.041
R$_1$	0.0751	0.0461	0.0537

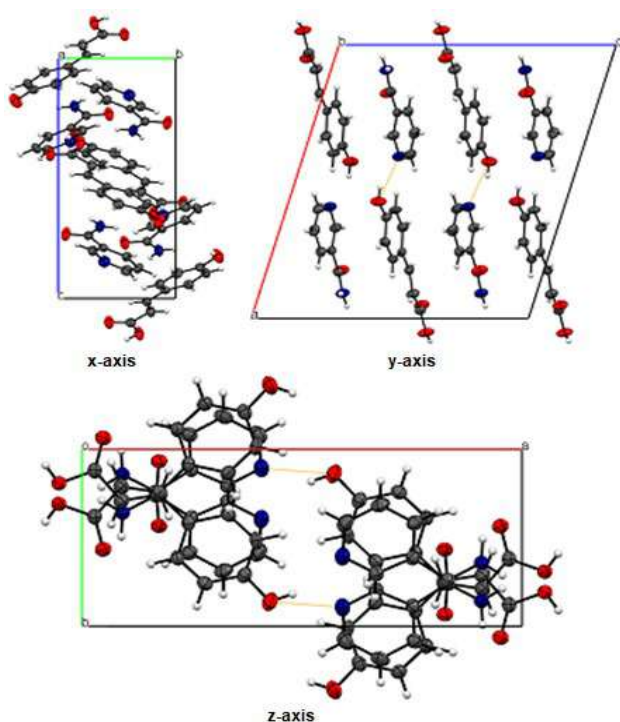*Indones. J. Chem., 2020, 20 (3), 661 - 679*

671

Fig 6. The crystal packing of NIC:COU (1:1) cocrystal

The crystal packing of NIC:COU (1:1) cocrystal from the x, y, and z views is illustrated in Fig. 6. The crystal lattice of NIC:COU (1:1) cocrystal is composed of the NIC and COU molecules alternately aligned with head to head stacking motif in the crystal lattice, observed from the y-axis. The differences in the molecular orientation are due to the non-centrosymmetric properties, differences in the hydrogen bonding patterns between the NIC and COU molecules, and also between the asymmetric pairs in the crystal lattice. The alignment of molecules and interaction between molecules in the crystal packing have a significant impact on the morphology of the crystal [41], which will be discussed in the crystal morphology prediction section.

Intermolecular Assessment using Molecular Modelling Technique

Table 5 shows the calculated lattice energy corresponds to the charge sets and force fields applied. The lattice energy was observed to be highly reliant on the charge set/force field applied. The lattice energy varies from -110.874 kcal/mol (Hirshfeld/Compass) to -292.740 kcal/mol (ESP/Compass). The $-NH_2$ and $-COOH$ groups undoubtedly contribute to the lattice energy value due to their participation in the hydrogen bonding formation

within the crystal lattice [47]. The use of ESP charge results in the strong electrostatic interaction between the positive oxygen atom of OH in COU and the negative regions of the NIC. Similar trend was observed between 2,4,5,8,10,12-hexanitro-2,4,6,8,10,12-hexaazaisowurtzitane (CL-20) and trinitrotoluene (TNT) [65]. Thus, it can be concluded that ESP/Compass pair forms the strongest hydrogen bonding interaction, while the Hirshfeld/Compass pair forms the weakest hydrogen bonding interaction between the NIC and COU molecules in the crystal lattice.

Morphological Prediction of NIC:COU (1:1) Cocrystal

Fig. 7(a) shows the crystal shape of NIC:COU (1:1) cocrystal grown from acetonitrile, and Fig. 7(b) shows the

Table 5. Lattice energies (kcal/mol) of NIC:COU (1:1) cocrystal computed using different charge sets and force fields

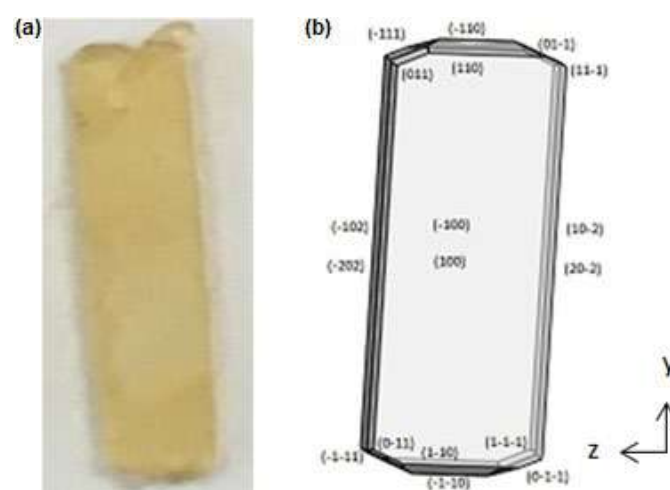| Force field	Type of charge	E_{latt} (kcal/mol)
Compass	Mulliken	-247.403
	Hirshfeld	-110.874
	ESP	-292.740
Universal	Mulliken	-210.824
	Hirshfeld	-146.484
	ESP	-226.753
Dreiding	Mulliken	-282.145
	Hirshfeld	-194.309
	ESP	-271.440

Fig 7. (a) NIC:COU (1:1) cocrystal grown in acetonitrile and (b) simulated NIC:COU (1:1) crystal morphology, predicted using Dreiding force field and ESP charge set

predicted NIC:COU (1:1) cocrystal morphology using MS with AE method. The most acceptable morphology was accomplished using ESP charge set with Dreiding force field (E_{latt} = -271.440 kcal/mol) with similar predicted crystal shape with the experimental morphology. The predicted crystal morphology produces 18 crystal facets with elongated (along the y-axis) octagonal shape with the dominant facets of (100) and (-100). The long and thin sides comprise of (10-2), (20-2), (-102), and (-202) facets, while the top and bottom sides of the crystal composed of (110), (-110), (1-10), and (-1-10) facets. The edges of the crystal are bounded with (11-1), (-111), (-1-11), (1-1-1), (011), (01-1), (0-11), and (0-1-1). The published NIC:COU (1:1) cocrystal [7] simulated with similar force field/charge set pair (Dreiding/ESP) resulted in lower lattice energy of -270.739 kcal/mol, indicating the similar crystal structure with the same lattice energy.

The distribution of lattice energy was calculated using Eq. (1) is presented in Table 6. The dominant facet of (100), with its symmetry (-100) facet has the minimum attachment energy of -22.020 kcal/mol (8.112%), the largest d_{100} of 15.915 Å, and the largest total facet area of 66.942%, thus being the slowest growing rate face with high stability (Fig. 8(a)). The (100) facets were constructed with the COU, and NIC molecules alternatingly positioned, making every layer downward from the surface. The small crystal facet results with a higher growth rate, thus small slice energy, which makes (11-1) facet to be the least morphologically important crystal facet [47,53].

The molecular packing of each NIC:COU (1:1) cocrystal facets are presented in Fig. 8(a–j). The molecular packing of NIC:COU (1:1) cocrystal facets reveal the hydrogen bonding interactions mainly occur at the amide group of NIC and the carboxylic acid group of COU. Most of the crystal facets show the open and rough surface topographies with large voids [39], except for the (20-2) facet, which forms a flat and smooth surface. In most cases, the crystal facet with flat and smooth surface results in a slow growth rate compared to the rough surface [66]. The slow growth rate crystal facet may also be due to the preferential adsorption of solvent molecules, as the growth kinetics is transferred to the polar surface [53,66].

It was observed that NH_2, -COOH, and -OH (phenol) groups are exposed on most of the crystal facets. The exposed group may affect the polarities of the crystal facet, which then affects the interaction with the solvent [39-40]. The crystal facet with exposed oxygen atoms (high polarity) will contribute to the high electrostatic energy for the particular facets [53]. The assessment of (20-2) facet with its symmetry (Fig. 8(c) and (d)) also shows significant conformational difference [53] (shown in red circle), which results in polar crystal facets.

Since the acidic proton is the best hydrogen bond donor, while the nitrogen atom of the pyridine ring is the best hydrogen bond acceptor, it was suggested that the facets exposed with these groups are ready to interact first with the solvent. Since the acetonitrile is a polar aprotic solvent, the (100) facet with exposed polar –OH groups hinders the growth of the facet resulting in larger a surface area. The (100), (1-10), (11-1), (1-1-1), (011), and (01-1) facets with exposed best hydrogen bond donor groups are expected to form the strongest hydrogen bond with the external compounds. It was also observed that the non-aggregated molecular arrangement patterns as (100) and (202) facets result with

Table 6. The distribution of attachment and slice energies for the NIC:COU (1:1) cocrystal facets, calculated using Eq. (1)

Facet	Multiplicity	d-spacing	Attachment energy		Slice energy		Total facet
			(kcal/mol)	(%)	(kcal/mol)	(%)	area (%)
(100)	2	15.915	-22.020	8.112	-249.420	91.888	66.942
(20-2)	2	7.654	-65.950	24.296	-205.490	75.704	18.227
(10-2)	2	7.615	-72.416	26.678	-199.024	73.322	3.891
(110)	4	5.881	-148.176	54.589	-123.264	45.411	6.222
(011)	4	5.653	-156.696	57.728	-114.744	42.272	1.154
(11-1)	4	5.849	-158.195	58.280	-113.245	41.720	3.565
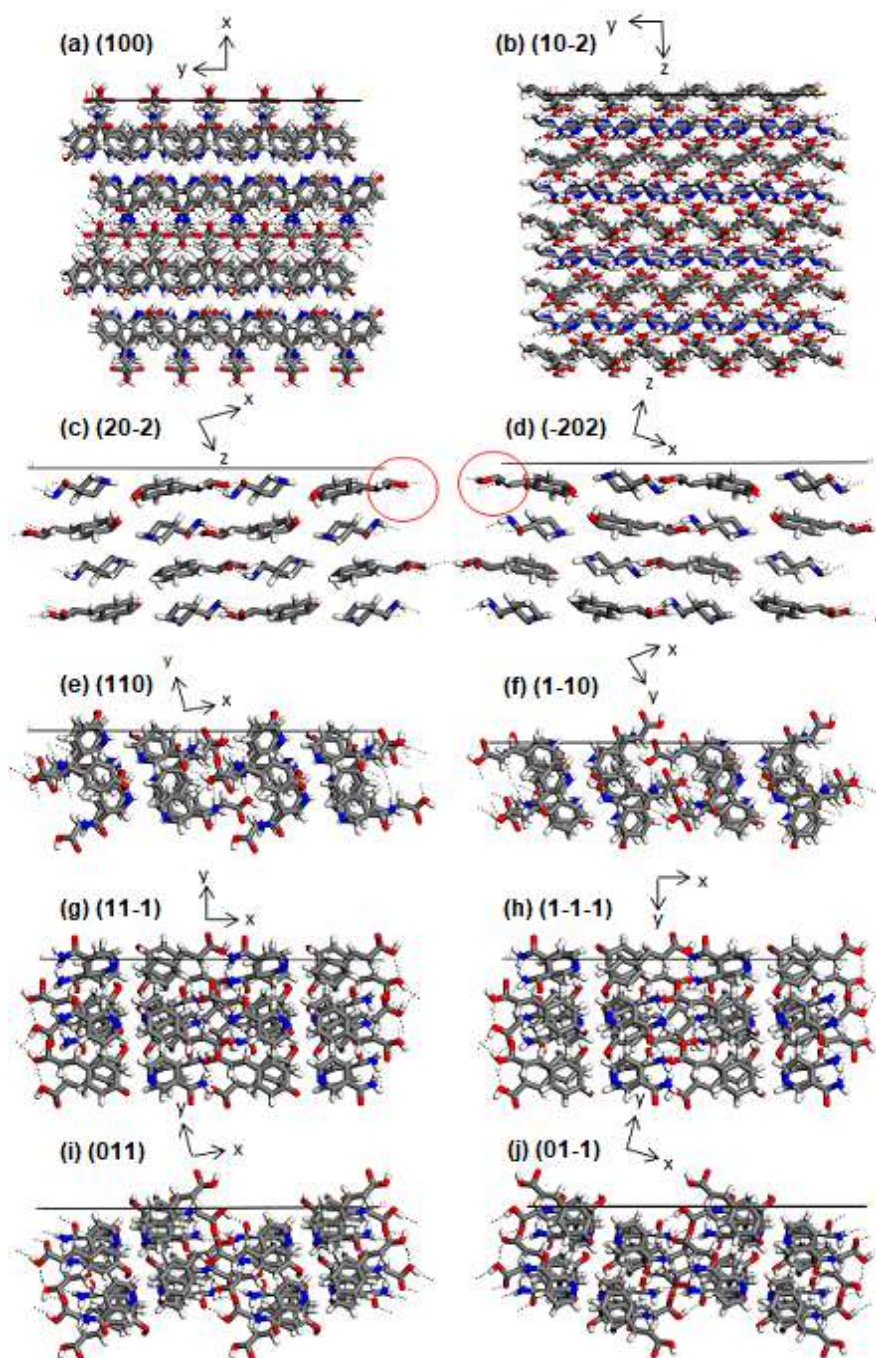
Fig 8. Molecular packing diagram of NIC:COU (1:1) cocrystal illustrating the surface chemistry of crystal facets, determined using the routine available in the Material Studio program package; forcefield used was Dreiding with ESP charge set

higher slice energy, compared to the aggregated molecular arrangements in other facets with lower slice energy. This shows that the molecular arrangement behavior within the crystal lattice has a compelling impact on the slice energy of the growing crystal.

Solubility Determination

Fig. 9 illustrates the experimental solubility-temperature profile of NIC:COU (1:1) cocrystal compared to NIC from 10 °C to 60 °C. The experimental solubility of NIC is within reasonable agreement with the
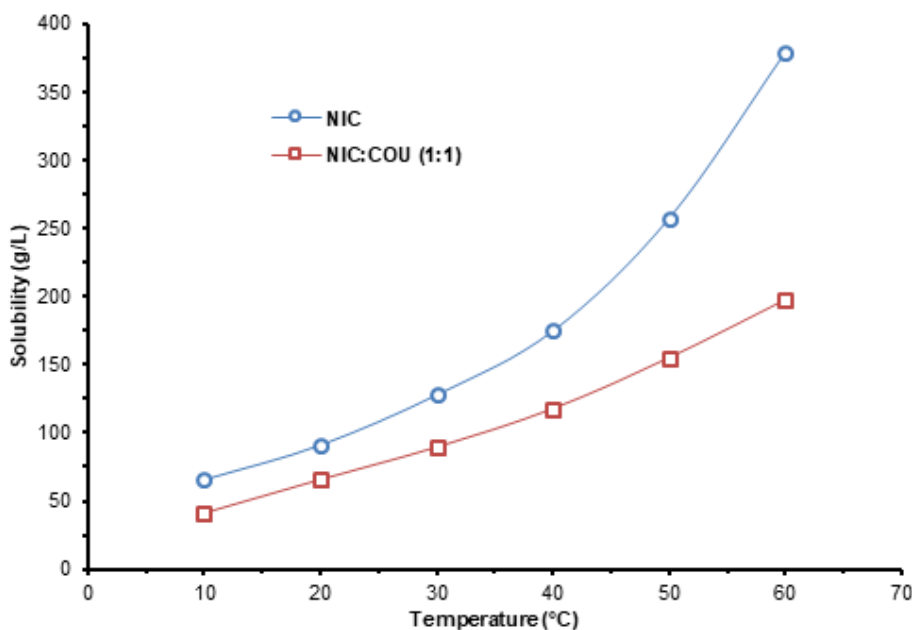
Fig 9. Solubility-temperature dependence of NIC and NIC:COU (1:1) cocrystal

result obtained by the previous researcher [67]. The solubility of NIC:COU (1:1) cocrystal significantly reduced in ethanol compared to NIC. The reduced cocrystal solubility may be due to the changes in the solvating interaction between the molecules and the solvent (varying from van der Waals to hydrogen bonding) [5,68].

The solvent used in the solubility determination affects the most to the solubility result, which generally follows the solubility of solute principle, 'like dissolves like' [68]. The solubility drop may also be due to the different solvent used during the crystallization process and the solubility analysis. Acetonitrile (polarity = 46, dielectric constant = 37.5) is a polar aprotic solvent, while ethanol (polarity = 65.4, dielectric constant = 24.3) is a polar protic solvent [67]. The simulation of cocrystal facets also shows the polar functional group exposed on most of the crystal facets, which makes the crystal as a polar compound. The assessment of structural conformation between (20-2) facet with its symmetry also shows the polar facet characteristic, explaining the reduced solubility of cocrystal in ethanol.

Higher melting temperature and heat content of NIC:COU (1:1) cocrystal (159.07 °C) compared to the compound with higher solubility, NIC (129.94 °C) also being one of the factors of low solubility [21]. Although

the decrease in solubility was not desired in the pharmaceutical industry, it was preferred by some other application of specialty chemicals [69].

Antioxidant Activity Determination

NIC and NIC:COU (1:1) cocrystal scavenging activities were analyzed by the reduction of the stable radical DPPH to non-radical stable diamagnetic compound with the presence of hydrogen-donating antioxidant [60,70]. The color change observed was from purple to colorless solution, which signifies that the DPPH radical has accepted the hydrogen donated from the antioxidant sample. The results of the *in vitro* antioxidant capability of NIC and NIC:COU (1:1) cocrystal by DPPH radical scavenging activity assay are tabulated in Table 7. The results show the increase in the radical scavenging capability of the cocrystal at several concentrations compared to NIC individually. This confirms that the NIC:COU (1:1) cocrystal is a more effective proton donor to the DPPH radical compared to NIC. The scavenging capability increase varies from 2.23% to 77.06%. The highest increment recorded is 77.06% at a concentration of 31.3 μM. The reported antioxidant activity of COU was 182.75 μM with 55.6% inhibition [60], which is lower compared to the

Table 7. Scavenging activity of NIC and NIC:COU (1:1) cocrystal

Concentration, μM	% Scavenging activity		% Increased scavenging activity
	NIC	NIC:COU (1:1)	
2.0	8.97	7.94	-
3.9	8.57	12.34	43.99
7.8	11.01	8.36	-
15.6	8.68	9.56	10.14
31.3	8.02	14.20	77.06
62.5	9.43	9.64	2.23
125.0	9.53	8.86	-
250.0	8.61	13.84	60.74
500.0	9.93	6.48	-
1000.0	8.56	13.24	54.67

synthesized cocrystal. The increased antioxidant capability of the cocrystal is due to the combined cocrystal structure of NIC and COU, which summates the number of hydrogen atom donors to react with the DPPH radical.

■ **CONCLUSION**

The NIC:COU (1:1) cocrystal was successfully synthesized using a slow evaporation method with acetonitrile. The comparison of the crystal data between the synthesized cocrystal with the published cocrystal data revealed similar cocrystal of NIC:COU (1:1) was produced, the synthesized cocrystal showed greater stability where the melting temperature is higher than the published cocrystal. The characterization data also discovered new crystal phases for the NIC:COU cocrystals with 1:2 and 2:1 feed molar ratios, which were not successfully grown into a single crystal. The molecular dynamics simulation work predicted the morphology of the NIC:COU (1:1) cocrystal using ESP/Dreiding pair resulted in lattice energy of -271.440 kcal/mol, which was in reasonable agreement with the experimental cocrystal morphology. The predicted cocrystal morphology was characterized as elongated (along the *y*-axis) octagonal shape with 18 total crystal facets, in which the morphological importance (100) was the strongest and the (11-1) facet was the weakest. The hydrogen-bonding interactions simulated in the MS were also concurrent with the result from SCD.

Nonetheless, the solubility of the cocrystal significantly reduced as the temperature was increased in ethanol. This occurrence was assisted with the increased melting temperature of NIC:COU (1:1) cocrystal compared to the NIC with the highest solubility compound used in this study. The simulation of crystal facets also showed the exposed polar functional groups, which technically will have low solubility in less polar solvent ethanol. The NIC:COU (1:1) cocrystal was found to be an effective antioxidant in the DPPH radical assay with the highest scavenging activity increase of 77.06% compared to NIC individually at 31.3 μM. The improved radical scavenging capacity of NIC:COU (1:1) cocrystal offers the potential value to become a new oral or transdermal formulation with better bioavailability.

■ **ACKNOWLEDGMENTS**

■ **REFERENCES**

[1] Song, J.X., Chen, J.M., and Lu, T.B., 2015, Lenalidomide–gallic acid cocrystals with constant high solubility, *Cryst. Growth Des.*, 15 (10), 4869–4875.

[2] Huang, Y., Zhang, B., Gao, Y., Zhang, J., and Shi, L., 2014, Baicalein-nicotinamide cocrystal with

676

Indones. J. Chem., 2020, 20 (3), 661 - 679

enhanced solubility, dissolution, and oral bioavailability, *J. Pharm. Sci.*, 103 (8), 2330–2337.

[3] Cheney, M.L., Weyna, D.R., Shan, N., Hanna, M., Wojtas, L., and Zaworotko, M.J., 2010, Supramolecular architectures of meloxicam carboxylic acid cocrystals, a crystal engineering case study, *Cryst. Growth Des.*, 10 (10), 4401–4413.

[4] Raghuram, M., Sarwar Alam, M., Prasad, M., and Has Khanduri, C., 2014, Pharmaceutical cocrystal of prulifloxacin with nicotinamide, *Int. J. Pharm. Pharm. Sci.*, 6 (10), 180–184.

[5] Shayanfar, A., Velaga, S., and Jouyban, A., 2014, Solubility of carbamazepine, nicotinamide and carbamazepine–nicotinamide cocrystal in ethanol–water mixtures, *Fluid Phase Equilib.*, 363, 97–105.

[6] Hino, T., Ford, J.L., and Powell, M.W., 2001, Assessment of nicotinamide polymorphs by differential scanning calorimetry, *Thermochim. Acta*, 374 (1), 85–92.

[7] Bevill, M.J., Vlahova, P.I., and Smit, J.P., 2014, Polymorphic cocrystals of nutraceutical compound *p*-coumaric acid with nicotinamide: Characterization, relative solid-state stability, and conversion to alternate stoichiometries, *Cryst. Growth Des.*, 14 (3), 1438–1448.

[8] Aakeröy, C.B., Beatty, A.M., and Helfrich, B.A., 2002, A high-yielding supramolecular reaction, *J. Am. Chem. Soc.*, 124 (48), 14425–14432.

[9] Aakeröy, C.B., Beatty, A.M., Helfrich, B.A., and Nieuwenhuyzen, M., 2003, Do polymorphic compounds make good cocrystallizing agents? A structural case study that demonstrates the importance of synthon flexibility, *Cryst. Growth Des.*, 3 (2)., 159–165.

[10] Bhogala, B.R., Basavoju, S., and Nangia, A., 2005, Tape and layer structures in cocrystals of some di- and tricarboxylic acids with 4,4′-bipyridines and isonicotinamide. From binary to ternary cocrystals, *CrystEngComm*, 7 (90), 551–562.

[11] Fábián, L., Hamill, N., Eccles, K.S., Moynihan, H.A., Maguire, A.R., McCausland, L., and Lawrence, S.E., 2011, Cocrystals of fenamic acids with nicotinamide, *Cryst. Growth Des.*, 11 (8), 3522–3528.

[12] Lemmerer, A., Báthori, N.B., and Bourne, S.A., 2008, Chiral carboxylic acids and their effects on melting-point behaviour in co-crystals with isonicotinamide, *Acta Crystallogr., Sect. B: Struct. Sci.*, 64 (Pt 6), 780–790.

[13] Vishweshwar, P., Nangia, A., and Lynch, V.M., 2003, Supramolecular synthons in phenol–isonicotinamide adducts, *CrystEngComm*, 5 (31), 164–168.

[14] Vishweshwar, P., Nangia, A., and Lynch, V.M., 2003, Molecular complexes of homologous alkanedicarboxylic acids with isonicotinamide: X-ray crystal structures, hydrogen bond synthons, and melting point alternation, *Cryst. Growth Des.*, 3 (5), 783–790.

[15] Berry, D.J., Seaton, C.C., Clegg, W., Harrington, R.W., Coles, S.J., Horton, P.N., Hurtshouse, M.B., Storey, R., Jones, W., and Friscic, T., 2008, Applying hot-stage microscopy to co-crystal screening: A study of nicotinamide with seven active pharmaceutical ingredients, *Cryst. Growth Des.*, 8 (5), 1697–1712.

[16] Zhang, S.W., Harasimowicz, M.T., de Villiers, M.M., and Yu, L., 2013, Cocrystals of nicotinamide and (R)-mandelic acid in many ratios with anomalous formation properties, *J. Am. Chem. Soc.*, 135 (50), 18981–18989.

[17] Setyawan, D., Sari, R., Yusuf, H., and Primaharinastiti, R., 2014, Preparation and characterization of artesunate–nicotinamide co-crystal by solvent evaporation and slurry method, *Asian J. Pharm. Clin. Res.*, 7 (Suppl. 1), 62–65.

[18] Rahman, Z., Agarabi, C., Zidan, A.S., Khan, S.R., and Khan, M.A., 2011, Physico-mechanical and stability evaluation of carbamazepine cocrystal with nicotinamide, *AAPS PharmSciTech*, 12 (2), 693–704.

[19] Remenar, J.F., Peterson, M.L., Stephens, P.W., Zhang, Z., Zimenkov, Y., and Hickey, M.B., 2007, Celecoxib: Nicotinamide dissociation: Using excipients to capture the cocrystal's potential, *Mol. Pharmaceutics*, 4 (3), 386–400.

[20] Nicoli, S., Bilzi, S., Santi, P., Caira, M. R., Li, J., and Bettini, R., 2008, Ethyl-paraben and nicotinamide mixtures: Apparent solubility, thermal behavior and X-ray structure of the 1:1 co-crystal, *J. Pharm. Sci.*, 97 (11), 4830–4839.

[21] Sopyan, I., Fudholi, A., Muchtaridi, M., and Sari, I.P., 2017, Simvastatin-nicotinamide co-crystal: Design, preparation and preliminary characterization, *Trop. J. Pharm. Res.*, 16 (2), 297–303.

[22] Keramatnia, F., Shayanfar, A., and Jouyban, A., 2015, Thermodynamic solubility profile of carbamazepine-cinnamic acid cocrystal at different pH, *J. Pharm. Sci.*, 104 (8), 2559–2565.

[23] Shayanfar, A., Asadpour-Zeynali, K., and Jouyban, A., 2013, Solubility and dissolution rate of a carbamazepine–cinnamic acid cocrystal, *J. Mol. Liq.*, 187, 171–176.

[24] Lemmerer, A., Esterhuysen, C., and Bernstein, J., 2010, Synthesis, characterization, and molecular modeling of a pharmaceutical co-crystal: (2-Chloro-4-nitrobenzoic acid):(nicotinamide), *J. Pharm. Sci.*, 99 (9), 4054–4071.

[25] Etter, M.C., 1990, Encoding and decoding hydrogen-bond patterns of organic compounds, *Acc. Chem. Res.*, 23 (4), 120–126.

[26] Bernstein, J., Davis, R.E., Shimoni, L., and Chang, N.L., 1995, Patterns in hydrogen bonding: Functionality and graph set analysis in crystals, *Angew. Chem. Int. Ed.*, 34 (15), 1555–1573.

[27] Etter, M.C., MacDonald, J.C., and Bernstein, J., 1990, Graph-set analysis of hydrogen-bond patterns in organic crystals, *Acta Crystallogr., Sect. B: Struct. Sci.*, 46, 256–262.

[28] Karki, S., Friščić, T., and Jones, W., 2009, Control and interconversion of cocrystal stoichiometry in grinding: Stepwise mechanism for the formation of a hydrogen-bonded cocrystal, *CrystEngComm*, 11 (3), 470–481.

[29] Nićiforović, N., and Abramovič, H., 2014, Sinapic acid and its derivatives: Natural sources and bioactivity, *Compr. Rev. Food Sci. Food Saf.*, 13 (1), 34–51.

[30] Kulik, T.V., Lipkovska, N.O., Barvinchenko, V.M., Palyanytsya, B.B., Kazakova, O.A., Dudik, O.O., Menyhard, A., and Laszlo, K., 2016, Thermal transformation of bioactive caffeic acid on fumed silica seen by UV-Vis spectroscopy, thermogravimetric analysis, temperature programmed desorption mass spectrometry and quantum chemical methods, *J. Colloid Interface Sci.*, 470, 132–141.

[31] Schultheiss, N., Roe, M., and Boerrigter, S.X.M., 2011, Cocrystals of nutraceutical *p*-coumaric acid with caffeine and theophylline: polymorphism and solid-state stability explored in detail using their crystal graphs, *CrystEngComm*, 13 (2), 611–619.

[32] Ravikumar, N., Gaddamanugu, G., and Solomon, K.A., 2013, Structural, spectroscopic (FT-IR, FT-Raman) and theoretical studies of the 1:1 cocrystal of isoniazid with *p*-coumaric acid, *J. Mol. Struct.*, 1033, 272–279.

[33] Du, N., Cao, S., and Yu, Y., 2011, Research on the adsorption property of supported ionic liquids for ferulic acid, caffeic acid and salicylic acid, *J. Chromatogr. B*, 879 (19), 1697–1703.

[34] Kumar, N., Pruthi, V., and Goel, N., 2015, Structural, thermal and quantum chemical studies of *p*-coumaric and caffeic acids, *J. Mol. Struct.*, 1085, 242–248.

[35] Jacobs, A., and Noa, F.M.A., 2013, Hybrid salt–cocrystal solvate: p-coumaric acid and quinine system, *J. Chem. Crystallogr.*, 44 (2), 57–62.

[36] Swapna, B., Maddileti, D., and Nangia, A., 2014, Cocrystals of the tuberculosis drug isoniazid: Polymorphism, isostructurality, and stability, *Cryst. Growth Des.*, 14 (11), 5991–6005.

[37] Shi, W., Xia, M., Lei, W., and Wang, F., 2014, Solvent effect on the crystal morphology of 2,6-diamino-3,5-dinitropyridine-1-oxide: A molecular dynamics simulation study, *J. Mol. Graphics Modell.*, 50, 71–77.

[38] Zhang, M., Liang, Z., Wu, F., Chen, J.F., Xue, C., and Zhao, H., 2017, Crystal engineering of ibuprofen compounds: From molecule to crystal

structure to morphology prediction by computational simulation and experimental study, *J. Cryst. Growth*, 467, 47–53.

[39] Chen, G., Xia, M., Lei, W., Wang, F., and Gong, X., 2014, Prediction of crystal morphology of cyclotrimethylene trinitramine in the solvent medium by computer simulation: A case of cyclohexanone solvent, *J. Phys. Chem. A*, 118 (49), 11471–11478.

[40] Han, G., Li, Q.F., Gou, R.J., Zhang, S.H., Ren, F.D., Wang, L., and Guan, R., 2017, Growth morphology of CL-20/HMX cocrystal explosive: Insights from solvent behavior under different temperatures, *J. Mol. Model.*, 23 (12), 360.

[41] Hassan, S., Adam, F., Abu Bakar, M.R., and Abdul Mudalip, S.K., 2018, Evaluation of solvents' effect on solubility, intermolecular interaction energies and habit of ascorbic acid crystals, *J. Saudi Chem. Soc.*, 23 (2), 239–248.

[42] Hod, I., Mastai, Y., and Medina, D.D., 2011, Effect of solvents on the growth morphology of dl-alanine crystals, *CrystEngComm.*, 13 (2), 502–509.

[43] Wang, C., Zhang, X., Du, W., Huang, Y.H., Guo, M.X., Li, Y., Zhang, Z.X., Hou, B.H., and Yin, Q.X., 2016, Effects of solvent and supersaturation on crystal morphology of cefaclor dihydrate: A combined experimental and computer simulation study, *CrystEngComm.*, 18 (47), 9085–9094.

[44] Rohl, A.L., 2003, Computer prediction of crystal morphology, *Curr. Opin. Solid State Mater. Sci.*, 7 (1), 21–26.

[45] Liu, J., Sun, J., Zhang, H., and Wen, Y., 2016, Prediction of crystal morphology of 1,3,5-triamino-2,4,6-trinitrobenzene in dimethyl sulfoxide via modified attachment energy modeling and its experimental validation, *Mol. Cryst. Liq. Cryst.*, 634 (1), 97–103.

[46] Liu, N., Li, Y.N., Zeman, S., Shu, Y.J., Wang, B.Z., Zhou, Y.S., Zhao, Q.L., and Wang, W.L., 2016, Crystal morphology of 3,4-bis(3-nitrofurazan-4-yl)furoxan (DNTF) in a solvent system: Molecular dynamics simulation and sensitivity study, *CrystEngComm.*, 18 (16), 2843–2851.

[47] Rosbottom, I., Roberts, K.J., and Docherty, R., 2015, The solid state, surface and morphological properties of *p*-aminobenzoic acid in terms of the strength and directionality of its intermolecular synthons, *CrystEngComm*, 17 (30), 5768–5788.

[48] Coombes, D.S., Catlow, C.R.A., Gale, J.D., Hardy, M.J., and Saunders, M.R., 2002, Theoretical and experimental investigations on the morphology of pharmaceutical crystals, *J. Pharm. Sci.*, 91 (7), 1652–1658.

[49] ter Horst, J.H., Kramer, H.J.M., van Rosmalen, G.M., and Jansens, P.J., 2002, Molecular modelling of the crystallization of polymorphs. Part I: The morphology of HMX polymorphs, *J. Cryst. Growth*, 237-239, 2215–2220.

[50] Erk, P., 2001, Crystal design of organic pigments–A prototype discipline of materials science, *Curr. Opin. Solid State Mater. Sci.*, 5 (2-3), 155–160.

[51] Millan, A., 2001, Crystal growth shape of whewellite polymorphs: Influence of structure distortions on crystal shape, *Cryst. Growth Des.*, 1 (3), 245–254.

[52] Grimsey, I.M., Osborn, J.C., Doughty, S.W., York, P., and Rowe, R.C., 2002, The application of molecular modelling to the interpretation of inverse gas chromatography data, *J. Chromatogr. A*, 969 (1-2), 49–57.

[53] Anuar, N., Wan Daud, W.R., Roberts, K.J., Kamarudin, S.K., and Tasirin, S.M., 2012, Morphology and associated surface chemistry of L-isoleucine crystals modeled under the influence of L-leucine additive molecules, *Cryst. Growth Des.*, 12 (5), 2195–2203.

[54] Shen, F., Lv, P., Sun, C., Zhang, R., and Pang, S., 2014, The crystal structure and morphology of 2,4,6,8,10,12-hexanitro-2,4,6,8,10,12-hexaazaisowurtzitane (CL-20) *p*-xylene solvate: A joint experimental and simulation study, *Molecules*, 19 (11), 18574–18589.

[55] McMahon, J.A., Bis, J.A., Vishweshwar, P., Shattock, T.R., McLaughlin, O.L., and Zaworotko, M.J., 2005, Crystal engineering of the composition of pharmaceutical phases. 3. Primary amide supramolecular heterosynthons and their role in

the design of pharmaceutical co-crystals, *Z. Kristallogr. Cryst. Mater.*, 220 (4), 340–350.

[56] Aitipamula, S., Chow, P.S., and Tan, R.B.H., 2009, Trimorphs of a pharmaceutical cocrystal involving two active pharmaceutical ingredients: potential relevance to combination drugs, *CrystEngComm*, 11 (9), 1823–1827.

[57] Spek, A.L., 2003, Single-crystal structure validation with the program PLATON, *J. Appl. Crystallogr.*, 36 (1), 7–13.

[58] Shahidi, F., and Zhong, Y., 2015, Measurement of antioxidant activity, *J. Funct. Foods*, 18, 757–781.

[59] Chen, Z., Bertin, R., and Froldi, G., 2013, EC_{50} estimation of antioxidant activity in DPPH assay using several statistical programs, *Food Chem.*, 138 (1), 414–420.

[60] Kiliç, I., and Yeşiloğlu, Y., 2013, Spectroscopic studies on the antioxidant activity of *p*-coumaric acid, *Spectrochim. Acta, Part A*, 115, 719–724.

[61] Gholizadeh, R., Wang, Y., and Yu, Y.X., 2017, Molecular dynamics simulations of stability at the early stages of silica materials preparation, *J. Mol. Struct.*, 1138, 198–207.

[62] Manin, A.N., Voronin, A.P., Drozd, K.V., Manin, N.G., Bauer-Brandl, A., and Perlovich, G.L., 2014, Cocrystal screening of hydroxybenzamides with benzoic acid derivatives: A comparative study of thermal and solution-based methods, *Eur. J. Pharm. Sci.*, 65, 56–64.

[63] Ezawa, T., Kawashima, Y., Noguchi, T., Jung, S., and Imai, N., 2017, Amidation of carboxylic acids via the mixed carbonic carboxylic anhydrides and its application to synthesis of antidepressant (1 *S*,2 *R*)-tranylcypromine, *Tetrahedron: Asymmetry*, 28 (12), 1690–1699.

[64] Teranishi, K., 2016, *trans-p*-Hydroxycinnamic acid as a bioluminescence-activating component in the pileus of the luminous fungus *Mycena chlorophos*, *Tetrahedron.*, 72 (5), 726–733.

[65] Ren, C., Li, X., and Guo, L., 2019, Chemical insight on decreased sensitivity of CL-20/TNT cocrystal revealed by ReaxFF MD simulations, *J. Chem. Inf. Model.*, 59 (5), 2079–2092.

[66] Singh, M., 2006, First principle study of crystal growth morphology: An application to crystalline urea, *arXiv:cond-mat.mtrl-sci*, 0602385.

[67] Wu, H., Dang, L., and Wei, H., 2014, Solid–liquid phase equilibrium of nicotinamide in different pure solvents: Measurements and thermodynamic modeling, *Ind. Eng. Chem. Res.*, 53 (4), 1707–1711.

[68] Ji, W., Meng, Q., Ding, L., Wang, F., Dong, J., Zhou, G., and Wang, B., 2016, Measurement and correlation of the solubility of caffeic acid in eight mono and water + ethanol mixed solvents at temperatures from (293.15 to 333.15) K, *J. Mol. Liq.*, 224, 1275–1281.

[69] Aakeröy, C.B., Forbes, S., and Desper, J., 2009, Using cocrystals to systematically modulate aqueous solubility and melting behavior of an anticancer drug, *J. Am. Chem. Soc.*, 131 (47), 17048–17049.

[70] Gülçin, I., 2006, Antioxidant activity of caffeic acid (3,4-dihydroxycinnamic acid), *Toxicology*, 217 (2-3), 213–220.

Application of Fourier Transform Near-Infrared (FT-NIR) and Fourier Transform Infrared (FT-IR) Spectroscopy Coupled with Wavelength Selection for Fast Discrimination of Similar Color of Tuber Flours

Rudiati Evi Masithoh[1,*], Hanim Zuhrotul Amanah[1,2], and Byoung Kwan Cho[2]

[1]Department of Agricultural and Biosystems Engineering, Faculty of Agricultural Technology, Universitas Gadjah Mada, Yogyakarta 55281, Indonesia

[2]Department of Biosystems Machinery Engineering, College of Agricultural and Life Science, Chungnam National University, 99 Daehak-ro, Yuseoung-gu, Daejeon 305-764, Republic of Korea

Abstract: *This research aimed at providing a fast and accurate method in discriminating tuber flours having similar color by using Fourier transform near-infrared (FT-NIR) and Fourier transform infrared (FT-IR) spectroscopy in order to minimize misclassification if using human eye, or to avoid adulteration. Reflectance spectra of three types of tubers (consisted of* Canna edulis, *modified cassava, and white sweet potato) were collected to develop a multivariate model of partial least-squares discriminant analysis (PLS-DA). Several spectra preprocessing methods were applied to obtain the best calibration and prediction model, while variable importance in the projection (VIP) wavelength selection method was used to reduce variables in developing the model. The PLS-DA model achieved 100% accuracy in predicting all types of flours, both for FT-NIR and FT-IR. The model was also able to discriminate all flours with coefficient of determination (R^2) of 0.99 and a standard error of prediction (SEP) of 0.03% by using 1st Savitzky Golay (SG) derivative method for the FT-NIR data, as well as R^2 of 0.99 and SEP of 0.08% by using 1st Savitzky Golay (SG) derivative method for the FT-IR data. By applying the VIP method, the variables were reduced from 1738 to 608 variables with R^2 of 0.99 and SEP of 0.09% for FT IR and from 1557 to 385 variables with R^2 of 0.99 and SEP of 0.05% for FT NIR.*

Keywords: *FT-NIR; FT-IR; VIP; PLS-DA; tuber flour*

■ INTRODUCTION

Tubers, such as cassava, sweet potato, arrowroot, taro, and *Canna edulis*, are abundantly cultivated in several regions in Indonesia and usually consumed as a staple food to alternate rice. Those crops are rich in carbohydrate, providing about 1/3 of that of an equivalent weight of rice or wheat due to their high moisture content, and also sources of a number of compounds such as saponins, phenolic compounds, glycoalkaloids, phytic acids, carotenoids, and ascorbic acid [1]. Tubers have a high metabolic activity after harvest; therefore, they are more perishable than grains [2]. One method to prolong the tuber self-life is by making them into flours. In flour form, the crops can be utilized for several food productions such as for noodles, biscuits, snacks, or bread.

Among the tubers, *Canna edulis*, modified cassava, and white sweet potato have white color in flour form. Their colors are similar, making them difficult to be differentiated by the human eye. Although similar in color, those flours are different in composition and also in price. Chemical compositions are required to determine the method in food processing as well as to provide nutrition information for people susceptible to certain compounds. Due to the difference in price, adulteration of flours is sometimes inevitable. Low quality and price products are added to other products for economic reasons [3]. Based on seller price in

Indonesia, white sweet potato has the most expensive price, followed by *Canna edulis* and modified cassava flours. Therefore, an incorrect judgment of the type of flours may bring about health or economic consequences.

Quality determination of flours is usually done by sensory analysis using trained panelists [4], GC-MS for aroma [5], colorimeter, and spectrophotometer for color [6], as well as quantitative analysis in the laboratory [7]. Those methods require intense sample preparation, time-consuming, and skilled labors, especially for sensory analysis. For massive and large products, fast and rapid discrimination methods are needed.

Spectroscopy is now becoming popular as a fast and rapid method for qualitative and quantitative food analysis. Infrared spectroscopic covers wide range of electromagnetic regions consisting of near-infrared (NIR) at 14000–4000 cm^{-1}, mid-infrared (MIR) at 4000–400 cm^{-1} and far infrared at 400–50 cm^{-1}; however, MIR and NIR regions are commonly used for food quality analysis [8]. Whereas spectra in the MIR region contain information on the fundamental molecular vibrations, the absorption spectra in the NIR region contain information on the overtones and combinations of fundamental vibrations [9]. MIR spectroscopy is able to identify very similar and complex molecular structures, so it is useful for compound identification, while NIR spectroscopy is able to identify molecular interactions and chemical groups [10].

Both NIR and IR spectroscopy have been applied for quality identification of flour from wheat [11], rice [12], cassava, taro, and yam [13], and sweet potato [14]. Other applications combine chemometrics analysis with NIR and IR spectroscopy for detecting adulteration of flour products [15-16]. Classification of products using NIR and IR spectroscopy are also studied [17-18], but study about distinguishing flours that have a similar color has not been conducted. Therefore, this paper aims at discriminating flours from tuber crops that have similar color by applying Fourier transform near-infrared (FT-NIR) and Fourier transform infrared (FT-IR) spectroscopy. This study also applies variable importance in the projection (VIP) wavelength selection method in order to reduce processing time.

■ EXPERIMENTAL SECTION

Materials

Canna edulis, modified cassava, and white sweet potato flours were purchased from ten different sellers to obtain large varieties of samples. The sample of this study was *Canna edulis*, modified cassava, and white sweet potato flours obtained from several farmers in Indonesia to provide a wide range of variety shown from different brands. There were ten brands for each flour, making in a total of 30 batches of flour. For every batch, 3 samples were taken for spectra analysis, making a total of 90 spectra data.

Instrumentation

FT-NIR spectrophotometer (Antaris II FT-NIR analyzer, Thermo Scientific Co., Waltham, MA, USA) assembled with an InGaAs detector module, beam splitter, sample holder, moving mirror, laser diode, and halogen NIR light source, as well as FT-IR spectrometer (Nicolet 6700, Thermo Scientific Co., Waltham, MA, USA) using an attenuated total reflectance (ATR) sampling technique, a deuterated triglycine sulfate (DTGS) detector, and a KBr beam splitter, were used for spectra measurement.

Procedure

FT-NIR spectra acquisition

The reflectance spectra of 90 flours were acquired using the FT-NIR spectrophotometer (Antaris II FT-NIR analyzer, Thermo Scientific Co., Waltham, MA, USA) assembled with an InGaAs detector module, beam splitter, sample holder, moving mirror, laser diode, and halogen NIR light source. Each sample was scanned for 32 scans at the wavelength range of 4000–10,000 cm^{-1} at 4 cm^{-1} spectral resolution. The background scan was conducted with a golden slit frequently before acquiring the spectrum from each flour. In total, there were 1557 variables for FT-NIR.

FT-IR spectra acquisition

The spectra of 90 flours were obtained using the Nicolet 6700 FT-IR spectrometer with a range of 650–4000 cm^{-1}, using an attenuated total reflectance (ATR)

sampling technique, a highly sensitive deuterated triglycine sulfate (DTGS) detector, and a KBr beam splitter. A total of 32 successive scans of each sample with a spectral resolution of 3 cm^{-1} was recorded from the bare diamond ATR crystal. A background was recorded before every group of samples scanned with a clean ATR crystal. In total, there were 1738 variables for FT-IR.

Spectra pre-treatment and analysis

All spectra collections were done using Thermo Scientific™ OMNIC™ Series Software. The spectra data were transformed to MS Excel® 2013 and then imported to the Matlab version R2018a (The MathWorks, Inc., Natick, MA, USA) for spectra preprocessing and chemometrics analysis. Two multivariate data analysis techniques were applied, namely principal component analysis (PCA) and partial least-squares discriminant analysis (PLS-DA), to develop a classification model for *Canna edulis*, modified cassava, and white sweet potato flours. PCA was used for reducing dimensions and visualizing data distribution concerning discrimination of samples. For developing the PLS-DA model, the FT-NIR and FT-IR spectra were preprocessed through normalization methods (minimum, maximum, and range), standard normal variate transformation (SNV), multiple scatter correlation (MSC), and Savitzky-Golay (SG) smoothing (1st and 2nd derivatives). The 3rd order of polynomial fit and 5 smoothing points were used for SG smoothing. Variable importance in the projection (VIP) wavelength selection method was used to reduce variables

in developing the model. Of 90 spectra data, 60% and 40% of the data were used for calibration and prediction, respectively. A full-cross validation method (leave-one-out) was used in developing a calibration model using the PLS-DA method. The coefficient of determination (R^2) and a standard error of prediction (SEP) were used to justify the accuracy of the model.

■ RESULTS AND DISCUSSION

The analysis results from the spectra obtained using FT-NIR and FT-IR were used to compare the performance accuracy of the two spectroscopic techniques in distinguishing *Canna edulis*, modified cassava, and white sweet potato flours.

Spectra Data Exploration

Original spectra of all flours collected from FT-NIR and FT-IR systems are presented in Fig. 1. Fig. 1(a) shows the FT-NIR in the wavenumber range of 4000–10000 cm^{-1} in which all spectra are widely distributed between samples and have a similar pattern. However, the relative absorbance of *Canna edulis* flour is characterized by higher relative absorbance compared to other flours. Although not too distinct, several peaks on FT-NIR spectra can be observed, which may reflect particular chemical compounds. Original spectra of flours acquired from FT-IR at a wavenumber of 650–4000 cm^{-1} (Fig. 1(b)) shows sharper fundamental absorptions; therefore, they can be easily assigned to specific chemical compounds [19].
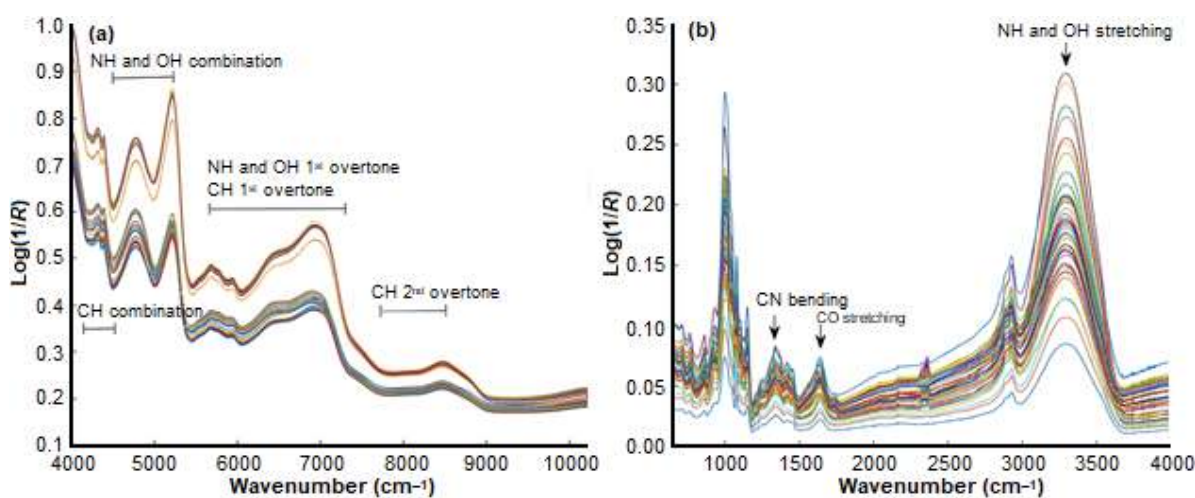

Fig 1. Original spectra of (a) FT-NIR and (b) FT-IR

The typical absorptions in the NIR region (Fig. 1(a)) are dominated by CH second overtone bands (7692–8695 cm⁻¹), NH and OH first overtone bands (5882–7142 cm⁻¹), CH first overtone bands (5882–7142 cm⁻¹), NH, and OH combination bands (4444–5263 cm⁻¹) and CH combination bands (4166–4444 cm⁻¹) [17]. Fig. 1(b) shows the FT-IR spectra of *Canna edulis*, modified cassava, and white sweet potato. In general, FT-IR spectra can be classified into two regions: below 1500 cm⁻¹, which are the fingerprint region, and 1500–4000 cm⁻¹, known as the functional group region [20]. Absorption peaks at a range of 3000–3500 cm⁻¹ show NH and OH stretching, while at 1456 and 1643 cm⁻¹ show CN bending and CO stretching, respectively [21].

Principle Component Analysis

The Principal Component Analysis (PCA) is applied for dimensional reduction and data exploration of the three tuber flours. By using original spectra for both FT-NIR and FT-IR data, the flours are clearly classified, as shown in Fig. 2(a) and Fig. 3(b). The loading plots (Fig. 2(b) and Fig. 3(b)) provide information about absorption bands, which largely contribute to the discrimination of flours according to the PC values.

As illustrated in Fig. 2(a), the plot of PC-1 and PC-2 provides better visualization of discrimination among the groups of samples for FT-NIR data. PC-1 and PC-2 altogether account for 99.5% the total variability. The PC
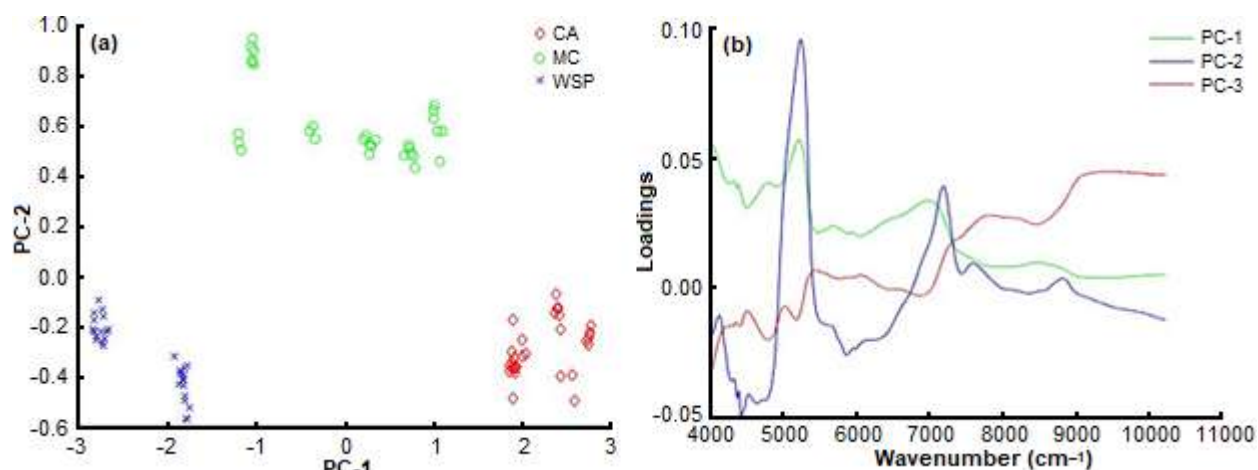

Fig 2. PCA of FT-NIR spectra of CA (*Canna edulis*), MC (modified cassava), and WSP (white sweet potato): (a) score plot and (b) loadings plot of PC-1 and PC-2
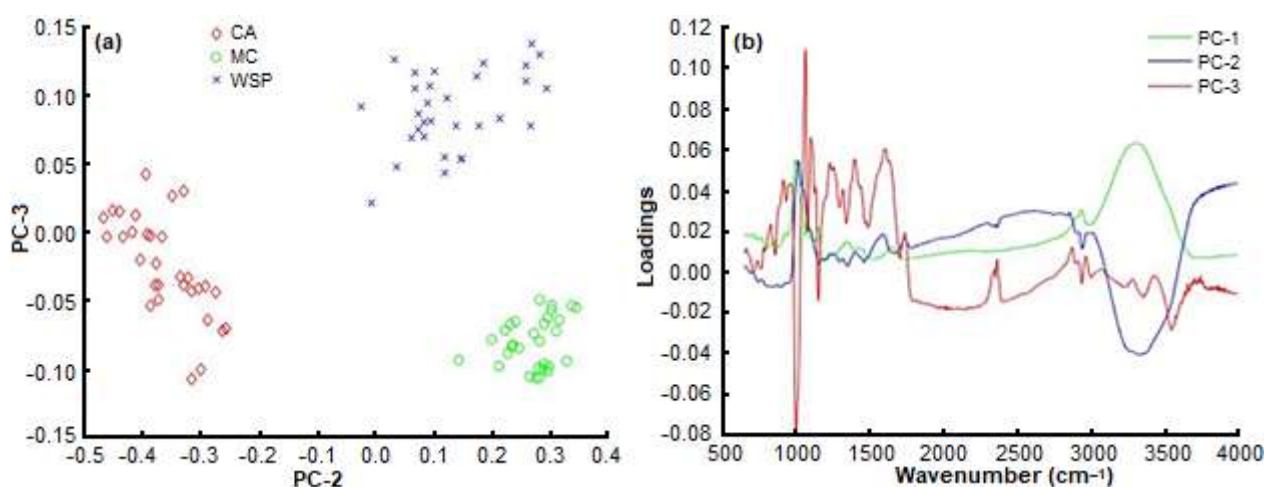

Fig 3. PCA of FT-IR spectra of CA (*Canna edulis*), MC (modified cassava), and WSP (white sweet potato): (a) score plot and (b) loadings profile of PC-2 and PC-3

loading plot (Fig. 2(b)) shows the highest value for PC-1 at 5208 cm^{-1} corresponding to CO stretch second overtone assigned to CONH structure and 6944 cm^{-1} CH combination corresponding to CH$_2$. On the other hand, PC-2 shows the peaks at 5208 cm^{-1} similar to that of PC-1, at which 7184 cm^{-1} is CH combination of CH$_2$ [22].

Fig. 3(b) shows a clear separation of three types of flour indicated by PC-2 and PC-3 for FT-IR data, which account for 13% of the total variability, but in total, the first three principal components account for 99.7% the total variability. The loadings of PC-2 (Fig. 3(b)) showed a negative influence of the bands at 3304 cm^{-1} associated with NH of amines and OH of alcohols, phenols, carboxylic acids, and water, as well as at 1018 cm^{-1} associated to CO of alcohols. The PC-3 shows several peaks on the fingerprint region, which shows several absorption peaks between 1000–1300 cm^{-1}, which are assigned to CO stretch of esters, ethers, alcohols, and carboxylic acids, as well as at 1600 cm^{-1} assigned to CC of the aromatic bond.

Partial Least Square Discriminant Analysis Model

A PLS-DA model is used to distinguish three types of tuber flour that have a similar color. The PLS-DA models are developed using the preprocessed spectra of samples from FT-NIR and FT-IR spectroscopy. The PLS-DA calibration model classified *Canna edulis*, modified cassava, and white sweet potato flour with 100% accuracy for calibration and predictive model for both FT-NIR and

FT-IR spectroscopy (data not shown), by using original spectra and applying all preprocessed methods, from normalization to derivatives. The high classification accuracy demonstrates that tuber flours having a similar color can be correctly identified by FT-NIR and FT-IR instruments.

The highest coefficient determination and standard error of prediction (SEP) of prediction, which are R^2 of 0.99 and 0.012, are obtained by applying the Savitzky-Golay 1st derivative preprocessed for FT-NIR spectra. For FT-IR, the coefficient determination and SEP of prediction, which are R^2 of 0.99 and 0.042, are obtained by also applying the Savitzky-Golay 1st derivative preprocessed. The 1st derivative provided the best PLS model since it removed the baseline offset and provided lesser peaks compared to other derivatives but was able to be distinctly observed. The PLS-DA results are listed in Table 1 for the FT-NIR and FT-IR spectral data.

Fig. 4 shows the beta coefficient of the PLS-DA model resulted from the Savitzky-Golay 1st derivative of FT-NIR and FT-IR spectra, which give the best calibration and prediction model for discriminating *Canna edulis*, modified cassava, and sweet potato flour. Several distinct peaks can be observed on FT-NIR spectra (Fig. 4(a)) at 4048 cm^{-1} symmetrical CNC stretch first overtone relating to protein, 4404 cm^{-1} OH stretch or CO stretch combination relating to cellulose, 5172 cm^{-1} OH stretch or HOH deformation combination relating to starch [22],
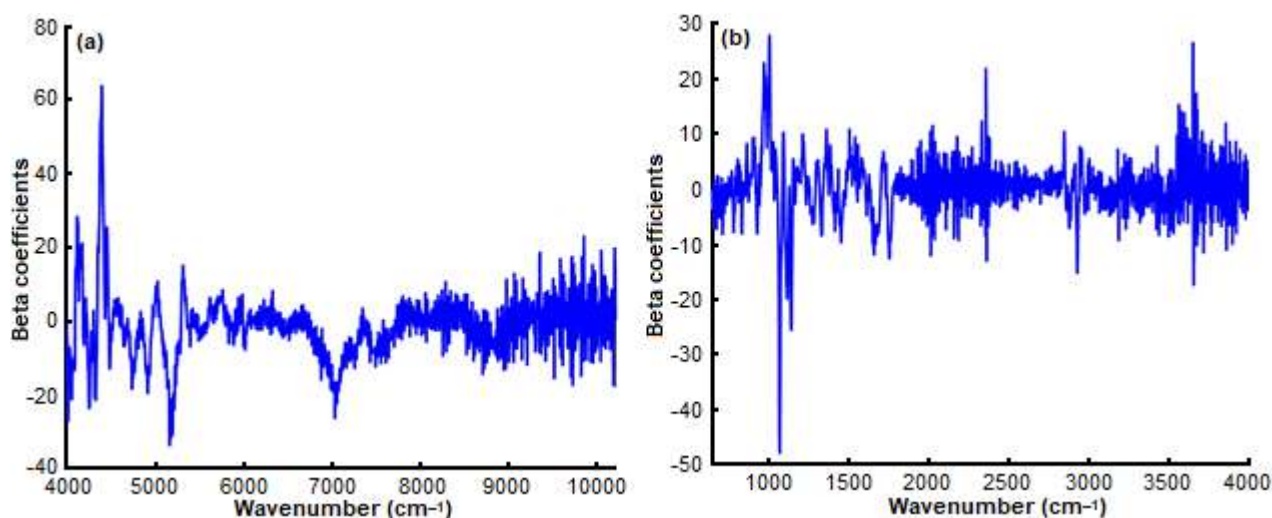

Fig 4. Beta coefficients of Savitzky-Golay 1st derivative of (a) FT-NIR spectra and (b) FT-IR spectra

Table 1. Comparison of original PLS-DA model versus VIP model with various preprocessing methods on FT-NIR and FT-IR spectra

Spectroscopy	Preprocessing	PLS-DA					PLS-DA VIP				
		Calibration		Prediction		LV	Calibration		Prediction		LV
		R^2	SEC	R^2	SEP		R^2	SEC	R^2	SEP	
FT-NIR	Mean norm	0.994	0.062	0.994	0.062	5	0.994	0.066	0.988	0.091	4
	Max norm	0.994	0.065	0.994	0.065	5	0.992	0.072	0.987	0.096	4
	Range norm	0.995	0.060	0.995	0.060	5	0.996	0.054	0.991	0.080	6
	MSC	0.998	0.040	0.998	0.040	7	0.997	0.045	0.995	0.060	6
	SNV	0.997	0.043	0.997	0.043	7	0.996	0.051	0.995	0.060	6
	SG1	0.999	0.012	0.999	0.012	5	0.998	0.034	0.996	0.050	5
	SG2	0.999	0.0121	0.999	0.0121	5	0.998	0.033	0.995	0.057	5
	Original	0.998	0.0409	0.998	0.0409	6	0.998	0.039	0.995	0.060	5
	Variables			1557					385		
FT-IR	Mean norm	0.995	0.059	0.995	0.059	5	0.99	0.08	0.98	0.11	5
	Max norm	0.994	0.066	0.994	0.066	5	0.99	0.07	0.99	0.09	6
	Range norm	0.987	0.097	0.987	0.097	3	0.97	0.14	0.96	0.18	3
	MSC	0.995	0.061	0.995	0.061	5	0.99	0.08	0.99	0.10	5
	SNV	0.995	0.059	0.995	0.059	5	0.99	0.07	0.99	0.09	5
	SG1	0.998	0.042	0.998	0.042	5	0.99	0.06	0.96	0.17	6
	SG2	0.995	0.057	0.995	0.057	5	0.99	0.06	0.95	0.19	6
	Original	0.986	0.100	0.986	0.100	5	0.98	0.11	0.95	0.19	5
	Variables			1738					608		

Note: R^2 = coefficient of determination; SEC = standard error of calibration' SEP = standard error of prediction; LV = latent variable; Mean norm = mean normalization; Max norm = maximum normalization; Range norm = range normalization; MSC = multiplicative scatter correction; SNV = standard normal variate, SG1 = Savitzky-Golay 1st derivative; SG2 = Savitzky-Golay 2rd derivative

and 7040 cm^{-1} relating to water [23]. Results indicate that starch, protein, cellulose, and water may contribute to flour discrimination based on FT-NIR spectra.

Clear peaks in the FT-IR region (Fig. 4(b)) can be observed at 3330, 2929, and 1641 cm^{-1}, which are related to water and protein absorption bands [24]. Other bands below 1500 cm^{-1} contain complex spectra, but it can be observed that at 1078 cm^{-1} are due to CC bond vibrations as well as 1011 and 1144 cm^{-1} are due to COC stretching bonds relate to the carbohydrate [25]. The distinct peak at 3649 cm^{-1} indicates the OH stretching bond relates to water. Those imply that carbohydrate and water contents among samples contribute to the discrimination of samples based on FT-IR spectra.

FT-NIR and FT-IR spectra contain lots of variables (in this study, there are 1557 and 1738 variables), although only parts of the variables are related to the property of interests. Therefore, the variable selection method is used

to select the number of variables that are able to improve the performance of the model and to ease the interpretation [26]. The variable selection used in this study is the variable importance on projection (VIP), which considers all variables for initialization and then filters the unimportant variables based on some criterions [26]. VIP cut off used is 1.0. The new PLS-DA model developed using VIP selection is compared with the original PLS-DA model, as shown in Table 1. VIP selection is able to reduce variables from 1557 to 385 for FT-NIR and 1738 to 608 for FT-IR. The VIP-PLS-DA model achieves R^2 of 0.99 and SEP of 0.05% for FT NIR with the Savitzky-Golay 1st derivative preprocessed spectra, as well as R^2 of 0.99 and SEP of 0.09% for FT IR with the maximum normalization data preprocessing methods. The VIP selection will provide a faster process and lesser computer memory required for computation.

◼ CONCLUSION

This study aimed to differentiate three types of tuber flours made of *Canna edulis*, modified cassava, and white sweet potato. The PLS-DA model achieved 100% accuracy in predicting all types of flours, both with a coefficient of determination (R^2) of 0.99 and a standard error of prediction (SEP) of 0.03% for FT-NIR and R^2 of 0.99 and SEP of 0.08% for FT-IR. The VIP method is used to develop PLS-DA models, which result in reducing variables from 1738 to 608 variables for FT-IR and from 1557 to 385 variables for FT-NIR. The VIP-PLS-DA also achieves high accuracy models with R^2 of 0.99 and SEP of 0.09% as well as R^2 of 0.99 and SEP of 0.05% for FT-IR and FT-NIR, respectively. Both FT-NIR and FT-IR provide high accuracy and fast methods in the discriminating types of tuber flours that have similar color, which will be beneficial for large samples.

◼ ACKNOWLEDGMENTS

◼ REFERENCES

[1] Chandrasekara, A., and Kumar, T.J., 2016, Roots and tuber crops as functional foods: A review on phytochemical constituents and their potential health benefits, *Int. J. Food Sci.*, 2016, 3631647.

[2] More, S.J., Ravi, V., and Raju, S., 2019, "Tropical tuber crops" in *Postharvest Physiological Disorders in Fruits and Vegetables*, 1st Ed., Eds. de Freitas, S.T., and Pareek, S., CRC Press., 719–758.

[3] Manning, L., 2016, Food fraud: Policy and food chain, *Curr. Opin. Food Sci.*, 10, 16–21.

[4] Starr, G., Bredie, W.L.P., and Hansen, Å.S., 2013, Sensory profiles of cooked grains from wheat species and varieties, *J. Cereal Sci.*, 57 (3), 295–303.

[5] Pico, J., Tapia, J., Bernal, J., and Gómez, M., 2018, Comparison of different extraction methodologies for the analysis of volatile compounds in gluten-free flours and corn starch by GC/QTOF, *Food Chem.*, 267, 303–312.

[6] Hidalgo, A., Fongaro, L., and Brandolini, A., 2017, Colour screening of whole meal flours and discrimination of seven *Triticum* subspecies, *J. Cereal Sci.*, 77, 9–16.

[7] Aprianita, A., Vasiljevic, T., Bannikova, A., and Kasapis, S., 2014, Physicochemical properties of flours and starches derived from traditional Indonesian tubers and roots, *J. Food Sci. Technol.*, 51 (12), 3669–3679.

[8] Esteki, M., Simal-Gandara, J., Shahsavari, Z., Zandbaaf, S., Dashtaki, E., and Heyden, Y.V., 2018, A review on the application of chromatographic methods, coupled to chemometrics, for food authentication, *Food Control*, 93, 165–182.

[9] Manley, M., 2014, Near-infrared spectroscopy and hyperspectral imaging: Non-destructive analysis of biological materials, *Chem. Soc. Rev.*, 43 (24), 8200–8214.

[10] Shi, H., Lei, Y., Prates, L.L., and Yu, P., 2019, Evaluation of near-infrared (NIR) and Fourier transform mid-infrared (ATR-FT/MIR) spectroscopy techniques combined with chemometrics for the determination of crude protein and intestinal protein digestibility of wheat, *Food Chem.*, 272, 507–513.

[11] Chen, J., Zhu, S., and Zhao, G., 2017, Rapid determination of total protein and wet gluten in commercial wheat flour using siSVR-NIR, *Food Chem.*, 221, 1939–1946.

[12] Sampaio, P.S., Soares, A., Castanho, A., Almeida, A.S., Oliveira, J., and Brites, C., 2018, Optimization of rice amylose determination by NIR-spectroscopy using PLS chemometrics algorithms, *Food Chem.*, 242, 196–204.

[13] Lebot, V., Champagne, A., Malapa, R., and Shiley, D., 2009, NIR determination of major constituents in tropical root and tuber crop flours, *J. Agric. Food Chem.*, 57 (22), 10539–10547.

[14] Ding, X., Ni, Y., and Kokot, S., 2015, NIR spectroscopy and chemometrics for the

discrimination of pure, powdered, purple sweet potatoes and their samples adulterated with the white sweet potato flour, *Chemom. Intell. Lab. Syst.*, 144, 17–23.

[15] Li, X., Lu, R., Wang, Z., Wang, P., Zhang, L., and Jia, P., 2018, Detection of corn and whole wheat adulteration in white pepper powder by near infrared spectroscopy, *Am. J. Food Sci. Technol.*, 6 (3), 114–117.

[16] Chen, H., Tan, C., Lin, Z., and Li, H., 2019, Quantifying several adulterants of notoginseng powder by near-infrared spectroscopy and multivariate calibration, *Spectrochim. Acta, Part A*, 211, 280–286.

[17] Ding, X., Ni, Y., and Kokot, S., 2015, NIR spectroscopy and chemometrics for the discrimination of pure, powdered, purple sweet potatoes and their samples adulterated with the white sweet potato flour, *Chemom. Intell. Lab. Syst.*, 144, 17–23.

[18] Giraudo, A., Grassi, S., Savorani, F., Gavoci, G., Casiraghi, E., and Geobaldo, F., 2019, Determination of the geographical origin of green coffee beans using NIR spectroscopy and multivariate data analysis, *Food Control*, 99, 137–145.

[19] Agelet, L.E., and Hurburgh, C.R., 2010, A tutorial on near infrared spectroscopy and its calibration, *Crit. Rev. Anal. Chem.*, 40 (4), 246–260.

[20] Jawaid, S., Talpur, F.N., Sherazi, S.T.H., Nizamani, S.M., and Khaskheli, A.A., 2013, Rapid detection of melamine adulteration in dairy milk by SB-ATR-Fourier transform infrared spectroscopy, *Food Chem.*, 141 (3), 3066–3071.

[21] Hell, J., Prückler, M., Danner, L., Henniges, U., Apprich, S., Rosenau, T., Kneifel, W., and Böhmdorfer, S., 2016, A comparison between near-infrared (NIR) and mid-infrared (ATR-FTIR) spectroscopy for the multivariate determination of compositional properties in wheat bran samples, *Food Control*, 60, 365–369.

[22] Aenugu, H.P.R., Kumar, D.S., Srisudharson, Parthiban, N., Ghosh, S.S., and Banji, D., 2011, Near infra red spectroscopy- An overview, *Int. J. ChemTech Res.*, 3 (2), 825–836.

[23] Shi, H., and Yu, P., 2017, Comparison of grating-based near-infrared (NIR) and Fourier transform mid-infrared (ATR-FT/MIR) spectroscopy based on spectral preprocessing and wavelength selection for the determination of crude protein and moisture content in wheat, *Food Control*, 82, 57–65.

[24] Kong, J., and Yu, S., 2007, Fourier transform infrared spectroscopic analysis of protein secondary structures, *Acta Biochim. Biophys. Sin.*, 39 (8), 549–559.

[25] Lohumi, S., Lee, S., Lee, W.H., Kim, M.S., Mo, C., Bae, H., and Cho, B.K., 2014, Detection of starch adulteration in onion powder by FT-NIR and FT-IR spectroscopy, *J. Agric. Food Chem.*, 62 (38), 9246–9251.

[26] Yun, Y.H., Li, H.D., Deng, B.C., and Cao, D.S., 2019, An overview of variable selection methods in multivariate analysis of near-infrared spectra, *TrAC, Trends Anal. Chem.*, 113, 102–115.

Silver Nanoparticles Capped with *p*-Hydroxybenzoic Acid as a Colorimetric Sensor for the Determination of Paraquat

Gusrizal Gusrizal[1,*], Sri Juari Santosa[2], Eko Sri Kunarti[2], and Bambang Rusdiarso[2]

[1]*Department of Chemistry, Faculty of Mathematics and Natural Sciences, Universitas Tanjungpura, Jl. Prof. Dr. H. Hadari Nawawi, Pontianak 78124, Indonesia*

[2]*Department of Chemistry, Faculty of Mathematics and Natural Sciences, Universitas Gadjah Mada, Sekip Utara, Yogyakarta 55281, Indonesia*

Abstract: *Highly stable silver nanoparticles capped with* p-*hydroxybenzoic acid were synthesized by reducing silver ion with* p-*hydroxybenzoic acid and used for the detection of paraquat. The synthesized silver nanoparticles, which are yellow, exhibited an absorption peak at 420 nm when measured with a UV-visible spectrophotometer due to the surface plasmon resonance. In the presence of paraquat, the color of silver nanoparticles changed from yellow to purple accompanied by the appearance of a new peak at 580 nm in addition to the peak at 420 nm. In order to obtain optimum experimental conditions, temperature, and time of reaction were optimized, and the ratio of absorbance obtained at 580 nm and 420 nm (A_{580}/A_{420}) were monitored. The A_{580}/A_{420} is proportional to the concentration of paraquat. Under the most favorable condition, the calibration curve showed a high level of linearity ranging from 6.0×10^{-4} to 1.0×10^{-3} M, and the detection limit was found to be 8.30×10^{-6} M. Silver nanoparticles capped with* p-*hydroxybenzoic acid was found to be useful for the colorimetric determination of paraquat in the aqueous medium.*

Keywords: *nanoparticles; paraquat;* p-*hydroxybenzoic acid; sensor; silver*

■ INTRODUCTION

Over the past few years, scientific publications have shown a significant increase in research on the exploration of nanoparticles. Among the metal nanoparticles, silver nanoparticles have attracted significant interest. Silver nanoparticles have been familiar as an antibacterial agent [1]. In addition to being an antibacterial agent, silver nanoparticles have been used in the development of analytical methods.

There is an increase in research using silver nanoparticles as a colorimetric sensor. The basis of measurement is a change in surface plasmon resonance spectra of silver nanoparticles caused by the aggregation of nanoparticles which results from the interaction of an analyte with the capping agent molecules covering the surface of the nanoparticles [2-3].

Surface plasmon resonance is an optical property of metal nanoparticles originating from the interaction of

light with the mobile conduction electron of the metal and is spectrally observed as a maximum absorbance in the visible range. Silver and gold nanoparticles display different positions of absorbance maxima, e.g., at the wavelength of 415 and 525 nm, respectively [4]. In addition to the type of metal, the position of absorbance maxima is dependent on the size of particles that could be controlled by the reducing and capping agent used in the synthesis [5-6].

Many methods for the synthesis of silver nanoparticles are available. In the chemical reduction method, the precursor of silver, the reducing agent, and the stabilizer or capping agent are needed [7]. Sodium borohydride and sodium citrate are usually used in the reduction of silver ions to produce silver nanoparticles, and polymers such as polyvinyl alcohol stabilize the silver nanoparticles during and after the formation of nanoparticles [5].

Silver nanoparticles were used as colorimetric sensors for metal ions such as Cu(II) [8], Cr(VI) [2], Mn(II), Hg(II) [9], Cr(III) [10], and Fe(III) [11]. The application of silver nanoparticles as a colorimetric sensor for organic compounds is still limited. They were used for the determination of melamine [12] and herbicide sulfurazon-ethyl [13]. In this paper, silver nanoparticles capped with *p*-hydroxybenzoic acid were used for the development of a colorimetric paraquat determination.

Paraquat (1,1′-dimethyl-4-4′-bipyridinium dichloride) is one of the most widely used herbicides in agriculture. However, it is a highly toxic herbicide. The risk of Parkinson's disease has been associated with exposure to paraquat [14-15]. In considering the effect of paraquat, it is essential to monitor the existence of paraquat in the environment. Several analytical methods have been available for paraquat determination such as liquid chromatography/ electrospray ionization-mass spectrometry [16], ultra-performance liquid chromatography-mass spectrometry/ mass spectrometry (UPLC-MS/MS) [17]. Because of the high cost of the equipment for determination, it is necessary to replace it with a rapid and straightforward method.

Previously, we have successfully synthesized highly stable silver nanoparticles capped with *p*-hydroxybenzoic acid [18], however their application has not been explored. As presented in this paper, we have developed an analytical method for paraquat determination using silver nanoparticles capped with *p*-hydroxybenzoic acid. The data presented in this paper is taken from the doctoral dissertation submitted to the Department of Chemistry Universitas Gadjah Mada by one of the authors [19].

It is predicted that paraquat initiates the aggregation of silver nanoparticles capped with *p*-hydroxybenzoic acid. Paraquat interacts with the *p*-hydroxybenzoic acid covering the silver nanoparticles through the mechanism of ion-pair as well as the formation of charge transfer complex. Paraquat acts as a bridge between the nanoparticles and causes the distance between the particles to become closer and produces a change in surface plasmon resonance spectra. The change of surface plasmon resonance spectra is estimated to be proportional to the concentration of paraquat. Therefore, silver nanoparticles

capped with *p*-hydroxybenzoic acid was used for the quantitative determination of paraquat.

■ EXPERIMENTAL SECTION

Materials

Sodium hydroxide (Merck), silver nitrate (Merck), potassium chloride (Merck), ammonium chloride (Merck), disodium hydrogen phosphate (Merck), *p*-hydroxybenzoic acid (Sigma-Aldrich), and paraquat (Sigma-Aldrich) were used as received without any further purification. Throughout the experiment, we used double distilled water.

Instrumentation

UV-visible spectrophotometer (Shimadzu UV-1700 PharmaSpec) was used to obtain the surface plasmon resonance spectra, and the transmission electron microscope (JEOL JEM-1400) was used to determine the size and morphology of the silver nanoparticles.

Procedure

Synthesis of silver nanoparticles

Silver nanoparticles capped with *p*-hydroxybenzoic acid were synthesized through the chemical reduction of silver nitrate with *p*-hydroxybenzoic acid as a reducing agent without additional capping agents in an aqueous medium [20]. A 5-mL of 2.0×10^{-4} M silver nitrate were added to 5 mL pH 11-adjusted 4.0×10^{-3} M *p*-hydroxybenzoic acid and was then heated in a boiling water bath for 1 h. A UV-visible spectrophotometer and a transmission electron microscope were used to characterize the synthesized silver nanoparticles.

Colorimetric detection of paraquat

The procedure for the colorimetric detection of paraquat is as follows: 1 mL of paraquat standard was introduced to 2 mL of synthesized silver nanoparticles and heated in a boiling water bath for 10 min. When the reaction was complete, the mixture was then cooled in tap water. The color of the solution changed from yellow to purple, and the change of color and absorbance intensity was monitored using a UV-visible

spectrophotometer. The performance of silver nanoparticles capped with *p*-hydroxybenzoic acid in the detection of paraquat was evaluated.

■ **RESULTS AND DISCUSSION**

Synthesis of Silver Nanoparticles

The formation of silver nanoparticles was visible because of the appearance of the yellow color in the mixtures of reaction. The color was due to the surface plasmon resonance and confirmed by measurement with a UV-visible spectrophotometer. The UV-visible spectra of silver nanoparticles synthesized by the reduction of silver nitrate with *p*-hydroxybenzoic acid are shown in Fig. 1(a). The spectra exhibited absorbance maxima at a wavelength of 420 nm. The transmission electron microscope image, as shown in Fig. 2, proves the formation of silver nanoparticles. In a previous paper, we reported that the reduction of silver nitrate with *p*-hydroxybenzoic acid without additional capping agents produced silver nanoparticles capped with *p*-hydroxybenzoic acid with an average size of 26 ± 11 nm [20].

The size of the particles and the position of the peak maxima at the surface plasmon resonance spectra of the silver nanoparticles varies with reducing and capping agents used in the synthesis. The reduction of the silver ion with glucose using polyvinylpyrrolidone as a capping agent produces silver nanoparticles with a peak at 420 nm and a size of 50 nm [21]. The synthesis of silver nanoparticles using aniline and dodecylbenzene sulfonic acid as a reducing and capping agent resulted in silver nanoparticles of 10 nm and a peak at 410 nm [22]. The reducing and capping agent determines the size and shape of the silver nanoparticles, and the position of the maximum peak depends on the size and shape of the nanoparticles [23].

Interaction of Silver Nanoparticles and Paraquat

Silver nanoparticles have been used for colorimetric detection of chemical compounds. The property of silver nanoparticles used in the detection of chemical compounds is the change in surface plasmon resonance spectra due to the interaction of silver nanoparticles with an analyte. In general, surface plasmon resonance spectra
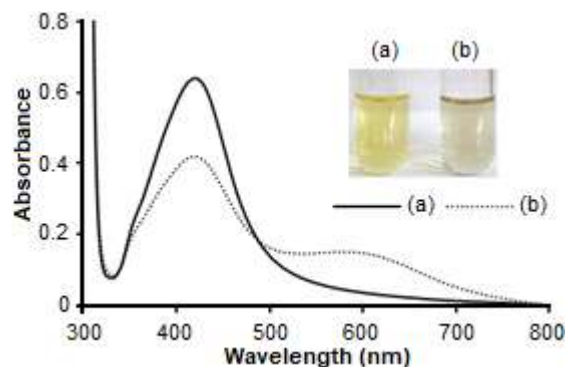

Fig 1. The surface plasmon resonance spectra of silver nanoparticles capped with *p*-hydroxybenzoic acid; (a) after synthesis and (b) after addition of paraquat
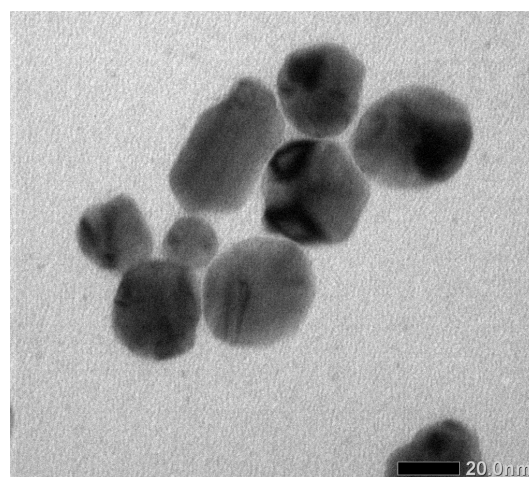

Fig 2. The TEM image of silver nanoparticles capped with *p*-hydroxybenzoic acid

of nanoparticles are sensitive to composition, size, shape, media, and the degree of aggregation of nanoparticles [24].

The addition of analytes to silver nanoparticles causes aggregation of silver nanoparticles. Surface plasmon resonance spectra of silver nanoparticles that experience aggregation are different when compared to the spectra of silver nanoparticles which do not experience aggregation. The difference that arises as a result of aggregation is the decrease in absorbance intensity at the main peak and the presence of secondary peaks at larger wavelengths. The ratio between the secondary peak and the main peak is used as a parameter for determining the amount of analyte because it represents the degree of aggregation due to the presence of the analyte [25].

The addition of paraquat to silver nanoparticles resulted in a change in the color of the nanoparticles from yellow to purple. This change was followed by changes in the surface plasmon resonance spectra of the nanoparticles, as shown in Fig. 1(b). The intensity of the main peak at 420 nm decreased, and there was a new peak at 580 nm. The existence of secondary peaks at larger wavelengths indicates the presence of larger silver nanoparticles due to aggregation [26]. The change of spectra represented by the ratio of absorbance obtained at 580 nm and 420 nm (A_{580}/A_{420}) was used as the basis for paraquat determination.

It is predicted that paraquat interacts with silver nanoparticles capped with *p*-hydroxybenzoic acid through the mechanism of ionic interaction between the positive charge of paraquat with the anionic group *p*-hydroxybenzoic acid covering silver nanoparticles and the formation of charge transfer complexes by π-π stacking of aromatic rings. In the formation of charge transfer complexes, paraquat with high electronegativity acts as an electron acceptor, and the aromatic ring of *p*-hydroxybenzoic acid which caps silver nanoparticles acts as electron donors [27-28]. The interaction between paraquat and *p*-hydroxybenzoic acid covering silver nanoparticles places paraquat as a bridge between nanoparticles and results in a closer distance between the nanoparticles. This causes changes in the surface plasmon resonance spectra [29]. The model of interaction between paraquat and silver nanoparticles capped with *p*-hydroxybenzoic acid, which causes aggregation is proposed as shown in Fig. 3.

A similar principle in the detection of chemicals using silver nanoparticles has been applied. The binding
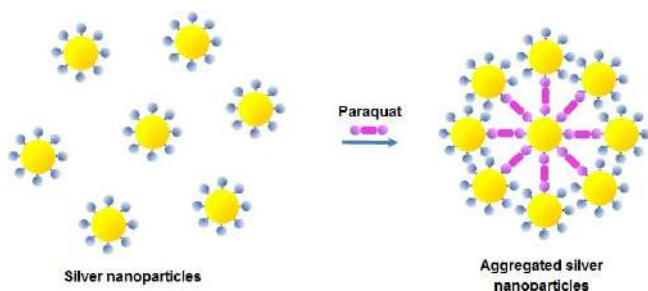

Fig 3. Model of interaction between paraquat and silver nanoparticles capped with p-hydroxybenzoic acid which causes aggregation

between melamine as an analyte with dopamine functionalized the surface of silver nanoparticles and produces the aggregation of nanoparticles [12]. Interaction of Cr(III) with trisodium citrate that acts as a capping agent of silver nanoparticles induces the aggregation of silver nanoparticles [2]. The aggregation of silver nanoparticles causes a change in the surface plasmon resonance spectra, and the change of spectra is proportional to the concentration of the analyte.

Optimization of Temperature and Reaction Time for the Reaction of Silver Nanoparticles with Paraquat

The reaction of synthesized silver nanoparticles capped with *p*-hydroxybenzoic acid with paraquat (1.0×10^{-3} M) was performed under room temperature and heating in a boiling water bath. The reaction was monitored during a specific time by determination of A_{580}/A_{420} to obtain the best experimental condition. Fig. 4 shows the change of surface plasmon resonance spectra of silver nanoparticles during the incubation. For the reaction under room temperature, the A_{580}/A_{420} continually increases until 150 min of incubation. On the other hand, stable aggregate formation was faster when the reaction was kept in a boiling water bath. The data shows that temperature affected the formation of a stable aggregate. We used 10 min incubation in a boiling water bath as the optimum condition for the reaction of paraquat with silver nanoparticles capped with *p*-hydroxybenzoic acid.

Analytical Performance of Paraquat Determination

The analytical performance parameter such as linear range or linearity, the limit of detection, precision, and accuracy were evaluated to validate the performance of silver nanoparticles capped with *p*-hydroxybenzoic acid for the determination of paraquat. Linearity shows that the measured response is proportional to the quantity of analyte. Linearity study was performed by plotting the A_{580}/A_{420} toward the concentration of paraquat. In this study, the concentration of paraquat used was varied from 1.0×10^{-4} M to 1.0×10^{-3} M with three replications. As shown in Fig. 5, the intensity of
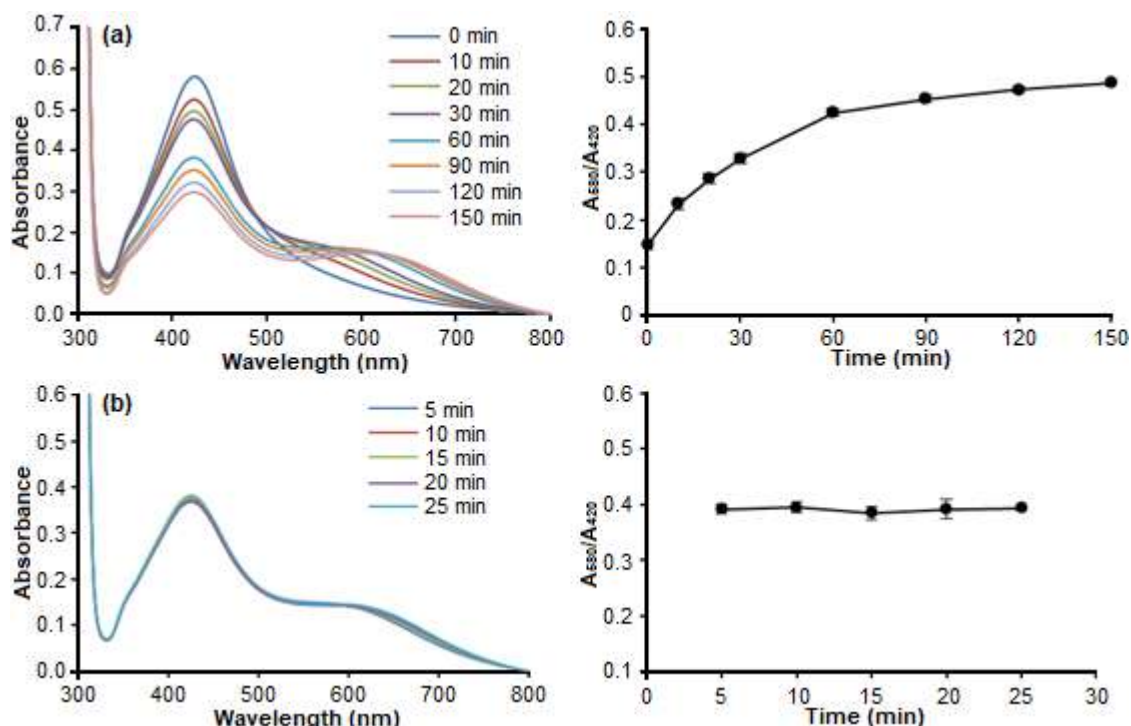
Fig 4. The change of surface plasmon resonance spectra and variation of A_{580}/A_{420} of silver nanoparticles capped with *p*-hydroxybenzoic acid with the presence of paraquat during the incubation under (a) room temperature and (b) heating in boiling water bath
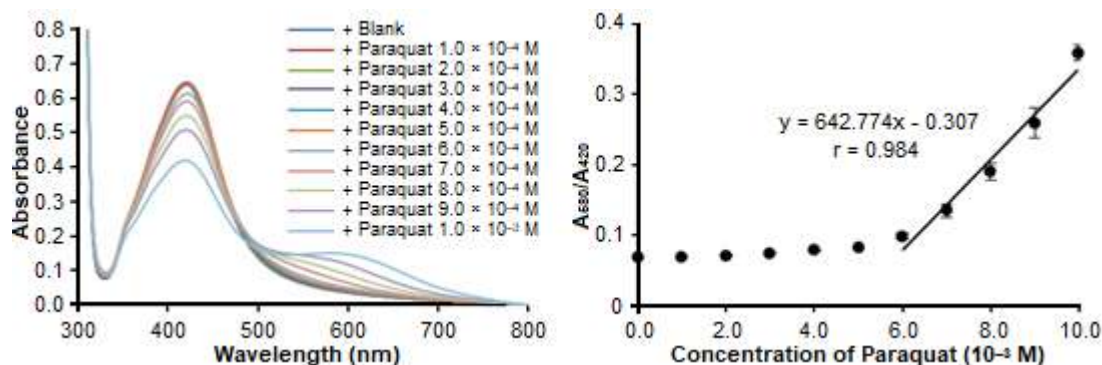

Fig 5. The surface plasmon resonance spectra of silver nanoparticles capped with *p*-hydroxybenzoic acid after the addition of paraquat with different concentration and the plot of A_{580}/A_{420} towards the concentration of paraquat

spectra at 420 nm decreased gradually by the increase of paraquat concentration and followed by the increase in peak intensity at 580 nm. The A_{580}/A_{420} increased linearly with the concentration of paraquat ranging from 6.0×10^{-4} to 1.0×10^{-3} M and the coefficient of regression (r) was 0.984.

The limit of detection was evaluated by measurement of several replications of a blank solution and defined as three times the standard deviation (n = 7). The limit of detection obtained was 8.30×10^{-6} M.

The evaluation of precision was carried out by measurement of a known concentration of paraquat with several replications. The precision was represented by the coefficient of variance from seven replications of measurement. The coefficient of variance obtained was 3%.

Accuracy was determined by spiking the standard solution of paraquat with the real water sample. The water sample was collected from the small canal in the

area of the chili farm. The amount of paraquat spiked into the water sample was estimated, and then the recovery percentage was calculated. The recovery percentage for the determination of paraquat in the water sample was 121%.

Effect of Other Substances

The universal inorganic and organic matrix in water from the farm area such as ammonium (NH_4Cl), phosphate (Na_2HPO_4), potassium (KCl), and humic acid was tested to check whether they could interfere in the determination of paraquat using silver nanoparticles capped with *p*-hydroxybenzoic acid. The NH_4Cl, Na_2HPO_4, KCl, and humic acid, individually were mixed with paraquat. The concentration of NH_4Cl, Na_2HPO_4, KCl in the mixture was 1.0×10^{-3} M and the concentration of humic acid was 1 ppm. Fig. 6 shows the interference effect of these matrices to the spectra of the mixture of silver nanoparticles and paraquat. The NH_4Cl, Na_2HPO_4, and KCl changed the A_{580}/A_{420} by 1%, 21%, and 7%, respectively.

The presence of Na_2HPO_4 resulted in a significant interference effect on the A_{580}/A_{420}. The presence of Na_2HPO_4 decreased the intensity of the main peak at 420 nm. Because phosphate is in the same group with carboxylic as hard bases[30], it is predicted that phosphate interacted with the surface of silver nanoparticles capped with *p*-hydroxybenzoic acid and replaced the *p*-hydroxybenzoic acid that acts as capping agent on the surface of the silver nanoparticles. This caused the destabilization of silver nanoparticles followed by aggregation.

The presence of humic acid in the mixture of silver nanoparticles and paraquat changed their spectra. There was an increase in the peak at 420 nm, but the peak at 580 nm disappeared. These results indicate that humic acids inhibit the aggregation of silver nanoparticles by paraquat. It is predicted that the interaction of paraquat with humic acid was stronger than that of silver nanoparticles so that the aggregation of silver nanoparticles capped with *p*-hydroxybenzoic acid facilitated by paraquat became blocked. Paraquat can interact with humic acid through ionic interactions as well as the formation of charge transfer complex [28].
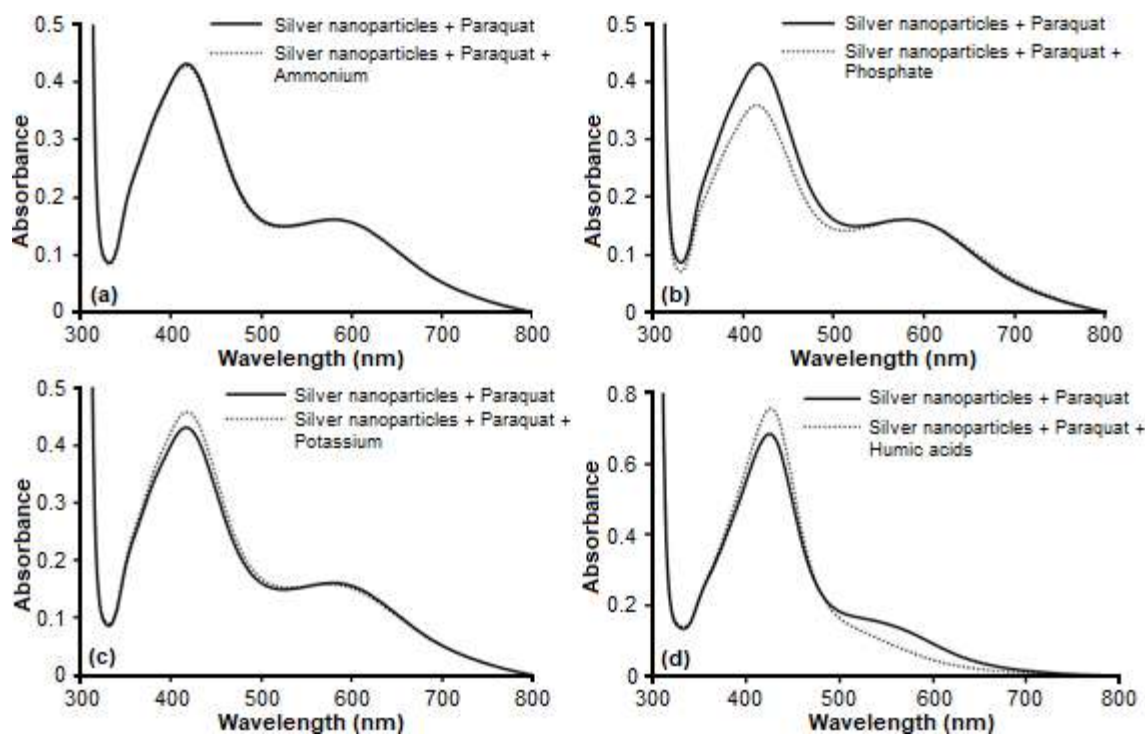

Fig 6. Effect of inorganic and organic matrices on the surface plasmon resonance spectra of the mixture of silver nanoparticles and paraquat

Comparison with another Method

The result of the determination of paraquat using silver nanoparticles capped with *p*-hydroxybenzoic acid was compared to another spectrophotometric method [31]. In this method, paraquat is reduced by ascorbic acid in alkaline solution resulting in the blue paraquat radical. The paraquat radical is measured with a UV-visible spectrophotometer at 600 nm.

Four concentrations of standard paraquat ranging from 1.0×10^{-3} to 4.0×10^{-3} M were measured by these two methods. A comparison of the result of the determination from different methods can be made by plotting the result in an x-y graph. The confidence interval for the slope and intercept of the line is used to find out whether these two methods produce the same or different results [32]. Our results are presented in Fig. 7. The equation of the line obtained is y = 0.9105x - 0.00005 (r = 0.9991). The confidence interval for the slope and intercept of the line lies between 0.9278 to 1.1508 and -0.00033 to 0.00025, respectively. Because the confidence interval for the slope and intercept includes one and zero, it is concluded that the difference of the results obtained using silver nanoparticles capped with *p*-hydroxybenzoic acid and ascorbic acid method is not significant. Because of the instability of the paraquat radical, silver nanoparticles capped with *p*-hydroxybenzoic acid is more suitable for the determination of paraquat.
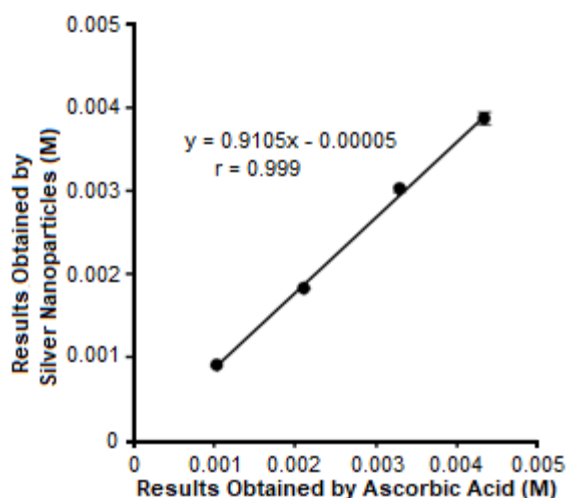

Fig 7. Comparison of the result of the determination obtained using ascorbic acid and silver nanoparticles capped with p-hydroxybenzoic acid

■ CONCLUSION

In this work, a simple method for the determination of paraquat in aqueous medium was developed based on the aggregation of silver nanoparticles capped with *p*-hydroxybenzoic acid. Paraquat acts as a bridge between the nanoparticles and causes the aggregation of nanoparticles followed by the change of the ratio of absorbance obtained at 580 and 420 nm. The absorbance ratio is linearly correlated with the concentration of paraquat. Validation of the developed method indicates that this method could be useful for the colorimetric determination of paraquat in the aqueous medium.

■ REFERENCES

[1] Durán, N., Durán, M., de Jesus, M.B., Seabra, A.B., Fávaro, W.J., and Nakazato, G., 2016, Silver nanoparticles: A new view on mechanistic aspects on antimicrobial activity, *Nanomed. Nanotechnol. Biol. Med.*, 12 (3), 789–799.

[2] Ravindran, A., Elavarasi, M., Prathna, T.C., Raichur, A.M., Chandrasekaran, N., and Mukherjee, A., 2012, Selective colorimetric detection of nanomolar Cr(VI) in aqueous solutions using unmodified silver nanoparticles, *Sens. Actuators, B*, 166-167, 365–371.

[3] Wu, X., Xu, Y., Dong, Y., Jiang, X., and Zhu, N., 2013, Colorimetric determination of hexavalent chromium with ascorbic acid capped silver nanoparticles, *Anal. Methods*, 5 (2), 560–565.

[4] Frost, M.S., Dempsey, M.J., and Whitehead, D.E., 2017, The response of citrate functionalised gold

and silver nanoparticles to the addition of heavy metal ions, *Colloids Surf., A*, 518, 15–24.

[5] Lee, P.C., and Meisel, D., 1982, Adsorption and surface-enhanced Raman of dyes on silver and gold sols, *J. Phys. Chem.*, 86 (17), 3391–3395.

[6] Ajitha, B., Reddy, Y.A.K., Reddy, P.S., Jeon, H.J., and Ahn, C.W., 2016, Role of capping agents in controlling silver nanoparticles size, antibacterial activity and potential application as optical hydrogen peroxide sensor, *RSC Adv.*, 6 (42), 36171–36179.

[7] Rycenga, M., Cobley, C.M., Zeng, J., Li, W., Moran, C.H., Zhang, Q., Qin, D., and Xia, Y., 2011, Controlling the synthesis and assembly of silver nanostructures for plasmonic applications, *Chem. Rev.*, 111 (6), 3669–3712.

[8] Ratnarathorn, N., Chailapakul, O., Henry, C.S., and Dungchai, W., 2012, Simple silver nanoparticle colorimetric sensing for copper by paper-based devices, *Talanta*, 99, 552–557.

[9] Annadhasan, M., Muthukumarasamyvel, T., Sankar Babu, V.R., and Rajendiran, N., 2014, Green synthesized silver and gold nanoparticles for colorimetric detection of Hg^{2+}, Pb^{2+}, and Mn^{2+} in an aqueous medium, *ACS Sustainable Chem. Eng.*, 2 (4), 887–896.

[10] Shrivas, K., Sahu, S., Patra, G.K., Jaiswal, N.K., and Shankar, R., 2016, Localized surface plasmon resonance of silver nanoparticles for sensitive colorimetric detection of chromium in surface water, industrial wastewater and vegetable samples, *Anal. Methods*, 8 (9), 2088–2096.

[11] Roto, R., Marcelina, Aprilita, N.H., Mudasir, Natsir, T.A., and Mellisani, B., 2017, Investigation on the effect of the addition of Fe^{3+} ion into the colloidal AgNPs in PVA solution and understanding its reaction mechanism, *Indones. J. Chem.*, 17 (3), 439–445.

[12] Ma, Y., Niu, H., Zhang, X., and Cai, Y., 2011, One-step synthesis of silver/dopamine nanoparticles and visual detection of melamine in raw milk, *Analyst*, 136 (20), 4192–4196.

[13] Dubas, S.T., and Pimpan, V., 2008, Humic acid assisted synthesis of silver nanoparticles and its application to herbicide detection, *Mater. Lett.*, 62 (17-18), 2661–2663.

[14] Lee, P.C., Bordelon, Y., Bronstein, J., and Ritz, B., 2012, Traumatic brain injury, paraquat exposure, and their relationship to Parkinson disease, *Neurology*, 79 (20), 2061–2066.

[15] Pezzoli, G., and Cereda, E., 2013, Exposure to pesticides or solvents and risk of Parkinson disease, *Neurology*, 80 (22), 2035–2041.

[16] Takino, M., Daishima, S., and Yamaguchi, K., 2000, Determination of diquat and paraquat in water by liquid chromatography/electrospray-mass spectrometry using volatile ion-pairing reagents, *Anal. Sci.*, 16 (7), 707–711.

[17] Pizzutti, I.R., Vela, G.M.E., de Kok, A., Scholten, J.M., Dias, J.V., Cardoso, C.D., Concenço, G., and Vivian, R., 2016, Determination of paraquat and diquat: LC-MS method optimization and validation, *Food Chem.*, 209, 248–255.

[18] Gusrizal, G., Santosa, S.J., Kunarti, E.S., and Rusdiarso, B., 2018, Two highly stable silver nanoparticles: Surface plasmon resonance spectra study of silver nanoparticles capped with *m*-hydroxybenzoic acid and *p*-hydroxybenzoic acid, *Molekul*, 13 (1), 30–37.

[19] Gusrizal, 2017, Sintesis nanopartikel perak melalui reduksi ion perak dengan asam 2-, 3-, dan 4-hidroksibenzoat serta aplikasinya untuk penentuan parakuat, *Dissertation*, Department of Chemistry, Universitas Gadjah Mada, Indonesia.

[20] Gusrizal, G., Santosa, S.J., Kunarti, E.S., and Rusdiarso, B., 2016, Dual function of *p*-hydroxybenzoic acid as reducing and capping agent in the rapid and simple formation of stable silver nanoparticles, *Int. J. Chemtech Res.*, 9 (9), 472–482.

[21] Wang, H., Qiao, X., Chen, J., Wang, X., and Ding, S., 2005, Mechanisms of PVP in the preparation of silver nanoparticles, *Mater. Chem. Phys.*, 94 (2-3), 449–453.

[22] Yang, J., Yin, H., Jia, J., and Wei, Y., 2011, Facile synthesis of high-concentration, stable aqueous dispersions of uniform silver nanoparticles using aniline as a reductant, *Langmuir*, 27 (8), 5047–5053.

[23] Khodashenas, B., and Ghorbani, H.R., 2019, Synthesis of silver nanoparticles with different shapes, *Arabian J. Chem.*, 12 (8), 1823–1838.

[24] Wei, H., Abtahi, S.M.H., and Vikesland, P.J., 2015, Plasmonic colorimetric and SERS sensors for environmental analysis, *Environ. Sci.: Nano*, 2 (2), 120–135.

[25] Jin, W., Huang, P., Wu, F., and Ma, L.H., 2015, Ultrasensitive colorimetric assay of cadmium ion based on silver nanoparticles functionalized with 5-sulfosalicylic acid for wide practical applications, *Analyst*, 140 (10), 3507–3513.

[26] Pinto, V.V., Ferreira, M.J., Silva, R., Santos, H.A., Silva, F., and Pereira, C.M., 2010, Long time effect on the stability of silver nanoparticles in aqueous medium: Effect of the synthesis and storage conditions, *Colloids Surf., A*, 364 (1-3), 19–25.

[27] Senesi, N., D'Orazio, V., and Miano, T.M., 1995, Adsorption mechanisms of s-triazine and bipyridylium herbicides on humic acids from hop field soils, *Geoderma*, 66 (3-4), 273–283.

[28] Roldán, M.L., Corrado, G., Francioso, O., and Sanchez-Cortes, S., 2011, Interaction of soil humic acids with herbicide paraquat analyzed by surface-enhanced Raman scattering and fluorescence spectroscopy on silver plasmonic nanoparticles, *Anal. Chim. Acta*, 699 (1), 87–95.

[29] Vilela, D., González, M.C., and Escarpa, A., 2012, Sensing colorimetric approaches based on gold and silver nanoparticles aggregation: Chemical creativity behind the assay. A review, *Anal. Chim. Acta*, 751, 24–43.

[30] Pearson, R.G., 1968, Hard and soft acid and bases, HSAB, Part I: Fundamental principles, *J. Chem. Educ.*, 45 (9), 581–587.

[31] Shivhare, P., and Gupta, V.K., 1991, Spectrophotometric method for the determination of paraquat in water, grain and plant materials, *Analyst*, 116 (4), 391–393.

[32] Miller, J.N., and Miller, J.C., 2010, *Statistics and Chemometrics for Analytical Chemistry*, 6th Ed., Pearson Education, Canada.

Prediction of Rashba Effect on Two-dimensional MX Monochalcogenides (M = Ge, Sn and X = S, Se, Te) with Buckled Square Lattice

Ibnu Jihad*, Juhri Hendrawan, Adam Sukma Putra, Kuwat Triyana, and Moh. Adhib Ulil Absor

*Department of Physics, Faculty of Mathematics and Natural Sciences, Universitas Gadjah Mada,
Sekip Utara BLS 21, Yogyakarta 55281, Indonesia*

Abstract: *The Rashba splitting are found in the buckled square lattice. Here, by applying fully relativistic density-functional theory (DFT) calculation, we confirm the existence of the Rashba splitting in the conduction band minimum of various two-dimensional MX monochalcogenides (M = Ge, Sn and X = S, Se, Te) exhibiting a pair inplane Rashba rotation of the spin textures. A strong correlation has also been found between the size of the Rashba parameter and the atomic number of chalcogen atom for Γ and M point in the first Brillouin zone. Our investigation clarifies that the buckled square lattice are promising for inducing the substantial Rashba splitting suggesting that the present system is promising for spintronics device.*

Keywords: *Ge monochalcogenides; Sn monochalcogenides; DFT method; spintronics; square lattice; Rashba effect; spin textures*

■ INTRODUCTION

Spintronics is a combinational word from spin transport electronics or spin electronics, which is the next generation of electronics. Spintronics explores the spin properties of electrons rather than the charge properties in electronics device, in which give us more degree of freedom [1]. This fact makes spintronics device have higher information density and also energetically efficient because the smaller movement is needed for changing (reading and writing) the spin structure. One branch of the spintronics research field is spin-orbitronics, which is focused on the exploitation of non-equilibrium material properties using spin-orbit coupling (SOC). In the spin-orbitronics, the investigation is aiming for searching materials that have large enough SOC energy splitting, especially the Rashba effect type to build spin field-effect transistor (SFET) [2].

The Rashba splitting in the electronics band structures is caused by the lack of inversion symmetry of the materials [3], which occurred in a two-dimensional (2D) structures of materials. Graphene as the first example of the 2D materials having hexagonal structure have been considered for this purpose. However, due to the weak SOC, this material is not suitable for spin-orbitronics [4-6]. Another example of 2D materials having hexagonal structure is coming from the transition metal dichalcogenides (TMDs) family [7]. Here, the breaking of inversion symmetry in the hexagonal crystal, together with the strong SOC of transition metal atom leads to the strong SOC splitting. Recently, the 2D Group-IV monochalcogenides in square lattice with black phosphorus structure have been recently studied and proved as a suitable semiconductor with sizeable Rashba splitting [9].

Although the SOC has been widely studied on the 2D materials with the hexagonal structure and black phosphorus structure, this effect should apparently appear on the other non-centrosymmetric 2D materials. One of the candidates is 2D material which posses a square lattice structure. The square lattice structure with buckling has also been experimentally observed on Bismuth (Bi) [10], making the realization of this structure is plausible. Computational research on buckled square lattice of lead chalcogenides showing significant first-order Rashba effect in this structure [8]. Previously, a preliminary study on the electronic structure of the MX monochalcogenides (M = Ge, Sn

and X = S, Se) has been conducted with buckled squared lattice and also the calculation of Rashba splitting size up to the-third order correction that was showing a sizeable Rashba splitting in these materials [9].

This work showed that the Rashba splitting is also observed in the MTe monochalcogenides (M = Ge, Sn) with buckled squared lattice as additional materials to MX monochalcogenides (M = Ge, Sn and X = S, Se) buckled square lattice. It is found that the substantial Rashba splitting is achieved in the conduction band minimum of various 2D MX monochalcogenides showing clockwise-anticlockwise rotation of the spin in the momentum space. From these various TMDs materials, the size of the Rashba parameter is strongly affected by the atomic number of chalcogen atoms for different high symmetry points in the first Brillouin zone.

■ COMPUTATIONAL METHOD

This work was started by modeling the two-dimensional monolayer buckled square lattice crystal (Fig. 1). The distance between slabs is set to 30 Å to prevent interaction between slabs. The coordinate axis is x = a, y = b, and c = z. The geometry is relaxed until the force of each atom less than 1 meV/Å.

The calculation was performed using a density functional theory (DFT) approach implemented on OPENMX code [10] within the generalized gradient approximation (GGA) for the exchange-correlation energy [11]. The norm-conserving pseudopotentials [12] was set to energy cut off 300 rydberg for charge density. The optimum k-point sampling for the calculation is 8 × 8 × 1. The wave function was expanded by a confinement scheme of a linear combination of multiple pseudoatomic orbitals [13-14]. The numerical pseudoatomic orbitals

used for M atom was two-s, two-p, three-d, and one-f, and for X atom was three-s, three-p, two-d, and one-f. The j-dependent pseudopotentials were applied for SOC [15]. After gaining the stable structure of the materials, the process continue to calculate the electronics band structures with the corresponding density of states (DOS) projected to the atomic orbitals.

■ RESULTS AND DISCUSSION

The optimized structure and the related parameters, are summarized in Table 1 and have good agreement with previous report [9]. The PbS and PbSe calculations have been presented to confirm the computational results with previously reported data [8].

The result of the electronic band structures is displayed in Fig. 2. It is observed that in the calculation without including SOC (blue lines in band structure), the valence band maximum (VBM) located in Y (and X') point for all MX. While In conduction band, the extremum valley or the conduction band minimum occurred along the Y-M line, for all MX. This result has a similarity with the previous result of MX with black phosphorene lattice structure. However, in black phosphorene, the different band structure was observed [16]. Our calculated DOS projected to the atomic orbitals confirmed that the VBM is dominated by a mixture of X-p_z and M-p_z. The CBM is contributed by the coupling of M-p_z and M-p_y. The band gap energy of all MX buckled square lattice monolayer has an indirect type. These calculated values are different from black phosphorene structure [9]. However, both structures have typical pattern in the band gap properties. The band gap are decreased along with the increasing chalcogen atomic mass in the buckles square lattice, thus
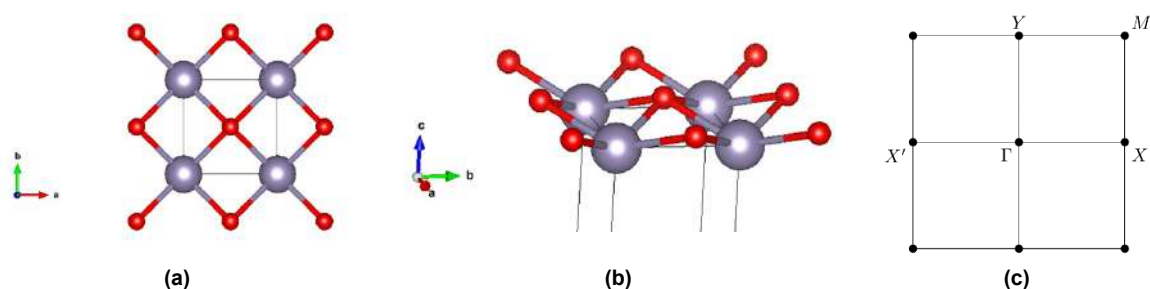

Fig 1. 2D buckled square lattice (drawing using Vesta) (a) from top and (b) side and (c) the first Brillouin zone

Table 1. Calculation result of lattice constant, buckling distance, and buckling angle

	Calculation			References			
	a(Å)	d_z(Å)	θ (°)	a(Å)	d_z(Å)	θ (°)	Source
PbS	3.76	1.04	21.4	3.76	1.0841	22.17	[8]
PBSe	3.79	1.27	25.4	3.85	1.2087	23.92	[8]
GeO	2.86	0.76	20.6	-	-	-	This work
GeS	3.25	1.14	26.4	3.31	1.10868	25.35	[9]
GeSe	3.42	1.22	26.8	3.46	1.18338	25.83	[16]
GeTe	3.69	1.30	26.5	-	-	-	This work
SnO	3.16	0.76	18.8	-	-	-	This work
SnS	3.54	1.20	25.6	3.55	1.18601	25.32	[16]
SnSe	3.62	1.34	27.6	3.68	1.27148	26.07	[16]
SnTe	3.94	1.41	26.8	-	-	-	This work
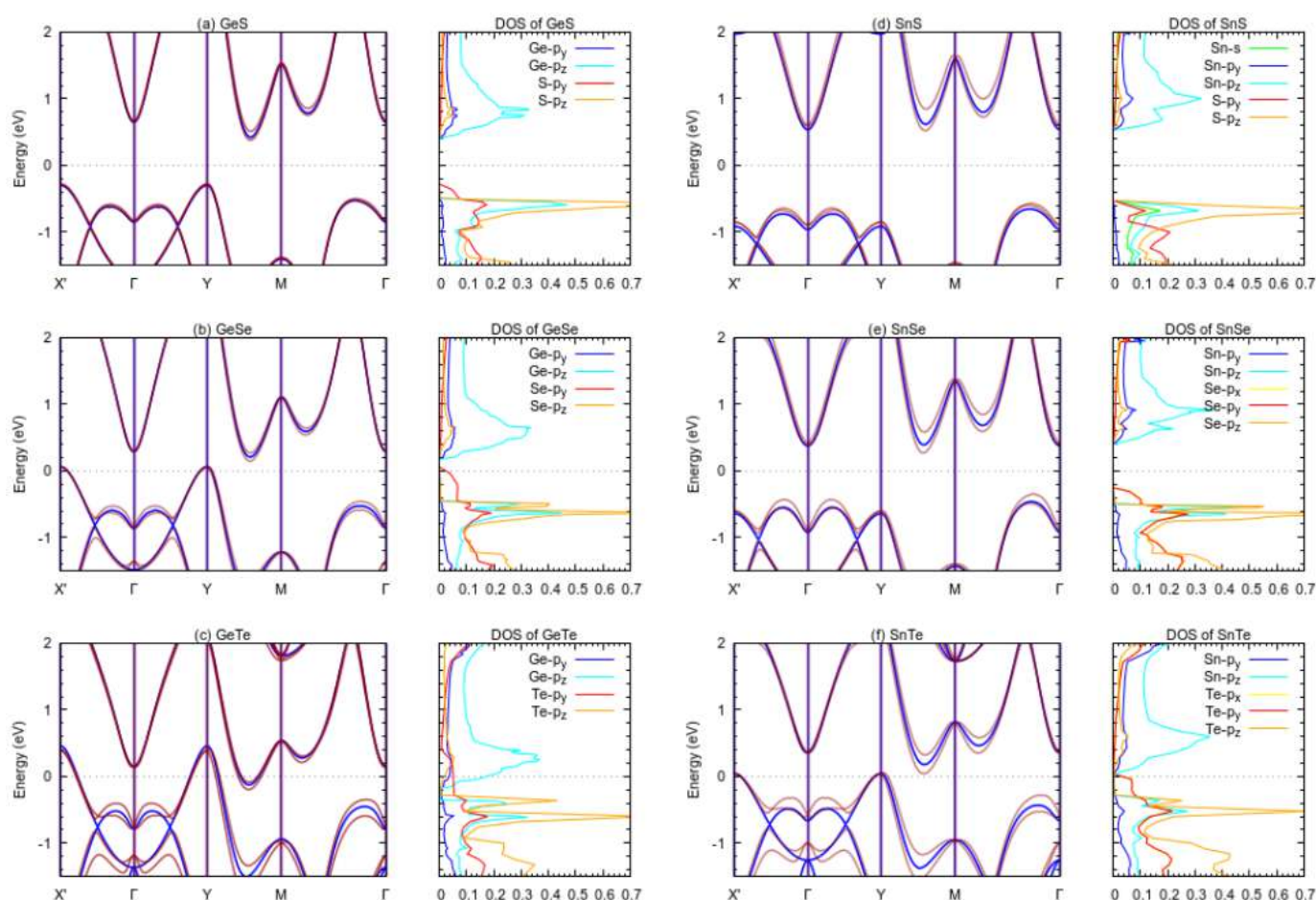
Fig 2. The Brillouin zone in k-space of the square lattice structure. Blue and pink line indicating the energy band without SOC and with SOC, respectively. The dominant DOS is displayed with corresponding orbitals

resulting in a lower band gap [17-19]. The band gap values are GeS = 0.660 eV, GeSe = 0.085 eV, GeTe = no band gap, SnSe = 1.097 eV, SnSe = 0.627 eV, and SnTe = no bandgap. From this band gap, all of MX is semiconductor except GeTe and SnTe, which is metallic.

When the calculation includes the SOC term, all of the bands are split due to the lack of inversion symmetry, which is occurs in all MX. The clarification of the

occurrence of the spin-split states is by considering the characteristic of the atomic orbitals of the band. From atomic point of view, coupling between atomic orbitals will contribute to the non-zero SOC matrix element through the relation $\zeta_l \langle \vec{L} \cdot \vec{S} \rangle_{u,v}$, where ζ_l is the angular-momentum-resolved atomic SOC strength, with $l = (s, p, d)$, $\vec{L}$ and $\vec{S}$ are the orbital angular momentum and Pauli spin operator, respectively, for the (u, v) atomic orbitals. It is revealed that the dominant contribution in CBM is coming from coupling between p orbitals of M atom and p orbitals of chalcogen atom for all MX. This p-p coupling is enhanced by increasing the atomic number of chalcogen atom. This finding is consistent with the enhancement of the spin splitting size around the Γ point. The more detailed discussion about the quantitative size of the splitting will be presented later.

Next, the spin-splitting near Γ and M-points of the CBM is claimed as Rashba-type splitting because the spin orientation is rotational [3], and we will show the calculation of this spin orientation (which is known as spin textures). It is well-known that there are three kinds

of SOC splitting in non-centrosymmetric and non-magnetic materials, namely Rashba, Dresselhaus, and Zeeman-like splitting [20], where the spin splitting and their corresponding spin textures are displayed in Fig. 3. The figure shows that the Rashba and Dresselhaus splitting is very similar except for the spin textures.

Next, the calculation of the size of the Rashba splitting in the buckled MX square lattice materials and the spin textures is conducted to clarify the claim that this is an actual Rashba splitting. To calculate the size of Rashba splitting (Rashba parameter) for higher-order, first is to use symmetry analysis to derive the effective Hamiltonian via k.p perturbation approximation. This approximation allows us to describe the electronic properties of our 2D MX monochalcogenides and can be used to analyze the properties of the band structure, such as spin splitting and spin texture for points around VBM and CBM. This method has already successfully used in various 2D material [7,21-25]. The symmetry group of the 2D square lattice structure is isomorphic to the C_{2v} or 2 mm two-dimensional space group [26], and from

(a) Rashba effect

(b) Dresselhauss effect

(c) Zeeman effect

The three bottom figures in the spin texture of the corresponding energy band splitting for energy E_0
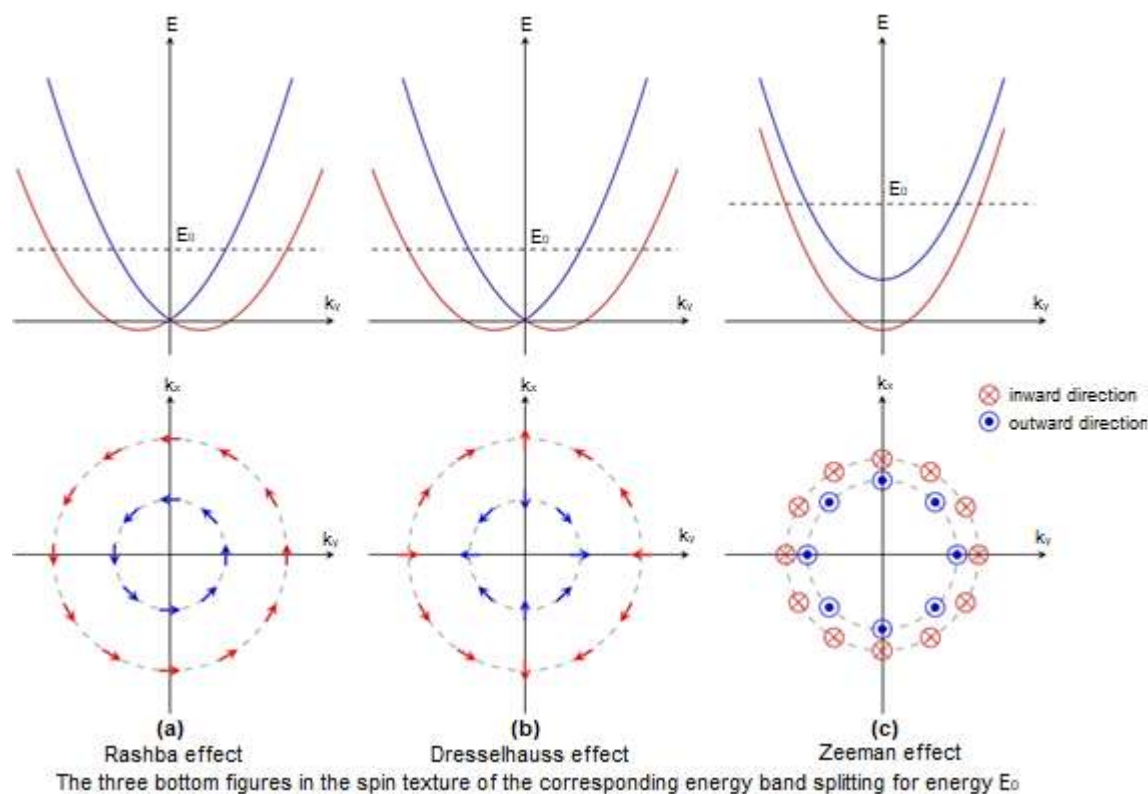
Fig 3. Three kinds of SOC splitting with the spin orientation

previous analysis using group theory [24], by deriving the general Hamiltonian using the direct product of irreducible representations. The elements of the group are denoted by $E: \{x, y, z\}$, $C_2: \{-x, -y, z\}$, $T_x: \{-x, y, z\}$, and $T_y: \{x, -y, z\}$. This group has four one-dimensional irreducible representations, A_1, A_2, B_1, and B_2 with the character table is written in Table 2.

The corresponding component of the irreducible representation is set to the polar-vector k and the axial-vector σ for the first order combination that corresponds to the A_1 irreducible representation is $B_1: k_x, \sigma_y$, $B_2: k_y, \sigma_x$, and $A_2: \sigma_z$. For the second-order, $A_1: k_x^2, k_y^2, k_y^2$, and $A_2: k_x k_y$, which is this second-order implies the form of kinetic energy. Finally, the third-order term is the possible product of $B_1: k_x^3, k_x k_y^2$, and $B_2: k_y^3, k_y k_x^2$ with σ_i. Then a new total Hamiltonian, that leaves the old one invariant, is constructed to get the new Hamiltonian related to SOC up to third-order as:

$$H(k) = E_0(k) + \alpha_1^{(1)}k_x\sigma_y + \alpha_1^{(2)}k_y\sigma_x + \alpha_3^{(1)}k_x^3\sigma_y +$$
$$\alpha_3^{(2)}k_x^2 k_y\sigma_x + \alpha_3^{(3)}k_x k_y^2\sigma_y + \alpha_3^{(4)}k_y^3\sigma_x \qquad (1)$$

where $E_0(k) = \hbar^2(\frac{k_x^2}{2m_x^*} + \frac{k_y^2}{2m_y^*})$ is the nearly free-electron energy, $\alpha_j^{(i)}$ is the i-th coefficient of the j-order, $\sigma_x, \sigma_y, \sigma_z$ is the Pauli spin matrices, (k_x, k_y) is the position in k-space and $k = \sqrt{k_x^2 + k_y^2}$. The eigenvalues problems for Eq. (1) gives us the splitting energy:

$$E_\pm(k, \theta) = E_0(k) \pm \sqrt{X^2 + Y^2} \qquad (2)$$

with

$$Y = \alpha_1^{(2)}k\sin\theta + \alpha_3^{(2)}k^3\cos^2\theta\sin\theta + \alpha_3^{(4)}k^3\sin^3\theta$$
$$X = \alpha_1^{(1)}k\cos\theta + \alpha_3^{(1)}k^3\cos^3\theta + \alpha_3^{(3)}k^3\sin^2\theta\cos\theta$$

where $k_x = k\cos\theta$, $k_y = k\sin\theta$, and θ is the angle of k with x-axis in k-space. The eigenvectors related to the $\pm\sqrt{(X^2 + Y^2)}$ eigenvalues is

$$\psi_\pm(k) = \begin{pmatrix} 0 \\ \pm\frac{(Y+iX)}{\sqrt{X^2+Y^2}} \end{pmatrix} \qquad (3)$$

The square of the difference of energy eigenvalue can be calculated using:

$$(\Delta E(k))^2 = 4(\alpha_1^{(1)}k_x + \alpha_3^{(1)}k_x^3 + \alpha_3^{(3)}k_x k_y^2)^2 + 4(\alpha_1^{(2)}k_y + \alpha_3^{(2)}k_x^2 k_y + \alpha_3^{(4)}k_y^3)^2 \qquad (4)$$

This equation is used to fit the plot of $(\Delta E(k))^2$ along Γ-X and Y-M and get the non-vanishing first-order coefficient as the Rashba parameter. The fitting results for the Rashba parameter are displayed in Table 3 with PbS calculation is shown as a confirmation. The table shows that for Γ-point, the size of the Rashba parameter increases depending on the atomic number of chalcogen atom, while on the M-point, the parameter is decreased.

Next, the spin texture of the band structures is determined as follows. For a given k point, its spin polarization of each eigenstates $\psi_\pm(k)$ is define as $S(k) = [S_x(k), S_y(k), S_z(k)]$ where $S_i(k) = \frac{\hbar}{2}\langle\psi(k)|\sigma_i\psi(k)\rangle$ is

Table 2. Character table of C$_{2v}$ group

	E	C_2	T_x	T_y
A_1	1	1	1	1
A_2	1	1	-1	-1
B_1	1	-1	-1	1
B_2	1	-1	1	-1

Table 3. Calculation result of band gap and Rashba parameter in CBM

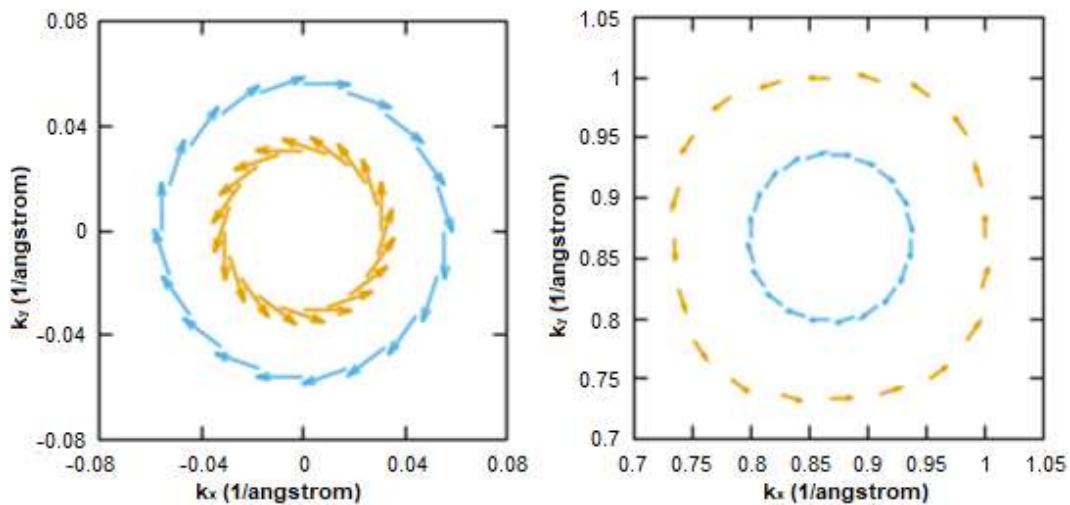| MX	Band Gap (eV)	Fitting Result (eVÅ)		Reference (eVÅ)		Source
		Γ-point ($\alpha_1^{(1)}$)	M-point ($\alpha_1^{(2)}$)	Γ-point	M-point	
PbS	0.747	1.20	3.19	1.03	5.10	[8]
GeS	0.660	0.20	0.68	0.201	0.583	[9]
GeSe	0.085	0.27	0.52	0.320	0.468	[16]
GeTe	Conductor	0.38	0.34	-	-	This work
SnS	1.097	0.42	2.36	0.429	2.354	[16]
SnSe	0.627	0.58	1.48	0.548	1.746	[16]
SnTe	Conductor	0.59	1.05	-	-	This work

Ibnu Jihad et al.

Fig 4. (left) Spin texture of SnTe for energy 0.4 eV around Γ-point, (right) Spin texture of SnSe for energy 1.15 eV around M-point. Both have zero z-component of spin. A similar form also occurred in other MX

the i-direction of spin component. This spin polarization is calculated in k-space around Γ point by using the spin density matrix of the spinor wave functions obtained from the DFT calculation [21-23]. The calculation result is shown in Fig. 4. It is revealed that constant-energy surface shows the inner and outer circles with counterclockwise and clockwise rotation of spin direction with no z-component of spin. This feature is consistent with the characteristic of the Rashba effect splitting.

The observed spin texture can be explained based on our derived SOC Hamiltonian given in Eq. (1). The expectation value of the spin polarization can be calculated from this to get $\langle S_x \rangle_\pm = \frac{\pm Y\hbar}{\sqrt{(X^2+Y^2)}}$, $\langle S_y \rangle_\pm = \frac{\pm X\hbar}{\sqrt{(X^2+Y^2)}}$, and $\langle S_z \rangle_\pm = 0$. This result shows that the spin textures are consistent with Fig. 4.

■ **CONCLUSION**

Investigation of the Rashba effect on two-dimensional MX Monochalcogenides (M = Ge, Sn and X = S, Se, Te) with buckled square lattice has shown that this structure is appropriate to create the Rasbha splitting. We also confirmed the properties of the spin texture of SOC splitting with the calculation from our DFT results. We found that some of MX have semiconductor properties (except GeTe and SnTe) and have different Rashba parameter. There is a strong correlation between the size of the Rashba parameter with the chalcogen atomic

number. In Γ-point, the escalation of the chalcogen atomic number increases the Rasha parameter, but in M-point the effect is inverting. These various size of the Rashba parameter make these materials, and this buckled square lattice is potential to be developed for spintronics materials.

■ **REFERENCES**

[1] Bhatti, S., Sbiaa, R., Hirohata, A., Ohno, H., Fukami, S., and Piramanayagam, S.N., 2017, Spintronics based random access memory: A review, *Mater. Today*, 20 (9), 530–548.

[2] Datta, S., and Das, B., 1990, Electronic analog of the electro-optic modulator, *Appl. Phys. Lett.*, 56 (7), 665–667.

[3] Manchon, A., Koo, H.C., Nitta, J., Frolov, S.M., and Duine, R.A., 2015, New perspectives for Rashba spin-orbit coupling, *Nat. Mater.*, 14 (9), 871–882.

[4] Tombros, N., Jozsa, C., Popinciuc, M., Jonkman, H.T., and van Wees, B.J., 2007, Electronic spin

transport and spin precession in single graphene layers at room temperature, *Nature*, 448 (7153), 571–574.

[5] Yan, W., Phillips, L.C., Barbone, M., Hämäläinen, S.J., Lombardo, A., Ghidini, M., Moya, X., Maccherozzi, F., van Dijken, S., Dhesi, S.S., Ferrari, A.C., and Mathur, N.D., 2016, Long spin diffusion length in few-layer graphene flakes, *Phys. Rev. Lett.*, 117 (14), 147201.

[6] Dlubak, B., Martin, M.B., Deranlot, C., Servet, B., Xavier, S., Mattana, R., Sprinkle, M., Berger, C., De Heer, W.A., Petroff, F., Anane, A., Seneor, P., and Fert, A., 2012, Highly efficient spin transport in epitaxial graphene on SiC, *Nat. Phys.*, 8 (7), 557–561.

[7] Absor, M.A.U., Santoso, I., Harsojo, Abraha, K., Kotaka, H., Ishii, F., and Saito, M., 2017, Polarity tuning of spin-orbit-induced spin splitting in two-dimensional transition metal dichalcogenides, *J. Appl. Phys.*, 122 (15), 153905.

[8] Hanakata, P.Z., Rodin, A.S., Carvalho, A., Park, H.S., Campbell, D.K., and Castro Neto, A.H., 2017, Two-dimensional square buckled Rashba lead chalcogenides, *Phys. Rev. B: Condens. Matter*, 96 (16), 161401.

[9] Hendrawan, J., Absor, M.A.U., Arifin, M., Jihad, I., and Abraha, K., 2019, Electronics structure of monochalcogenide materials MX (M = Ge, Sn and Pb; X = S and Se) buckled square lattice, *IOP Conf. Ser.: Mater. Sci. Eng.*, 515 (1), 012105.

[10] Ozaki, T., Kino, H., Yu, J., Han, M.J., Kobayashi, N., Ohfuti, M., Ishii, F., Ohwaki, T., Weng, H., and Terakura, K., 2009, *OpenMX: Open source package for Material eXplorer*, http://www.openmx-square.org/.

[11] Perdew, J.P., Burke, K., and Ernzerhof, M., 1996, Generalized gradient approximation made simple, *Phys. Rev. Lett.*, 77 (18), 3865–3868.

[12] Troullier, N., and Martins, J.L., 1991, Efficient pseudopotentials for plane-wave calculations, *Phys. Rev. B: Condens. Matter*, 43 (3), 1993–2006.

[13] Ozaki, T., 2003, Variationally optimized atomic orbitals for large-scale electronic structures, *Phys. Rev. B: Condens. Matter*, 67 (15), 155108.

[14] Ozaki, T., and Kino, H., 2004, Numerical atomic basis orbitals from H to Kr, *Phys. Rev. B: Condens. Matter*, 69 (19), 195113.

[15] Theurich, G., and Hill, N.A., 2001, Self-consistent treatment of spin-orbit coupling in solids using relativistic fully separable ab initio pseudopotentials, *Phys. Rev. B: Condens. Matter*, 64 (7), 073106.

[16] Absor, M.A.U., and Ishii, F., 2019, Intrinsic persistent spin helix state in two-dimensional group-IV monochalcogenide MX monolayers (M = Sn or Ge and X = S, Se or Te), *Phys. Rev. B: Condens. Matter*, 100 (11), 115104.

[17] Gomes, L.C., and Carvalho, A., 2015, Phosphorene analogues: Isoelectronic two-dimensional group-IV monochalcogenides with orthorhombic structure, *Phys. Rev. B: Condens. Matter*, 92 (8), 085406.

[18] Xu, L., Yang, M., Wang, S.J., and Feng, Y.P., 2017, Electronic and optical properties of the monolayer group-IV monochalcogenides MX (M = Ge, Sn; X = S, Se, Te), *Phys. Rev. B: Condens. Matter*, 95 (23), 235434.

[19] Wan, W., Liu, C., Xiao, W., and Yao, Y., 2017, Promising ferroelectricity in 2D group IV tellurides: A first-principles study, *Appl. Phys. Lett.*, 111 (13), 132904.

[20] Acosta, C.M., Fazzio, A., and Dalpian, G.M., 2019, Zeeman-type spin splitting in nonmagnetic three-dimensional compounds, *npj Quantum Mater.*, 4 (1), 41.

[21] Absor, M.A.U., Santoso, I, Harsojo, Abraha, K., Kotaka, H., Ishii, F., and Saito, M., 2018, Strong Rashba effect in the localized impurity states of halogen-doped monolayer PtSe2, *Phys. Rev. B: Condens. Matter*, 97 (20), 205138.

[22] Kotaka, H., Ishii, F., and Saito, M., 2013, Rashba effect on the structure of the Bi one-bilayer film: Fully relativistic first-principles calculation, *Jpn. J. Appl. Phys.*, 52 (3R), 035204.

[23] Absor, M.A.U., Kotaka, H., Ishii, F., and Saito, M., 2016, Strain-controlled spin splitting in the conduction band of monolayer WS2, *Phys. Rev. B: Condens. Matter*, 94 (11), 115131.

[24] Vajna, S., Simon, E., Szilva, A., Palotas, K., Ujfalussy, B., and Szunyogh, L., 2012, Higher-order contributions to the Rashba-Bychkov effect with application to the Bi/Ag(111) surface alloy, *Phys. Rev. B: Condens. Matter*, 85 (7), 075404.

[25] Affandi, Y., and Absor, M.A.U., 2019, Electric field-induced anisotropic Rashba splitting in two dimensional tungsten dichalcogenides WX_2 (X: S, Se, Te): A first-principles study, *Physica E*, 114, 113611.

[26] Dresselhaus, M.S., Dresselhaus, G., and Jorio, A., 2008, *Group Theory – Application to the Physics of Condensed Matter*, Springer-Verlag, Heidelberg, Germany.

Six-Armed Structures Based on Benzene Ring, Synthesis and Characterization via Sonogashira Coupling

Mohammed Hadi Ali Al-Jumaili[1,2,*], Ahmed Solaiman Hamed[3], Nihat Akkurt[4], and Lokman Torun[5,**]

[1]*Department of Chemistry, Faculty of Science and Arts, Yildiz Technical University, İstanbul, Turkey*

[2]*College of Dentistry, Al Turath University College, Baghdad, Iraq*

[3]*Department of Chemistry, College of Applied Science, University of Fallujah, Al-Anbar, Iraq*

[4]*Department of Chemistry, Faculty of Science and Art, Kirklareli University, Kirklareli, Turkey*

[5]*TORKIM ARGE, Inc., Yildiz Technical University, Technology Developing Zone, Incubation Center, 34220 Esenler, İstanbul, Turkey*

* Corresponding author:

tel: +90-536-2077645
email: Mo2006h2000@yahoo.com[*];
ltorun@yildiz.edu.tr[**]

Abstract: *New six-armed compounds consist of benzene ring as a central core substituted with aromatic ring and three rod-like armed of 2-chloro-4,6-bis(dodecyloxy)-1,3,5-triazine as the peripheral arms unit which were obtained by sequential nucleophilic substitution of chlorine atoms in cyanuric chloride. The substitution took place at the acetylenic periphery on the central benzene ring by cross-coupling. Equimolar mixtures of the six-armed compounds based on the benzene core with the complementary 4-dodecyloxybenzoic acid, which already possessed liquid crystal property, resulting in the organic salt. The organic salts and structures were investigated by differential scanning calorimetry (DSC) and confirmed by spectroscopic methods (^{1}H-NMR, ^{13}C-NMR, Mass spectrometry, and FT-IR).*

Keywords: *triazine; liquid crystals; hydrogen bonding; benzene core derivatives; synthesis; characterization*

■ INTRODUCTION

Multi-arm liquid crystals exhibited very specific electro-optical phenomena and wide applications [1-2]. Chiral liquid crystalline materials use in flexible color display applications [3-5]. Branched-arm LCs have a higher molecular weight in comparing with the conventional low molecular mass compounds, which usually contain a core and a few mesogenic units as the side arm; that is why it attracted much attention for their special molecular structures and interesting properties. Derivatives of benzene [6-8], condensed aromatic rings [9], are often used as cores of the multi-arm compounds. The multi-arm liquid crystal shows different properties such as lower melting temperature, lower viscosity, good solubility, etc., from the linear dimers, trimers, and oligomers [10-12]. One of the most interested classes in the liquid crystal is the star-shaped, which has been paid much attention in recent years [13-16].

Heterocycles are important in the design and synthesis of organic functional materials, especially in the development of thermotropic liquid crystals, since phase structure, polarity, geometry, luminescence, and many other molecular properties can be varied by the introduction of heteroatoms [17-20]. In recent years, much interest focus on the synthesis and characterization of compounds containing a 1,3,5-triazine unit or used as a central core due to their interesting properties, such as liquid crystalline and nonlinear optical properties as well as their applications in other fields [21-24]. The 1,3,5-triazine is an electron-accepting unit, which can be substituted at the 2,4,6-positions with an appropriate aromatic rigid core through linking groups at the side arms to give a C$_3$-symmetrical system (star-shaped) that is able to form columnar mesophases [25]. Moreover, the extension of the electronic conjugation of these types of mesogens

should give CLCs with luminescent properties and high charge-carrier mobility [26-27].

Supramolecular liquid crystals (LCs), obtained via intermolecular hydrogen bonding have attracted considerable attention due to their ability of existence of the mesophase. In these cases, the hydrogen bonded complexes are formed between two identical molecules, and the system can be considered as self-complementary [28].

In this study, our research focuses on star-shaped molecules bearing three aromatic arms and three rod-like armed of 2-chloro-4,6-bis(dodecyloxy)-1,3,5-triazine as the peripheral arms unit linking through triple bond on the benzene core, started from 1,3,5-trichloro-2,4,6-triiodobenzene, which is derived from 1,3,5-trichlorobenzene and 2-chloro-4,6-bis(dodecyloxy)-1,3,5-triazine which is derived from 2,4,6-trichloro-1,3,5-triazine. The synthesis of organic salts was obtained via intermolecular hydrogen bonding between six-armed compounds and 4-dodecyloxybenzoic acid, which is already possessed liquid crystal property to increase the possibility of liquid crystalline of the mixture [29].

■ **EXPERIMENTAL SECTION**

Materials

The reagents and solvents used were obtained from Merck with pro analysis grade without further purification, i.e., cyanuric chloride, dodecan-1-ol, ethynylbenzene, 1,3,5-trichlorobenzene, 2-iodo-thiophene, 2-ethynyl benzene, ethynyltrimethylsilane, copper iodide, potassium carbonate, tetrakis (triphenylphosphine)palladium and triethylamine, tetrahydrofuran, dimethylformamide, and dioxane. Thin-layer chromatography was performed using aluminum plates (20 × 20 cm) coated with silica gel 60 F254 (Merck), while column chromatography was carried out using silica gel 60 (0.063–0.200 mm) from Merck.

Instrumentation

Structure elucidation of compounds was carried out using HRMS (High resolution mass spectrometry), FT-IR (Shimadzu Prestige-21, KBr discs), ^{1}H-NMR (500 MHz) and ^{13}C-NMR (125 MHz) (CDCl$_3$, standard internal TMS) spectrometers. Liquid crystalline evaluation of the organic salts was performed using DSC (Differential scanning calorimetry).

Procedure of Six-armed Compounds

2-chloro-4,6-bis(dodecyloxy)-1,3,5-triazine (2)

A mixture of 2,4,6-trichloro-1,3,5-triazine (**1**) (1.90 g, 10.3 mmol), dodecan-1-ol (3.84 g, 20.6 mmol) and K$_2$CO$_3$ (2.84 g, 20.6 mmol) were dissolved in 10.0 mL of THF (Scheme 2). The mixture was stirred at 50 °C for 5 h under argon atmosphere. The solution was poured into a mixture of ethyl acetate (20.0 mL) and water (20.0 mL). The organic layer after separation was dried with sodium sulfate. Under vacuum, the solvent was evaporated and the crude product was purified by column chromatography with hexane/ethyl acetate (5% EtOAc) as an eluent to give white solid materials with a yield (3.50 g, 70%). ^{1}H-NMR (500 MHz, CDCl$_3$) δ 3.70 (t, J = 6.7 Hz, 4H, OCH$_2$), 1.81–1.51 (m, 4H, CH$_2$), 1.58–1.20 (m, 36H, CH$_2$), 0.94 (t, J = 6.9 Hz, 6H, CH$_3$) ^{13}C-NMR (126 MHz, CDCl$_3$) δ 173.17 (O-C$_{het}$), 172.18 (Cl-C$_{het}$), 68.54 (OCH$_2$), 31.95, 29.68, 29.66, 29.61, 29.56, 29.38, 29.33, 28.68, 25.86, 22.72, 14.14). HRMS = m/z M$^+$ and [M+K]$^+$ calcd for C$_{27}$H$_{50}$ClN$_3$O$_2$: 483.36; found: 483.35, 523.3282 respectively.

2,4-bis(dodecyloxy)-6-((trimethylsilyl)ethynyl)-1,3,5-triazine (3)

A mixture of 2-chloro-4,6-bis(dodecyloxy)-1,3,5-triazine (**2**) (1.20 g, 2.47 mmol), K$_2$CO$_3$ (0.40 g, 22.0 mmol), ethynyltrimethylsilane (0.29 g, 2.96 mmol), Pd(Pph$_3$)$_4$ (0.28 g, 0.24 mmol), CuI (0.09 g, 0.49 mmol), were dissolved in 10.0 mL of THF (Scheme 2). The mixture was refluxed for 6 h under argon atmosphere. The solution was poured into a mixture of ethyl acetate (20.0 mL) and water (20.0 mL). The organic layer after separation was dried with sodium sulfate. Under vacuum, the solvent was evaporated to give brown oily material with a yield (1.10 g, 81%). HRMS = m/z [M+H]$^+$ calcd for C$_{32}$H$_{59}$N$_3$O$_2$Si: 545.44; found: 546.39.

Trimethyl(thiophen-2-ylethynyl) silane (5)

A mixture of 2-iodothiophene (**4**) (0.40 g, 1.90 mmol), K$_2$CO$_3$ (0.394 g, 2.85 mmol), 2-methylbut-3-yn-2-ol (0.17 g, 2.09 mmol), Pd(Pph$_3$)$_4$ (0.021 g, 0.019 mmol), CuI (0.007 g, 0.038 mmol), were dissolved in 10.0 mL of

THF under argon atmosphere (Scheme 2). The mixture was refluxed for 6 h. The solution was poured into a mixture of ethyl acetate (20.0 mL) and water (20.0 mL). The organic layer after separation was dried with sodium sulfate. Under vacuum, the solvent was evaporated to give brown oily material with a yield (0.27g, 87%). HRMS = m/z [M+H]$^+$ calcd for $C_9H_{10}OS$: 166.0; found: 167.05.

2-ethynylthiophene (6)

A mixture of trimethyl(thiophen-2-ylethynyl) silane (**5**) (0.25 g, 1.38 mmol) and K_2CO_3 (0.249 g, 1.80 mmol) were dissolved in 10.0 mL of toluene (Scheme 2). The mixture was stirred for 12 h at 80 °C. The solution was poured into a mixture of dichloromethane (20.0 mL) and water (20.0 mL). The organic layer after separation was dried with sodium sulfate. Under vacuum, the solvent was evaporated to give brown oily material with a yield (0.1 g, 83%). HRMS = m/z [2M$^+$] calcd for C_6H_4S: 108; found: 108.

1,3,5-trichloro-2,4,6-triiodobenzene (8)

Periodic acid (3.00 g, 13.2 mmol) was added slowly to 50.0 mL of concentrated sulfuric acid and stirred for 1 h then Potassium iodide (6.50 g, 39.5 mmol) was added to the mixture slowly at 0 °C, after the reaction reached room temperature, 1,3,5-trichlorobenzene (**7**) (0.789 g, 4.38 mmol) was added (Scheme 3). The solution was poured into a mixture of ethyl acetate (50.0 mL) and water (50.0 mL). The organic layer after separation was dried with sodium sulfate. Under vacuum, the solvent was evaporated to give light yellow solid materials with a yield (1.50 g, 62%), MP. 280 °C. HRMS = m/z M$^+$ and [M+H]$^+$ calcd for $C_6Cl_3I_3$: 557.6; found: 558.6.

((2,4,6-trichlorobenzene-1,3,5-triyl) tris(ethyne-2,1-diyl)) tribenzene (9a)

A mixture of 1,3,5-trichloro-2,4,6-triiodobenzene (**8**) (0.50 g, 0.90 mmol), ethynylbenzene (0.28 g, 2.68 mmol), Pd (Pph$_3$)$_4$ (0.01 g, 0.09 mmol), CuI (0.03 g, 0.18 mmol) and K_2CO_3 (0.28 g, 2.86 mmol) were dissolved in 10.0 mL of dioxane (Scheme 3). The mixture was stirred at 75 °C for 6 h under argon atmosphere. The solution was poured into a mixture of ethyl acetate (20.0 mL) and water (20.0 mL). The organic layer after separation was dried with sodium sulfate. Under vacuum, the solvent was evaporated and the crude product was purified by column chromatography

with hexane/ethyl acetate (5% EtOAc) as an eluent to give white powder with a yield (0.35 g, 81%). MP. 140–145 °C. ^{1}H-NMR (500 MHz, CDCl$_3$) (7.6 (m, 1H), 7.4 (m, 2H). ^{13}C-NMR (142, 132.5, 129.2, 128.5, 121.8, 81.6, 74). HRMS = m/z [M+H]$^+$ calcd for $C_{30}H_{15}Cl_3$: 481.80; found: 483.02.

2,2',2''-((2,4,6-trichlorobenzene-1,3,5-triyl) tris (ethyne-2,1diyl)) trithiophene (9b)

A mixture of 1,3,5-trichloro-2,4,6-triiodobenzene (**8**) (0.50 g, 0.89 mmol), 2-ethynylthiophene (**6**) (0.48 g, 2.69 mmol), Pd (Pph$_3$)$_4$ (0.10 g, 0.089 mmol), CuI (0.03 g, 0.178 mmol) and K_2CO_3 (0.39 g, 2.84 mmol) were dissolved in 10.0 mL of dioxane (Scheme 3). The mixture was stirred at 75 °C for 6 h under argon atmosphere. The solution was poured into a mixture of ethyl acetate (20.0 mL) and water (20.0 mL). The organic layer after separation was dried with sodium sulfate. Under vacuum, the solvent was evaporated and the crude product was purified by column chromatography with hexane/ethyl acetate (5% EtOAc) as an eluent to give pale yellow powder with a yield (0.37 g, 84%), MP.124–127 °C. ^{1}H-NMR: (CDCl$_3$) (7.3 (m, 1H) 3× (1H), 7.17 (m, 1H) 3× (1H), 6.7 (dt, J = 6.8, 3.4 Hz, 1H) 3× (1H)), ^{13}C-NMR: (146, 141, 138, 132, 131, 129, 100, 98). HRMS = m/z M$^+$ and [M+H]$^+$ calcd for $C_{24}H_9Cl_3S_3$: 499.88; found: 499.89 and 500.88, respectively.

6,6',6''-((2,4,6-tris(phenylethynyl)benzene-1,3,5-triyl) tris(ethyne-2,1-diyl)) tris(2,4-bis(dodecyloxy)-1,3,5-triazine) (10a)

((2,4,6-trichlorobenzene-1,3,5-triyl)tris(ethyne-2,1-diyl))tribenzene (**9a**) (0.15 g, 0.31 mmol), 2,4-bis(dodecyloxy)-6-((trimethylsilyl)ethynyl)-1,3,5-triazine (**3**) (0.51 g, 0.93 mmol), Pd(Pph$_3$)$_4$ (0.035 g, 0.031 mmol), CuI (0.011 g, 0.06 mmol) and K_2CO_3 (0.136 g, 0.99 mmol) were dissolved in 10.0 mL of dioxane (Scheme 3). The mixture was stirred at 80 °C for 16 h under argon atmosphere. The organic layer after separation was dried with sodium sulfate. Under vacuum, the solvent was evaporated and the crude product was purified by column chromatography with hexane/ethyl acetate (5% EtOAc) as an eluent to obtain light brown with a yield (0.42 g, 75%). ^{1}H-NMR: (CDCl$_3$) (7.3 (dt, J = 11.1, 5.4 Hz, 6H), 7.18 (m, 9H), 4.15 (t, J = 6.8 Hz, 12H, OCH$_2$), 1.64–1.50 (m, 12H, CH$_2$), 1.44–1.1 (m, 108H, CH$_2$), 0.7 (t, J = 6.8 Hz, 18H, CH$_3$). ^{13}C-NMR: (173, 171, 142, 139, 132, 129, 128, 122, 108, 98, 81,

74, 68, 32, 31, 30, 29, 28, 24, 22, 12). MS = m/z [M+2]$^+$ calcd for C$_{117}$H$_{165}$N$_9$O$_6$: 1793.6; found: 896.64 × 2 = 1793.28.

6,6',6''-((2,4,6-tris(thiophen-2-ylethynyl) benzene-1,3,5-triyl) tris(ethyne-2,1-diyl)) tris(2,4-bis(dodecyloxy)-1,3,5-triazine) (10b)

2,2',2''-((2,4,6-trichlorobenzene-1,3,5-triyl)tris(ethyne-2,1-diyl))trithiophene **(9b)** (0.15 g, 0.3 mmol), 2,4-bis(dodecyloxy)-6-((trimethylsilyl)ethynyl)-1,3,5-triazine (**3**) (0.49 g, 0.90 mmol), Pd(Pph$_3$)$_4$ (0.034 g, 0.03 mmol), CuI (0.011 g, 0.06 mmol) and K$_2$CO$_3$ (0.13 g, 0.96 mmol) were dissolved in 10.0 mL of dioxane (Scheme 3). The mixture was stirred at 80 °C for 16 h under argon atmosphere. The solution was poured into a mixture of ethyl acetate (20.0 mL) and water (20.0 mL). The organic layer after separation was dried with sodium sulfate. Under vacuum, the solvent was evaporated and the crude product was purified by column chromatography with hexane/ethyl acetate (5% EtOAc) as an eluent to obtain light brown with a yield (0.41g, 76%). ^{1}H-NMR: (CDCl$_3$) (7.25 (m, 6H), 6.95 (d, 3H), 4.3 (t, J = 6.8 Hz, 12H, OCH$_2$), 1.6 (m, 12H, CH$_2$), 1.4–1.1 (m, 108H, CH$_2$), 0.8 (t, J = 6.8 Hz, 18H, CH$_3$). ^{13}C-NMR: (173, 166, 162, 134, 131, 128, 127, 121, 114, 98, 87, 68.5, 32, 31, 30, 29, 28, 24, 22, 12). HRMS = m/z [M+2H]$^{+2}$ calcd for C$_{111}$H$_{159}$N$_9$O$_6$S$_3$: 1811.7; found: (906.58 × 2 - 2 = 1811.16).

Second route of synthesis compounds 10(a-b): 6,6',6''-((2,4,6-trichlorobenzene-1,3,5-triyl) tris(ethyne-2,1-diyl)) tris(2,4-bis(dodecyloxy)-1,3,5-triazine) (11)

1,3,5-trichloro-2,4,6-triiodobenzene (**8**) (0.50 g, 0.89 mmol), 2,4-bis(dodecyloxy)-6-((trimethylsilyl)ethynyl)-1,3,5-triazine (**3**) (1.47 g, 2.69 mmol), K$_2$CO$_3$ (0.39 g, 2.84 mmol), Pd(Pph$_3$)$_4$ (0.01 g, 0.089 mmol), CuI (0.033 g, 0.178 mmol), were dissolved in 10.0 mL of dioxane under argon atmosphere (Scheme 4). The mixture was stirred at 70 °C for 12 h. The solution was poured into a mixture of ethyl acetate (20.0 mL) and water (20.0 mL). The organic layer was washed and dried over sodium sulphate. The solvent was removed under vacuum to give yellow solid material with yield (1.10 g, 76%). ^{1}H-NMR: (CDCl$_3$) (4.3 (t, 12H, OCH$_2$), 1.65 (m, 4H, CH$_2$), 1.35 (m, 18H, CH$_2$), 0.95 (t, 6H, CH$_3$)). ^{13}C-NMR (173.5, 171.3, 145.6, 126. 100.3, 97.89, 68.5, 31.9, 29.65, 29.6, 29.5, 29.3, 28.6, 25.8, 22.7, 14.1). HRMS = m/z [M+2] and [M+2(NH$_4$)]$^{+2}$ calcd

for C$_{93}$H$_{150}$Cl$_3$N$_9$O$_6$: 1594.1; found: 797.52 (797.52 × 2 = 1595.04), 816.09 (816.09 × 2 - 36 = 1596.1) respectively.

4-(dodecyloxy) benzoic acid (4-DBA) (12)

A solution of 4-hydroxy benzoic acid (8.20 mmol), 1-bromododecane (5.50 mL, 23.0 mmol, 2.8 eq) and KOH (1.30 g, 23.0 mmol, 2.8 eq) in ethanol (25.0 mL) was heated under reflux for 2 days (Scheme 5). By adding 10% aqueous KOH (25.0 mL) to the mixture and refluxed overnight, the hydrolysis was carried out. After cooling down, the reaction mixture was acidified with HCl (6.0 M), the precipitate was filtered, washed with water and recrystallized from ethanol to obtain the pure product 4-dodecyloxybenzoic acid, a white solid material with yield (4.55 g, 91%). ^{1}H-NMR (500 MHz, CDCl$_3$) showed peaks at (δ 8.10 (d, 2H), 6.98 (d, 2H),4.07 (t, 2H), 1.84 (m, 2H), 1.48 (m, 2H), 1.37–1.28 (m, 16H), 0.91 (t, 3H). The FT-IR (2914, 2848, 2559, 1670, 1604) cm^{-1}.

Synthesis of organic salt

4-DBA mesogenic unit (**12**) with a carboxyl group was added into a solution of compound **10 (a-b)** in 10 mL of dry THF with one to one ratio (Scheme 5). The resulting solution was sonicated for 15 min until a transparent solution was observed. Then, the solvent was removed in vacuum.

The organic salt (13a). ^{1}H-NMR (7.9 (d, 2H), 7.4 (d, 2H), 7.15 (m, 3H), 6.8 (d, 2H), 4.2 (t, 12H, OCH$_2$), 3.85 (t, (OCH$_2$), 1.75 (m, 12H, CH$_2$), 1.15 (m, 108H, CH$_2$), 0.7 (t, J = 7.0 Hz, 18H, CH$_3$). FT-IR (2917, 2855, 2564, 1694, 1609, 1560, 1477, 1419, 1332, 1274). MS = m/z [M+3(HCOO)]$^{-3}$ calcd for C$_{136}$H$_{195}$N$_9$N$_9$O$_9$: 2098.5; found: 744.496 (744.496 × 3 – 3 × 45 = 2098.48).

The organic salt (13b). ^{1}H-NMR (7.85 (d, 2H), 7.25 (m, 2H), 6.95 (d, 1H), 6.75 (d, 2H), 4.26 (t, 12H, OCH$_2$), 3.8 (t, (OCH$_2$), 1.75 (m, 12H, CH$_2$), 1.3–1.15 (m, 108H, CH$_2$), 0.75 (t, 18H, CH$_3$). FT-IR (2915, 2844, 1680, 1584, 1530, 1560, 1490, 1419, 1278, 1156).

■ RESULTS AND DISCUSSION

In this contribution, six arms structures based on benzene ring were synthesized via Sonogashira-reaction using different substituted started with 1,3,5-trichlorobenzene and 2,4,6-trichloro-1,3,5-triazine as described in (Scheme 1-5). The structures were confirmed

Indones. J. Chem., 2020, 20 (3), 705 - 715

709
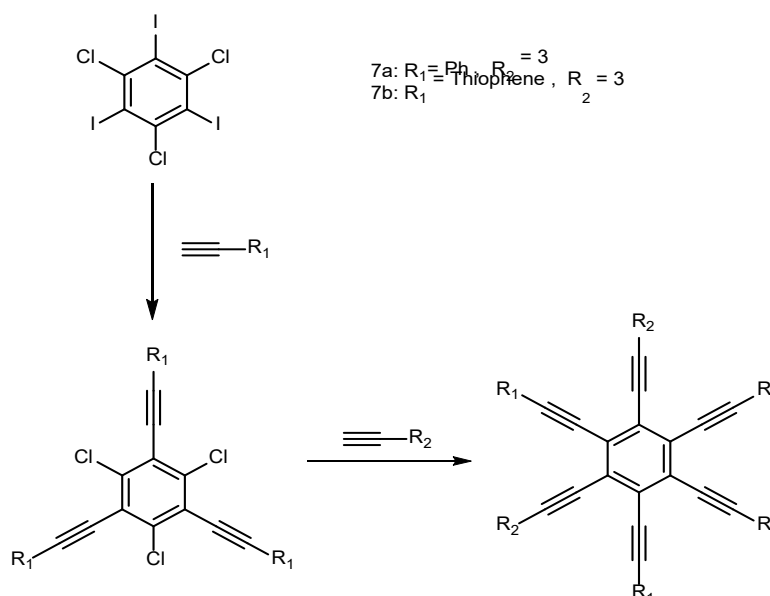
Scheme 1. Synthesis route of six arms compounds
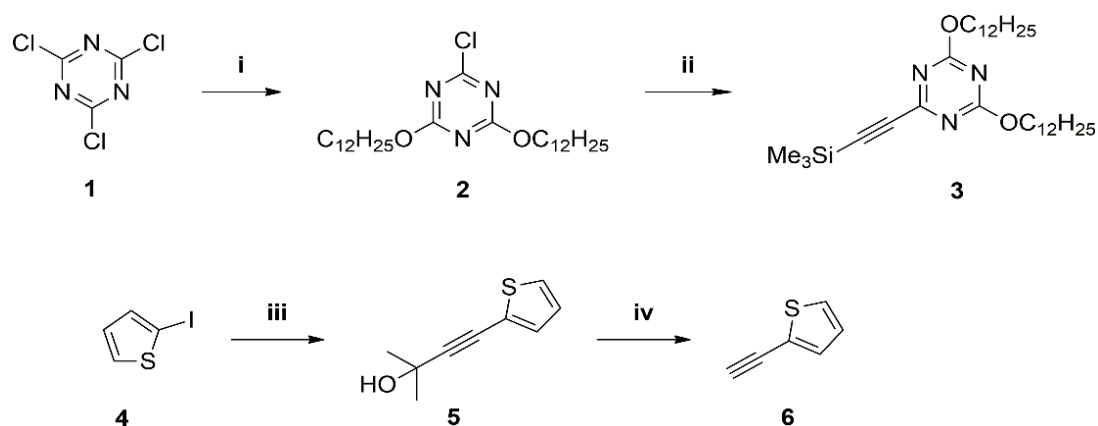
Scheme 2. Synthesis route of intermediate compounds. Reaction and condition: **i)** K_2CO_3, dodecan-1-ol, 0–50 °C, 5 h, THF, **ii)** Ethynyltrimethylsilane, K_2CO_3, Pd(PPh$_3$)$_4$, CuI, THF, Reflux, **iii)** 2-methylbut-3-yn-2-ol, Pd(PPh$_3$)$_4$, CuI, K_2CO_3, THF, Reflux, **iv)** K_2CO_3, toluene, 80 °C, 12 h
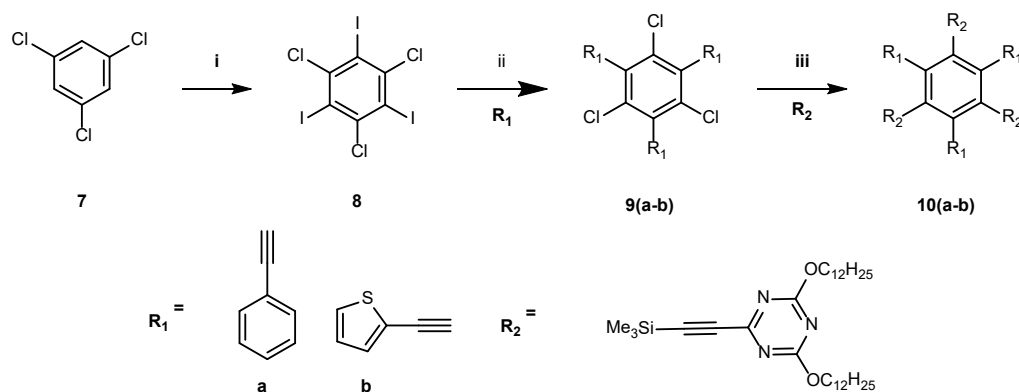
Scheme 3. Synthesis route of six arms on the benzene ring. Reaction and condition: **i)** H_5IO_6, H_2SO_4, KI, 0 °C 10.0 min, r.t., **ii)** Pd(PPh$_3$)$_4$, CuI, Et$_3$N (3.2 eq), Dioxane, 75 °C, 6 h, **iii)** Pd(PPh$_3$)$_4$, CuI, K_2CO_3, Dioxane, 80 °C, 12 h
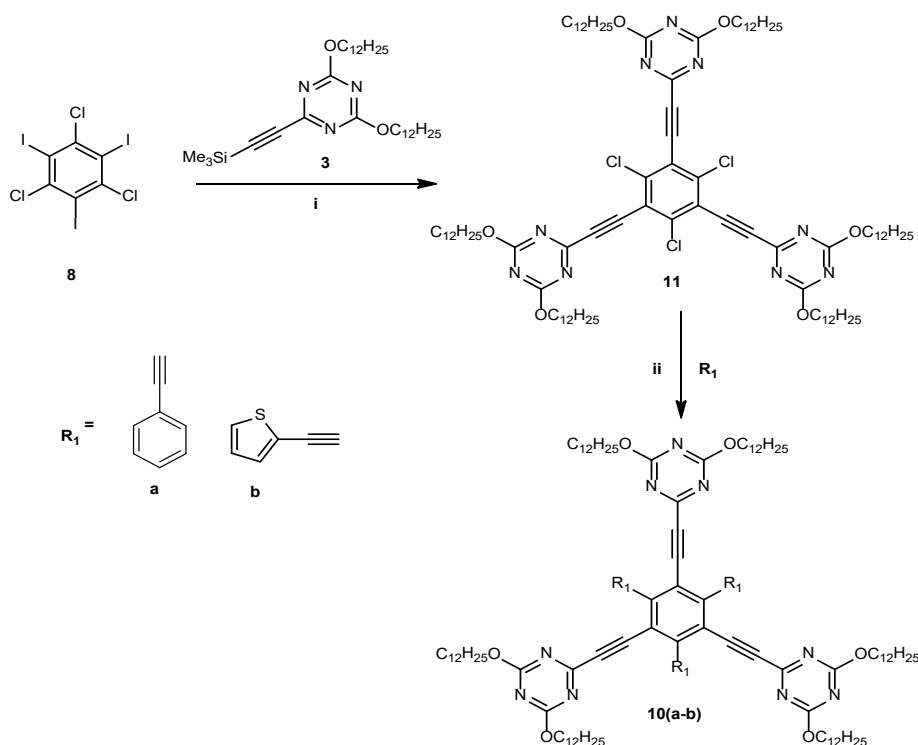
Scheme 4. Synthesis route of six arms compounds **10(a-b)**. Reaction and condition: **i)** Pd (PPh$_3$)$_4$, CuI, K$_2$CO$_3$, Dioxane, 70 °C, 6 h, **ii)** Pd(PPh$_3$)$_4$, CuI, K$_2$CO$_3$, Dioxane, 80 °C, 12 h
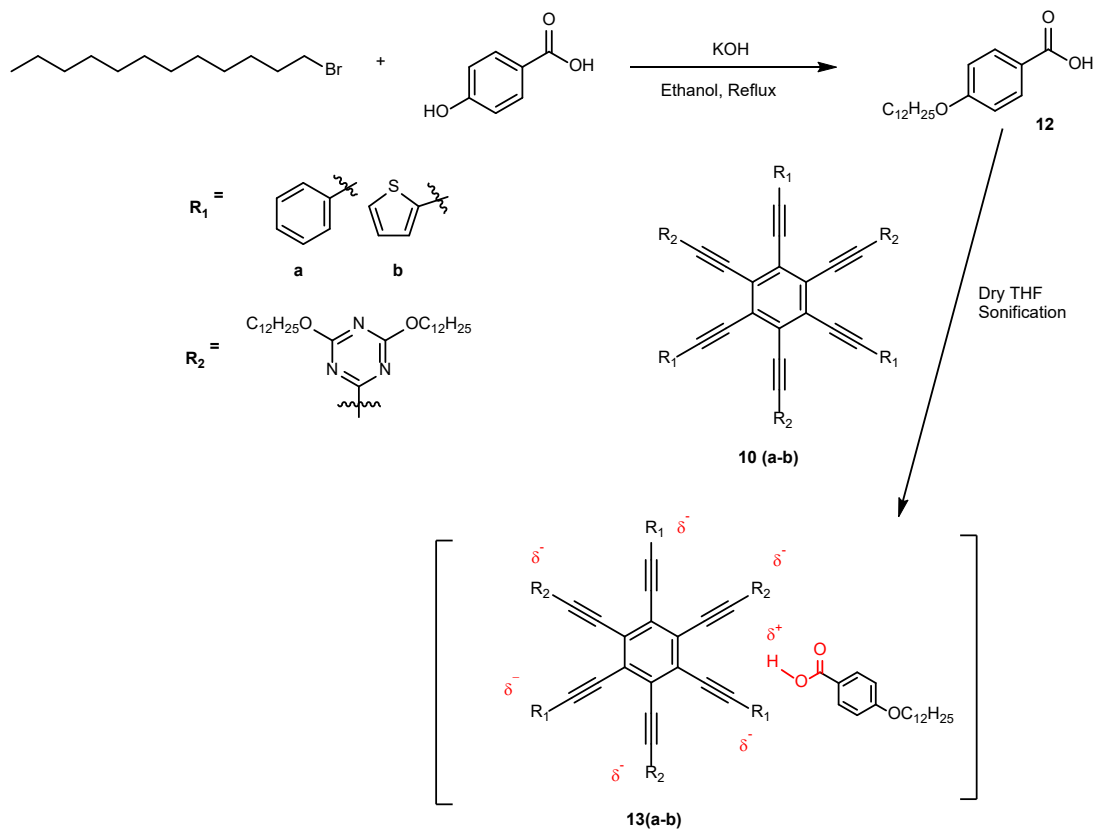
Scheme 5. Synthesis procedure of organic salt **13(a-b)**

by spectroscopic analysis and investigated by differential scanning calorimetry (DSC).

The compounds (**10a**, **10b**) were obtained in two routes (Scheme 3, Scheme 4). In comparison, the yield of product in the second route was higher than the first route, which may occur due to the chloride that has more reactivity to couple with aromatic (ethynylbenzene, 2-ethynylthiophene) than to couple with 2,4-bis(dodecyloxy)-6-((trimethylsilyl)ethynyl)-1,3,5-triazine, and the reaction to achieve the product was also shorter as well [30] (Table 1).

The formation of ionic interaction between the six-armed π-conjugated system and the mesogenic carboxyl group was mainly studied by FTIR. The sharp peak belongs to the carboxylic (Fig. 1). Moreover, asymmetric stretching carboxylate peak at $1670 \, cm^{-1}$ of pure 4-DBA was shifted in both organic salt to $1680 \, cm^{-1}$ and $1694 \, cm^{-1}$, respectively, after ionic interaction. In addition, peaks at 2900 and $2800 \, cm^{-1}$ are belonged to hydrogen stretching.

The formation of ionic interaction between the six-armed π-conjugated system and the mesogenic carboxyl group was also checked by NMR spectroscopy. The signals corresponding to the aromatic protons of alkoxy benzoate unit shift to (7.95, 6.8) ppm in compound (**13a**) and (7.85, 6.75) ppm in compounds (**13b**) comparing to pure **4-DBA** signals at (8.05, 6.95) ppm — these shifting due to an increase in electron density of the aromatic ring. Similarly, the signals of oxymethylene protons of 4-DBA in ion complex shift to higher field 3.85 ppm in compound (**13a**) and 3.8 ppm in compound (**13b**) as

compared with the signals of pure **4-DBA** at 4.05 ppm (Fig. 2). Additionally, the oxymethylene protons and aromatic protons of both organic salts show no shifting since their electronic environment did not change.

Additionally, unambiguous support for the structures of (**13a**), came from the QTOF analysis. The mass spectra of the organic salt indicate the presence of $[M+3(HCOO)]^{-3}$ at 744.496 and 744.84, as seen in Fig. 3.

Compound **4-DBA**, which has an n-dodecyloxy terminal chain, shows enantiotropic liquid crystalline properties that are in agreement with the behavior observed for analogous benzoic acids carrying an alkoxy chain with the different numbers of carbon atoms at 4-position of the aromatic ring [31-33]. Upon heating, **4-DBA** showed three peaks corresponding to Cr–SmC–N–Iso transitions. On cooling from the isotropic phase, the same behavior of reverse transitions was observed. In addition to this, a calorimetric peak corresponding to Cr-Cr transition at 65.86 °C was detected in the cooling DSC thermogram (34). A typical texture of the SmC mesophase observed for **4-DBA** is shown in Fig. 4.

Table 1. Comparison of the percentage yield

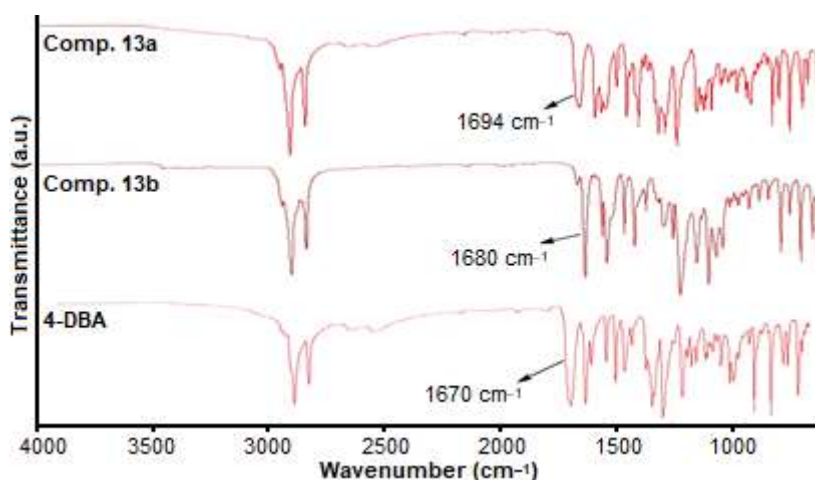| Comp. 10(a-b)	R₁	R₂	Time/h	Yield/%
Scheme 3	9a	3	16	75
	9b	3	16	76
Scheme 4	11	ethynylbenzene	12	85
	11	2-ethynylthiophene	12	81

Fig 1. FT-IR spectra of organic salt (**13a**, **13b**) and benzoic acid (**4-DBA**)
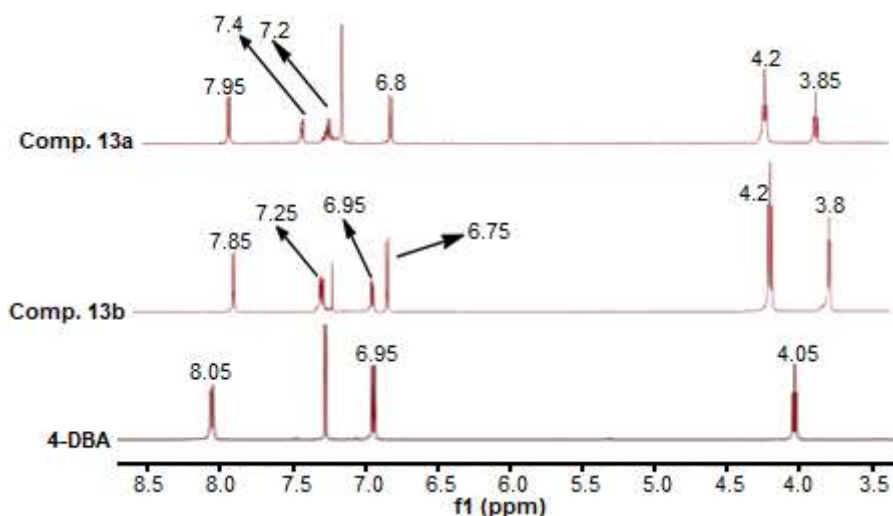
Fig 2. The comparison of ^{1}H-NMR spectra (in CDCl$_3$) of organic salts (**13a**, **13b**) and benzoic acid (**4-DBA**)
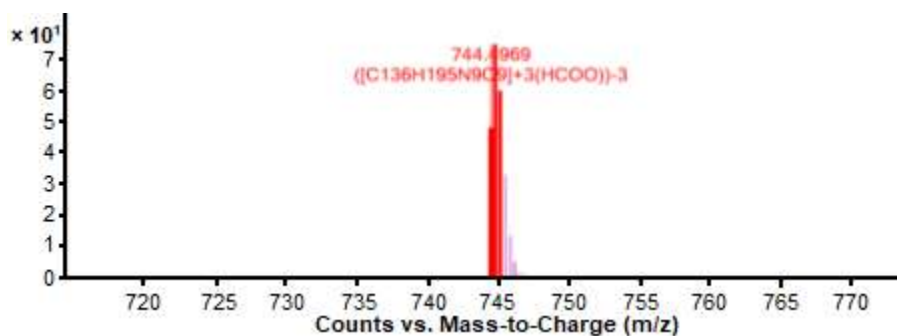

Fig 3. Q-TOF LC/MS result of organic salt (**9a**)

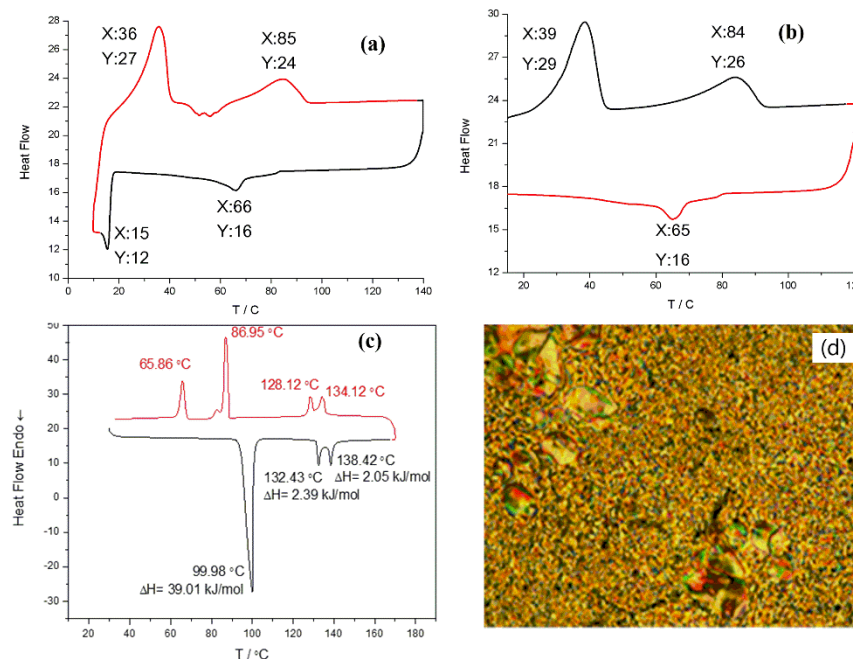**Fig 4.** (a) DSC thermograms of (a) **organic salt 13a**, (b) **organic salt 13b**, (c) **4-DBA** on 1st heating and cooling (10 °C min^{-1}), (d) A typical texture of the smectic C mesophase of compound **4-DBA** T = 118.0 °C as observed between crossed polarizers in ordinary glass-plates on cooling

Table 2. Mesophases and phase transition temperatures as observed on heating (H→) and cooling (←C) and corresponding transition enthalpies of the organic salts **13a**, **13b**, and **4-DBA**

Comp.	T/°C [ΔH kJ/mol]
4-DBA[b]	H →: Cr 99.98 [39.01] SmC 132.43 [2.39] N 138.42 [2.05] Iso
OS (13a)	H →: Cr 12 [14.9] Col 16 [66] Iso: ← **C**
	Cr 29.3 [38.7] Col 25.6 [83.6] Iso: ← **C**
OS (13b)	H →: Cr 15.7 [65.2]
	Cr 27 [36] Col 23.9 [84.9] Iso: ← **C**

[a]Perkin-Elmer DSC-6; enthalpy values in italics in brackets taken from the 1st heating and cooling scans at a rate of 10 °C min⁻¹; Abbreviations: Cr = crystalline, SmC = tilted smectic phase, N = nematic phase; Col = columnar mesophase, Iso = isotropic liquid phase
[31-32] Cr 95.1 SmC 128.9 N 137.2 Iso
[33] Cr 92.4 SmC 131.5 N 142.0 Iso

The transition phase determined by differential scanning calorimetry (DSC), organic salt **13a**, exhibits a phase transition, which is in agreement with two endotherms in the DSC heating curves. On heating, two peaks were observed at 84–27 °C. On the cooling form, the isotropic liquid, two peaks corresponding to the transition phase were observed at 66–15 °C, as shown in Fig. 4. However, for the organic salt **13b**, on heating, two endotherm peaks were observed at 83–38 °C, whereas in the cooling cycle, one peak was observed at 65 °C, the results were summarized in (Table 2).

Both organic salts with multi-side chains, the differential scanning calorimetry revealed textures suggesting liquid crystalline states below the transitions at higher temperatures. An increase in the length of the alkoxy side chains leads to a steady decrease in the temperatures for the phase transition [35].

By the differential scanning calorimetry (DSC), two endothermic peaks were observed in the heating and cooling cycle of the compound **13a**, which expected to exhibit liquid crystal phases (Fig. 4). Besides, compound **13b** also showed two endothermic peaks in the heating cycle but showed one peak only in the cooling cycle, which may also exhibit a transition phase.

■ CONCLUSION

A new six arms compounds based on benzene ring as a central core substituted with different aromatic compounds and three rod-like armed of 2-chloro-4,6-bis(dodecyloxy)-1,3,5-triazine, using 2,4,6-trichloro-1,3,5-triazine and 1,3,5-trichlorobenzene in the presence of palladium catalyst through the cross-coupling was efficiently synthesized. The structures were investigated by differential scanning calorimetry (DSC) and confirmed by the spectroscopic analyses (¹³C-NMR, ¹H-NMR, and MS). The compounds were evaluated for their liquid crystal's behaviors. The results from the DSC suggested that liquid crystals behaviors of both organic salt at low temperatures are due to the ionic interaction with the complementary of 4-dodecyloxybenzoic acid, which already possessed a liquid crystal at low temperatures.

■ ACKNOWLEDGMENTS

■ REFERENCES

[1] He, X.H., Han, L., Meng, F.B., Tian, M., and Zhang, B.Y., 2012, The effect of different arms on the properties of chiral branched-arm liquid crystals based on isosorbide as the chiral core, *Liq. Cryst.*, 39 (6), 779–787.

[2] Wang, X., Bai, L., Kong, S., Song, Y., and Meng, F., 2019, Star-shaped supramolecular ionic liquid crystals based on pyridinium salts, *Liq. Cryst.*, 46 (4), 512–522.

[3] Novotná, V., Bobrovsky, A., Shibaev, V., Pociecha, D., Kašpar, M., and Hamplová, V., 2016, Synthesis, phase behavior and photo-optical properties of bent-core methacrylate with azobenzene group and

corresponding side-chain polymethacrylate, *RSC Adv.*, 6 (70), 65747–65755.

[4] He, W.L., Huang, Q., Yang, Z., Cao, H., Wang, D., and Yang, H., 2015, Effect of bent-shape and calamitic-shape of hydrogen-bonded mesogens on the liquid crystalline properties, *Liq. Cryst.*, 42 (8), 1191–1200.

[5] Doganci, E., and Davarci, D., 2019, Synthesized and mesomorphic properties of cholesterol end-capped poly (ε-caprolactone) polymers, *J. Polym. Res.*, 26 (7), 165.

[6] Zhang, B.Y., Yao, D.S., Meng, F.B., and Li, Y.H., 2005, Structure and properties of novel three-armed star-shaped liquid crystals, *J. Mol. Struct.*, 741 (1-3), 135–140.

[7] Judele, R., Laschat, S., Baro, A., and Nimtz, M., 2006, Gallic esters of 4,5-dinitrocatechol as potential building blocks for thermotropic liquid crystals, *Tetrahedron*, 62 (41), 9681–9687.

[8] Salisu, A.A., 2016, Synthesis and characterization of three-arm star-shaped glassy liquid crystal containing biphenyl esters, *ChemSearch J.*, 7 (1), 37–42.

[9] Caminade, A.M., and Majoral, J.P., 2018, Engineering CNDP's of dendrimers containing phosphorous interior compositions to produce new emerging properties, *J. Nanopart. Res.*, 20 (3), 74.

[10] Imrie, C.T., Henderson, P.A., and Yeap, G.Y., 2009, Liquid crystal oligomers: going beyond dimers, *Liq. Cryst.*, 36 (6-7), 755–777.

[11] Iftime, M.M., Cozan, V., Airinei, A., Varganici, C., Ailiesei, G., Timpu, D., and Sava, I., 2019, Asymmetric azomethine amines with azobenzene moieties–liquid crystalline and optical properties, *Liq. Cryst.*, 46 (10), 1584–1594.

[12] Osman, F., Yeap, G.Y., Maeta, N., Ito, M.M., Lin, C.M., and Lin, H.C., 2017, Liquid crystalline non-linear S-shaped oligomers consisting of azobenzene and biphenylene units: Synthesis, characterisation and influence of central spacer, *Liq. Cryst.*, 44 (14-15), 2355–2365.

[13] Wang, Y.J., Sheu, H.S., and Lai, C.K., 2007, New star-shaped triarylamines: Synthesis, mesomorphic behaviour, and photophysical properties, *Tetrahedron*, 63 (7), 1695–1705.

[14] Bao, R., Pan, M., Qiu, J.J., and Liu, C.M., 2010, Synthesis and characterization of six-arm star-shaped liquid crystalline cyclotriphosphazenes, *Chin. Chem. Lett.*, 21 (6), 682–685.

[15] Ge, L.N., Xian, S.W., Huang, Y., Min, Y., Lv, J.M., Tian, M., and Yao, D.S., 2018, Synthesis and mesomorphism of novel multi-arm liquid crystals with cholic acid as chiral center linking Schiff base moieties as mesogens, *Liq. Cryst.*, 45 (7), 1055–1067.

[16] Barberá, J., Bardají, M., Jiménez, J., Laguna, A., Martínez, M.P., Oriol, L., Serrano, J.L., and, and Zaragozano, I., 2005, Columnar mesomorphic organizations in cyclotriphosphazenes, *J. Am. Chem. Soc.*, 127 (25), 8994–9002.

[17] Kanibolotsky, A.L., Perepichka, I.F., and Skabara, P.J., 2010, Star-shaped π-conjugated oligomers and their applications in organic electronics and photonics, *Chem. Soc. Rev.*, 39 (7), 2695–2728.

[18] Tuzimoto, P., Santos, D.M.P.O., Moreira, T.S., Cristiano, R., Bechtold, I.H., and Gallardo, H., 2014, Luminescent liquid crystals containing a sulphur-based heterocyclic core, *Liq. Cryst.*, 41 (8), 1097–1108.

[19] Gallardo, H., and Westphal, E., 2015, Importance of organic synthesis in the development of liquid crystals, *Curr. Org. Synth.*, 12 (6), 806–821.

[20] Sarhan, A.A.O., and Izumi, T., 2003, Design and synthesis of new functional compounds related to ferrocene bearing heterocyclic moieties: A new approach towards electron donor organic materials, *J. Organomet. Chem.*, 675 (1-2), 1–12.

[21] Salisu, A.A., and Kogo, A.A., 2010, New Liquid crystals in the series of 1,3,5-triazine compounds containing azobenzene at the peripheral arms, *Bayero J. Pure Appl. Sci.*, 3 (1), 54–58.

[22] Didehban, K., Namazi, H., and Entezami, A.A., 2009, Triazine-based dendrimers as liquid crystals: synthesis and characterization, *Iran. Polym. J.*, 18 (9), 731–741.

[23] Tan, L.S., Dalton, M., and Kannan, R., 2012, *Two-photon absorbing cross-linked polyurethanes*

containing delphenylamino-dialkyffluorene-1,3,5-triazine units, U.S. Patent 8,318,888.

[24] Bhagavath, P., Shetty, R., and Sunil, D., 2019, 1,3,5-Triazine-based liquid crystals: An up-to-date appraisal of their synthetic design and mesogenic properties, *Crit. Rev. Solid State Mater. Sci.*, 1–32.

[25] Meier, H., Holst, H.C., and Oehlhof, A., 2003, Star-shaped compounds having 1,3,5-triazine cores, *Eur. J. Org. Chem.*, 2003 (21), 4173–4180.

[26] Lee, C.H., and Yamamoto, T., 2002, Synthesis of liquid-crystalline, highly luminescent π-conjugated 1,3,5-triazine derivatives by palladium-catalyzed cross-coupling reaction, *Mol. Cryst. Liq. Cryst.*, 378 (1), 13–21.

[27] Beltrán, E., Serrano, J.L., Sierra, T., and Giménez, R., 2012, Functional star-shaped tris(triazolyl)triazines: Columnar liquid crystal, fluorescent, solvatofluorochromic and electrochemical properties, *J. Mater. Chem.*, 22 (16), 7797–7805.

[28] Sundaram, S., Subhasri, P., Rajasekaran, T.R., Jayaprakasam, R., Senthil, T.S., and Vijayakumar, V.N., 2017, Observation of induced new smectic phase in supramolecular hydrogen bonded liquid crystals between mesogenic and non-mesogenic aliphatic compounds, *Ferroelectrics*, 510 (1), 103–120.

[29] Ambrožič, G., and Zigon, M., 2005, Hydrogen bonded liquid-crystalline polyurethane complexes with 4-dodecyloxybenzoic acid, *Acta Chim. Slov.*, 52, 207–214.

[30] Nishihara, Y., Ikegashira, K., Hirabayashi, K., Ando, J., Mori, A., and, Hiyama, T., 2000, Coupling reactions of alkynylsilanes mediated by a Cu(I) salt: Novel syntheses of conjugate diynes and disubstituted ethynes, *J. Org. Chem.*, 65 (6), 1780–1787.

[31] Kumar, C.R.S., Jha, A., and Sastry, S.S., 2010, Induced crystal G phase of liquid crystalline amide through inter molecular hydrogen bonding, *J. Non-Cryst. Solids*, 356 (6-8), 334–339.

[32] Sıdır, Y.G., Sıdır, İ., and Demiray, F., 2017, Dipole moment and solvatochromism of benzoic acid liquid crystals: Tuning the dipole moment and molecular orbital energies by substituted Au under external electric field, *J. Mol. Struct.*, 1137, 440–452.

[33] Stackhouse, P.J., Wilson, A., Lacey, D., and Hird, M., 2010, Synthesis and properties of novel columnar liquid crystals based on symmetrical and non-symmetrical 1,3,5-trisubstituted benzene derivatives, *Liq. Cryst.*, 37 (9), 1191–1203.

[34] Akkurt, N., Al-Jumaili, M.H.A., Eran, B.B., Ocak, H., and Torun, L., 2019, Acetylene-bridged triazine π-conjugated structures: synthesis and liquid crystalline properties, *Turk. J. Chem.*, 43, 1436–1444.

[35] Yang, R., Ding, L., Chen, W., Zhang, X., and Li, J., 2019, Molecular-weight dependence of phase structure and viscosity in a liquid crystalline polyester with strong π–π interaction, *Liq. Cryst.*, 46 (3), 422-429.

Evaluation of Total Flavonoid, Total Phenolic Contents, and Antioxidant Activity of Strychnobiflavone

Sana Ullah and Chang-Gu Hyun[*]

Department of Chemistry and Cosmetics, Jeju National University, Jeju 63243, South Korea

[*] Corresponding author:

email: cghyun@jejunu.ac.kr

Abstract: *This work evaluates the antioxidant activity of strychnobiflavone due to the increasing demand of the antioxidant agents day by day. Various in vitro antioxidants assays such as 2,2-diphenyl-1-picrylhydrazyl (DPPH) and 2,2'-azino-bis(3-ethylbenzothiazoline-6-sulfonic acid) (ABTS) were used to investigate the antioxidant activity of strychnobiflavone. The results of both DPPH and ABTS show that strychnobiflavone increase the scavenging activity in a concentration-dependent manner due to the phenolic and flavonoid contents. This study revealed that strychnobiflavone is one of the promising and an effective compound for the antioxidant agent.*

Keywords: *antioxidant activity; total flavonoid; strychnobiflavone*

■ INTRODUCTION

The quality of drugs and their impact on human health is regarded as one of the most attractive research interests [1]. For thousands of years, mankind is using plant sources to either alleviate or cure illnesses [2]. Most of the developing countries are investigating and struggling to enhance the quality of their foods. For this purpose, people use different compounds and herbal drugs in their everyday foods as prevention from any diseases [3-5]. Approximately 5–7% of inhaled oxygen, or even more, is converted into reactive oxygen species (ROS) such as O^{2-}, H_2O_2 and •HO [6-7]. These reactive oxygen species are the side products of mitochondrial complex reaction, which can cause Fenton reaction in the body and generally result in degradation of proteins, lipids peroxidation, and oxidation of DNA [8]. It causes many diseases such as cancer, diabetes, atherosclerosis and many chronic diseases [9-12].

Antioxidants are defined as a free radical scavenger that protects us from various diseases like ischemia, anemia, asthma, Parkinson's diseases, inflammation, to name a few [13-14]. They can be used to quench the free radicals in our bodies. Antioxidant compounds in food play an important role as a health-protecting factor. The primary source of natural antioxidants is whole grains, fruits, and vegetables. There are also some known compounds like vitamin C, carotenes, polyphenols, and flavonoids used as antioxidants [15-19].

Many studies are investigating different kinds of fruits, vegetables, and plant extracts as an antioxidant for reducing the risk of the diseases caused by free radicals [20-22]. Strychnobiflavone was previously used as an anti-leishmanial and anti-aging [23-24]. The structure of strychnobiflavone contains phenolic and flavonoid functional groups. Phenols and flavonoids are recently demonstrated as good antioxidants [25-27]. In this paper, the antioxidant activity of Strychnobiflavone hydroethanolic (SHE) was evaluated and compared to vitamin C (ascorbic acid) as one of the most commonly used antioxidants.

■ EXPERIMENTAL SECTION

Materials

Strychnobiflavone (purchased from Sigma-Aldrich), ethanol, water, quercetin, DPPH, ABTS, Folin-Ciocalteau's reagent, gallic acid, potassium persulfate, sodium carbonate, ascorbic acid.

Procedure

Determination of total phenolic contents

The total phenolic contents of SHE was evaluated

using the Folin-Ciocalteau's reagent as a previously described method [28] with slight modification. The sample was mixed with Folin-Ciocalteau's reagent (100 µL) and distilled water (900 µL) and kept for 3 min. Sodium carbonate (200 µL, 15%) was then added. The volume was adjusted to 3 mL with distilled water. The absorbance was measured at 700 nm using 96 well plates. A standard curve was prepared using gallic acid with a concentration range from 150 to 1000 µg/mL.

Determination of total flavonoid contents

The flavonoid contents were determined as previously described [29] with slight modification. One milliliter of 2% aluminium chloride in ethanol was mixed with 1 mL of SHE with various concentrations (62.5 µg/mL to 1 mg/mL). The absorbance was measured at 415 nm after kept for 15 min. The total flavonoid contents were determined using a standard curve of quercetin (0 to 256 µg/mL).

DPPH radical scavenging activity assay

The free radical scavenging activity of SHE was determined using 2,2-diphenyl-1-picrylhydrazyl free radical. Samples with various concentration (ranging from 200 µg/mL to 1 mg/mL) were treated against 0.2 mM DPPH radical using 96 well plates. Ascorbic acid was used as a positive control with the range of concentration of 16 µg/mL to 1 mg/mL. The absorbance was measured at 517 nm.

ABTS radical scavenging activity assay

A mixture of 7 mM ABTS and 2.45 mM potassium persulfate was prepared. It was then mixed in distilled water with a ratio of 1:1 and kept in the dark for 16 h at 4 °C. The sample was diluted in ethanol at the ratio of 1:30, and the absorbance is fixed to 0.7–0.8. With 96 well plates, 20 µL of SHE and 180 µL of ABTS solutions were added to each well. Ascorbic acid was used as a positive control. The absorbance was measured at 700 nm.

■ RESULTS AND DISCUSSION

Total Phenolic Contents

The total phenolic contents in strychnobiflavone were determined using the spectrophotometric method. The standard curve was obtained from different concentrations of gallic acid. The standard curve of gallic acid was compared to the SHE sample. As indicated in Table 1, the gallic acid equivalency (GAE) increases with the increase in the concentration of SHE. It indicated that SHE has a phenolic functional group in its structure, which beneficial for scavenging and stabilizing free radicals. At the concentration of 62.5 µg/mL, the GAE is 29.77. It reaches 126.106 at 1000 µg/mL. It shows that the GAE value increases with the increase in concentration; hence, it is concentration-dependent.

Total Flavonoid Contents

The total flavonoid contents of SHE is also determined using spectrophotometric method. The total flavonoid contents were estimated by the standard curve of quercetin in Fig. 2. From Table 2, the quercetin equivalency (QE) increases with the increase in SHE concentration. At a concentration of 1000 µg/mL, the QE value is 269.32, almost twice larger than that of 125 µg/mL. Therefore, the flavonoid contents increase in a dose-dependent manner. SHE has more flavonoid contents than phenolic contents (Table 1).

Table 1. Gallic acid equivalent (GAE) of the total phenolic contents in strychnobiflavone

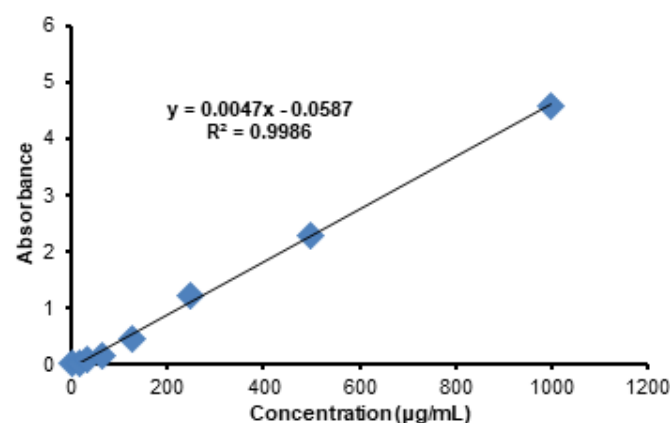| Concentration (µg/mL)	Absorbance of SHE	Gallic acid equivalent (mg)
62.5	0.08122	29.770213
125	0.1214	38.3191489
250	0.2103	57.234043
500	0.3123	78.9361702
1000	0.5340	126.106383

$y = 0.0047x - 0.0587$
$R^2 = 0.9986$

Fig 1. Standard curve of gallic acid

Table 2. Quercetin equivalent (QE) of the total flavonoid contents in strychnobiflavone

| Concentration (µg/mL)	Absorbance of SHE	Quercetin equivalent (mg)
62.5	0.0657	132.3548
125	0.1329	154.0323
250	0.2203	182.2258
500	0.3002	208
1000	0.4903	269.3226

Result for DPPH Assay

The antioxidant activity of SHE was determined from the scavenging activity of stable 1,1-diphenyl-2-picrylhydrazyle radical, as shown in Fig. 3. Ascorbic acid (Vit. C) is used as a positive control. The scavenging activity of SHE increases in dose-dependent manners. The SHE has the phenolic and flavonoid content to scavenge the free radical of DPPH. Therefore the more concentration of SHE, the higher scavenging activity will be obtained. Even though SHE shows less activity than the ascorbic acid, it can be considered as one of the promising candidates for stabilizing the toxic radical.

Result for ABTS Assay

The scavenging activity of SHE against ABTS radicals was investigated at various concentrations.

$y = 0.0031x + 0.3446$
$R^2 = 0.8794$
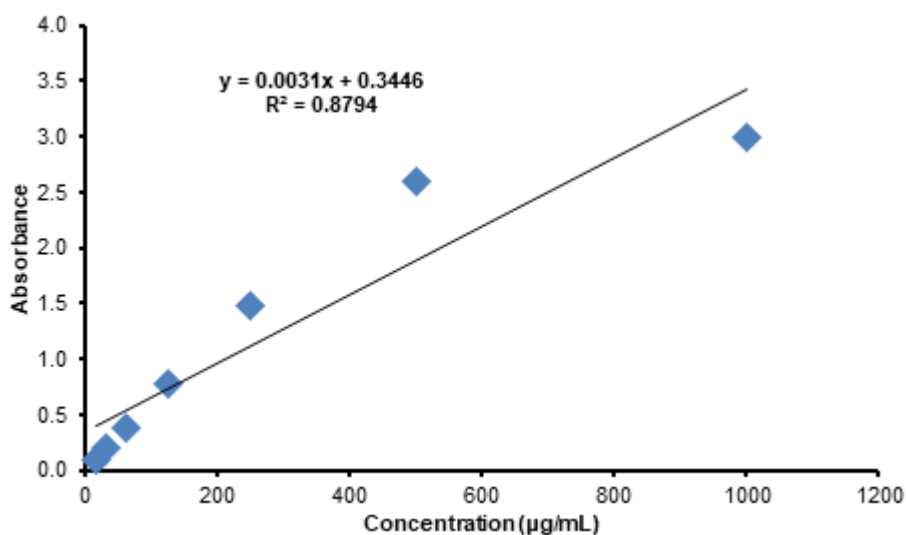
Fig 2. Standard curve of quercetin
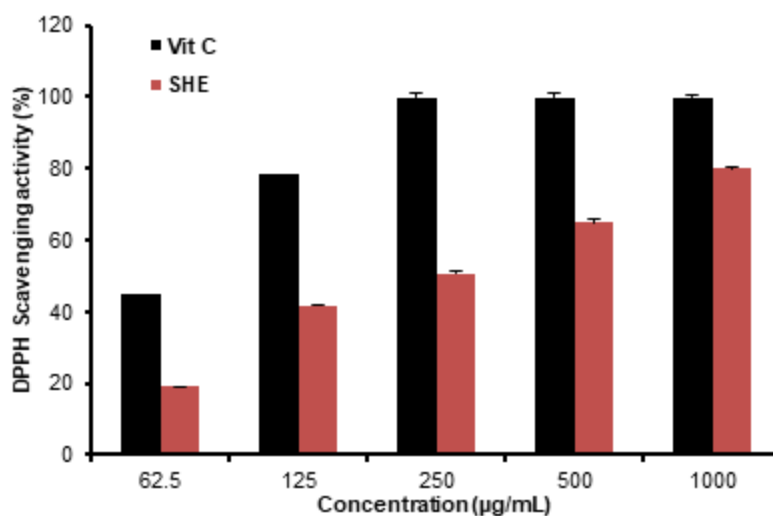
Fig 3. Scavenging activity of SHE against DPPH free radicals at various concentrations. Ascorbic acid was used as a positive control. The SHE scavenge the DPPH radical in a dose-dependent manner
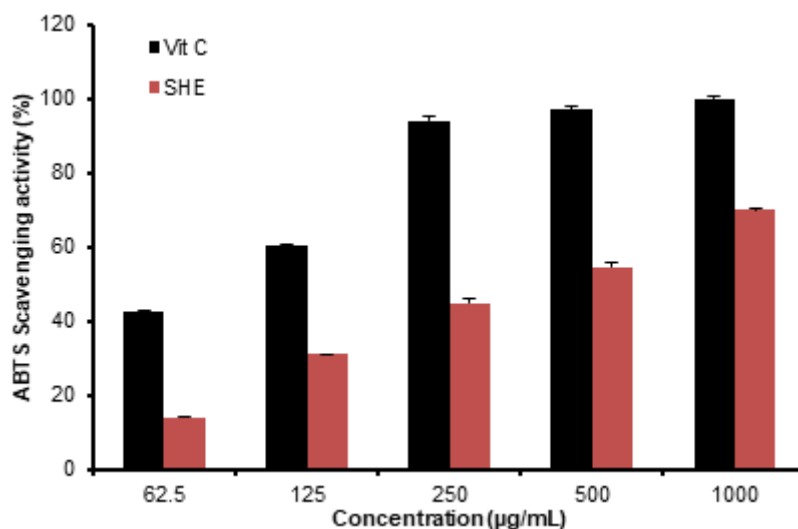
Fig 4. Scavenging activity of SHE against ABTS radicals at various concentrations. Ascorbic acid was used as a positive control. SHE suppresses the free radical in a dose-dependent manner

Ascorbic acid was used as a positive control for comparison. ABTS radical cation was produced in a stable form using potassium persulfate. After a stable absorbance was obtained, the antioxidant SHE is added into the reaction medium, and the antioxidant activity was measured based on the decolorization phenomenon. The scavenging activity of the SHE increases with an increase in concentration. The scavenging activity of SHE showed a slightly higher percentage in DPPH assay (Fig. 4) compared to the ABTS assay. This is because DPPH is soluble in the hydroethanolic system while ABTS is in aqueous. Most organic compounds are less soluble in aqueous media; thus, DPPH is more convenient to be scavenged.

This study confirms the presence of phenolic and flavonoid contents in SHE. The results indicate that the value of total flavonoid is higher than that of total phenolic contents. The SHE shows antioxidant activity on the DPPH and ABTS assays. The scavenging of a stable free-radical molecule like DPPH or ABTS determines the antioxidant capacity of strychnobiflavone. The performance of SHE against DPPH and ABTS radical was compared with the well-known strong antioxidant ascorbic acid. Hence, this work revealed that SHE can be considered as one of the good candidates for an antioxidant that suppresses the free radicals generated by UV radiation.

■ CONCLUSION

The strychnobiflavone hydroethanolic soluble compound was first investigated in term of the phenolic and flavonoid contents. The results showed that SHE has total phenolic contents as well as flavonoid contents which are known for the scavenging of free radicals. We also found that SHE has more flavonoid contents than the phenolic one. Furthermore, the DPPH and ABTS assays were performed to evaluate the antioxidant scavenging activity. Both DPPH and ABTS results confirm the antioxidant activity of SHE for the scavenging of the toxic free radicals.

■ REFERENCES

[1] Mandal, M., Misra, D., Ghosh, N.N., and Mandal, V., 2017, Physicochemical and elemental studies of *Hydrocotyle javanica* Thunb. for standardization as herbal drug, *Asian Pac. J. Trop. Biomed.*, 7 (11), 979–986.

[2] Qi, Z., 2015, WHO Traditional medicine strategy 2014-2023, *Global Health History Seminar on Traditional Medicine and Ayurveda*, 19 March 2015,WHO-HQ, Geneva.

[3] Tilburt, J.C., and Kaptchuk, T.J., 2008, Herbal medicine research and global health: An ethical analysis, *Bull. World Health Organ.*, 86 (8), 594–599.

[4] Kamboj, A., 2012, "Analytical evaluation of herbal drugs" in *Drug Discovery Research in Pharmacognosy*, Eds. Vallisuta, O., and Olimat, S.M., IntechOpen, Rijeka, Croatia, 23–60.

[5] Gupta, V.K., Kumria, R., Garg, M., and Gupta, M., 2010, Recent updates on free radicals scavenging flavonoids: An overview, *Asian J. Plant Sci.*, 9 (3), 108–117.

[6] Roy, P., Abdulsalam, F.I., Pandey, D.K., Bhattacharjee, A., Eruvaram, N.R., and Malik, T., 2015, Evaluation of antioxidant, antibacterial, and antidiabetic potential of two traditional medicinal plants of India: *Swertia cordata* and *Swertia chirayita*, *Pharmacogn. Res.*, 7 (Suppl. 1), S57–S62.

[7] Tachakittirungrod, S., Okonogi, S., and Chowwanapoonpohn, S., 2007, Study on antioxidant activity of certain plants in Thailand: Mechanism of antioxidant action of guava leaf extract, *Food Chem.*, 103 (2), 381–388.

[8] Joseph, J., Cole, G., Head, E., and Ingram, D., 2009, Nutrition, brain aging, and neurodegeneration, *J. Neurosci.*, 29 (41), 12795–12801.

[9] Riley, P.A., 1994, Free radicals in biology: oxidative stress and the effects of ionizing radiation, *Int. J. Radiat. Biol.*, 65 (1), 27–33.

[10] Willcox, J.K., Ash, S.L., and Catignani, G.L., 2004, Antioxidants and prevention of chronic disease, *Crit. Rev. Food Sci. Nutr.*, 44 (4), 275–295.

[11] Wan, C., Yu, Y., Zhou, S., Liu, W., Tian, S., and Cao, S., 2011, Antioxidant activity and free radical-scavenging capacity of *Gynura divaricata* leaf extracts at different temperatures, *Pharmacogn. Mag.*, 7 (25), 40–45.

[12] Pisoschi, A.M., and Negulescu, G.P., 2011, Methods for total antioxidant activity determination: A review, *Biochem. Anal. Biochem.*, 1 (1), 106.

[13] Liyana-Pathirana, C.M., Shahidi, F., and Alasalvar, C., 2006, Antioxidant activity of cherry laurel fruit (*Laurocerasus officinalis* Roem.) and its concentrated juice, *Food Chem.*, 99 (1), 121–128.

[14] de Quirós, A.R.B., and Costa, H.S., 2006, Analysis of carotenoids in vegetable and plasma samples: A review, *J. Food Compos. Anal.*, 19 (2-3), 97–111.

[15] Gey, K.F., 1990, The antioxidant hypothesis of cardiovascular disease: Epidemiology and mechanisms, *Biochem. Soc. Trans.*, 18 (6), 1041–1045.

[16] Thompson, M., Williams, C.R., and Elliot, G.E.P., 1976, Stability of flavonoid complexes of copper(II) and flavonoid antioxidant activity, *Anal. Chim. Acta*, 85 (2), 375–381.

[17] Gey, K.F., Puska, P., Jordan, P., and Moser, U.K., 1991, Inverse correlation between plasma vitamin E and mortality from ischemic heart disease in cross-cultural epidemiology, *Am. J. Clin. Nutr.*, 53 (1), 326S–334S.

[18] Olmedilla, B., Granado, F., Gil-Martinez, E., Blanco, I., and Rojas-Hidalgo, E., 1997, Reference values for retinol, tocopherol, and main carotenoids in serum of control and insulin-dependent diabetic Spanish subjects, *Clin. Chem.*, 43 (6), 1066–1071.

[19] Weisburger, J.H., 1999, Mechanisms of action of antioxidants as exemplified in vegetables, tomatoes and tea, *Food Chem. Toxicol.*, 37 (9-10), 943–948.

[20] Gillman, M.W., Cupples, L.A., Gagnon, D., Posner, B.M., Ellison, R.C., Castelli, W.P., and Wolf, P.A., 1995, Protective effect of fruits and vegetables on development of stroke in men, *JAMA*, 273 (14), 1113–1117.

[21] Rimm, E.B., Ascherio, A., Giovannucci, E., Spiegelman, D., Stampfer, M.J., and Willett, W.C., 1996, Vegetable, fruit, and cereal fiber intake and risk of coronary heart disease among men, *JAMA*, 275 (6), 447–451.

[22] Cohen, J.H., Kristal, A.R., and Stanford, J.L., 2000, Fruit and vegetable intakes and prostate cancer risk, *J. Natl. Cancer Inst.*, 92 (1), 61–68.

[23] Lage, P.S., Chávez-Fumagalli, M.A., Mesquita, J.T., Mata, L.M., Fernandes, S.O.A., Cardoso, V.N., Soto, M., Tavares, C.A.P., Leite, J.P.V., Tempone, A.G., and Coelho, E.A.F., 2015, Antileishmanial activity and evaluation of the mechanism of action of strychnobiflavone flavonoid isolated from *Strychnos pseudoquina* against *Leishmania infantum*, *Parasitol. Res.*, 114 (12), 4625–4635.

[24] Travasarou, A., Angelopoulou, M.T., Vougogiannopoulou, K., Papadopoulou, A., Aligiannis, N., Cantrell, C.L., Kletsas, D., Fokialakis, N., and Pratsinis, H., 2019, Bioactive metabolites of the stem bark of *Strychnos aff. darienensis* and evaluation of their antioxidant and UV protection activity in human skin cell cultures, *Cosmetics*, 6 (1), 7.

[25] Xiao, L., Takada, H., Maeda, K., Haramoto, M., and Miwa, N., 2005, Antioxidant effects of water-soluble fullerene derivatives against ultraviolet ray or peroxylipid through their action of scavenging the reactive oxygen species in human skin keratinocytes,

Biomed. Pharmacother., 59 (7), 351–358.

[26] Mu'nisa, A., Hala, Y., and Muflihunna, A., 2007, Analysis of phenols and antioxidants infused sappan wood (*Caesalpiniasappan* L.), *IJSDR*, 2 (9), 89–93.

[27] Martins, N., Barros, L., and Ferreira, I.C.F.R., 2016, *In vivo* antioxidant activity of phenolic compounds: Facts and gaps, *Trends Food Sci. Technol.*, 48, 1–12.

[28] Panche, A.N., Diwan, A.D., and Chandra, S.R., 2016, Flavonoids: An overview, *J. Nutr. Sci.*, 5, e47.

[29] Harman, D., 1962, Role of free radicals in mutation, cancer, aging, and the maintenance of life, *Radiat. Res.,* 16 (5), 753–763.

NOTE:

Antibacterial and Antioxidant Activities of Polyeugenol with High Molecular Weight

Erwin Abdul Rahim[*]**, Nur Istiqomah, Gilang Almilda, Ahmad Ridhay, Ni Ketut Sumarni, and Indriani**

Department of Chemistry, Tadulako University, Jl. Sukarno-Hatta Km 9, Palu 94148, Central Sulawesi, Indonesia

* *Corresponding author:*

email: erwin_abdulrahim@yahoo.com

Abstract: *This study was aimed to prepare polyeugenol with high molecular weight and to evaluate its antibacterial and antioxidant activities. First, polyeugenol was synthesized from eugenol in the presence of H_2SO_4-CH_3COOH (4:1) as catalyst. The synthesized polyeugenol was weighed by using viscometer, revealing its high molecular weight of $(7.76–21.9) \times 10^5$ g/mol. Furthermore, the antibacterial activity of the polyeugenol was conducted against* Staphylococcus aureus *and* Escherichia coli *bacteria. It was conducted by applying well diffusion method at 1, 2, 3, 4 and 5% concentrations to observe inhibition zones, in which the tests showed that the antibacterial activity of the polyeugenol against* S. aureus *were 17.42, 17.76, 18.79, 21.42 and 22.55 mm, while those against* E. coli *were 15.87, 17.23, 17.56, 18.24 and 19.21 mm, respectively. In short, these results indicated a strong antibacterial activity. Then, tests on antioxidant activity against free radical DPPH (2,2-diphenyl-1-pycrylhydrazyl) gave the IC_{50} value of 80.47 μg/mL, indicating a strong antioxidant activity. Therefore, the polymer synthesized in this work has a high potential to be applied in various biomedical applications.*

Keywords: *polyeugenol; high molecular weight; antibacterial activity; antioxidant activity*

■ INTRODUCTION

Eugenol is the major component in clove oil (*Syzygium aromaticum*), reaching 70–96% of oil content. Eugenol ($C_{10}H_{12}O_2$) contains several functional groups, including allyl (-CH_2-CH=CH_2), phenol (-OH) and methoxy (-OCH_3). These functional groups allow eugenol to act as the base material for the synthesis of more valuable compounds, including polyacetylene containing eugenol moiety [1-4], epoxy resin with extremely high biomass content from eugenol [5], bio-renewable thermosetting copolymer based on eugenol [6], renewable eugenol-based polymeric oil-absorbent microspheres [7], and UV-cured thiol-ene eugenol/ZnO composite [8].

In fact, eugenol compound and its various derivative compounds have been recognized to have strategic roles in various industries such as pharmaceutical, cosmetics, food and beverage, cigarette, vegetable, fishery, mining, active packaging and other chemical industries [9]. Practically, eugenol can be further processed into a variety of more useful products, including polyeugenol. Besides isoeugenol, polyeugenol is a result of further derivatization

of eugenol. In the literature, various researches have successfully developed techniques and methods to create polymers that suit certain purposes such as having antibacterial and antioxidant properties. Those advances have made the polymer industry to undergo rapid developments [10].

In a recent study, Prasetya et al. [11] had synthesized polyeugenol with low molecular weight. The polymer, however, showed low antibacterial activity towards *Staphylococcus aureus* and *Escherichia coli*. Therefore, the purpose of this study was to synthesize polyeugenol with high molecular weight and to improve the antibacterial and antioxidant activities compared to eugenol. Practically, this work would result in creating a polymer from eugenol with considerably good antibacterial and antioxidant properties.

■ EXPERIMENTAL SECTION

Materials

This study used various materials for the experiments, including eugenol (99.99% purity; obtained

from Happy Green Co.), H_2SO_4, CH_3COOH glacial, silica gel, distilled water, ethanol (98%), Whatman filter paper no. 1, 1,1-diphenyl-2-pycrylhydrazyl (DPPH), *S. aureus* and *E. Coli* bacteria (Obtained from Health Laboratory, Palu, Central Sulawesi), dimethyl sulfoxide (DMSO), *n*-hexane, petroleum ether (technical grade), nutrient agar (NA), Chloramphenicol, aluminum foils and plastic wraps.

Instrumentation

In terms of equipment and instruments, this research used measuring cups (250 mL, 50 mL, 25 mL), magnetic stirrer/mixer, spray bottle, dropper drip, pipettes (5 mL, 1 mL), petri dishes, aluminum foil, hot plate, analytical balance, dry cloth, spatulas, test tubes, micropipettes, tube racks, instruments for UV-VIS analysis, autoclave, incubator, rotary vacuum evaporator, Ostwald viscometer (U-tube), stopwatch, skates, Bunsen burner, needles and other glass-based tools commonly used in the laboratory.

Procedure

Polymerization of eugenol [12]

As much as 10 g of eugenol was placed into a 250 mL measuring cup. Next, 2.5 mL of catalyst (H_2SO_4-CH_3COOH; 4 mol H_2SO_4:1 mol CH_3COOH ratio) was gradually added into the cup while being continuously mixed (room temperature, 5 min) by using a magnetic stirrer. Polymer formation was indicated by the release of concentrated white smoke and the appearance of formed polymer. To stop the polymerization, methanol (1 mL) was added to the cup. After that, the polymer was settled at room temperature for 24 h and was then identified. Next, as much as 2 g of polyeugenol was decentered in a 250 mL Erlenmeyer. An amount of 40 mL of diethyl ether was later added to the bottle. The bottle was sealed with a plug to then be shaken until the polyeugenol was completely dissolved. After that, the dissolved polyeugenol was divided into two 250 mL cups. For each cup, a toe of 100 mL was added, then each cup was shaken and kept for one night. In the following day, the bottom and upper layers was segregated, in which the upper part had its restored form. Then, they were washed 3 times. Practically, the top layer would be soluble in ether but not soluble in water. To ensure no water residual in the polyeugenol, 1 g of anhydrous Na_2SO_4

was added and filtered. Then, the filtrate was placed in a petri dish and kept for 48 h at room temperature.

Determination of molecular weight of polyeugenol

Polyeugenol was dissolved in ethanol to a concentration of 0.02 g/mL in a 50 mL flask. After that, the polymer was divided into five, and each of them was diluted with ethanol to the following concentrations: 0.01500; 0.01000; 0.00500; 0.00250 and 0.00125 g/mL. Next, the percentage of pure ethanol solvent was measured in Ostwald viscometer to discover the concentration of the polymer solution, producing t_0, t_1, t_2, t_3, t_4, t_5, and t_6. Using the Poisseuille equation (ηsp/C) versus C was obtained. The curve was then extrapolated to zero concentration (C = 0) to obtain [η]. Using the Mark-Houwink equation (η = K.M^a), the molecular weight of the polymer was calculated by taking the corresponding K and a into account.

Antibacterial activity assay of polyeugenol using well diffusion method

This study applied a well diffusion method to test the inhibition zone of bacteria. First, 25 mL of nutrient agar (NA) medium was mixed with 25 µL suspension of test bacteria (*S. aureus* and *E. coli*). Next, it was homogenized and poured in sterilized petri dishes and left to get solidified. After that, ± 9 mm holes/wells were made by using a piercing device. Three holes were made to the first cup (i.e. first hole for polyeugenol with 1% concentration, second hole for polyeugenol 2%, third hole for polyeugenol 3%). Meanwhile, two holes/wells were made to the second plate (i.e. first hole for polyeugenol 4%, second hole for polyeugenol 5%). Then, two holes/wells were made to the third plate (i.e. first hole for negative control, second hole for positive control of chloramphenicol 250 µL/50 µL). The treatment was repeated three times, incubated for 24 h at 37 °C, and then observed to measure the diameter of the drag zone by using a sliding range. Three replicates were tested for each experiment.

Antioxidant activity assay of polyeugenol using DPPH method

25 mg of polyeugenol with high molecular weight was weighed and placed into a 25 mL measuring flask.

Next, ethanol was gradually added to reach 1000 ppm concentration to be used as a stock solution. Later, 10 mL of the stock solution was taken by using a volumetric flask, then filled into a 100 mL measuring flask. Ethanol was then added to the flask to obtain a solution with 100 ppm concentration. To investigate the antioxidant activity, 0.2 mL of each concentration was piped by using a micropipette as sample solutions and placed into a vial. Next, 3.8 mL of DPPH solution 50 μM was added into the vial. After that, the mixture was homogenized and kept in a dark room for 30 min. Then, the uptake was measured by a UV-VIS spectrophotometer at a 517 nm wavelength. Absorption at DPPH 50 μM was measured as a control. The antioxidant activity was expressed in terms of the percentage of inhibition and calculated by using Eq. (1).

$$I(\%) = \frac{\text{Control Absorbance} - \text{Sample Absorbance}}{\text{Control Absorbance}} \times 100\% \quad (1)$$

where: Control Absorbance = absorbance of DPPH 50 μM; Sample Absorbance = Absorbance of test sample

The IC_{50} value of each concentration was calculated by using the linear regression equation formula obtained from the relationship curve between the percentages of inhibition to the sample concentration.

■ **RESULTS AND DISCUSSION**

Synthesis of Polyeugenol

In general, cationic polymerization is limited to monomers with electron-donating substituents where double bond polarization makes them sensitive to electrophilic attacks by carbonyl [13]. According to Cowd [9], only monomers have electron-donating groups that can undergo cationic polymerization. The use of acetic acid as co-catalyst will be corresponding to high molecular weight polymer. Cationic olefins monomers polymerization occurs with olefins $CH_2=CHR$ containing electron-donating substituents, $R_2C=Z$ compounds with hetero Z groups or hetero atoms, and cyclic molecules with hetero atoms as a structural part of the ring [13].

Synthesis of polyeugenol was conducted in this study through the cationic polymerization reaction with H_2SO_4-CH_3COOH as the catalyst. During the polymerization process, the synthesis was observed by thickened white smoke, in which the resulting polymer

was attached to the beaker and the color became purplish black.

The purification step resulted in the formation of two layers. The bottom layer was water and the catalyst, while the top layer was the produced polyeugenol. Diethyl ether was used as a polyeugenol solvent because it was nonpolar and would not get mixed with water during the washing process. Fig. 1 shows the IR spectra of eugenol and polyeugenol. Results of the FTIR spectrum of polyeugenol showed a wide absorption at wavenumber 3448 cm^{-1}, indicating vibration of -OH groups. In the FTIR spectrum of eugenol, the -OH group was located at wavenumber 3518 cm^{-1}. Next, peaks at 2870–2931 cm^{-1} showed the vibration of Csp^3-H stretches. Meanwhile, the presence of a conjugated aromatic compound was shown by absorption bands at 1604 and 1512 cm^{-1}. Besides that, peaks at wavenumber 2839–2908 cm^{-1} within the IR spectrum of eugenol showed a Csp^3-H vibration, while the presence of an aromatic compound was indicated by absorption bands at 1604 and 1512 cm^{-1}. The C=C aromatic spectrum was observed at wavenumber of 1500–1600 cm^{-1}, while the stretching vibration of Csp^3-H was indicated by the absorption at 3000–2840 cm^{-1}. The presence of absorption bands within the IR spectrum of eugenol showed that the absorption at 1635 cm^{-1} was a characteristic of absorption band for the range C=C,
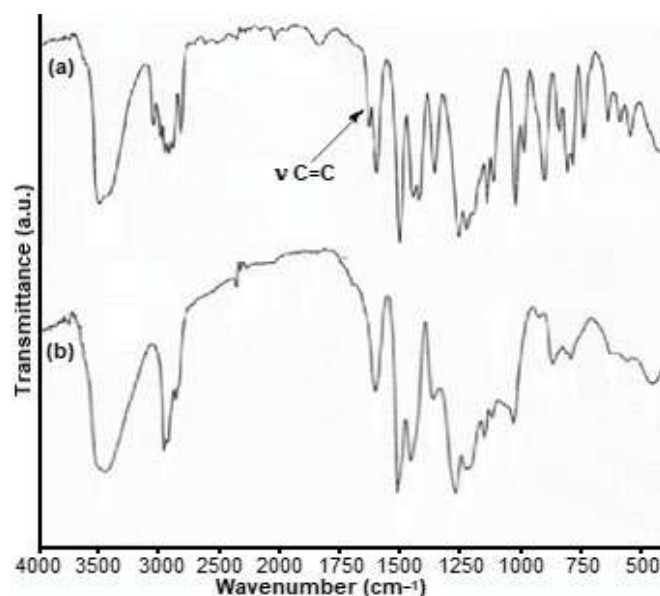

Fig 1. IR spectra of (a) eugenol and (b) polyeugenol

which was strengthened by absorption bands out of the field at 900–648 cm^{-1}. Then, peaks at 995 and 910 cm^{-1} showed unsaturated groups in the form of vinyl groups (-CH=CH$_2$-). Based on the explanation above, the compound contained ether (C-O-C-); -OH; methyl (-CH$_3$), methylene (-CH$_2$-) and vinyl groups.

Furthermore, peaks at wavenumber 1637 and 995 cm^{-1}, which was typical for the absorption for the vinyl group, appeared within the IR spectrum of eugenol, while it did not appear at the spectrum of polyeugenol. Hence, it indicated the formation of polyeugenol. Apparently, the purification, the IR spectrums and the ratio between eugenol and H$_2$SO$_4$ catalyst (4:1) are the same as the results of a previous work by Ngadiwiyana [14]. Fig. 2 illustrates the polymerization of eugenol with H$_2$SO$_4$-CH$_3$COOH catalyst. The polyeugenol was obtained in 88.28% yield together with an unknown compound (11.27% yield) which is soluble in water.

Determination of Molecular Weight of Polyeugenol

Based on the calculation on the molecular weight of polyeugenol, the resulting polymer was obtained as a solid form with (7.76–21.9) × 10^5 g/mol (n = 13.134 repeating unit) molecular weight, indicating that this study successfully produced polyeugenol with high molecular weight. The molecular weight of polyeugenol obtained in this study is higher than that obtained by Ngadiwiyana [14] which was 7.800 g/mol. In addition, the molecular weight after purification was, in fact, greater than that of Junaidi`s work [15], in which the weight of polyeugenol produced during an ether fraction was 5.140 g/mol.

Antibacterial Activity Test of Polyeugenol

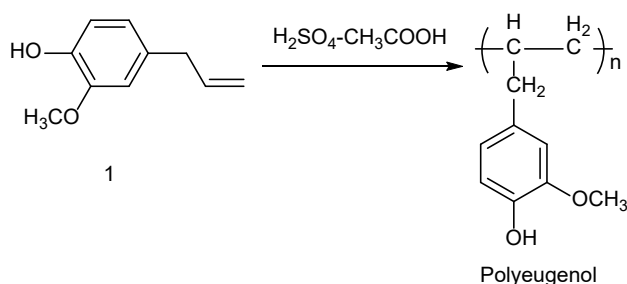This test applied dimethyl sulfoxide (DMSO) as a solvent with 1, 2, 3, 4 and 5% concentrations. DMSO was

Fig 2. Synthesis of polyeugenol

employed since it could dissolve almost all polar and non-polar compounds. Besides, DMSO would prevent the inhibition of bacterial growth, hence it would not be interfering with the result of observations on antibacterial activity. Looking at the test results (Table 1), the diameters of inhibition zones for the *S. aureus* and *E. coli* test bacteria increased in parallel with the increase in concentration. The results showed that the inhibition zones of polyeugenol tested against *S. aureus* were relatively higher than those tested against *E. coli*. *E. coli* is recognized as Gram-negative bacteria, while *S. aureus* is known as Gram-positive bacteria. Thus, polyeugenol with high molecular weight showed a stronger inhibitory power against Gram-positive bacteria compared to Gram-negative bacteria.

In general, the cationic bactericidal mechanism occurs due to the interactions and destructions of cell membrane structures. In Gram-positive bacteria, the cell membrane is covered by a cell wall, which is composed of 30–40 peptidoglycan layers [16]. Furthermore, there are the bound location of the positive charge of polyeugenol hydroxyl group, causing distortion and breakdown of the cell wall due to osmotic shock and cytoplasmic exudation of the content. In contrast, Gram-negative bacteria have an outer membrane layer (containing lipopolysaccharide and protein), one or two peptidoglycan (cell wall) and cell membranes (consisting of two layers of fat), transmembrane proteins and an inner membrane layer. Practically, the O-chain negative charge of lipopolysaccharide is bound to the positive charge of the polyeugenol's hydroxyl group, hence blocking the flow of nutrients in bacteria that ultimately leads to cell death due to the strong association between the O-chain and the outer membrane. In addition, the eugenol-free hydroxyl group can bind negative charge on the surface of bacterial cells, which will eventually perform antibacterial effects [17].

Table 1 and Fig. 3 shows antibacterial activities of polyeugenol at every concentration level and repetition. The inhibition zone appears to be larger in parallel to the increase of concentrations. The differences in inhibitory power of an antibacterial compound against Gram-positive and Gram-negative bacteria were particularly
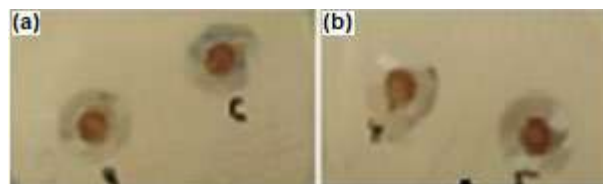
Table 1. Inhibition zones of polyeugenol

Bacterial	Repeated	Inhibition Zones (mm)							Eugenol [17]
		Concentration (%)					Control		
		1	2	3	4	5	(+)	(-)	
S. Aureus	Average	17.42	17.76	18.79	21.42	22.55	37.14	-	7.75
E. Coli	Average	15.87	17.23	17.56	18.24	19.21	44.40	-	9.25

caused by the structures of their cell walls. The cell wall of Gram-positive bacteria consists of several peptidoglycan layers, forming a thick and rigid structure and contains teichoic acid. Meanwhile, the cell wall of Gram-negative bacteria consists of one or more thin peptidoglycan layers, hence the cell wall is more susceptible to physical shocks, including antibiotics or other antibacterial agents. The difference in cell wall structure has caused both bacteria to respond to Gram staining [18].

The previous study conducted by Prasetya et al. [11] had prepared polyeugenol by applying cationic polymerization method with BF_3 catalyst and conducted the antibacterial test against *S. aureus* and *E. coli* bacteria. The work demonstrated that the activities against *S. aureus* and *E. coli* were lower than our study. Apparently, the results of this study (Table 1) differ from previous results, particularly on the non-existence of antibacterial activity in Gram-negative bacteria (*E. coli*). It was probably due to the differences in polyeugenol molecular weight (Mw) and the catalyst being used. The prior study showed that the antibacterial activity of eugenol could inhibit lower growth of pathogenic bacterial *E. coli,* and *S. aureus*. Yalpani et al. [18] had also reported that the degree of polymerization was directly proportional to increased inhibitory activity. The spacer length or alkyl chain length refers to the length of the carbon chain that composes the polymer backbone. The chain length has been investigated to see if it affects the antimicrobial activity of the polymer. The results have generally shown that the longer alkyl chains have resulted in higher activity.

Some of the major chemical compounds that have antibacterial properties include phenols as well as phenolic compounds, alcohols, halogens, heavy metals, aldehydes and detergents [19]. In particular, the 3-(3,4-dimethoxyphenyl)-1-propanol unit in polyeugenol is alcohol primarily produced from the synthesis, making the

Fig 3. Inhibition zones of polyeugenol against (a) *S. aureus* and (b) *E. coli*

antibacterial mechanism to be similar to other alcohols. Looking at the study, polyeugenol with high molecular weight would have higher antibacterial activity than its previous forms as eugenol compound.

According to Davis and Stout [20], the antibacterial activity could be considered as strong when it produces inhibition area between 10–20 mm. Meanwhile, inhibition zone with 5–10 mm diameter was considered to have medium antibacterial activity, and less than 5 mm diameter was categorized as having a low antibacterial activity. Based on these classifications, the antibacterial inhibition of polyeugenol with high molecular weight against *S. aureus* test bacteria at 1, 2 and 3% concentrations were considered strong, while at 4 and 5% concentrations were considered very strong. On the other hand, the antibacterial inhibition against *E. coli* test bacteria at 1, 2, 3, 4 and 5% concentrations were considered strong. Thus, the best concentration for inhibiting bacteria was at 5% concentration. In other words, the higher the presence of polyeugenol in a medium, the higher the number of bacterial cell diffusions.

Antioxidant Activity Test using DPPH Method

The antioxidant activity of eugenol and polyeugenol compounds were performed by applying DPPH method with vitamin C as a control. In this study, the IC_{50} value of eugenol compound was found to be 128.59 µg/mL, while that of polyeugenol was 80.47 µg/mL. Then, the IC_{50} value of vitamin C was revealed to be 42.94 µg/mL (Table 2).

Table 2. Antioxidant activity of polyeugenol using DPPH method

Compounds	IC$_{50}$ (µg/mL)			Average of IC$_{50}$
	I	II	III	(µg/mL)
Eugenol	135.22	125.60	125.44	128.59
Polyeugenol	84.13	78.01	79.83	80.47
Vitamin C	43.72	42.25	42.81	42.94

In terms of relationships between the concentrations of extract to the percentage of inhibition, in short, the lower the concentration of a sample, the lower the value of inhibition to free radical activity. In other words, inhibition of free radicals would increase if the sample concentration increased. In terms of IC$_{50}$ values, they appeared to be inversely proportional to the antioxidant capability of a compound. The smaller the value of IC$_{50}$, the greater the antioxidant ability of a compound. In general, IC$_{50}$ value is stated as a value indicating the amount of sample concentration that can capture DPPH free radical by 50%. Therefore, this study discovered polyeugenol compound to have a considerably strong antioxidant activity.

In detail, the presence of phenolic compounds in polyeugenol would cause the compound to have good antioxidant activity. This occurs because the phenolic compound is known to have hydroxyl groups (OH). Practically, hydrogen atom of the phenolic group would be donated to a radical compound to get stabilized. Besides, this study had produced polyeugenol with high molecular weight, hence its antioxidant properties would surely be higher than eugenol. Increased antioxidant activity of the synthesized polyeugenol compound, in fact, was due to electronic and steric effects of the phenol ring, resulting in stability of free radical inhibition [19]. Therefore, the polyeugenol synthesized in this research offered great potentials as a source of antioxidants.

■ **CONCLUSION**

Polyeugenol with high molecular weight was synthesized by using H_2SO_4-CH_3COOH catalyst and was discovered to have antibacterial properties. Its highest inhibitory power was revealed at a 5% concentration with very strong inhibition diameter (22.55 mm) for *S. aureus* and strong inhibition diameter (19.21 mm) for *E. coli* bacteria. In terms of antioxidant activity, on the other hand, polyeugenol was discovered to demonstrate its antioxidant activity with a strong IC$_{50}$ value category (IC$_{50}$ = 80.47 µg/mL). Therefore, the polymer can be considered as being highly applicable for various biomedical applications.

■ **REFERENCES**

[1] Rahim, E.A., Sanda, F., and Masuda, T., 2004, Synthesis and properties of novel polyacetylene containing eugenol moieties, *J. Macromol. Sci. Part A Pure Appl. Chem.*, 41 (2), 133–141.

[2] Rahim, E.A., Sanda, F., and Masuda, T., 2004, Synthesis and properties of novel eugenol-based polymers, *Polym. Bull.*, 52 (2), 93–100.

[3] Rahim, E.A., 2018, Unique polymerization and new smart material of eugenol-based helical polymers, *Int. J. Sci. Res.*, 7 (11), 990–996.

[4] Rahim, E.A., Sanda, F., and Masuda, T., 2006, Synthesis and properties of optically active amino acid-based polyacetylenes bearing eugenol and fluorene moieties, *J. Polym. Sci., Part A: Polym. Chem.*, 44 (2), 810–819.

[5] Miao, J.T., Yuan, L., Guan, Q., Liang, G., and Gu, A., 2017, Biobased heat resistant epoxy resin with extremely high biomass content from 2,5-furandicarboxylic acid and eugenol, *ACS Sustainable Chem. Eng.*, 5 (8), 7003–7011.

[6] Liu, K., Madbouly, S.A., and Kessler, M.R., 2015, Biorenewable thermosetting copolymer based on soybean oil and eugenol, *Eur. Polym. J.*, 69, 16–28.

[7] Deng, J., Yang, B., Chen, C., and Liang, J., 2015, Renewable eugenol-based polymeric oil-absorbent

728

Indones. J. Chem., 2020, 20 (3), 722 - 728

microspheres: Preparation and oil absorption ability, *ACS Sustainable Chem. Eng.*, 3, 599–605.

[8] Modjinou, T., Tobias, H.R., Morales, G., Versache, D.L., Langlois, V., Grande, D., and Renard, E., 2016, UV-cured thiol-ene eugenol/ZnO composite materials with antibacterial properties, *RSC Adv.*, 6, 88135.

[9] Cowd, M.A., 1982, *Polymer Chemistry*, John Murray Publishers Ltd, London.

[10] Rojo, L., Barcenilla, J.M., Vázquez, B., Gonzáles, R., and Román, J.S., 2008, Intrinsically antibacterial material based on polymeric derivatives of eugenol for biomedical applications, *Biomacromolecules*, 9 (9), 2530–2535.

[11] Prasetya, N.B.A., Ngadiwiyana, Ismiyarto, and Sarjono, P.R., 2019, Synthesis and study of antibacterial activity of polyeugenol, *IOP Conf. Ser.: Mater. Sci. Eng.*, 509, 012101.

[12] Sitti, A.H., Erwin, A.R., and Musafira, 2018, Sintesis dan karakteristik polyeugenol dari eugenol menggunakan katalis $H_2SO_4 – CH_3COOH$, *Kovalen*, 4 (3), 285–296.

[13] Remmp, P., and Merril, E.W., 1991, *Polymer Synthesis*, Hutting and Wept, New York.

[14] Ngadiwiyana, 2005, Polimerisasi eugenol dengan katalis asam sulfat pekat, *JKSA*, 8 (2), 43–47.

[15] Djunaidi, M.C., Jumina, J., Siswanta, D., and Ulbricht, M., 2015, Synthesis of Fe ionic-imprinted polyeugenol using polyethylene glycol diglycidilether as cross-linking agent for sorption of Fe(III), *Indones. J. Chem.*, 15 (3), 305–314.

[16] Kittur, F.S., Kumar, A.B.V., Varadaraj, M.C., and Tharanathan, R.N., 2005, Chitooligosaccharides–Preparation with the aid of pectinase ribozyme from *Aspergillus niger* and their antibacterial activity, *Carbohydr. Res.*, 340 (6), 1239–1245.

[17] Rastina, Sudarwanto, M., and Wientarsih, I., 2015, Aktivitas antibakteri ekstrak etanol daun kari (*Murraya koenigii*) terhadap *Staphylococcus aureus*, *Escherichia coli*, dan *Pseudomonas* sp., *J. Ked. Hewan*, 9 (2), 185–188.

[18] Yalpani, M., Johnson, F., and Robinson, L.E., 1992, "Antimicrobial activity of some chitosan derivatives" in *Advances in Chitin and Chitosan*, Eds. Brine, C.J., Sandford, P.A., and Zikakis, J.P., Elsevier, London, 543–548.

[19] da Silva, F.F.M., Monte, F.J.Q., de Lemos, T.L.G., do Nascimento, P.G.G., de Medeiros Costa, A.K., and de Paiva, L.M.M., 2018, Eugenol derivatives: Synthesis, characterization, and evaluation of antibacterial and antioxidant activities, *Chem. Cent. J.*, 12, 34.

[20] Davis, W.W., and Stout, T.R., 1971, Disc plate method of microbiological antibiotic assay, *Appl. Microbiol.*, 22 (4), 659–666.